FOSSIL ENERGY

DOE/MC/26253-9
(DE93000126)

Scale-up of Miscible Flood Processes

Final Report

By
Franklin M. Orr, Jr.

February 1993

Performed Under Contract No. FG21-89MC26253

Stanford University
Stanford, California

Bartlesville Project Office
U. S. DEPARTMENT OF ENERGY
Bartlesville, Oklahoma

DISCLAIMER

This report was prepared as an account of work sponsored by an agency of the United States Government. Neither the United States Government nor any agency thereof, nor any of their employees, makes any warranty, express or implied, or assumes any legal liability or responsibility for the accuracy, completeness, or usefulness of any information, apparatus, product, or process disclosed, or represents that its use would not infringe privately owned rights. Reference herein to any specific commercial product, process, or service by trade name, trademark, manufacturer, or otherwise does not necessarily constitute or imply its endorsement, recommendation, or favoring by the United States Government or any agency thereof. The views and opinions of authors expressed herein do not necessarily state or reflect those of the United States Government or any agency thereof.

This report has been reproduced directly from the best available copy.

Available to DOE and DOE contractors from the Office of Scientific and Technical Information, P.O. Box 62, Oak Ridge, TN 37831; prices available from (615)576-8401, FTS 626-8401.

Available to the public from the National Technical Information Service, U.S. Department of Commerce, 5285 Port Royal Rd., Springfield, VA 22161.

DOE/MC/26253-9
Distribution Category UC-122

Scale-up of Miscible Flood Processes

Final Report

By
Franklin M. Orr, Jr.

February 1993

Work Performed Under Contract No. DE-FG21-89MC26253

Prepared for
U.S. Department of Energy
Assistant Secretary for Fossil Energy

Royal J. Watts, Project Manager
Morgantown Energy Technology Center
P. O. Box 880
Morgantown, WV 26505

Prepared by
Stanford University
Petroleum Engineering Department
Stanford, CA 94305-2220

Abstract

Results of a wide-ranging investigation of the scaling of the physical mechanisms of miscible floods are reported.

Advanced techniques for analysis of crude oils are considered in Chapter 2. Application of supercritical fluid chromatography is demonstrated for characterization of crude oils for equation-of-state calculations of phase equilibrium. Results of measurements of crude oil and phase compositions by gas chromatography and mass spectrometry are also reported. They demonstrate that the presence of significant quantities of multi-ring aromatic compounds in a crude oil can increase substantially the minimum miscibility pressure for CO_2 injection.

The theory of development of miscibility is considered in detail in Chapter 3. The theory is extended to four components, and sample solutions for a variety of gas injection systems are presented. The analytical theory shows that miscibility can develop even though standard tie-line extension criteria developed for ternary systems are not satisfied. In addition, the theory includes the first analytical solutions for condensing/vaporizing gas drives.

In Chapter 4, the interactions of viscous fingering and permeability heterogeneity are examined. Results of flow visualizations are reported for unstable displacements in synthetic heterogeneous porous media. In addition, predictions of a particle-tracking simulator for the same displacements are compared with the experimental observations. Both experiments and simulations show that even modest permeability heterogeneity can dominate the pattern of fingering in unstable displacements. Finally, a suite of unstable displacements in laboratory samples is interpreted with the particle-tracking simulator to examine the affects of changes in mobility ratio for displacements in which dispersion, heterogeneity, and viscous instability interact.

In Chapter 5, the combined effects of capillary and gravity-driven crossflow are considered. The experimental results presented show that very high recovery can be achieved by gravity segregation when interfacial tensions are moderately low. We argue that such crossflow mechanisms are important in multicontact miscible floods in heterogeneous reservoirs. In addition, results of flow visualization experiments are presented that illustrate the interplay of crossflow driven by gravity with that driven by viscous forces.

Contents

1 Introduction **1**

2 Phase Behavior **3**

2.1 Prediction of CO_2/Hydrocarbon Phase Behavior Using SFC 3

2.1.1 SFC Apparatus 4

2.1.2 CO_2/Hydrocarbon Binary Systems 6

2.1.3 Crude Oil Characterization 17

2.1.4 Solubility in Dense CO_2 30

2.1.5 Conclusions 35

2.2 Component Partitioning in CO_2/Crude Oil Mixtures 36

2.2.1 Experimental Apparatus and Procedures 36

2.2.2 Experimental Results 41

2.2.3 Numerical Modelling 65

2.2.4 Conclusions 77

2.3 Summary 77

3 Development of Miscibility in Four-Component Gas Drives **79**

3.1 Displacement of $CH_4/C_4/C_{10}$ Mixtures by CO_2 80

3.1.1 Mathematical Model 80

3.1.2 Solution Structure 82

3.1.3 Solution Construction 86

3.1.4 Determination of the Crossover Tie Line 88

3.1.5 Continuity 89

3.1.6 Minimum Miscibility Pressure 89

3.1.7 Sample Solutions 90

3.1.8 Discussion 95

3.1.9 Conclusions 97

3.2 Analytical Theory of Condensing/Vaporizing Gas Drives 98

3.2.1 Shocks 98

3.2.2 $CH_4/C_3/C_6/C_{16}$ Displacements 100
3.2.3 Solution Construction 101
3.2.4 Generalized Crossover Tie-Line Construction 101
3.2.5 Condensing/Vaporizing Mechanism 106
3.2.6 $CH_4/C_2/C_6/C_{16}$ Displacements 113
3.2.7 Discussion 116
3.2.8 Conclusions 116
3.3 Classification of Three- and Four-Component Displacements 117
3.3.1 K-Value Effect on Phase Behavior 117
3.3.2 Self-Sharpening Shocks vs. Expansion Waves 118
3.3.3 Classification of Three-Component Solutions 121
3.3.4 Classification of Four-Component Solutions 126
3.4 Effects of Volume Change on Mixing in Four-Component Gas Drives 132
3.4.1 Mathematical Model 133
3.4.2 Sharpening Behavior on Nontie-Line Paths 136
3.4.3 Displacement by Carbon Dioxide 141
3.4.4 Displacement by Nitrogen 142
3.4.5 Comparison of Theory and Experiment 146
3.4.6 Development of Miscibility 153
3.4.7 Conclusions 154
3.5 Summary 157

4 Modeling of Viscous Fingering 159
4.1 Experimental Investigation of Viscous Fingering in Heterogeneous Porous Media 159
4.1.1 Experimental Apparatus and Procedures 159
4.1.2 Estimation of Permeability 161
4.1.3 Viscous Fingering in Heterogeneous Porous Media 164
4.1.4 Discussion 193
4.1.5 Conclusions 194
4.2 Dispersion, Permeability Heterogeneity and Viscous Fingering: Acoustic Experimental Observations and Particle-tracking Simulations 194
4.2.1 Experimental Apparatus and Procedures 195
4.2.2 Particle-Tracking Simulations 197
4.2.3 Stable Displacements 201
4.2.4 Unstable Displacements 208
4.2.5 Conclusions 226
4.3 Summary 226

5 Crossflow: Effects of Gravity, Capillary and Viscous Forces in Heterogeneous Porous Media 228
5.1 Capillary Imbibition and Gravity Drainage in Low IFT Systems 228
5.1.1 Literature Review 229
5.1.2 Experimental Procedure 233
5.1.3 Results and Discussion 235
5.1.4 Drainage 240
5.1.5 Discussion 243

5.1.6 Conclusions 249
5.2 Visualization of Gravity Segregation, Capillary and Viscous Crossflow in Near-Miscible Displacement in a Two-Layered Model 249
5.2.1 Experimental Apparatus and Procedures 249
5.2.2 Experimental Results 252
5.2.3 Discussion 266
5.2.4 Conclusions 274
5.3 Summary 274

6 Summary **276**

List of Tables

2.1 Capacity factors for docosane at 131°F. 9
2.2 Calculated $\bar{V}_1^{\infty,s}$ for n-alkanes. 12
2.3 Calculated $\bar{V}_1^{\infty,s}$ for aromatics. 13
2.4 Calculated $\bar{V}_1^{\infty,s}$ for naphthenes. 13
2.5 SFC-calculated δ_{12}'s. 13
2.6 Binary phase behavior for the CO_2/tetracosane mixture at 212°F. 14
2.7 CO_2/octacosane phase behavior at 167°F. 14
2.8 CO_2/hexatriacontane phase behavior at 212°F. 15
2.9 CO_2/tetratetracontane phase behavior at 212°F. 15
2.10 Composition of Means and Maljamar stock tank oils. 20
2.11 Results of flash and lumping of Means stock tank oil with 80 mol % CO_2 at 90°F and 1000 psia. 21
2.12 Results of flash and lumping of Maljamar stock tank oil with 80 mol % CO_2 at 160°F and 1600 psia. 26
2.13 Results of flash and lumping of Wasson stock tank oil + 312 scf/bbl gas with 60 mol % CO_2 at 90°F and 1500 psia. 28
2.14 Solubility of naphthalene in CO_2 at 95°F. 32
2.15 Solubility of naphthalene in CO_2 at 131°F. 32
2.16 Solubility of naphthalene in CO_2 at 140°F. 33
2.17 Solubility of naphthalene in CO_2 at 149°F. 33
2.18 PVT Sampling Conditions 42
2.19 K-values for C_{13} Molecules in Sample 1 47
2.20 Means, Oil W, and Kubiki - Chemical Type Distribution 63
2.21 Measured or Estimated Critical Properties for Multi-ring Aromatics 67
2.22 Measured Boiling Points and Specific Gravities for Multi-ring Aromatics . . 67
2.23 Critical Pressures for Multi-ring Aromatics 68
2.24 Critical Temperatures for Multi-ring Aromatics 68
2.25 Acentric Factors for Multi-ring Aromatics 69
2.26 Nine Pseudocomponent Oil Description – non-MRA Base Case 71
2.27 Nine Pseudocomponent Oil Description – First Aromatic Case 71
2.28 Nine Pseudocomponent Oil Description – Second Aromatic Case 73

3.1 Component Properties. 81
3.2 MOC Solution for the Composition Route at 1600 psia, 160° F. 85
3.3 MOC Solution for the Composition Route at 1730 psia, 160° F. 92
3.4 Component properties. 134

3.5 Method of characteristics solution for a quaternary displacement with volume change on mixing at 1600 psia and 160°F, (CO2-3). 141
3.6 Method of characteristics solution for a quaternary displacement with volume change on mixing at 1600 psia and 160°F, (NIT-1). 142
3.7 Method of characteristics solution for a quaternary displacement with volume change on mixing at 1406.7 psia and 160°F. 151
3.8 Method of characteristics solution for a quaternary displacement with no volume change on mixing at 1406.7 psia and 160°F. 153

4.1 Densities and viscosities of the fluids used in the experiments. 160

5.1 Core Properties 233
5.2 Phase Properties for Three Equilibrium Tie-Lines 234
5.3 Inverse Bond Number for Imbibition Experiments 238
5.4 Capillary Number for Injection Experiments in 500 md Berea 240

List of Figures

2.1 Experimental apparatus. 5
2.2 Example chromatogram of methane and docosane. 8
2.3 Capacity factors of docosane at 131°F. 9
2.4 Correlation for $\bar{V}_1^{\infty,s}$. 10
2.5 CO_2/tetracosane, /octacosane, and /hexatriacontane phase behavior. 16
2.6 Phase diagram for the CO_2/Means stock tank oil mixture. 22
2.7 Modified phase diagram for the CO_2/Means stock tank oil mixture. 23
2.8 Phase behavior of Maljamar stock tank oil with CO_2 at 160°F and 1600 psia. 25
2.9 Phase behavior of Wasson stock tank oil + 312 scf/bbl gas with CO_2 at 90°F. 29
2.10 Solubility of naphthalene in CO_2. 34
2.11 Pressure-temperature diagram for a highly asymmetric binary mixture. . . . 35
2.12 Schematic of Sampling System 39
2.13 Simulated Distillation Analyses for Means, Oil W, and Kubiki. 43
2.14 K-values versus Carbon Number for Sample 1, Means at 3000 psi, 105°F. . . 44
2.15 K-values versus Elution Time for Sample 1, Means at 3000 psi, 105°F. 45
2.16 Alkane K-values Sample 1, Means at 3000 psi, 105°F. 46
2.17 Cyclic K-values for Sample 1, Means at 3000 psi, 105°F. 48
2.18 Multi-ring Aromatic K-values for Sample 1, Means at 3000 psi, 105°F. 49
2.19 K-values versus Elution Time for Sample 2, Means at 1500 psi, 105°F. 50
2.20 Pressure-Composition Diagram for Means Crude Oil and CO_2 at 105°F. (Data from Stessman, 1991). 52
2.21 Slim Tube Displacement Data for Means at 105°F. (Data provided by Exxon). 53
2.22 Pressure-Composition Diagram for Means Crude Oil and CO_2 at 120°F. (Data from Stessman, 1991). 54
2.23 K-values versus Elution Time for Sample 3, Means at 3950 psi, 125°F. 55
2.24 Slim Tube Displacement Data for Oil W at 170°F. (Data provided by donor of Oil W). 56
2.25 K-values versus Elution Time for Sample 4, Oil W at 3100 psi, 170°F. 57
2.26 K-values versus Elution Time for Sample 5, Oil W at 2000 psi, 125°F. 58
2.27 Slim Tube Displacement Data for Kubiki at 125°F. (Data provided by the Teikoku Oil Co.) 59
2.28 K-values versus Elution Time for Sample 6, Kubiki at 2000 psi, 125°F. . . . 60
2.29 K-values versus Elution Time for Sample 7, Kubiki at 3950 psi, 125°F 61
2.30 Oil W Carbon Number Distribution by Chemical Type 64
2.31 Kubiki Carbon Number Distribution by Chemical Type 66
2.32 Boiling Point versus Elution Time for Pure Components in Crude Oil. 70

2.33 Slim Tube Simulation, Kubiki 9-component Base and Aromatic Lumped Descriptions. 72
2.34 Slim Tube Simulation, Kubiki 9-component Aromatic Lumped Descriptions. 74
2.35 Slim Tube Simulation, Effect of Multi-ring Aromatic Binary Interaction Parameters. 75
2.36 Slim Tube Simulation, Effect of All Binary Interaction Parameters. 76

3.1 Composition route for displacement of a $CH_4/C_4/C_{10}$ mixture by pure CO_2 at 1600 psia, 160° F. 83
3.2 Composition profiles for the composition route at 1600 psia, 160° F. 84
3.3 Determination of the MMP for initial mixture **a**. 91
3.4 Composition route for displacement of oil mixture by pure CO_2 at 1730 psia, 160° F. 93
3.5 Composition profiles for the nearly miscible composition route at 1730 psia, 160° F. 94
3.6 Comparison of experimental MMP results with the crossover tie-line criterion. 96
3.7 Composition route for displacements of oil **O** by CH_4/C_3 gas mixtures at 2000 psia, 200 °F. Geometric construction of crossover tie line is shown for injection gas $\mathbf{I_2}$. 102
3.8 Composition and saturation profiles for the routes shown in Fig. 3.7 at 2000 psia, 200 °F. 103
3.9 Comparison of analytical and numerical profiles with $\triangle x_D = 0.001$ and $\triangle t_D = 0.0001$ for solution with gas $\mathbf{I_2}$. 104
3.10 Ternary representation of C/V displacement of oil **O** by gas $\mathbf{I_2}$. 107
3.11 Fluid properties for nearly miscible C/V displacement of oil **O** by gas $\mathbf{I_3}$. . . 108
3.12 Illustration of ruled surfaces upon which the displacement is either condensing or vaporizing. 110
3.13 Pseudoternary diagrams constructed from the ruled surfaces like those in Fig. 3.12 by lumping C_6 and C_{16}. 111
3.14 Pseudoternary diagrams constructed from the ruled surfaces like those in Fig. 3.12 by lumping C_3 and C_6. 112
3.15 Composition route for displacements of oil **O** by CH_4/C_2 gas mixtures at 2000 psia, 200 °F. Geometric construction of crossover tie line is shown for injection gas $\mathbf{I_4}$. 114
3.16 Composition and saturation profiles for the routes shown in Fig. 3.15. 115
3.17 Types of phase behavior found in three-component systems based on component volatilities. 119
3.18 Slopes of tie lines and their extensions for type HVI and LVI phase behavior (plait points are shown). 120
3.19 122
3.20 Vaporizing and condensing drives for HVI and LVI phase behavior. 123
3.21 MMP for vaporizing and condensing drives of type HVI and LVI phase behavior. 124
3.22 Typical solution routes in composition space for type HVI and LVI phase behavior with either condensing or vaporizing gas drives. 125
3.23 Typical solution profiles for type HVI and LVI phase behavior with either condensing or vaporizing gas drives. 127

3.24 Types of phase behavior found in four-component systems based on component volatility. 128
3.25 Illustration of a typical solution route in a four-component system. 130
3.26 Illustration of displacement mechanisms for four-component systems. 131
3.27 Composition routes, ruled surfaces and the structure of the envelopes formed by two different families of tie lines. 137
3.28 Ruled surface of tie lines generated by a nontie-line path and the envelope curve in that surface. 139
3.29 Composition route for displacement of a $CH_4/C_4/C_{10}$ mixture by pure CO_2 at 1600 psia and 160°F. 143
3.30 Composition, saturation and velocity profiles for displacement of a $CH_4/C_4/C_{10}$ mixture by pure CO_2 at 1600 psia and 160°F. 144
3.31 Comparison of composition, saturation and velocity profiles with and without volume change on mixing for displacement of a $CH_4/C_4/C_{10}$ mixture by pure CO_2 at 1600 psia and 160°F. 145
3.32 Composition route for displacement of a $CH_4/C_4/C_{10}$ mixture by pure N_2 at 1600 psia and 160°F. 147
3.33 Composition, saturation and velocity profiles for displacement of a $CH_4/C_4/C_{10}$ mixture by pure N_2 at 1600 psia and 160°F. 148
3.34 Composition route for displacement of a $CH_4/C_4/C_{10}$ mixture by pure CO_2 with VC at 1406.7 psia and 160°F. 149
3.35 Composition route for displacement of a $CH_4/C_4/C_{10}$ mixture by pure CO_2 with NVC at 1406.7 psia and 160°F. 150
3.36 Comparison of effluent mole fractions with the experimental data for displacement of a $CH_4/C_4/C_{10}$ mixture by pure CO_2 at 1406.7 psia and 160°F. . . . 152
3.37 Effect of CH_4 on N_2 MMP for dead oil (48% C_4, 52% C_{10}), **A**. 155
3.38 Determination of the critical tie line at 5011 psia and 160°F in the interior of quaternary diagram for the live oil (35% CH_4, 31.2% C_4, 33.8% C_{10}), **a**. . . . 156

4.1 Dimensions of two-dimensional bead packs. 160
4.2 Schematic of equipment for flow visualization experiments. 162
4.3 Measured front positions during displacement of undyed oil by dyed oil with the same viscosity and density. 163
4.4 Permeability distribution estimated from the front position of Fig. 4.3 for the two-layer model of Fig. 4.1. 165
4.5 The four models used in experiments. 166
4.6 Injected fluid concentrations in an experimental displacement at M=40 and $q = 6\,cm^3/min$ in the homogeneous model (Panels a-c). 167
4.7 Injected fluid concentrations in an experimental displacement at M=40 and $q = 6\,cm^3/min$ in the homogeneous model (Panels d-f). 168
4.8 Simulated concentration distributions for a displacement at M=40 in the homogeneous model (Panels a-c). 170
4.9 Simulated concentration distributions for a displacement at M=40 in the homogeneous model (Panels d-f). 171

4.10 Comparison of the appearance of fingers in the simulation (a) and experiment (b) for a displacement at M=40 and q = 6 cm^3 / min in the homogeneous model. 172
4.11 Comparison of cross-sectional averaged compositions in experiment and simulation of a displacement at M=40 and q = 6 cm^3 / min in the homogeneous model. 173
4.12 Comparison of the 0-2 concentration contour in experiment (a) and simulation (b) at M=40 and q = 6 cm^3 / min in the homogeneous model. 174
4.13 Comparison of the effluent composition curves in experiment and simulation at M=40 and q = 6 cm^3 / min in the homogeneous model. 175
4.14 Injected fluid concentration in an experimental displacement at M=40 and q = 6 cm^3 / min in the two-layer model (Panels a-c). 176
4.15 Injected fluid concentration in an experimental displacement at M=40 and q = 6 cm^3 / min in the two-layer model (Panels d-f). 177
4.16 Simulated concentration distributions for displacement at M=40 in the two-layer model (Panels a-c). 179
4.17 Simulated concentration distributions for displacement at M=40 in the two-layer model (Panels d-f). 180
4.18 Injected fluid concentration in an experimental displacement at M=40 and q = 6 cm^3 / min in the streak model (Panels a-c). 181
4.19 Injected fluid concentration in an experimental displacement at M=40 and q = 6 cm^3 / min in the streak model (Panels d-f). 182
4.20 Simulated concentration distributions for displacement at M=40 in the streak model (Panels a-c). 183
4.21 Simulated concentration distributions for displacement at M=40 in the streak model (Panels d-f). 184
4.22 Injected fluid concentration in an experimental displacement at M=1 and q = 6 cm^3 / min in the checkered model (Panels a-c). 186
4.23 Injected fluid concentration in an experimental displacement at M=1 and q = 6 cm^3 / min in the checkered model (Panels d-f). 187
4.24 Injected fluid concentration in an experimental displacement at M=40 and q = 6 cm^3 / min in the checkered model (Panels a-c). 188
4.25 Injected fluid concentration in an experimental displacement at M=40 and q = 6 cm^3 / min in the checkered model (Panels d-f). 189
4.26 Injected fluid concentration in an experimental displacement at M=40 and q = 6 cm^3 / min in the checkered model (Panels g-i). 190
4.27 Simulated concentration distributions for displacement at M=40 in the checkered model (Panels a-c). 191
4.28 Simulated concentration distributions for displacement at M=40 in the checkered model (Panels d-f). 192
4.29 Schematic of a cross-section of the experimental apparatus and typical data. 196
4.30 Permeability maps of the millstone slab and three faces of a limestone core . 198
4.31 Dispersivity (α_L) vs. mobility ratio (M) from flow experiments in the millstone and limestone cores, and from simulations using limestone Face 1. 202
4.32 Semivariograms for the permeability distributions of the millstone slab and limestone core. 203

4.33 Concentration grayscale maps and transversely averaged concentration profiles for M = 1 and 0.08 at 0.4 PVI from simulations of limestone Face 1. . . 205
4.34 Concentration grayscale maps and transversely averaged concentration profiles for M = 1 and 0.08 at 0.4 PVI from simulations of limestone Face 3. . . 206
4.35 (a) Concentration distribution (black = 1, white = 0), and (b) Pressure distribution for unstable (M = 10) and stable (M = 0.1) displacements. 207
4.36 Concentration grayscale maps and transversely averaged concentration profiles at 0.2 and 0.4 PVI in a homogeneous medium for M = 3.1. 209
4.37 Concentration grayscale maps and transversely averaged concentration profiles at 0.2 and 0.4 PVI in a homogeneous medium for M = 13.5. 210
4.38 Experimental concentration histories at the ten locations for the millstone (M = 3.1) and limestone (M = 3.4) cores. 211
4.39 Fingered zone time-sizes from experimental concentration histories for limestone (M = 2.2 & 3.4), and millstone (M = 3.1). 212
4.40 Millstone core. Experimental (dashed) and simulation (solid) concentration histories for M = 3.1. 213
4.41 Millstone core. Experimental (dashed) and simulation (solid) concentration histories. for M = 13.5. Locations 1, 3, 5, 7, 9. 214
4.42 Millstone core. Experimental (dashed) and simulation (solid) concentration histories. for M = 13.5. Locations 2, 4, 6, 8, 10. 215
4.43 Concentration histories at 10 locations from 2D (dashed) and 3D (solid) simulations in a homogeneous medium at M =3.1. 217
4.44 Experimental concentration histories at locations 2, 4, 6, 8, 10 in the limestone core at M = 2.2, 3.4 and 12.5. 219
4.45 Limestone experimental concentration histories and Face 1 simulation at locations 2, 4, 6, 8, 10 for M = 3.4. 220
4.46 Concentration grayscale maps and transversely averaged concentration profiles at 0.2 and 0.4 PVI using Face 1 permeability distribution for M = 3.4. . 221
4.47 Leading (c = 5%) and trailing (c = 95%) edge velocities extracted from the millstone experimental curves and numerical simulations at M = 3.1. The corresponding base-state solution velocities are also shown. 222
4.48 20% concentration contour at PVI = 0.05 and 0.10 for a dispersion anisotropy 20. M = 5. α_L (cm) = 0.10 (top), 0.075 (middle), 0.05 (bottom) 225

5.1 Interfacial profiles for different Bond numbers (after Concus[21]). 232
5.2 Entrapment on the left if capillary effects dominate. Suppression of entrapment on the right for large values of Bond number. After Morrow and Songkran [84]. 233
5.3 Phase diagram for IC_8, IPA and brine system. 234
5.4 Recovery curve for 15 md limestone at three different IFT's. 236
5.5 Recovery curve for 100 md Berea at three different IFT's. 237
5.6 Residual saturation vs. capillary to gravity ratio for imbibition experiments. 239
5.7 Capillary desaturation curve of continuous oil for imbibition and injection compared with data obtained from Chatzis and Morrow. 241
5.8 Drainage of brine, IFT = 0.1 and 1.0 mN/m, from 500 md Berea. 243

5.9 Drainage recovery curves for 700 md Brown sandstone at two different IFT's compared to imbibition at 0.1 mN/m. 244
5.10 Imbibition recovery curves for 100 md Berea at high and low IFT's compared to drainage at an IFT = 0.1 mN/m. 245
5.11 Summary of flow behavior for imbibition and drainage experiments. 246
5.12 IFT vs. density difference for phases approaching miscibility. 248
5.13 Schematic Diagram of the Glass-bead Pack. 250
5.14 IPA-Brine-IC_8 phase diagram. 251
5.15 Dependence of mixture density on composition. 252
5.16 Dependence of viscosity on composition. 252
5.17 Fluid distributions during displacement of IPA by IC_8 at 0.5 ml/min. 254
5.18 Fluid distributions during displacement of IPA by IC_8 at 1.0 ml/min. 255
5.19 Fluid distributions during displacement of IPA by IC_8 at 2.0 ml/min. 256
5.20 Fluid distributions during displacement of IPA by IC_8 at 4.0 ml/min. 257
5.21 Production curves for the displacements of IPA by IC_8. 258
5.22 Fluid distributions during displacement of LMO by C_{10} at 1.0 ml/min. . . . 259
5.23 Fluid distributions during displacement of LMO by C_{10} at 2.0 ml/min. . . . 260
5.24 Fluid distributions during displacement of LMO by C_{10} at 4.0 ml/min. . . . 261
5.25 Production curves for the displacements of LMO by C_{10}. 262
5.26 Fluid distributions during displacement of LMO by IC_8 at 1.0 ml/min. . . . 263
5.27 Fluid distributions during displacement of LMO by IC_8 at 2.0 ml/min. . . . 264
5.28 Fluid distributions during displacement of LMO by IC_8 at 4.0 ml/min. . . . 265
5.29 Production curves for the displacements of LMO by IC_8. 266
5.30 Fluid distributions of near-miscible displacements after 0.1 PVI. 267
5.31 Fluid distributions of near-miscible displacements after 0.2 PVI. 268
5.32 Fluid distributions of near-miscible displacements after 0.3 PVI. 269
5.33 Fluid distributions of near-miscible displacements after 0.4 PVI. 270
5.34 Production curves for near-miscible displacements. 271
5.35 Recoveries of IPA after 0.75, 1.0 and 1.5 PVI. 272
5.36 Pressure distribution during flow in a two-layered system with gravity effects. 273

1. Introduction

This report summarizes results of a wide-ranging investigation of the fundamental physical mechanisms that control displacement performance in miscible floods: phase behavior, viscous fingering, reservoir heterogeneity, viscous crossflow, capillary crossflow, and gravity segregation. The central objective of the research effort is to quantify scaling behavior of multicontact miscible (MCM) displacement processes, so that experimental observations at laboratory scale can be interpreted and translated with confidence to the much larger displacement scales appropriate to oil reservoirs.

The translation of scales requires an understanding of the flow processes that control displacement performance. Phase behavior, the partitioning of components between phases, and the resulting chromatographic separations that occur when phases flow at different rates are responsible for multicontact miscibility in one-dimensional flow settings. In reservoir flows, however, flow is anything but one dimensional. Permeability heterogeneities will induce nonuniform flow, as will viscous fingering. Crossflow, whether due to capillary, viscous or gravity forces, will induce mixing that cannot occur in one-dimensional flow. Thus, in reservoir scale flows, displacement performance will depend on the interplay of nonuniform flow, phase behavior and transverse mixing mechanisms. In this report we present new results that improve understanding of the physical mechanisms operating in all three areas.

In the interests of conciseness, we rely on the detailed descriptions given previously of experimental equipment, mathematical methods, and numerical techniques [90, 91, 92] and focus on new results. Significant progress has been made in several areas. In Chapter 2, we demonstrate a new technique based on supercritical fluid chromatography (SFC) for characterization of a crude oil for phase behavior computations with an equation of state (EOS) and show that results of PVT experiments for a CO_2-crude oil are *predicted* with good accuracy. We also report results of detailed analyses by gas chromatography and mass spectrometry (GCMS) of hydrocarbons present in oil-rich and CO_2-rich phases. Those results illuminate the question of how crude oil composition influences the supercritical extraction that is an essential part of development of miscibility. They show, for example, that oils that contain significant quantities of aromatic hydrocarbons with two and three rings will have minimum miscibility pressures much higher than those of oils containing primarily saturated alkanes.

In Chapter 3, we explore development of miscibility in one-dimensional flow, the interaction of phase equilibrium with two-phase flow. In a significant extension of the well known three-component theory for vaporizing and condensing gas drives, we show that the standard criteria for miscibility, based on tie-line extensions through the initial and injection compositions, are not sufficient to explain displacement behavior in multicomponent systems. Instead, we use analytical solutions for four-component systems to show that an additional tie line, which we call the "crossover" tie line, can often control development of miscibility. We also show that the displacement behavior that has come to be known as a "condensing/vaporizing" gas drive [157, 129] is observed when a crossover tie line controls

development of miscibility. We show that it is easy to determine what type of displacement behavior (condensing, vaporizing, or condensing/vaporizing) will occur from the relative magnitudes of the K-values of the components present in the oil and injected gas. We also examine the effects of volume change as components transfer between phases.

In Chapter 4 we turn to the question of nonuniform flow, and its impact on displacement performance. Nonuniform flow can arise from permeability heterogeneity or from viscous fingering. In most miscible floods, viscous fingering and permeability heterogeneity must interact to determine sweep efficiency. Numerical simulations of fingering behavior in heterogeneous porous media [1, 2] suggest that heterogeneity can dominate the patterns of fingering. In Section 4.1 we report results of a detailed test of that prediction. We show that the particle-tracking simulation technique developed previously [1, 2, 114] reproduces accurately behavior observed in flow visualization experiments in which viscous fingering takes place in flow models with known permeability distributions. We emphasize that history matching is not required to make the predictions reproduce the experimental observations. We then make use of the particle-tracking technique to interpret in detail a series of displacement experiments in real porous media. Those experiments, and the simulation interpretations, explore the relationship between dispersion, heterogeneity, and viscous fingering.

In Chapter 5, we examine effects of crossflow in an experiment that combines the effects of gravity-driven flow, interfacial tension (IFT) gradients, and low IFT's. The experimental results reported show that significant crossflow can be expected when interactions of phase behavior and multiphase flow create mixtures on tie lines close to a critical tie line. Thus, crossflow will have significant impact on mixing of oil and injected gas in heterogeneous reservoirs if the displacement is MCM or nearly so. That result suggests that interactions of crossflow, heterogeneity and phase behavior will have significant impact on development of miscibility during MCM flow in heterogeneous reservoirs. Also presented in Chapter 5 are results of flow visualization experiments that illustrate how permeability heterogeneity, viscous crossflow, and gravity segregation interact to determine displacement performance. Those experiments also suggest that significant compositional effects are also possible when interactions of crossflow and equilibrium phase behavior are also present.

2. Phase Behavior

The partitioning of components between phases is responsible for the chromatographic separations of components that lead to the development of multicontact miscibility in CO_2 floods and other miscible gas injection processes. Hence, the prediction of equilibrium phase compositions is a fundamental part of any detailed description of a miscible flood process. This chapter reports results of two sets of experiments designed to improve understanding of the use of an equation of state (EOS) to predict phase equilibria.

Section 2.1 outlines the thermodynamic theory behind use of supercritical fluid chromatography as part of the experimental data used to characterize an oil for EOS calculations. The technique is then demonstrated for well characterized hydrocarbon systems and for a CO_2/crude oil system. The calculations show that phase diagrams that agree well with conventional PVT observations can be predicted with minimal adjustment of parameters.

Section 2.2 reports results of experiments in which samples of equilibrium CO_2-rich and oil-rich phases were analyzed by gas chromatography and mass spectrometry (GC-MS). That technique permits identification of specific hydrocarbon molecules, and hence the analysis is much more detailed than that detained by gas chromatography alone. The detailed analyses are then used to explore how oil composition affects extraction by CO_2 and hence development of miscibility. A combination of EOS calculations and compositional simulations demonstrates conclusively that the presence of multi-ring aromatic compounds leads to higher minimum miscibility pressures.

2.1 Prediction of CO_2/Hydrocarbon Phase Behavior Using SFC

Maurice P. Stadler

The traditional method of studying the phase behavior of reservoir fluids is by pressure-volume-temperature (PVT) experiments. A typical PVT experiment requires loading a vessel with the mixture to be studied, controlling the pressure and temperature in the vessel, and sampling and analyzing the phase or phases that result. The PVT measurements may then used to adjust parameters in an EOS representation of phase behavior, which can then be used to interpolate between known results and to predict the phase behavior of new systems. However, PVT experiments are relatively difficult to perform. Thus, development of new methods to adjust EOS parameters could reduce the cost of experimentation.

One such method is supercritical fluid chromatography (SFC). SFC is similar to gas chromatography except that the carrier fluid is a relatively dense, supercritical fluid, in this case, high-pressure CO_2. Mixtures of hydrocarbons, such as crude oils, can be separated by SFC. Chromatography and thermodynamics are used to relate the time needed for a given component to pass through a chromatographic column to the interaction of the component with the CO_2 carrier fluid. In other words, SFC elution times of the various hydrocarbon compounds can be used to help characterize CO_2/hydrocarbon systems. Three different applications are studied.

First, SFC is used to determine CO_2/hydrocarbon binary interaction parameters for the Peng-Robinson EOS. Binary interaction parameters are the adjustable parameters used to improve the accuracy of EOS's. An equation is derived that relates the SFC elution time of a hydrocarbon component to its interaction parameter with CO_2. Binary interaction parameters for CO_2 and several n-alkanes measured using SFC are reported.

Second, SFC is used to characterize crude oils for calculation of phase behavior of CO_2/crude oil mixtures with an EOS. SFC is used in two different ways for this application. First, the carbon number distribution of the crude oil is determined by simulated distillation using SFC. SFC is a natural tool for characterizing CO_2/oil mixtures because hydrocarbons that elute together during an SFC run are likely to partition together into a phase rich in CO_2. (See Section 2.2 for confirmation of this point.) Second, unknown CO_2/n-alkane binary interaction parameters, which are needed for the EOS calculations, are determined using the technique described before. A method for prediction of CO_2/crude oil phase behavior is proposed and tested by comparing the results to those of PVT experiments.

Finally, SFC is used to determine the solubility of a hydrocarbon in dense CO_2. This application is based on the work of Bartle *et al.* [6]. Additional details of all the work described in this section are given by Stadler [123, 125].

2.1.1 SFC Apparatus

The apparatus, supplied by Applied Biosystems, is basically a gas chromatograph (GC) that has been modified to accept supercritical CO_2 as the carrier fluid. This was done by placing a pump between the CO_2 supply vessel and the injection port. A schematic diagram of the apparatus is shown in Fig. 2.1.

An SFC MicroGradient System pump (Applied Biosystems) delivered the CO_2 at high pressures. This pump is designed to deliver fluids accurately at low flow rates. An important feature of the pump is that it can be programmed to deliver fluid at fixed or steadily changing pressures. That feature is similar to temperature programming in gas chromatography. The maximum allowable pressure is 5500 psig.

The injector is a Valco Model CI4W injection valve. Two different packed columns were used in this work. The first is a Polysiloxane PM, 20 cm $\times$ 1.0 mm column (Applied Biosystems), which was used for simulated distillation and the binary interaction parameter work. The second is a Spherisorb ODS2, 10 cm $\times$ 4.6 mm, 10 μm particle-size column (Jones Chromatography), which was used for the solubility work. The columns were installed in a Hewlett-Packard (HP) Model 5890 GC. A flame ionization detector was used to detect the material eluted from the column. This type of detector is ideal for analysis of hydrocarbons with a CO_2 carrier fluid because hydrocarbons burn easily, whereas CO_2 does not.

The experiments and data acquisition were partially automated by linking the components electronically. An HP 3396A Integrator and the HP 5890 GC were linked via the Instrument Network (INET). INET digitally transfers the raw detector data to the integrator. Also, the integrator can control all of the setpoints (oven temperature, detector temperature, etc.) of the GC. The pump also has features for networking—relays for activating four external devices. Those relays are opened and closed by commands in the pump program. One relay is wired to the integrator's remote start

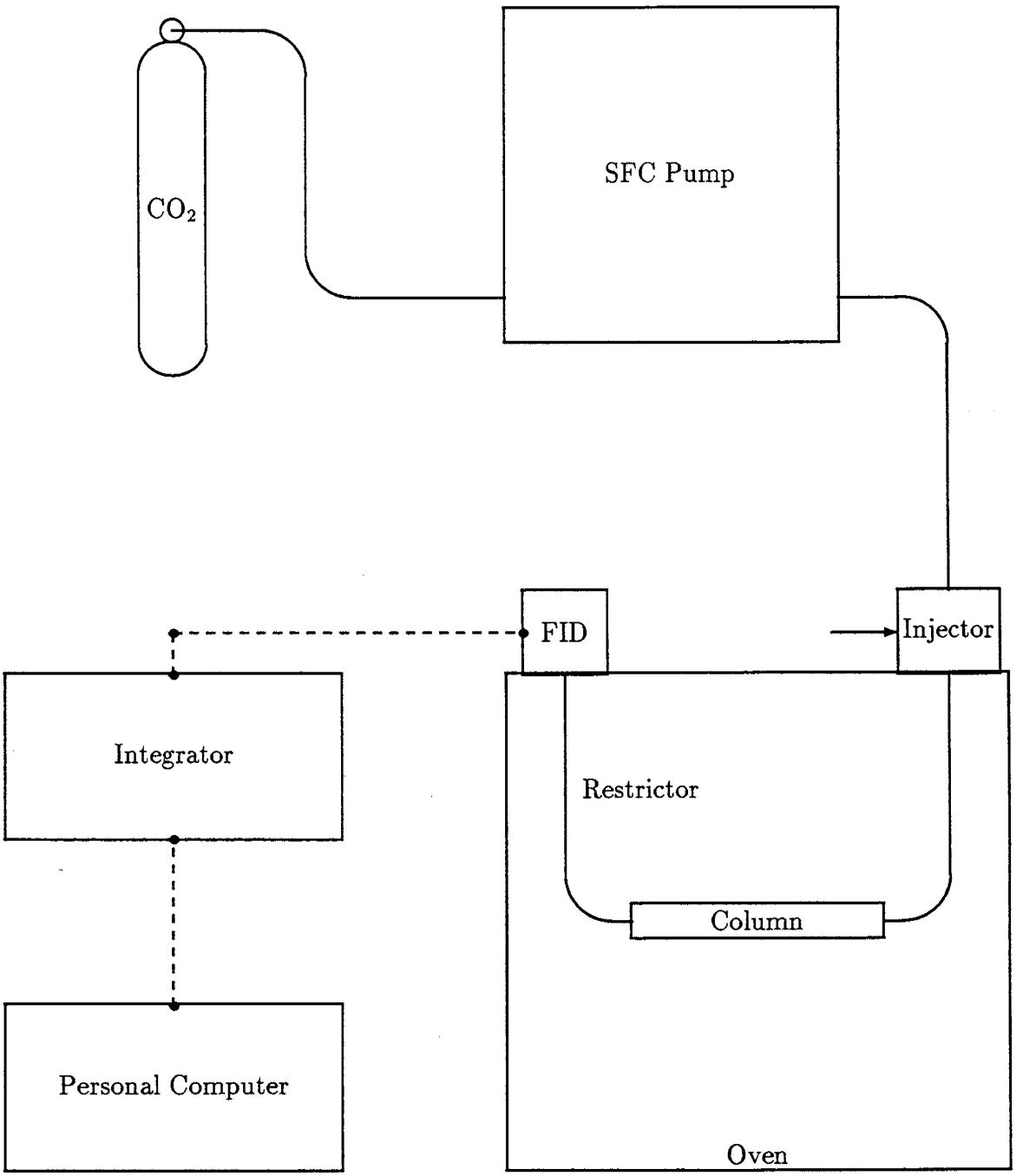

Figure 2.1: Experimental apparatus.

connection. Another relay is wired to the injector. In a typical pump program, these two relays close at the same time. Finally, the integrator was linked to an IBM Personal Computer AT through an RS232C port. That link allows chromatographic data to be stored on the hard drive of the computer.

2.1.2 CO_2/Hydrocarbon Binary Systems

We begin with a description of a method for determination of CO_2/hydrocarbon binary interaction parameters. We present first a derivation that relates CO_2/hydrocarbon binary interaction parameters to the capacity factor (a chromatographic measurement). The method was tested by comparison of results with those for well-characterized hydrocarbons.

Thermodynamic Development

In order to use SFC to measure properties of CO_2/hydrocarbon systems, equations that relate chromatography to thermodynamic properties are needed. An equation used to determine binary interaction parameters from SFC is derived as follows.

Separation in the chromatographic column is modeled with the aid of Henry's law, since hydrocarbon solutes are present at very low concentrations in the column's mobile and stationary phases during a typical SFC experiment. The partial molar Gibbs function of a solute in a solution modeled by Henry's law, $\bar{G}_1^{\mathrm{id}}$, is given by [143]

$$\bar{G}_1^{\mathrm{id}} = G_1^{\circ} + RT \ln x_1, \tag{2.1}$$

where G_1° is the Gibbs function of the solute at the Henry's law standard state (infinite dilution), R is the universal gas constant, T is temperature, and x_1 is the mole fraction of the solute in solution.

The mobile phase flow rate through the column is slow enough that the mobile (m) and stationary (s) phases can be assumed to be in chemical equilibrium at any point along the column. In this case, $\bar{G}_1^{\mathrm{id,m}} = \bar{G}_1^{\mathrm{id,s}}$, or

$$G_1^{\circ,\mathrm{m}} + RT \ln x_1^{\mathrm{m}} = G_1^{\circ,\mathrm{s}} + RT \ln x_1^{\mathrm{s}}. \tag{2.2}$$

Assuming ideal chromatographic separation, the capacity factor, k_1', is given by [142]

$$k_1' = \frac{x_1^{\mathrm{s}}}{x_1^{\mathrm{m}}} \frac{V^{\mathrm{m}}}{V^{\mathrm{s}}} \frac{V^{\mathrm{t,s}}}{V^{\mathrm{t,m}}} = \frac{t_1}{t_2} - 1, \tag{2.3}$$

where V is molar volume, V^{t} is total volume, t_1 is the chromatographic retention time of the solute, and t_2 is the time required for the carrier fluid to pass through the column, also called the "dead time." (The dead time is assumed to be equal to the elution time of methane.) The second equality in Eq. 2.3 is used to calculate the capacity factor experimentally. If we combine Eqs. 2.2 and 2.3, take the derivative with respect to pressure, and assume that

$$\left[\frac{\partial}{\partial P}\left(\frac{V^{\mathrm{t,s}}}{V^{\mathrm{s}} V^{\mathrm{t,m}}}\right)\right]_T = 0, \tag{2.4}$$

we obtain [7]

$$\left(\frac{\partial \ln k_1'}{\partial P}\right)_T = \frac{1}{RT}(\bar{V}_1^{\infty,\mathrm{m}} - \bar{V}_1^{\infty,\mathrm{s}}) + \left(\frac{\partial \ln V_2}{\partial P}\right)_T, \tag{2.5}$$

where $\bar{V}_1^{\infty}$ is the partial molar volume of the solute at infinite dilution (Henry's law standard state) and V_2 is the molar volume of the CO_2 mobile phase. Upon expansion of $\bar{V}_1^{\infty,m}$, Eq. 2.5 becomes [153]

$$\left(\frac{\partial \ln k_1'}{\partial P}\right)_T = -\frac{n}{RT}\lim_{n_1\to 0}\left(\frac{\partial P}{\partial n_1}\right)_{V_2,T,n_2}\left(\frac{\partial V_2}{\partial P}\right)_T - \frac{\bar{V}_1^{\infty,s}}{RT} + \left(\frac{\partial \ln V_2}{\partial P}\right)_T, \tag{2.6}$$

where n_1 is number of moles of the solute, n_2 is number of moles of CO_2, and n is total number of moles.

Any EOS can be used to calculate the first and third terms on the right hand side of Eq. 2.6. In the examples that follow, the derivatives for the Peng-Robinson EOS [103] are used. If we substitute these expressions into Eq. 2.6, assume that δ_{12}, the binary interaction parameter between CO_2 and the solute, and $\bar{V}_1^{\infty,s}$ are not functions of pressure, and integrate, Eq. 2.6 becomes

$$A = \delta_{12}B + \bar{V}_1^{\infty,s}C + D, \tag{2.7}$$

where

$$\begin{aligned} A &= \frac{1}{RT}\int_{P_i}^{P}\left[\frac{RT}{(V_2-b_2)} + \frac{RTb_1}{(V_2-b_2)^2} + \frac{2a_2b_1(V_2-b_2)}{(V_2^2+2b_2V_2-b_2^2)^2} - \frac{RT}{V_2} - \frac{2\sqrt{a_1a_2}}{V_2^2+2b_2V_2-b_2^2}\right] \\ &\times \left[\frac{2a_2(V_2+b_2)}{(V_2^2+2b_2V_2-b_2^2)^2} - \frac{RT}{(V_2-b_2)^2}\right]^{-1} dP + \ln k_1', \end{aligned} \tag{2.8}$$

$$B = -\frac{1}{RT}\int_{P_i}^{P}\left(\frac{2\sqrt{a_1a_2}}{V_2^2+2b_2V_2-b_2^2}\right)\left[\frac{2a_2(V_2+b_2)}{(V_2^2+2b_2V_2-b_2^2)^2} - \frac{RT}{(V_2-b_2)^2}\right]^{-1} dP, \tag{2.9}$$

$$C = -\frac{P-P_i}{RT}, \tag{2.10}$$

$$D = \ln k_{1i}', \tag{2.11}$$

where a_1, a_2, b_1, and b_2 are the Peng-Robinson EOS parameters. P_i is the lowest pressure at which the experiments are performed, and k_{1i}' is the capacity factor at the lowest pressure. The unknowns in Eq. 2.7 are δ_{12} and $\bar{V}_1^{\infty,s}$. All other terms can be calculated using the EOS except for the capacity factors, which are determined experimentally. Eq. 2.7 is expressed in integral form because it is more accurate to integrate an analytical expression numerically than to differentiate discrete experimental data.

One way to calculate δ_{12} from Eq. 2.7 is to use SFC to measure the capacity factor of the solute at several pressures. The terms A, B, C, and D can be calculated using the measured capacity factors and the Peng-Robinson EOS. A least-squares, two-variable regression can then be performed to calculate δ_{12} and $\bar{V}_1^{\infty,s}$. However, that approach was not found to be reliable because δ_{12} and $\bar{V}_1^{\infty,s}$ have a high statistical correlation.

A better way to determine δ_{12} is to note that δ_{12}'s for several CO_2/hydrocarbon pairs can be found in the literature. For these hydrocarbons, the capacity factors at several pressures were determined using SFC. Because δ_{12} is known, Eq. 2.7 becomes

$$(A - \delta_{12}B) = \bar{V}_1^{\infty,s}C + D. \tag{2.12}$$

$\bar{V}_1^{\infty,s}$ can be determined from a least-squares fit. With several values of $\bar{V}_1^{\infty,s}$, a correlation can be made.

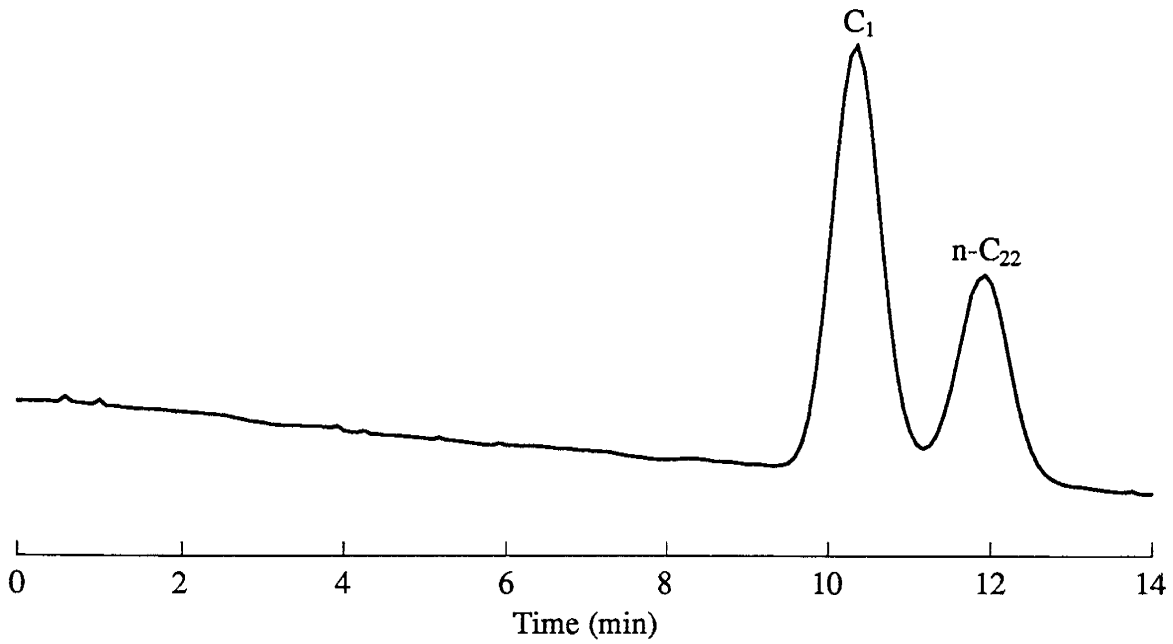

Figure 2.2: Example chromatogram of methane and docosane.

To estimate an unknown δ_{12}, $\bar{V}_1^{\infty,s}$ can be determined from the correlation, and Eq. 2.7 can be rearranged to yield

$$(A - \bar{V}_1^{\infty,s}C) = \delta_{12}B + D. \tag{2.13}$$

A least-squares fit can be performed on capacity factor measurements to estimate δ_{12}.

Results and Discussion

A correlation is needed in order to estimate $\bar{V}_1^{\infty,s}$. In order to calculate $\bar{V}_1^{\infty,s}$ from Eq. 2.12, reported δ_{12}'s are required. Those δ_{12}'s are taken from Deo *et al.* [26] because they list a set of δ_{12}'s for a large number of hydrocarbons. For many of those hydrocarbons, SFC was used to measure the capacity factor at several pressures. An illustration of how the capacity factor at a particular pressure and temperature was determined for docosane, n-C_{22}, is given in Fig. 2.2. Several measurements for docosane at 131°F are given in Table 2.1 and Fig. 2.3.

The next step is to calculate $\bar{V}_1^{\infty,s}$ using a linear least-squares fit of Eq. 2.12 to the experimental data. The result of the regression for the data listed in Table 2.1 is that $\bar{V}_1^{\infty,s} = 848$ cm^3/mol. As shown by the curve in Fig. 2.3, this procedure matches the capacity factor versus pressure data well, which partially vindicates the assumptions made in deriving Eq. 2.7.

Values of $\bar{V}_1^{\infty,s}$ were estimated by the procedure just described for many of the hydrocarbons included in the work of Deo *et al.* The results of those experiments and linear least-squares regressions for $\bar{V}_1^{\infty,s}$ are given in Tables 2.2–2.4 and Fig. 2.4. The SFC experiments were performed at 131°F. Because Deo *et al.* list δ_{12}'s over a wide range of temperatures, interpolation was used where possible to obtain the δ_{12}'s of Tables 2.2–2.4. When interpolation of Deo *et al.*'s data was not possible, the δ_{12} at the temperature closest to 131°F was chosen. Nevertheless, the dependence of δ_{12} on temperature is not large [86].

Table 2.1: Capacity factors for docosane at 131°F.

Pressure (psia)	t_o (min)	t_1 (min)	$\ln k_1'$
1715	14.71	67.32	1.274
1915	15.59	33.66	0.148
2115	15.51	25.39	-0.451
2315	14.12	20.56	-0.785
2515	13.49	17.95	-1.107
2715	12.60	15.74	-1.388
2915	11.79	14.34	-1.535
3115	11.15	13.20	-1.694
3315	10.62	12.31	-1.838
3515	10.10	11.57	-1.927

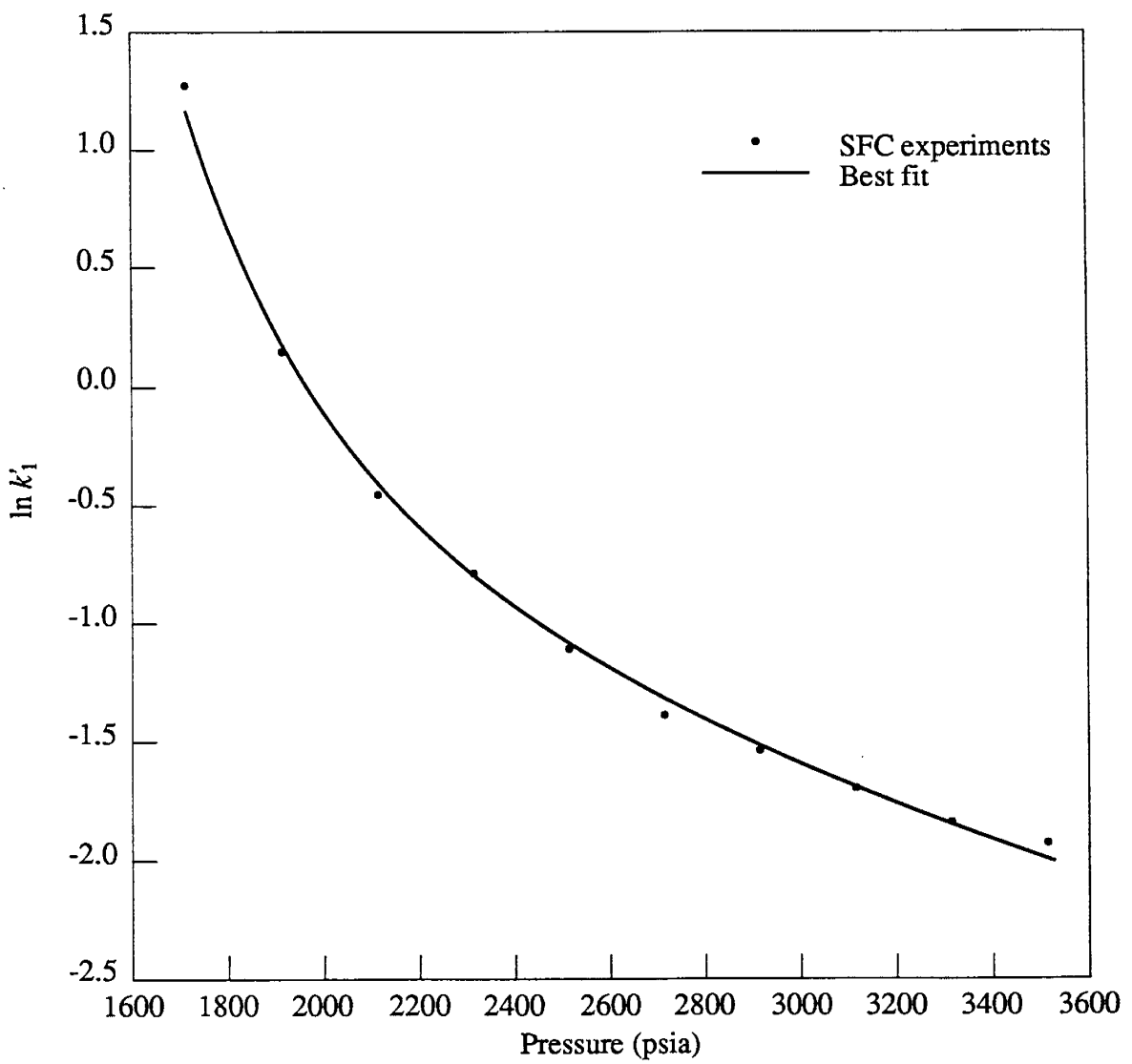

Figure 2.3: Capacity factors of docosane at 131°F.

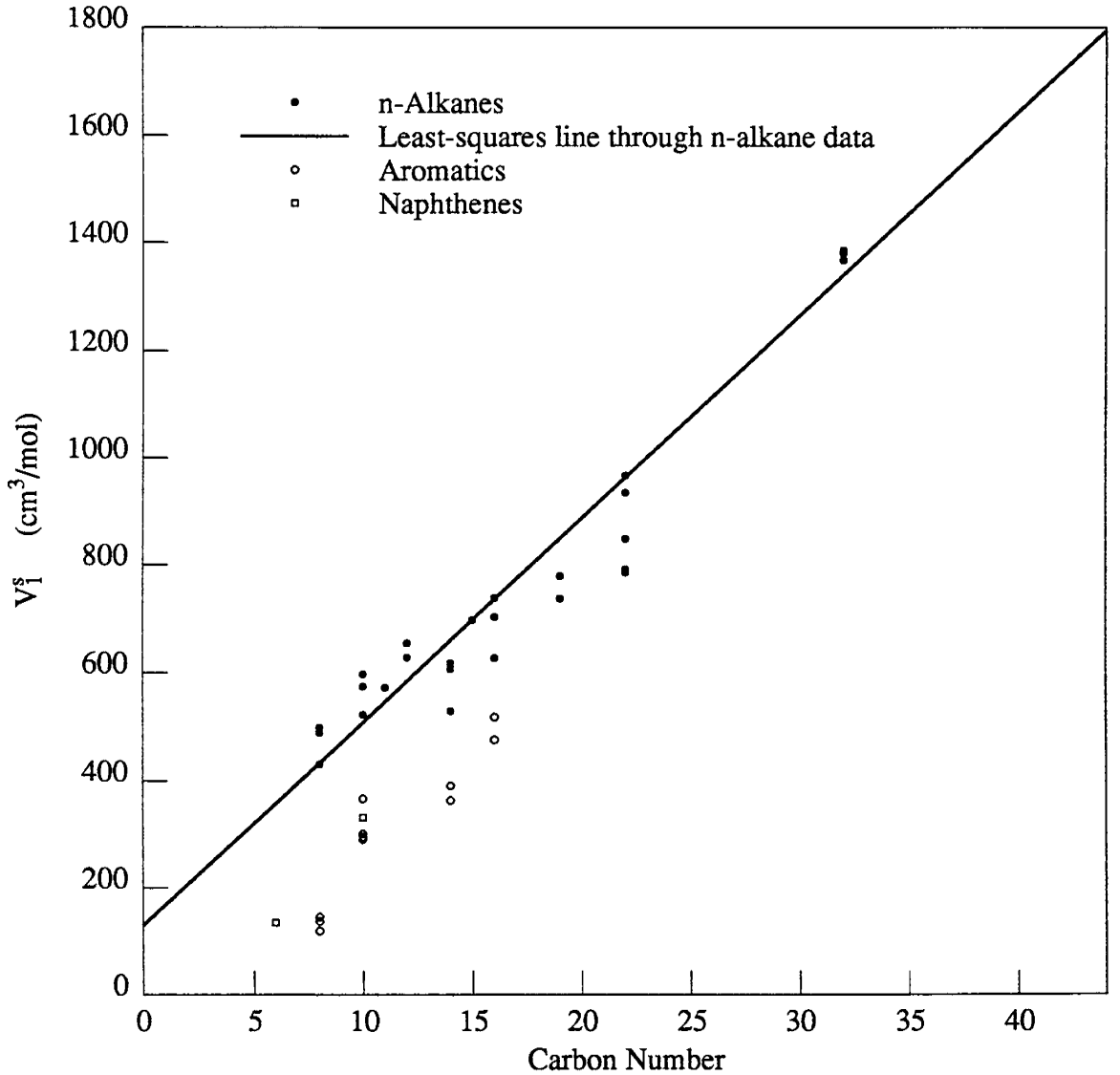

Figure 2.4: Correlation for $\bar{V}_1^{\infty,s}$. The equation for the line that passes through the n-alkane data is $\bar{V}_1^{\infty,s} = 37.9n + 131$ where n is the carbon number.

As Table 2.2 shows, there is considerable scatter for the calculated values of $\bar{V}_1^{\infty,s}$ for a given component. Evidently, $\bar{V}_1^{\infty,s}$ is sensitive to slight differences between different sets of capacity factor experiments. Therefore, multiple, sets of experiments, each yielding a value for $\bar{V}_1^{\infty,s}$, were performed for most of the solutes in order to improve the accuracy of the correlation.

As shown in Fig. 2.4, the results for the n-alkane data appear to fall more or less on a straight line. Deviations from this straight line could be due to the variety of pressures, temperatures, and experimental techniques for which the δ_{12}'s are reported and to the experimental error in the original data used to determine δ_{12}. The line that passes through these data is a least-squares line. Although, this correlation may depend on temperature, that dependence is not significant because the correlation is only used to calculate δ_{12}, which does not depend strongly on temperature.

As Fig. 2.4 shows, the aromatics and naphthenes have a smaller partial molar volume in the stationary phase than the n-alkanes, probably because aromatic molecules have a more compact molecular structure (rings) than n-alkanes (chains).

No line was constructed through the aromatic or naphthenic data because of the small number of data points, which is due to the scarcity of PVT data for aromatics and naphthenes. In addition, the aromatic and naphthenic hydrocarbons represented in Fig. 2.4 do not constitute a homologous series. The aromatic and naphthenic data are included only for illustrative purposes and for comparison with the data for n-alkanes. As more PVT data become available for binary mixtures of CO_2 and aromatic or naphthenic hydrocarbons, a correlation can be constructed for those hydrocarbon groups.

To measure δ_{12} for a hydrocarbon that is not included in the work of Deo *et al.,* the following steps should be taken. First, measure the capacity factor for the hydrocarbon at several pressures. Then, use the correlation provided in Fig. 2.4 to obtain $\bar{V}_1^{\infty,s}$. Perform a linear least-squares fit to the data with Eq. 2.13. The slope of this line is δ_{12}.

That procedure was applied to four hydrocarbons for which δ_{12} was not calculated by Deo *et al.* Table 2.5 lists the results of those experiments and calculations. $\bar{V}_1^{\infty,s}$ was taken from the correlation in Fig. 2.4. The SFC-determined δ_{12} for each hydrocarbon is the average of at least two separate δ_{12} determinations. The SFC experiments were performed at 131°F.

One way to check the validity of these measured δ_{12}'s is to use them with the Peng-Robinson EOS to calculate phase behavior data and compare the results with PVT experiments. Fig. 2.5 illustrates the results for the first three CO_2/hydrocarbon systems. The points are PVT data taken from Tsai and Yau [138] and Gasem and Robinson [41]. For each CO_2/hydrocarbon pair, two curves were calculated using the Peng-Robinson EOS. The solid line was calculated with a δ_{12} that results in a best fit of the EOS to the data; the dashed line was calculated with the δ_{12} determined using the SFC method outlined before. The results of the comparisons between the calculated and PVT-observed data are listed in Tables 2.6–2.9. In these tables, x_2 is the mole fraction of CO_2 in the liquid phase, and y_2 is the mole fraction of CO_2 in the vapor phase. Also required for the EOS calculations are the critical pressure, critical temperature, and acentric factor for each hydrocarbon (Table 2.5). The critical properties were estimated using the correlation of Twu [139], and the acentric factor was estimated using the correlation of Kesler and Lee [60]. Correlations were used for these hydrocarbons because the properties have not been determined experimentally.

Table 2.2: Calculated $\bar{V}_1^{\infty,s}$ for n-alkanes with δ_{12} reported in Deo *et al.* [26].

Component	δ_{12}	$\bar{V}_1^{\infty,s}$ (cm^3/mol)
Octane	0.109	491.
		500.
		431.
Decane	0.100	523.
		598.
		575.
Undecane	0.102	572.
Dodecane	0.104	655.
		628.
Tetradecane	0.110	618.
		607.
		612.
		529.
Pentadecane	0.093	698.
Hexadecane	0.098	703.
		627.
		738.
Nonadecane	0.105	737.
		799.
Docosane	0.093	791.
		848.
		785.
		934.
		965.
Dotriacontane	0.063	1386.
		1384.
		1381.
		1367.
		1380.

Table 2.3: Calculated $\bar{V}_1^{\infty,s}$ for aromatics with δ_{12} reported in Deo *et al.* [26].

Compound	Carbon number	δ_{12}	$\bar{V}_1^{\infty,s}$ (cm^3/mol)
m-Xylene	8	0.074	120.
			146.
			139.
Naphthalene	10	0.124	367.
			294.
			291.
			296.
			301.
Phenanthrene	14	0.154	364.
			391.
Pyrene	16	0.282	476.
			519.

Table 2.4: Calculated $\bar{V}_1^{\infty,s}$ for naphthenes with δ_{12} reported in Deo *et al.* [26].

Compound	Carbon number	δ_{12}	$\bar{V}_1^{\infty,s}$ (cm^3/mol)
cyclo-Hexane	6	0.107	136.
Decalin	10	0.167	331.

Table 2.5: SFC-calculated δ_{12} for hydrocarbons not studied by Deo *et al* [26]. The value for $\bar{V}_1^{\infty,s}$ was determined from the correlation.

Compound	$\bar{V}_1^{\infty,s}$ (cm^3/mol)	δ_{12}		P_c (bar)	T_c (K)	ω
		SFC	Best fit			
Tetracosane	1017	0.124	0.068	9.38	806	1.00
Octacosane	1165	0.080	0.079	7.95	836	1.11
Hexatriacontane	1460	0.006	0.020	5.99	884	1.27
Tetratetracontane	1794	-0.266	0.020	3.96	946	1.52

Table 2.6: Binary phase behavior for the CO_2/tetracosane mixture at 212°F. Comparison of published PVT data [138] with calculations using the Peng-Robinson EOS with the SFC-determined and best fit δ_{12}'s.

Pressure	Published		Calculated			
			$\delta_{12} = 0.124$ (SFC)		$\delta_{12} = 0.068$ (Best fit)	
(psia)	x_2	y_2	x_2	y_2	x_2	y_2
147.	0.0819	1.0000	0.0728	1.0000	0.0853	1.0000
294.	0.1720	1.0000	0.1397	1.0000	0.1635	1.0000
441.	0.2437	1.0000	0.2011	1.0000	0.2352	1.0000
588.	0.3004	1.0000	0.2574	1.0000	0.3008	1.0000
735.	0.3531	1.0000	0.3091	1.0000	0.3608	1.0000

Table 2.7: CO_2/octacosane phase behavior at 167°F. Comparison of published PVT data [41] with calculations using the Peng-Robinson EOS with the SFC-determined and best fit δ_{12}'s.

Pressure	x_2		
		Calculated	
(psia)	Published	$\delta_{12} = 0.080$ (SFC)	$\delta_{12} = 0.079$ (Best fit)
122.5	0.099	0.085	0.085
210.0	0.160	0.142	0.141
325.0	0.231	0.211	0.210
453.0	0.301	0.281	0.281
670.5	0.399	0.387	0.386
860.5	0.470	0.466	0.465
1120.0	0.551	0.556	0.557
1393.0	0.617	0.632	0.633

Table 2.8: CO_2/hexatriacontane phase behavior at 212°F. Comparison of published PVT data [41] with calculations using the Peng-Robinson EOS with the SFC-determined and best fit δ_{12}'s.

Pressure (psia)	x_2		
		Calculated	
	Published	$\delta_{12} = 0.006$ (SFC)	$\delta_{12} = 0.020$ (Best fit)
126.5	0.101	0.094	0.091
229.0	0.172	0.165	0.159
241.0	0.178	0.173	0.167
282.5	0.206	0.200	0.192
416.0	0.280	0.282	0.272
528.5	0.335	0.345	0.333
621.0	0.375	0.393	0.380
653.5	0.390	0.410	0.395
852.5	0.459	0.501	0.484

Table 2.9: CO_2/tetratetracontane phase behavior at 212°F. Comparison of published PVT data [41] with calculations using the Peng-Robinson EOS with the SFC-determined and best fit δ_{12}'s.

Pressure (psia)	x_2		
		Calculated	
	Published	$\delta_{12} = -0.266$ (SFC)	$\delta_{12} = 0.020$ (Best fit)
136.0	0.122	0.202	0.106
233.0	0.188	0.331	0.175
290.0	0.238	0.401	0.214
486.0	0.343	0.605	0.334
607.0	0.401	0.704	0.399
886.5	0.502	0.852	0.529

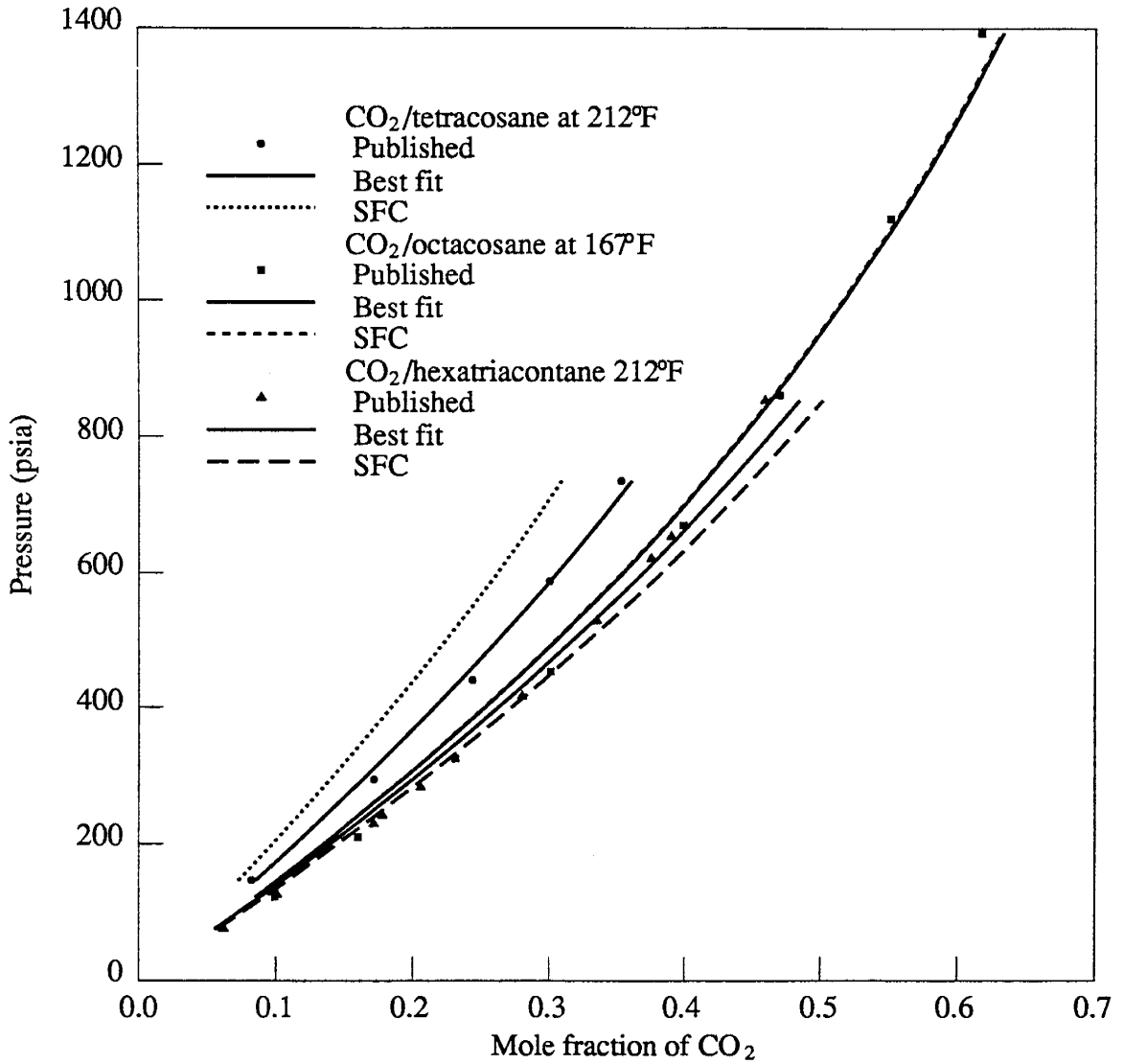

Figure 2.5: CO_2/tetracosane, /octacosane, and /hexatriacontane phase behavior. Comparison of literature PVT data [138, 41] with calculations using the Peng-Robinson EOS with the SFC-determined and best fit δ_{12}'s.

As shown in Fig. 2.5, the SFC-determined δ_{12} improves the Peng-Robinson EOS prediction of the experimental data for the first three binary mixtures. In addition, for the CO_2/octacosane pair, the SFC-determined δ_{12} is very close to the best fit δ_{12}.

However, for the CO_2/tetratetracontane pair, the SFC method described above does a poor job of producing a useful δ_{12} for the Peng-Robinson EOS, as Table 2.9 shows. Application of the linear correlation for $\bar{V}_1^{\infty,s}$ yields -0.266 for the value of δ_{12}. That value produces poor agreement with the phase equilibria measurements summarized in Table 2.9. One possible explanation for poor agreement is that determination of the critical properties, acentric factor, and $\bar{V}_1^{\infty,s}$ all involve extrapolations of data for hydrocarbons much smaller than tetratetracontane. Thus, many of the properties needed to determine δ_{12} are not accurately known. This lack of information results in an inaccurate value for δ_{12}.

2.1.3 Crude Oil Characterization

Obtaining accurate CO_2/hydrocarbon binary interaction parameters is part of a larger problem: computing the phase behavior of CO_2/crude oil mixtures. Accurate prediction of phase compositions is an essential part of fundamental understanding of the development of miscibility in CO_2/crude oil displacements [93, 94] (see section 2.2). Development of cubic EOS's has proceeded to the point that phase equilibrium calculations can be made routinely if the crude oil can be characterized adequately. An adequate characterization includes (1) division of the crude oil into an appropriate number of pseudocomponents and (2) specification of properties such as critical pressure, P_c, critical temperature, T_c, and acentric factor, ω, for each pseudocomponent. In addition, essentially all modern EOS's use binary interaction parameters, δ, to improve the accuracy of calculated phase compositions.

The use of pseudocomponents is required because crude oils contain hundreds of hydrocarbon constituents (Section 2.2). Even if all components could be identified, and the amount of each determined, the computational demands of phase equilibria calculations would be too high for use in compositional simulations of the CO_2 flood process, for example. Some uncertainty inevitably arises from the lumping of real components into pseudocomponents, however, because the parameters required for EOS calculations (P_c, T_c, ω, δ) cannot be measured directly. The approach most commonly used is to estimate P_c, T_c, and ω from correlations and to adjust those values and δ's to improve agreement between calculated phase behavior and observations from PVT experiments [20]. The disadvantage of that approach is that time-consuming PVT experiments are required if accurate phase equilibria calculations are to be made.

In this chapter, another approach to crude oil characterization is proposed for CO_2 flood applications, and the proposed method is investigated to determine whether it can make reasonably accurate predictions of CO_2/crude oil phase behavior. A key part of the characterization procedure is the use of SFC. Mixtures of hydrocarbons are separated by SFC because hydrocarbon components partition differently between the mobile CO_2 phase and the stationary phase in a packed column. Thus, the physical mechanism that produces the separation is similar to the mechanism that produces high displacement efficiency in a multicontact miscible CO_2 flood. SFC with CO_2 as a carrier is used in two ways: the composition of the oil is determined by performing simulated distillation using SFC, and SFC is used to estimate δ's not available elsewhere for CO_2 and moderately heavy hydrocarbon components, as shown in the previous section.

The proposed characterization procedure was tested for three CO_2/crude oil mixtures. Reported in this section are comparisons of predicted phase behavior with PVT observations for mixtures of CO_2 and oil from the Means, Maljamar, and Wasson fields.

Characterization Procedure

The approach to crude oil characterization taken here is specialized for mixtures of oil with CO_2 and, with CO_2-enhanced oil recovery in mind, is based upon how the components of a crude oil partition from an oil-rich phase into a CO_2-rich phase. The intent is to group hydrocarbon that partition similarly into dense CO_2. The proposed lumping procedure is:

1. Acquire a few milliliters of the crude oil to be studied, and determine its carbon number distribution by simulated distillation using SFC. Simulated distillation is a commonly used laboratory technique for characterizing crude oils [131, 17, 74, 124].

   Although simulated distillation is usually performed by gas chromatograph, SFC is used here because the elution order of the components during an SFC run depends on how the components partition into the CO_2 mobile phase. Thus, SFC is a natural tool for lumping hydrocarbons because components that elute together partition into CO_2 together.

   Simulated distillation typically results in 37 or so carbon number fractions.

2. Use an EOS to perform a flash calculation for a mixture of CO_2 with the crude oil (represented by carbon number fractions) at a pressure and temperature in the range of interest. Adjust the overall mole fraction of CO_2 so that a two-phase mixture results. The estimated K value for each carbon number fraction is obtained from this calculation. (The critical pressure, critical temperature, acentric factor, and molecular weight assigned to each carbon number fraction are taken from correlations that are included in the EOS computer program.)

3. Group the carbon number fractions into a small number of pseudocomponents so that the difference between the K value of each carbon number fraction and the K value of the pseudocomponent to which it is assigned is minimized—the lumping scheme of Newley and Merrill [88], except that they used the K values of the oil components at the oil's dew-point pressure without additional CO_2. This minimization procedure can be expressed mathematically. Assume that we wish to group N_c carbon number fractions (index i) into N_{pc} pseudocomponents (index j). The jth pseudocomponent group is given the label $m(j), j = 1, 2, \ldots, N_{pc}$.

   The objective function, σ, to be minimized is given by [88]

$$\sigma = \sum_{j=1}^{N_{pc}} \sum_{i \in m(j)} \left(\frac{K_i - \bar{K}_j}{K_i} \right)^2 \tag{2.14}$$

   where

$$K_i = y_i / x_i \tag{2.15}$$

$$\bar{K}_j = \sum_{i \in m(j)} y_i \Big/ \sum_{i \in m(j)} x_i \tag{2.16}$$

and y_i is the mole fraction of carbon number fraction i in the vapor phase, and x_i is the mole fraction in the liquid phase.

4. Estimate P_c, T_c, ω, and molecular weight (MW) for each pseudocomponent. This is done by obtaining those values for each carbon number fraction and using the mixing rules taken from Newley and Merrill [88]. In addition, δ's must be assigned.

5. Use an appropriate EOS to calculate the desired phase diagram. In the examples that follow, the Peng-Robinson EOS [103] was used.

Results

The proposed lumping scheme was tested for mixtures of CO_2 with Means stock tank oil. The crude oil was characterized according to the scheme outlined above, and the Peng-Robinson EOS was used to generate a phase diagram, which is compared to experimental results.

The Means oil comes from the San Andres unit of the Permian Basin in Andrews County, Texas [77]. Table 2.10 presents the simulated distillation results obtained by SFC for Means stock tank oil. The first three components are specific compounds; the other components are carbon number fractions. The weight percent values come directly from simulated distillation. Those values are converted to mole percent values (z) using the molecular weight of each component or carbon number fraction. The properties of C_{45} were used, arbitrarily, for the C_{41+} fraction.

To estimate the K values needed in the Newley-Merrill lumping scheme, a flash calculation was performed for a mixture of Means stock tank oil and 80 mol % CO_2 at 90°F and 1000 psia. The results of that flash—the K values and liquid phase mole fraction (x) of each carbon number fraction or component—are given in Table 2.11. The term w is the mole percent of each of the components or carbon number fractions for the flash calculation.

Table 2.11 includes the results of the pseudocomponent lumping scheme. Seven pseudocomponents were chosen. Seven pseudocomponents are sufficient to give reasonable resolution of the mixture composition. Each pseudocomponent group is enclosed in horizontal lines along with P_c, T_c, ω, and MW estimated for each pseudocomponent. The term z is the mole percent of each pseudocomponent. The binary interaction parameter between each pseudocomponent and CO_2 (δ_{12}) was taken to be that for one of the n-alkanes near the middle of the lumped carbon number fractions. Those values were taken from Deo *et al.* [26] and from SFC experiments. The source of each binary interaction parameter is indicated in the table. All other binary interaction parameters were set to zero.

The Peng-Robinson EOS was used with the pseudocomponent representation of the CO_2/Means stock tank oil to calculate a pressure-composition phase diagram. The results are presented as solid lines in Fig. 2.6. In addition, Fig. 2.6 shows the results of PVT experiments for the Means stock tank oil [130]. The points are actual experimental data; the dashed lines indicate interpolation or extrapolation.

The overall agreement in Fig. 2.6 is fair. Large differences between the calculated and experimental results occur in the liquid-liquid region. No parameters were adjusted in calculating that phase diagram.

Pressure-composition phase diagrams of the type shown in Fig. 2.6 are usually sensitive to the δ_{12} between CO_2 and the high-MW pseudocomponent [68]. As discussed in

Table 2.10: Composition of Means and Maljamar stock tank oils by simulated distillation using SFC.

	Means		Maljamar	
	(weight %)	z (mol %)	(weight %)	z (mol %)
n-C_4	0.43	1.68	0.22	0.81
i-C_5	0.86	2.71	0.46	1.33
n-C_5	0.86	2.71	0.46	1.33
C_6	1.57	4.16	1.81	4.40
C_7	2.85	6.76	3.63	7.93
C_8	3.89	8.28	5.16	10.1
C_9	3.35	6.30	5.04	8.72
C_{10}	3.55	6.03	4.61	7.21
C_{11}	3.07	4.76	3.88	5.53
C_{12}	3.62	5.12	4.44	5.77
C_{13}	2.83	3.68	3.30	3.95
C_{14}	3.22	3.86	3.51	3.87
C_{15}	3.06	3.38	3.47	3.53
C_{16}	2.89	2.96	4.00	3.78
C_{17}	3.19	3.06	3.14	2.78
C_{18}	2.64	2.39	2.32	1.94
C_{19}	2.29	1.98	2.47	1.97
C_{20}	2.23	1.85	2.45	1.87
C_{21}	2.19	1.71	2.46	1.77
C_{22}	2.20	1.67	2.01	1.40
C_{23}	2.12	1.55	2.45	1.64
C_{24}	2.05	1.44	1.87	1.21
C_{25}	1.38	0.93	1.80	1.12
C_{26}	2.00	1.30	2.11	1.27
C_{27}	1.36	0.86	1.63	0.95
C_{28}	1.99	1.22	1.60	0.90
C_{29}	1.35	0.80	1.59	0.87
C_{30}	1.31	0.76	1.58	0.84
C_{31}	1.49	0.84	1.51	0.78
C_{32}	1.22	0.67	1.45	0.73
C_{33}	1.15	0.61	1.03	0.51
C_{34}	1.23	0.64	1.30	0.62
C_{35}	1.15	0.59	1.19	0.56
C_{36}	0.96	0.48	1.14	0.53
C_{37}	1.18	0.58	0.80	0.36
C_{38}	0.65	0.31	1.02	0.45
C_{39}	0.93	0.44	0.94	0.41
C_{40}	0.74	0.34	0.67	0.28
C_{41+}	25.0	10.6	15.5	6.01

Table 2.11: Results of flash and lumping of Means stock tank oil with 80 mol % CO_2 at 90°F and 1000 psia.

				Lumping Results					
	K	w (mol %)	x (mol %)	z (mol %)	P_c (atm)	T_c (K)	ω	MW	δ_{12}
CO_2	1.90×10^{0}	80.00	52.31		72.80	304.2	0.225	44.0	
n-C_4	1.98×10^{-1}	0.337	0.639	38.6	28.26	576.1	0.352	102	0.109[a]
i-C_5	1.21×10^{-1}	0.543	1.126						
n-C_5	1.02×10^{-1}	0.543	1.152						
C_6	5.54×10^{-2}	0.831	1.875						
C_7	2.97×10^{-2}	1.352	3.158						
C_8	1.74×10^{-2}	1.655	3.933						
C_9	9.49×10^{-3}	1.261	3.029						
C_{10}	5.42×10^{-3}	1.206	2.915						
C_{11}	3.12×10^{-3}	0.951	2.306	23.8	19.43	699.4	0.556	179	0.110[a]
C_{12}	1.77×10^{-3}	1.024	2.487						
C_{13}	1.05×10^{-3}	0.736	1.791						
C_{14}	6.06×10^{-4}	0.772	1.878						
C_{15}	3.47×10^{-4}	0.676	1.646						
C_{16}	2.04×10^{-4}	0.593	1.443						
C_{17}	1.25×10^{-4}	0.613	1.492	14.2	14.27	786.1	0.722	270	0.099[a]
C_{18}	8.44×10^{-5}	0.479	1.166						
C_{19}	5.85×10^{-5}	0.396	0.965						
C_{20}	3.83×10^{-5}	0.369	0.899						
C_{21}	2.65×10^{-5}	0.343	0.834						
C_{22}	1.79×10^{-5}	0.334	0.813						
C_{23}	1.28×10^{-5}	0.309	0.753						
C_{24}	2.17×10^{-6}	0.288	0.702	5.75	11.37	844.2	0.999	347	0.102[b]
C_{25}	1.29×10^{-6}	0.186	0.454						
C_{26}	8.29×10^{-7}	0.261	0.635						
C_{27}	5.32×10^{-7}	0.172	0.419						
C_{28}	3.40×10^{-7}	0.244	0.593						
C_{29}	2.38×10^{-7}	0.161	0.392	3.68	9.82	881.5	1.108	403	0.063[a]
C_{30}	1.50×10^{-7}	0.151	0.369						
C_{31}	1.01×10^{-7}	0.168	0.409						
C_{32}	6.70×10^{-8}	0.134	0.326						
C_{33}	4.64×10^{-8}	0.123	0.299						
C_{34}	3.28×10^{-8}	0.128	0.312	14.0	7.26	954.1	1.317	520	0.006[c]
C_{35}	2.37×10^{-8}	0.118	0.287						(0.1)[d]
C_{36}	1.67×10^{-8}	0.096	0.233						
C_{37}	1.26×10^{-8}	0.116	0.282						
C_{38}	8.88×10^{-9}	0.062	0.152						
C_{39}	6.81×10^{-9}	0.087	0.213						
C_{40}	4.85×10^{-9}	0.068	0.166						
C_{41+}	1.37×10^{-9}	2.112	5.143						

[a]Taken from Deo et al. (1989) for an n-alkane near the middle of the pseudocomponent.
[b]The average of the two SFC-determined δ_{12}'s for n-C_{24} and n-C_{28}.
[c]The SFC-determined δ_{12} for n-C_{36}.
[d]A more reasonable value.

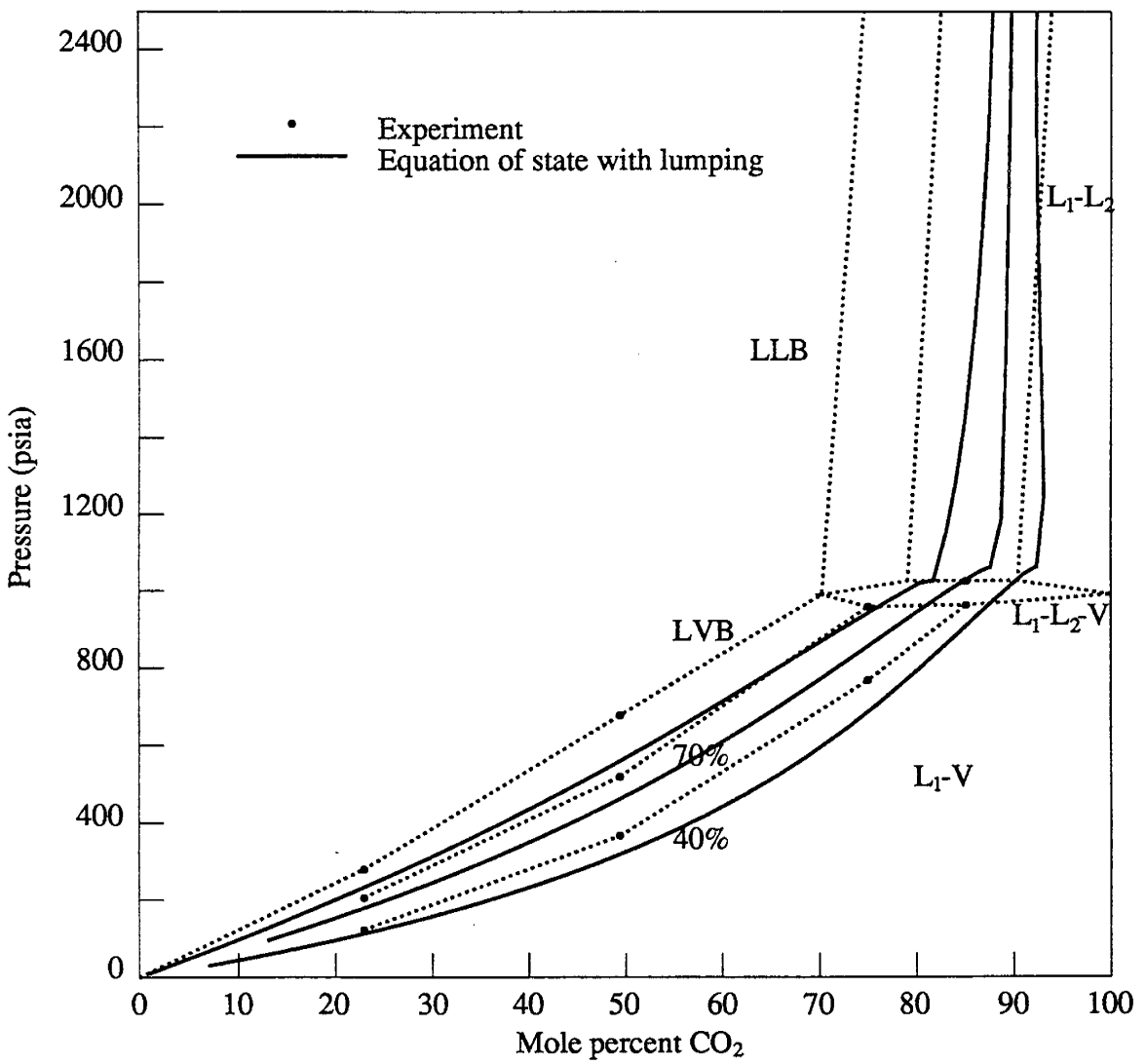

Figure 2.6: Pressure-composition phase diagram for the CO_2/Means stock tank oil mixture at 90°F. Comparison of experiments [130] and calculations.

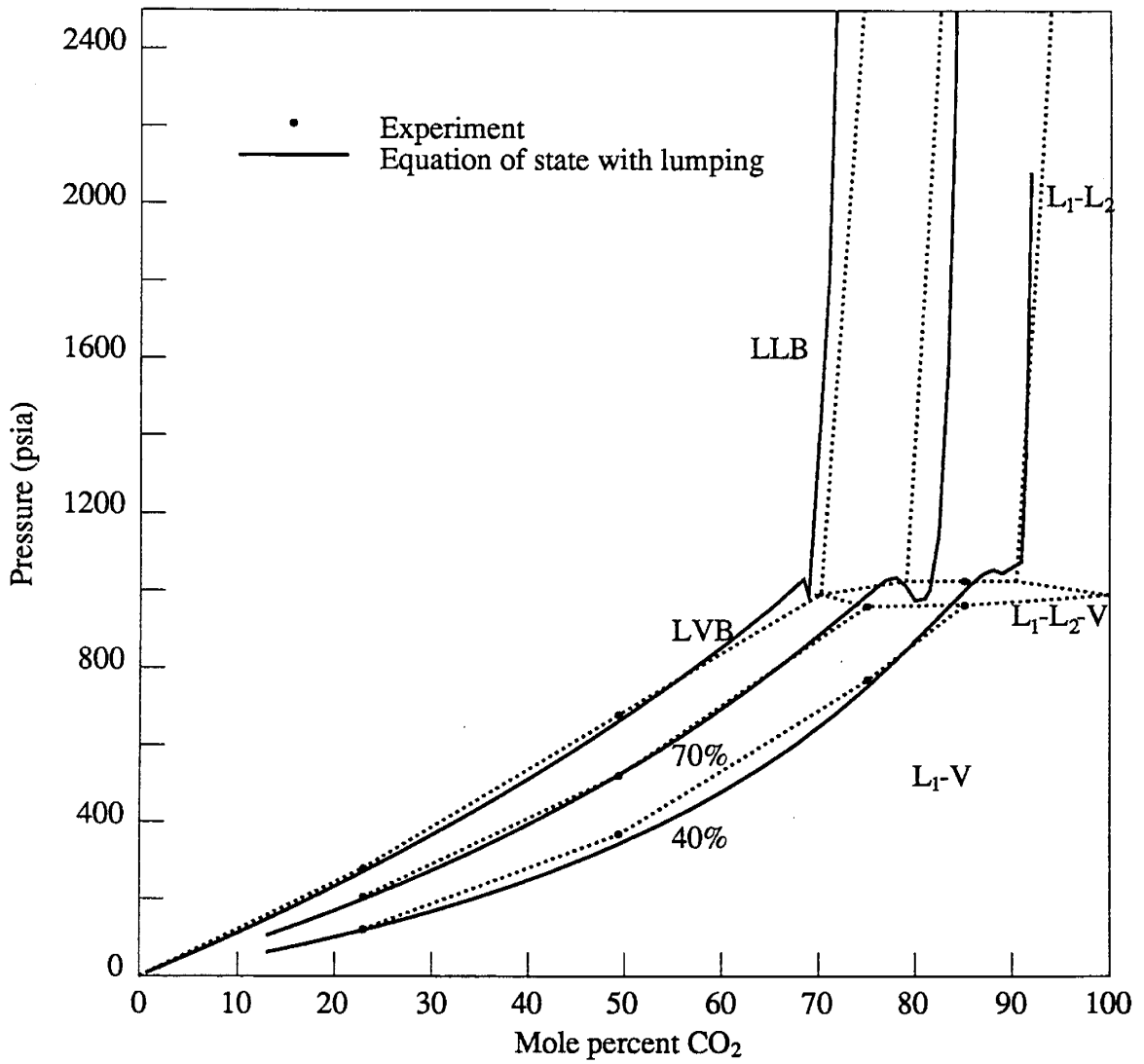

Figure 2.7: Pressure-composition phase diagram for the CO_2/Means stock tank oil mixture at 90°F. Comparison of experiments [130] and calculations with δ_{12} for the CO_2/high-MW pseudocomponent pair equal to 0.1.

Section 2.1.2, however, δ_{12} for very high-MW hydrocarbons could not be determined accurately using SFC. As a result, the value for that δ_{12} was changed. A value of 0.1 was chosen because that number is roughly in line with the other binary interaction parameters (Table 2.11). The results of this recalculated phase diagram are shown in Fig. 2.7. The agreement is much improved.

A three-phase region was observed experimentally, but could not be generated using the Peng-Robinson EOS and the pseudocomponent properties given in Table 2.11. Adjustments to the properties of the heavy hydrocarbon pseudocomponent could be made to force the Peng-Robinson EOS to match the observed three-phase region [68].

Near the three-phase region, the EOS calculations yield a peculiar dip in the lines. A possible explanation for this quirk is that the EOS computer program calculates a point on the saturation, or constant percent volume line, by starting with the previously calculated point, increasing the mole percent CO_2 by a small increment, and calculating the pressure

iteratively until the equilibrium conditions are satisfied. When a mole percent CO_2 addition places the mixture slightly out of the L_1-V region and into the L_1-L_2 region, the equation of state may still find a metastable, L_1-V equilibrium state. That solution extends the line with the same L_1-V trend. However, with additional increases in the mole percent CO_2, the metastable state no longer exists, and the EOS finds the stable, L_1-L_2 equilibrium state. When this occurs, the pressure of the mixture drops because a more stable equilibrium state has been found, and the calculated phase diagram line exhibits a sharp, downward bend. The prediction of false phase-equilibria solutions using an EOS is also explained by Baker *et al.* [4].

The above results show that the initialization scheme presented in this section can be used to predict the phase behavior of a CO_2/crude oil mixture. Slight adjustment of δ_{12} between CO_2 and the high-MW pseudocomponent can improve the agreement to experimental results.

Similar agreement was also observed for mixtures of CO_2 with Means stock tank oil at 105°F and 120°F [123, 125].

A second stock tank oil was studied in order to test the characterization procedure further. That oil comes from the Maljamar Field of Lea County, New Mexico. Table 2.10 presents the carbon number distribution determined by simulated distillation using SFC. The weight percent values were converted to mole percent values using the same carbon number fraction MW's that were used for the Means stock tank oil. Instead of pressure-composition phase diagrams, a ternary diagrams will be used to describe the CO_2/crude oil phase behavior.

Fig. 2.8 presents a ternary phase diagram of mixtures of CO_2 and Maljamar stock tank oil at 160°F and 1600 psia. As before, the phase behavior was computed using the characterization scheme described before and compared with PVT observations [121]. The Peng-Robinson EOS was used to perform a flash calculation for a mixture of 80 mol % CO_2 and Maljamar crude oil, which is represented by the carbon number fractions. The results of that calculation, performed at 160°F and 1600 psia, are given in Table 2.12.

Table 2.12 presents the optimized pseudocomponents. An additional pseudocomponent was created by splitting the C_{11}–C_{16} pseudocomponent into a C_{11}–C_{12} pseudocomponent and a C_{13}–C_{16} pseudocomponent. This was done to facilitate graphing because the ternary diagram divides the crude oil at the C_{12} and C_{13} carbon number fractions. The value of the binary interaction parameter between CO_2 and the heaviest pseudocomponent was kept at the SFC-determined value of 0.006.

Using the eight pseudocomponents of Table 2.12, the Peng-Robinson EOS was used to calculate a ternary diagram for mixtures of CO_2 and the Maljamar stock tank oil at 160°F and 1600 psia. The PVT-observed and calculated phase compositions shown in Fig. 2.8 agree well. The vapor phase compositions agree very well. The calculated liquid phase compositions contain about 2 mol % (absolute) less CO_2 than the experimentally determined compositions, which show some scatter. The slopes of the calculated and observed tie lines are similar. The orientation of the tie lines plays an important role in the development of miscibility in CO_2 floods (Section 3). No parameters were adjusted for the calculations presented in Fig. 2.8.

Ternary phase diagrams for CO_2/Maljamar stock tank oil mixtures were generated using the SFC characterization scheme at other temperatures and pressures, and those results were compared with PVT-observed results [123]. Agreement similar to that of Fig. 2.8 was

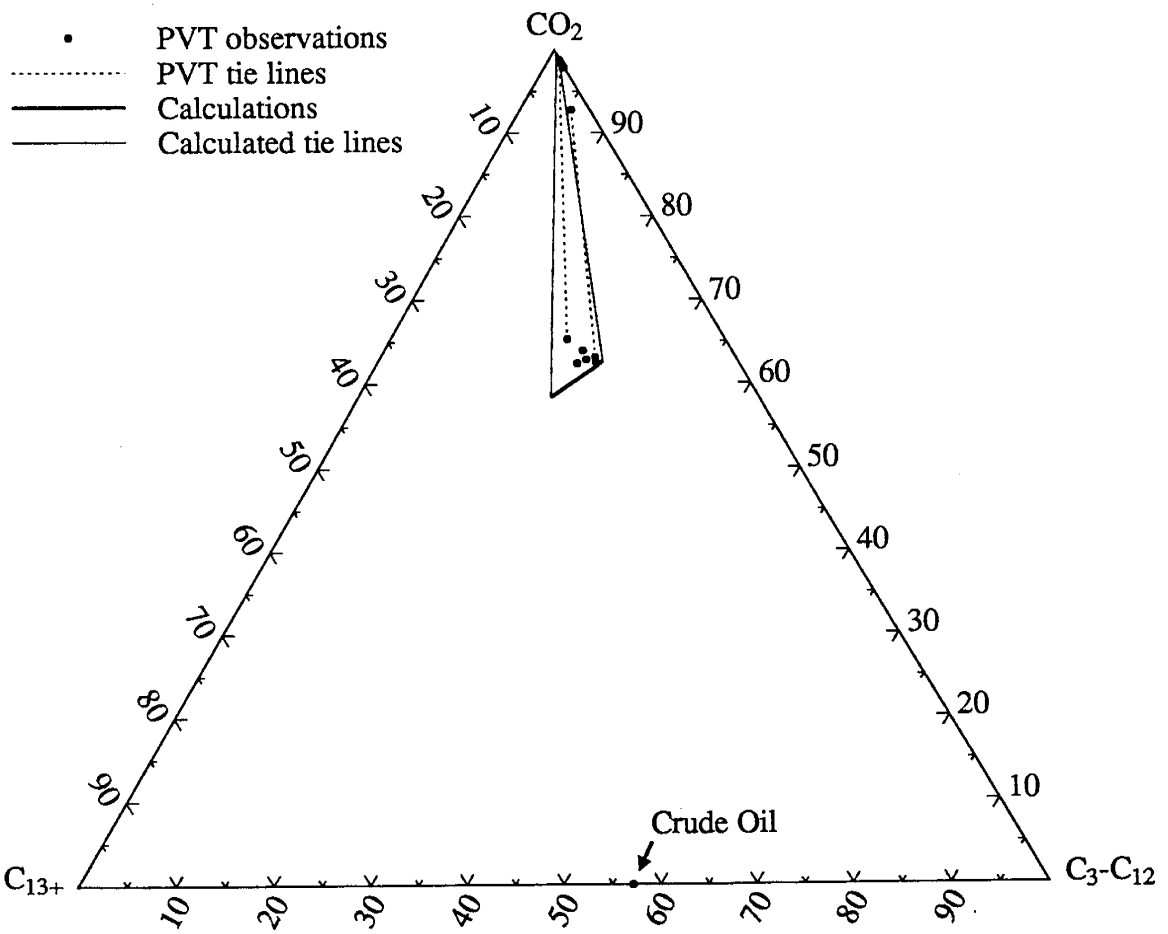

Figure 2.8: Phase behavior of Maljamar stock tank oil with CO_2 at 160°F and 1600 psia. Comparison of PVT observations [121] and calculations.

Table 2.12: Results of flash and lumping of Maljamar stock tank oil with 80 mol % CO_2 at 160°F and 1600 psia.

				Lumping Results					
	K	w (mol %)	x (mol %)	z (mol %)	P_c (atm)	T_c (K)	ω	MW	δ_{12}
CO_2	1.88×10^{0}	80.00	52.36		72.80	304.2	0.225	44.0	
n-C_4	3.32×10^{-1}	0.162	0.269	41.8	28.23	577.9	0.353	107	0.098[a]
i-C_5	2.34×10^{-1}	0.265	0.489						
n-C_5	2.09×10^{-1}	0.265	0.503						
C_6	1.30×10^{-1}	0.881	1.837						
C_7	8.25×10^{-2}	1.585	3.515						
C_8	5.61×10^{-2}	2.021	4.643						
C_9	3.63×10^{-2}	1.743	4.117						
C_{10}	2.44×10^{-2}	1.441	3.462						
C_{11}	1.65×10^{-2}	1.106	2.688	11.3	22.31	655.0	0.476	154	0.104[a]
C_{12}	1.10×10^{-2}	1.155	2.828						
C_{13}	7.57×10^{-3}	0.791	1.947	15.1	18.55	712.8	0.581	198	0.110[a]
C_{14}	5.14×10^{-3}	0.773	1.911						
C_{15}	3.45×10^{-3}	0.705	1.747						
C_{16}	2.38×10^{-3}	0.755	1.873						
C_{17}	1.68×10^{-3}	0.555	1.379	13.4	14.36	784.5	0.718	271	0.099[a]
C_{18}	1.27×10^{-3}	0.388	0.963						
C_{19}	9.84×10^{-4}	0.394	0.979						
C_{20}	7.32×10^{-4}	0.373	0.928						
C_{21}	5.65×10^{-4}	0.354	0.881						
C_{22}	4.28×10^{-4}	0.280	0.698						
C_{23}	3.38×10^{-4}	0.328	0.817						
C_{24}	9.96×10^{-5}	0.242	0.603	5.45	11.45	842.3	0.994	347	0.102[b]
C_{25}	6.97×10^{-5}	0.223	0.556						
C_{26}	5.10×10^{-5}	0.254	0.631						
C_{27}	3.74×10^{-5}	0.190	0.474						
C_{28}	2.74×10^{-5}	0.180	0.449						
C_{29}	2.14×10^{-5}	0.174	0.434	3.73	9.87	879.9	1.103	402	0.063[a]
C_{30}	1.55×10^{-5}	0.168	0.418						
C_{31}	1.17×10^{-5}	0.156	0.390						
C_{32}	8.86×10^{-6}	0.146	0.365						
C_{33}	6.86×10^{-6}	0.101	0.253						
C_{34}	5.41×10^{-6}	0.125	0.311	9.22	7.41	949.8	1.305	512	0.006[c]
C_{35}	4.31×10^{-6}	0.112	0.280						
C_{36}	3.39×10^{-6}	0.105	0.262						
C_{37}	2.78×10^{-6}	0.072	0.179						
C_{38}	2.19×10^{-6}	0.090	0.224						
C_{39}	1.83×10^{-6}	0.081	0.202						
C_{40}	1.45×10^{-6}	0.056	0.141						
C_{41+}	6.13×10^{-7}	1.202	2.992						

[a]Taken from Deo et al. (1989) for an n-alkane near the middle of the pseudocomponent.
[b]The average of the two SFC-determined δ_{12}'s for n-C_{24} and n-C_{28}.
[c]The SFC-determined δ_{12} for n-C_{36}.

obtained except when the mixture temperature was near the critical temperature of CO_2 (88°F) and the mixture pressure was above the critical pressure of CO_2 (1070 psia). For those conditions, liquid-liquid behavior is observed, and predictions of phase behavior are difficult. In that case, the binary interaction parameter between CO_2 and the high-MW pseudocomponent was adjusted to force good agreement between the calculated and observed phase behavior.

All of the previously studied oils are stock tank oils; however, fluids found in petroleum reservoirs often contain significant concentrations of dissolved gas. In order to test the characterization scheme for such mixtures, Wasson tank oil + 312 scf/bbl gas at 90°F was studied. An actual sample of Wasson oil was not available for simulated distillation by SFC in our laboratory. Instead, the carbon number distribution of the Wasson reservoir fluids measured by Orr and Jensen [95] using gas chromatography was used. As a result, the first step in the crude oil lumping procedure—determination of the oil composition using SFC—was skipped.

As might be expected, crude oil characterization becomes more complicated for reservoir fluids that contain large amounts of methane because the assumption that all hydrocarbon/hydrocarbon binary interaction parameters can be set to zero is no longer valid. This is due to the small size of the methane molecules relative to the other hydrocarbon molecules. In the EOS calculations that follow, a constant binary interaction parameter is assigned to each pair of pseudocomponents that includes the lowest-MW pseudocomponent. That binary interaction parameter is determined by matching the bubble-point pressure of the crude oil without CO_2. Therefore, the bubble point of the reservoir fluid is assumed to be known beforehand, and the results that follow only test the validity of the SFC characterization scheme for the effect of adding CO_2 to the mixture.

Table 2.13 gives the results of the flash of Wasson stock tank oil + 312 scf/bbl gas with 60 mol % CO_2 at 90°F and 1500 psia. Table 2.13 also presents the results of the lumping of the carbon number fractions into pseudocomponents. Without constraints, the lumping procedure puts CO_2 and some of the low-MW components into the same pseudocomponent. However, in order to facilitate the plotting of the results on the pressure-composition phase diagrams, the lumping computer program was modified so that one pseudocomponent consists only of CO_2. The binary interaction parameter between the lowest-MW pseudocomponent and all other pseudocomponents, including CO_2, was set to a constant value of 0.13. That value was determined by matching the 900 psia bubble-point pressure of the reservoir fluid without added CO_2. All other hydrocarbon/hydrocarbon binary interaction parameters were kept at zero, and the CO_2/hydrocarbon binary interaction parameters (except that for the CO_2/lowest-MW pseudocomponent pair) were determined as before.

Fig. 2.9 shows both the PVT-observed and the calculated results. The PVT observations shown were constructed from the raw experimental data provided by Jensen and Orr [14]. Unlike the previously presented phase diagrams, Fig. 2.9 exhibits a critical point (C).

The calculated results shown in Fig. 2.9 were obtained using the Peng-Robinson EOS and the characterization scheme given in Table 2.13. The calculated phase diagram does not show a critical point. Usually, more pseudocomponents and tuning are required to match a critical point and sharp bends in constant liquid volume fraction lines. CO_2 floods are usually not designed at conditions near a critical point for typical CO_2/oil mixtures, however, so accurate representation of that portion of the phase diagram is frequently not

Table 2.13: Results of flash and lumping of Wasson stock tank oil + 312 scf/bbl gas with 60 mol % CO_2 at 90°F and 1500 psia.

				Lumping Results					
	K	w (mol %)	x (mol %)	z (mol %)	P_c (atm)	T_c (K)	ω	MW	δ_{12}
CO_2	1.66×10^{0}	60.00	49.48		72.80	304.2	0.225	44.0	
C_1	1.31×10^{0}	8.601	7.816	35.1	45.26	259.1	0.063	23.9	0.13[a]
C_2	7.91×10^{-1}	2.983	3.197						
C_3	5.66×10^{-1}	2.443	2.838						
i-C_4	4.70×10^{-1}	0.484	0.583	27.1	30.01	548.8	0.317	96.5	0.116[b]
n-C_4	4.21×10^{-1}	0.484	0.594						
i-C_5	3.47×10^{-1}	0.686	0.867						
n-C_5	3.21×10^{-1}	0.686	0.877						
C_6	2.20×10^{-1}	1.344	1.791						
C_7	1.64×10^{-1}	1.851	2.529						
C_8	1.29×10^{-1}	3.111	4.316						
C_9	9.77×10^{-2}	2.175	3.060						
C_{10}	7.59×10^{-2}	1.596	2.267	16.2	21.38	670.8	0.504	163	0.104[b]
C_{11}	5.93×10^{-2}	1.148	1.643						
C_{12}	4.60×10^{-2}	1.156	1.665						
C_{13}	3.64×10^{-2}	0.972	1.406						
C_{14}	2.85×10^{-2}	0.896	1.301						
C_{15}	2.22×10^{-2}	0.712	1.037						
C_{16}	1.77×10^{-2}	0.644	0.940	9.15	14.90	774.6	0.699	261	0.109[b]
C_{17}	1.42×10^{-2}	0.632	0.924						
C_{18}	1.20×10^{-2}	0.448	0.655						
C_{19}	1.03×10^{-2}	0.548	0.802						
C_{20}	8.59×10^{-3}	0.384	0.563						
C_{21}	7.35×10^{-3}	0.356	0.522						
C_{22}	6.23×10^{-3}	0.336	0.493						
C_{23}	5.41×10^{-3}	0.312	0.458						
C_{24}	2.32×10^{-3}	0.284	0.417	3.01	11.51	841.1	0.990	346	0.102[c]
C_{25}	1.86×10^{-3}	0.268	0.394						
C_{26}	1.53×10^{-3}	0.256	0.376						
C_{27}	1.26×10^{-3}	0.164	0.241						
C_{28}	1.04×10^{-3}	0.232	0.341						
C_{29}	8.96×10^{-4}	0.156	0.229	9.53	8.21	925.8	1.236	472	0.1[d]
C_{30}	7.39×10^{-4}	0.152	0.224						
C_{31}	6.22×10^{-4}	0.148	0.218						
C_{32}	5.25×10^{-4}	0.204	0.300						
C_{33}	4.50×10^{-4}	0.112	0.165						
C_{34}	3.91×10^{-4}	0.104	0.153						
C_{35}	3.41×10^{-4}	0.132	0.194						
C_{36}	2.96×10^{-4}	0.072	0.106						
C_{37+}	1.81×10^{-4}	2.731	4.019						

[a] All binary interaction parameters with this pseudocomponent are set to 0.13.
[b] Taken from Deo et al. (1989) for an n-alkane near the middle of the pseudocomponent.
[c] The average of the SFC-determined δ_{12}'s for n-C_{24} and n-C_{28}.
[d] A reasonable value.

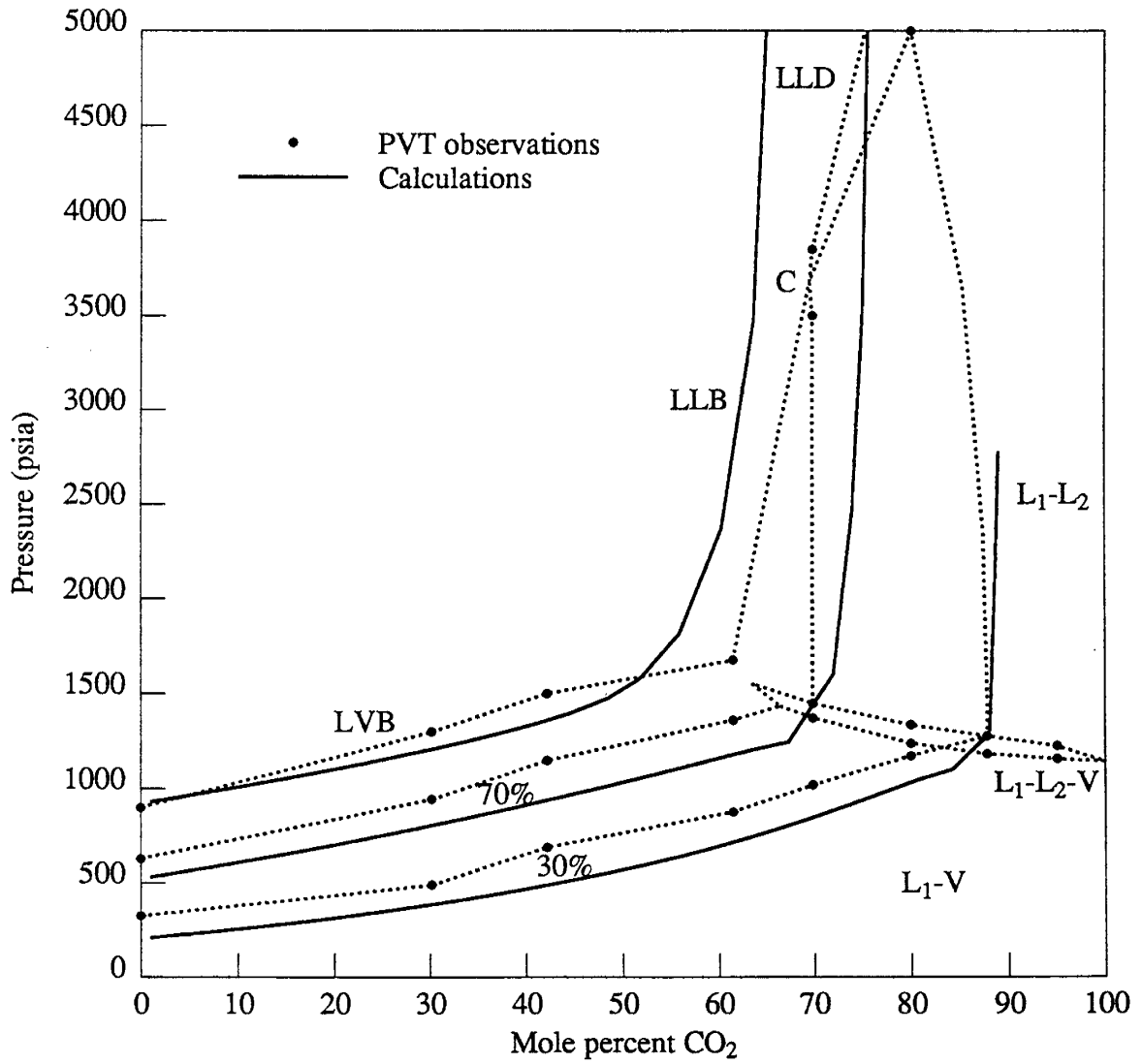

Figure 2.9: Phase behavior of Wasson stock tank oil + 312 scf/bbl gas with CO_2 at 90°F. Comparison of PVT observations [14] and calculations.

required. Agreement similar to that of Fig. 2.9 was obtained for other mixtures of CO_2 and Wasson stock tank oil with various amounts of gas and at other temperatures [123].

Discussion

The results of Sections 2.1.2 and 2.1.3 show that it is possible in some cases to predict with reasonable accuracy the phase behavior of CO_2/hydrocarbon mixtures using SFC. The main advantage of SFC over the use of PVT experiments is that SFC experiments are easier to perform, yet still involve direct observation of CO_2/hydrocarbon interactions.

One limitation in using SFC is that the properties (P_c, T_c, and ω) of the hydrocarbons injected into the SFC column must be known for EOS calculations; however, these properties are not known accurately for heavy components. Also, the correlation used for assigning molecular weights to the carbon number fractions may not be accurate for some oils. The characterization scheme will probably work best for oils that are not too aromatic because CO_2/n-alkane binary interaction parameters were used in characterizing the pseudocomponents. Characterization by SFC could be extended to other systems with determination of $\bar{V}_1^{\infty,s}$ for other classes of compounds. Finally, prediction of phase behavior at high pressures (> 2000 psi), where liquid-liquid behavior is observed, was found to be difficult.

Despite those limitations, the crude oil characterization scheme described in Sections 2.1.2 and 2.1.3 offers several possible applications for studying CO_2 floods. For example, SFC can be used to quickly estimate the phase behavior of CO_2/oil mixtures for the initial evaluation of a potential CO_2 flood. Once PVT studies have been performed, SFC can be used to help develop an EOS model because SFC adds additional experimental constraints to that model.

2.1.4 Solubility in Dense CO_2

In addition to CO_2-enhanced oil recovery applications, SFC and thermodynamics can be used to estimate solubility of a solute in CO_2. This application is described in the work of Bartle *et al.* [6]. Their work is investigated further here.

First, a derivation of the equation that relates the chromatographic capacity factor to solubility is presented. Second, experimentally determined solubilities are compared to published values.

Thermodynamic Development

Rewriting Eq. 2.1 for the mobile CO_2 carrier fluid phase gives

$$\bar{G}_1^{\mathrm{id,m}} = G_1^{\mathrm{o,m}} + RT \ln x_1^{\mathrm{m}}. \tag{2.17}$$

Combination of Eqs. 2.2, 2.3, and 2.17 yields

$$\ln\left(k_1' \frac{V^{\mathrm{s}}}{V^{\mathrm{m}}} \frac{V^{\mathrm{t,m}}}{V^{\mathrm{t,s}}}\right) = \frac{1}{RT}(\bar{G}_1^{\mathrm{id,m}} - RT \ln x_1^{\mathrm{m}} - G_1^{\mathrm{o,s}}). \tag{2.18}$$

After some rearrangement, this equation becomes

$$x_1^{\mathrm{m}} = \frac{V_2}{k_1'}\left\{\frac{V^{\mathrm{t,s}}}{V^{\mathrm{s}}V^{\mathrm{t,m}}} \exp\left[\frac{1}{RT}(\bar{G}_1^{\mathrm{id,m}} - G_1^{\mathrm{o,s}})\right]\right\}, \tag{2.19}$$

where V^{m} has been replaced by V_2 because the mobile phase is essentially pure CO_2. If the solute-rich phase remains in the pure solid state, the expression in braces is approximately constant with respect to pressure, and Eq. 2.19 becomes [6]

$$x_1^{\mathrm{m}} = \frac{V_2}{k_1'} C(T), \tag{2.20}$$

where C is a constant that is a function of temperature and the identity of solute 1. Eq. 2.20 can be rewritten as

$$x_1^{\mathrm{m}} = \frac{C(T)}{k_1' \rho_2}, \tag{2.21}$$

where ρ_2 is the density of the CO_2, and $C(T)$, therefore, may have different units from the $C(T)$ of Eq. 2.20.

Eq. 2.21 can be used to determine the solubility of a solute in CO_2, x_1^{m}. The capacity factor of the solute, k_1', can be determined using SFC, and the density of CO_2, ρ_2, using an EOS. Both are determined at the pressure and temperature at which the solubility value is desired. In order to calculate C, Eq. 2.21 can be rearranged to yield

$$C = k_1' x_1^{\mathrm{m}} \rho_2. \tag{2.22}$$

One solubility measurement for the solute at the desired temperature must be be known.

Once the value of C is fixed, the solubility of the solute in CO_2 at the same temperature can be determined at another pressure by measuring the capacity factor of the solute at that pressure and using Eq. 2.21 to convert this capacity factor to solubility.

Results and Discussion

The procedure described above was used to determine the solubility of naphthalene in CO_2. The results are compared with measured values. McHugh and Paulaitis [79] measured the solubility of naphthalene in CO_2 over a range of pressure at four temperatures: 95°F, 131°F, 141°F, and 149°F. These solubilities are given in Tables 2.14–2.17, one table for each of the four temperatures.

Table 2.14 will be used to illustrate how SFC capacity factors are converted into solubility values. The first column gives the pressures at which the published solubility measurements are reported. At each of those pressures and at 95°F, an SFC experiment was performed to calculate the capacity factor of naphthalene. The third column gives the density of pure CO_2 at the stated pressure and temperature.

The next step is to calculate C using Eq. 2.22 and one of the published solubility measurements, the "match point," indicated in Table 2.14 as the row without an error. The other SFC solubilities were calculated using Eq. 2.21. The SFC-derived solubilities are listed in the fourth column and compared with the measured solubilities.

The solubility results of Tables 2.14–2.17 are presented in Fig. 2.10. At 95°F and 131°F, SFC results agree well with the published solubilities of naphthalene in CO_2. The errors are within ±10% except for the 95°F case, for which the solubilities approach zero at low pressure. Also, as the pressure difference between the match point and another solubility measurement gets larger, so does the error, in general.

However, at 141°F the agreement between the SFC results and the data of McHugh and Paulaitis is poor at pressures below the match point. The errors at 149°F are large,

Table 2.14: Solubility of naphthalene in CO_2 (x_1^m) at 95°F. Comparison of SFC and measured [79] results. $C = 0.0144$ g/cm^3.

Pressure (psia)	k_1'	ρ_2 (g/cm^3)	x_1^m (mole fraction) SFC	x_1^m (mole fraction) Published	Error (%)
1260	3.989	0.628	0.00577	0.00750	-23.1
1424	2.967	0.703	0.00692	0.00975	-29.0
1545	2.008	0.733	0.00982	0.01066	-7.9
1930	1.449	0.791	0.01261	0.01410	-10.6
2452	1.104	0.837	0.01563	0.01605	-2.6
2894	0.976	0.866	0.01709	0.01709	
3226	0.894	0.883	0.01829	0.01830	-0.1
3517	0.837	0.897	0.01923	0.01908	0.8
3704	0.808	0.905	0.01976	0.01922	2.8

Table 2.15: Solubility of naphthalene in CO_2 (x_1^m) at 131°F. Comparison of SFC and measured [79] results. $C = 0.0404$ g/cm^3.

Pressure (psia)	k_1'	ρ_2 (g/cm^3)	x_1^m (mole fraction) SFC	x_1^m (mole fraction) Published	Error (%)
1933	3.607	0.586	0.01912	0.02114	-9.5
2084	2.683	0.630	0.02390	0.02544	-6.1
2330	1.958	0.681	0.03030	0.03053	-0.8
2490	1.726	0.706	0.03316	0.03387	-2.1
2537	1.616	0.713	0.03509	0.03473	1.0
2750	1.393	0.739	0.03928	0.03928	
3051	1.177	0.768	0.04471	0.04224	5.8
3242	1.100	0.784	0.04689	0.04366	7.4
3449	1.008	0.799	0.05018	0.04586	9.4
3649	0.939	0.812	0.05297	0.04969	6.6
4174	0.830	0.842	0.05786	0.05382	7.5

Table 2.16: Solubility of naphthalene in CO_2 (x_1^m) at 140°F. Comparison of SFC and measured [79] results. $C = 0.0684$ g/cm^3.

Pressure (psia)	k_1'	ρ_2 (g/cm^3)	x_1^m (mole fraction) SFC	Published	Error (%)
1942	5.261	0.528	0.02461	0.01516	62.
2212	2.857	0.612	0.03914	0.02589	51.
2383	2.198	0.648	0.04799	0.03401	41.
2547	1.821	0.677	0.05551	0.04296	29.
2665	1.715	0.694	0.05746	0.04436	29.
2794	1.511	0.711	0.06370	0.05386	18.
2959	1.348	0.729	0.06956	0.05903	18.
2989	1.334	0.733	0.07000	0.06259	12.
3148	1.209	0.748	0.07559	0.06963	8.6
3154	1.223	0.749	0.07466	0.06990	6.8
3286	1.165	0.760	0.07720	0.07720	
3364	1.121	0.767	0.07960	0.07721	3.1
3422	1.079	0.771	0.08214	0.08306	-1.1
3599	1.024	0.785	0.08511	0.09064	-6.1
3699	0.994	0.792	0.08694	0.09204	-5.5
3739	0.983	0.794	0.08763	0.09583	-8.6
3964	0.939	0.808	0.09008	0.09756	-7.7
4227	0.882	0.823	0.09421	0.09802	-3.9

Table 2.17: Solubility of naphthalene in CO_2 (x_1^m) at 149°F. Comparison of SFC and measured [79] results. $C = 0.0583$ g/cm^3.

Pressure (psia)	k_1'	ρ_2 (g/cm^3)	x_1^m (mole fraction) SFC	Published	Error (%)
2202	3.579	0.561	0.02903	0.02427	19.6
2490	2.515	0.628	0.03691	0.03765	-2.0
2687	1.871	0.661	0.04707	0.04428	6.3
2790	1.717	0.676	0.05015	0.05015	
3089	1.400	0.713	0.05837	0.06440	-9.4
3264	1.272	0.731	0.06265	0.07309	-14.3
3369	1.185	0.741	0.06637	0.07902	-16.0
3476	1.139	0.750	0.06822	0.3206	-78.7
3714	1.035	0.768	0.07327	0.3237	-77.4
3989	0.960	0.787	0.07710	0.2999	-74.3

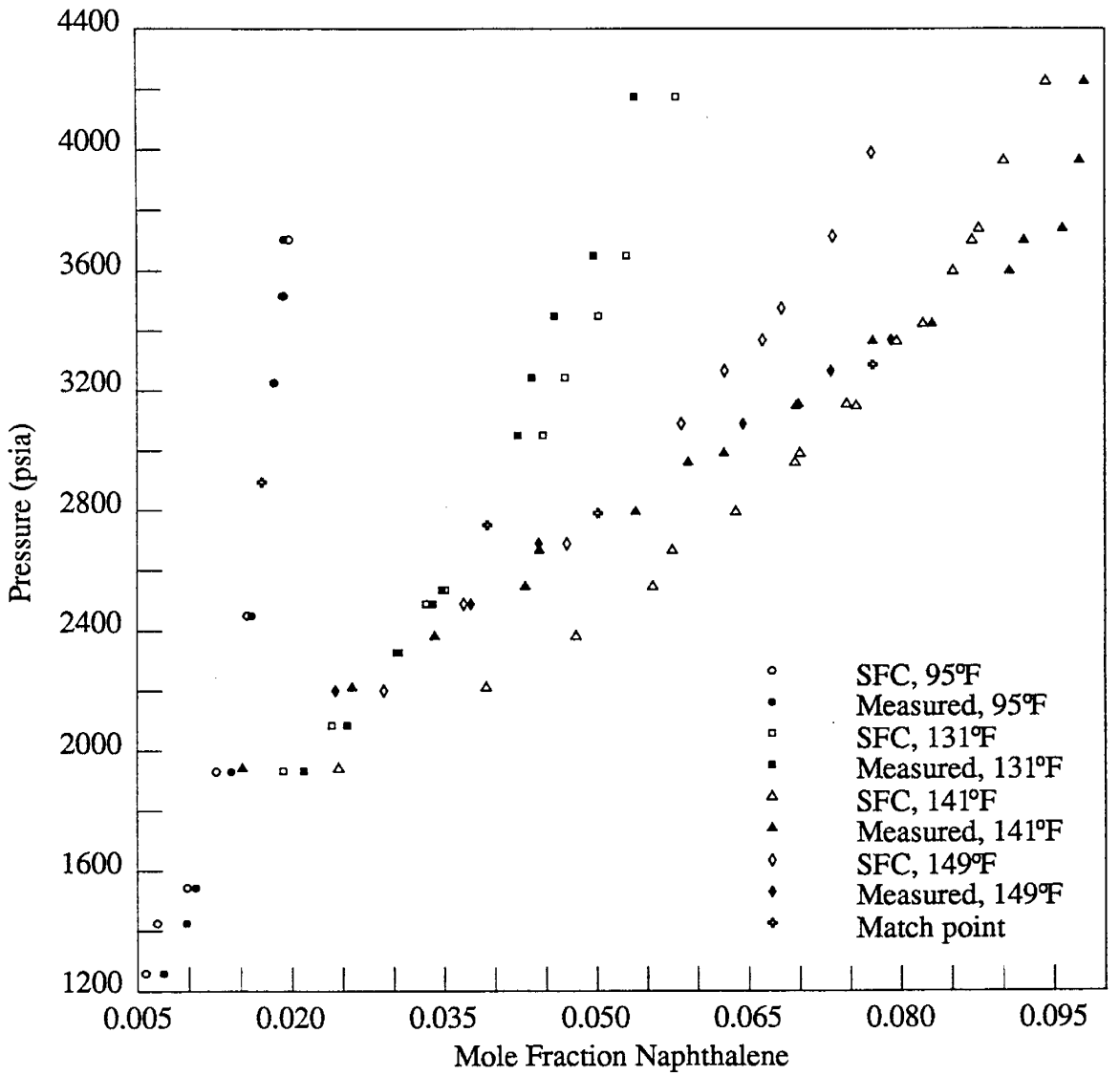

Figure 2.10: Solubility of naphthalene in CO_2. Comparison of SFC and measured [79] results.

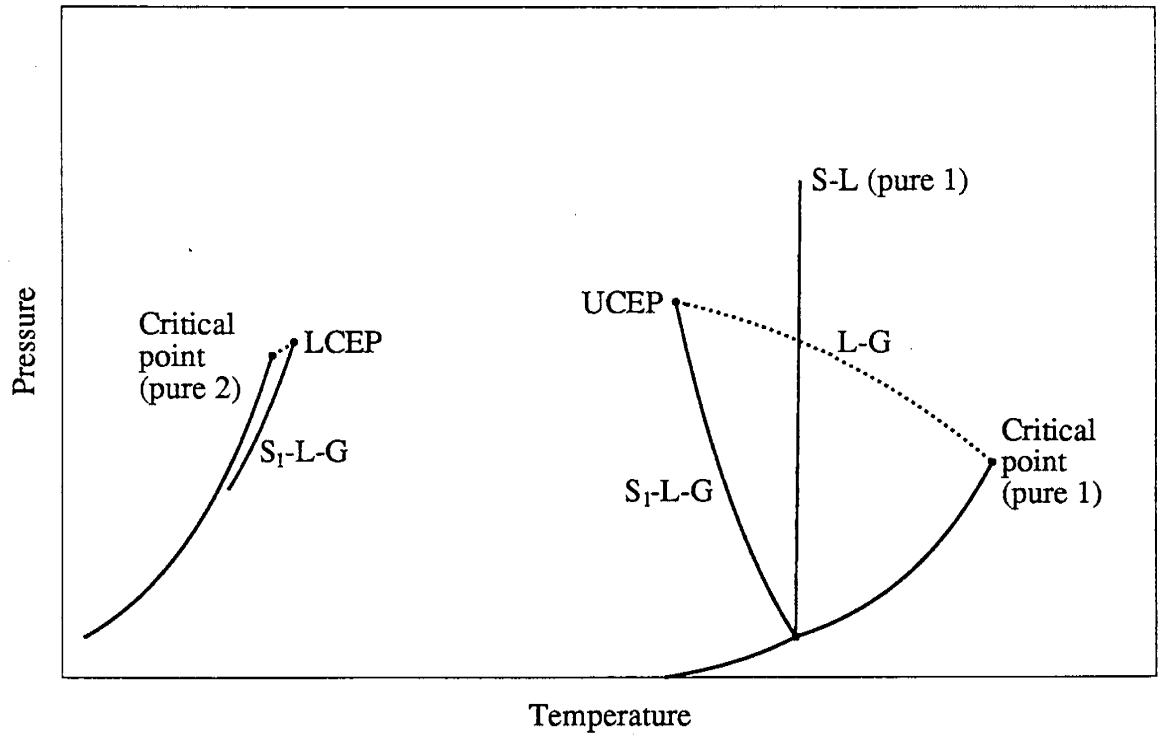

Figure 2.11: Pressure-temperature diagram for a highly asymmetric binary mixture indicating the upper critical end point (UCEP) [115].

too. This behavior can be explained by noting that the upper critical end point for the CO_2/naphthalene binary system is about 145°F and 3500 psi [79]. The upper critical end point temperature is the minimum temperature at which a solute-rich liquid phase can form (Fig. 2.11). As the CO_2/naphthalene mixture temperature approaches the upper critical point end point temperature, the solute-rich phase can no longer be approximated by a pure solid solute. That behavior invalidates one of the assumptions made in the thermodynamic development. Thus, the proximity of the CO_2/naphthalene system to the upper critical end point explains why the SFC-determined solubilities are so different from the measured results at the higher temperatures.

The solubility of a solute becomes quite sensitive to changes in pressure and temperature in the region of the upper critical end point. Table 2.17 shows, for example, that the measured solubility of naphthalene increases considerably at about 3400 psi.

This SFC method of determining the solubility of solids in dense CO_2 has been applied to biphenyl, phenanthrene, anthracene, fluorene, and pyrene with similar results and limitations [123].

2.1.5 Conclusions

1. A method for determining binary interaction parameters of n-alkanes using SFC has been demonstrated.

2. SFC is useful for characterizing crude oils because components that elute together also partition into CO_2 together. A characterization scheme is proposed and tested for mixtures of CO_2 and oil from the Means, Maljamar, and Wasson fields.

3. SFC can also be used to measure solubility of individual hydrocarbons in dense CO_2 provided that the solubility at one pressure is known.

2.2 Component Partitioning in CO_2/Crude Oil Mixtures

Karen D. Hagedorn

The extraction of light to intermediate hydrocarbons from the oil into a CO_2-rich upper phase governs the development of miscibility in a CO_2 displacement process. Therefore, it is important to understand how different types of hydrocarbon compounds present in a crude oil are extracted into this upper phase. Knowledge of how individual components partition can then be extended to show how the distribution of these components in an oil affects the phase behavior of a miscible process.

Miscible processes are usually modelled using compositional simulation. Because of computing time constraints, compositional descriptions for crude oils are generally limited to a small number of pseudocomponents. These pseudocomponents, or cuts, are usually based on chromatographic retention time. This technique, called simulated distillation (SIMDIS, see Section 2.1), assumes that compounds that elute together from a GC behave similarly with respect to the process of interest, in this case extraction by dense CO_2. Knowledge of how different types of components are extracted with respect to elution time is important, therefore, in determining how the hundreds of components present in a crude oil should be assigned to a small number of pseudocomponents in order to represent the total oil composition accurately.

In this section, detailed compositional analyses of crude oils and of samples of equilibrium CO_2-rich and oil rich phases are reported. The composition information, obtained by gas chromatography and mass spectrometry (GC/MS), is the most comprehensive ever obtained for CO_2/crude oil mixtures.

2.2.1 Experimental Apparatus and Procedures

The equipment employed in the experimental portion of this study includes a computerized GC/MS system and a PVT system used to generate the equilibrium phase samples. The experimental GC/MS system consists of a Varian 3400 gas chromatograph in tandem with a Finnigan MAT TSQ 70 mass spectrometer.

Gas Chromatograph

The gas chromatograph serves as an inlet separation device for the mass spectrometer. It is equipped with both on-column and split/splitless injectors. Carrier gas flow is controlled by an inlet pressure controller. Cryogenic cooling of the GC oven is achieved by flash

expansion of liquid CO_2 into the oven. Flow of the coolant is controlled by a solenoid valve, which is actuated by the oven temperature sensor. The GC is connected to the mass spectrometer by a one inch diameter transfer line. The GC column runs through the transfer line and directly into the ion source of the mass spectrometer. The transfer line is maintained at a constant temperature by an auxiliary heater connected to the GC. Control of the GC and transfer line operating conditions can be achieved either through the instrument control capability of the GC/MS operating system or directly from the front of the GC.

Mass Spectrometer

The TSQ 70 instrument used in this study is a triple quadrupole instrument. The instrument is capable of running in single stage (MS) or two-stage (MS/MS) modes. Only the single stage mode was used in the analyses performed.

The basic design of the mass spectrometer includes an ion source, a mass analyzer, and an electron multiplier. The entire system is maintained under high vacuum. As molecules elute from the GC column, they enter the ion source, where they are bombarded with electrons, causing them to fragment into positively charged ions. Ions from the ion source are separated by mass-to-charge ratio (m/z) in the mass analyzer.

The electron multiplier consists of two conversion dynodes and a continuous dynode electron multiplier. Eventually, enough electrons are generated to produce a measurable current at the end of the multiplier, where the electrons are collected by the anode. The current is then processed by the data system to yield the intensity of a given m/z value for a particular scan. The plot of ion intensity vs all m/z values for a particular scan is known as the mass spectrum. The summation of the intensities of all the ions in a particular scan is related to the amount of the component present.

Operating Conditions

The GC column used in all of the analyses was a fused silica capillary column 25m long with an external diameter of 0.32mm. The stationary phase was crosslinked dimethyl polysiloxane with a phase thickness of 0.52 microns. Helium was used as the carrier gas with an inlet pressure of 6 psig. Samples of 0.35μl were injected using the split injection technique. The injector temperature was 300° C. The GC column was temperature programmed with an initial isothermal period at -10° C for 5 minutes, a temperature ramp from -10° to 300° C at 3° C per minute, and a final isothermal period at 300° C for 10 minutes. Thus, the total time for one run was approximately 2 hours. Transfer line temperature was 300° C for the entire run.

Ionization of the sample was achieved by electron impact (EI) ionization with an ionization potential of 70 eV. The mass analyzer was scanned over an m/z range from 50 to 500 mass units in 1 second, representing a carbon number range of about C_5 to C_{30}.

Phase Sample Generation

The phase samples used in this analysis were generated in a conventional PVT system centered around a windowed RUSKA cell enclosed in a constant temperature oven. The volume, and hence the pressure, in the cell was controlled by movement of a mercury interface. The entire system is fully described by Stessman [130].

Phases were sampled individually through the uppermost sampling port of the PVT cell. The sampled phase passed through a densitometer and then was flashed to atmospheric conditions through a back-pressure regulator (BPR). The resultant vapor phase was collected in an evacuated sampling vessel. The liquid phase was collected in a centrifuge tube. Liquid phase amounts were determined by weight, and vapor phase amounts were determined by applying the ideal gas law to the pressure change in the sampling vessel. The vapor phase was immediately passed to a gas chromatograph equipped with a thermal conductivity (TCD) detector. The liquid phase was analyzed by GC/MS. Thus, a two phase system in the PVT cell actually resulted in 4 sample analyses: upper phase vapor, upper phase liquid, lower phase vapor, and lower phase liquid. A schematic diagram of the sampling system is given as Fig. 2.12.

Data Analysis

Raw output data from a GC/MS analysis consist of ion intensities for the entire range of m/z values recorded at each scan. Summation of the intensities of all ions present in a particular scan permits construction of a Total Ion Chromatogram (TIC). The TIC is a plot of total ion intensity versus scan time. Philp and Gilbert [109] showed for four Australian oils that the TIC is virtually identical to an FID (flame ionization detector) trace from a GC analysis. Therefore, area percent from the TIC, if the instrument is tuned properly, can be directly related to weight percent for all compounds present. In actuality, a response factor unique to each compound should be used to convert area percent to weight percent; however, with the large number of components present in crude oil, it is not possible to estimate response factors for each of them. Therefore, in this analysis, all response factors were assumed to be 1. For the partition coefficient calculations, the response factor is irrelevant, as long as it is independent of composition, because it is present for both phases and divides out of the K-value equation.

Peak Quantitation

The areas for labelled peaks are calculated automatically by the GC/MS data analysis system and are stored in a quantitation file along with their respective scan numbers. The scan number for a given peak (which actually covers several scans) is that scan which corresponds to the highest intensity point of the peak. The mass spectrum for the peak is then the mass spectrum corresponding to the peak scan number.

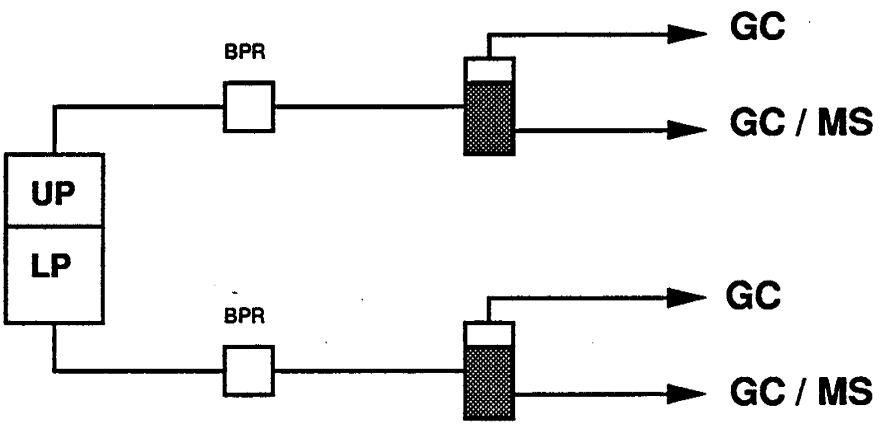

Figure 2.12: Schematic of Sampling System

Spectrum Identification

The mass spectrum of a particular component is a function of its molecular structure. When bombarded with electrons in the source, a molecule fragments based on the stability of the fragment ions formed. For saturated compounds, each carbon atom has four bond sites. In a pure hydrocarbon, each of these sites will be occupied by either another carbon atom or a hydrogen atom. A carbon atom that is bonded to four other carbon atoms is called a quaternary carbon, one that is bonded to three carbons and one hydrogen is a tertiary carbon, etc. When one of the carbon-carbon bonds fragments, the resulting positive ion has an order of one less than the original carbon. For example, fragmentation of quaternary carbon-carbon bond results in a tertiary ion. The order of decreasing stability for these fragment ions is: tertiary, secondary, primary. Fragmentation will occur so as to produce the most stable ions (tertiary or secondary). Therefore, a molecule is most likely to fragment at quaternary and tertiary carbons, which represent positions of branching on straight chain compounds and positions of alkylation on cycloalkanes.

Aromatic molecules are extremely stable, as are aromatics with only methyl groups attached. Fragmentation in aromatic molecules will generally occur only in alkyl groups of two carbon atoms or more. Fragmentation of alkyl groups follows the same rules as for aliphatic molecules.

A second type of ion that forms in the source in addition to the fragment ions is the molecular ion, which results from the removal of an electron. The molecular ion is easily identified because it is the highest m/z peak (for spectra of only one component) and is generally the only even-valued m/z peak. The intensity of the molecular ion depends on the degree of fragmentation. For highly branched alkanes, the molecular ion is sometimes absent.

Identification of components is based on molecular weight (from the molecular ion), elution order, library spectrum identification, and "user experience." While it is not always possible to identify individual isomers, especially for high carbon numbers, the molecular weight, carbon number, and chemical type can be identified for most compounds.

For carbon numbers greater than ten, many of the peaks consist of multiple components that coelute from the GC. The library search routines are unable to resolve spectra of multiple components, so it is up to the user to identify which m/z peaks are associated with which components. The identification process is largely based on user expertise. In order to separate quantitatively the coeluting components, the intensities of the ions associated with each component are summed and then the total area of the peak is divided between the components based on the ratios of the ion summations.

Once the quantitation and identification process is completed, the GC/MS analysis of the sample has resulted in a complete list of elution times, weight fractions, molecular weights, carbon numbers, and chemical types for approximately 400 components in the C_5 to C_{30} fraction. The GC/MS procedure can be run on any liquid sample, including whole crude oils or the liquid portions of the equilibrium phase samples.

Phase Sample Analysis

The separate vapor and liquid analyses of a sampled phase, by GC and GC/MS, respectively, are recombined mathematically using the known sampled quantities of the two portions. Because C_6 to C_8 hydrocarbons are present in both phases and are analyzed with different degrees of resolution, an assumption must be made about how the components in the less-resolved vapor phase should be divided to match the more detailed component analysis of the liquid phase. The assumption employed here was that components of the same carbon number (for these low carbon numbers) partition similarly into the two phases. Therefore, the C_6 fraction (for example) of the vapor phase was divided up to match the more detailed compositional description of the liquid phase based on the distribution of C_6 components in the liquid phase.

Once the upper and lower phases have been mathematically recombined, K-values can be calculated for selected components based on the amount of that component in the two phases. Therefore, in order to be selected for K-value calculation, a component must be detectable in both phases and may not be part of a peak that contains more than two components.

Whole crude oil samples were analyzed under operating conditions identical to those used for the phase samples. However, for the oils, all peaks were identified, if possible, and all coeluting components were separated quantitatively. No internal standard run was performed on any GC/MS analysis; therefore, no account was taken of the uneluted fraction. Standard SIMDIS analyses, including an internal standard run, were performed on the whole oil samples for quantitative purposes.

These SIMDIS analyses required three runs; a baseline run (no sample), the sample itself, and the sample with a known quantity of internal standard added. Single carbon number cuts, based upon normal alkane elution times, were quantified by calculating the area under the GC trace between the two normal alkanes, after the baseline had been subtracted. The purpose of the internal standard run was to quantify the uneluted fraction. The SIMDIS procedure for crude oils was that described in Section 2.1 and also by Worman and Green [152].

2.2.2 Experimental Results

Phase Equilibrium Samples

This section presents the results of the component partitioning experiments described in Section 2.2.1. Partitioning data are presented in terms of K-values of individual molecules. Carbon dioxide is normalized out of the compositions of both phases to isolate only the hydrocarbon behavior. Therefore, K-values presented here are defined as:

$$K_i = \frac{\frac{w_{i,u}}{1-w_{CO_2,u}}}{\frac{w_{i,l}}{1-w_{CO_2,l}}}$$

where $w_{i,u}$ and $w_{i,l}$ are the weight fractions of component i in the upper and lower phases, respectively, and $w_{CO_2,u}$ and $w_{CO_2,l}$ are the weight fractions of CO_2 in the upper and lower phases. Weight fractions were used in place of mole fractions because they were measured directly in the GC/MS analysis. Conversion of the weight fraction based K-values to the traditional mole fraction based value would require simply multiplying the K-value by the ratio of the individual phase molecular weights.

The sampling conditions for the partitioning experiments are summarized in Table 2.18. CO_2 density at sampling conditions is also included.

Table 2.18: PVT Sampling Conditions

Sample	Oil	Pressure (psia)	Temp. (°F)	CO_2 density (gm/cc)
1	Means	3000	105	.844
2	Means	1500	105	.618
3	Means	3950	125	.844
4	Oil W	3100	170	.647
5	Oil W	2000	125	.647
6	Kubiki	2000	125	.647
7	Kubiki	3950	125	.844

Three crude oils were selected for the partitioning experiments: Means (Permian Basin), Oil W (Gulf Coast), and Kubiki (Japan). These oils were selected on the basis of their carbon number distributions and on the types of molecules known to be present. The carbon number distributions for these three oils as obtained from simulated distillation (SIMDIS) are presented in Fig. 2.13. More detailed compositional analyses of these oils will be presented later in this section.

Means Oil The first oil studied was Means crude oil. PVT sample 1 was generated at the reservoir temperature of 105°F and a pressure of 3000 psia. Fig. 2.14 shows K-values for sample 1 plotted versus carbon number as determined directly from the mass spectrum. While there is clearly a trend of decreasing K-value with an increase in the size of the molecule, there is also significant variation in K-value with chemical structure at a given carbon number. K-values for the molecules with a carbon number of 13 are presented in Table 2.19. The range of K-values for a particular carbon number is quite large, as Table 2.19 indicates. Apparently, the K-value is a strong function of molecular structure for C_{13} molecules. Thus, carbon number is a rather poor correlating parameter for partitioning behavior. These data confirm previous binary results [25, 38]. In typical hydrocarbon analyses, however, compositions are determined based on elution time from a chromatographic column (SIMDIS). This technique is based on the assumption that compounds that elute together from a GC partition similarly. Therefore, it makes sense to plot the partitioning data versus GC elution time. The same K-value data from sample 1 are plotted versus elution time in Fig. 2.15. While the correlation is certainly improved, different classes of compounds still show distinctive behavior. Fig. 2.16 shows the K-values for branched alkanes versus a reference curve of normal alkanes for sample 1. While there is some scatter in the data, the K-values

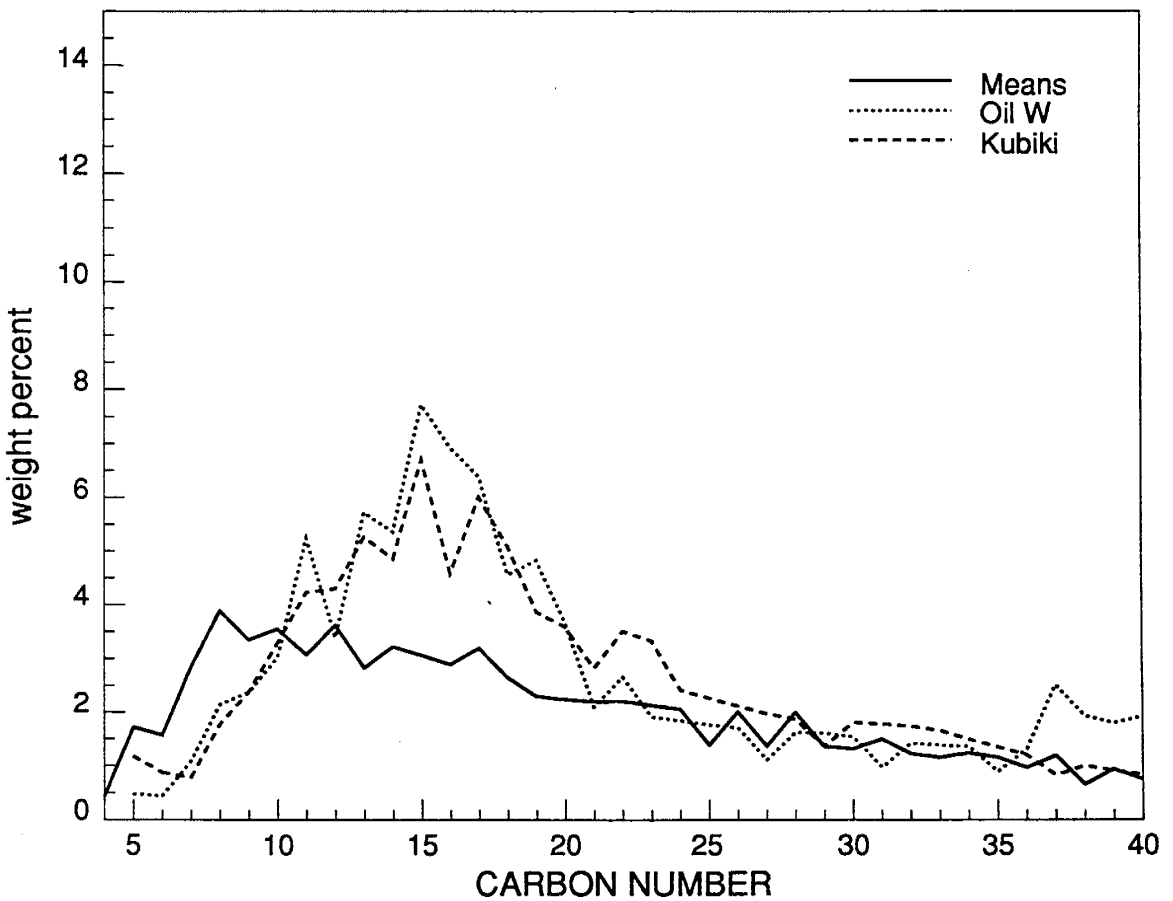

Figure 2.13: Simulated Distillation Analyses for Means, Oil W, and Kubiki.

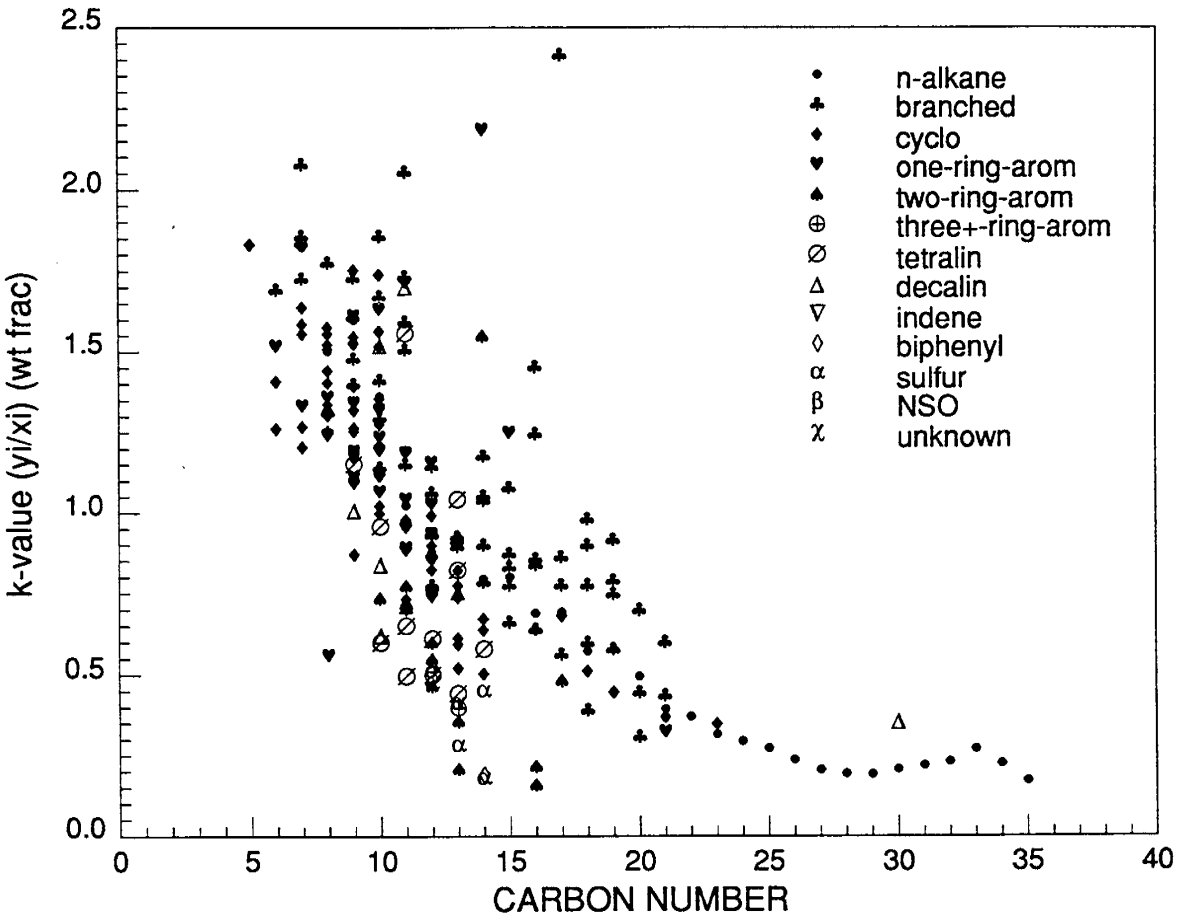

Figure 2.14: K-values versus Carbon Number for Sample 1, Means at 3000 psi, 105°F.

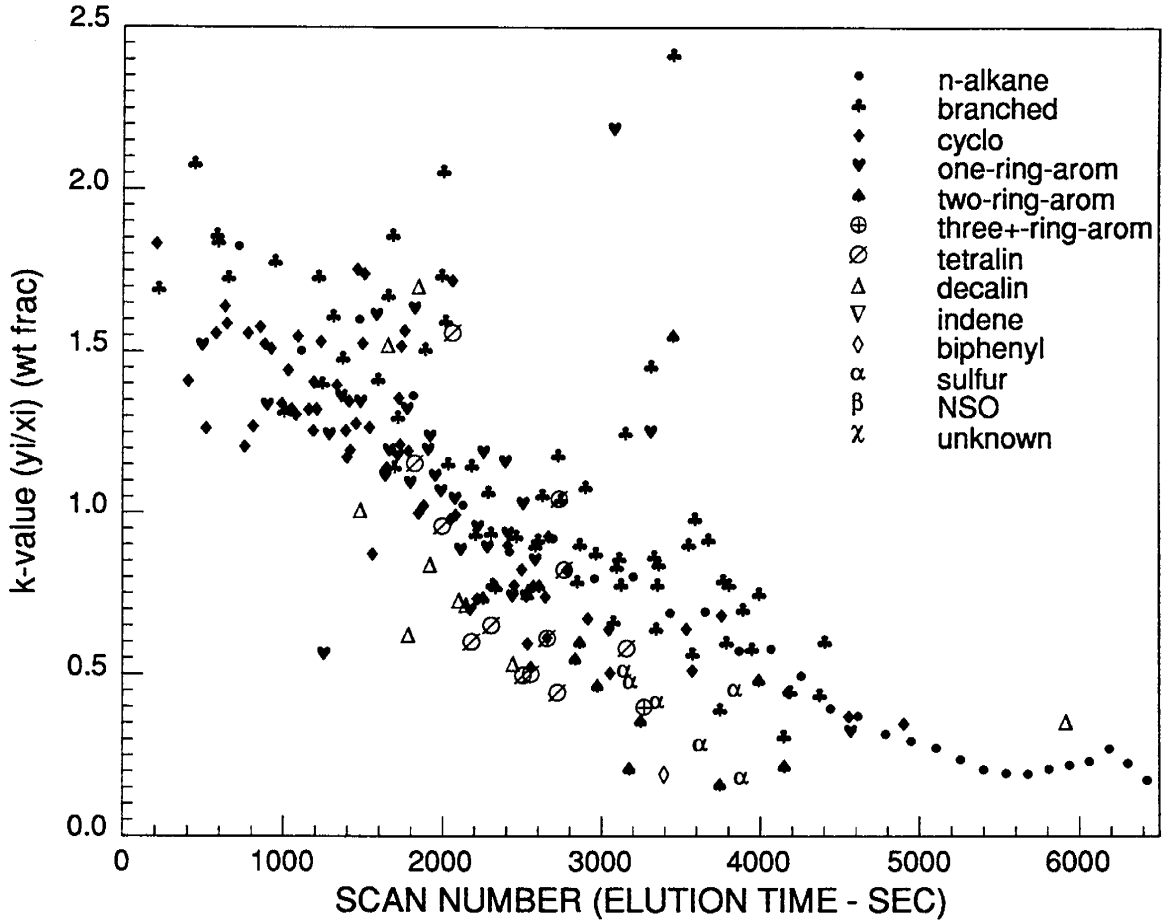

Figure 2.15: K-values versus Elution Time for Sample 1, Means at 3000 psi, 105°F.

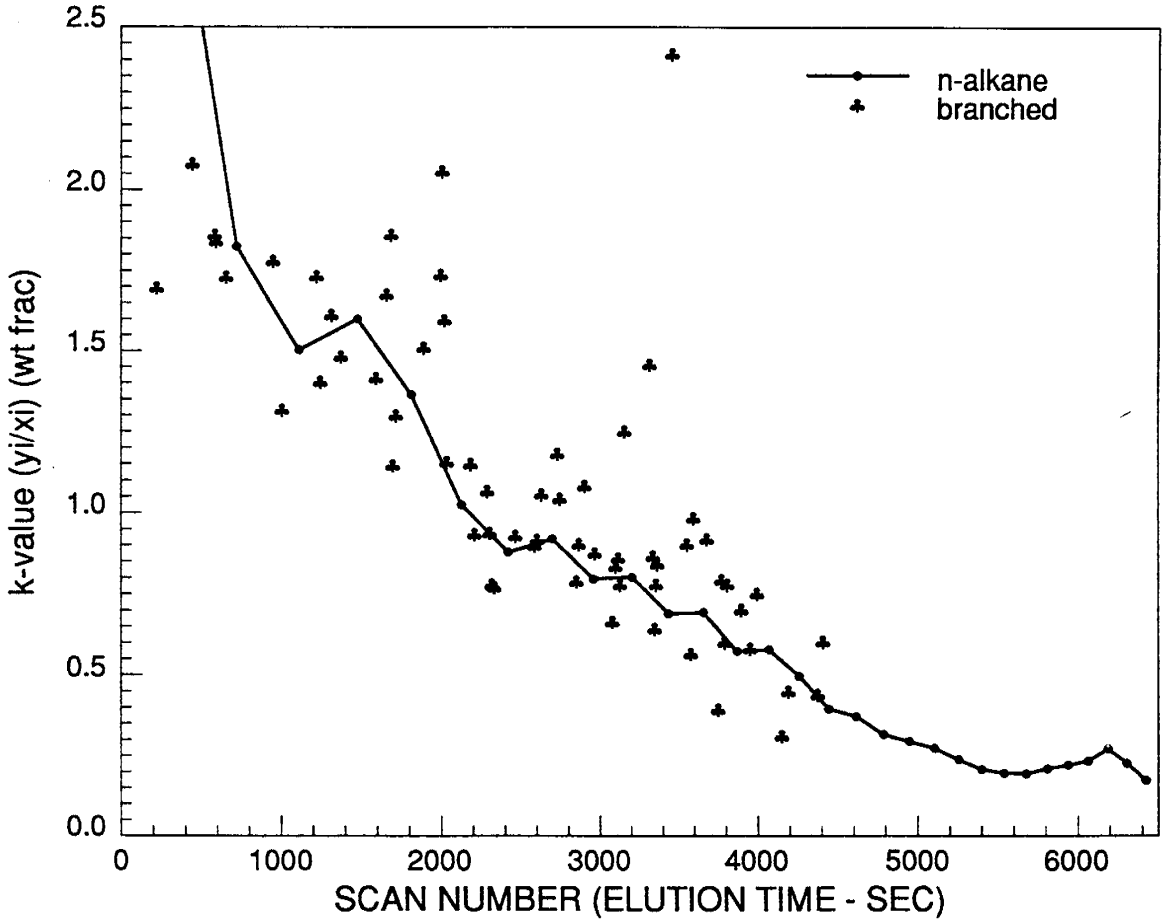

Figure 2.16: Alkane K-values Sample 1, Means at 3000 psi, 105°F.

Table 2.19: K-values for C_{13} Molecules in Sample 1

K-value	type
0.9273030	br alkane
0.9256641	cycloalkane
0.9191930	n-alkane
0.9147595	br alkane
0.8966523	br alkane
0.8221080	tetralin
0.8216525	cycloalkane
0.7732788	cycloalkane
0.7562973	decalin
0.7404297	cycloalkane
0.7381052	cycloalkane
0.6120179	cycloalkane
0.5942336	cycloalkane
0.5217079	cycloalkane
0.4432040	tetralin
0.4153269	sulfur
0.3994214	3-ring arom
0.3581294	2-ring arom
0.2831350	sulfur
0.2106793	2-ring arom

for branched alkanes tend to be slightly higher than those of n-alkanes with similar elution times. In contrast, Fig. 2.17 shows the K-values for saturated cyclic compounds versus those of normal alkanes. Both one and two-ring cyclics are included in this figure. Clearly, the K-values for the cyclic compounds are lower than those of the normal alkanes. However, the differences in K-values between both cyclic and branched molecules and the normal alkanes are much less pronounced than the difference in K-values between multi-ring aromatics and the other types of molecules. The K-values for these multi-ring aromatics in sample 1 are plotted with the normal alkane data for comparison in Fig. 2.18. Substituted naphthalenes represent most of the multi-ring aromatic compounds in the Means crude oil. The K-values for these molecules are considerably lower than the K-values for other, coeluting molecules. These data imply that the SIMDIS assumption that components that elute together from a GC partition similarly is not strictly valid for the extraction of multi-ring aromatics by CO_2.

A second experiment (sample 2) was run using Means at a lower pressure (1500 psia) and the same temperature as the first sample to investigate the effect of pressure on partitioning behavior. Fig. 2.19 shows the individual compound K-values versus elution time for the second experiment. While the K-values for the larger molecules (latest elution times) decrease somewhat more rapidly for the low pressure case, samples 1 and 2 show that a 1500 psi drop in pressure did not have a significant effect on partitioning behavior. The only observable trend is a slight steepening in the slope of the data. It should be noted that both of these pressures were above the three-phase region at this temperature (Fig. 2.20).

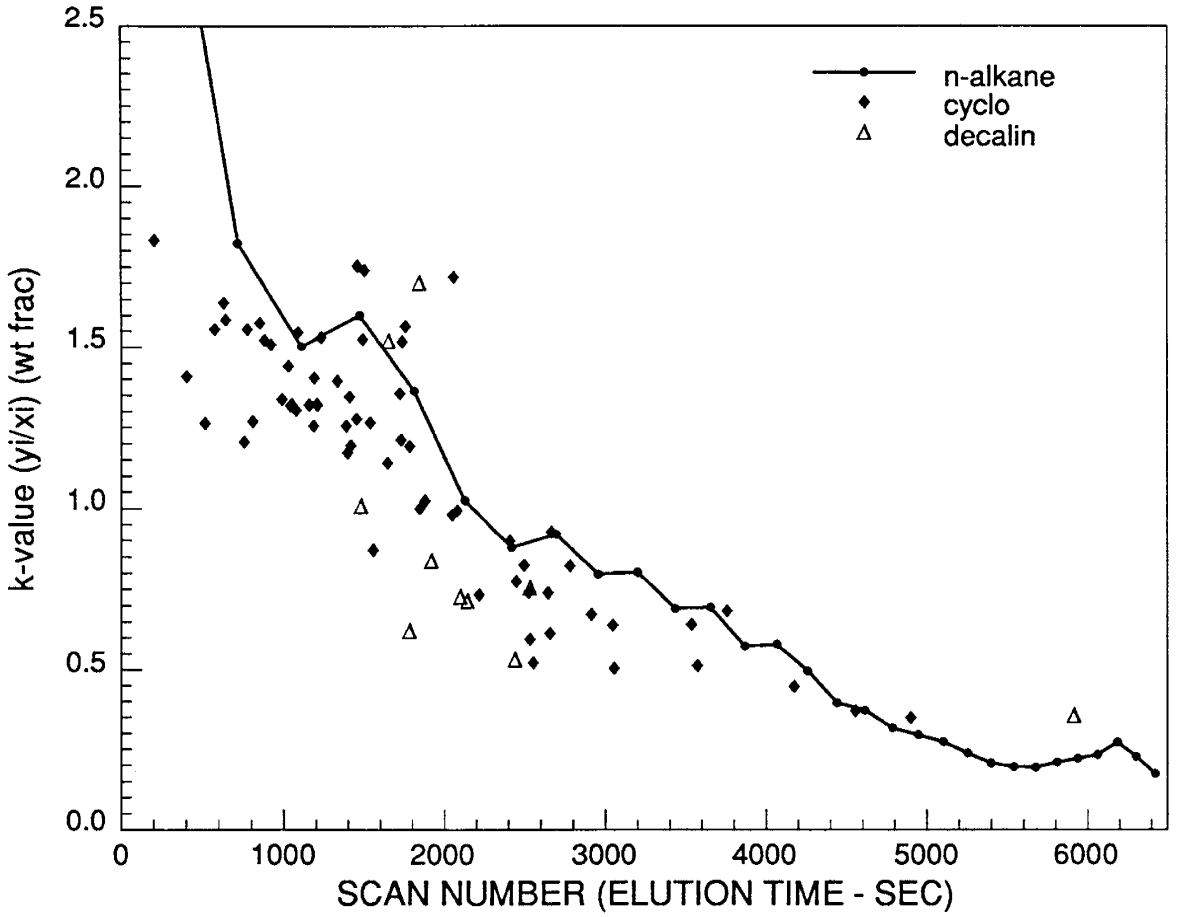

Figure 2.17: Cyclic K-values for Sample 1, Means at 3000 psi, 105°F.

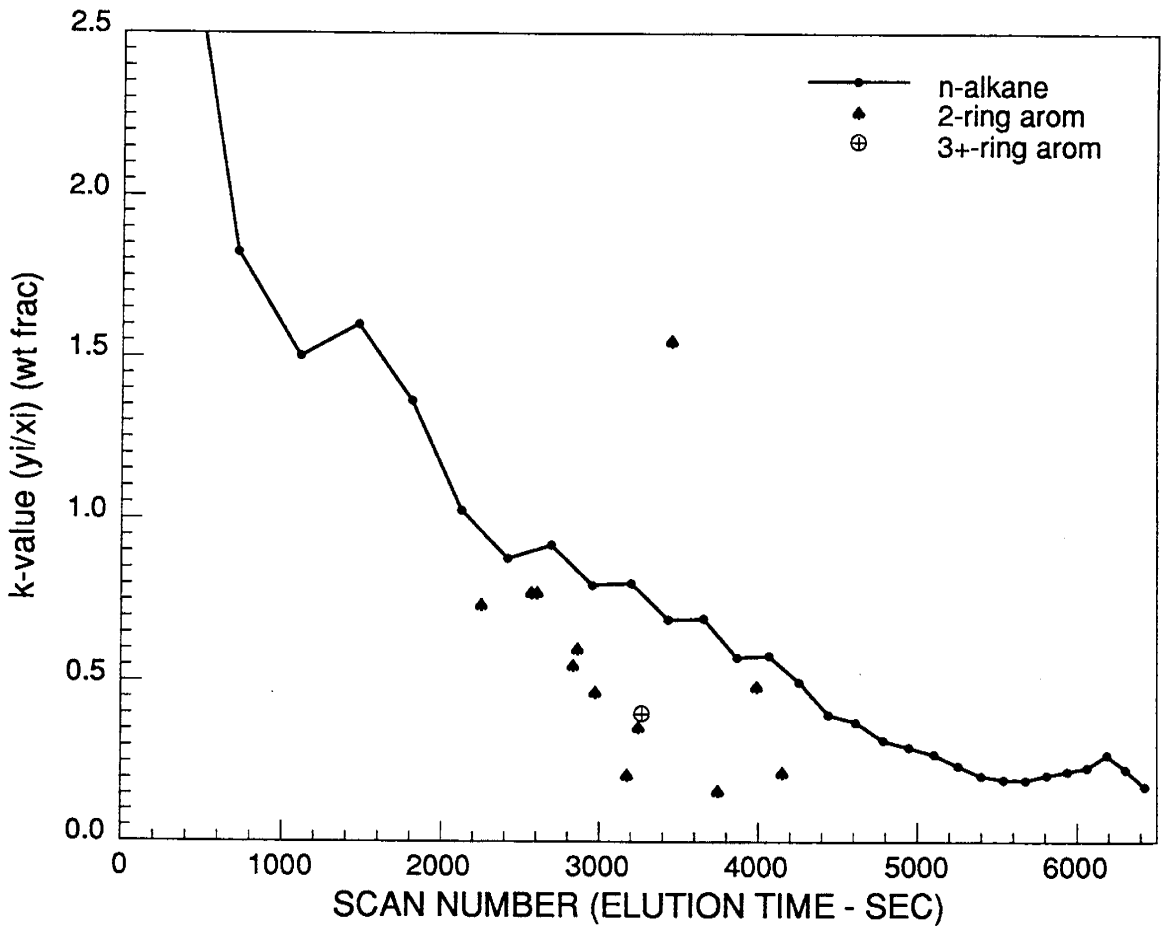

Figure 2.18: Multi-ring Aromatic K-values for Sample 1, Means at 3000 psi, 105°F.

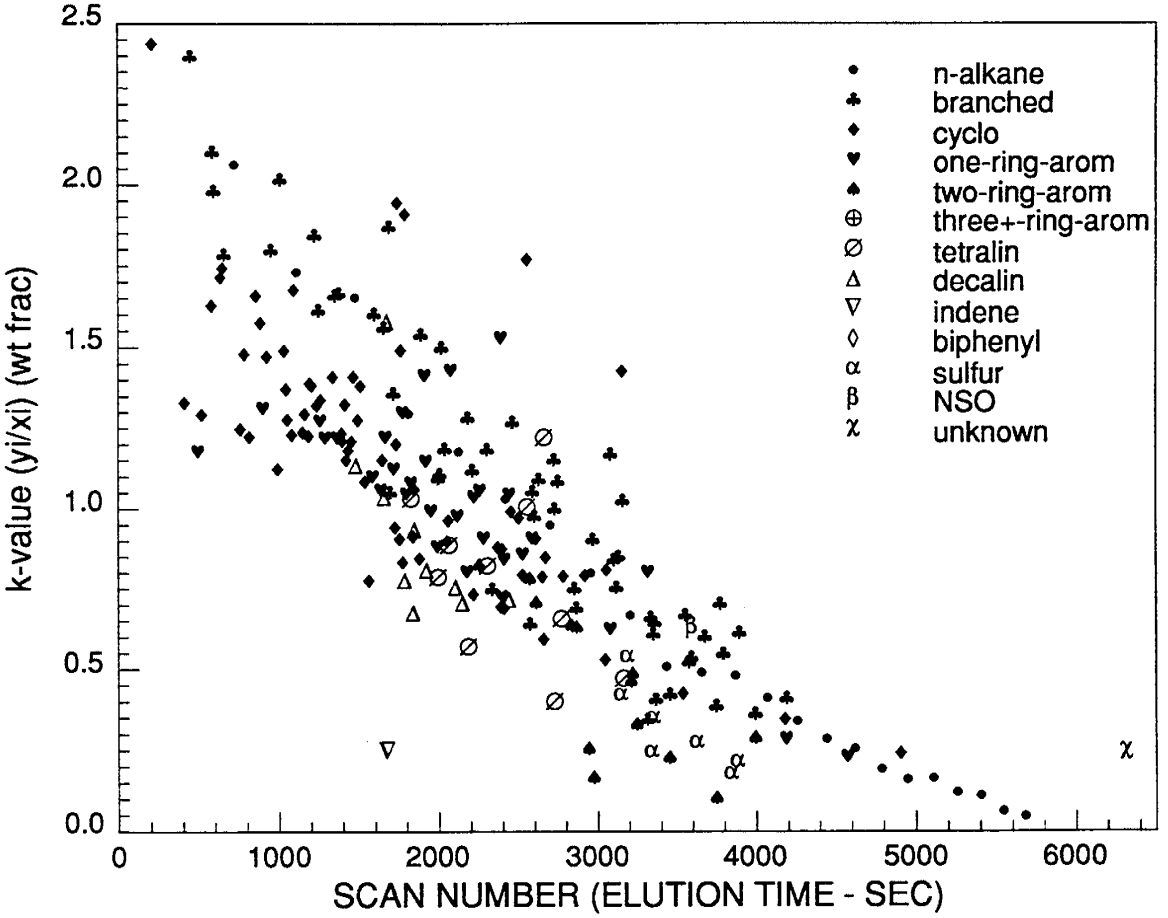

Figure 2.19: K-values versus Elution Time for Sample 2, Means at 1500 psi, 105°F.

Therefore, both of these samples represented liquid-liquid behavior. The phase behavior of Means stock tank oil and CO_2 mixtures was fully described by Stessman [130].

The almost negligible change in extraction behavior with pressure for Means at these conditions agrees with the results of a slim tube displacement experiment also performed at reservoir temperature. Fig. 2.21 shows slim tube recovery as a percent of the original oil in place (%OOIP) versus pressure at 1.2 pore volumes of injection. The relatively flat recovery curve above about 1200 psia confirms that there is minimal effect of pressure on phase behavior, and hence on displacement performance, at the pressures investigated in samples 1 and 2.

To investigate the effect of temperature and of the upper phase state, sample 3 was run at a higher temperature (125°F) than samples 1 and 2. At this temperature, a three phase region does not occur in Means (Fig. 2.22). Sample 3 was run at a pressure that resulted in the same CO_2 density as sample 1. K-values for this experiment, shown in Fig. 2.23, are very similar to those of sample 1 (Fig. 2.15). Thus, samples 1 and 3 confirm that temperature and upper phase state do not have a significant effect on extraction behavior, as long as CO_2 density remains constant.

Oil W The second set of samples was run using a Gulf Coast oil (Oil W), which has a carbon number distribution somewhat heavier than that of Means (Fig. 2.13). Oil W is relatively depleted in the smaller, more extractable molecules. The slim tube displacement data for Oil W at the reservoir temperature of 170°F are presented in Fig. 2.24. Sample 4 was run at 170°F and the slim tube minimum miscibility pressure for this oil of 3100 psia. Partitioning data for sample 4 are shown in Fig. 2.25. Comparison of Figs. 2.15 and 2.25 indicates that the relative extraction behavior for various types of compounds is similar to that observed in the Means experiments, except that the differences seem less pronounced. For example, the branched alkanes still lie somewhat above the normal alkane curve and the substituted naphthalenes lie below it, but the relative differences are much smaller than those observed in Means.

For comparison purposes, sample 5 was run at the same CO_2 density as sample 4, but at a temperature of 125°F. This represented a pressure of 2000 psia. A problem with the back pressure regulator during sampling led to difficulties in the analysis of the upper phase vapor sample, and consequently, in recombining the upper phase samples. As a result, the magnitude of the K-values from this sample may be somewhat suspect. However, the relative partitioning data for the various compounds is acceptable. Sample 5 also shows that a significant amount of material is being extracted at these conditions. This agrees with the sample 3 observation that temperature does not affect extraction as long as CO_2 density is constant. Fig. 2.26 confirms the results of sample 4. It demonstrates that chemical type has a smaller effect on extraction behavior for Oil W than was observed in the Means experiments.

Kubiki Oil The final oil studied in the partitioning experiments was Kubiki. Kubiki was selected because it displays unusual slim tube behavior, shown in Fig. 2.27. Because Kubiki and Oil W have similar carbon number distributions (Fig. 2.13), the first Kubiki sample (sample 6) was run at the same conditions as sample 5. These conditions represent Kubiki's reservoir temperature and the minimum miscibility density for Oil W. This pressure on the Kubiki slim tube displacement curve corresponds to a very low recovery, an indication of

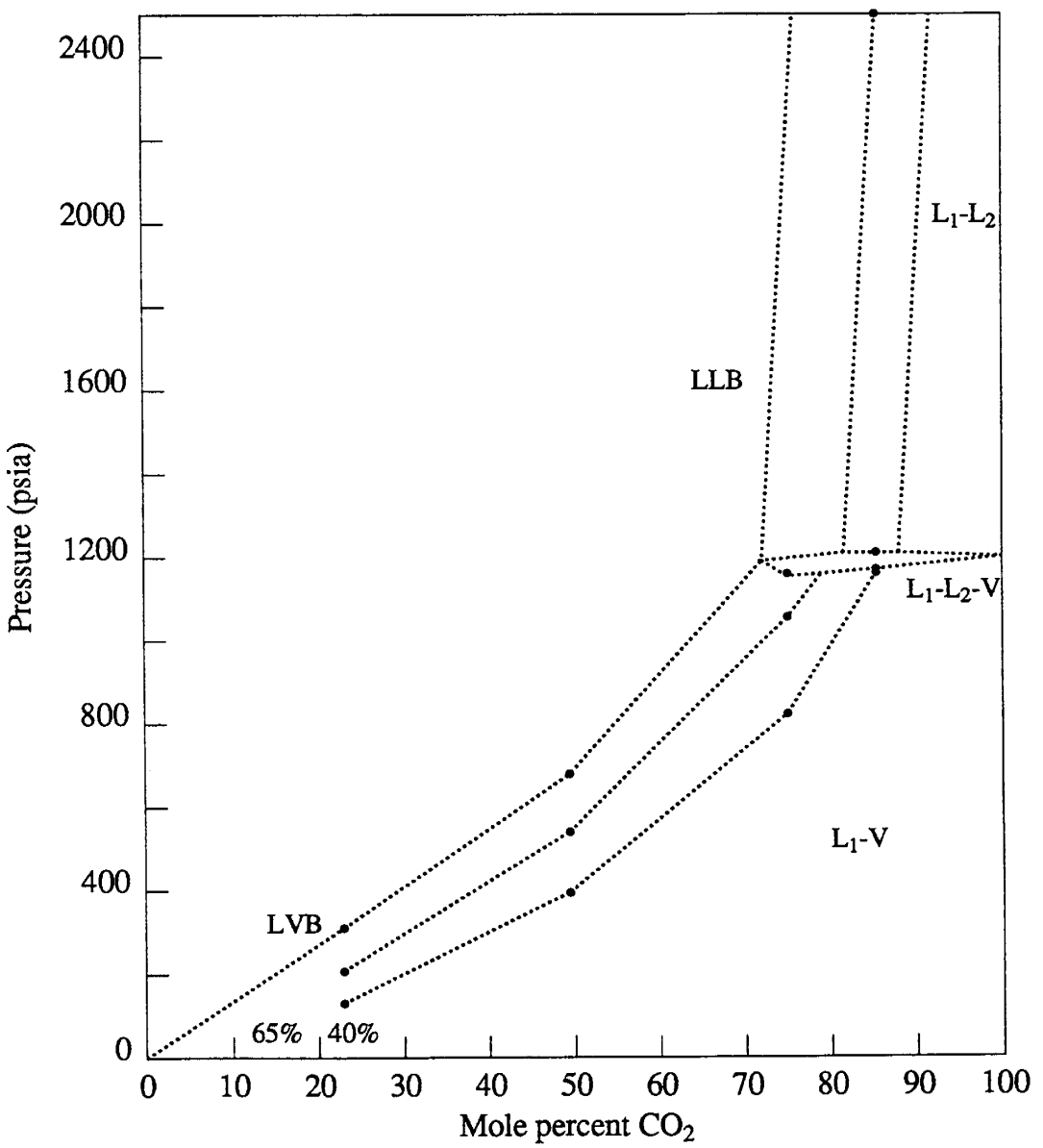

Figure 2.20: Pressure-Composition Diagram for Means Crude Oil and CO_2 at 105°F. (Data from Stessman, 1991).

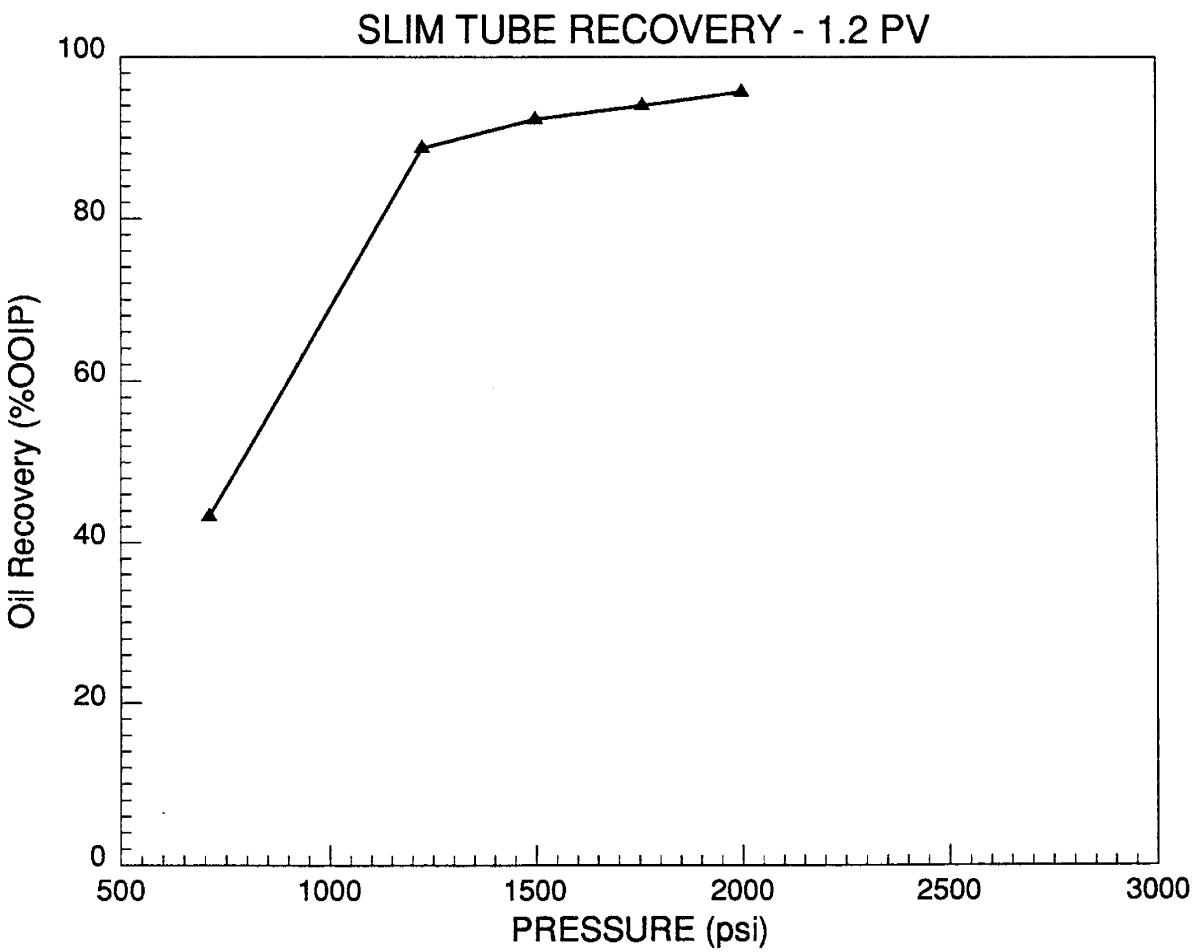

Figure 2.21: Slim Tube Displacement Data for Means at 105°F. (Data provided by Exxon).

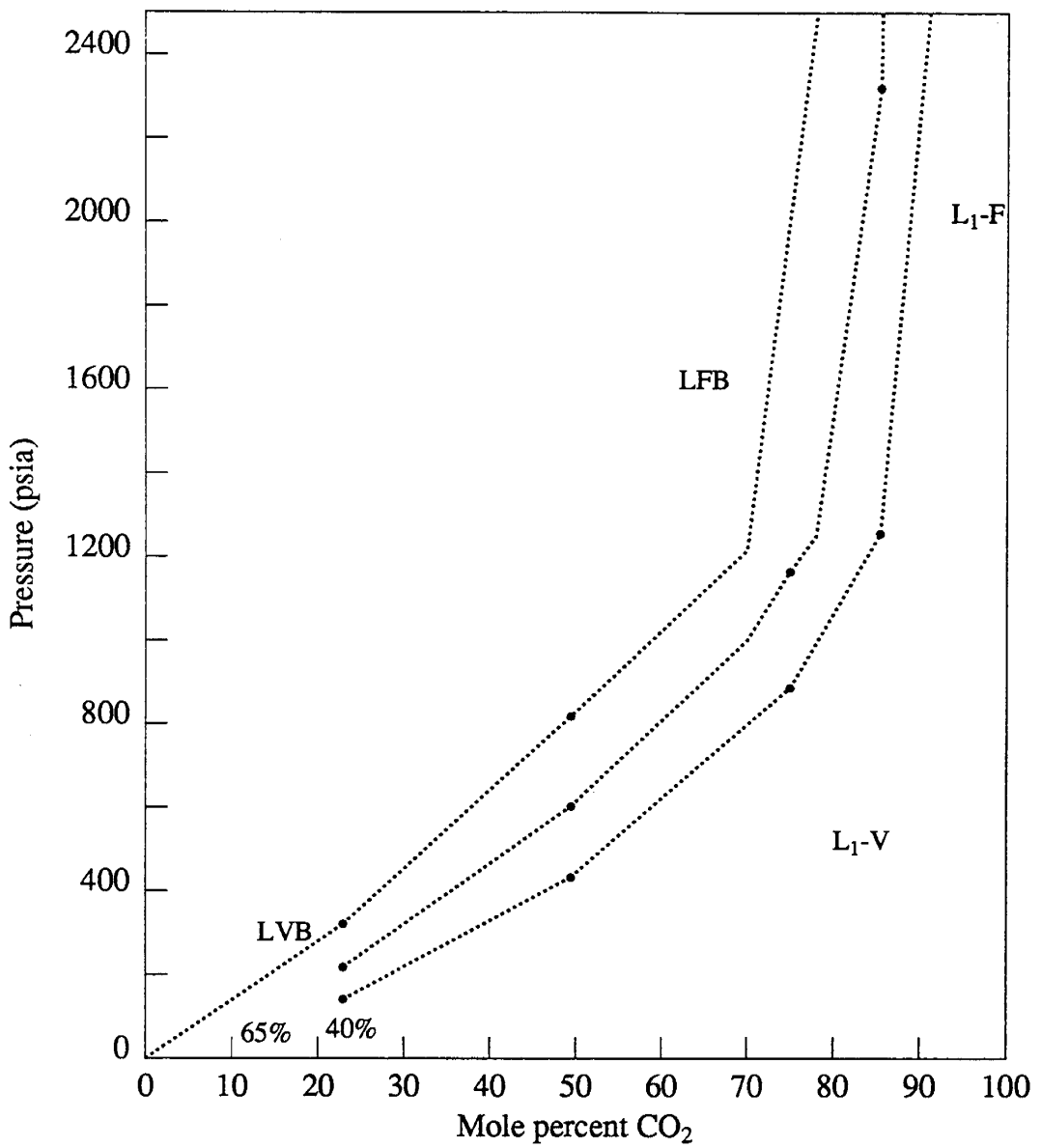

Figure 2.22: Pressure-Composition Diagram for Means Crude Oil and CO_2 at 120°F. (Data from Stessman, 1991).

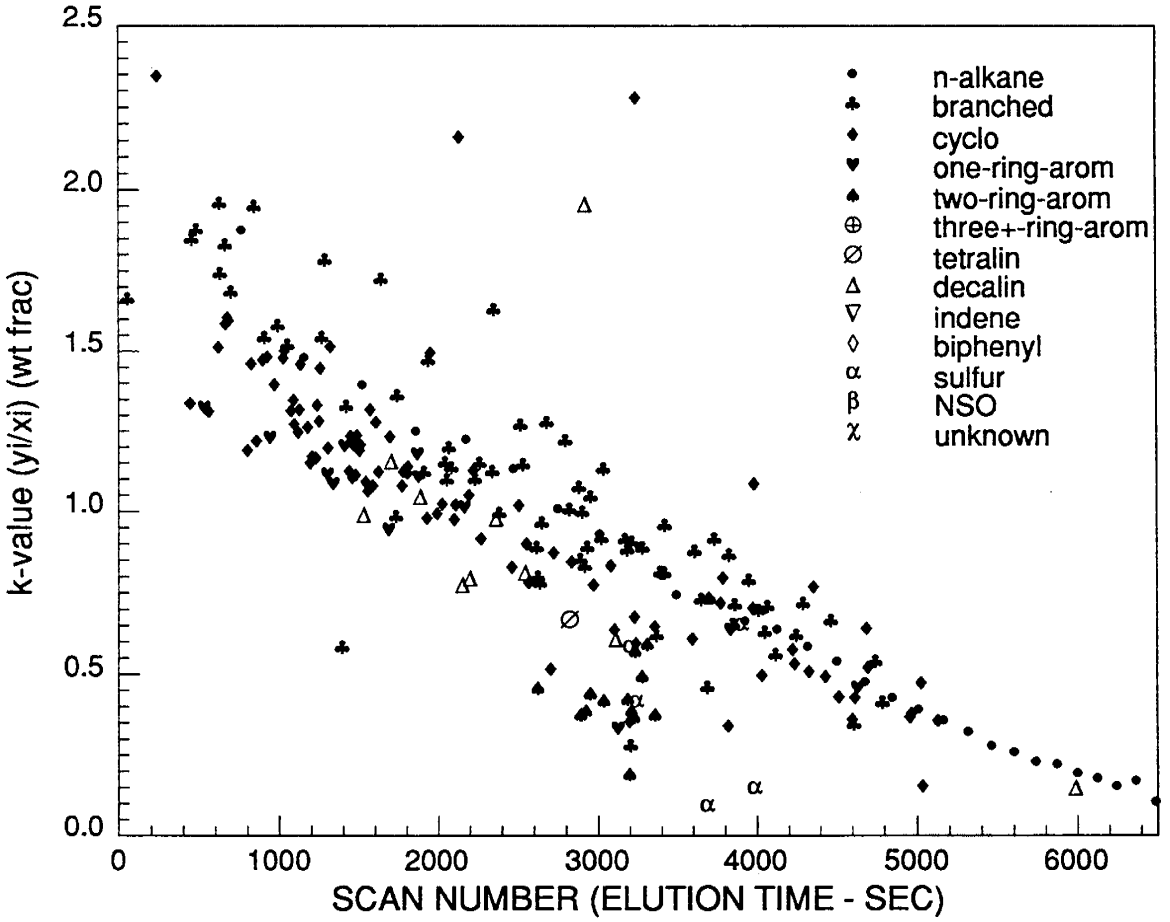

Figure 2.23: K-values versus Elution Time for Sample 3, Means at 3950 psi, 125°F.

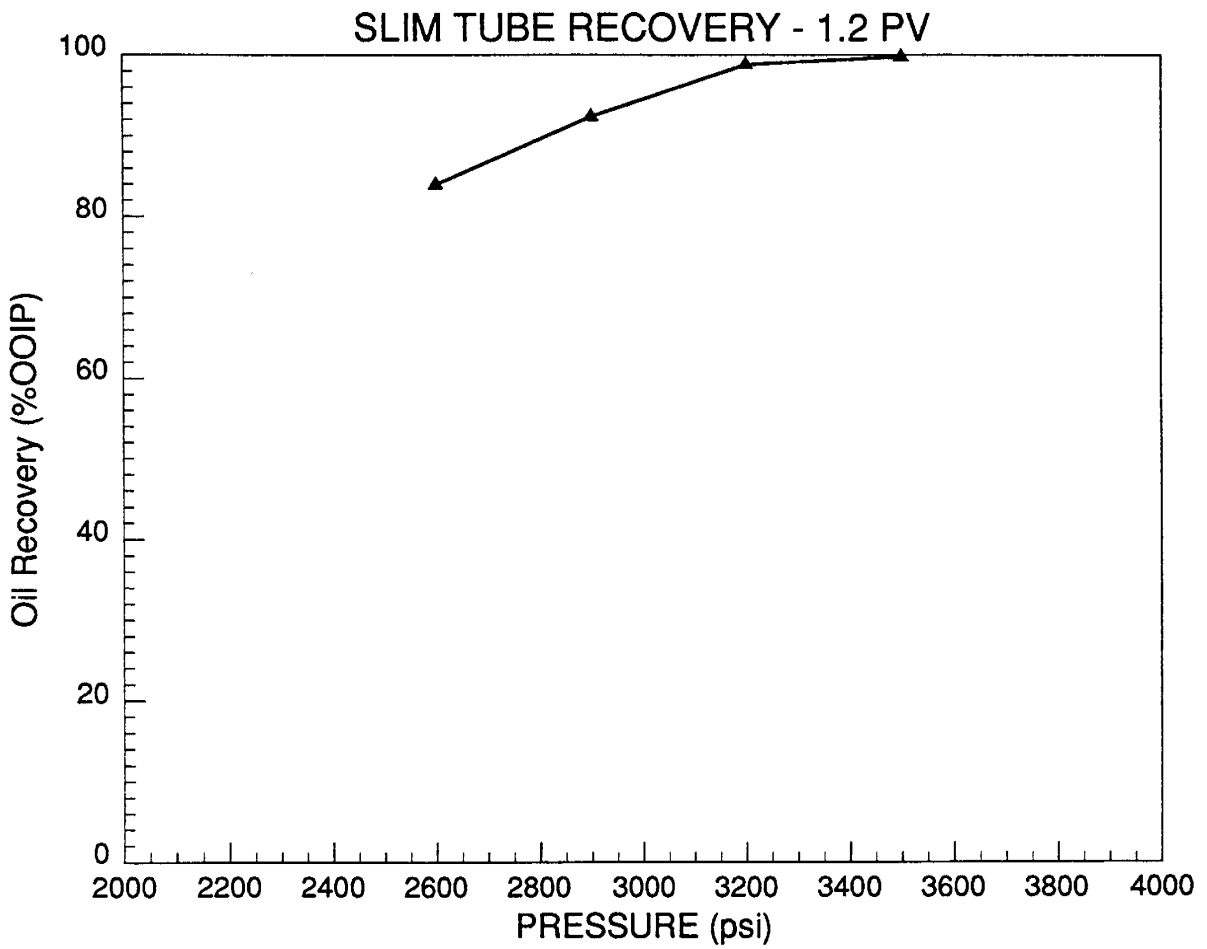

Figure 2.24: Slim Tube Displacement Data for Oil W at 170°F. (Data provided by donor of Oil W).

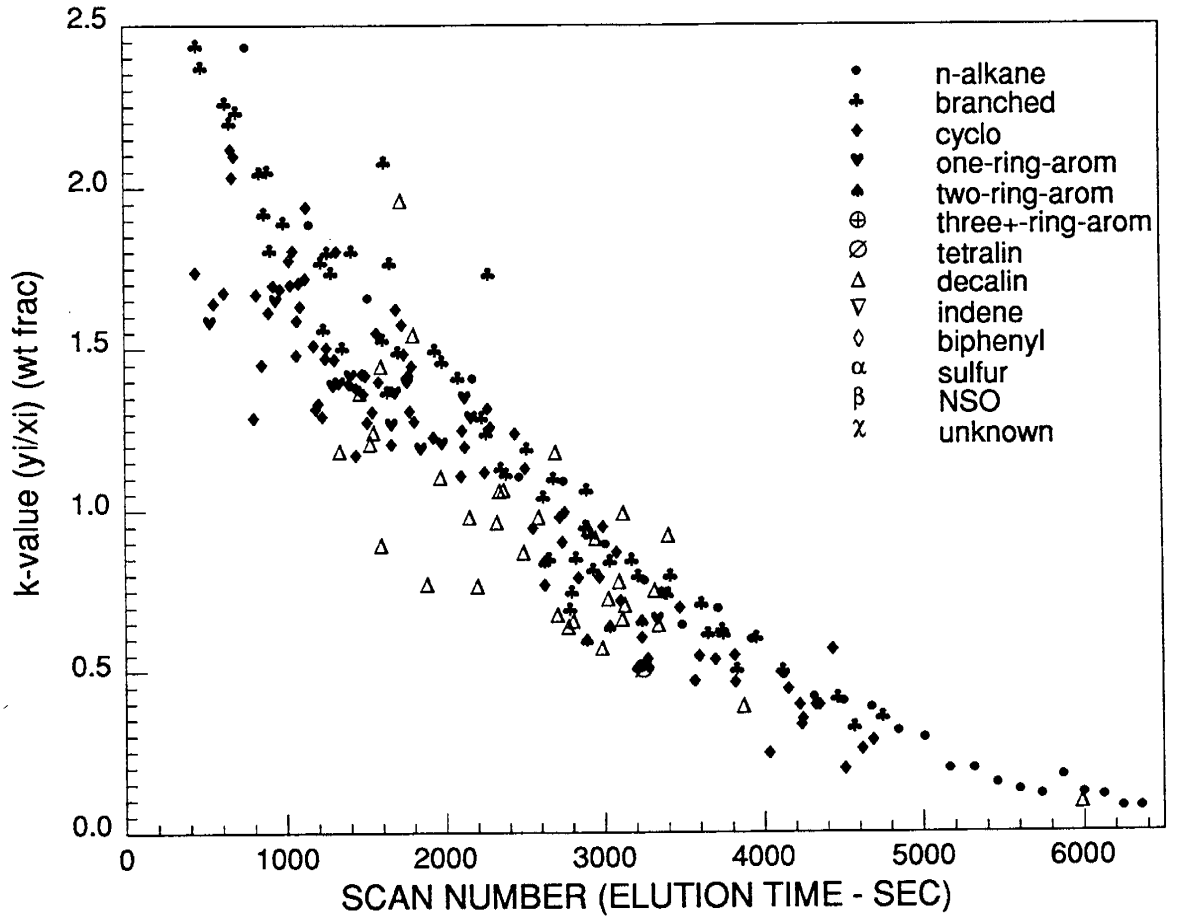

Figure 2.25: K-values versus Elution Time for Sample 4, Oil W at 3100 psi, 170°F.

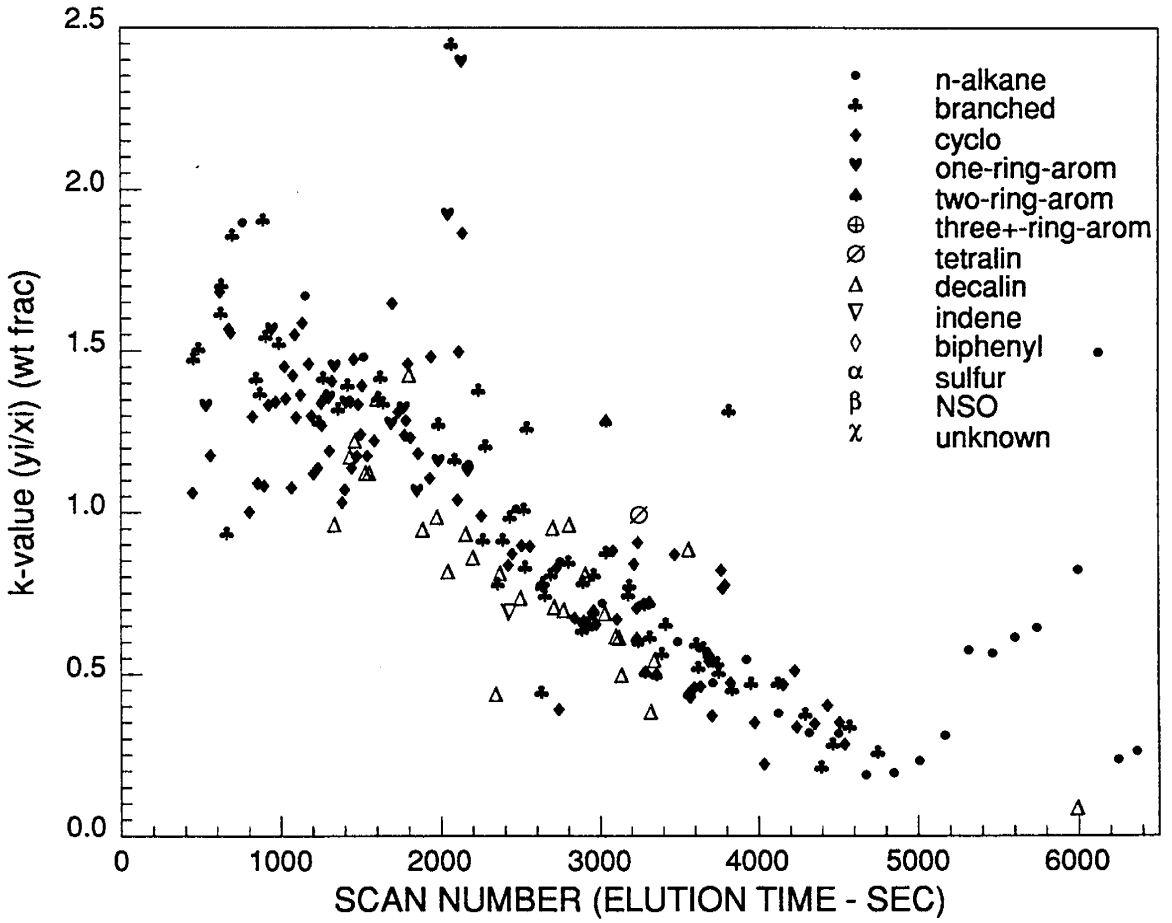

Figure 2.26: K-values versus Elution Time for Sample 5, Oil W at 2000 psi, 125°F.

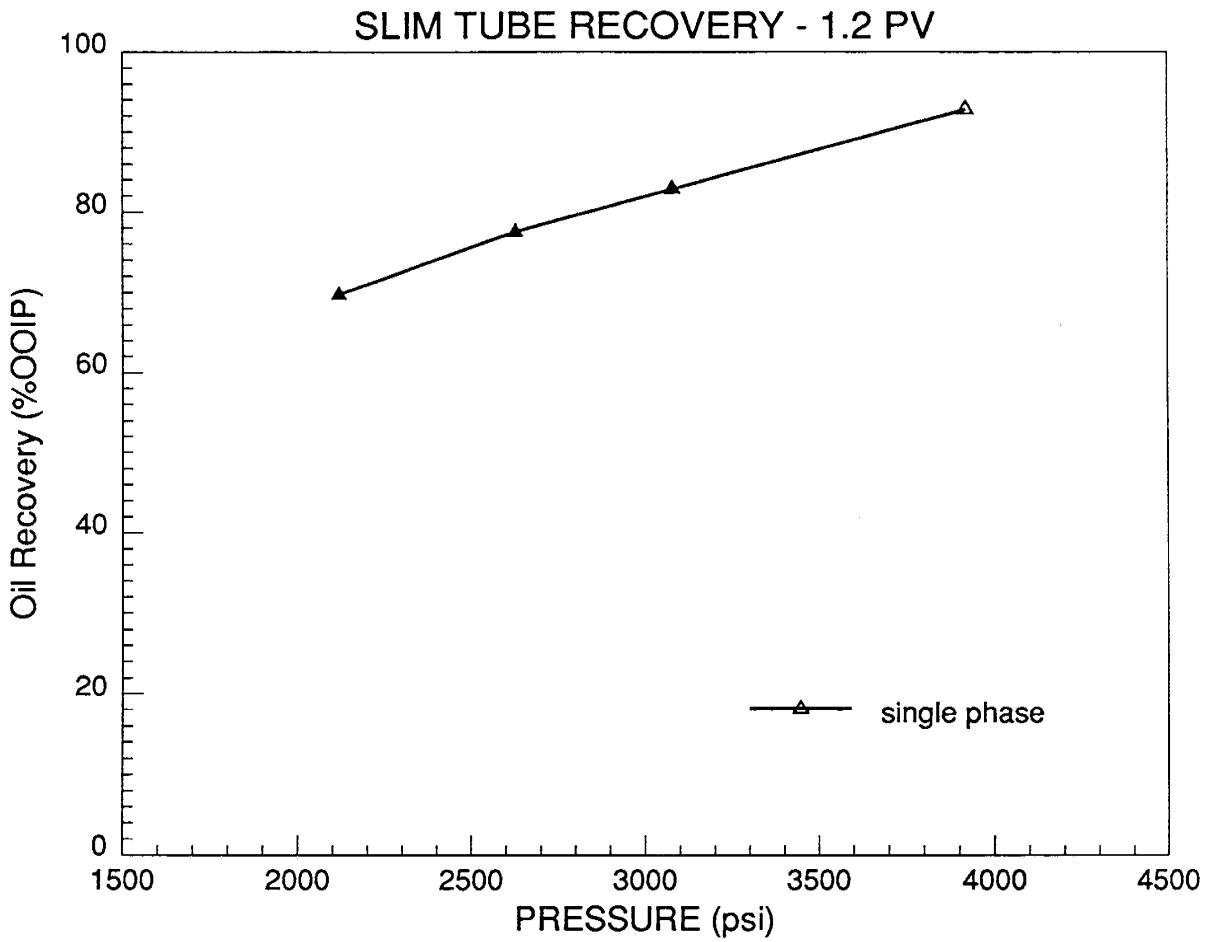

Figure 2.27: Slim Tube Displacement Data for Kubiki at 125°F. (Data provided by the Teikoku Oil Co.)

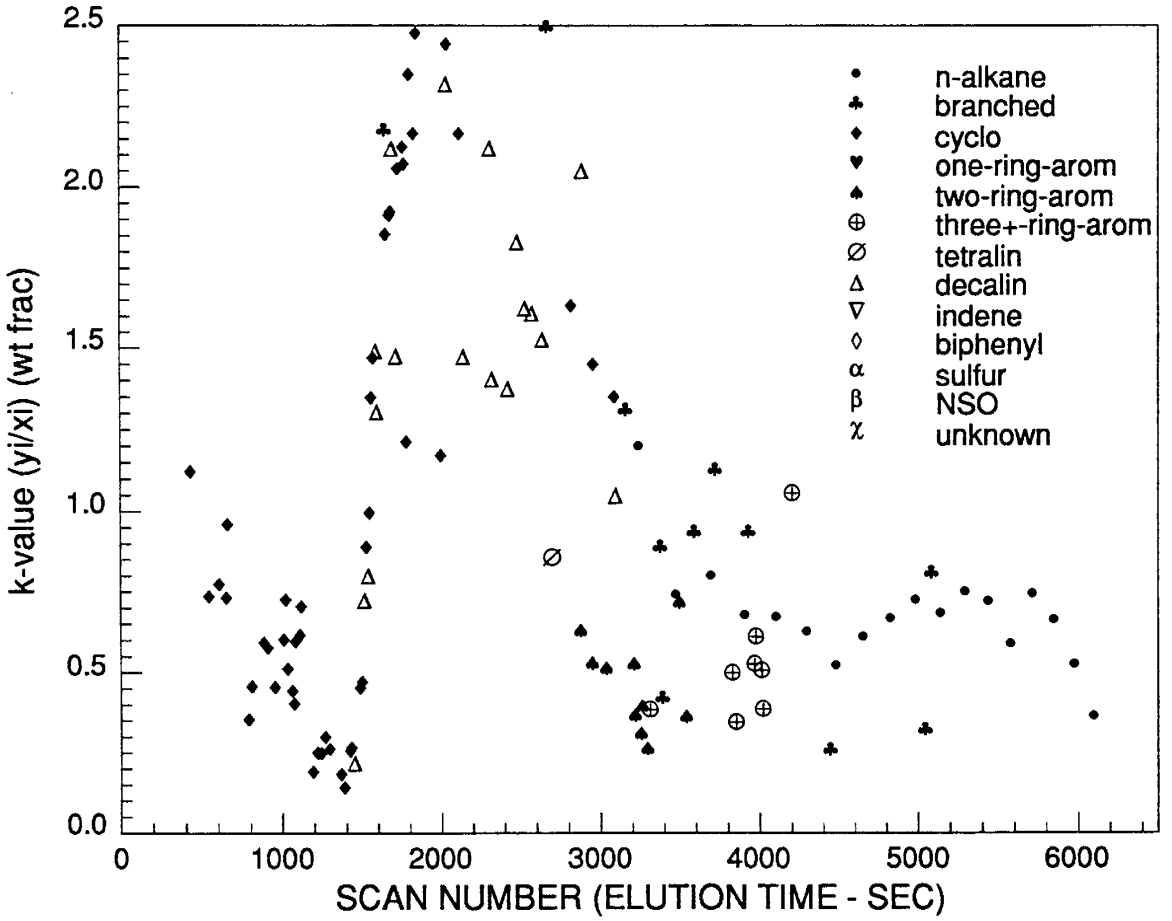

Figure 2.28: K-values versus Elution Time for Sample 6, Kubiki at 2000 psi, 125°F.

an immiscible displacement. Therefore, one would expect rather poor extraction behavior. The upper phase sample for these conditions was so volatile that the technique used here of separating gas and liquid samples was inadequate to maintain a proper material balance. As a result, many of the light ends (less than C_{11}) were lost, and the magnitudes of the remaining K-values were affected. The loss of the light ends resulted in a relative increase in the weight fractions of the heavier components. This, in turn, resulted in higher K-values for the heavier components than would have occurred had the light ends been present. However, the relative K-values of the different compounds can again provide some useful information. Fig. 2.28 shows a portion of the data for sample 6. The most useful information added from this sample is the data for an abundance of substituted naphthalenes and for aromatics with 3 or more rings. As was seen in the Means samples, these multi-ring aromatics are extracted much less efficiently than other compounds with similar elution times.

The final PVT sample was run at the Kubiki MMP of 3950 psia at 125°F. The behavior of the multi-ring aromatics, shown in Fig. 2.29 again shows much poorer extraction than other compounds with similar elution times. However, overall extraction is much better at this pressure. This corresponds to the higher recovery observed in the slim tube displacement.

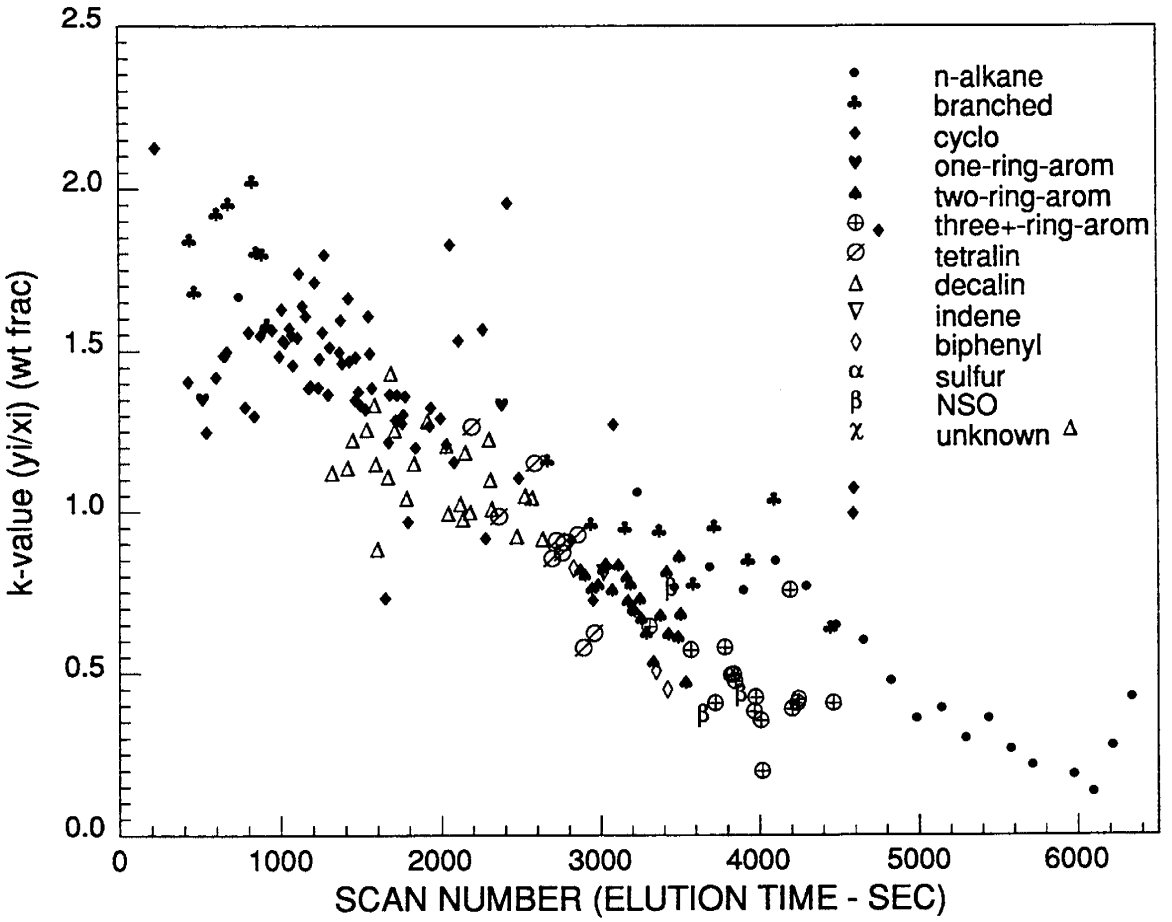

Figure 2.29: K-values versus Elution Time for Sample 7, Kubiki at 3950 psi, 125°F

The increased pressure also seems to have improved the extraction of the two-ring aromatics. Substituted naphthalene K-values increased with pressure to become closer to other similarly eluting components. However, extraction of compounds with three or more rings did not show the same improvement.

Whole Oil Analyses and Slim Tube Displacements

The partitioning data of Section 2.2.2 clearly show the effects of chemical structure on extraction of individual hydrocarbons by dense CO_2. However, the phase behavior of an oil with CO_2 is also a function of the quantities and distribution of these compounds within the oil. A detailed GC/MS analysis of the oil itself, combined with the partitioning information of Section 2.2.2 can then be used to explain or predict the phase behavior of the oil with CO_2.

Slim tube displacements are a commonly performed experiment used to evaluate the effects of phase behavior on displacement performance. These experiments have an advantage over single contact PVT experiments on displacement performance in that they more closely mimic the actual multicontact displacement process that occurs in a reservoir flow situation. The results of several slim tube experiments were presented in Section 2.2.2 to illustrate the similarity between the effects of CO_2 density on slim tube phase behavior and on partitioning behavior. The knowledge of how different molecules behave in a CO_2/crude oil mixture, as obtained from the partitioning behavior data, can be used to illustrate the effect of oil composition on slim tube phase behavior.

Fig. 2.21 presented the slim tube results for Means oil. Means is a medium gravity (30°API) Permian Basin oil. The data for Means represent fairly typical slim tube behavior. Recovery increases sharply with pressure until a "breakover" point, after which additional increases in pressure have a smaller impact on recovery. This breakover point is one commonly used criterion for evaluating the minimum miscibility pressure (MMP) of an oil. It has been shown [96] that, for low temperatures (less than 120°F), the extrapolated vapor pressure (EVP) of CO_2 is a reasonable estimate of MMP. The EVP of CO_2 at 105°F is approximately 1200 psia, which agrees well with the experimentally determined breakover point. This relatively low MMP for Means is a result of the presence of a significant quantity of easily extractable material. Fig. 2.13 shows that Means contains a much larger percent of the lighter hydrocarbons (less than C_{12}) than either of the other oils studied in the partitioning experiments. Table 2.20 shows the chemical type breakdown by weight for the C_5 to C_{35} fractions of the oils studied in Section 2.2.2. This fraction in Means is largely dominated by normal and branched alkanes, 1-ring cycloalkanes, and 1-ring substituted benzenes. The partitioning data of Section 2.2.2 indicate that these compounds are extracted with roughly equal efficiency, depending on molecular size alone. The much less extractable compounds, the multi-ring aromatics, are not present in sufficient quantities to be detrimental to the development of miscibility.

It was mentioned previously and in other works [50, 25] that CO_2 density governs extraction behavior. The CO_2 density at miscibility conditions of 1250 psia and 105°F for Means is 0.388 gm/cc.

The second oil discussed in Section 2.2.2, Oil W, has a much smaller fraction of the light hydrocarbons than Means. Therefore, one would expect a higher CO_2 density to

Table 2.20: Means, Oil W, and Kubiki - Chemical Type Distribution

Type	Means (%)	Oil W (%)	Kubiki (%)
n-alkane	30.27	5.01	5.55
br alkane	23.26	34.19	19.67
cycloalkane	24.70	27.02	32.77
1-ring arom	12.37	11.52	3.28
2-ring arom	2.71	6.83	9.03
3+-ring arom	0.95	0.11	8.98
tetralin	1.33	2.79	4.46
decalin	2.37	11.79	12.11
indene	0.00	0.00	0.56
biphenyl	0.39	0.45	1.26
sulfur	1.33	0.00	0.00
NSO	0.00	0.00	1.33
unknown	0.33	0.29	1.00
Temp (°F)	105	170	125
MMP (psia)	1200	3100	3950

be required for development of miscibility in Oil W, even if chemical type did not have an effect. Fig. 2.24 shows an MMP of about 3100 psia at reservoir temperature of 170°F. This condition corresponds to a CO_2 density of 0.647 gm/cc, which is significantly higher than the miscibility density for Means. Partitioning data showed that temperature did not have a significant effect on extraction behavior, as long as CO_2 density remained constant. Therefore, the increase in CO_2 density required for miscibility in Oil W must be attributed to the oil composition. The chemical type distribution of Oil W, shown in Table 2.20, is somewhat different than that of Means. Specifically, Oil W has a much lower concentration of normal alkanes, and much higher concentrations of branched alkanes and substituted decalins. However, Oil W is still composed predominantly of saturated compounds, which were not shown to differ substantially in extraction behavior. Therefore, the higher CO_2 density required for miscibility is attributable primarily to the carbon number distribution.

It was pointed out in Section 2.2.2 that substituted naphthalenes in Oil W did not show the significantly poorer extraction behavior that was observed for those compounds in Means. A potential explanation for this phenomenon may be found by looking at how the different molecular structures are distributed in terms of carbon number. Fig. 2.30 shows the carbon number distribution for Oil W, broken down into chemical types.

The single carbon number "bars" in Fig. 2.30 were calculated by summing the amounts of all molecules eluting between two normal alkanes, including the second normal alkane. This last normal alkane is the "carbon number" on the x-axis. These data are analogous to a single carbon number "slice" from SIMDIS, except that they also include the identification of the individual molecules present. Fig. 2.30 shows the relatively small amount of carbon number 5, 6, and 7 compounds present in Oil W. The depletion of the C_5 - C_{12} fraction means that significant extraction of the intermediate (C_{12} - C_{20}) hydrocarbons will be required for miscibility. The substituted naphthalenes fall in this range. A possible explanation for the

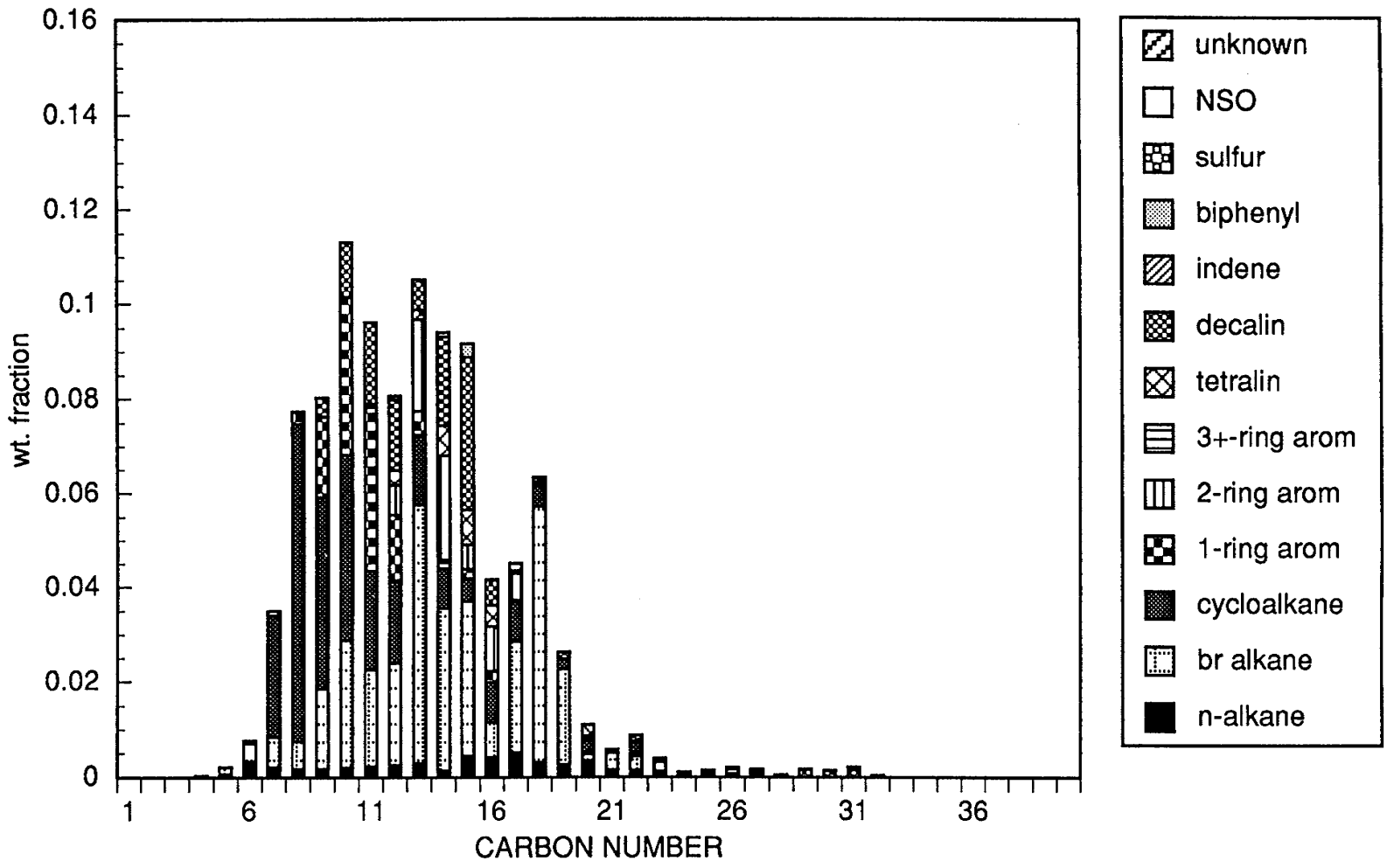

Figure 2.30: Oil W Carbon Number Distribution by Chemical Type

poorer extraction of these compounds in Means, even at high CO_2 densities, is that the presence of a large quantity of easily extractable material in the upper phase eliminates the need for further extraction. This argument is consistent with the results of samples 1 and 2 that showed little additional extraction with an increase in CO_2 density.

The Japanese oil, Kubiki, was chosen for the partitioning experiments because of its unusual slim tube behavior (Fig. 2.27). The partitioning data showed that there were a significant number of two and three or more ring aromatics present in Kubiki, and that these molecules were not extracted as well as the other compounds present. Table 2.20 shows that Kubiki does have a much higher concentration of multi-ring aromatics (2-ring, 3+-ring, biphenyl, NSO) than either of the other two oils. However, the carbon number distribution (SIMDIS analysis) for Kubiki is very similar to that of Oil W. Given the similar "compositions" (based on SIMDIS alone), one would expect the higher temperature oil (Oil W) to have a higher MMP (to achieve the same CO_2 density). Instead, the MMP for Kubiki (as determined by an outlet sight glass) is considerably higher than that of Oil W. In other words, the miscibility density for Kubiki (.844 gm/cc) is much higher than for Oil W (.647 gm/cc). This increase in required density cannot be attributed to size distribution, but must be associated with the types of compounds present. The partitioning data for Kubiki at the miscibility density of Oil W (.647 gm/cc) showed that these multi-ring aromatics were not extracted well. When the pressure (density) was increased to the MMP, however, the naphthalene extraction improved, similar to what was observed for Oil W. Fig. 2.31 shows the carbon number distribution with chemical type breakdown for Kubiki. The data are very similar to Oil W in carbon number, but not in type. As mentioned previously, when the C_5 to C_{12} range is depleted (as in Oil W and Kubiki), the intermediate hydrocarbons must be extracted in sufficient quantities to develop miscibility. In Oil W, this range contains primarily saturated compounds. In Kubiki, however, significant quantities of aromatics are present. Therefore, increased CO_2 density is required to extract enough material into the upper phase to develop miscibility. The unusual, flat shape of the slim tube curve for Kubiki, then, results from the fact that significant increases in density are required to extract more material into the upper phase. This type of behavior has also been observed for heavier oils [39]. Kubiki behaves like a heavy oil because the multi-ring aromatics present behave like higher carbon number aliphatics.

In summary, the experimental results demonstrate that both molecular size and structure affect the way a component is extracted by dense CO_2. While elution time is a reasonable correlating parameter with extraction behavior in most cases, certain classes of compounds, especially the multi-ring aromatics, show anomalous behavior that cannot be accounted for with simple GC compositional analyses.

2.2.3 Numerical Modelling

The availability of a full GC/MS analysis for an oil presents both opportunity and challenge in terms of characterizing the oil for EOS calculations. Obviously, the more information that is available on an oil's composition, the more accurately it can be described. However, while GC/MS provides detailed component by component identification, it does not yield any information on the properties of these components. In order for the data to be useful for numerical modelling, some estimation must be made of either the critical properties

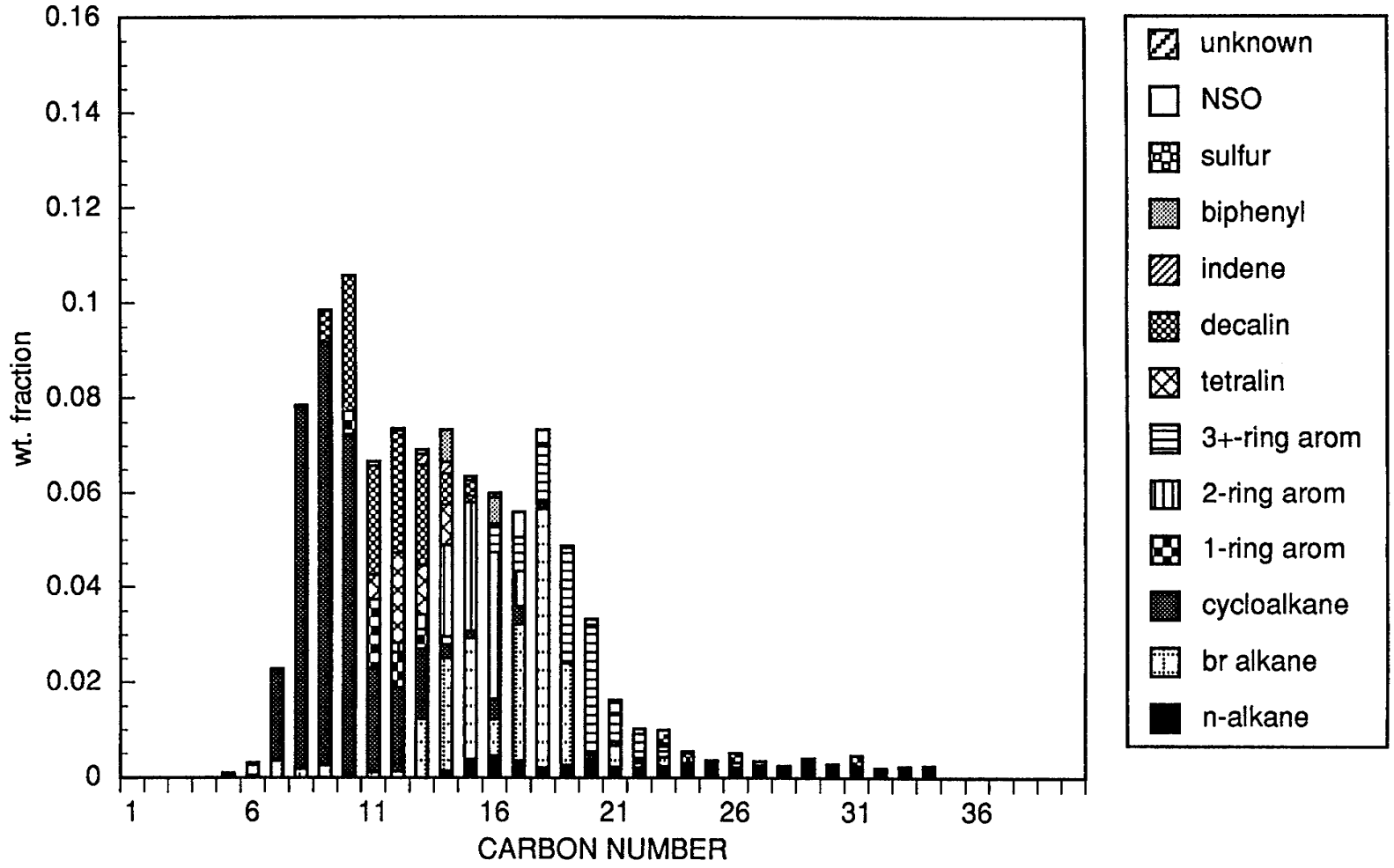

Figure 2.31: Kubiki Carbon Number Distribution by Chemical Type

Table 2.21: Measured or Estimated Critical Properties for Multi-ring Aromatics

Compound	T_c (K)	P_c (atm)	ω	ref
naphthalene	748.4	39.97	.3020	[113]
phenanthrene	873.2	32.57	.5400	[5]
phenanthrene	882.55	31.30	.3299	[62]
anthracene	869	30.83	.3531	[62]
pyrene	938.2	25.65	.3440	[5]

Table 2.22: Measured Boiling Points and Specific Gravities for Multi-ring Aromatics

Compound	T_b (°C)	SG	MW	ref
naphthalene	218	1.015	128	[150]
Me naphthalene	244.6	1.02	142	[23]
di-Me naphthalene	265	1.015	156	[23]
tri-Me naphthalene	263	1.010	170	[23]
fluorene	294	1.203	166	[23]
phenanthrene	340	1.179	178	[107]
pyrene	393	1.271	202	[23]

or, at least, of the boiling point and specific gravity. Measured critical properties are rarely available for any but the most simple structures present in crude oil. Critical properties are especially difficult to find for multi-ring aromatics. Boiling points and specific gravities are available for a few aromatic components.

Multi-ring Aromatic Critical Properties

The problem of assigning critical properties of multi-ring aromatic compounds is two-fold. The first problem is the lack of experimentally measured data. Measured properties are generally available only for the simplest, unsubstituted structures. Properties for some of the heavier compounds such as phenanthrene and pyrene have been estimated from thermal property measurements [65, 66]. These measured and estimated values are not always consistent. Table 2.21 lists some of the measured or estimated properties reported for multi-ring aromatics.

The two reported property values of phenanthrene differ slightly in T_c and P_c and substantially in acentric factor.

Measured boiling points and specific gravities are available for these compounds and for a few other multi-ring aromatics. These data can be used to compare critical property correlation values to the measured data and to predict properties when no measured critical properties are available. Table 2.22 lists the boiling points, specific gravities, and molecular weights of some multi-ring aromatics, including those from Table 2.21.

Table 2.23: Critical Pressures for Multi-ring Aromatics

Compound	Measured (atm)	Twu [139]	Wilson *et al.* [150]
naphthalene	39.97	36.61	38.84
Me naphthalene	N/A	33.83	35.68
di-Me naphthalene	N/A	31.40	32.49
tri-Me naphthalene	N/A	31.30	32.23
fluorene	N/A	33.65	48.77
phenanthrene	32.57	30.29	39.54
pyrene	25.65	27.20	41.90

Table 2.24: Critical Temperatures for Multi-ring Aromatics

Compound	Measured (K)	Twu [139]	Wilson *et al.* [150]
naphthalene	748.4	733.9	740.7
Me naphthalene	N/A	761.1	768.67
di-Me naphthalene	N/A	779.4	787.20
tri-Me naphthalene	N/A	776.3	783.80
fluorene	N/A	839.5	871.00
phenanthrene	873.2	881.5	910.35
pyrene	938.2	944.3	990.65

The second problem that arises in assigning properties to these compounds is the choice of critical property correlation. Most correlations were developed for lighter, paraffinic fractions. The critical property correlations that appear to be most applicable to these higher boiling point, multi-ring structures are those of Twu [139] and Wilson *et al.* [150]. However, neither of these authors presents a correlation for acentric factor. The correlation of Kesler and Lee [60] is commonly used.

Table 2.23 compares the measured critical pressures with those calculated from boiling point and specific gravity using the Twu and Wilson *et al.* correlations. Clearly, the Twu correlation performs better, especially for the larger molecules, phenanthrene and pyrene. It was mentioned previously that extension of the Wilson *et al.* correlation to 3 or more ring compounds was questionable due to the absence of these molecules in the database from which the correlation was derived. The Wilson *et al.* P_c correlation gives values for the 3- and 4-ring structures that are substantially higher than measured values, and even the trend in P_c with molecular size is wrong.

The Wilson *et al.* critical temperature correlation also overpredicts the properties of the 3 and 4 ring molecules, although the deviation is not as severe. Table 2.24 compares the measured T_c values with those from the two correlations. Again, the Twu correlation performs much better.

The Kesler and Lee acentric factor correlation overpredicts this value. Whitson [148] claimed that the Edmister [33] correlation yields lower acentric factors for fractions over

Table 2.25: Acentric Factors for Multi-ring Aromatics

Compound	Measured	Kesler & Lee [60]	Edmister [33]
naphthalene	.302	.3557	.3546
me naphthalene	N/A	.3946	.3932
di-me naphthalene	N/A	.4313	.4298
tri-me naphthalene	N/A	.4307	.4297
fluorene	N/A	.3625	.3617
phenanthrene	.504,.3299	.4504	.4494
pyrene	.344	.4723	.4713

C_{20}. Table 2.25 shows the measured versus calculated acentric factors using both the Kesler and Lee and Edmister correlations. The Edmister correlation does result in lower acentric factors, although the difference is negligible.

From Tables 2.23, 2.24, and 2.25, it is clear that the Twu correlations for critical temperature and critical pressure and the Edmister correlation for acentric factor should be used to estimate the critical properties of the aromatic fractions. The Twu correlation does require the specific gravity of a cut, which may not be known from GC/MS. However, the Twu correlation for molecular weight may be rearranged to solve for specific gravity, given the molecular weight determined directly from the GC/MS data.

Oil Characterization

Full characterization of a crude oil for equation of state calculations requires the quantity of each component or pseudocomponent and the critical properties of that component. While the GC/MS analysis could yield a type of SIMDIS quantitative analysis, the uneluted fraction was not accounted for in these analyses. Also, the possible quantitation errors associated with the GC/MS system that were discussed in Section 2.2.1 make this method undesirable. For a purely quantitative weight fraction distribution, it is faster and more accurate to perform a standard SIMDIS analysis, including an internal standard run to quantify the uneluted fraction, using conventional gas chromatography (GC).

This section presents a new method that has been developed for characterizing a crude oil that has a significant multi-ring aromatic fraction. The only data required are the weight fraction distribution from SIMDIS and the GC/MS quantitative data that was presented for the whole oils in Section 2.2.2. This method requires that the SCN cuts from SIMDIS be divided into two parts; multi-ring aromatics (MRA), and everything else (non-MRA). The fraction of a SCN cut that is multi-ring aromatic is easily determined from the GC/MS data. The non-MRA properties can be determined using the Katz and Firoozabadi [59] SCN boiling points and specific gravities, and any appropriate correlation.

Because the Twu [139] correlation requires the boiling point of a cut, some estimate must be made of the boiling point of the MRA fraction. Wilson *et al.* [150] showed that a plot of boiling point versus elution time resulted in two straight lines; one for normal alkanes and one for multi-ring aromatics. This plot can be constructed for the particular column

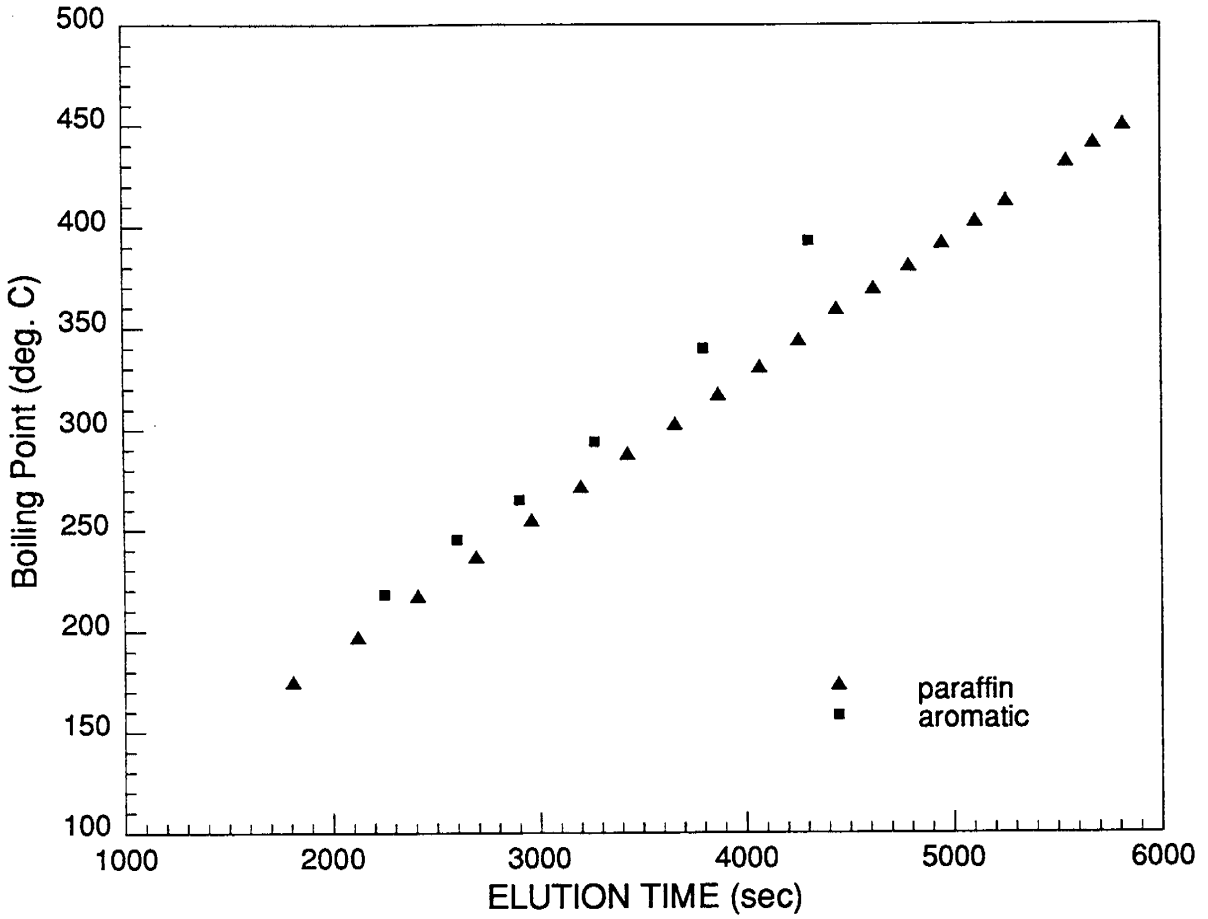

Figure 2.32: Boiling Point versus Elution Time for Pure Components in Crude Oil.

and conditions, using the GC/MS analysis of the oil itself. No additional experiments are required. Such a plot is shown in Fig. 2.32.

The boiling point of a SCN MRA fraction is obtained from Fig. 2.32 by locating the elution time corresponding to the SCN n-alkane on the lower curve, and then reading the boiling point of the coeluting MRA fraction from the upper curve.

The molecular weight for the MRA fraction is calculated directly from the GC/MS analysis. Boiling point and molecular weight are sufficient for the Twu correlation to determine the critical temperature and pressure for the MRA fraction. Acentric factor can be calculated using either the Kesler and Lee or Edmister correlations.

Binary interaction parameters (BIPs) for multi-ring aromatic compounds with CO_2 have been reported in the literature [26]. Appropriate BIPs for the MRA cuts can be estimated from the pure component values of similarly eluting molecules.

Table 2.26: Nine Pseudocomponent Oil Description – non-MRA Base Case

Components	mole frac.	P_c (atm)	T_c (K)	ω	MW
PC5-PC8	.1115	30.79	524.6	0.2820	89.4
PC9-PC11	.1575	24.00	628.6	0.3981	135.8
PC12-PC14	.1847	20.08	687.6	0.4938	175.2
PC15-PC16	.1292	17.63	731.9	0.5724	212.7
PC17-PC18	.1034	16.03	761.8	0.6334	243.1
PC19-PC20	.0728	14.85	784.8	0.6844	268.9
PC21-PC22	.0553	13.77	808.0	0.7379	298.8
PC23-PC25	.0560	12.80	831.3	0.7935	329.1
PC26+	.1296	9.74	917.9	1.0989	492.0

Table 2.27: Nine Pseudocomponent Oil Description – First Aromatic Case

Components	mole frac.	P_c (atm)	T_c (K)	ω	MW
PC5-PC8	.1115	30.79	524.6	0.2820	89.4
PC9-PC11	.1575	24.00	628.6	0.3981	135.8
PC12A-PC16A	.0958	30.49	811.3	0.4577	165.5
PC12-PC15	.1995	19.74	693.7	0.5038	180.0
PC17A-PC22A	.1085	27.19	897.4	0.5454	201.6
PC16-PC19	.1086	16.06	761.0	0.6319	242.5
PC20-PC25	.0775	13.26	820.2	0.7665	314.2
PC23A-PC26+A	.0505	14.75	1005.3	0.9515	390.6
PC26+	.0907	9.74	917.9	1.0989	492.0

Slim Tube Simulations

In order to study the effect of multi-ring aromatics in a crude oil on the displacement process, slim tube experiments were simulated using the full Kubiki oil description presented by Hagedorn [43]. The 40-foot slim tube was modelled using 80 grid blocks. Cubic relative permeability functions were used for simplicity.

A non-MRA oil was set up using the nine pseudocomponents with only non-MRA properties. For the first aromatic case, the MRA and non-MRA components were lumped separately by carbon number, with each pseudocomponent containing entirely MRA or entirely non-MRA constituents. The pseudocomponents and their properties are given in Tables 2.26 and 2.27.

Fig. 2.33 shows the results of slim tube simulations at 125°F, using the two 9-component cases with all of the CO_2/hydrocarbon binary interaction parameters set to 0.08. Clearly, inclusion of the multi-ring aromatic properties in the oil description results in a higher minimum miscibility pressure.

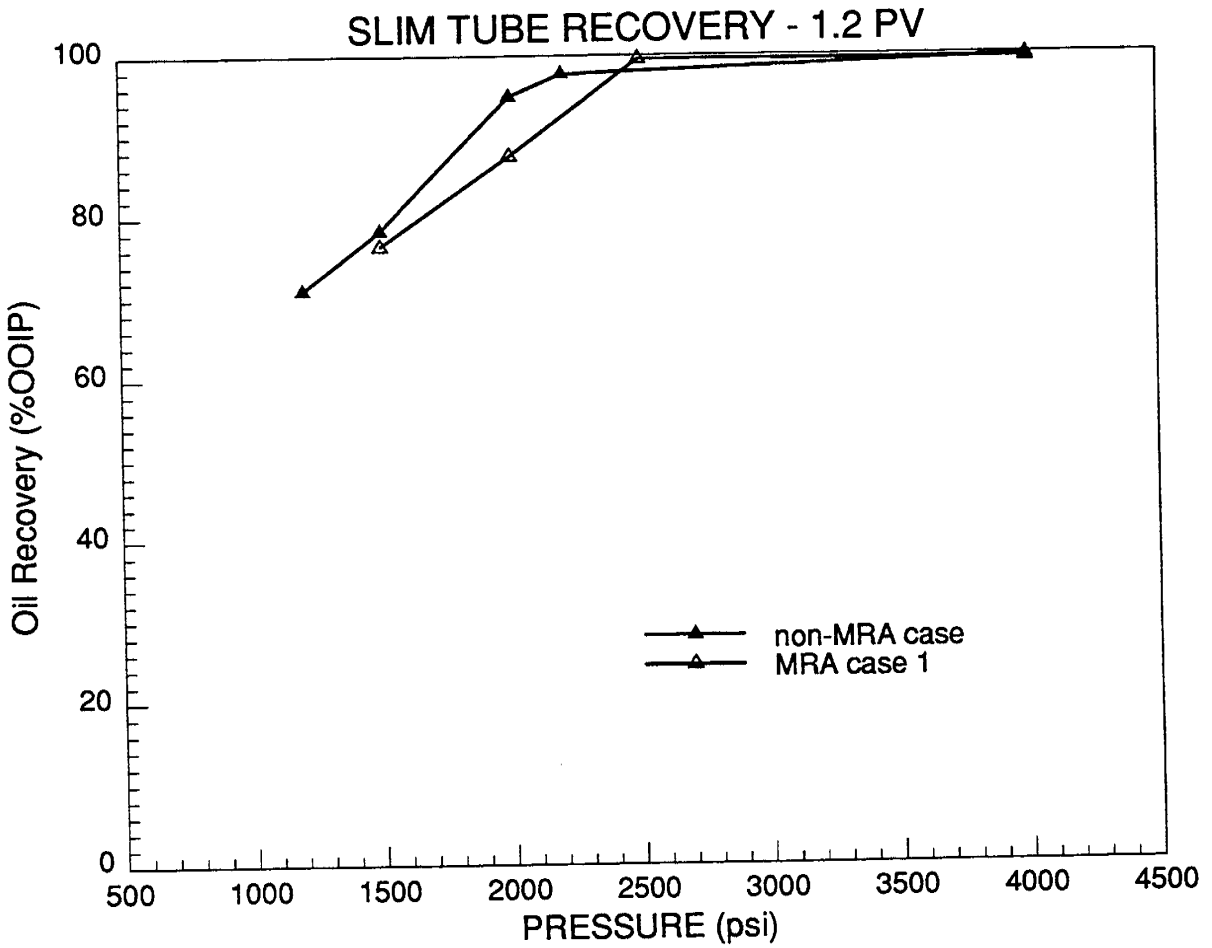

Figure 2.33: Slim Tube Simulation, Kubiki 9-component Base and Aromatic Lumped Descriptions.

Table 2.28: Nine Pseudocomponent Oil Description – Second Aromatic Case

Components	mole frac.	P_c (atm)	T_c (K)	ω	MW
PC5-PC8	.1115	30.79	524.6	0.2820	89.4
PC9-PC11	.1575	24.00	628.6	0.3981	135.8
PC12-PC14	.1847	21.33	696.4	0.4812	170.9
PC15-PC16	.1292	23.26	774.8	0.5145	188.2
PC17-PC18	.1034	18.39	783.3	0.6023	228.0
PC19-PC20	.0728	22.63	858.9	0.5817	219.2
PC21-PC22	.0553	18.52	864.4	0.6558	257.7
PC23-PC25	.0560	14.46	853.9	0.7567	309.8
PC26+	.1296	10.56	944.9	1.0849	475.5

To evaluate the effect of lumping MRA and non-MRA components, a second aromatic description was set up with the MRA components lumped with non-MRA components. This oil description is given in Table 2.28. The binary interaction parameters for all CO_2/hydrocarbon pairs were set to 0.08 for this comparison.

The slim tube simulation results for the two MRA-inclusive descriptions of Tables 2.27 and 2.28 are shown in Fig. 2.34. The lumping procedure does have an effect on the slim tube recoveries, with slightly lower recoveries resulting from the lumping scheme that combined MRA and non-MRA components into a single pseudocomponent. The difference between the two schemes is small, though. Therefore, the first nine component description can be used to illustrate the effects of the various parameters on slim tube results. It is recognized, however, that the lumping scheme does affect the simulation results and should be studied more carefully for tuning or prediction purposes.

Although the relative accuracies of the two specific lumping schemes presented here are unknown, the method of lumping employed in the first MRA-inclusive scheme (Table 2.27) is preferable. Because the MRA components have such distinctive partitioning behavior and because they have considerably different properties from other, coeluting components, it makes more physical sense to lump them separately. Tuning the various critical properties and interaction parameters is much more realistic if the pseudocomponents include this narrower range of behavior.

To evaluate the effect of the CO_2/MRA interaction parameters, another set of slim tube simulations was performed using the oil description of Table 2.27 with non-MRA interaction parameters of 0.08 and interaction parameters of the respective MRA pseudocomponents of 0.135, 0.15, and 0.25. These MRA interaction parameters were based on the BIPs of the individual components comprising the MRA pseudocomponents. The results of this set of simulations are compared with those of the same oil description with constant interaction parameters of 0.08 in Fig. 2.35. The effect of the higher MRA interaction parameters is to decrease recoveries and flatten the shape of the recovery versus pressure curve.

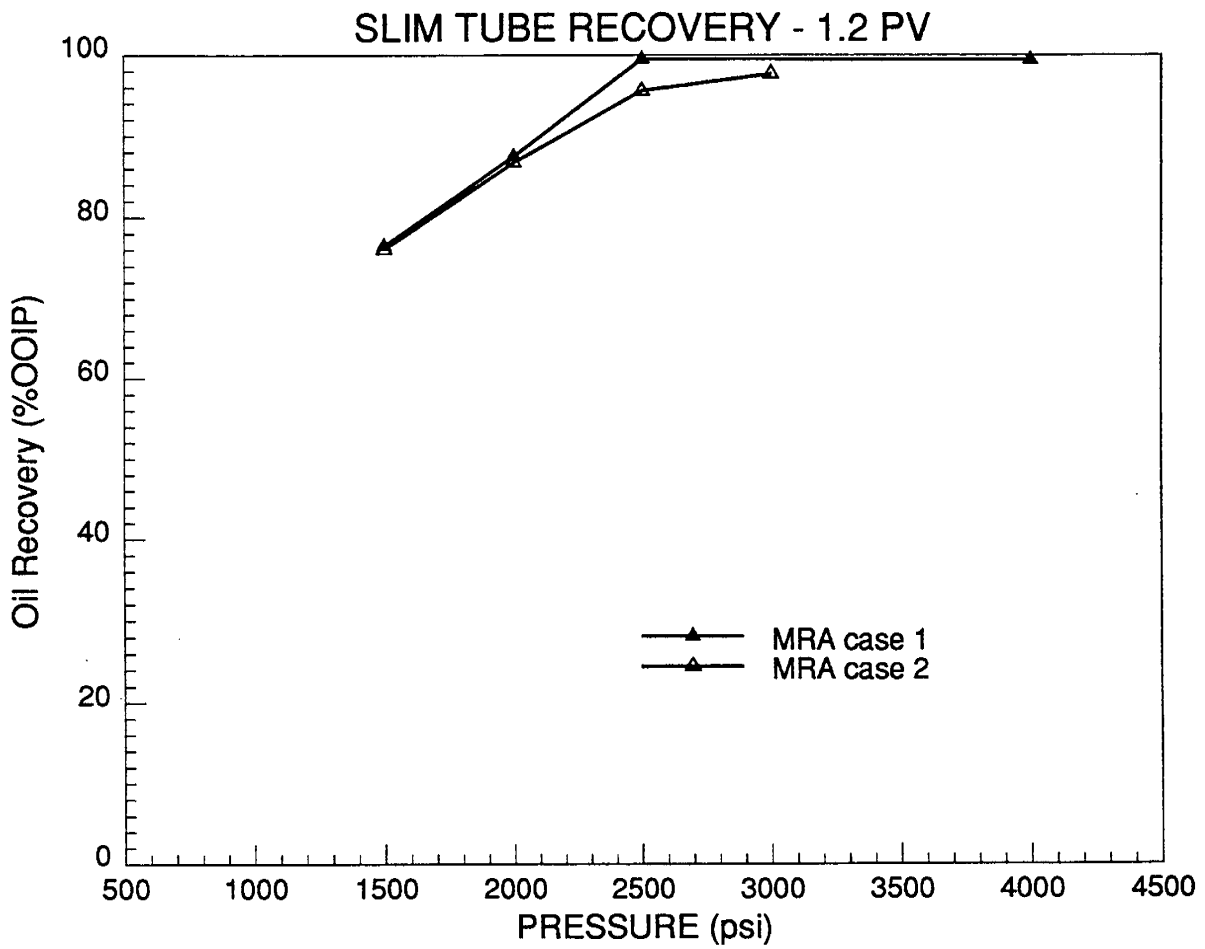

Figure 2.34: Slim Tube Simulation, Kubiki 9-component Aromatic Lumped Descriptions.

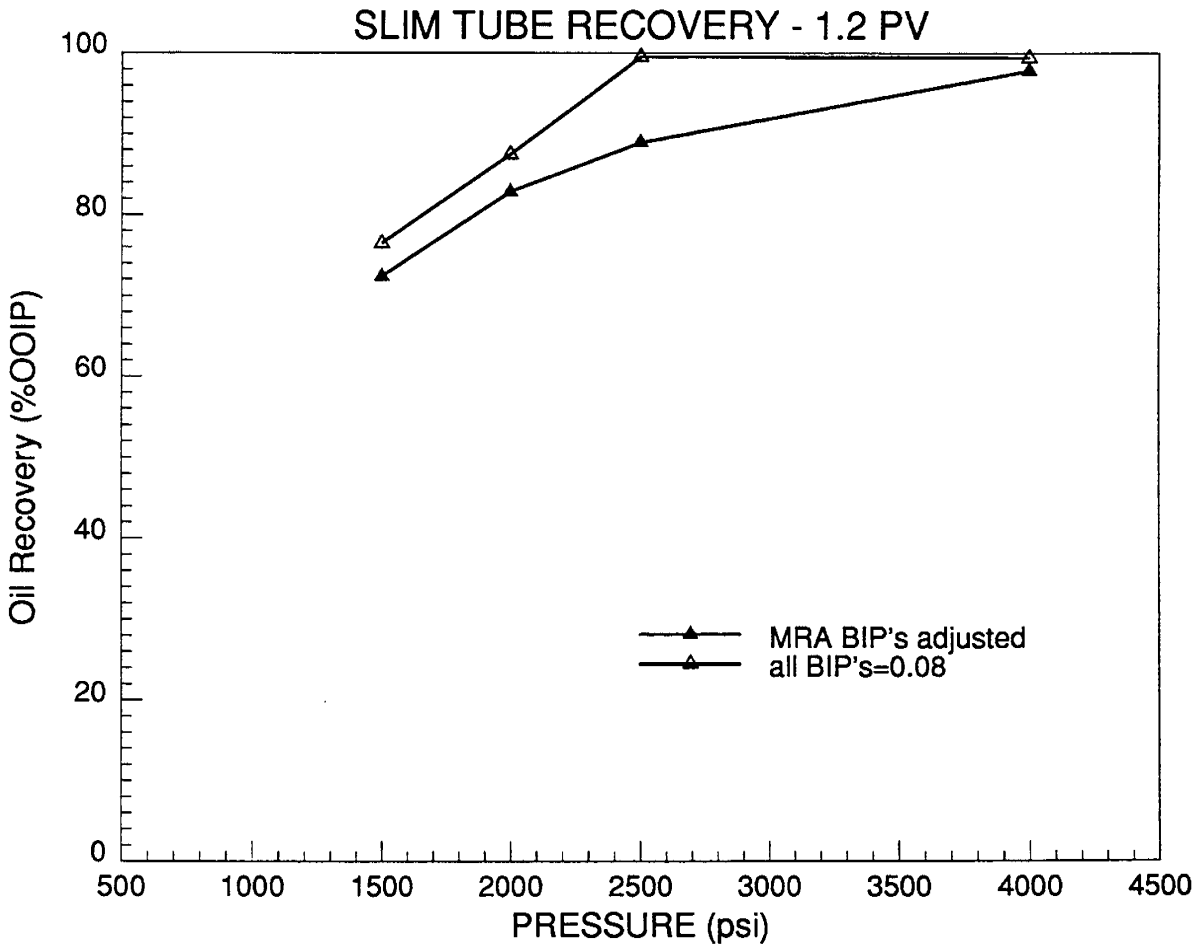

Figure 2.35: Slim Tube Simulation, Effect of Multi-ring Aromatic Binary Interaction Parameters.

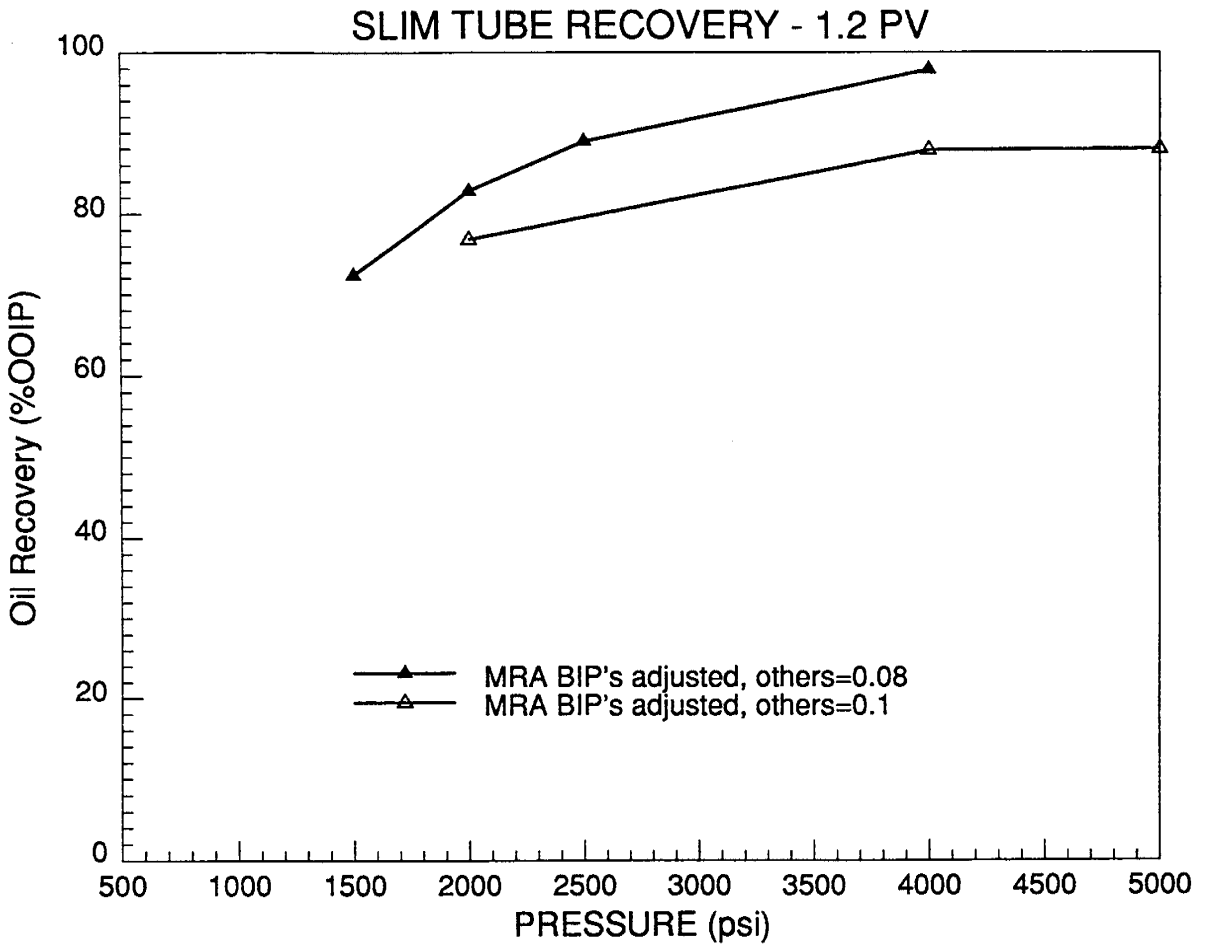

Figure 2.36: Slim Tube Simulation, Effect of All Binary Interaction Parameters.

When the non-MRA interaction parameters are also increased, the recovery versus pressure curve becomes flatter, with even lower recoveries, as Fig. 2.36 shows. The lower curve in the figure results from using the oil description of Table 2.27 with the CO_2/MRA interaction parameters of 0.135, 0.15, and 0.25, respectively, and the CO_2/non-MRA interaction parameters of 0.1. The effect of increasing all of the interaction parameters is to flatten the recovery curve to a shape much like that observed for Kubiki.

The results of this series of slim tube simulations confirm that including multi-ring aromatic properties in an oil description increases the MMP, and indicate that the binary interaction parameters of both the MRA and non-MRA components have a very strong effect on the phase behavior. While no attempt was made in this study to determine the true interaction parameters for Kubiki or any other oil, it is clear that the choice of binary interaction parameters is very important if the experimental slim tube recoveries are to be reproduced. Binary interaction parameters are functions of chemical structure, just as are critical properties [26]. Therefore, the entire oil composition, as obtained from the GC/MS analyses, should be included in the selection of binary interaction parameters.

The use of higher non-MRA interaction parameters for the oil description with MRA components included than for the non-MRA description is justifiable, based on the entire compositional descriptions of Kubiki and Oil W. Cyclic compounds, present in significant quantities in the lighter fraction of Kubiki, have higher interaction parameters than branched alkanes or 1-ring aromatics, which make up a significant portion of the same carbon number range in Oil W [26]. Therefore, the variation in interaction parameters from the non-MRA description in Fig. 2.35 to the MRA description with non-MRA BIPs of 0.1 in Fig. 2.36 easily falls within the range of physically reasonable parameters, and is able to reproduce the effect of multi-ring aromatics on slim tube performance that was observed experimentally for Oil W and Kubiki.

2.2.4 Conclusions

Based on the experimental and simulation results presented in this work, the following conclusions have been drawn:

1. Molecular size is the dominant factor in determining how well a component is extracted by CO_2, but chemical structure does have an effect.

2. Multi-ring aromatic components in crude oils are extracted significantly less efficiently by dense CO_2 than other components of similar size or similar GC elution time.

3. The presence of significant quantities of multi-ring aromatic compounds in a crude oil is detrimental to the development of miscibility with CO_2.

4. Elution time from a gas chromatograph is an appropriate way to characterize an oil, as long as the multi-ring aromatic fraction, if present, is treated separately.

5. The Twu [139] correlation for critical temperature and critical pressure should be used for multi-ring aromatics. The Kesler and Lee or Edmister correlations should be used for acentric factor.

6. Including the MRA properties in the oil characterization results in a decrease in slim tube recovery a given pressure, and a correspondingly higher MMP.

7. Calculated slim tube recoveries are very sensitive to the CO_2/hydrocarbon binary interaction parameters. These interaction parameters are also functions of molecular type.

2.3 Summary

The thermodynamic theory and experimental results presented in Section 2.1 show that supercritical fluid chromatography data can be tied to the characterization of a crude oil for calculations of phase equilibria with an equation of state. The use of simulated distillation by SFC with CO_2 as the carrier is attractive as an analytical method for crude oils because it lumps together hydrocarbons that partition similarly into CO_2. The crude oil characterization scheme proposed in Section 2.1 permits prediction of CO_2/crude oil

phase behavior based on minimal compositional inforamtion, and it reduces the need for arbitrary adjustment of parameters such as P_c, T_c, w and $\delta_i j$ for pseudocomponents. The characterization scheme is likely to perform best for oils that are dominated by alkanes, because the EOS parameters and interaction parameters used were drawn from alkane data. Thus, the results obtained show that it is possible to add additional experimental constraints to a fluid characterization with little more effort than is required to obtain compositional information about the oil in the first place. Because that information is required anyway, the approach described is a significant improvement over existing techniques.

The detailed compositional data obtained in the GC/MS analyses of crude oils and phases also demonstrate how information about the distribution of molecular types can be used to explain anomalous slim tube displacement behavior. The phase composition data show clearly that multiring aromatics are extracted less efficiently by dense CO_2 than are alkanes, whether branched or normal. The presence of such compounds in an oil results from the geochemistry of the origins of the oil and, of course, from the subsequent thermal and migratory history of the oil. The results presented suggest that geochemical information about sources and alteration of the oil, which is frequently obtained as part of the exploration process, can be used to advantage to determine when a detailed GC/MS analysis of the oil is needed.

Phase equilibrium calculations with the Peng-Robinson EOS as well as compositional simulations indicate clearly that oils such as the Kubiki crude oil, which contain significant quantities of multi-ring aromatics, require a more detailed characterization than that described in Section 2.1. While many options exist for characterization of oils with multi-ring aromatics, one technique that works well is to represent aromatic cuts separately. The use of physically reasonable EOS parameters for those cuts produces calculated slim-tube behavior that is similar to that measured for Kubiki. The results presented for that oil establish that reservoir engineers planning a CO_2 flood should consult with exploration geochemists to determine whether an analytical techniques more sophisticated than simulated distillation should be used in the development of the oil characterization.

3. Development of Miscibility in Four-Component Gas Drives

In this chapter we examine how phase behavior interacts with two-phase flow in one dimension. Because the flow is one dimensional, effects of viscous fingering, heterogeneity and crossflow, all inherently two- and three-dimensional features, are necessarily absent. We also neglect dispersive mixing. In effect, we assume that there is sufficient diffusion to mix fluids at the pore level, so that any phases present are in chemical equilibrium, but the level of diffusion is too low to cause growth of a significant dispersive transition zone during flow. Such an assumption only applies when the porous medium has minimal local variation in permeability, a situation that is approximated well in slim tube displacements, for example.

Under those assumptions, a minimum miscibility pressure (MMP) can be defined unambiguously. The traditional analysis of development of miscibility is based on ternary systems [112, 46, 80]. It is now well established that in ternary systems, multicontact miscibility can develop in only two ways. If the initial composition of the oil eventually lies on the extension of a critical tie line (a tie line tangent to the binodal curve at the plait point) as the pressure is increased, the displacement is known as a vaporizing gas drive. If, on the other hand, the composition of the injected fluid is the one that lies on a critical tie-line extension as the pressure is increased or the composition of the injected mixture is changed, then the displacement is known as a condensing gas drive.

In this chapter we show that the ternary arguments used to describe development of miscibility do not tell the whole story if more than three components are present. Several investigators have argued that real miscible flood systems show important behavior that cannot be represented adequately on ternary diagrams. For example, Zick [157] and Stalkup [129] used composition simulations to show that multicomponent displacements have characteristics of both condensing and vaporizing gas drives. Jensen and Michelsen [53] used four-component systems to demonstrate that direct application of the critical tie-line criterion from ternary systems leads to incorrect estimates of the minimum miscibility pressure (MMP) in some cases. Stalkup [127] argued that quaternary phase diagrams were required in the analysis of displacements by nitrogen and methane (CH_4). However, none of the previous investigators has developed a rigorous extension of the three-component tie-line criterion for miscibility to systems with more than three components.

This work extends significantly the solution technique described by Monroe *et al.* [83] for one-dimensional, dispersion-free flow of four-component mixtures. Using the method of characteristics (MOC), analytical solutions can be found by geometric constructions not much more difficult than those performed in the Buckley-Leverett solution for displacement of oil by water. A completely general tie-line extension criterion for development of miscibility in quaternary displacements is presented.

To illustrate the range of behavior possible in four-component systems, we consider several model systems. We begin in Section 3.1 with an analysis displacement of mixtures of methane (CH_4), butane (C_4), and decane (C_{10}) by CO_2. That analysis demonstrates a way that miscibility can develop that has not been previously identified. In Section 3.2, we examine systems similar to those described by Zick [157] and Stalkup [129], and we show

that the four-component theory proves the existence of condensing/vaporizing gas drives. We also resolve the questions raised by Jensen and Michelsen [53] about tie-line extension criteria in multicomponent systems. In Sections 3.1, 3.2 and 3.3, we simplify the analysis somewhat by assuming that there is no change in volume as components transfer between phases. In Section 3.3 we show that there are many possible combinations of vaporizing and condensing mechanisms, and we report a simple classification of displacement types based on equilibrium K-values. In Section 3.4 we relax the assumption of no volume change as components transfer between phases, and we demonstrate the effects of numerical dispersion in comparisons of the analytical solutions with finite difference numerical solutions. We return to the model CH_4/ C_4/ C_{10} system in Section 3.3, where we consider displacements by CO_2/ C_4 mixtures and N_2. In Section 3.4 we resolve the questions raised by Stalkup [127] about the representation of the displacements with N_2 and CH_4 present.

The analytical solutions presented here illustrate the variety of compositional behavior that can occur in four-component systems, and they provide considerable guidance about systems with more than four components. Hence, they represent a significant extension of the previously existing theory of the development of miscibility.

3.1 Displacement of $CH_4/C_4/C_{10}$ Mixtures by CO_2

Franklin M. Orr Jr., Russell T. Johns, and Birol Dindoruk

3.1.1 Mathematical Model

Consider one-dimensional, dispersion-free flow of four-component mixtures under the same assumptions stated by Monroe *et al.* [83]. In this section we assume that components do not change volume as they transfer between phases, though we emphasize that the tie-line extension criteria presented below do not change if that assumption is relaxed (see Section 3.4 or references [28] or [27] for proof of this statement).

The resulting material balance equations are

$$\frac{\partial C_i}{\partial t_D} + \frac{\partial F_i}{\partial x_D} = 0, \quad i = 1, \cdots, n_c \tag{3.1}$$

with,

$$C_i = \sum_{j=1}^{n_p} c_{ij} S_j \,, \quad F_i = \sum_{j=1}^{n_p} c_{ij} f_j \,, \quad c_{ij} = \frac{x_{ij}}{\rho_i} \Big/ \sum_{k=1}^{n_c} \frac{x_{kj}}{\rho_k} \,,$$

where C_i and F_i are the overall volume fraction and fractional flow of component i, S_j is the saturation of phase j, c_{ij} and x_{ij} are the volume and mole fractions of component i in phase j, ρ_i is the density of component i, and x_D and t_D are dimensionless distance and time.

Phase equilibrium calculations were performed with the Peng-Robinson equation of state [103] (PREOS) with critical properties, acentric factors, and binary interaction parameters given in Table 3.1. Component densities used to convert mole fractions to volume fractions are also given in Table 3.1. Phase viscosities were calculated with the Lohrenz-Bray-Clark [75] correlation with values of the critical volumes reported in Table 3.1. Under the assumption of no volume change on mixing, phase densities calculated with the PREOS

Table 3.1: Component Properties.

Component	M_w	P_c (psia)	T_c (deg F)	V_c (ft^3/mol)	ω	s_i (ft^3/mol)
CO_2	44.01	1071.0	87.90	1.5060	0.2250	0.0600
CH_4	16.04	667.8	-116.63	1.5899	0.0104	-0.0661
$n-C_4$	58.12	550.7	305.65	4.0828	0.2010	-0.0074
C_{10}	142.29	305.7	652.10	9.6610	0.4900	0.1602

Component	ρ_i (mol/ft^3)		δ_{ij}			
	1600 psia	1730 psia	CO_2	CH_4	$n-C_4$	C_{10}
CO_2	0.4237	0.4843	0.0000	0.1000	0.1257	0.0942
CH_4	0.2627	0.2848	0.1000	0.0000	0.0270	0.0420
$n-C_4$	0.5859	0.5886	0.1257	0.0270	0.0000	0.0080
C_{10}	0.3041	0.3045	0.0942	0.0420	0.0080	0.0000

were not used to calculate phase saturations, but the PREOS densities were used in phase viscosity calculations. Volume translation parameters listed in Table 3.1 were used to improve estimates of phase density for use in those phase viscosity calculations. The fractional flow function was

$$f_g = \frac{S_g^{e_g}/\mu_g}{(1-S_g-S_{or})^{e_o}/\mu_o + S_g^{e_g}/\mu_g}, \tag{3.2}$$

with $S_{or} = 0.20$, $e_o = 2.0$, and $e_g = 2.0$.

Eq. 3.1 is a system of first-order hyperbolic equations. The solution is found by calculating the velocity at which each overall composition propagates through the porous medium [46]. Because dispersion is absent, the mixture compositions that form during the displacement lie on a single composition route that connects the initial composition to the injection composition. The problem then is to find the appropriate route for given initial and injection compositions. Potential solution routes or paths are obtained by solving an eigenvalue problem [46]. Path directions are given by eigenvectors and composition propagation rates (wave velocities) by eigenvalues. Tie lines, for example, are paths, and there are also

two additional nontie-line paths through each composition point [46, 83]. The solution route must then be selected from the infinite set of composition paths subject to the additional "velocity constraint" that requires the propagation velocity for compositions within the two-phase region to increase monotonically as the solution route is traced from the injection composition to the initial composition. For additional details of the solution procedures, see references [27] and [56].

The solution route that satisfies those constraints includes shocks (jumps from one composition to another), continuous variations (spreading waves) along a composition path, and zones of constant state, which arise when the solution route switches from one path to another. Shocks occur when it is impossible to satisfy the velocity constraint with continuous variations. A material balance for each component across a shock shows that the wave velocity of the shock is given by

$$\Lambda = \frac{F_i^I - F_i^{II}}{C_i^I - C_i^{II}} \cdot \tag{3.3}$$

where I and II refer to opposite sides of the shock.

Eq. 3.3 can be used to prove that the solution route can enter or leave a two-phase region only via a shock in which the single-phase composition lies on an extension of an equilibrium tie line [70, 46]. That proof establishes that the solution route will avoid the two-phase region if either the injection composition or the initial composition does not lie on any tie-line extension, and it applies to systems with any number of components. In other words, the displacement will be miscible in the multicontact sense.

In ternary systems, a displacement is multicontact miscible (MCM) only if either the initial or injection composition lies on the edge of or outside the region of tie-line extensions. In this section we consider how miscibility develops when more than three components are present. Monroe *et al.* [83] showed that addition of CH_4 to a C_4/C_{10} mixture induces two-phase flow, but did not investigate how miscibility develops for the live oil. Instead they speculated that strict multicontact miscibility would develop only when that same criterion is met. For four-component systems, however, the three-component tie-line extension criterion is too restrictive. Instead, it is possible to achieve miscibility when both the initial and injection compositions fall well within the region of tie-line extensions.

3.1.2 Solution Structure

Consider the displacement of an initial mixture containing 10% CH_4, 20% C_4 and 70% C_{10} by pure CO_2. Fig. 3.1 shows the composition path solution obtained by the method described in detail by Monroe *et al.* [83]. The corresponding composition profiles are shown as solid lines in Fig. 3.2. The positions of compositions in the profiles in Fig. 3.2 are expressed in terms of wave velocity. To convert to actual position, the wave velocity is simply multiplied by the dimensionless time, in pore volumes. Table 3.2 reports the compositions and wave velocities of the points labeled **a**-**f** in Fig. 3.1.

From the initial composition, **a**, there is a shock to composition **b**, which is on the tie line in the $CH_4/C_4/C_{10}$ plane that extends through composition **a**. From point **b**, there is a second shock to point **c** on the $CO_2/C_4/C_{10}$ face. That shock occurs because wave velocities (eigenvalues) increase along the composition paths that connect the $CH_4/C_4/C_{10}$ face to the $CO_2/C_4/C_{10}$ face. Hence continuous variation along this nontie-line path is prohibited by

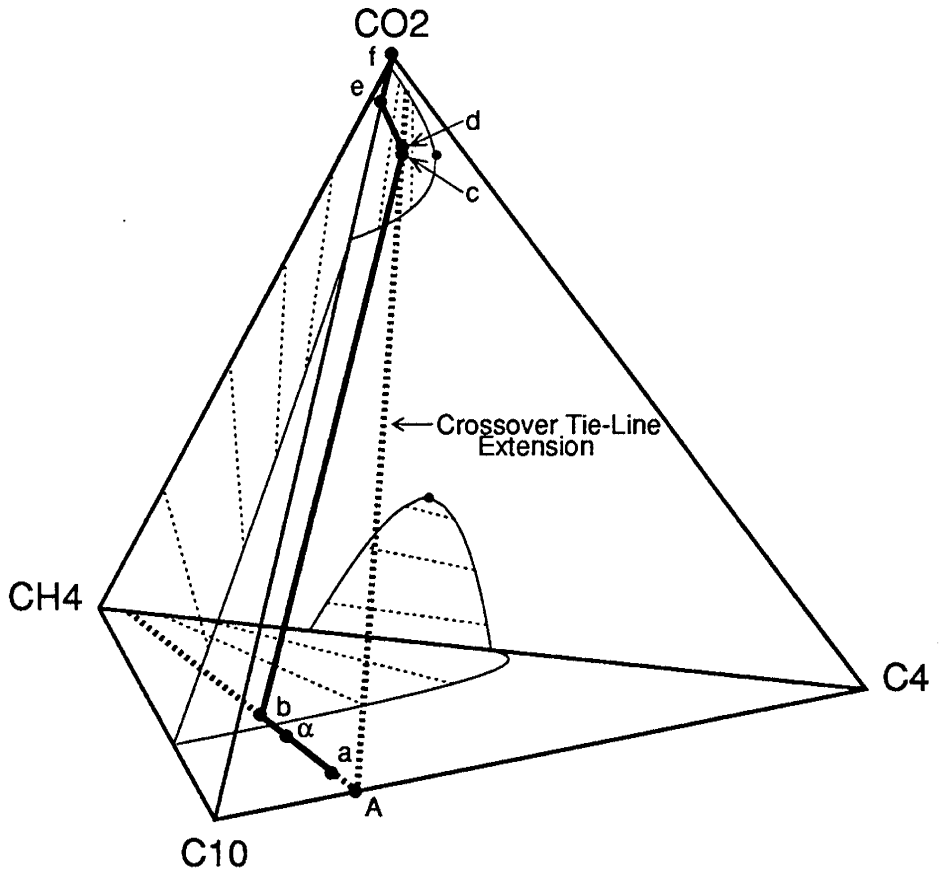

Figure 3.1: Composition route for displacement of a $CH_4/C_4/C_{10}$ mixture by pure CO_2 at 1600 psia, 160° F.

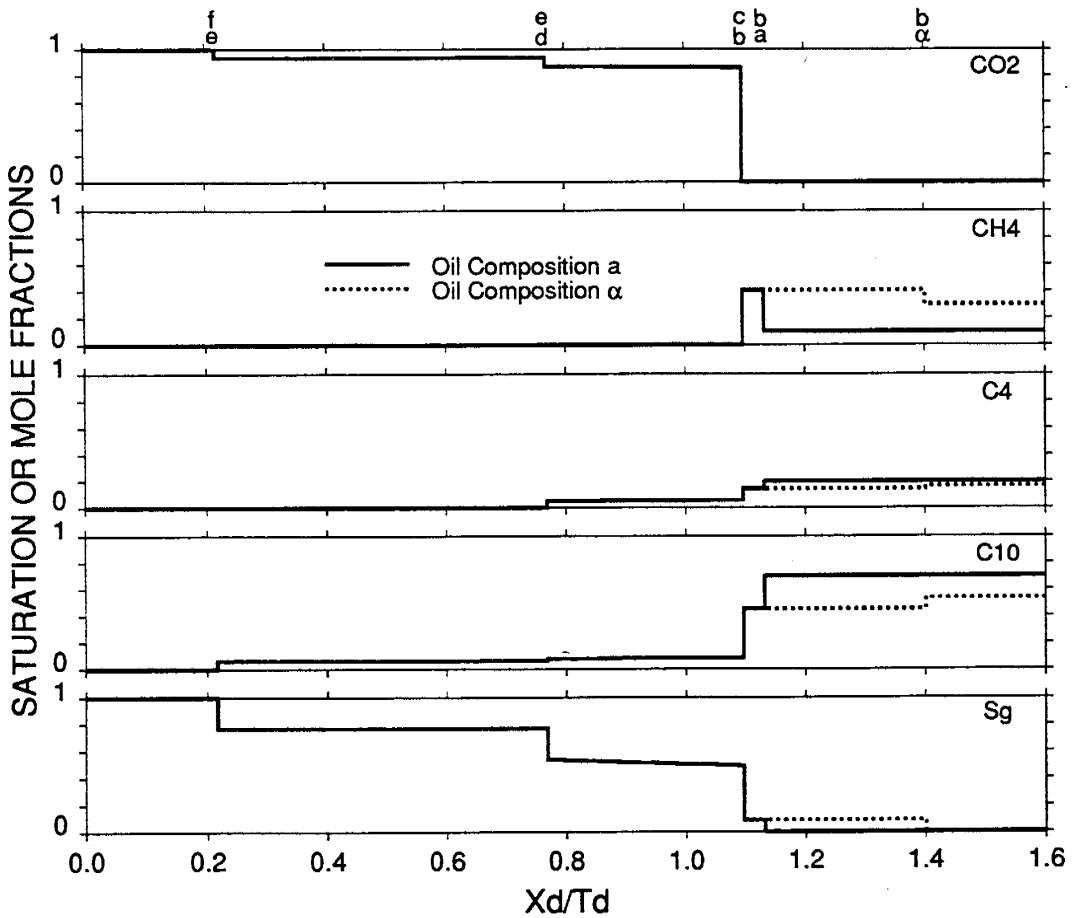

Figure 3.2: Composition profiles for the composition route at 1600 psia, 160° F.

Table 3.2: MOC Solution for the Composition Route at 1600 psia, 160° F.

Composition Label	Composition (Mole Fraction)				Gas Saturation (Vol. Fraction)	Wave Velocity
	CO_2	CH_4	$n-C_4$	C_{10}		
A	0.0000	0.0000	0.2188	0.7812	0.0000	-
a	0.0000	0.1000	0.2000	0.7000	0.0000	1.1308
b	0.0000	0.4046	0.1427	0.4527	0.0899	1.1308-1.0958
c	0.8615	0.0000	0.0531	0.0854	0.4893	1.0958
d	0.8698	0.0000	0.0515	0.0787	0.5379	0.7687
e	0.9376	0.0000	0.0000	0.0624	0.7685	0.7686-0.2166
f	1.0000	0.0000	0.0000	0.0000	1.000	0.2166
Oil Composition α						
α	0.0000	0.3000	0.1624	0.5376	0.0000	1.4013
b	0.0000	0.4046	0.1427	0.4527	0.0899	1.4013-1.0958

the velocity constraint. Note that the CH_4 concentration increases in the shock from **a** to **b** and then drops to zero in the **b**→**c** shock. Hence all the CH_4 from hydrocarbons left behind the leading **a**→**b** shock appears in a CH_4 bank.

Point **c** lies on a very important tie line, which Monroe *et al.* [83] called the *crossover* tie line. Development of miscibility in four-component systems depends on the location of the crossover tie line with respect to the critical locus. Thus, a key result is to demonstrate a simple method for determination of the crossover tie line.

When the solution route reaches point **c**, only three components remain, and the composition route from point **c** to the injection composition, point **f** at the pure CO_2 apex, is the same as that described for a ternary vaporizing gas drive. Between **c** and **d** there is a continuous variation along the crossover tie line, the only continuous variation in the solution to this problem. It is the multicomponent equivalent of the region of continuous saturation variation in a Buckley-Leverett problem. At point **d**, the route jumps to point **e** on the injection tie line, and from point **e**, there is a shock to the injection composition. Hence in this example problem, the properties of the solution are largely governed by the behavior of the **a**→**b**, **b**→**c**, **d**→**e**, and **e**→**f** shocks.

Fig. 3.2 shows that the interplay of phase behavior and two-phase flow causes a chromatographic sorting of components present in the original oil into banks and waves in order of their equilibrium K-values. K-values depend on composition, but for the range of compositions investigated, the values were near 1.8 for CH_4, 1.3 for CO_2, 0.4 for C_4, and 0.09 for C_{10}. Hence, all of the CH_4, which has the largest K-value, appears in a leading bank. CO_2, with the next highest K-value, first appears at the shock in which the CH_4 disappears. Hence, in this example where the injection gas contains none of the components present in the oil and the oil contains no CO_2, no more than three components are present at any spatial location (Fig. 3.2). Because C_4 has the third highest K-value, hydrocarbons present between **c** and **d** are much richer in C_4 than is the original oil. C_4 then disappears at the **d**→**e** shock. C_{10}, with the lowest K-value, is the last to disappear at the slow-moving, trailing evaporation shock. The velocity of that shock is controlled by the solubility of C_{10} in the injected CO_2. That solubility is low when the C_{10} K-value is low.

3.1.3 Solution Construction

When the crossover tie line is connected to the initial and injection tie lines only by shocks (i.e. if the shocks **b** → **c** and **d** → **e** exist), the solutions illustrated in Figs. 3.1 and 3.2 can be constructed by the following sequence of straightforward calculations:

1. Find the crossover tie line for the given initial and injection compositions.

2. Calculate the composition **c** on the crossover tie line and hence the velocity of the **b**→**c** shock, Λ^{bc}.

3. Find composition **b** on the initial tie line and calculate the velocities of the **a**→**b** shock, Λ^{ab}.

4. Find the composition **d** on the crossover tie line and the composition **e** on the injection tie line and calculate the velocities of the **d**→**e** and **e**→**f** shocks, Λ^{de} and Λ^{ef}.

The crossover tie line can be found by a simple geometric construction:

1. Find the tie line in the $CH_4/C_4/C_{10}$ face that extends through the initial composition **a**. Extend that tie line further to find point **A** where it intersects the C_4/C_{10} edge of the ternary face (see Fig. 3.1).

2. The crossover tie line is the tie line in the $CO_2/C_4/C_{10}$ face that also extends through point **A**.

A detailed proof that the crossover tie line is so defined is given in the next section. For the example given here, there is only one tie line in the $CH_4/C_4/C_{10}$ face that intersects the initial composition **a**. Hence there is no question of uniqueness of composition paths for the solutions given here [55].

Point **c** on the crossover tie line is determined from a shock material balance on CO_2, as is shown in the next section. At point **c**,

$$\lambda_t^c = \frac{df_g^c}{dS_g} = \frac{F_{CO_2}^c}{C_{CO_2}^c}, \tag{3.4}$$

in which the eigenvalue for variation along the crossover tie line, λ_t, is simply given by $\frac{df_g}{dS_g}$. Eq. 3.4 is equivalent to the Welge tangent construction for the saturation at the shock that forms during displacement of oil by water.

Once point **c** is known, point **b** on the initial tie line can be found easily from a shock balance on CH_4.

$$\frac{F_{CH_4}^b}{C_{CH_4}^b} = \lambda_t^c \tag{3.5}$$

From composition **b**, the velocity of the leading **a**→**b** shock is given by a shock balance written for any of the three components present in the initial mixture, for example,

$$\Lambda^{ab} = \frac{F_{CH_4}^a - F_{CH_4}^b}{C_{CH_4}^a - C_{CH_4}^b}. \tag{3.6}$$

Points **d** and **e** can be found similarly. The wave velocity of the **d**→**e** shock satisfies another tangent construction of the form,

$$\lambda_t^d = \frac{df_g^d}{dS_g} = \frac{F_{C_4}^d}{C_{C_4}^d}. \tag{3.7}$$

When the composition **d** is known, point **e** is determined from a shock balance on CO_2 or C_{10}.

$$\frac{F_{CO_2}^d - F_{CO_2}^e}{C_{CO_2}^d - C_{CO_2}^e} = \lambda_t^d. \tag{3.8}$$

Finally, the wave velocity of the trailing shock can be found from

$$\Lambda^{ef} = \frac{F_{C_{10}}^e}{C_{C_{10}}^e}. \tag{3.9}$$

Thus, the full solution can be found easily if the crossover tie line is known. Hence, the simple geometric construction given for the determination of the crossover tie line simplifies construction of solutions significantly. We emphasize, however, that this procedure applies only when the crossover tie line is connected to the initial and injection tie lines by shocks, and the injection gas is pure CO_2. Shocks between tie lines occur when eigenvalues increase along nontie-line paths from points near **b** to points near **c** and also increase for paths from **d** to **e**. If eigenvalues decrease along either of those paths then a continuous variation along the nontie-line path will occur. In such cases, the crossover tie line must be found by integration along nontie-line paths.

The crossover tie-line construction given here is a special case of a more general construction. The general construction is based on the fact that if two tie lines are connected by a shock, the extensions of the tie lines <u>must</u> intersect. That statement is proved in Section 3.2 for systems without volume change on mixing and again in Section 3.4 for systems in which components change volume as they transfer between phases (see also references [56, 27, 57, 28, 58].)

3.1.4 Determination of the Crossover Tie Line

The wave velocity of the **a**→**b** shock is given by

$$\Lambda^{ab} = \frac{F_i^a - F_i^b}{C_i^a - C_i^b} \qquad i = CH_4, C_4, C_{10}\,. \tag{3.10}$$

Eq. 3.10 can be written for any two components and the velocity Λ^{ab} eliminated, which yields

$$\frac{F_{CH_4}^a - F_{CH_4}^b}{C_{CH_4}^a - C_{CH_4}^b} = \frac{F_i^a - F_i^b}{C_i^a - C_i^b} \qquad i = C_4, C_{10}\,. \tag{3.11}$$

Eq. 3.11 applies to any point **a** on the extension of the tie line through point **b**. In particular it applies in the limit as the concentration of CH_4 goes to zero, in which case the initial composition is the point **A**. The result for composition **A** is,

$$\frac{F_{CH_4}^b}{C_{CH_4}^b} = \frac{F_i^A - F_i^b}{C_i^A - C_i^b} \qquad i = C_4, C_{10}\,. \tag{3.12}$$

Now consider the material balances for the **b**→**c** shock.
They have the form,

$$\lambda_t^c = \frac{df_g^c}{dS_g} = \frac{F_i^b - F_i^c}{C_i^b - C_i^c} \qquad i = CO_2, CH_4, C_4, C_{10}\,. \tag{3.13}$$

Because CH_4 is missing on the $CO_2/C_4/C_{10}$ face, $F_{CH_4}^c = 0$. Also, CO_2 is not present on the $CH_4/C_4/C_{10}$ face, so $F_{CO_2}^b = C_{CO_2}^b = 0$. Hence, for CH_4 and CO_2, Eq. 3.13 reduces to

$$\lambda_t^c = \frac{F_{CH_4}^b}{C_{CH_4}^b} = \frac{df_g^c}{dS_g}\,, \tag{3.14}$$

$$\lambda_t^c = \frac{F_{CO_2}^c}{C_{CO_2}^c} = \frac{df_g^c}{dS_g}\,. \tag{3.15}$$

Rearrangement of Eq. 3.13 written for C_4 or C_{10} gives

$$F_i^b = F_i^c + \lambda_t^c(C_i^b - C_i^c) \qquad i = C_4, C_{10}\,. \tag{3.16}$$

Rearrangement of Eq. 3.12 with substitution of Eq. 3.14 gives

$$F_i^b = F_i^A + \lambda_t^c(C_i^b - C_i^A) \qquad i = C_4, C_{10}\,. \tag{3.17}$$

Elimination of F_i^b from Eqs. 3.16 and 3.17 gives

$$\lambda_t^c = \frac{F_i^c - F_i^A}{C_i^c - C_i^A} = \frac{df_g^c}{dS_g} \qquad i = C_4, C_{10}\,. \tag{3.18}$$

Eq. 3.18 is exactly equivalent to a set of material balances written for a tangent shock from point **A** to point **c**. Those shock balances require that points **A** and **c** lie on the same tie-line extension [46]). Thus, point A, which lies on the extension of the tie line through point **b** by definition also lies on the extension of the tie line through **c**. Hence, the tie line through **A** and **c** is the crossover tie line.

3.1.5 Continuity

Now consider the effect of variations in the position of point **a** along the same tie-line extension. Once the crossover tie line has been determined for a given initial composition, **a**, the location of point **c** on that tie line is determined from Eq. 3.15 which is independent of the amount of CH_4 in the mixture **a** (because $\lambda_t^c = \frac{df_g^c}{dS_g}$, which depends only on S_g^c for overall composition variations along a single tie line). Once λ_t^c has been found from Eq. 3.15, point **b** is given by Eq. 3.14, which is also independent of the amount of CH_4 present at **a**. Hence points **b** and **c** are invariant for changes in the composition **a** as long as the compositions all lie on the same tie-line extension. Eqs. 3.7 and 3.8 are also independent of the CH_4 fraction in composition **a** as long as the crossover tie line is fixed, which it is as long as point **a** lies on the same tie line extension, and hence points **d** and **e** are also invariant.

Therefore, only the velocity of the leading shock, given by Eq. 3.10, changes if the CH_4 fraction is varied along the same tie-line extension. The solutions given here must be continuous with respect to variations in the initial CH_4 fraction, and the solution reduces continuously to the three-component solution as **a** approaches **A**. In the limit as **a** approaches **A**, the wave velocity of the **A**→**b** shock from Eq. 3.14 is λ_t^c. The wave velocity of the **b**→**c** shock is also λ_t^c from Eq. 3.15. But λ_t^c is exactly the wave velocity of a shock from **A** to point **c**, the leading shock of the ternary solution. Thus, the **a**→**b** and **b**→**c** shocks merge and hence, the four-component solution reduces continuously to the three-component solution as the initial CH_4 fraction goes to zero.

3.1.6 Minimum Miscibility Pressure

The simple geometric construction for the crossover tie line can be put to good use to determine MMP behavior. Consider what happens to the crossover tie line as the displacement pressure is increased while the initial composition is held fixed. As the pressure increases, the two-phase region on the $CO_2/C_4/C_{10}$ face shrinks, and the crossover tie line becomes shorter as it approaches the plait point on that face. If the displacement is to be

MCM, one of the three key tie lines (initial, injection, or crossover) must be a critical tie line. In the example considered here, the crossover tie line approaches the critical plait point at a lower pressure than do the initial and injection tie lines, and hence, the MMP for injection of pure CO_2 to displace $CH_4/C_4/C_{10}$ mixtures is the pressure at which the crossover tie line is the critical tie line in the $CO_2/C_4/C_{10}$ face. Thus, the MMP for a given initial composition can be found by the following steps (see reference [94]) for a proof that piston-like displacement results when the crossover tie line is a critical tie line):

1. Estimate the MMP. Extend the initial tie line in the $CH_4/C_4/C_{10}$ face at the estimated pressure to zero CH_4 concentration, point **A**.

2. Find the pressure at which the critical tie line in the $CO_2/C_4/C_{10}$ face extends through point **A**. That pressure is the updated estimate of the MMP.

3. If the new MMP differs significantly from the previous estimate repeat steps (1) and (2) to convergence.

The procedure outlined is illustrated in Fig. 3.3 in which the change in the MMP when a dead oil is saturated with CH_4 is determined. As Fig. 3.3 shows, a C_4/C_{10} mixture containing 48 mole % C_4 has an MMP of about 1600 psia. Addition of about 35% CH_4 to mixture **A** gives a saturated mixture, **a**, at 1600 psia. Extension of the tie line at 1600 psia through **a** gives composition **B** as Fig. 3.3 shows. Composition **B** lies on a critical tie line at about 1625 psia. Recalculation of the tie line through **a** at 1625 psia gives a new tie-line extension to the C_4/C_{10} axis. In this case, the new tie line differs only slightly from the previous one. Hence, convergence is achieved in only one step. Thus, addition of 35% CH_4 to the original oil changes the MMP, but for this system, in which tie lines in the $CH_4/C_4/C_{10}$ face cross the dilution line at a small angle, the magnitude of the change is small.

Fig. 3.3 shows that addition of CH_4 to a dead oil mixture at its MMP causes the composition route for displacement of the live oil at the same pressure to enter the two-phase region, as Monroe *et al.* [83] observed. Because the resulting crossover tie line lies quite close to the critical point at 1600 psia, however, the displacement is still quite efficient. The simple geometric construction for the tie line makes it clear why empirical correlations for MMP's call for use of the bubblepoint pressure as the MMP if the oil contains so much dissolved CH_4 that its bubblepoint exceeds the MMP estimated or measured for the dead oil. The dispersion-free theory given here proves that the empirical proviso is not strictly correct, though it also shows that, in this system, the change in the MMP is likely to be small. In fact, the change in the MMP of 25 psia in the example given would be smaller than the typical pressure increment in slim tube tests, and hence below the typical resolution of an MMP measurement. We note, however, that MMP's other systems, such as those containing N_2 and CH_4, are much more sensitive to changes in the initial composition. Hence, the technique outlined here should be used to determine how sensitive MMP's are to the initial oil composition.

3.1.7 Sample Solutions

In the example given above, dilution of a C_4/C_{10} mixture with CH_4 changed the crossover tie line. If, however, the initial mixture is modified in such a way that the composition of the point **a** always remains on the same tie-line extension, only the wave velocity of

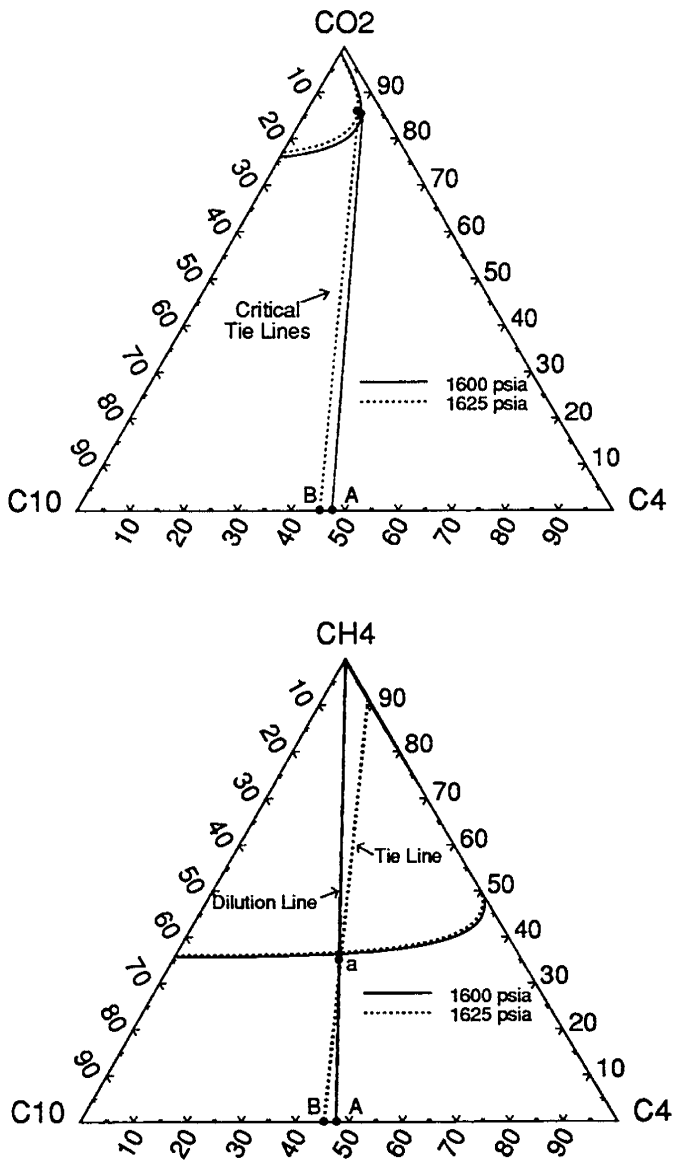

Figure 3.3: Determination of the MMP for initial mixture **a**.

Table 3.3: MOC Solution for the Composition Route at 1730 psia, 160° F.

Composition Label	Composition (Mole Fraction)				Gas Saturation (Vol. Fraction)	Wave Velocity
	CO_2	CH_4	C_4	C_{10}		
A	0.0000	0.0000	0.2189	0.7811	0.0000	-
a	0.0000	0.1000	0.2000	0.7000	0.0000	1.0405
b	0.0000	0.4160	0.1404	0.4436	0.0676	1.0405-1.0302
c	0.8934	0.0000	0.0475	0.0591	0.5784	1.0302
d	0.8942	0.0000	0.0473	0.0585	0.5919	0.9295
e	0.9643	0.0000	0.0000	0.0357	0.9081	0.9295-0.6200
f	1.0000	0.0000	0.0000	0.0000	1.000	0.6200
Oil Composition α						
α	0.0000	0.3000	0.1623	0.5377	0.0000	1.1142
b	0.0000	0.4160	0.1404	0.4436	0.0676	1.1142-1.0302

the leading shock changes as, the continuity arguments that prove the invariance of points **b**, **c**, **d** and **e** for initial compositions on the same tie-line extension show. Fig. 3.2 also shows composition profiles for mixture α in Fig. 3.1, and the resulting velocity of the leading shock is given in Table 3.2. Composition α lies on the same tie-line extension, but it contains three times as much CH_4 as composition **a**. The profiles shown in Fig. 3.2 indicate that the leading CH_4 bank is larger for initial composition α, but the composition profiles upstream of the **b**→**c** shock are unchanged. Thus, the crossover tie line is fixed for all compositions that lie on the same tie-line extension in the $CH_4/C_4/C_{10}$ face.

Any change in initial composition or displacement pressure that results in a crossover tie line closer to the plait point in the $CO_2/CH_4/C_{10}$ face improves displacement efficiency. For example, Fig. 3.4 shows the composition route for displacement of the initial mixture in Figs. 3.1 and 3.2 and Table 3.2, but this time at a pressure of 1730 psia. Details of the analytical solution are given in Table 3.3. As Fig. 3.4 shows, the crossover tie line is much closer to the plait point. Fig. 3.5 shows the resulting composition profiles. Comparison of

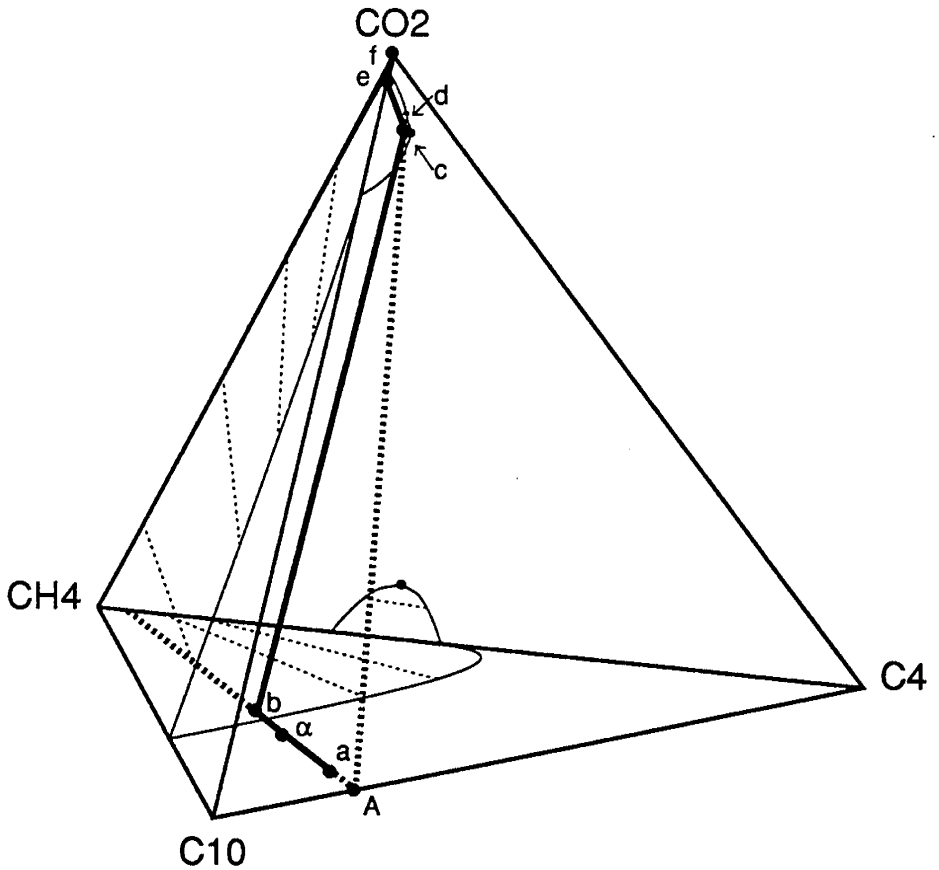

Figure 3.4: Composition route for displacement of oil mixture by pure CO_2 at 1730 psia, 160° F.

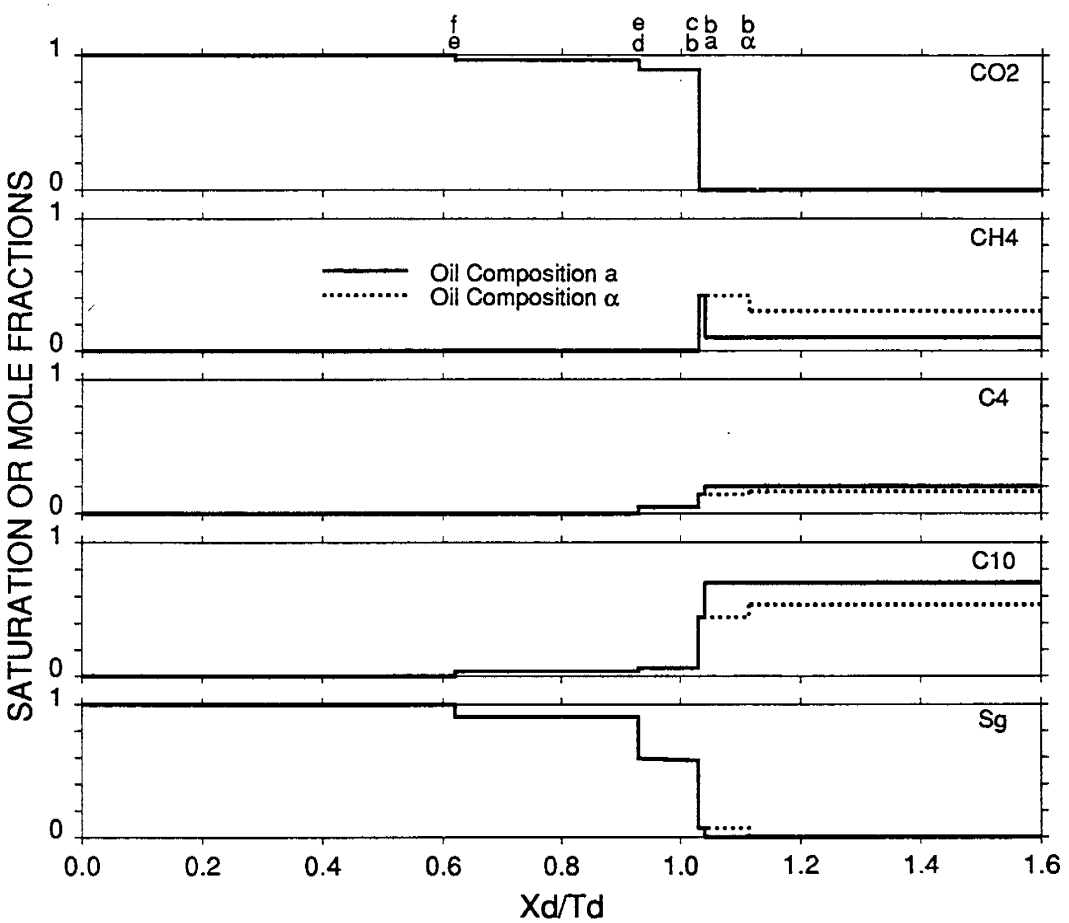

Figure 3.5: Composition profiles for the nearly miscible composition route at 1730 psia, 160° F.

Figs. 3.2 and 3.5 and Tables 3.2 and 3.3 indicates that at the higher pressure the leading shock is slower and the trailing shocks move faster. If the pressure were increased still further to 1750 psia, the MMP according to the crossover tie-line criterion, the trailing, intermediate and leading shocks would all merge, and a piston-like displacement would result.

3.1.8 Discussion

In the examples given here, it is the approach of the crossover tie line to the plait point that determines miscibility. In the next sections we will describe other systems in which either the initial tie line or the injection tie line will control development of miscibility. The examples shown indicate that the crossover tie-line MMP criterion is satisfied for mixture **a** at approximately 1750 psia. At that pressure, both the initial and injection compositions lie well within the region of tie-line extensions. Hence, the crossover tie-line criterion shows that miscibility can develop even when both initial and injection compositions are on tie-line extensions. Thus, the behavior of four-component systems contrasts sharply with that of three-component systems, in which either the injection or initial oil composition must lie outside the region of tie-line extensions if the displacement is to be MCM. For this system, the crossover tie-line criterion is less restrictive than the requirement that either the initial or injection composition be outside the region of tie-line extensions. For example, the injection composition, pure CO_2, lies on a critical tie line at 1870 psia, the CO_2-C_{10} critical pressure. The initial mixture **a** lies on a critical tie line at approximately 4500 psia. Hence, it is clear that the pressure given by the crossover tie-line criterion is much lower than that obtained if the initial or injection composition is to be on a critical tie line. It is likely that many CO_2/crude oil systems containing dissolved CH_4 show similar behavior.

The solutions presented here allow interpretation of the experimental results reported by Metcalfe and Yarborough [80]. They performed displacement experiments for the $CO_2/CH_4/C_4/C_{10}$ system in a Berea sandstone core six feet in length. They reported displacement results at 1500 psia, 1700 psia, and 1900 psia, for an initial mixture containing 40% C_4 with 60% C_{10} and for the same mixture diluted with CH_4 (25 % CH_4, 30% C_4, 45% C_{10}). Phase diagrams calculated with the PREOS are shown in Fig. 3.6.

The displacements at 1500 psia for both initial compositions were immiscible according to the definition given here. Fig. 3.6 shows that composition **B**, the dead oil composition obtained by extending the initial tie line (at 1500 psia) to zero CH_4 concentration, yields a crossover tie line well inside the two-phase region on the $CO_2/C_4/C_{10}$ ternary diagram (Fig. 3.6). The live oil displacement at 1500 psia showed a significant CH_4 bank in effluent composition data, evidence of a chromatographic separation that can only occur if there is two-phase flow.

The live oil displacement at 1900 psia was first contact miscible as Metcalfe and Yarborough reported. A dilution line from the initial live oil composition to pure CO_2 passes close to the edge of the calculated two-phase region in the interior of the quaternary diagram, but does not penetrate it. No CH_4 bank was observed at 1900 psia, another indication that no two-phase flow occurred.

Metcalfe and Yarborough interpreted the displacements at 1700 psia to be MCM. According to the PREOS, at least, the composition **B** is outside the region of tie-line extensions (Fig. 3.6). Fig. 7 of Metcalfe and Yarborough indicates that the critical tie line in the

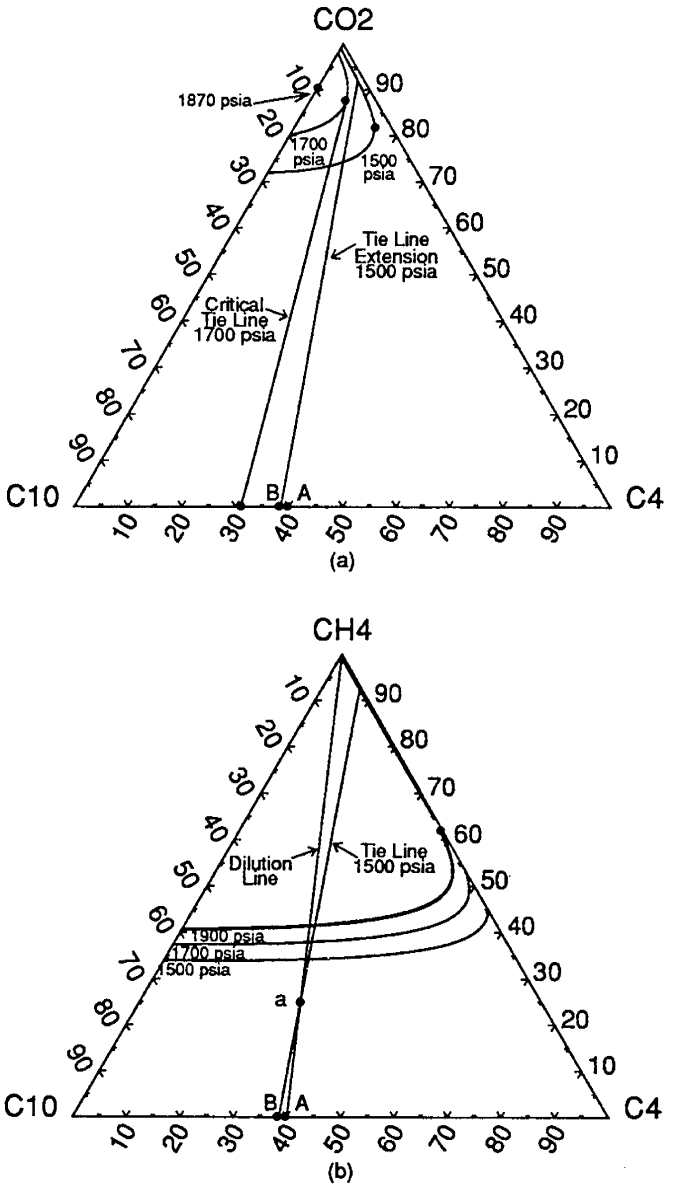

Figure 3.6: Comparison of experimental MMP results with the crossover tie-line criterion.

$CO_2/C_4/C_{10}$ face intersects the C_4/C_{10} axis very close to composition **B**. Hence, the analytical theory supports their interpretation that the displacement was MCM. However, a small CH_4 bank was reported at 1700 psia, clear evidence that two-phase flow occurred somewhere in the core. There are several potential explanations for the existence of the CH_4 bank. For example, the PREOS may not represent the actual phase behavior adequately in the critical region. With a slight change in phase behavior, however, the analytical theory could predict a nearly MCM displacement, which would produce a small CH_4 bank. In addition, two-phase flow may have been caused by other displacement mechanisms not considered in the analytical theory. For example, physical dispersion can cause two-phase flow in a one-dimensional flow that is MCM without dispersion[146]. Furthermore, the experimental displacement was not strictly one-dimensional. Instead, viscous fingering, gravity segregation, and local permeability heterogeneity may have caused some nonuniform flow. As Pande and Orr [98, 99, 100] showed, if crossflow driven by viscous, capillary or gravity forces is also present, it can induce two-phase flow even when the corresponding one-dimensional displacement is MCM. In real displacements some two-phase flow is probably inevitable because dispersion, nonuniform flow, and crossflow are always present. In the limit where these physical mechanisms have small effect, however, as in slim tube displacements, the four-component analytical theory allows unambiguous determination of the MMP.

3.1.9 Conclusions

Analysis of the behavior of dispersion-free MOC solutions for one-dimensional displacement of $CH_4/C_4/C_{10}$ mixtures by pure CO_2 injection shows that:

1. In four-component systems, miscibility can develop even though both the injection and initial oil compositions lie on tie-line extensions.

2. Development of miscibility in displacements of $CH_4/C_4/C_{10}$ mixtures by CO_2 occurs when the crossover tie line is the critical tie line in the $CO_2/C_4/C_{10}$ face.

3. The crossover tie line can be found from a straightforward geometric construction when the crossover tie line is connected to the injection and initial tie line by shocks.

4. If the initial composition is varied along a single tie-line extension, only the velocity of the leading shock (and hence the size of the CH_4 bank) changes. All other portions of the solution remain fixed.

5. Interactions of phase behavior and two-phase flow cause a chromatographic sorting of components present in the initial oil into banks and waves in K-value order. All CH_4 in the zone of two-phase flow appears in a leading CH_4 bank.

3.2 Analytical Theory of Condensing/Vaporizing Gas Drives

Russell T. Johns, Birol Dindoruk, Franklin M. Orr, Jr.

Pseudoternary diagrams have traditionally been used to explain the behavior of multicontact miscible (MCM) gas-drive processes [51]. According to three-component theory, only two types of displacements are possible, vaporizing or condensing gas drives. Both qualitative mixing cell arguments and more rigorous mathematical approaches show that a ternary displacement can be MCM only if either the oil composition (vaporizing gas drive) or the injection gas composition (condensing gas drive) lies outside the region of tie-line extensions on a ternary phase diagram [112, 46, 31]. Thus, a ternary displacement can be either a condensing or a vaporizing drive but not both simultaneously.

Zick [157], however, used experimental and simulation results to show that real oil displacements by gas have characteristics of both vaporizing and condensing gas drives. Stalkup [126, 127, 128] also observed that classical displacement mechanisms are too simple to explain the behavior of real oil displacements by enriched gases. Novosad *et al.* [89] agreed with this view, but concluded that at high temperatures a pure vaporizing mechanism is responsible for high recovery in enriched gas displacements. Tiffin *et al.* [135], however, concluded that enriched gas displacements were primarily condensing, and any vaporizing mechanism that might contribute would be inconsequential to the oil recovery. Lee *et al.* [72] attempted to explain these contradictory results by showing that real field displacements can be either vaporizing, condensing, or both.

To investigate whether both condensing and vaporizing mechanisms contribute to development of miscibility, we consider displacements in four-component systems. We report the first definitive, analytical proof that Zick's description of a combined condensing and vaporizing mechanism is correct for some enriched gas drives. We also extend significantly the analytical solution technique described by Orr *et al.* [94] and Monroe *et al.* [83] for pure gas injection to a two-component gas mixture. We show two types of solutions obtained for condensing/vaporizing (C/V) drives, and we illustrate these types for two enriched gas displacement systems. In the first, mixtures of methane (CH_4) and propane (C_3) displace an oil containing $/rmCH_4$, n-hexane (C_6), and n-hexadecane (C_{16}). In the second, the injection gas is a mixture of CH_4 and ethane (C_2), while the oil remains unchanged. In both solutions, flow behavior is strongly influenced by the crossover tie line defined in Section 3.1. We demonstrate how to find the crossover tie line in each case, and show that it is the volatility (equilibrium K-values) of the C_2 or C_3 that determines the type of solution. Finally, we examine how development of miscibility occurs for C/V systems.

3.2.1 Shocks

The material balance equations solved in this section are given in Section 3.1.1. Component properties used for phase equilibrium calculations are reported in Table 3.1. As in Section 3.1, the solution is composed of continuous variations and shocks. Shocks or discontinuities in the solution occur when a continuous variation along an eigenvector path violates

the velocity constraint. Shocks must satisfy the jump relations (integrated mass balance of Eq. 3.1) of the form

$$\Lambda = \frac{F_i^U - F_i^D}{C_i^U - C_i^D} \quad i = 1, \cdots, n_c \,, \tag{3.19}$$

where U is the upstream side of the shock, D is the downstream side of the shock, and Λ is the shock velocity. These jump relations specify the speed a shock must take if a component is to be conserved across the shock.

In the examples that follow, several types of shocks are important. The first type is a shock from an overall composition in a single-phase region to a two-phase overall composition. Larson [70] showed that the single-phase composition must lie on the extension of an equilibrium tie line for such shocks. The second type is a shock from one tie line to another in the two-phase region. This shock, sometimes referred to as a "self-sharpening wave" [15], occurs when the eigenvalue on the nontie-line path violates the velocity constraint. In the examples considered here the equilibrium K-value of the light intermediate component (C_2 or C_3) determines whether composition variations along nontie-line paths are self-sharpening or not. It is important to know whether such variations are self-sharpening because that determines the method used to find the crossover tie line. Either type of shock may be (1) an intermediate discontinuity (tangent shock [83]) in which the shock velocity is equal to the local eigenvalue on one side of the shock or (2) a genuine (nontangent) shock, in which the shock velocity does not match the local wave velocity on either side of the shock, and hence the shock lies between zones of constant state.

To see how self-sharpening waves depend on K-values, we transform Eq. 3.1 to a new set of dependent variables, C_i and y_i, the volume fraction of component i in the vapor phase [55]. For ternary systems,

$$\begin{pmatrix} \frac{\partial C_1}{\partial t_d} \\ \frac{\partial y_1}{\partial t_d} \end{pmatrix} + \begin{pmatrix} \frac{\partial F_1}{\partial C_1} & \frac{\partial F_1}{\partial y_1} \\ 0 & \frac{F_1+h}{C_1+h} \end{pmatrix} \begin{pmatrix} \frac{\partial C_1}{\partial x_d} \\ \frac{\partial y_1}{\partial x_d} \end{pmatrix} = 0 \,, \tag{3.20}$$

where the eigenvalues are easily identified as

$$\lambda_t = \frac{\partial F_i}{\partial C_i} = \frac{df_g}{dS_g} \quad \lambda_{nt} = \frac{F_1 + h}{C_1 + h} \,, \tag{3.21}$$

and the function h is

$$h(y_1) = \frac{\frac{db}{d\xi}}{\frac{da}{d\xi}} \,. \tag{3.22}$$

The function a is the tie-line slope ($a = \frac{y_2 - x_2}{y_1 - x_1}$) and b is the tie-line intercept ($b = \frac{y_1 x_2 - x_1 y_2}{y_1 - x_1}$), and ξ is a parameter (say arc length) that varies monotonically along the nontie-line path.

The eigenvector associated with the nontie-line eigenvalue is

$$\frac{dC_1}{d\xi} = 1.0 \quad \frac{dy_1}{d\xi} = \frac{\lambda_{nt} - \lambda_t}{\frac{\partial F_1}{\partial y_1}} \,. \tag{3.23}$$

The derivative of the nontie-line eigenvalue along the nontie-line path is

$$\frac{d\lambda_{nt}}{d\xi} = \frac{1}{C_1 + h}\left[\frac{dF_1}{d\xi} + \frac{dh}{d\xi} - \lambda_{nt}(\frac{dC_1}{d\xi} + \frac{dh}{d\xi})\right]. \tag{3.24}$$

Because $\frac{dF_1}{d\xi} = \lambda_{nt}$ (proved using the chain rule), Eq. 3.24 becomes

$$\frac{d\lambda_{nt}}{d\xi} = \frac{\frac{dh}{d\xi}}{C_1 + h}(1 - \lambda_{nt}). \tag{3.25}$$

The expression for the nontie-line eigenvalue can be substituted into this equation to obtain

$$\frac{d\lambda_{nt}}{d\xi} = \frac{-\frac{dh}{d\xi}}{(C_1 + h)^2}(F_1 - C_1). \tag{3.26}$$

Hence, in the region where $F_1 > C_1$ (the region of interest), the nontie-line eigenvalue decreases along the nontie-line path if $\frac{dh}{d\xi}$ is positive. Thus, the sign of $\frac{dh}{d\xi}$ determines how the nontie-line eigenvalue varies along the nontie-line path.

To show how self-sharpening behavior depends on component volatility, we assume that equilibrium K-values, $K_i = \frac{y_i}{x_i}$, do not change with composition variations. After significant algebra [56], we find that the derivative $\frac{dh}{d\xi}$ is proportional to a new function H,

$$H = \left[\frac{(K_1 - K_2)(K_2 - K_3)}{(1 - K_2)(1 - K_3)}\right]\frac{dx_2}{d\xi}. \tag{3.27}$$

If $H > 0$, the nontie-line eigenvalue decreases along the nontie-line path, while if $H < 0$, the nontie-line eigenvalue increases along the nontie-line path. For the case when K-values are independent of composition, the derivative $\frac{dx_2}{d\xi}$ is either positive or negative depending on the direction taken along the nontie-line path. To apply this result to the PREOS, however, typical K-values must be chosen. In the examples considered in this section, direct computation of the eigenvalues on nontie-line paths indicates that Eq. 3.27 also holds for phase behavior calculated with the PREOS.

3.2.2 $CH_4/C_3/C_6/C_{16}$ Displacements

We examine first the $CH_4/C_3/C_6/C_{16}$ hydrocarbon system at 2000 psia and 200°F. Direct computation with the PREOS shows that $K_{CH_4} > K_{C_3} > K_{C_6} > K_{C_{16}}$ for all compositions inside the two-phase region. Only CH_4 has a K-value greater than unity at this temperature and pressure.

Fig. 3.7 and Table 3.2 give the analytical solution for a three-component oil (labeled **O**) displaced by enriched mixtures of CH_4 and C_3 (labeled $\mathbf{I_1}$, $\mathbf{I_2}$, $\mathbf{I_3}$, $\mathbf{I_4}$, $\mathbf{I_5}$). Fig. 3.8 shows the corresponding composition and saturation profiles for the immiscible displacements by injection gas $\mathbf{I_1}$, $\mathbf{I_2}$ and $\mathbf{I_3}$. Consider the typical solution illustrated for the displacement by injection gas $\mathbf{I_2}$. The solution lies on three key tie lines: (1) the tie line whose extension passes through the injection gas composition (called the injection gas tie line), (2) the tie line whose extension passes through the oil composition (called the initial oil tie line), and (3) a key tie line known as the crossover tie line. The analytical solution includes: (1) a trailing nontangent shock from the injection gas composition $\mathbf{I_2}$ to $\mathbf{F_2}$ along the injection gas tie line, (2) a region of constant state at $\mathbf{F_2}$, (3) a self-sharpening tangent shock from $\mathbf{F_2}$ to $\mathbf{E_2}$ on

the crossover tie line, (4) a continuous variation from $\mathbf{E_2}$ to the equal eigenvalue point $\mathbf{D_2}$, with velocities given by the tie-line eigenvalue, (5) a continuous variation along the nontie-line path from $\mathbf{D_2}$ to $\mathbf{B_2}$ on the initial oil tie line, with velocities given by the nontie-line eigenvalue, (6) a region of constant state at $\mathbf{B_2}$, (7) and a nontangent shock from $\mathbf{B_2}$ to the oil composition $\mathbf{O}$. The $\mathbf{F_2} \rightarrow \mathbf{E_2}$ shock occurs because the nontie-line eigenvalue increases from $\mathbf{E_2}$ to $\mathbf{F_2}$, and a continuous variation there would violate the velocity constraint. A continuous variation along the $\mathbf{D_2} \rightarrow \mathbf{B_2}$ nontie-line path, however, is allowed because the nontie-line eigenvalue increases from $\mathbf{D_2}$ to $\mathbf{B_2}$.

Fig. 3.8 shows that the components in the oil are separated chromatographically according to their volatilities. CH_4, with the highest volatility, is displaced first followed by a small C_3 bank. C_6 disappears next at the self-sharpening shock from $\mathbf{E_2}$ to $\mathbf{F_2}$. C_{16} with the lowest volatility is completely evaporated at the slow moving trailing shock from $\mathbf{F_2}$ to $\mathbf{I_2}$. In this example, the nontie-line path intersects the constant-composition plane for CH_4 twice, and thus, the CH_4 concentration decreases and then increases from $\mathbf{B_2}$ to $\mathbf{D_2}$ (this effect is more pronounced from $\mathbf{B_3}$ to $\mathbf{D_3}$). Because the nontie-line eigenvalue does not vary significantly from $\mathbf{B_2}$ to $\mathbf{D_2}$, those composition points are close on the composition profiles of Fig. 3.8.

Fig. 3.9 gives a comparison of the analytical solution for injection gas $\mathbf{I_2}$ with a finite difference solution (fully explicit with single-point upstream weighting) using 1000 grid blocks and a time step size of 0.0001. As Fig. 3.9 shows, numerical dispersion smooths the shock fronts in the displacement. The nontie-line path is smoothed the most because it is nonsharpening. Otherwise, excellent agreement is obtained.

3.2.3 Solution Construction

The analytical solution can be computed easily once the crossover tie line is found. In Section 3.1 we demonstrated a simple construction to find the crossover tie line when a three-component oil ($CH_4/C_4/C_{10}$) was displaced by pure CO_2. In that system the crossover tie line could be found easily and was reached only by shocks.

For the more complex case of enriched gas injection, however, that simple geometric construction can be generalized. For example, in Fig. 3.7, nontangent and self-sharpening shocks occur at the trailing end of the displacement (near the injection gas composition). Next, we prove that for a series of successive shocks from one tie line to another, the extensions of these two tie lines must intersect, regardless of the number of components. Thus, in the $CH_4/C_3/C_6/C_{16}$ example, the extension of the injection gas tie-line must intersect the crossover tie-line extension. The intersection point (labeled $\mathbf{X_2}$) lies outside the quaternary diagram as illustrated in Fig. 3.7 for the displacement by injection gas $\mathbf{I_2}$.

3.2.4 Generalized Crossover Tie-Line Construction

Consider the displacement route shown in Fig. 3.7 for injection of a CH_4 and C_3 gas mixture. For n_c components, the jump relations for the $\mathbf{F} \rightarrow \mathbf{E}$ and $\mathbf{X} \rightarrow \mathbf{E}$ shock are

$$\Lambda^{\mathbf{FE}} = \frac{F_i^{\mathbf{F}} - F_i^{\mathbf{E}}}{C_i^{\mathbf{F}} - C_i^{\mathbf{E}}}, \qquad \Lambda^{\mathbf{XE}} = \frac{F_i^{\mathbf{X}} - F_i^{\mathbf{E}}}{C_i^{\mathbf{X}} - C_i^{\mathbf{E}}}. \tag{3.28}$$

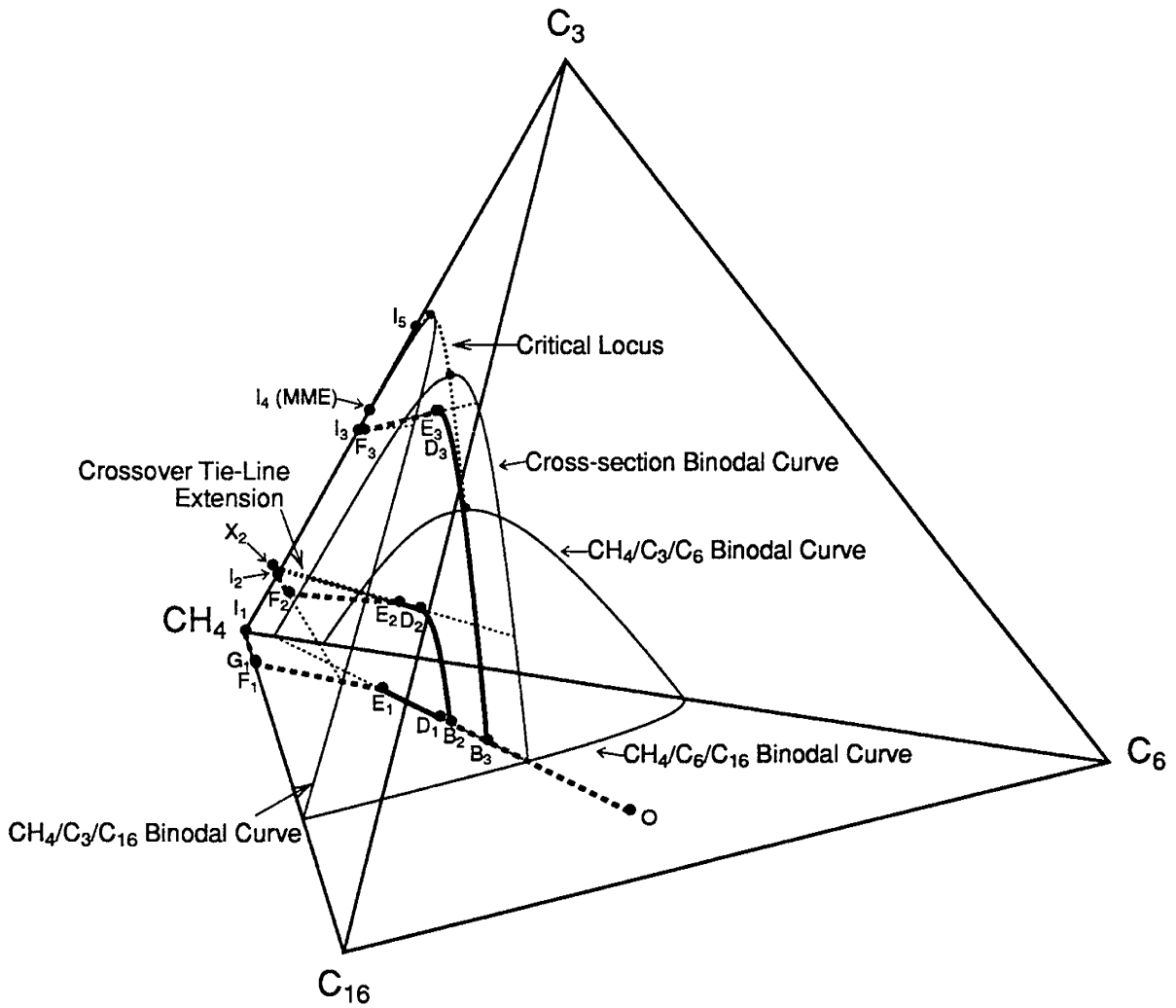

Figure 3.7: Composition route for displacements of oil **O** by CH_4/C_3 gas mixtures at 2000 psia, 200 °F. Geometric construction of crossover tie line is shown for injection gas $\mathbf{I_2}$.

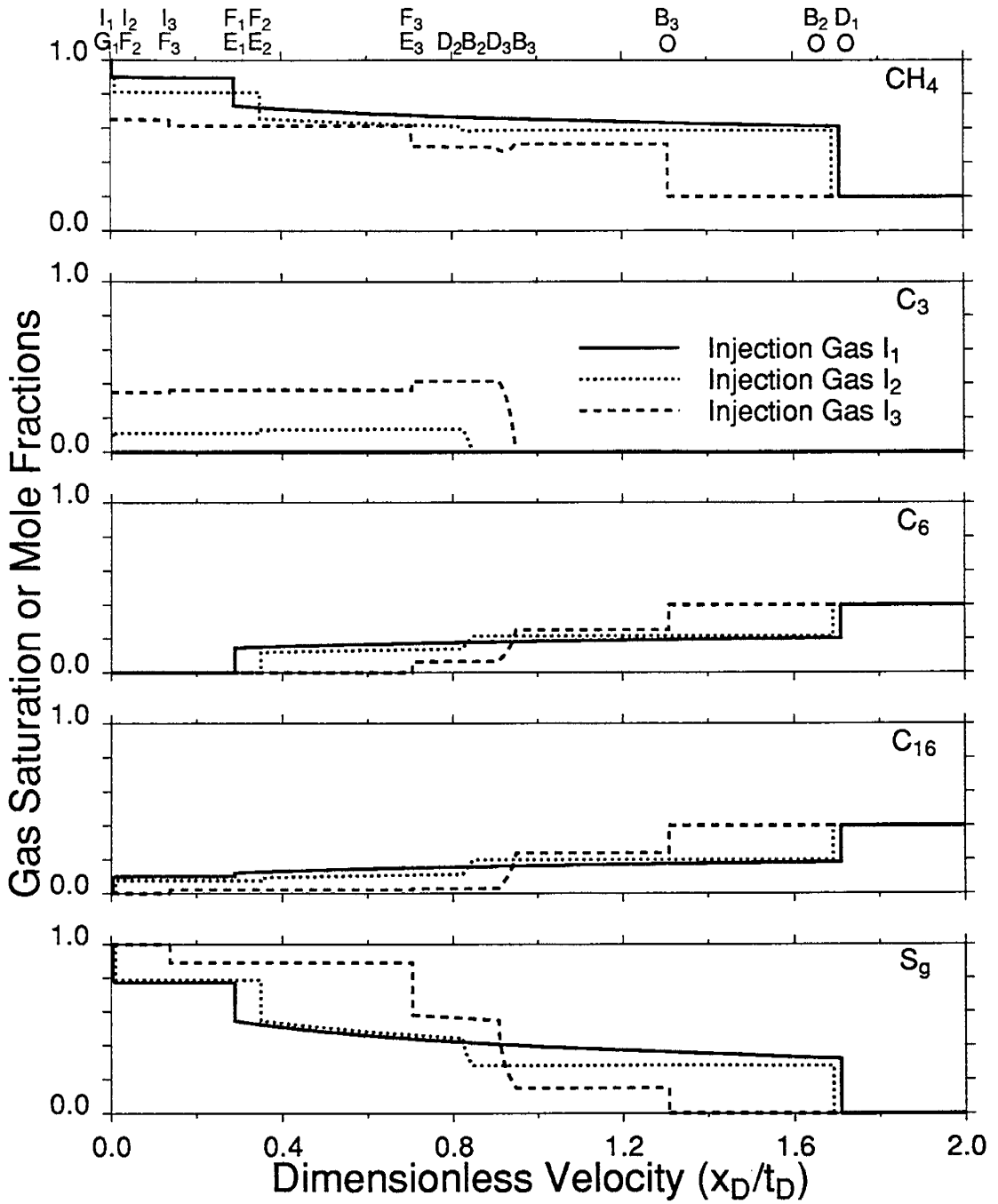

Figure 3.8: Composition and saturation profiles for the routes shown in Fig. 3.7 at 2000 psia, 200 °F.

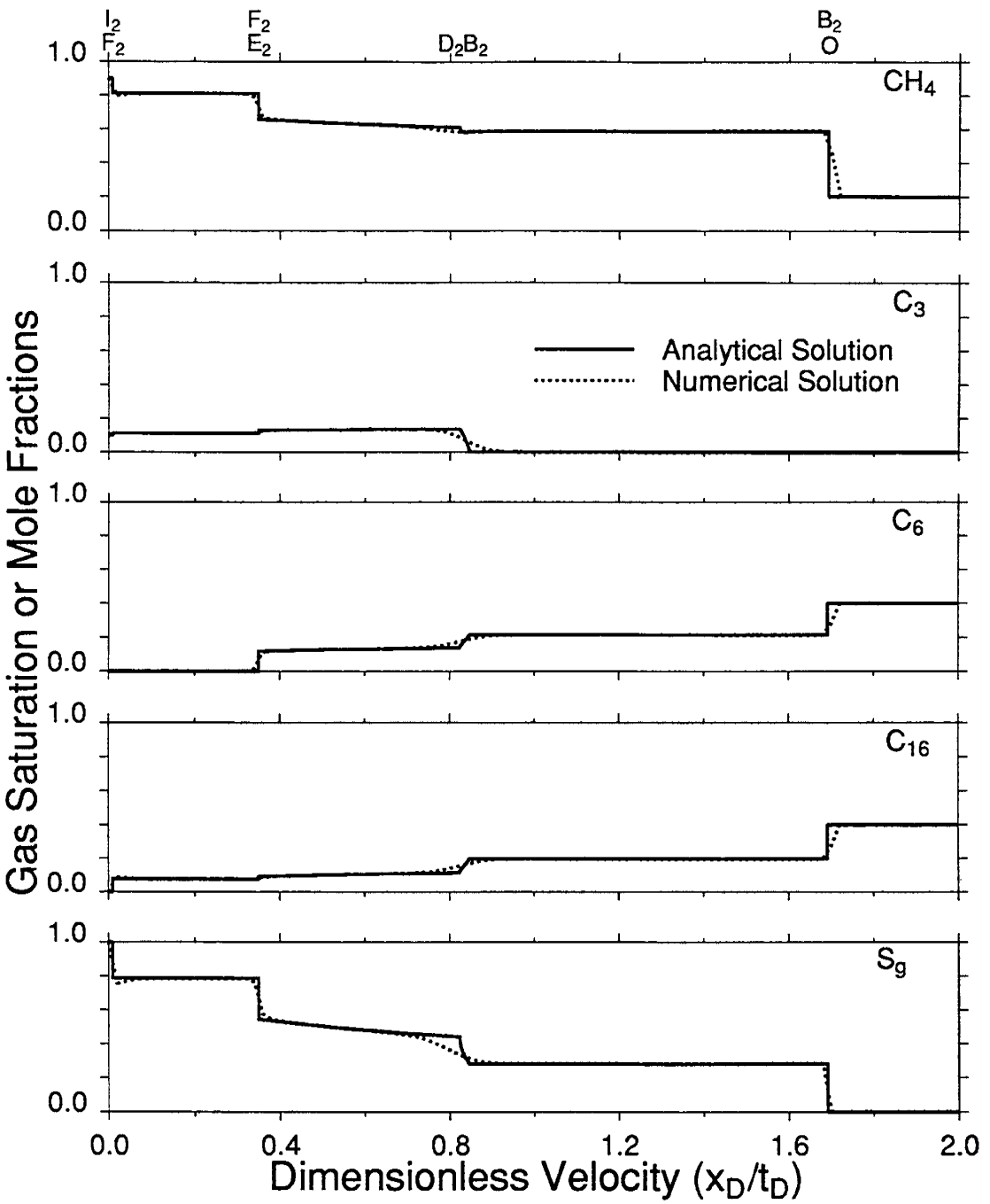

Figure 3.9: Comparison of analytical and numerical profiles with $\Delta x_D = 0.001$ and $\Delta t_D = 0.0001$ for solution with gas $\mathbf{I_2}$.

Because compositions $\mathbf{X}$ and $\mathbf{F}$ contain no C_6, $C_{C_6}^{\mathbf{F}} = F_{C_6}^{\mathbf{F}} = C_{C_6}^{\mathbf{X}} = F_{C_6}^{\mathbf{X}} = 0$, and from Eq. 3.28,

$$\Lambda^{\mathbf{XE}} = \Lambda^{\mathbf{FE}} . \tag{3.29}$$

Also, the $\mathbf{X} \rightarrow \mathbf{E}$ shock must be tangent to the fractional flow surface at $\mathbf{E}$ in order to satisfy appropriate entropy and velocity constraints (proof of this statement is given by Johns [56]). Thus, composition $\mathbf{E}$ can be found from a tangent construction along the crossover tie line in which $\Lambda^{\mathbf{XE}} = \lambda_t^E = \frac{df_g^{\mathbf{E}}}{dS_g}$.

Eq. 3.28 can be rearranged to eliminate F_i^E. That is,

$$\frac{F_i^{\mathbf{X}} - F_i^{\mathbf{F}}}{C_i^{\mathbf{X}} - C_i^{\mathbf{F}}} = \frac{\Lambda^{\mathbf{FE}}(C_i^{\mathbf{E}} - C_i^{\mathbf{F}}) + \Lambda^{\mathbf{XE}}(C_i^{\mathbf{X}} - C_i^{\mathbf{E}})}{C_i^{\mathbf{X}} - C_i^{\mathbf{F}}} . \tag{3.30}$$

Because $\Lambda^{\mathbf{XE}} = \Lambda^{\mathbf{FE}}$, Eq. 3.30 becomes

$$\frac{F_i^{\mathbf{X}} - F_i^{\mathbf{F}}}{C_i^{\mathbf{X}} - C_i^{\mathbf{F}}} = \Lambda^{\mathbf{XF}} = \Lambda^{\mathbf{FE}} = \Lambda^{\mathbf{XE}} = \lambda_t^E . \tag{3.31}$$

Hence, a triangle of equal velocity shocks from $\mathbf{X} \rightarrow \mathbf{F}$, $\mathbf{F} \rightarrow \mathbf{E}$, and $\mathbf{X} \rightarrow \mathbf{F}$ exists, where composition $\mathbf{X}$ is the intersection of the crossover tie-line and the injection gas tie-line extensions.

The generalized crossover tie-line construction makes finding compositions $\mathbf{E}$ and $\mathbf{F}$ straightforward. Point $\mathbf{E}$ can be found by constructing a tangent shock along the crossover tie line from the intersection point $\mathbf{X}$. The velocity of this shock is

$$\Lambda^{\mathbf{XE}} = \frac{F_i^{\mathbf{X}} - F_i^{\mathbf{E}}}{C_i^{\mathbf{X}} - C_i^{\mathbf{E}}} \quad i = 1, \cdots, n_c . \tag{3.32}$$

Because this is a tangent shock, the velocity of composition $\mathbf{E}$ is also

$$\Lambda^{\mathbf{XE}} = \lambda_t^{\mathbf{E}} = \frac{df_g^{\mathbf{E}}}{dS_g} . \tag{3.33}$$

Thus, according to Eq. 3.31, composition $\mathbf{F}$ can be found by constructing a shock from $\mathbf{X}$ to $\mathbf{F}$ such that its velocity is equal to $\lambda_t^{\mathbf{E}}$ [56].

Therefore, the solution procedure for the $CH_4/C_3/C_6/C_{16}$ displacement is a two-part process. First, the key tie lines and compositions must be found:

1. Find the tie lines that extend through the injection gas and oil compositions. The negative flash procedure described by Whitson and Michelson [149] can be used to find these tie lines.

2. Find the crossover tie line. To do so, integrate along a nontie-line path from the oil tie line and compute successive tie lines. The crossover tie line is the tie line along the nontie-line path that intersects the injection gas tie line.

3. Construct a tangent shock from $\mathbf{X}$ along the crossover tie line to locate composition $\mathbf{E}$. The velocity of this shock, $\lambda_t^{\mathbf{E}}$, is equal to the velocity, $\Lambda^{\mathbf{FE}}$, of the self-sharpening shock from $\mathbf{F}$ to $\mathbf{E}$.

4. Find composition **F** by constructing a nontangent shock from **X** along the injection gas tie line such that the shock velocity is equal to $\lambda_t^{\mathbf{E}}$.

Once the key tie lines and compositions are found, the location of each overall composition is found from its wave velocity. The velocity of the trailing shock from injection gas composition **I** to point **F** is given by the shock jump relations, Eq. 3.19. (In some instances, a tangent shock can be constructed from the injection gas composition along the injection gas tie line. This occurs only when point **F** is beyond the tangent point. In such cases, a small continuous variation along the injection gas tie line is possible. For example, as Fig. 3.7 shows, a small continuous variation occurs from $\mathbf{F_1}$ to $\mathbf{G_1}$ in the displacement by injection gas $\mathbf{I_1}$.) The velocity of compositions that vary continuously along the crossover tie line from **E** to the equal eigenvalue composition **D** is given by the tie-line eigenvalue, $\lambda_t = \frac{df_g}{dS_g}$. The velocities of compositions that vary continuously along the nontie-line path from **D** to **B** are given by the nontie-line eigenvalue. The path is obtained by taking small steps in composition space. The velocity of the shock from **B** to **O** is obtained from the shock jump relations, Eq. 3.19. (A continuous variation along the oil tie line may occur if point **B** lies before the tangent point from the oil tie line to **O**.)

3.2.5 Condensing/Vaporizing Mechanism

The displacements shown in Fig. 3.7 have features of both condensing and vaporizing mechanisms. In the $CH_4/C_3/C_6/C_{16}$ example, condensing behavior occurs at the leading edge of the displacements followed by a trailing vaporizing drive.

The combined condensing and vaporizing mechanism is best illustrated by constructing two limiting ternary solutions from the quaternary displacements of Fig. 3.7. Fig. 3.10 shows two ternary solutions constructed by removing (along a dilution line) components from the oil or injection gas. In Fig. a of Fig. 3.10, C_6 has been removed from the oil **O** (shown as **O′**) to illustrate the condensing portion of the solution. The ternary solution includes a continuous variation along the nontie-line path from **B′** to **D′** with C_3 condensing into the liquid phase. The nontie-line path can be taken because the nontie-line eigenvalue increases from the injection gas tie line to the initial oil tie line (see Section 3.2.2). A small continuous variation along the initial oil tie line occurs from **A′** to **B′**. The vaporizing portion of the solution is illustrated in Fig. b of Fig. 3.10 and in Fig. 3.7 by removing C_3 from the injection gas $\mathbf{I_2}$ (shown as $\mathbf{I_1}$). A self-sharpening shock occurs along the nontie-line path in this case which vaporizes C_6 from the oil.

Thus, the four-component solution can be decoupled approximately into two successive ternary solutions which exhibit condensing and vaporizing behavior. Fig. 3.11 illustrates this behavior further for the nearly miscible displacement by injection gas $\mathbf{I_3}$. In that case, the component K-values and phase densities both nearly converge at the crossover tie line. Thus, in the condensing portion of the displacement, the liquid-phase density decreases as heavier components are replaced by lighter components (C_3 and C_6), while in the trailing vaporizing portion, the liquid density increases as the lighter components in the oil are extracted. This result is similar to that presented by Zick [157] in his Fig. 12.

Fig. 3.12 further illustrates the C/V mechanism. It demonstrates that the analytical solution for the composition path lies on vertical- and horizontal-ruled surfaces (a ruled surface is generated by a sequence of lines) within the quaternary diagram. The ruled

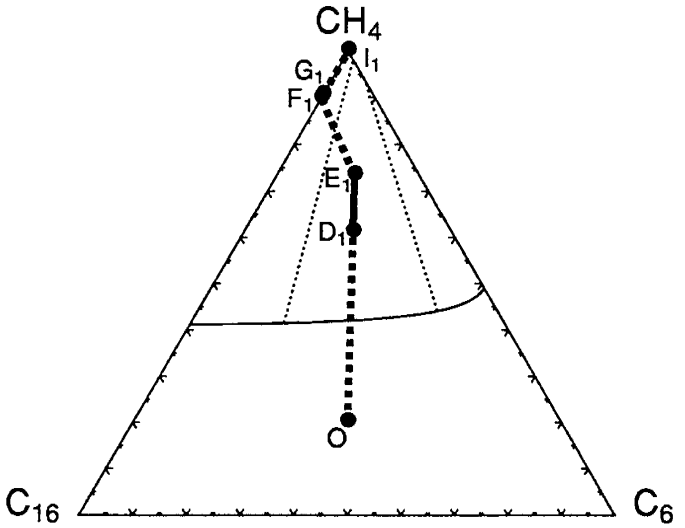

(b) Vaporizing Portion

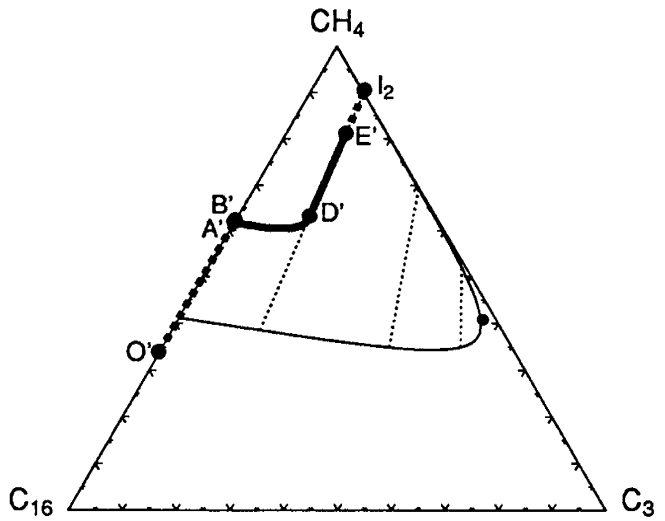

(a) Condensing Portion

Figure 3.10: Ternary representation of C/V displacement of oil **O** by gas $\mathbf{I_2}$.

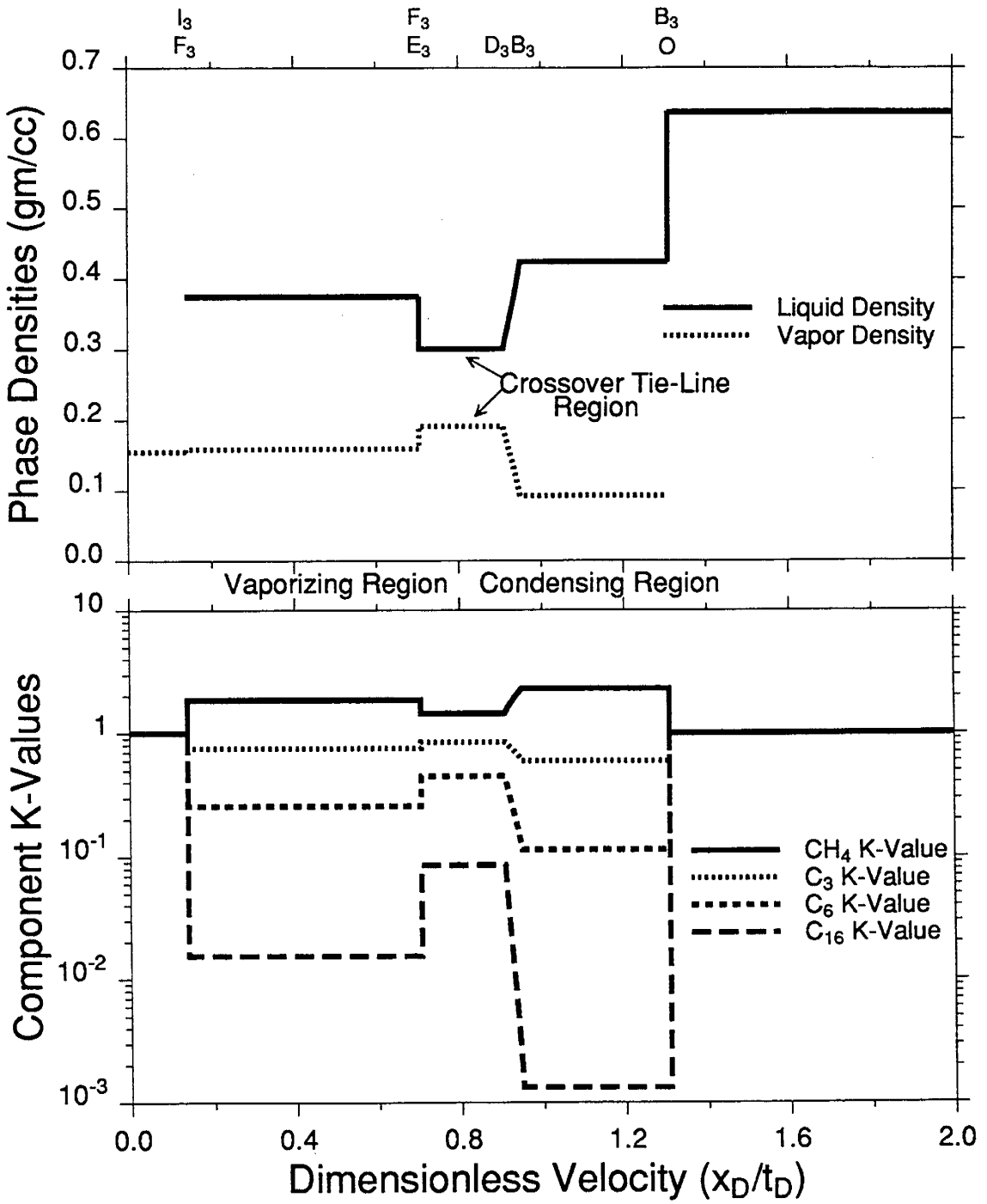

Figure 3.11: Fluid properties for nearly miscible C/V displacement of oil **O** by gas $\mathbf{I_3}$.

surfaces are composed of tie lines that intersect the composition path and may be thought of as cross sections of the quaternary diagram. (They are nearly planar for phase behavior calculated with the PREOS at these conditions. If K-values are independent of composition, they are strictly planar [27]). The condensing displacement occurs on the vertical-ruled surface (composed of tie lines along the nontie-line path), while the vaporizing displacement occurs along the horizontal-ruled surface (composed of tie lines which intersect the crossover tie-line extension). Hence, the crossover tie line can be defined as the intersection of the vertical- and horizontal-ruled surfaces.

Minimum Enrichment for Miscibility

Multicontact miscibility in C/V displacements is obtained when the crossover tie line becomes a critical tie line. Fig. 3.7 illustrates this for the $CH_4/C_3/C_6/C_{16}$ system in which the injection gas is enriched with C_3. As the gas is enriched to $\mathbf{I_3}$, the crossover tie line moves closer to the critical locus, and the shocks and waves approach unit velocity (see Fig. 3.8). That is, the two-phase transition zone shrinks, and flow approaches a piston-like displacement. If C_3 enrichment is increased to the minimum enrichment for miscibility (MME at $\mathbf{I_4}$), all shocks and waves have unit velocity.

Thus, it is the crossover tie line and not the injection gas tie line that determines miscibility here. For example, in Fig. 3.7, the crossover tie line approaches the critical locus at a mixture of 61.5% CH_4 and 38.5% C_3 ($\mathbf{I_4}$), while the injection gas tie line is a critical tie line at an enrichment of 47.0% CH_4 and 53% C_3 ($\mathbf{I_5}$). Thus, if the injection gas tie lines were used to determine miscibility in C/V displacements, the calculated MME would contain significantly more C_3. From experimental and simulation results, Zick [157] observed that "In between (the condensing and vaporizing zones) is the sharp, two-phase transition zone, the two phases of which are almost, but not quite miscible." Fig. 3.11 shows the distribution of K-values in the transition for injection gas $\mathbf{I_3}$. Fig. 3.11 clearly illustrates that the K-values in the middle of the transition zone are close to unity, and hence, the two-phase fluids are nearly miscible. As the crossover tie line approaches the critical locus, the K-values approach unity. Thus, an important result of this section is to demonstrate conclusively the existence of combined condensing and vaporizing displacement behavior in which multicontact miscibility is controlled by the approach of the crossover tie line to the plait point locus as the enrichment or pressure is increased. According to the definition given here, therefore, the CO_2 displacements of Section 3.1 are also C/V drives.

Pseudoternary Diagrams

Several authors have shown that pseudoternary diagrams can exhibit a two-phase region with a narrow neck displacement for multicomponent systems [157, 128, 89, 72]. Figs. 3.13 and 3.14 shows these same features for pseudoternary diagrams constructed by replotting the ruled-surface tie lines for injection gas enrichments $\mathbf{I_1}$, $\mathbf{I_2}$, $\mathbf{I_3}$, and $\mathbf{I_4}$. Fig. 3.13 is constructed by lumping C_6 and C_{16}, while Fig. 3.14 is constructed by lumping C_3 and C_6.

The pseudoternary phase diagrams in Fig. 3.13 reproduce the features of phase diagrams obtained by Zick and Stalkup from numerical simulations. Fig. 3.14, however, gives a different view of the same displacements and shows similar features to pseudoternary diagrams given by Lee *et al.* [72]. In the condensing portion of the displacement, the tie-line

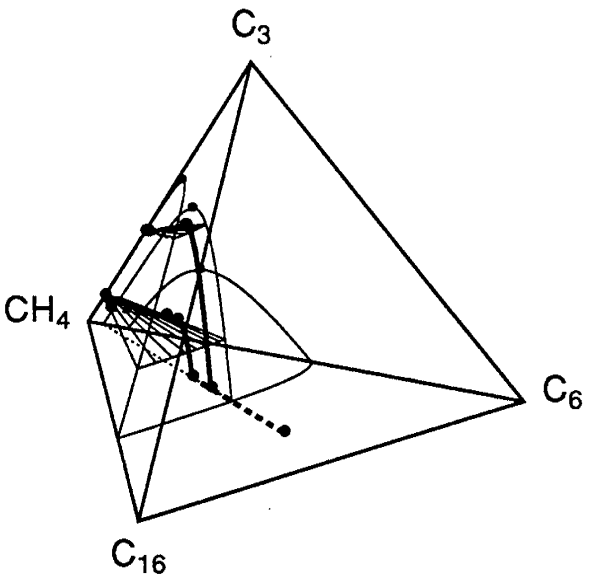

(b) Horizontal Ruled Surfaces (Vaporizing)

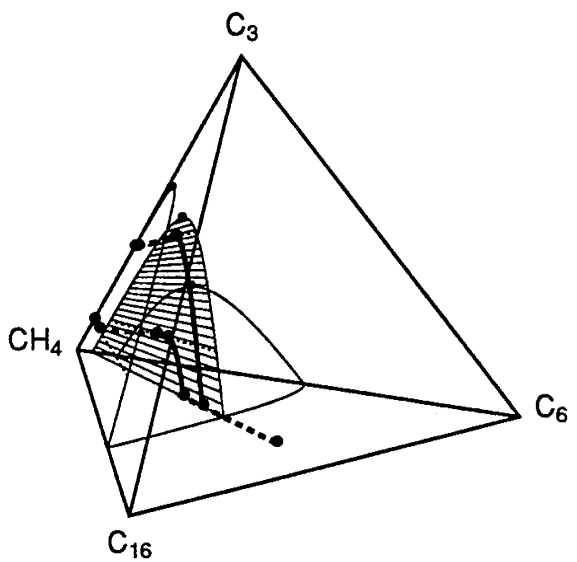

(a) Vertical Ruled Surface (Condensing)

Figure 3.12: Illustration of ruled surfaces upon which the displacement is either condensing or vaporizing.

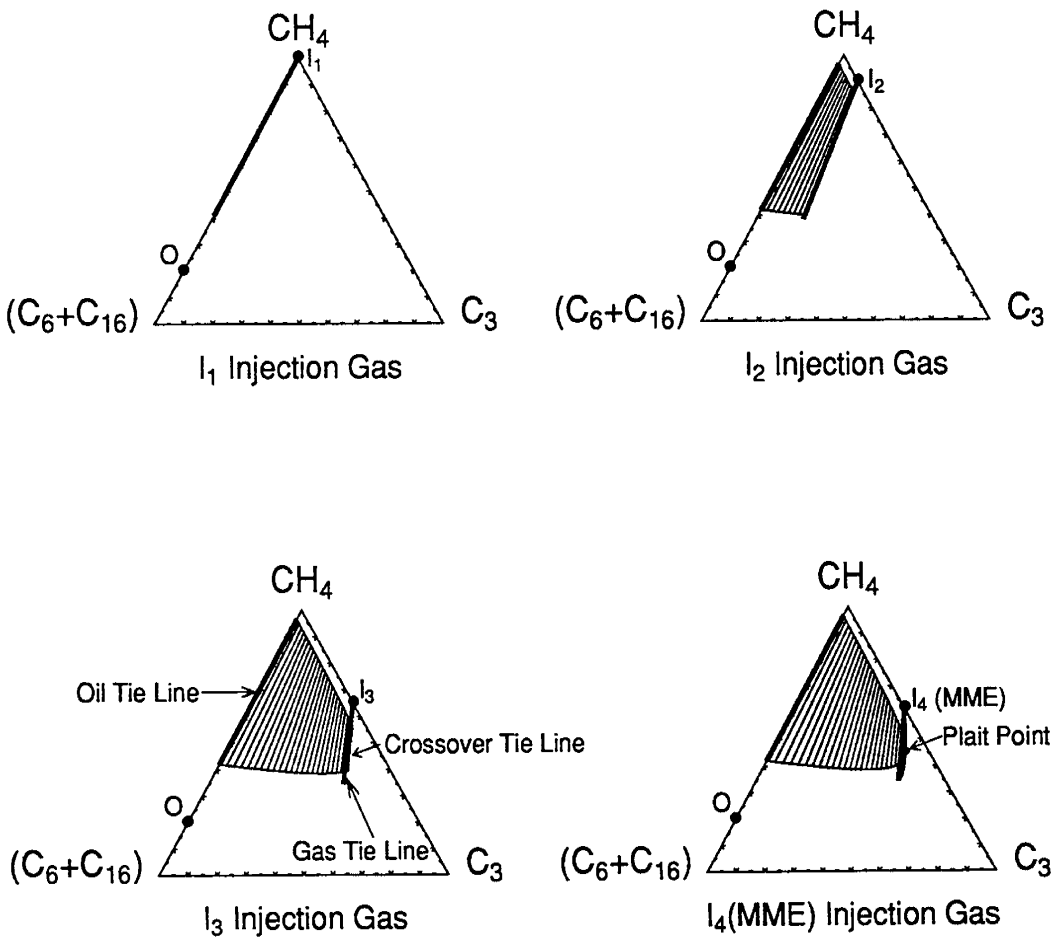

Figure 3.13: Pseudoternary diagrams constructed from the ruled surfaces like those in Fig. 3.12 by lumping C_6 and C_{16}.

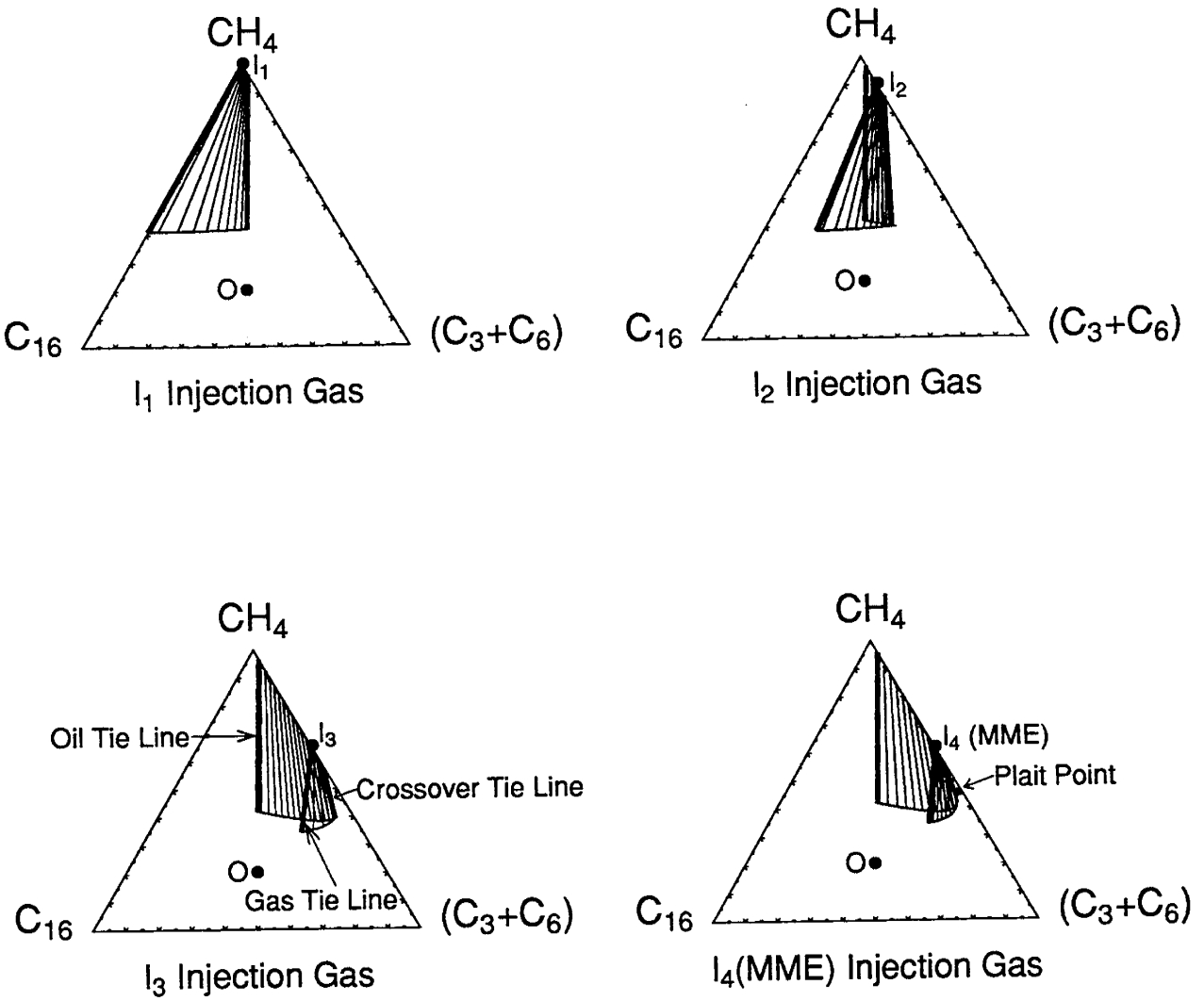

Figure 3.14: Pseudoternary diagrams constructed from the ruled surfaces like those in Fig. 3.12 by lumping C_3 and C_6.

lengths become smaller as the solution route approaches the crossover tie line (along the vertical-ruled surface as shown in Fig. a in Fig. 3.12). Because the crossover tie line is closest to the critical locus, it is the shortest length tie line obtained in the displacement. The vaporizing portion of the displacement begins at the crossover tie line, and tie-line lengths increase until the injection gas tie line is reached (along the horizontal-ruled surfaces in Fig. b in Fig. 3.12). Because the crossover tie-line length decreases as the displacement approaches miscibility, the neck region becomes thinner for nearly miscible floods. For example, the immiscible displacement with injection gas $\mathbf{I_2}$ shows less curvature in the two-phase region, while displacements closer to the MME (i.e. $\mathbf{I_3}$) give thinner necks in the two-phase region. If the injection gas enrichment is increased further to the MME $\mathbf{I_4}$, the neck becomes a single point, as the crossover tie line becomes a critical tie line. Because composition paths in numerical simulations are influenced by numerical dispersion, however, the crossover tie line obtained numerically would still have a small finite length at the MME.

3.2.6 $CH_4/C_2/C_6/C_{16}$ Displacements

In the next example, we replace C_3 in the injection gas with C_2 and hold the temperature, pressure, and initial oil composition constant. In this system, the two-phase region is larger due to the greater volatility of C_2 over that of C_3. Hence, the displacement by CH_4/C_2 gas mixtures should be less efficient than those with CH_4/C_3 gas injection. Figs. 3.15 and 3.16 and Table 3.3 show the analytical solutions for displacements with gas enrichments $\mathbf{I_1}$, $\mathbf{I_2}$, $\mathbf{I_3}$, $\mathbf{I_4}$, $\mathbf{I_5}$, and $\mathbf{I_6}$.

Because the volatility of ethane is greater than unity ($K_{C_2} > 1.0$), some features of the displacements differ. In particular, the continuous variation along the nontie-line path on the vertical-ruled surface is replaced by a self-sharpening shock. The K-value rule (Eq. 3.27) applied to the ternary $CH_4/C_2/C_{16}$ face verifies that a shock must occur along the nontie-line path. Hence, as was shown in Section 3.2.3, the crossover tie-line extension must intersect both the oil and injection gas tie-line extensions, and the crossover tie line can be found easily. The intersection with the oil tie line ($\mathbf{X^O}$) and the injection gas tie line ($\mathbf{X^I}$) is shown in Fig. 3.15 for the displacement with injection gas $\mathbf{I_4}$.

The solution consists primarily of shocks with only a small continuous variation along the crossover tie line. Just as before, the solution can be found from a two-step process in which the key tie lines, points **B**, **C**, **D**, **E**, and **F**, and the velocities of the overall compositions are calculated. The solution procedure differs from the $CH_4/C_3/C_6/C_{16}$ system only in that points **B** and **D** are identified from shock balances rather than by integration along a nontie-line path.

As is shown in Figs. 3.15 and 3.16, the displacements are less efficient (more immiscible) than the displacements of the $CH_4/C_3/C_6/C_{16}$ system. That is, the leading shocks are faster and the trailing shocks are slower. Also, the crossover tie line is further from the critical locus. Hence, the minimum enrichment needed for miscibility is higher (approximately 29% CH_4 and 71% C_2). Just as before, it would take significantly more C_2 (at $\mathbf{I_6}$) to make the injection gas tie line a critical tie line, and thus, the crossover criterion (MME at $\mathbf{I_5}$) is less restrictive.

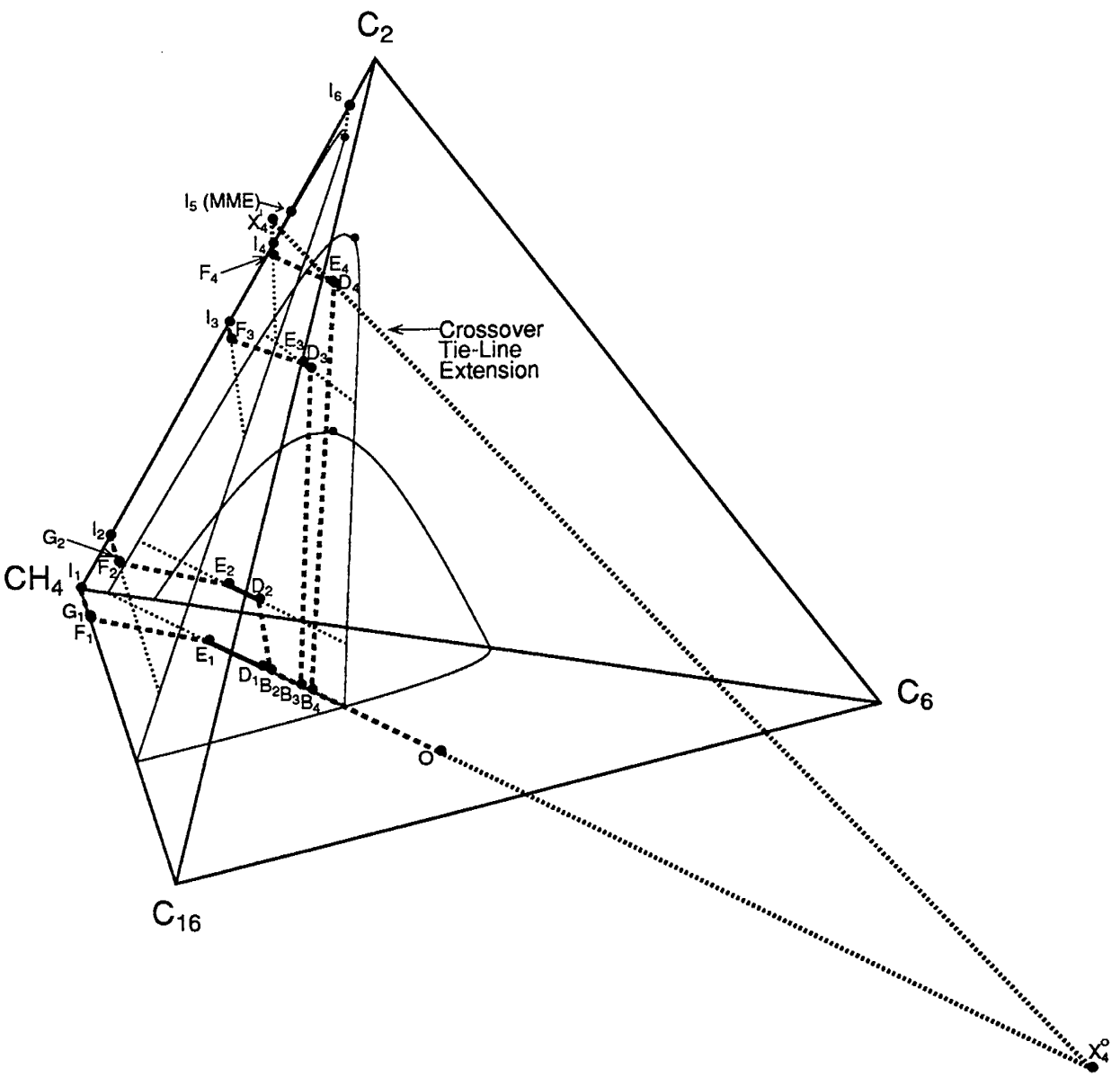

Figure 3.15: Composition route for displacements of oil **O** by CH_4/C_2 gas mixtures at 2000 psia, 200 °F. Geometric construction of crossover tie line is shown for injection gas $\mathbf{I_4}$.

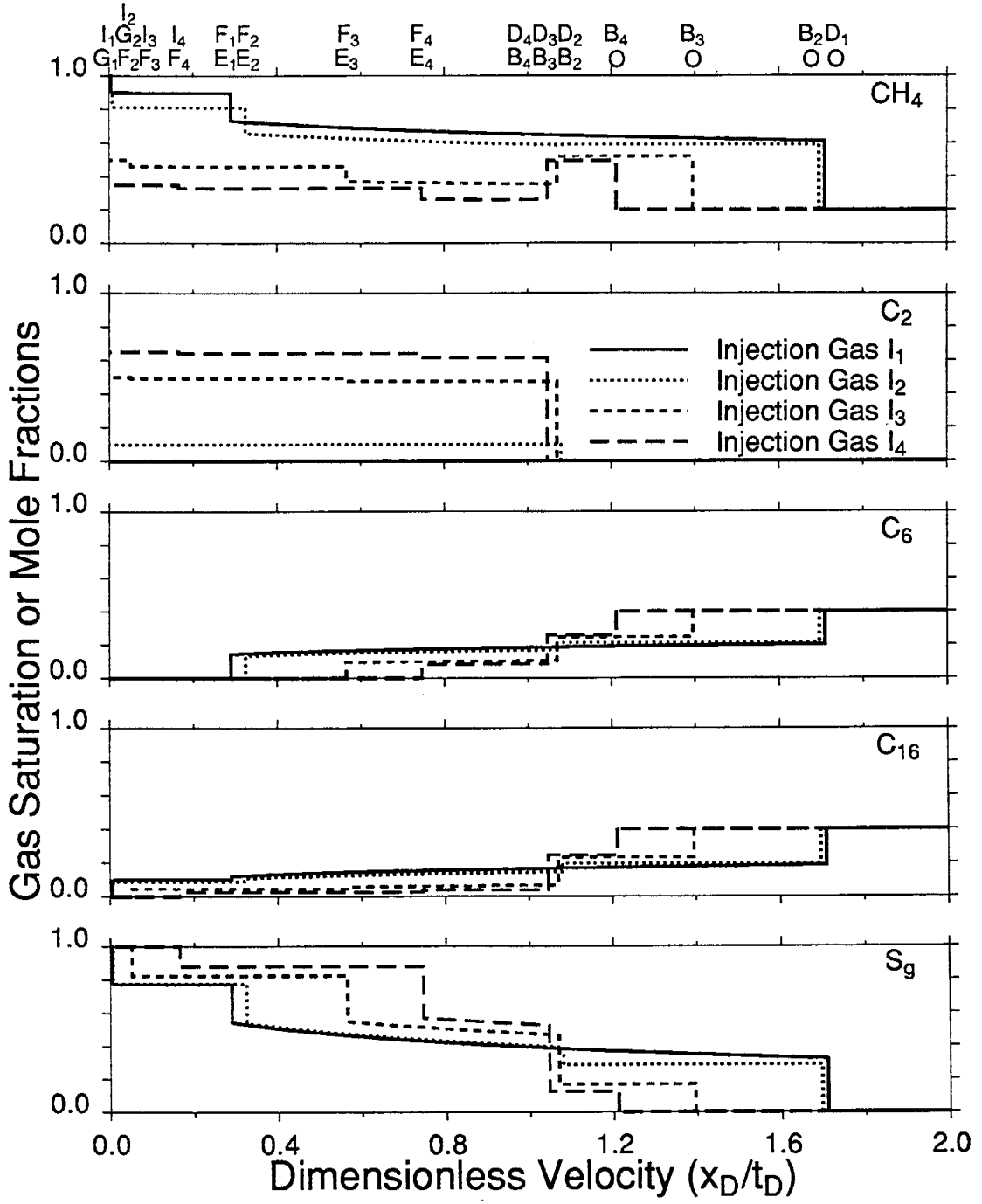

Figure 3.16: Composition and saturation profiles for the routes shown in Fig. 3.15.

3.2.7 Discussion

The examples shown illustrate that when a fourth component is added, it is possible to have a displacement with features of both condensing and vaporizing gas drives. Also, a third key tie line of the solution route, the crossover tie line, was shown to control the development of miscibility in these systems. Displacement mechanisms other than a combined condensing and vaporizing one, however, can exist in four-component drives. It is easy to conceive of oil and injection compositions that could give purely vaporizing, purely condensing, or combined vaporizing (leading) and condensing gas (trailing) drives. For these other mechanisms, the injection or oil tie line will control the development of miscibility, not the crossover tie line [56]. Thus, in four-component systems, there are four possible mechanisms of displacement, which helps to explain the contradictory conclusions by Novosad and Costain [89], Tiffin *et al.* [135] and Lee *et al.* [72].

It is likely, however, that many real oil displacements will have features of both condensing and vaporizing displacements. For example, many authors have assumed that carbon-dioxide floods are always purely vaporizing (especially at high temperature). The $CO_2/CH_4/C_4/C_{10}$ example given in Section 3, however, can now be clearly identified as a C/V displacement. The fact that the crossover tie line controls development of miscibility in C/V displacements has important implications for mixing algorithms [44, 67, 76] used to estimate MMP's and MME's. Those methods determine the MMP or MME as the pressure or enrichment at which either the initial or injection composition lies on the extension of a critical tie line. Jensen and Michelson [53], however, used the $CO_2/CH_4/C_4/C_{10}$ system as an example of a system for which such methods give incorrect results. The solutions presented here and in Section 3.1 show why. The mixing algorithms do not identify the crossover tie line, and hence, they give incorrect MMP's and MME's for C/V drives in which the crossover tie line controls the development of miscibility. We argue, therefore, that such methods should not be used unless it is known *a priori* that the displacement mechanism is purely vaporizing or condensing. In Section 3.3 we show how displacements can be classified as vaporizing, condensing, or some combination of the two according to the K-values of the components present.

3.2.8 Conclusions

We have shown through analytical calculations for four-component systems that:

1. In certain four-component enriched gas floods, the mechanism of displacement is a leading condensing drive followed by a trailing vaporizing one.

2. In C/V gas drives, miscibility is obtained when the injection gas is sufficiently enriched to drive the crossover tie line to the critical plait point locus. Thus, the crossover tie line, not the injection gas tie line, determines miscibility in such systems.

3. When the crossover tie line is reached only by self-sharpening shocks, it can be found easily from a geometric construction. In such cases, the crossover tie line is the only tie line that intersects both the initial and injection tie lines, regardless of the number of components.

4. The neck region of pseudoternary diagrams is directly related to the combined displacement mechanism. The crossover tie line is the shortest tie line in the neck region of the ternary diagram.

5. A simple rule based upon component K-values allows an *a priori* prediction of the type of wave (self-sharpening shock or continuous variation) along the nontie-line path.

3.3 Classification of Three- and Four-Component Displacements

Russell T. Johns

In the solutions reported in Sections 3.1 and 3.2 the volatilities or K-values of the components determine the eigenvalues, which are the wave velocities that indicate how fast particular compositions move. In this section we show that K-values are also important in the solution route seen in three- and four-component gas displacements. Here we make use of two key ideas. First, components present in the oil and gas are preferentially separated according to their K-value ranking. That is, the component with the highest K-value is generally recovered first, followed by the next highest K-value component. The chromatographic separation occurs because components with large K-values preferentially vaporize into the more mobile gas phase, while components with low volatility evaporate slowly and remain in the less mobile liquid phase. The second key idea is that the features of a solution route (the locations of shocks and expansion waves) can be determined from the K-value ordering prior to calculation of any eigenvalues or eigenvectors.

3.3.1 K-Value Effect on Phase Behavior

Consider a reservoir oil containing components 1, 2, and 3 with K-values ($K_1 > K_2 > K_3$). Assume also that the K-value ordering is strictly fixed for all tie lines in the two-phase region. If so, There are only four possible combinations of this ordering for three-component systems,

1. $K_1 > K_2 > K_3 > 1.0$
2. $K_1 > K_2 > 1.0$ and $1.0 > K_3$
3. $K_1 > 1.0$ and $1.0 > K_2 > K_3$
4. $1.0 > K_1 > K_2 > K_3$.

Cases 1 and 4 are trivial because a two-phase region does not exist, and any flood will be first-contact miscible, giving piston-like displacement. Hence, only two types,

1. Type HVI: $K_1 > K_2 > 1.0$ and $1.0 > K_3$
2. Type LVI: $K_1 > 1.0$ and $1.0 > K_2 > K_3$

are of interest. The HVI (high volatility intermediate component) system is so named because the intermediate component (component 2) has a K-value greater than unity, while in the LVI (low volatility intermediate component) system, the intermediate component has a K-value smaller than unity. Fig. 3.17 illustrates these types of three-component phase behavior for the PREOS. The figure shows the binodal curves for both high pressure, when a plait point exists, and low pressure, when no plait point exists. Whether or not a plait point exists does not change the overall features seen in the solution of an immiscible gas flood, but it does affect the development of miscibility. The plait point for type HVI is lower (contains less component 1) than the plait point for type LVI, and thus, the tie lines are skewed differently in the two systems.

Tie lines connecting the liquid and gas equilibrium compositions are also determined by the component K-values. In particular, the extensions of the tie lines (i.e. the slopes and intercepts) are governed by the K-value ordering. For a three-component system, a tie line can be written as a linear combination of the tie-line eigenvector, which points in the direction of the tie line, and an equilibrium tie-line composition.

$$\begin{pmatrix} C_1 \\ C_2 \end{pmatrix} = \alpha \begin{pmatrix} y_1 - x_1 \\ y_2 - x_2 \end{pmatrix} + \begin{pmatrix} x_1 \\ x_2 \end{pmatrix} . \tag{3.34}$$

Solving for α (i.e. the saturation) gives

$$\frac{C_1 - x_1}{y_1 - x_1} = \frac{C_2 - x_2}{y_2 - x_2} . \tag{3.35}$$

Eq. 3.35 can be written in terms of K-values, which leads to the result that when C_1 is zero,

$$C_2 = x_2 \left[1.0 - \left(\frac{K_2 - 1.0}{K_1 - 1.0} \right) \right] . \tag{3.36}$$

Thus, this equation gives the intersection of the tie-line extension and the Comp. 2/Comp. 3 axis (where $C_1 = 0.0$). For type HVI phase behavior ($K_1 > K_2 > 1.0$), the fraction $\frac{K_2 - 1.0}{K_1 - 1.0}$ is always positive but less than unity and therefore, $C_2 > 0.0$. Also, $C_2 < x_2$ because the minimum for K_2 is unity. Thus, type HVI tie-line extensions must intersect the Comp. 2/Comp. 3 axis where $0.0 < C_2 < x_2$.

The intersection of the tie-line extension and the Comp. 1/Comp. 3 axis can also be determined. In this case,

$$C_1 = x_1 \left[1.0 - \left(\frac{K_1 - 1.0}{K_2 - 1.0} \right) \right] . \tag{3.37}$$

Thus, type HVI tie-line extensions also intersect the Comp. 1/Comp. 3 axis but outside the ternary diagram (i.e. at $C_1 < 0.0$). Type HVI tie lines, therefore, are as shown in Fig. 3.18.

Type LVI tie-line extensions also intersect the Comp. 2/Comp. 3 axis where $0.0 < C_2 < 1.0$, but intersect the Comp. 1/Comp. 3 axis where $C_1 > 1.0$ (again, outside the ternary diagram). Type LVI tie lines, therefore, differ from type HVI as shown in Fig. 3.18.

3.3.2 Self-Sharpening Shocks vs. Expansion Waves

Eq. 3.27 in Section 3.2 determines the effect that K-values have on the change of the nontie-line eigenvalue along a nontie-line path. For K-values that are independent of

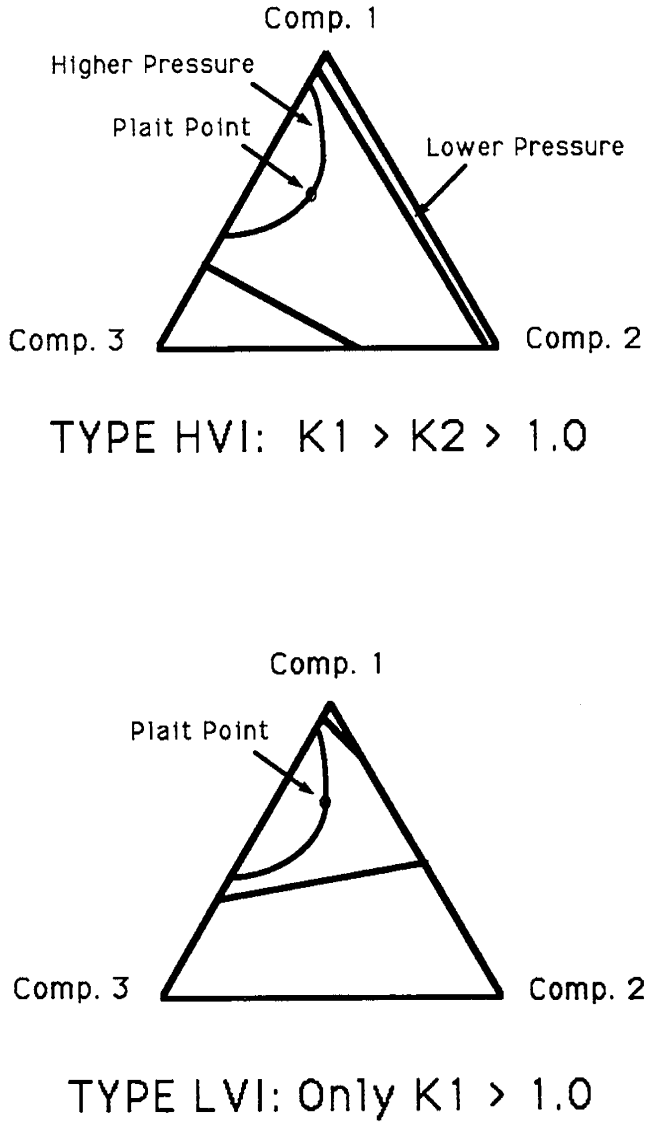

Figure 3.17: Types of phase behavior found in three-component systems based on component volatilities.

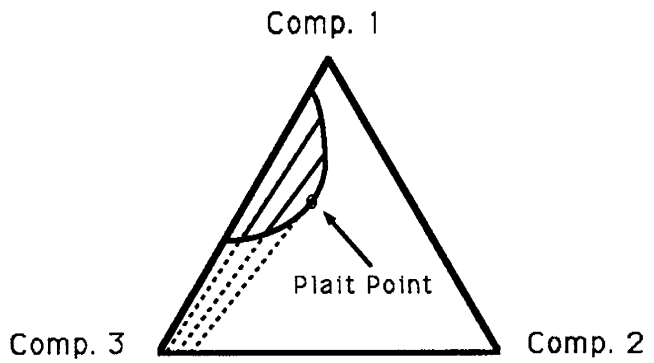

TYPE HVI: K1 > K2 > 1.0

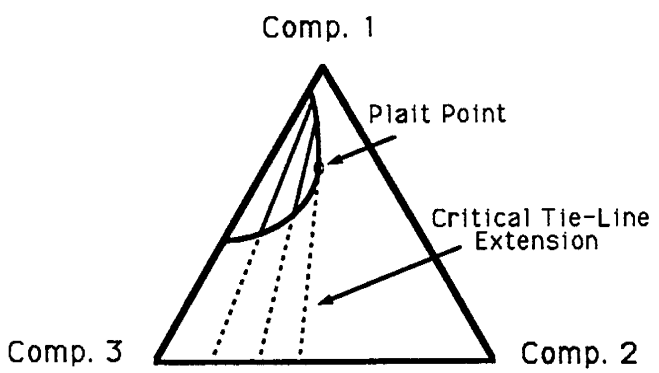

TYPE LVI: Only K1 > 1.0

Figure 3.18: Slopes of tie lines and their extensions for type HVI and LVI phase behavior (plait points are shown).

composition, the derivative $\frac{dx_2}{d\xi}$ is negative when a nontie-line path is traced from the right to the left on ternary diagrams (in the direction of decreasing values of Comp. 2). Thus, using Eq. 3.27, type HVI phase behavior gives $H > 0.0$ while type LVI phase behavior gives $H < 0.0$. Hence, the direction of the variation in the nontie-line eigenvalue is reversed for the two types, as is shown in Fig. 3.19. The arrows show the direction the nontie-line eigenvalue increases along the nontie-line path. The directions are reversed for the region across the equivelocity curve, where $F_i < C_i$. Thus, if the K-values are strictly ordered, the nontie-line eigenvalue must be either a maximum or a minimum at the umbilic point along a given nontie-line path.

3.3.3 Classification of Three-Component Solutions

In three-component systems, there are only two displacement mechanisms, vaporizing or condensing. The composition of the injection gas and oil determines which type occurs. A vaporizing displacement occurs if the injection gas composition lies on a tie-line extension that is to the left of the extension through the oil composition. That is, the middle intermediate component (component 2) will be vaporized at the leading edge of the displacement. If the reverse is true, and the injection gas composition lies on a tie-line extension which is to the right of the initial oil tie-line extension, then the middle intermediate component will be condensed at the leading edge of the displacement [51]. Thus, for each type of phase behavior (HVI or LVI), it is possible to have either a vaporizing or condensing gas drive. The two types of displacements are illustrated in Fig. 3.20.

Fig. 3.21 shows oils or injection gases which are at the MMP (or MME) for the four solution types. The MMP for vaporizing gas drives is the pressure at which the oil composition lies on the critical tie-line extension, while the MMP for condensing gas drives is the pressure at which the injection gas composition lies on the critical tie-line extension. Thus, in ternary systems, miscibility can develop only if either the initial oil or injection gas composition lies outside the region of tie-line extensions.

Because the eigenvalue variation along the nontie-line path is determined for type HVI and LVI phase behavior, the features of a solution route can be determined prior to calculation of any eigenvalues or eigenvectors. If the process is vaporizing or condensing, the leading shock and trailing shock must jump into or out of the two-phase region along the oil or gas tie-line extension [70]. Thus, the remaining portion of the solution connects these two tie lines in composition space. The only remaining question is: does a shock or an expansion wave occur along the nontie-line path?

Fig. 3.22 illustrates the four characteristic solution routes that are possible in ternary displacements. For type HVI-vaporizing displacements, the nontie-line eigenvalue decreases along the nontie-line path from the oil tie line to the injection gas tie line. Hence, the nontie-line eigenvalue satisfies the velocity constraint and an expansion wave ($\mathbf{B} \rightarrow \mathbf{C}$) connects the two tie lines. For a type HVI-condensing displacement, however, the reverse is true and a self-sharpening shock ($\mathbf{F} \rightarrow \mathbf{G}$) occurs. Type LVI phase behavior is the mirror image of type HVI. (If the definition for K-values were reversed so that a high K-value becomes low volatility, type HVI becomes type LVI). That is, the vaporizing displacement has a self-sharpening shock, while the condensing displacement shows an expansion wave.

Fig. 3.22 also illustrates the notion that components present in the oil are separated

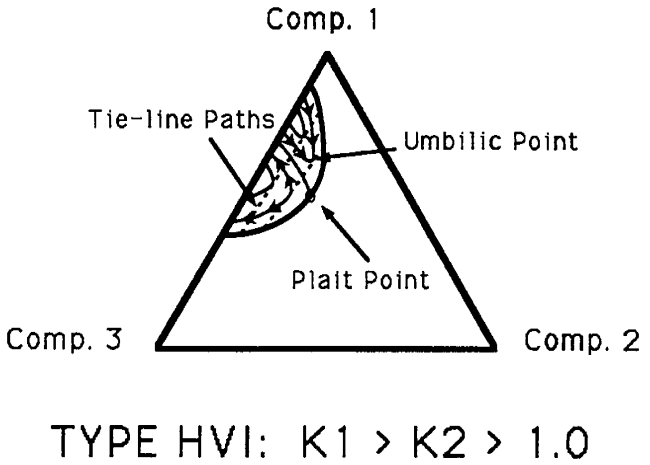
Comp. 1
Tie-line Paths
Umbilic Point
Plait Point
Comp. 3
Comp. 2
TYPE HVI: K1 > K2 > 1.0

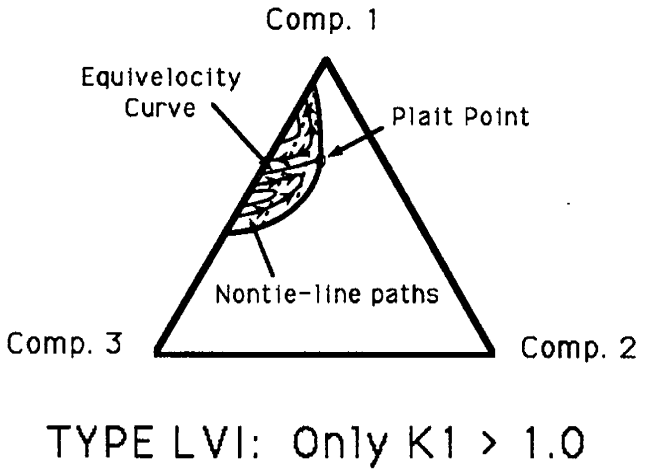
Comp. 1
Equivelocity
Curve
Plait Point
Nontie-line paths
Comp. 3
Comp. 2
TYPE LVI: Only K1 > 1.0

Figure 3.19:

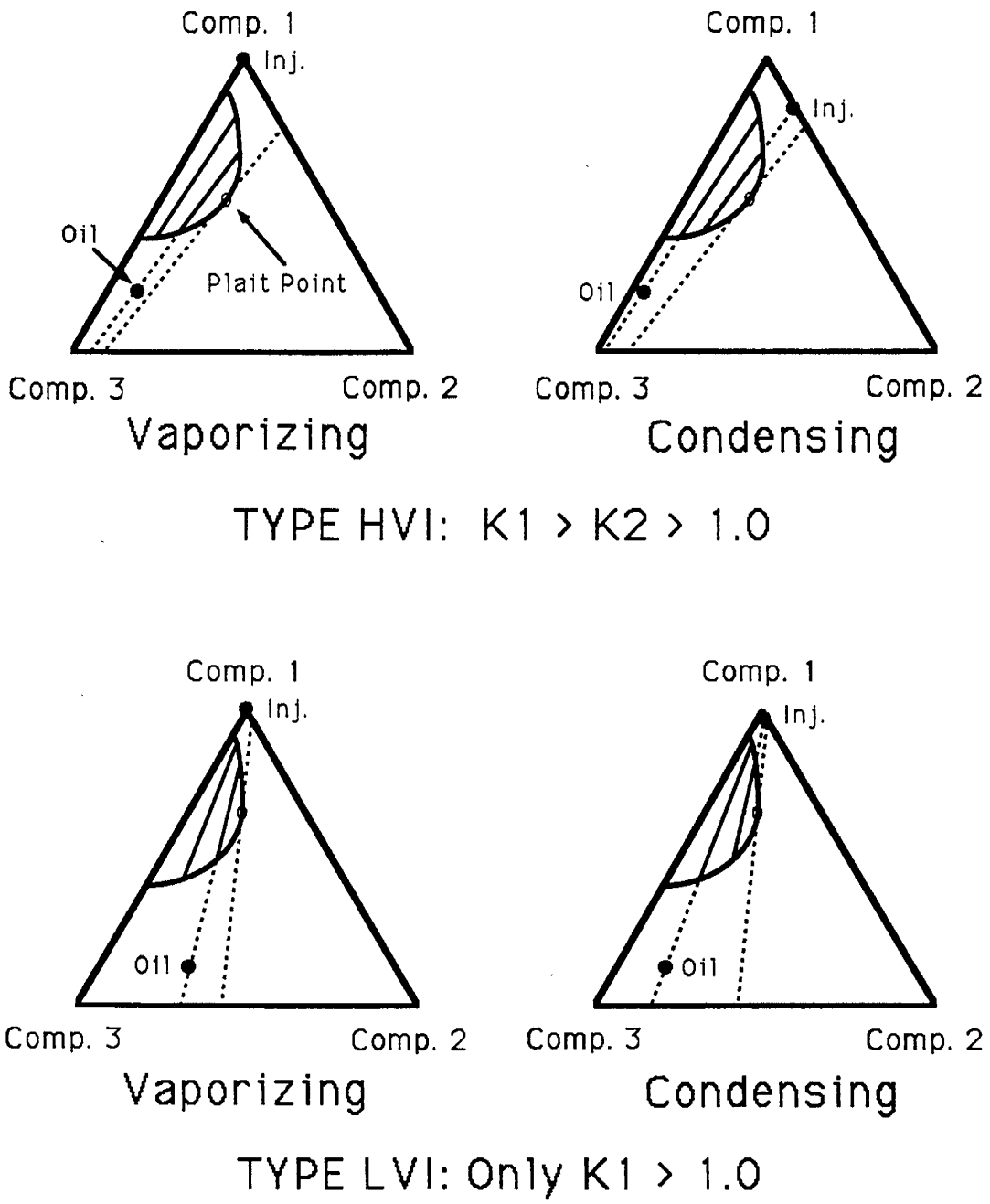

Figure 3.20: Vaporizing and condensing drives for HVI and LVI phase behavior.

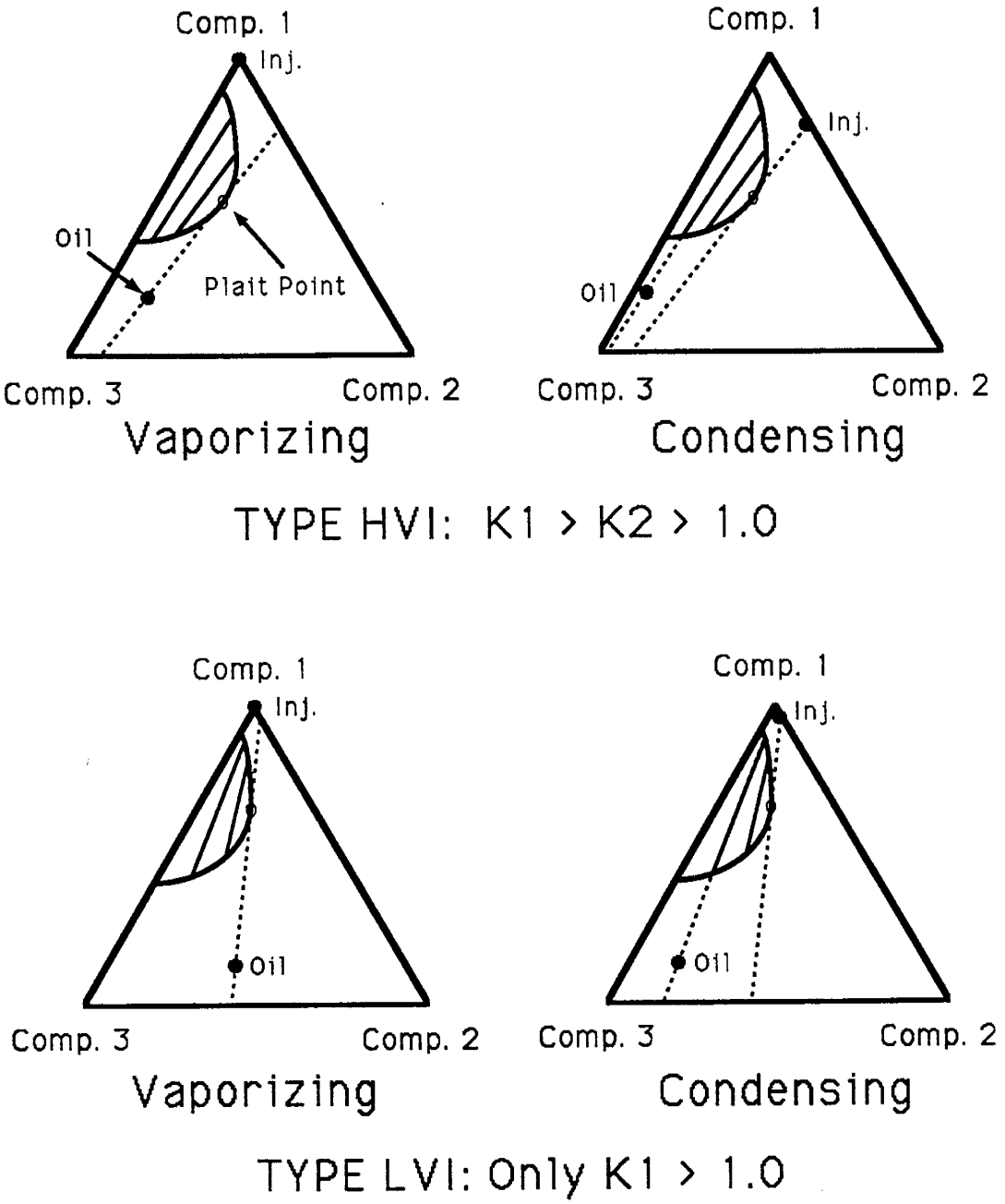

Figure 3.21: MMP for vaporizing and condensing drives of type HVI and LVI phase behavior.

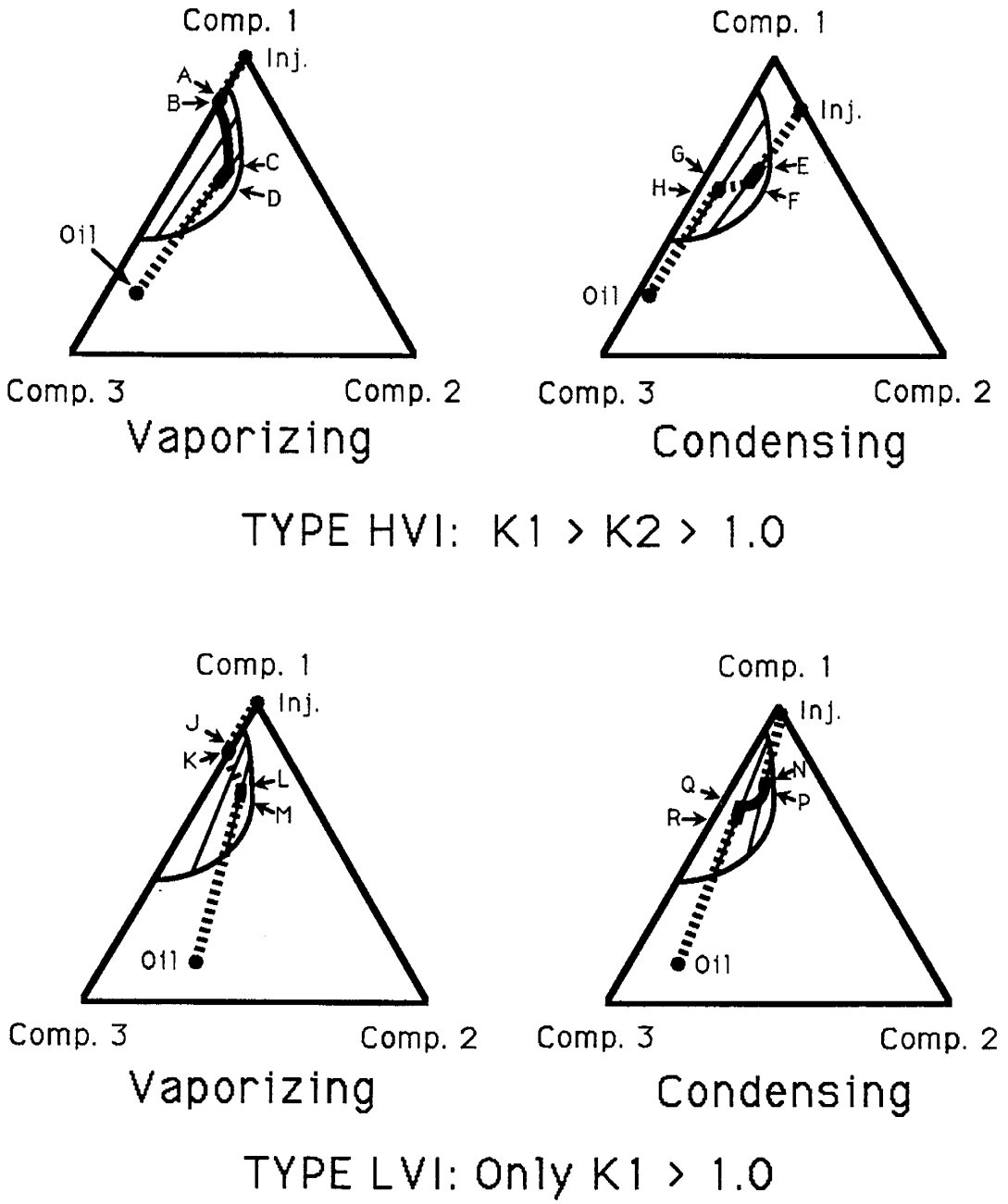

Figure 3.22: Typical solution routes in composition space for type HVI and LVI phase behavior with either condensing or vaporizing gas drives.

chromatographically according to their K-value ranking. That is, the components are preferentially separated because the solution route must first jump into the two-phase region along the oil tie-line extension and over to the injection gas tie line. For example, if an oil that contains only Comp. 2 and Comp. 3 is displaced by pure Comp. 1, then the solution route must eventually jump to the injection gas tie line in which the concentration of Comp. 2 is zero. Thus, Comp. 2 will be evaporated first, followed by Comp. 3 with the lowest volatility. For systems in which both the oil and gas contain all three components, the chromatographic separation becomes more obscure, but still occurs.

Fig. 3.23 summarizes the qualitative features of the saturation profiles for the four types of solutions that are possible in ternary systems. Segments that are marked with a question mark are ones that may or may not appear in a particular solution.

3.3.4 Classification of Four-Component Solutions

The results given in Sections 3.3.1 and 3.3.2 can be extended to systems with more than three components. Again, the component K-values can be used to categorize the solution phase behavior and structure. For four-component systems that have strictly ordered K-values, there are only three types of phase behavior that give a two-phase region. They are,

- Type HVI: $K_1 > K_2 > K_3 > 1.0$ and $1.0 > K_4$.
- Type MVI: $K_1 > K_2 > 1.0$ and $1.0 > K_3 > K_4$.
- Type LVI: $K_1 > 1.0$ and $1.0 > K_2 > K_3 > K_4$.

In HVI phase behavior (high volatility intermediate components), the intermediate components (those with K_2 and K_3 volatility) partition preferentially into the gas phase, while in LVI phase behavior (low volatility intermediate components), the intermediate components show higher concentrations in the liquid phase. In type MVI (medium volatility intermediate components), however, one of the intermediate components has high volatility, while the other low volatility. Fig. 3.24 illustrates these types for constant K-values by showing the binodal curve on each ternary face of the quaternary diagram. The dotted lines show the two-phase binodal curves on the back faces of the quaternary diagram. Plait points are not shown but are easily included by treating each side of the quaternary diagram as a ternary diagram.

For each type of phase behavior shown in Fig. 3.24, it is easy to prove that the tie-line extensions must intersect the Comp. 2/Comp. 3/Comp. 4 ternary plane. The proof of this statement is nearly identical to that given in Section 3.3.1. That is, the slope of the tie line and its tie-line extension is determined by the component K-values using the tie-line equation,

$$\frac{C_1/x_1 - 1}{K_1 - 1} = \frac{C_2/x_2 - 1}{K_2 - 1} = \frac{C_3/x_3 - 1}{K_3 - 1}. \tag{3.38}$$

and thus,

$$C_i = x_i \left[1 + (\frac{K_i - 1}{K_3 - 1})(C_3/x_3 - 1)\right], \quad i = 1, \cdots, n_c - 2 \tag{3.39}$$

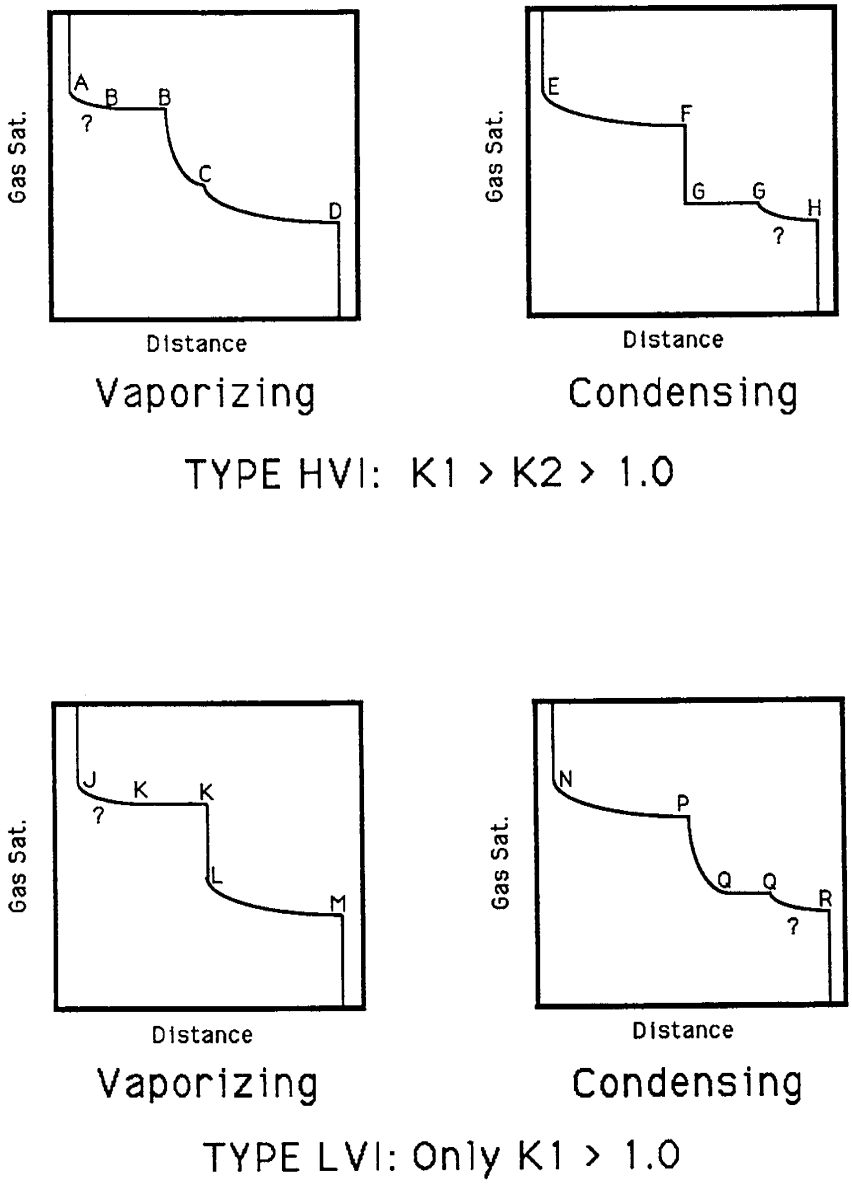

Figure 3.23: Typical solution profiles for type HVI and LVI phase behavior with either condensing or vaporizing gas drives.

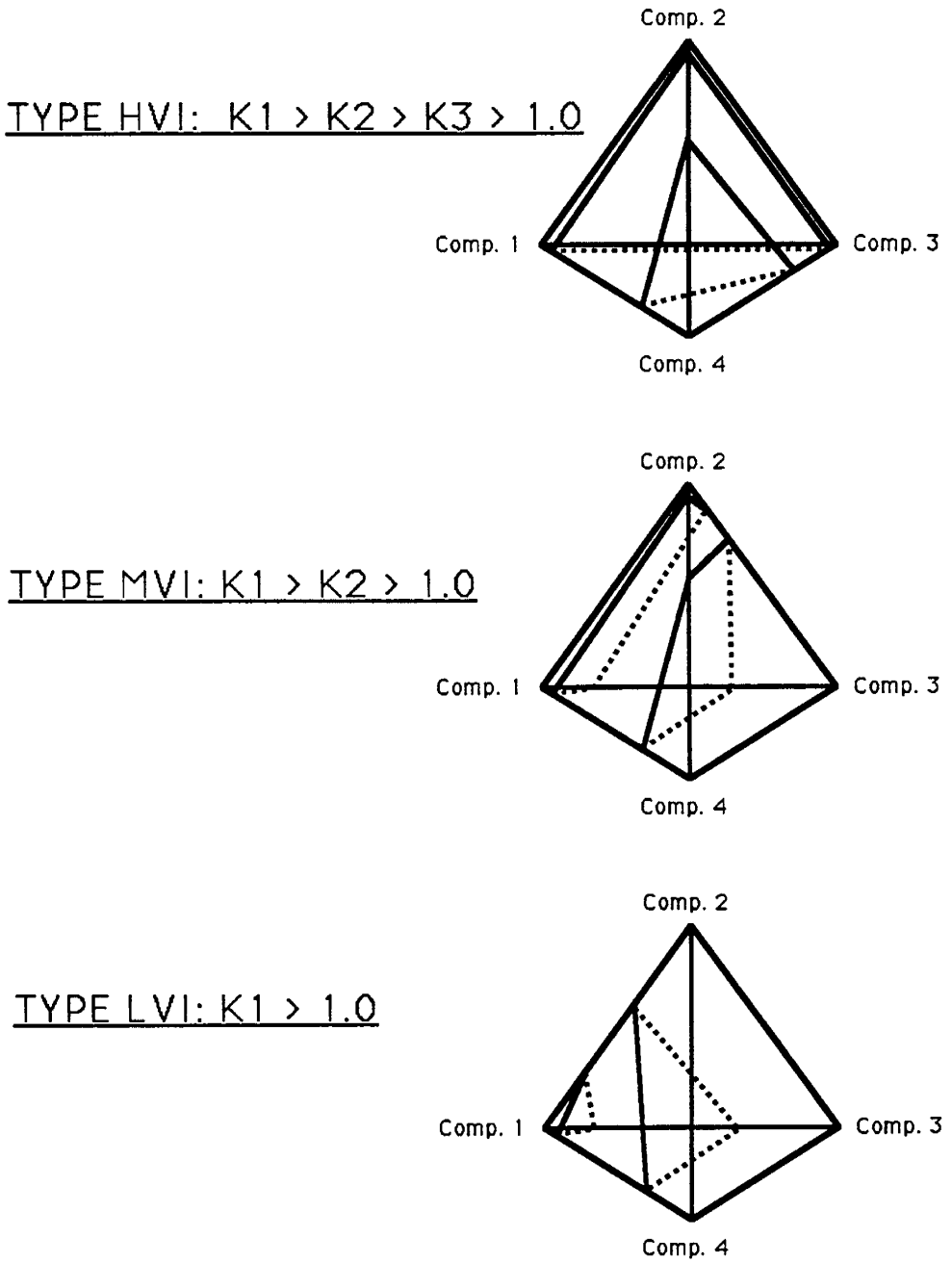

Figure 3.24: Types of phase behavior found in four-component systems based on component volatility.

which is similar to Eq. 3.37 given in Section 3.3.1.

In three-component displacements, there are two types of displacement mechanisms (condensing or vaporizing) for each type of phase behavior. Hence, for three-component systems, four types of solution routes are possible. For four-component displacements, however, there are four types of displacement mechanisms (pure condensing, pure vaporizing, leading condensing/trailing vaporizing, or leading vaporizing/trailing condensing) for each type of phase behavior. For example, the solutions reported in Sections 3.1 and 3.2 included a leading condensing segment connected to a trailing vaporizing segment by the crossover tie line. Hence, for four-component displacements there are twelve typical solution routes that are possible. The displacements can be classified into one of the following categories:

- Type HVI: Leading condensing/trailing condensing
- Type HVI: Leading vaporizing/trailing vaporizing
- Type HVI: Leading condensing/trailing vaporizing
- Type HVI: Leading vaporizing/trailing condensing
- Type MVI: Leading condensing/trailing condensing
- Type MVI: Leading vaporizing/trailing vaporizing
- Type MVI: Leading condensing/trailing vaporizing
- Type MVI: Leading vaporizing/trailing condensing
- Type LVI: Leading condensing/trailing vaporizing
- Type LVI: Leading vaporizing/trailing condensing
- Type LVI: Leading condensing/trailing vaporizing
- Type LVI: Leading vaporizing/trailing condensing

Fig. 3.25 illustrates a typical solution route for a four-component displacement of oil by gas. The quaternary diagram can be divided into four quadrants depending on the injection gas and initial oil composition. The quadrants are divided by surfaces that are nearly planar for the PREOS (Peng Robinson equation of state) and exactly planar for constant K-values. These surfaces are illustrated in Fig. 3.25 by the "vertical" and "horizontal" surfaces. The injection gas composition lies on the horizontal surface, while the initial oil composition on the vertical surface. The displacements in the next sections show that the solution must traverse or shock along these surfaces. That is, the leading portion of the solution travels along the vertical surface (from the oil tie line, which lies on the vertical surface) until it intersects the crossover tie line. The intersection of the horizontal and vertical surfaces occurs at this third key tie line, the crossover tie line. The solution route then follows the crossover tie line until a switch is made to the horizontal surface. From there, the trailing portion of the displacement begins (along the horizontal surface) and ends at the injection gas tie line (which lies on the horizontal surface).

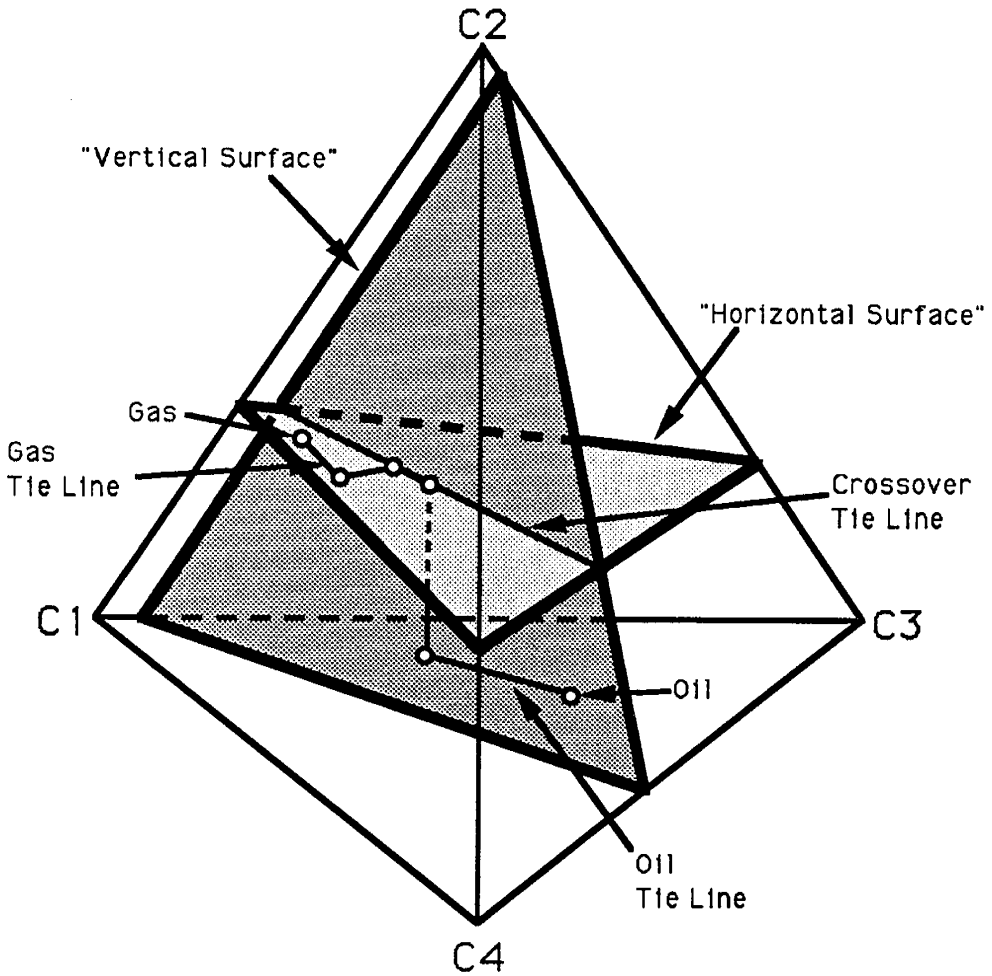

Figure 3.25: Illustration of a typical solution route in a four-component system.

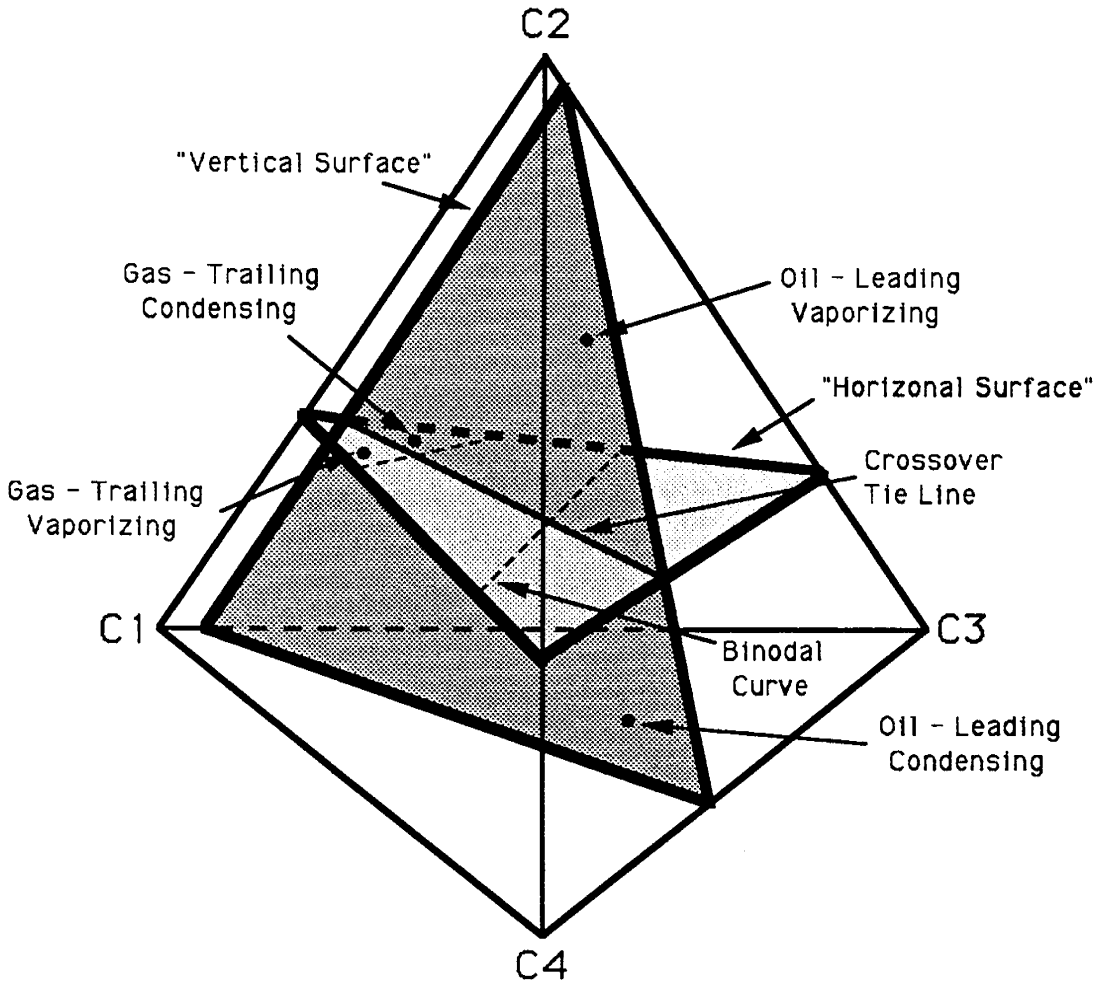

Figure 3.26: Illustration of displacement mechanisms for four-component systems.

Fig. 3.26 illustrates how the displacement mechanism is determined for a typical quaternary diagram. Along the horizontal and vertical surfaces, the displacement mechanism can be either vaporizing or condensing. It is the location of the injection gas and initial oil composition that determines the type of displacement mechanism along each surface. If the oil composition lies below the horizontal surface determined by the injection gas composition, then the leading portion of the displacement will be condensing. If, on the other hand, the oil composition lies above the horizontal surface then the leading portion of the displacement will be vaporizing. The trailing portion of the displacement is determined the same way. That is, if the injection gas composition lies to the right of the vertical surface, then the trailing portion of the displacement will be condensing, while if the injection gas composition lies to the left of the vertical surface, then the trailing portion will be vaporizing. Thus, a combination of four types of displacements is possible. For example, the typical displacement illustrated in Fig. 3.25 can now be recognized as a combined leading condensing/trailing vaporizing (C/V) gas drive. The pure vaporizing or condensing displacement occurs when both the leading and trailing portions of the displacement give the same type of displacement mechanism.

As a result of the solution structure, development of miscibility in four-component systems is more complex than was described for three-component problems (in which the solution lies on only one surface). For four-component systems, a third key tie line called the crossover tie line, plays an important role. In four-component systems then, either the injection gas tie line, the initial oil tie line or the crossover tie line can control the development of miscibility. That is, the tie line that is driven first to a critical tie line as the pressure or injection gas composition is changed is the one that controls the development of miscibility. Which tie line is the key tie line on the relative locations of the three key tie lines and the critical locus. The examples of Sections 3.1 and 3.2 were ones in which the crossover tie line controlled development of miscibility. In Section 3.4, examples are reported in which either the initial or injection tie lines are responsible for development of miscibility. Many additional examples are given by Johns [56] and Dindoruk [27].

3.4 Effects of Volume Change on Mixing in Four-Component Gas Drives

Birol Dindoruk

The theory presented in Sections 3.1-3.3 was developed based on the assumption that the partial molar volume of any component in a mixture is constant no matter what phase the component appears in. As a result, the local flow velocity also remains constant in one-dimensional flow. The assumption of no volume change on mixing (NVC) is reasonable if the pressure is high enough, but it is not necessarily reasonable at pressures of interest in many gas injection processes. Dumoré *et al.* [31] included effects of volume change (VC) as components transfer between phases, and calculated the varying local flow velocity that results. They showed that, just as in NVC analyses, mixture compositions that form during the displacement fall on a path that includes two key tie lines, the injection tie line, which is the tie line that extends through the injection composition, and the oil tie line, which extends through the initial oil composition. Just as in the theory of Sections 3.1 and 3.2,

the two key tie lines may be connected by a continuous variation along a nontie-line path or by a shock from one tie line to the other. They also showed that in ternary systems with VC, miscibility can develop in two ways, when the injection tie line becomes a critical tie line (a condensing gas drive), or when the oil tie line does so (a vaporizing gas drive). Thus, in ternary systems, the key features of the theory apply in both NVC and VC systems.

The next step in the development of analytical theory was taken by Monroe *et al.* [83], who extended the approach of Dumoré *et al.* [31] to a four-component system. They demonstrated that when a fourth component is added, a third key tie line, the crossover tie line, appears in the solution. In Sections 3.1 and 3.2 we showed how to use geometric constructions to find the crossover tie lines, and showed that miscibility can also develop when the crossover tie line becomes a critical tie line.

In this section, we show that the geometric constructions reported in Sections 3.1 and 3.2 can be generalized to apply when the effects of volume change are included. We report sample solutions for two quaternary systems that demonstrate important variations in solution structure, and we show how to determine easily which solution type will occur. The approach demonstrated can be used, therefore, to solve any four-component problems with or without volume change on mixing.

3.4.1 Mathematical Model

In the component transport equations, dissipative terms (diffusion, dispersion, capillary forces and gravity) are neglected, and one-dimensional flow is considered. The resulting material balance equations for isothermal flow of components in a homogeneous porous medium are,

$$\frac{\partial G_i}{\partial \tau} + \frac{\partial F_i}{\partial \xi} = 0 \qquad i = 1, n_c, \tag{3.40}$$

where τ and ξ are dimensionless time and space coordinates and the overall molar concentration and fractional flow of component i are

$$G_i = G_i(\vec{Z}) = \sum_{j=1}^{n_p} x_{ij}\rho_{jD}S_j \qquad i = 1, n_c, \tag{3.41}$$

$$F_i = F_i(\vec{Z}, v_D) = v_D \sum_{j=1}^{n_p} x_{ij}\rho_{jD}f_j \qquad i = 1, n_c. \tag{3.42}$$

Eq. 3.40 is nonstrictly hyperbolic when $n_c > 2$. The flow velocity, v_D, in Eq. 3.42 varies with spatial location when components change volume as they transfer between phases. Equilibrium compositions in Eqs. 3.41 and 3.42 were calculated with the Peng and Robinson [103] equation of state (PREOS). Phase densities were corrected using volume translation similar to that described by Peneloux *et al.* [102]. Phase viscosities were calculated with the correlation of Lohrenz *et al.* [75] from the phase composition data. Properties of components used are given in Table 3.4 [114, 26, 54]. Vapor and liquid relative permeability functions were assumed to have the form

$$k_{rv} = \left[\frac{S_v}{1 - S_{lr}}\right]^{n_v}, \qquad k_{rl} = \left[\frac{1 - S_v - S_{lr}}{1 - S_{lr}}\right]^{n_l}, \tag{3.43}$$

Table 3.4: Component properties.

Component	M_w	P_c (psia)	T_c (°F)	V_c $(ft^3/lb-mol)$	ω	s_i $(ft^3/lb-mol)$
N_2	28.01	493.0	-232.4	1.4403	0.040	-0.0014
CO_2	44.01	1071.0	87.90	1.5060	0.2250	0.0600
CH_4	16.04	667.8	-116.63	1.5899	0.0104	-0.0661
C_4	58.12	550.7	305.65	4.0828	0.2010	-0.0744
C_{10}	142.29	305.7	652.10	9.6610	0.4900	0.1602

Component	ρ_i $(lb-mol/ft^3)$	δ_{ij}				
	1600 psia	N_2	CO_2	CH_4	C_4	C_{10}
N_2	0.2370	0.0000	—	0.0310	0.1200	0.1200
CO_2	0.4237	—	0.0000	0.1000	0.1257	0.0942
CH_4	0.2627	0.0310	0.1000	0.0000	0.0270	0.0420
C_4	0.5859	0.1200	0.1257	0.0270	0.0000	0.0080
C_{10}	0.3041	0.1200	0.0942	0.0420	0.0080	0.0000

where $n_v = 3.0$, $n_l = 3.0$, and $S_{lr} = 0.05$. When gravity and capillary pressure effects are neglected, the fractional flow expression for phase j is

$$f_j = \frac{\frac{k_{rj}}{\mu_j}}{\sum_{j=1}^{n_p} \frac{k_{rj}}{\mu_j}} \tag{3.44}$$

Because phase compositions are fixed for overall compositions on a single tie line and because phase viscosities depend only on the composition of the phase, there is a single fractional flow curve for each tie line. The relative permeability functions on that tie line depend only on the vapor saturation, S_v, which is a function of the overall composition, Z_i, through the vapor mole fraction, V,

$$S_v = \frac{V}{V + \frac{\rho_v}{\rho_l}(1-V)}, \qquad V = \frac{Z_i - x_{il}}{x_{iv} - x_{il}} \tag{3.45}$$

The hyperbolic equation system is a Riemann problem, where the initial data are

prescribed as two different constant composition states connected by a discontinuity at $\xi = 0$,

$$\vec{Z}(\xi, 0) = \begin{cases} \vec{Z}_{inj} & \xi < 0 \ , \\ \vec{Z}_{ini} & \xi > 0 \ . \end{cases} \tag{3.46}$$

The solution path in the composition domain must connect $\vec{Z}_{inj}$ and $\vec{Z}_{ini}$.

Eq. 3.40 can be solved by the method of characteristics, whereby it is transformed into an eigenvalue problem of the form given by Dumoré *et al.* [31],

$$([F] - \lambda\,[G])\,\vec{X} = 0 \ , \tag{3.47}$$

where the elements of F are

$$[F] = \left[\frac{\partial F_i}{\partial Z_j}, \frac{\partial F_i}{\partial v_D}\right] \quad i = 1, n_c, \quad j = 1, n_c - 1 \ , \tag{3.48}$$

and those of $[G]$ are

$$[G] = \left[\frac{\partial G_i}{\partial Z_j}, 0\right] \quad i = 1, n_c, \quad j = 1, n_c - 1 \ . \tag{3.49}$$

For compositions in the two-phase region, the eigenvalues, λ, in Eq. 3.47 give the local wave velocity and the eigenvectors, $\vec{X}$, give composition path directions. Dumoré *et al.* [31] showed that tie lines are eigenvector directions, and there are two additional, nontie-line directions in four-component problems [83].

Solutions to Eqs. 3.40-3.46 include spreading waves and shocks, which arise when continuous variations would lead to a multivalued solution. A material balance for a component across a shock yields the familiar Rankine-Hugoniot expression for the velocity of the shock,

$$\Lambda = \frac{F_i^{II} - F_i^{I}}{G_i^{II} - G_i^{I}} \ , \tag{3.50}$$

where I and II refer to the upstream and the downstream sides of the shocks.

In the solutions reported below, two types of shocks are important. If a mixture composition on one side of shock forms only one phase, the two-phase composition on the other side must lie on the tie line that extends through the single-phase composition [70, 31]. Such phase transition shocks always occur when the number of phases changes. If a shock occurs within the two-phase region, however, it can connect two tie lines. The resulting self-sharpening waves arise when a continuous variation along a nontie-line path would cause fast-moving compositions to lie upstream of slow moving ones.

All of the solutions presented in this section were verified by finite difference in calculations. Detailed comparisons are given by Dindoruk [27]. The numerical solutions included the effects of numerical dispersion, which smears the shocks and causes other small differences in the solution, but the approximate solutions clearly show that the analytical solutions are correct.

3.4.2 Sharpening Behavior on Nontie-Line Paths

In the solutions reported below, a crossover tie line is connected to the initial oil and injection gas tie lines either by shocks or by continuous variations along nontie-line paths. Whether or not a spreading wave exists along a nontie-line path depends on how eigenvalues vary along it. If eigenvalues increase monotonically as the nontie-line path is traced from upstream to downstream, then a continuous variation is permitted. Otherwise the velocity constraint, which requires that fast compositions lie downstream of slow ones, is violated, the wave is self-sharpening, and a shock forms.

Each nontie-line composition path generates a ruled surface of tie lines that intersect the path. The extensions of the tie lines in the ruled surface also generate an envelope curve on the surface, as Fig. 3.27 illustrates. A similar approach was used by Wachmann [144] and Ceré and Zanotti [15] to examine self-sharpening behavior for ternary systems with no volume change on mixing. For the kth nontie-line path, the saturation value at a point where a tie line is tangent to the envelope curve is [27]

$$P_k = \frac{\overline{\rho} Z_i^e - \rho_l x_{il}}{\rho_v x_{iv} - \rho_l x_{il}} \tag{3.51}$$

where $\overline{\rho}$ is defined as

$$\overline{\rho} = P_k \rho_v + (1 - P_k)\rho_l \ . \tag{3.52}$$

Substitution of Eq. 3.52 into Eq. 3.51 yields

$$P_k = \frac{V^e}{V^e + \frac{\rho_v}{\rho_l}(1 - V^e)} \ , \tag{3.53}$$

where V^e is vapor mole fraction on the envelope.

It is convenient to define a parameter, ψ, that varies along the kth nontie-line path and to represent each tie line in terms of $P_k(\psi)$, and an additional function, $\varphi(\psi)$, defined as

$$\varphi(\psi) = \frac{\rho_l x_{il} - m\rho_l x_{jl}}{\frac{d}{d\psi}\left[\rho_v x_{iv} - \rho_l x_{il}\right] - m\frac{d}{d\psi}\left[\rho_v x_{jv} - \rho_l x_{jl}\right]} \ , \tag{3.54}$$

where, the slope, m, is defined as

$$m = \frac{\rho_v x_{iv} - \rho_l x_{il}}{\rho_v x_{jv} - \rho_l x_{jl}} \tag{3.55}$$

and i and j are the subscripts for two distinct components. The parameter, ψ, can be selected as the equilibrium mole fraction of one of the components in any of the phases. It can be shown [27] that the kth eigenvalue can then be expressed as

$$\lambda_k^* = \left[\frac{\left(f_v - P_k(\psi) + \frac{d\ln v_D}{d\psi}\varphi(\psi)\right)}{(S_v - P_k(\psi))}\right] \ . \tag{3.56}$$

A similar form for the nontie-line eigenvalues was also used by Welge *et al.* [147] and Larson and Hirasaki [71]. Whether a variation along a nontie-line path is self-sharpening as the path is traced in a given direction can be determined by differentiating Eq. 3.56. The result is

$$\frac{d\lambda_k^*}{d\psi} = \frac{(f_v - S_v)}{(S_v - P_k(\psi))^2}\frac{dP_k(\psi)}{d\psi} + \frac{\left(\frac{df_v}{dS_v} - \frac{f_v - P_k(\psi)}{S_v - P_k(\psi)}\right)}{(S_v - P_k(\psi))}\frac{dS_v}{d\psi} + \frac{d}{d\psi}\left[\frac{\frac{d\ln v_D}{d\psi}\varphi(\psi)}{S_v - P_k(\psi)}\right] \tag{3.57}$$

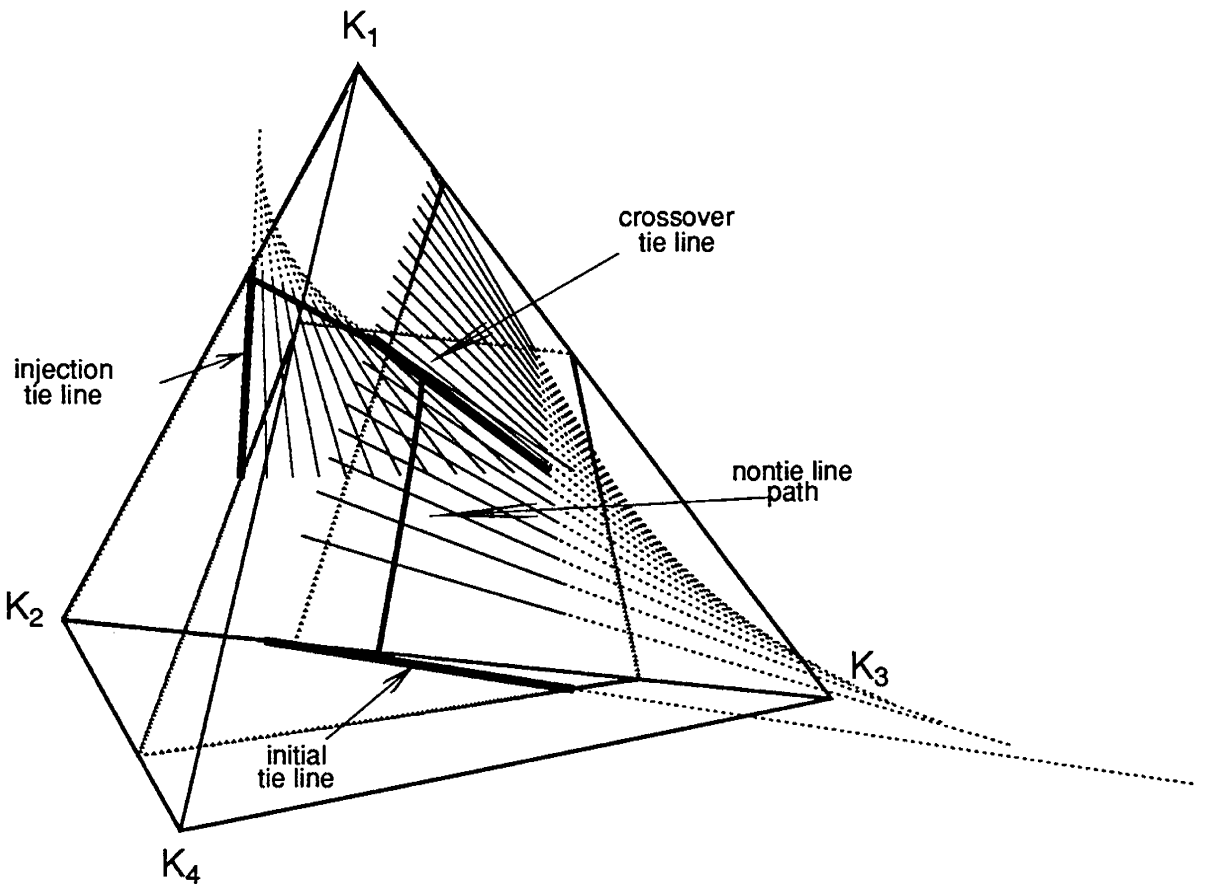

Figure 3.27: Composition routes, ruled surfaces and the structure of the envelopes formed by two different families of tie lines.

If two tie lines are connected by a continuous variation, the nontie-line path will be tangent to one of the tie lines at a point where the tie-line eigenvalue, $\lambda_t^* = \frac{df_v}{dS_v}$, is equal to λ_k^*, as Fig. 3.28 illustrates. An indication of the variation in λ_k^* can be seen from the behavior of Eq. 3.57 in the neighborhood of the equal eigenvalue point. At that point it can be shown [27] that

$$\frac{df_v}{dS_v} = \frac{f_v - P_k}{S_v - P_k}, \tag{3.58}$$

and the nontie-line path is tangent to the tie-line path. Furthermore, the local flow velocity, v_D, is fixed for variations along a tie line, because phase densities are also fixed. Hence, $\frac{dv_D}{d\psi}$ and $\frac{d^2 v_D}{d\psi^2}$ are also zero at the equal eigenvalue point. For points near the equal eigenvalue point but on the nontie-line path, therefore,

$$\lim_{\lambda_k^* \to \lambda_t^*} \left[\frac{df_v}{dS_v} - \frac{f_v - P_k}{S_v - P_k} \right] = 0 \tag{3.59}$$

also

$$\lim_{\lambda_k^* \to \lambda_t^*} \frac{d}{d\psi} \left[\frac{\frac{d \ln v_D}{d\psi} \varphi(\psi)}{S_v - P_k(\psi)} \right] = 0 \tag{3.60}$$

and hence, Eq. 3.57 reduces to

$$\lim_{\lambda_k^* \to \lambda_t^*} \frac{d\lambda_k^*}{d\psi} = \left[\frac{(f_v - S_v)}{(S_v - P_k(\psi))^2} \frac{dP_k(\psi)}{d\psi} \right]_{\lambda_k^* = \lambda_t^*} \tag{3.61}$$

Eq. 3.57 is similar to Eq. 3.27 in Section 3.2.

In the examples presented below, solution composition paths lie only in the region for which $f_v > S_v$, [46, 47, 31, 55] so the self-sharpening behavior is determined by the sign of $\frac{dP_k}{d\psi}$. In fact, direct evaluation of Eq. 3.57 for phase behavior calculated with the PREOS indicates that the sign of $\frac{d\lambda_k^*}{d\psi}$ does not change as the nontie-line path is traced away from the equal eigenvalue point. Because the velocity constraint requires that λ_k^* increase monotonically, as the solution path is traced downstream, Eq. 3.61 can be used to determine whether a variation along a nontie-line path is self-sharpening.

Calculations using Eq. 3.61 for the ruled surfaces shown in Fig. 3.27 indicate that nontie-line velocities increase from the initial tie line to the crossover tie line, and increase again from the crossover tie line to the injection tie line. Hence, two shocks connect the crossover tie line to the initial and injection tie lines.

Shocks Between Tie Lines

In cases where Eq. 3.57 or 3.61 indicates that variation along a nontie-line path is self-sharpening, the shock balances, Eq. 3.50 must be solved for the appropriate compositions on either side of the shock. In Section 3.2 we showed that for a four-component system without volume change that a shock between two tie lines implies that extensions of the tie lines intersect (outside of the quaternary diagram, in general). We now show that that statement is a special case of a more general result (for additional discussion of n_c component systems see Dindoruk [27] and Johns [56]): *If a shock connects two-phase compositions on different*

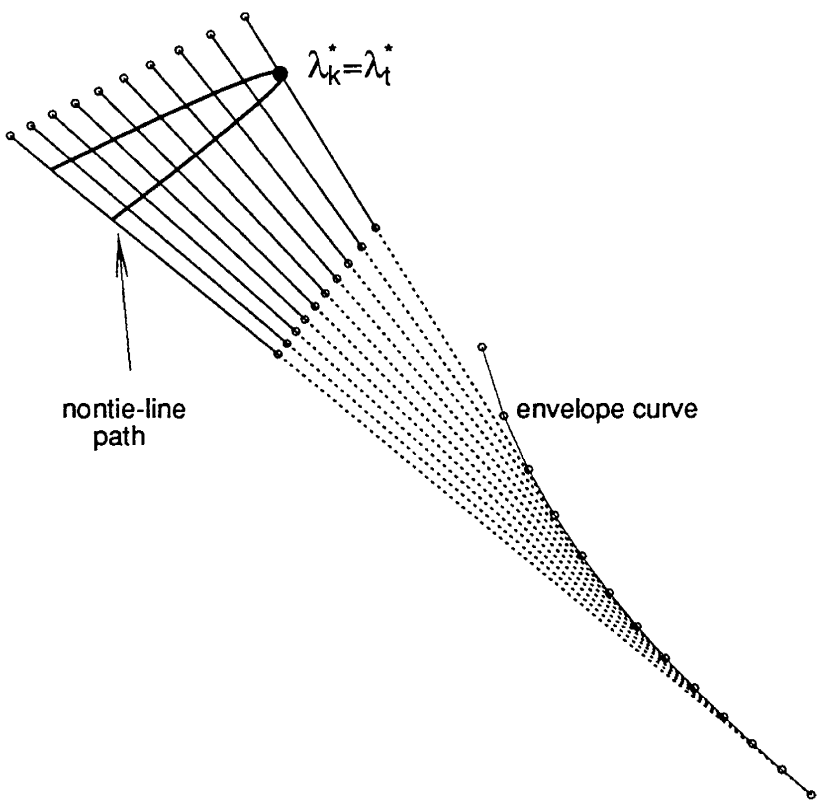

Figure 3.28: Ruled surface of tie lines generated by a nontie-line path and the envelope curve in that surface.

tie lines in n_c-component space, extensions of the two tie lines must intersect, whether or not volume changes as components change phase.

To prove this statement, we substitute the definitions of F_i and G_i into Eq. 3.50 and rearrange to obtain

$$\frac{\frac{v_D^{II} F_i^{*II} - \Lambda G_i^{II}}{v_D^I - \Lambda} - (\rho_{lD} x_{il})^I}{[\rho_{vD} x_{iv} - \rho_{lD} x_{il}]^I} = \frac{v_D^I f_v^I - \Lambda S_v^I}{v_D^I - \Lambda}, \qquad i = 1, n_c. \tag{3.62}$$

We now define an overall molar concentration, $\rho_D^s Z_i^s$, as

$$\rho_D^s Z_i^s = \frac{v_D^{II} F_i^{*II} - \Lambda G_i^{II}}{v_D^I - \Lambda}, \qquad i = 1, n_c\,. \tag{3.63}$$

Substitution of Eq. 3.63 into Eq. 3.62 gives the equation of a straight line in n_c-space,

$$\frac{\rho_D^s Z_i^s - (\rho_{lD} x_{il})^I}{[\rho_{vD} x_{iv} - \rho_{lD} x_{il}]^I} = \frac{v_D^I f_v^I - \Lambda S_v^I}{v_D^I - \Lambda}, \qquad i = 1, n_c\,. \tag{3.64}$$

Eq. 3.64 can be rewritten as

$$\rho_D^s Z_i^s = \alpha\,(\rho_{vD} x_{iv})^I + (1-\alpha)\,(\rho_{lD} x_{il})^I\,, \qquad i = 1, n_c\,, \tag{3.65}$$

where α is a parameter along the tie line independent of i defined as

$$\alpha = \frac{v_D^I f_v^I - \Lambda S_v^I}{v_D^I - \Lambda}\,. \tag{3.66}$$

According to Eq. 3.65, the molar concentration, $\rho_D^s Z_i^s$, must lie on a generalized tie line that passes through the equilibrium concentration points $(\rho_{vD} x_{iv})^I$ and $(\rho_{lD} x_{il})^I$.

Next, we substitute the definitions of F_i^{*II} and G_i^{II} into Eq. 3.63 and rearrange to obtain

$$\rho_D^s Z_i^s = \frac{v_D^{II} - \Lambda}{v_D^I - \Lambda}\left\{\beta\,(\rho_{vD} x_{iv})^{II} + (1-\beta)\,(\rho_{lD} x_{il})^{II}\right\}, \qquad i = 1, n_c\,, \tag{3.67}$$

where

$$\beta = \frac{v_D^{II} f_v^{II} - \Lambda S_v^{II}}{v_D^{II} - \Lambda}\,. \tag{3.68}$$

Eq. 3.67 indicates that the concentration, $\rho_D^s Z_i^s$, is also a linear combination of the equilibrium phase concentrations on the II side of the shock, $(\rho_{vD} x_{iv})^{II}$ and $(\rho_{lD} x_{il})^{II}$. Thus, the point $\rho_D^s Z_i^s$ is the intersection of the two generalized tie-line extensions.

Eqs. 3.65 and 3.67 are written in terms of molar concentrations (moles per unit volume) rather than mole fractions. For any overall composition, Z_i^s (in mole fractions), on tie line I, for example, an average molar density can be defined as

$$\rho_D^s = \alpha \rho_{vD}^I + (1-\alpha)\rho_{lD}^I\,, \tag{3.69}$$

Table 3.5: Method of characteristics solution for a quaternary displacement with volume change on mixing at 1600 psia and 160°F, (CO2-3).

Composition Label	Composition (Mole Fraction)				Total Flow Velocity	Gas Saturation (Vol. Fraction)	Wave Velocity (λ)
	CO_2	CH_4	C_4	C_{10}			
a	0.0000	0.1000	0.2000	0.7000	0.7982	0.0000	0.9321
b	0.0000	0.4586	0.1325	0.4088	0.8511	0.2481	0.9055-0.9321
c	0.8619	0.0000	0.0530	0.0850	0.9430	0.5810	0.9055
d	0.8680	0.0000	0.0518	0.0802	0.9430	0.6151	0.6301
e	0.9282	0.0000	0.0000	0.0717	0.9420	0.8019	0.1561-0.6301
f	1.0000	0.0000	0.0000	0.0000	1.0000	1.0000	0.1561

where α is given by Eq. 3.66. Substitution of Eq. 3.69 into 3.65 yields

$$Z_i^s = \frac{\alpha\rho_{vD}^I}{\alpha\rho_{vD}^I + (1-\alpha)\rho_{lD}^I} x_{iv}^I + \frac{(1-\alpha)\rho_{lD}^I}{\alpha\rho_{vD}^I + (1-\alpha)\rho_{lD}^I} x_{il}^I \,, \; i = 1, n_c. \tag{3.70}$$

Thus, the composition, Z_i^s, also lies on the extension of the equilibrium tie line in mole fraction composition space. Similar expressions can be derived for tie line II, and hence, the overall composition, Z_i^s, is the intersection of two tie lines in n_c-component space.

In the example solutions that follow, the tie-line intersection rule was used to identify the crossover tie line whenever it is connected to the initial or injection tie line by a shock. Once the crossover tie line has been identified, the appropriate shock velocities and compositions can be obtained from Eqs. 3.50 [94, 57, 28].

3.4.3 Displacement by Carbon Dioxide

We consider first displacement of an oil mixture of 10% CH_4, 20% C_4 and 70% C_{10} by pure CO_2 at 1600 psia and 160°F, exactly the same conditions as for Fig. 3.1 in Section 3.1. Fig. 3.29 shows that the composition path for this displacement is qualitatively equivalent to the path shown in Fig. 3.1. The relevant displacement profiles are shown in Fig. 3.30. The composition coordinates of the key points in the solution are given along with the associated wave velocities in Table 3.5. Comparison of the points given in Tables 3.2 and 3.5 indicates, while the same key tie lines appear in both solutions, the key points on the tie lines differ.

Again in this gas drive, there is a phase transition shock along the initial tie line from **a** to **b**. According to Eq. 3.61, continuous variations from the initial tie line toward the crossover tie line are self-sharpening. Therefore, a shock from **b** to **c** must connect the initial tie line and crossover tie line. That shock has a velocity equal to the tie-line eigenvalue at **c**. There is then a continuous variation along the crossover tie line from **c** to **d**.

The nontie-line paths from the crossover tie line to the injection tie line also show sharpening behavior according to Eq. 3.61, and hence there is a shock from **d** to **e**. Finally, there is a trailing shock along the injection tie line from point **e** to **f**.

Table 3.6: Method of characteristics solution for a quaternary displacement with volume change on mixing at 1600 psia and 160°F, (NIT-1).

Composition Label	Composition (Mole Fraction)				Total Flow Velocity	Gas Saturation (Vol. Fraction)	Wave Velocity (λ)
	N_2	CH_4	C_4	C_{10}			
a	0.0000	0.1000	0.2000	0.7000	0.9209	0.0000	1.6987
b	0.2215	0.2415	0.1300	0.4069	1.0859	0.4150	1.6987
c	0.2271	0.2451	0.1283	0.3995	1.0859	0.4294	1.4721
d	0.4831	0.0000	0.1245	0.3923	1.0105	0.5193	1.2570-0.5082
e	0.5343	0.0000	0.1145	0.3512	1.0105	0.5822	0.2457
f	0.6677	0.0000	0.0000	0.3323	0.9996	0.6913	0.2457-0.0529
g	0.7940	0.0000	0.0000	0.2060	0.9996	0.8184	0.0070
h	1.0000	0.0000	0.0000	0.0000	1.0000	1.0000	0.0070

In this case, the crossover tie line is connected to the initial and injection tie lines only by shocks. Hence, the crossover tie line must intersect both the initial and injection tie lines; it is the only tie line in Fig. 3.29 that does so [92, 56, 57, 27].

The comparison of the solutions for this system with and without volume change on mixing is shown in Fig. 3.31. The solution structure in both cases is determined largely by the initial, injection and crossover tie lines. In fact, a key result of this section is that the essential features of the solution are determined by the structure of the space of tie lines, whether or not there is volume change. The profiles indicate, however, that the CH_4 bank travels more rapidly when volume change is ignored. In fact, the volumetric shrinkage that occurs when CO_2 dissolves in the liquid phase in the transition zone slows the CH_4 bank and the CO_2 front enough that breakthrough of injected CO_2 occurs when more than one pore volume of CO_2 has been injected. Thus, the effect of volume change is to alter significantly the timing of oil recovery.

3.4.4 Displacement by Nitrogen

Next, we consider displacement of the same initial mixture, 10% CH_4, 20% C_4 and 70% C_{10}, by pure nitrogen (N_2). Thus, the initial composition and displacement conditions are exactly the same as in the CO_2 flood example shown. The composition path and the solution profiles for the system are given in Figs. 3.32 and 3.33. The labeled points and their associated wave velocities are presented in Table 3.6.

The solution structure for the N_2 displacement differs substantially from that of the CO_2 displacement. There is a leading shock from point **a** to point **b** along the initial tie line, followed by a continuous variation along the same tie line until the equal eigenvalue point, **c**, is reached. Continuous variation along a nontie-line path from the initial tie line

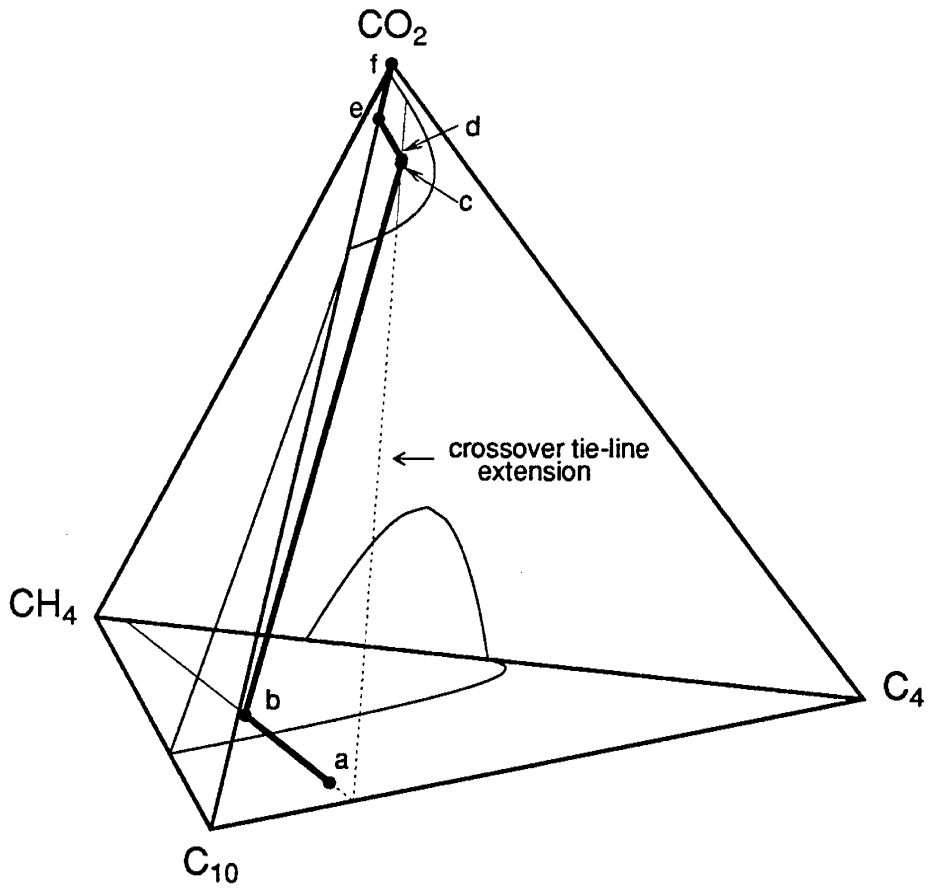

Figure 3.29: Composition route for displacement of a $CH_4/C_4/C_{10}$ mixture by pure CO_2 at 1600 psia and 160°F.

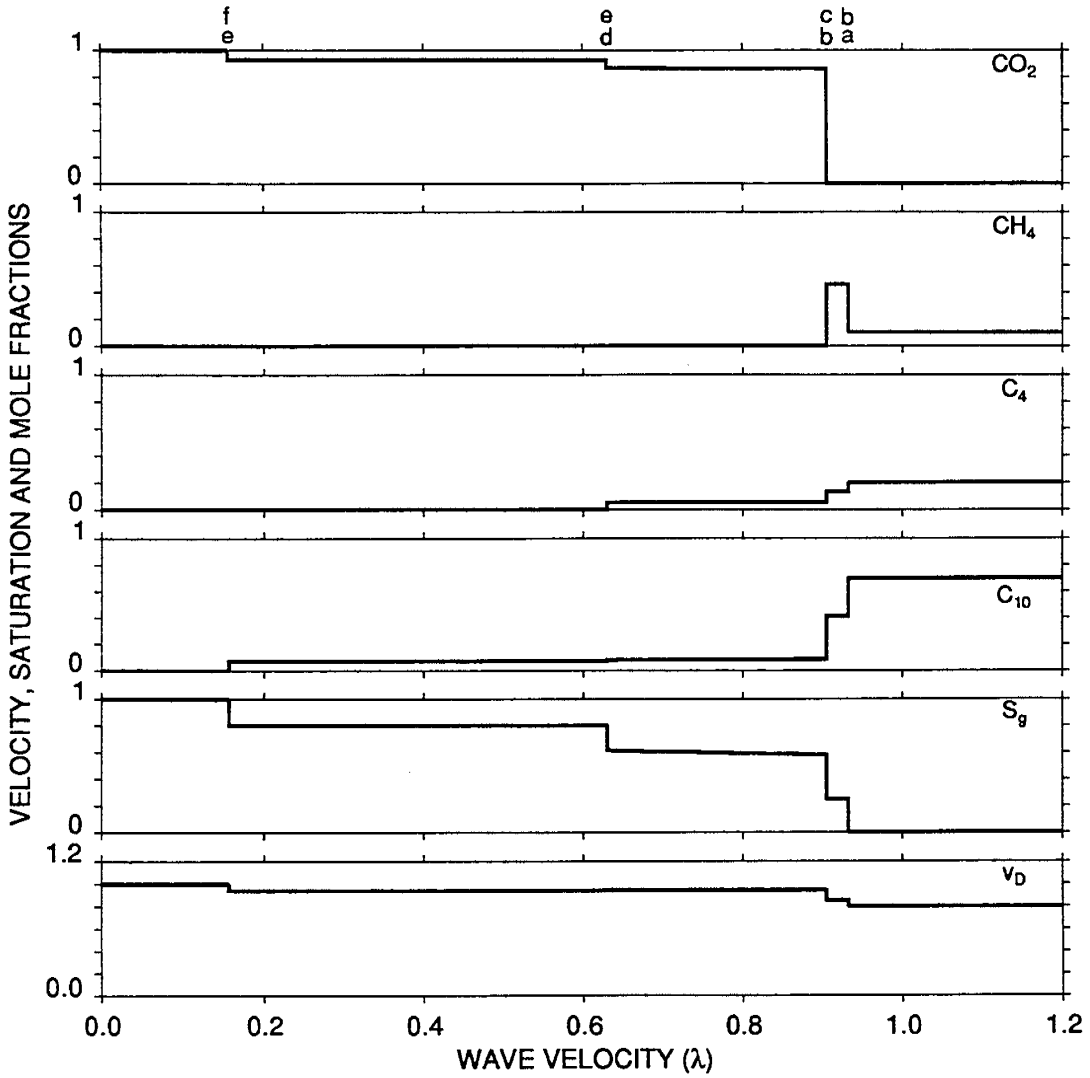

Figure 3.30: Composition, saturation and velocity profiles for displacement of a $CH_4/C_4/C_{10}$ mixture by pure CO_2 at 1600 psia and 160°F.

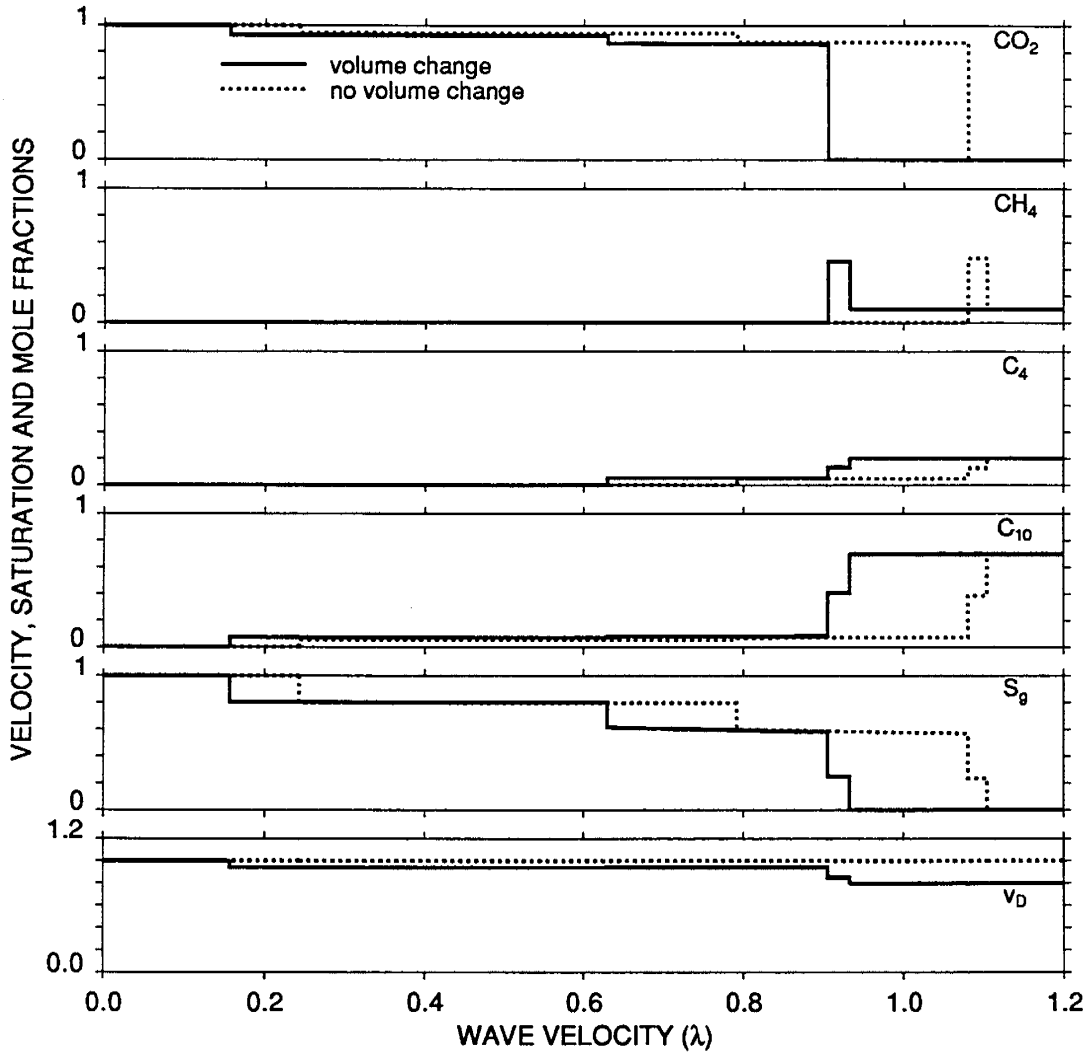

Figure 3.31: Comparison of composition, saturation and velocity profiles with and without volume change on mixing for displacement of a $CH_4/C_4/C_{10}$ mixture by pure CO_2 at 1600 psia and 160°F.

to the crossover tie line is permitted in this case because eigenvalues decrease as the path is traversed. Hence, a path switch occurs at **c**, followed by evolution along a nontie-line path. The nontie-line path extends until the crossover tie line is reached at point **d**. There is a large zone of constant state **d** $\rightarrow$ **d** (Fig. 3.33) because the wave velocity on the crossover tie line at **d** is lower than the wave velocity on the nontie-line path at point **d**. The constant state is followed by a continuous variation along the crossover tie line to point **e**. Point **e** is connected by a shock to **f** because the nontie-line path is self-sharpening according to Eq. 3.57. Finally, there is a continuous variation along the injection tie line to point **g**, where a trailing shock connects to the injection composition, **h**. In the N_2 displacement, therefore, the crossover tie line is the one tie line that intersects the injection tie line and also intersects the nontie-line path obtained by integration from the equal eigenvalue point, **c**, on the initial tie line.

The initial tie line in this example solution is not unique as long as the initial composition is strictly confined to the N_2-free face. In other words, two tie lines can be found that extend through the initial composition, **a**. Both are shown in Fig. 3.32. The first is the tie line in the interior of the quaternary diagram, along which the solution route is shown to enter the two-phase region. The second is a tie line that lies in the $CH_4/C_4/C_{10}$ face. A solution route that begins with a shock along the second tie line can also be found. That solution satisfies the requirement that wave velocities increase monotonically as the solution is traced through the two-phase region from the trailing shock to the leading shock. However, the second route can easily be eliminated by requiring that the solution be continuous with respect to the initial data, one of the conditions proposed by Hadamard [156] for a well-posed problem. This condition states that a slight variation of the initial data for the problem should cause the solution to vary only slightly. Addition of an infinitesimal amount of N_2 to the initial composition will resolve the nonuniqueness issue, because two tie lines will not intersect at this new point. If the initial point **a** is the limit of such points as the N_2 concentration goes to zero, it is clear that the solution will be continuous with respect to addition of N_2 only if the initial tie line is the tie line in the interior of the quaternary diagram. Therefore, the initial tie line in the interior of the quaternary diagram is selected. For additional discussion of the continuity condition, see Johns [56].

3.4.5 Comparison of Theory and Experiment

Experimental data obtained by Heller *et al.* [49] for injection of pure CO_2 into an artificial oil mixture 11.92% CH_4, 37.98% C_4, 50.10% C_{10} at 1406.7 psia and 160°F were selected for comparison with analytical solutions reported in this section. They reported results of displacement experiments at several pressures. That pressure was selected because it is farthest from the MMP. Hence, the separation of the component banks is clearer than that for displacements at pressures closer to the MMP. Responses at all the pressures were similar, however.

The composition paths for the displacement with CO_2 are shown in Figs. 3.7 and 3.8 for VC and NVC. The relative permeability functions used in the simulations were

$$k_{rg} = \left[\frac{S_g}{1 - S_{or}}\right]^{n_3}, \quad k_{rl} = \left[\frac{1 - S_g - S_{or}}{1 - S_{or}}\right]^3, \tag{3.71}$$

with $S_{or} = 0.05$.

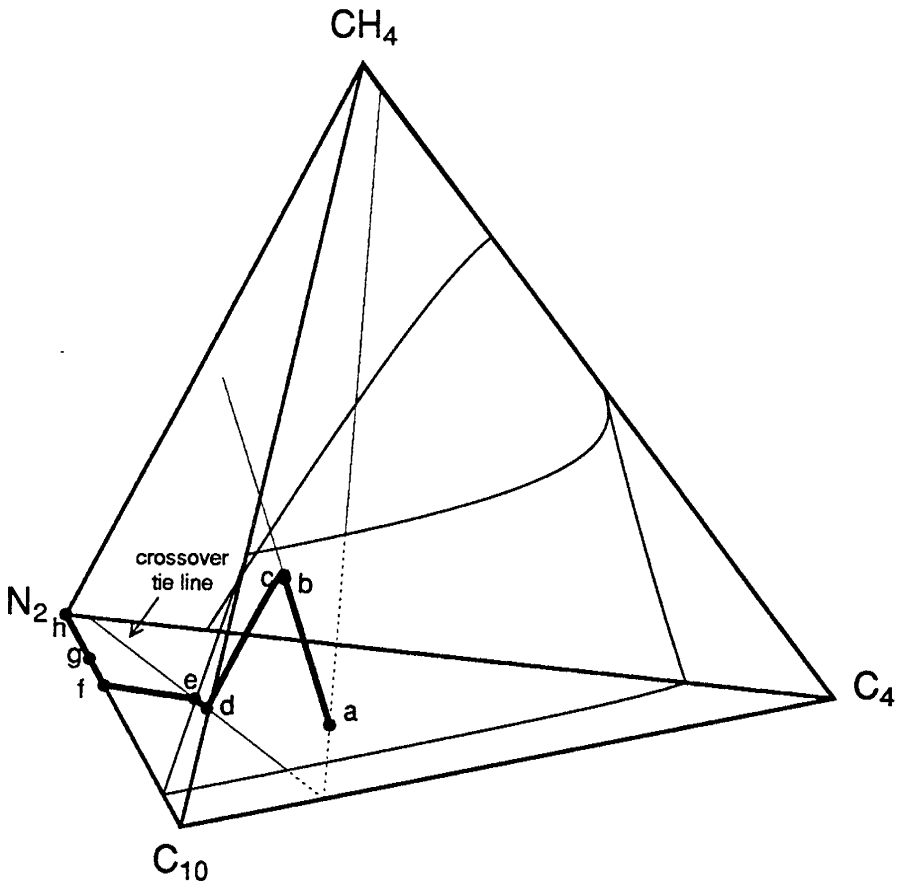

Figure 3.32: Composition route for displacement of a $CH_4/C_4/C_{10}$ mixture by pure N_2 at 1600 psia and 160°F.

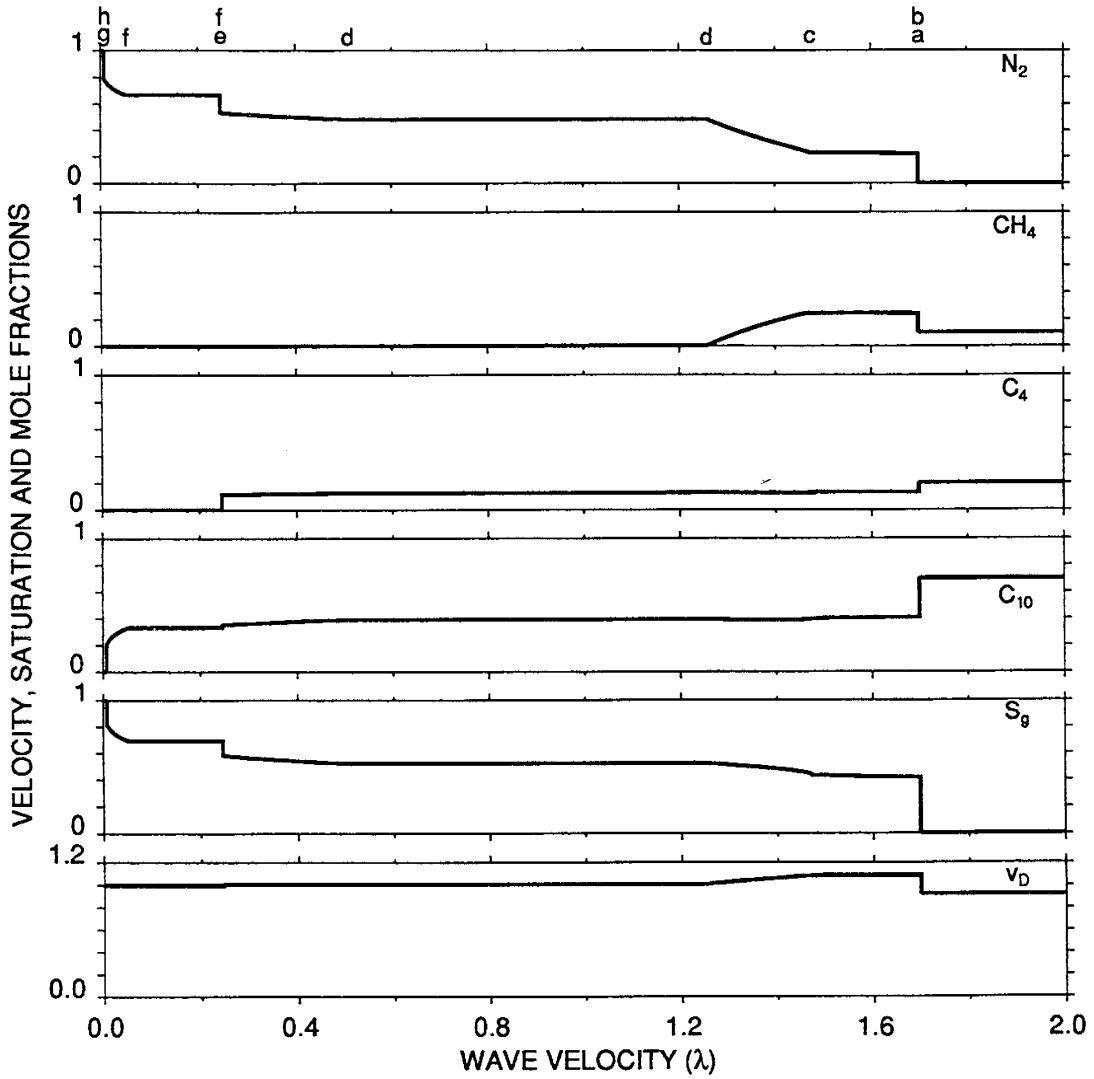

Figure 3.33: Composition, saturation and velocity profiles for displacement of a $CH_4/C_4/C_{10}$ mixture by pure N_2 at 1600 psia and 160°F.

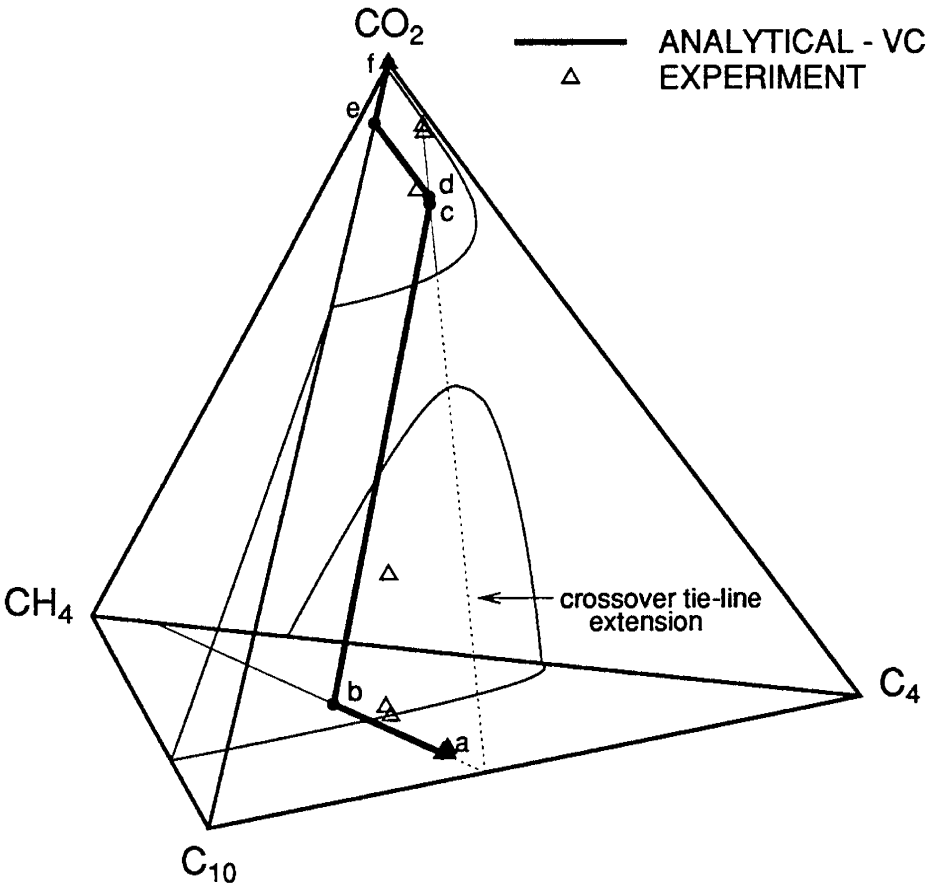

Figure 3.34: Composition route for displacement of a $CH_4/C_4/C_{10}$ mixture by pure CO_2 with VC at 1406.7 psia and 160°F.

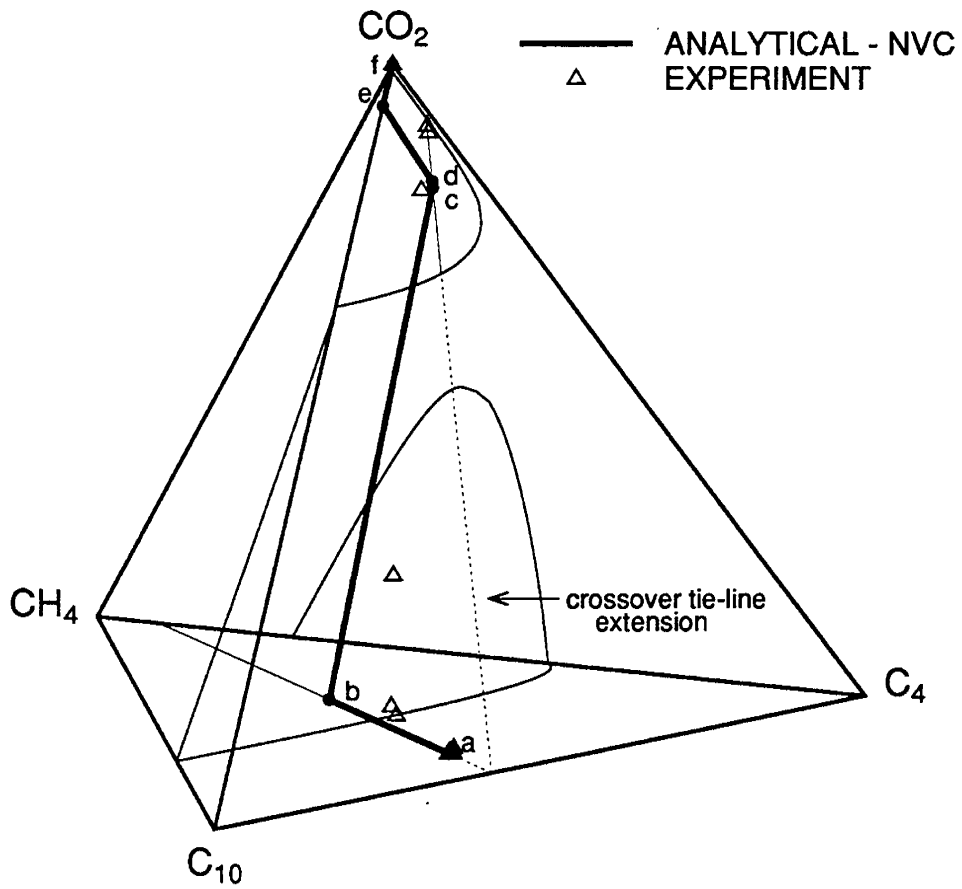

Figure 3.35: Composition route for displacement of a $CH_4/C_4/C_{10}$ mixture by pure CO_2 with NVC at 1406.7 psia and 160°F.

Table 3.7: Method of characteristics solution for a quaternary displacement with volume change on mixing at 1406.7 psia and 160°F.

Composition Label	Composition (Mole Fraction)				Total Flow Velocity	Gas Saturation (Vol. Fraction)	Wave Velocity (λ)
	CO_2	CH_4	C_4	C_{10}			
a	0.0000	0.1192	0.3798	0.5010	0.7850	0.0000	0.9520
b	0.0000	0.4225	0.2661	0.3114	1.8530	0.2764	0.9045-0.9520
c	0.7969	0.0000	0.1198	0.0832	0.9823	0.5726	0.9045
d	0.8071	0.0000	0.1159	0.0769	0.9823	0.6177	0.5556
e	0.9224	0.0000	0.0000	0.0776	0.9707	0.8498	0.0857-0.5556
f	1.0000	0.0000	0.0000	0.0000	1.0000	1.0000	0.0857

The compositions and the velocities of the key points are given in Tables 3.7 and 3.8. The comparison of the experimental effluent mole fractions with the two analytical solutions is presented in Fig. 3.36.

As in the example of Section 3.4.3, the crossover tie line is connected to the initial and injection tie lines by shocks, and hence, the crossover tie line is determined by the requirement that it intersect both the initial and injection tie lines. The solution structure is identical to that described in Sections 3.1.2 and 3.4.3.

Comparison of the effluent mole fractions with the experimental data (Fig. 3.36) indicates reasonable agreement. The solution with VC is clearly superior to the solution with NVC because only the VC solution predicts the breakthrough time after 1 PV of CO_2 injection, as was observed in the experiment [49]. In this case, the NVC assumption is not reasonable, and it leads to significant errors in the arrival time of the leading shock. The location and the strength of the CH_4 bank is also predicted more accurately with VC. A CH_4 bank was produced before CO_2 breakthrough, as was clearly observed in the experiment. However, the experimental CH_4 bank was wider and more dispersed, probably as a result of dispersion and nonuniform flow due to some viscous instability and gravity override in the inlet region of the slim tube. Therefore, not quite all of the bank is recovered before breakthrough. The existence of a CH_4 bank in a CO_2 flood indicates clearly that two-phase flow occurred during the displacement. Without that two-phase flow, the chromatographic separation that produces a CH_4 bank could not have occurred.

A variety of physical mechanisms could be responsible for the disagreement shown in Fig. 3.38. Dispersion undoubtedly caused some smearing of the shocks, and there was probably a limited region near the inlet of the slim tube where viscous instability and gravity override induced flow that was not strictly one dimensional. In addition, there must have been some effect of pressure drop over the length of the model, a physical mechanism that is not modeled in the one-dimensional analytical solutions. The changes in pressure over the flow length would have some effect on phase behavior (probably minor) and some effect on phase densities. Furthermore, the relative permeability functions appropriate to the

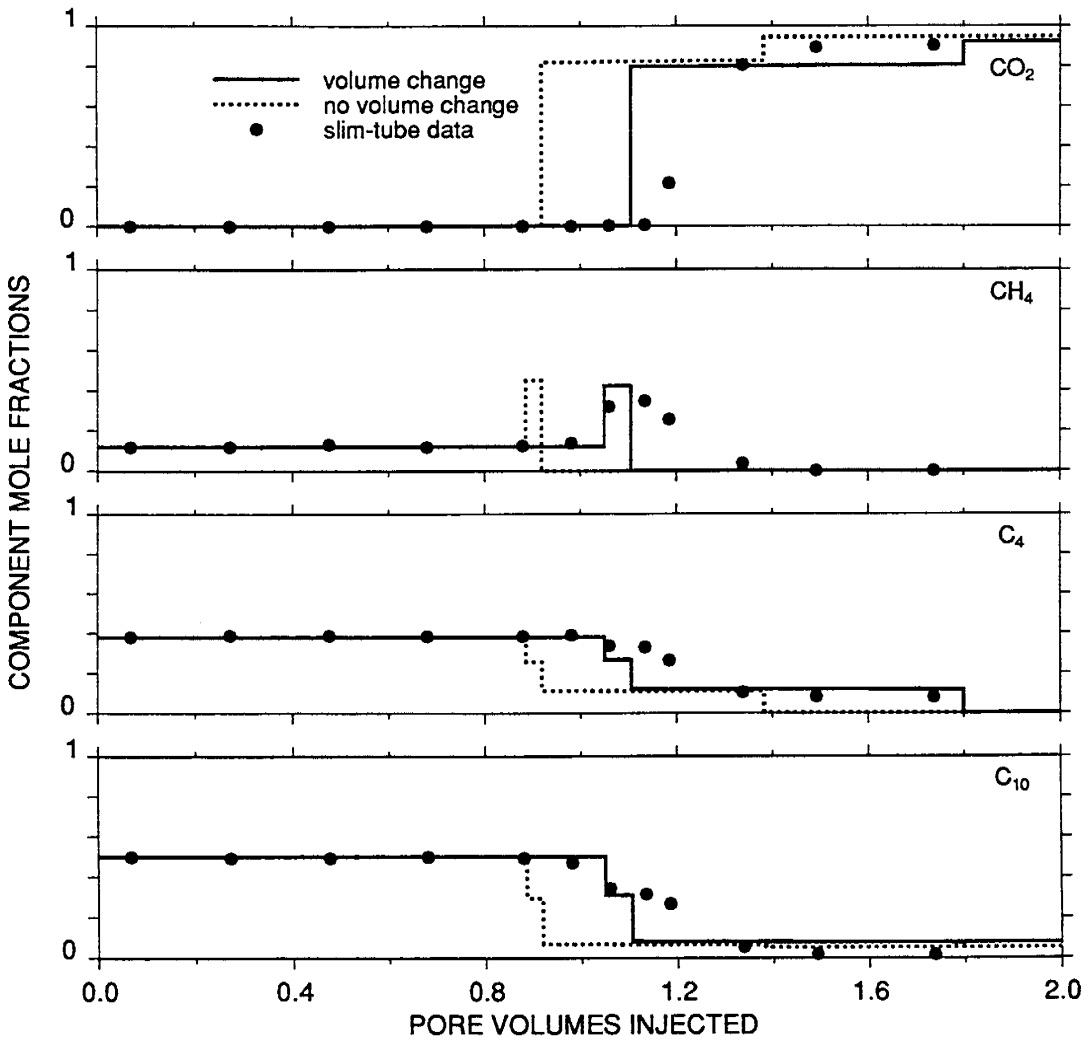

Figure 3.36: Comparison of effluent mole fractions with the experimental data for displacement of a $CH_4/C_4/C_{10}$ mixture by pure CO_2 at 1406.7 psia and 160°F.

Table 3.8: Method of characteristics solution for a quaternary displacement with no volume change on mixing at 1406.7 psia and 160°F.

Composition Label	Composition (Mole Fraction) CO_2	CH_4	C_4	C_{10}	Total Flow Velocity	Gas Saturation (Vol. Fraction)	Wave Velocity (λ)
a	0.0000	0.1192	0.3798	0.5010	1.0000	0.0000	1.1283
b	0.0000	0.4492	0.2561	0.2947	1.0000	0.2587	1.0877-1.1283
c	0.8193	0.0000	0.1113	0.0694	1.0000	0.5561	1.0877
d	0.8279	0.0000	0.1080	0.0641	1.0000	0.5955	0.7233
e	0.9461	0.0000	0.0000	0.0538	1.0000	0.8458	0.1440-0.7233
f	1.0000	0.0000	0.0000	0.0000	1.0000	1.0000	0.1440

slim tube in use were not known, and there is undoubtedly some error associated with the calculated phase densities and viscosities. Given the sampling frequency of the experiments, it is not possible to establish what combination of mechanisms produced the disagreement in Fig. 3.38. Indeed, given the complexity of the interactions of phase equilibrium and flow, even in a slim tube, the agreement observed in Fig. 3.38, which was obtained with no adjustment of parameters, is remarkable. All of the shocks predicted by the theory appear to be present (to the extent they can be resolved given the sampling frequency), and the quantitative agreement of changes in composition at the shocks is also good. Thus, we conclude that the available experimental evidence is completely consistent with the predictions of the theory.

3.4.6 Development of Miscibility

In four-component systems, miscibility can develop when any of the key tie lines, the initial tie line, injection tie line or crossover tie line approaches a critical locus whether or not volume change is present. As the pressure is increased in the CO_2 displacement, for example, miscibility develops as the two-phase region shrinks, and the crossover tie line [92] approaches the plait point on the $CO_2/C_4/C_{10}$ face of the quaternary diagram. At the MMP, the points **c** and **d** coincide because the crossover tie line is tangent to the binodal curve. The shock balances to the crossover tie line become

$$\Lambda^{bc} = v_D^b \frac{F_{CH_4}^{*b}}{G_{CH_4}^b} = v_D^c \frac{F_{CO_2}^{*c}}{G_{CO_2}^c} = v_D^c \frac{df_v^c}{dS_v} = v_D^c \ . \tag{3.72}$$

Because $f_v^c = S_v^c$ at the plait point, $F_i^{*c} = G_i^c$ and $v_D^b = v_D^c$. Similar shock balances between points **c** and **e** require that $v_D^e = v_D^c$. Point **e** is located on the binodal curve since

$$\Lambda^{ce} = v_D^c \frac{F_{C_4}^{*c}}{G_{C_4}^c} = \frac{v_D^e F_{CO_2}^{*e} - v_D^c F_{CO_2}^{*c}}{G_{CO_2}^e - G_{CO_2}^c} = v_D^c \frac{df_v^c}{dS_v} = v_D^c \ . \tag{3.73}$$

Finally, the Rankine-Hugoniot condition for the trailing shock along the injection tie line requires that $\Lambda^{ef} = v_D^e = 1$. Therefore, all the convective velocity terms approach unity, as do the shock speeds. Thus, flow velocity variations are eliminated and the displacement becomes piston-like at the MMP when the crossover tie line is a critical tie line. Thus, the addition of volume change does not alter the picture of development of miscibility developed in Sections 3.1 and 3.2.

In the $CO_2/CH_4/C_4/C_{10}$ system, the crossover tie line controls development of miscibility. If C_4 were added to the injected CO_2, however, the injection tie line could control development of miscibility [28]. If the injected mixture contains enough C_4 that it lies to the right of the crossover tie line in Fig. 3.29, for example, the injection tie line will reach the plait point first as the two-phase region shrinks with pressure increases, a condensing gas drive according to standard ternary definitions.

In the N_2 displacement, development of miscibility is controlled by the initial tie line. As pressure increases, of all the tie lines traversed in the solution, the initial tie line will be tangent to the locus of plait points at the lowest pressure (MMP). Thus, the N_2 displacement satisfies the traditional definition of vaporizing gas drive miscibility based on ternary systems. Thus, any of the key tie lines can approach the critical locus first as pressure and/or enrichment are changed. The theory presented in this chapter establishes that it is the geometry of the tie lines alone that determines how miscibility develops.

In Section 3.1, the effect on the MMP for CO_2 displacements of the addition of CH_4 to the oil was described. In those displacements, the crossover tie line controlled the development of miscibility. An increase in CH_4 concentration in the initial liquid increased the MMP of the system, but only slightly. The MMP behavior of the N_2 displacement is quite different when CH_4 concentration is increased, however. In that system, the initial tie line changes rapidly as the amount of CH_4 in the initial mixture increases. In fact, the MMP declines as the initial mixture is enriched with CH_4. As the amount of CH_4 in the initial mixture is increased, the initial tie line moves shorter, because it moves closer to the critical locus. Fig. 3.37 shows an example of the effect of adding CH_4 to a dead oil, **A**. The MMP for the dead oil is very high, approximately 18400 psia, as is shown in Fig. 3.37a. Addition of 35% CH_4 to the dead oil, reduces the N_2 MMP to about 5011 psia. At that pressure, the initial composition, **a**, is outside of the tie-line extensions on the $CH_4/C_4/C_{10}$ face as Fig. 3.37b shows. However, there is a critical tie line in the interior of the quaternary composition space extending through the initial composition, as is shown in Fig. 3.38. Thus, in the N_2 system considered, addition of 35% CH_4 leads to a reduction of MMP by 13400 psia, much greater sensitivity to CH_4 concentration than was observed for the CO_2 systems. That behavior is due to orientation of the tie lines in the quaternary space. Here again, it is the structure of the space of equilibrium tie lines that controls the important features of the solution.

3.4.7 Conclusions

The analytical solutions for gas flood systems with volume change on mixing lead to the following conclusions:

1. Variations in the total flow velocity can have significant impact on the timing of recovery.

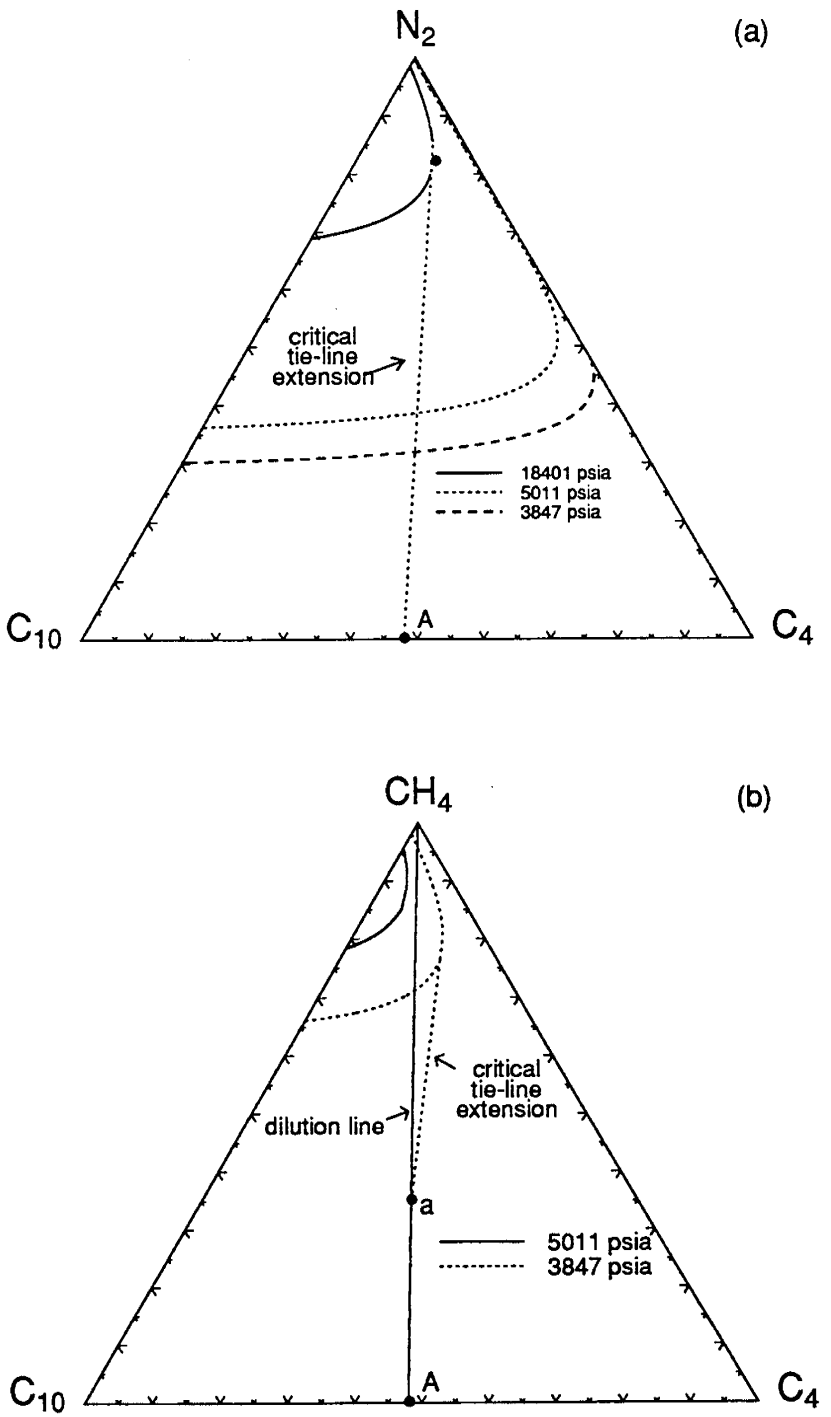

Figure 3.37: Effect of CH_4 on N_2 MMP for dead oil (48% C_4, 52% C_{10}), **A**.

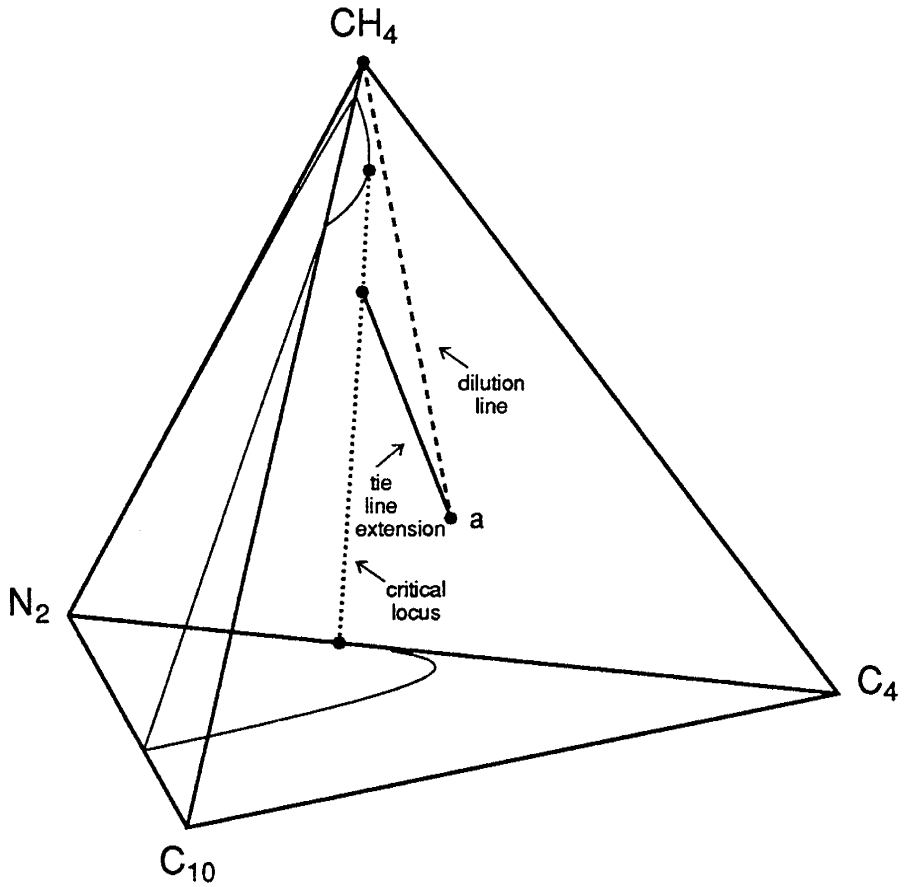

Figure 3.38: Determination of the critical tie line at 5011 psia and 160°F in the interior of quaternary diagram for the live oil (35% CH_4, 31.2% C_4, 33.8% C_{10}), **a**.

2. The crossover tie line may be connected to the initial and injection tie lines by spreading waves or self-sharpening waves. Sharpening behavior of the nontie-line paths can be predicted from the properties of an envelope curve associated with each nontie-line path.

3. If two tie lines are connected by a self-sharpening wave in the two-phase region, they must intersect, whether or not components change volume as they change phase.

4. Four-component solutions with volume change are constructed by linking three key tie lines: the initial, injection and crossover tie lines. The key tie lines are the same as those determined without volume change.

5. Miscibility develops if any of the key tie lines is a critical tie line.

3.5 Summary

This chapter represents a significant advance in the theory of multicontact miscible gas injection processes. The analytical solutions presented for four-component systems demonstrate conclusively that the standard ternary description of the development of miscibility is too simple to explain the mechanisms of gas injection processes that range from the CO_2 floods of West Texas to the miscible gas injection scheme used in a major Alaska reservoir to nitrogen floods of light-oil reservoirs. The analytical theory proves that condensing/vaporizing gas drives do exist, and it shows that CO_2 floods for oils that contain dissolved methane are actually condensing/vaporizing drives.

The value of the analytical solutions is particularly evident in the analysis of the development of miscibility. The theory shows that development of miscibility can be controlled by any of three tie lines in four-component systems. As in ternary systems, if either the initial or injection tie lines is a critical tie line, the displacement is multicontact miscible. In the four-component systems, a third key tie line, the crossover tie line, can also be a critical tie line. If so, it can also create multicontact miscibility. The CO_2 floods and enriched gas displacements in Sections 3.1 and 3.2 are examples of condensing/vaporizing drives in which the crossover tie line controls development of miscibility. The four-component theory also demonstrates why CO_2 flood minimum miscibility pressures are insensitive to the presence of dissolved methane in the oil, while N_2 floods are very sensitive. In addition, the theory proves that mixing cell methods produce incorrect estimates of minimum miscibility pressure when the crossover tie line controls miscibility.

Finally, extension of the theory to include the effects of volume change as components change phase shows that the three key tie lines do not change. That theory shows that the timing of recovery depends strongly on volume change but that the structure of the solutions does not. Thus, the foundations of the theory of development of miscibility do not change when the significant additional mathematical complexities that arise from volume change are included in the theory.

The key ideas of the analytical approach developed in this chapter also apply when more than four components are present. Examples of solutions with five and six components are reported by Dindoruk [27] and Johns [56]. Each additional component implies an additional crossover tie line, and hence it will be possible for some of the new crossover tie

lines to control development of miscibility. In practice, however, only the tie lines associated with light intermediate components will fill that role. Hence, the theory given here points the way to a general theory of the development of miscibility in truly multicomponent gas injection processes.

4. Modeling of Viscous Fingering

In most miscible floods, the viscosity of the injected gas will be substantially less than that of the oil being displaced. Hence, the displacement will be unstable, and viscous fingering will result. In such cases, displacement performance will depend on a complex interplay of viscous fingering, heterogeneity, crossflow, and phase behavior. Past work has focussed on the interaction of viscous fingering with permeability heterogeneity. A particle-tracking simulator developed originally by Araktingi [1, 2] and extended by Tchelepi [92] is applied in Section 4.1 to show that the simulation technique does a good job of capturing the transition from (1) flow dominated by viscous forces in homogeneous or randomly heterogeneous porous media to (2) flow dominated by the spatial distribution of permeability when there is significant correlation of high and low permeability.

In Section 4.2 we examine the interactions of dispersion, viscous fingering and permeability heterogeneity in laboratory core samples. There we use the particle-tracking technique to interpret measurements of apparent dispersion coefficients determined in displacements with favorable mobility ratios. In addition, we examine why displacements at similar unfavorable mobility ratios in sandstone and limestone cores were so different. Again we find that heterogeneity plays a dominant role. Thus, the results presented in this chapter demonstrate that the particle-tracking technique can be used with confidence to explore the scaling behavior of unstable displacements in heterogeneous porous media.

4.1 Experimental Investigation of Viscous Fingering in Heterogeneous Porous Media

David C. Brock

Given the complexity of miscible displacements at field scale, some sort of numerical simulation will be required for predictions of process performance. In this section we attempt to verify experimentally the physical representation of viscous instability used in the particle-tracking simulator developed by Araktingi [1]. Details of the formulation of the current version of the simulator are given in Section 4.2. If it can be shown that the simulator represents accurately the relevant physical mechanisms, then the simulator can be used to explore scaling issues. Because numerical simulations are the only technique available for predictions of the performance of large-scale flows, it is especially important that an experimental test of simulator accuracy be performed. This section describes such a test.

4.1.1 Experimental Apparatus and Procedures

To test the simulation representation of the combined effects of viscous instability and permeability heterogeneity, flow visualization experiments were performed in two-dimensional packs of glass beads. Properties of fluids used in displacement experiments are reported in Table 4.1. Dimensions of a typical flow model are shown in Fig. 4.1. The relatively thin bead pack (thickness 6.4 mm) is contained between glass plates. Inlet and outlet

Table 4.1: Densities and viscosities of the fluids used in the experiments.

Fluid	density, g/cm^3	viscosity, cp
Light Mineral Oil	0.836	23.0
Medium Mineral Oil	0.854	46.0
Fluid F	0.854	0.58
Fluid G	0.836	0.58

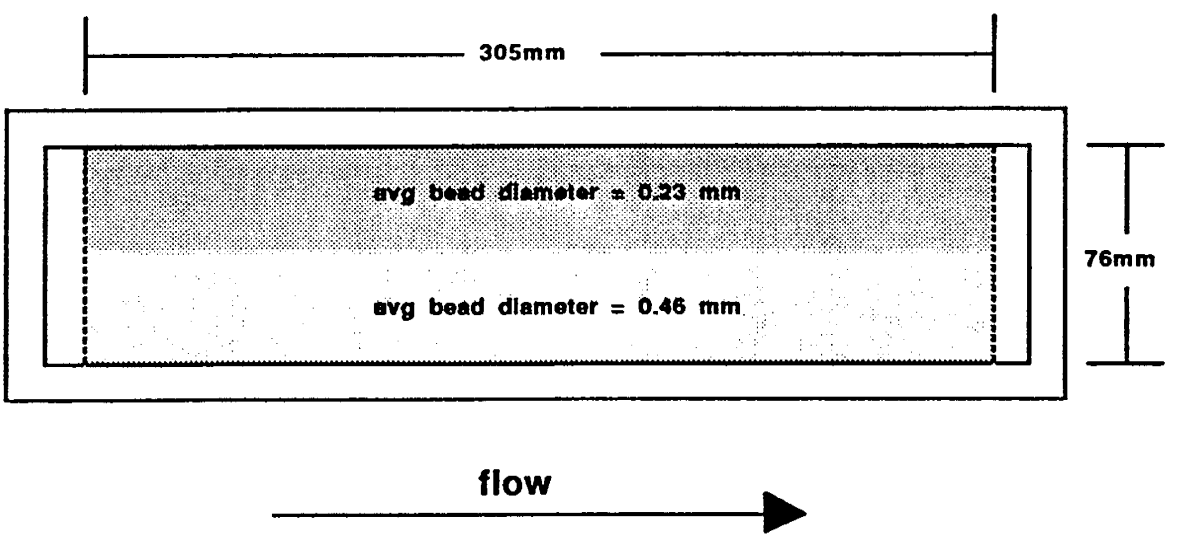

Figure 4.1: Dimensions of two-dimensional bead packs.

headers distribute fluid in such a way that the flow is nearly linear. In the model shown in Fig. 4.1, two layers with different permeabilities were created with beads of two diameters (0.23 and 0.46 mm). Permeability of a sphere pack can be estimated from the Blake-Kozeny equation as

$$k = \frac{d_p^2}{150} \frac{\phi_3}{1 - \phi^2} \tag{4.1}$$

According to Eq. (4.1), the permeabilities of the layers were 46 and 182 Darcies. In the displacements described below, the model was horizontal and fluids used had matched densities. Hence, gravity did not influence displacement performance.

A schematic of the flow system is shown in Fig. 4.2. In a typical displacement, oil containing a dye (Automate Red B) was injected into the model containing undyed oil, and the entire displacement was recorded on videotape. Video images were digitized to yield 512 x 480 arrays of integer intensities from 0 to 255. Intensities were calibrated pixel by pixel by performing displacements with mixtures of dyed and undyed fluid of known composition. Hence, video images could be converted to composition maps. From such maps, the location of the contour of 50% concentration of the injected fluid could be located as a function of displacement throughput.

Each flow model was packed (Brock [12]) using a combination of vibration and capillary and physical compaction in an attempt to create layers with uniform permeability. Displacements with fluids with matched viscosity and density indicated, however, that the presence of some local variations in permeability was unavoidable. Fig. 4.3 shows results of such a displacement for the model of Fig. 4.1, reported as the location of the displacement front at intervals of about 30 seconds. If the layers had been perfectly uniform, then piston-like fronts would have moved through each layer. While on average, fronts in the lower (high permeability) layer, moved about four times faster than those in the low permeability layer, the irregularity of the fronts shown in Fig. 4.3 indicates that the local flow velocity varied to some extent within each layer. Because the displaced and injected fluids were identical except for the presence of dye, the flow velocity variations must have been due to local permeability variations.

4.1.2 Estimation of Permeability

If measurements or estimates of the local pressure gradient are available, then successive contour positions of the type shown in Fig. 4.3 can be used to estimate local permeability. In the experiments described here, pressures were measured only at the inlet and outlet. Hence, only the average pressure gradient was known, though for the nearly linear flow, that estimate was certainly reasonable. Local flow velocities were determined from the contour data. The spacing between successive contours determines the minimum length scale on which permeability variations can be detected. To reduce the impact of noise in the concentration determination, the contours were smoothed by local averaging of the composition data. For each permeability block, the smoothed concentration was taken to be the average of the measured block concentration with the average of the eight surrounding block concentrations. Evenly spaced points were then selected along each contour, and vectors were drawn from each point along the direction of the pressure gradient. The local frontal

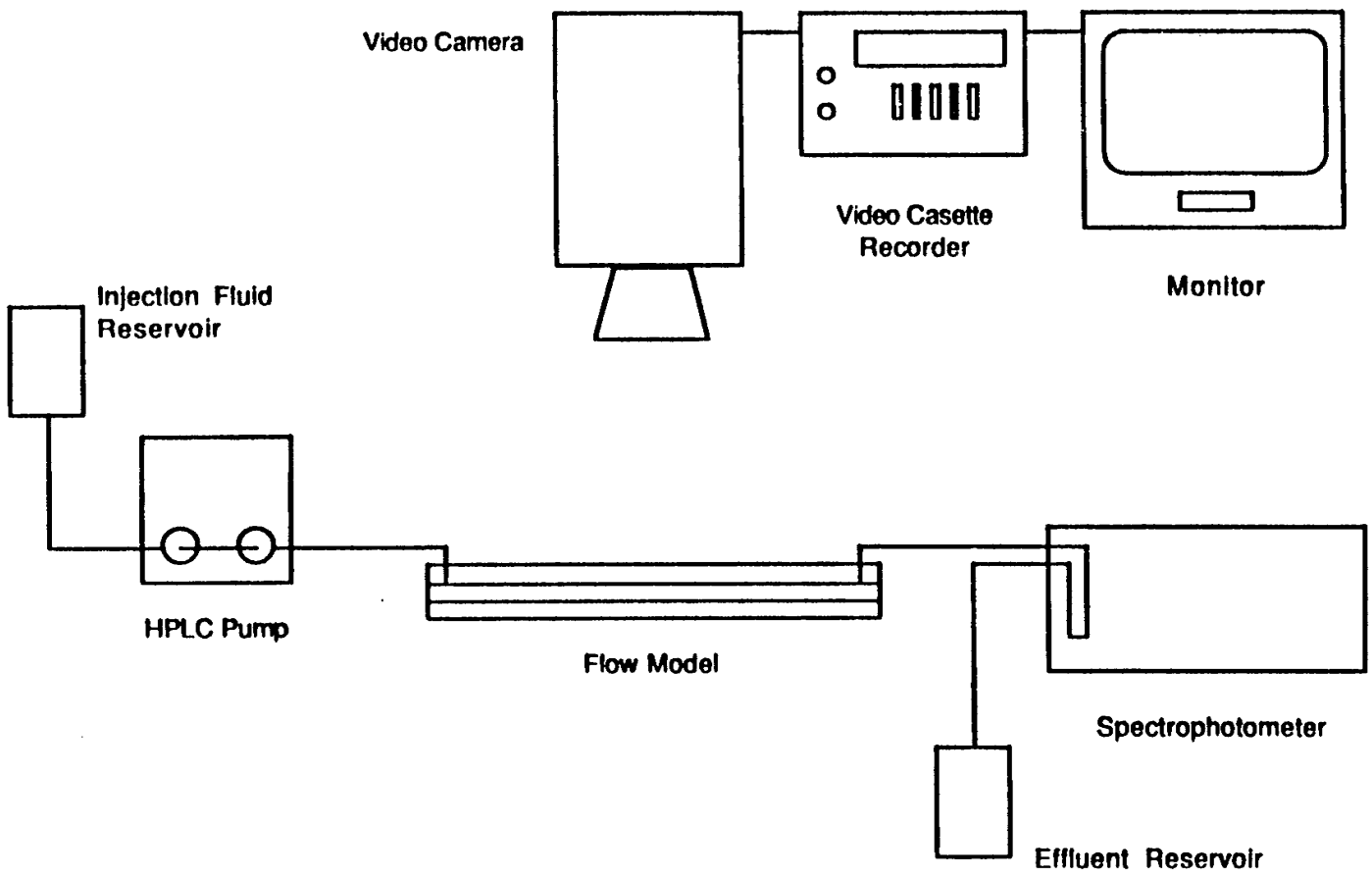

Figure 4.2: Schematic of equipment for flow visualization experiments.

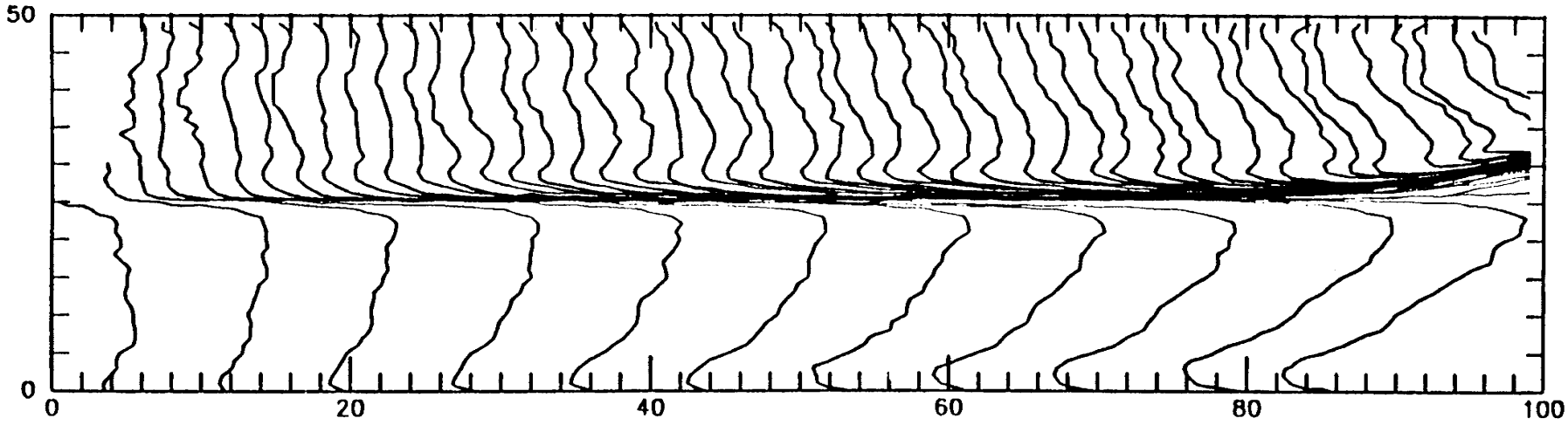

Figure 4.3: Measured front positions during displacement of undyed oil by dyed oil with the same viscosity and density.

velocity was measured from the length of the vector between successive contours and the time difference. The permeability at each vector position is then given by Darcy's law

$$\frac{k}{\phi} = \frac{v_f \mu}{\frac{\partial p}{\partial x}} \qquad (4.1-2)$$

The porosity was estimated by a material balance on the area between successive contours. For sphere packs, the porosity varies only slightly, so the corrections due to porosity variations were also small. Permeabilities estimated from the contour data in Fig. 4.3 are shown in Fig. 4.4. As expected from the Blake-Kozeny equation, the measured permeabilities in the fast layer were approximately four times those of the slow layer (note that the positions of the fast and slow layers in Fig. 4.3 have been reversed in Fig. 4.4). Apparently, there is a ridge of slightly higher permeability close to the boundary between the layers. Otherwise, the permeabilities show relatively small variations that are due, presumably, to local heterogeneities in the packing.

The technique described here allows the use of flow visualization data to improve estimates of local permeability obtained from the Blake-Kozeny equation, but it is not without limitations. For example, the layers used here were parallel to the flow direction, and hence, the difference in permeability was immediately obvious in the flow visualizations. If the layers had been arranged transverse to the direction of flow, the flow visualizations would have shown no distortion of the fronts. Either more detailed pressure data or, alternately, flow in the transverse direction would have been required to detect the permeability variations in such a case. If such data were available, then the technique demonstrated here could also be used to interpret flow visualizations obtained by X-ray tomography of core samples, for example.

4.1.3 Viscous Fingering in Heterogeneous Porous Media

Flow visualization experiments were performed in bead packs with four permeability distributions illustrated in Fig. 4.5. The first model was homogeneous; the others included heterogeneities created with sections of large and small beads. In each model, displacements were performed at three viscosity ratios (M = 1, M = 40, and M = 80) and at three different flow rates. Properties of fluids used are summarized in Table 4.1. Detailed descriptions of all the experimental results are given by Brock [12]. Here we illustrate typical results and compare them with simulations of the experiments.

Homogeneous Model

Results of an unstable displacement at an injection flow rate of $q = 6\,cm^3/min$ and a mobility ratio of M = 40 are shown in Fig. 4.6. Early in the displacement, at 0.05 PVI, fingers started to grow (Fig. a in Fig. 4.6). Because injection took place through a slotted baffle, the displacement started with 15 fingers. Already at 0.05 PVI, the 15 fingers were no longer in evidence. Instead, approximately seven fingers had formed. At 0.10 PVI (Fig. b in Fig. 4.6), fingers were still evolving, and one finger at the lower edge had moved ahead of the others, due to the higher permeability there. By 0.20 PVI (Fig. d in Fig. 4.7), only four main fingers remained. Although the total number of fingers was decreasing, fingers were continually being created as well as destroyed. As tips spread, they were seen to split into

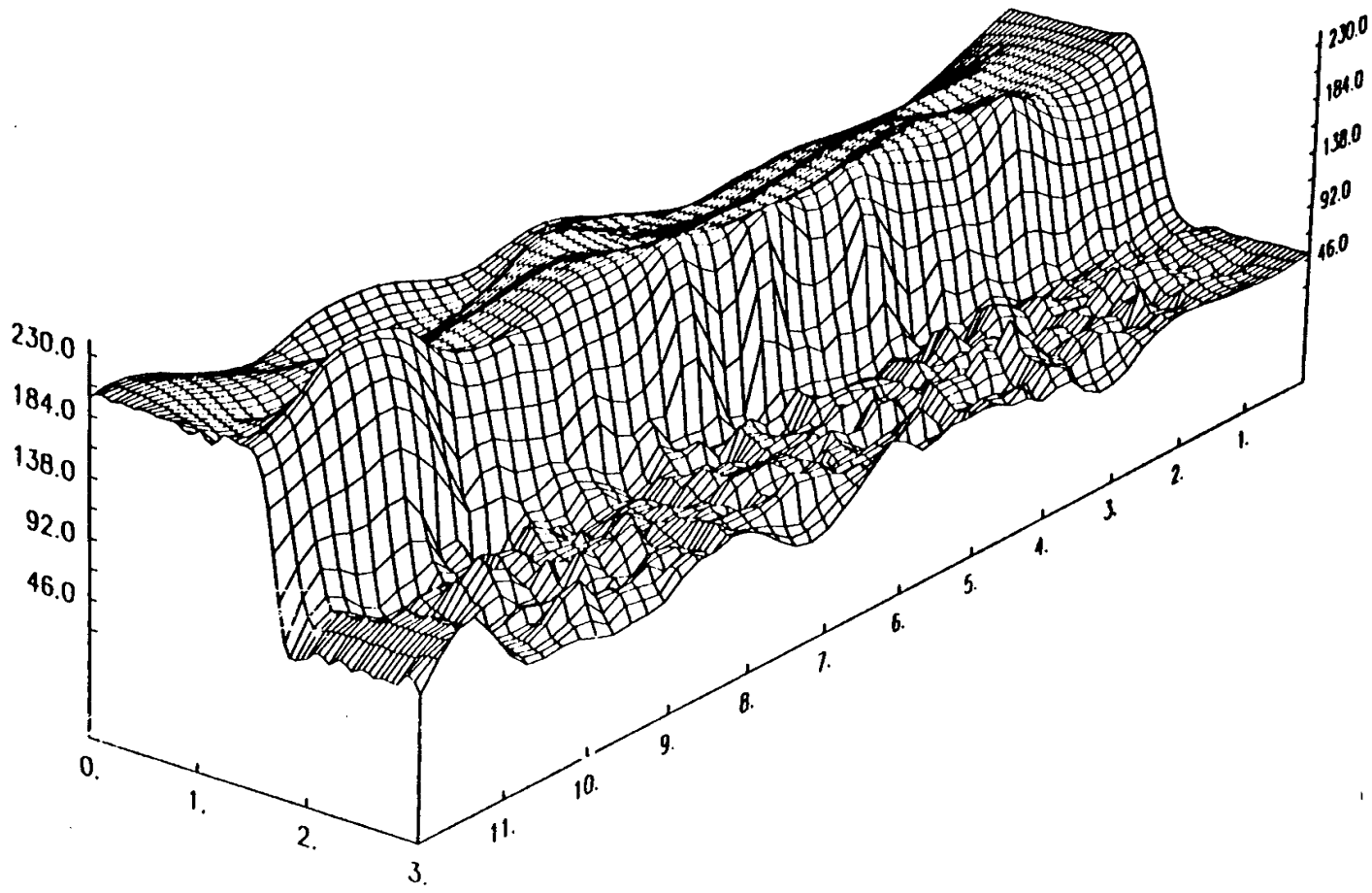

Figure 4.4: Permeability distribution estimated from the front position of Fig. 4.3 for the two-layer model of Fig. 4.1.

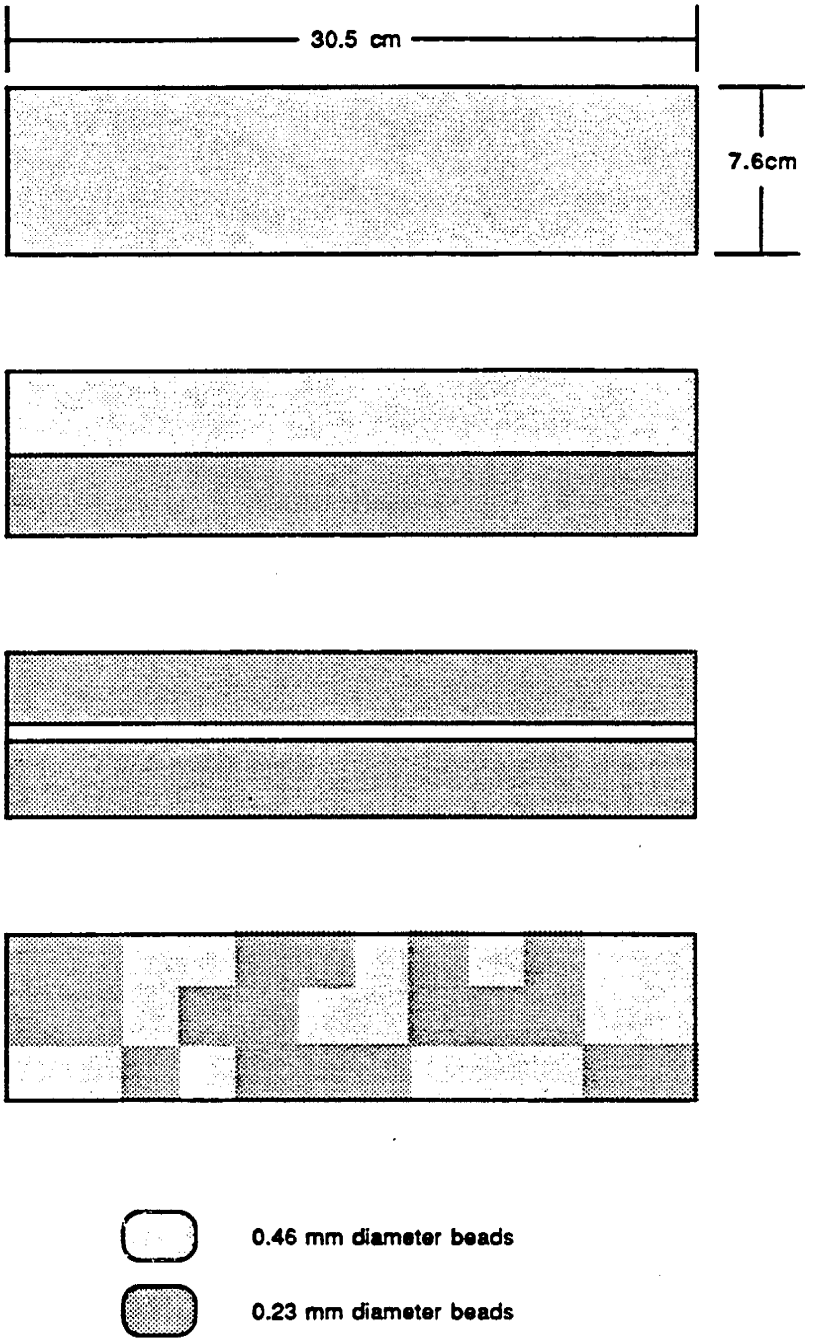

Figure 4.5: The four models used in experiments.

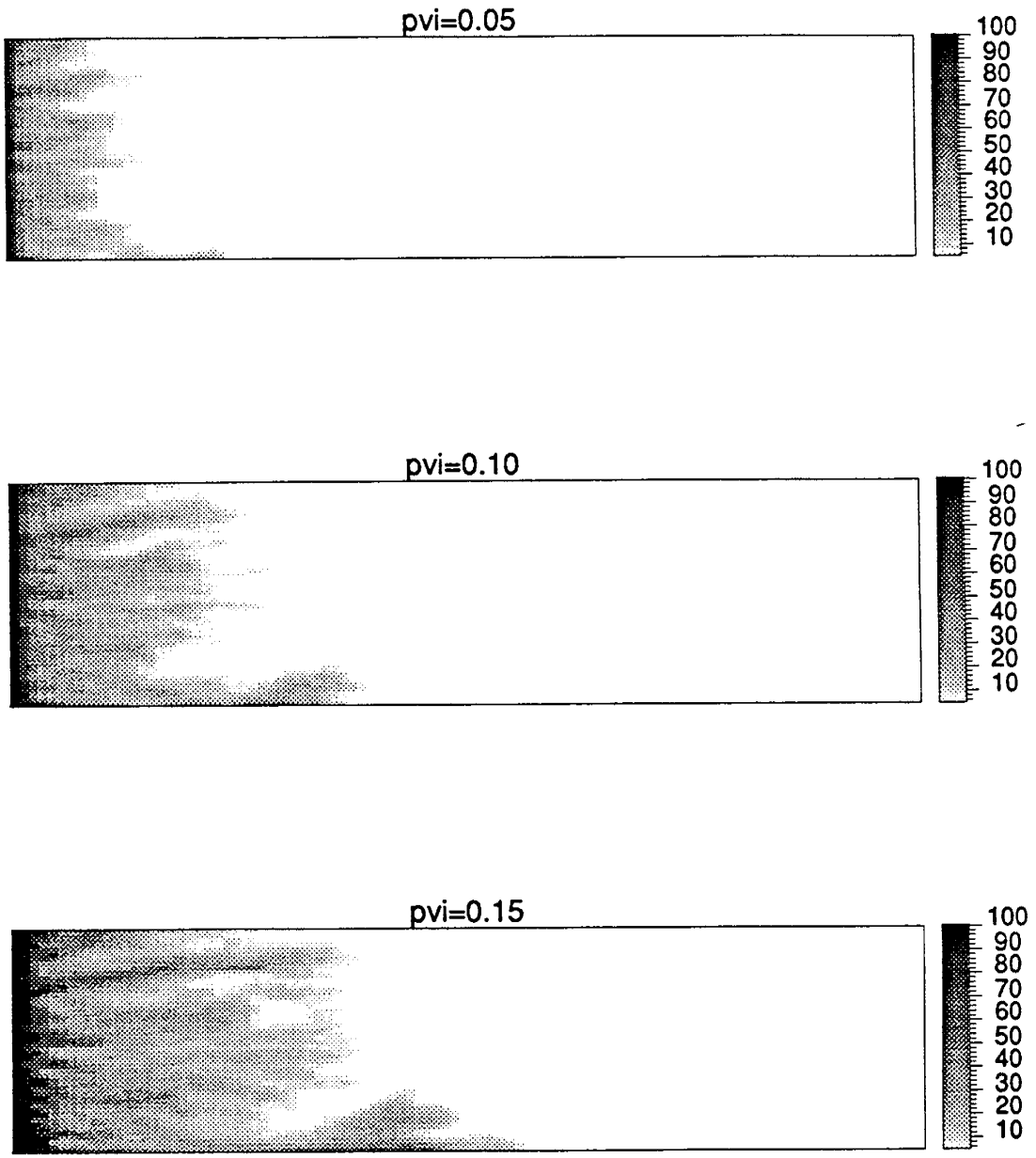

Figure 4.6: Injected fluid concentrations in an experimental displacement at M=40 and $q = 6\,cm^3/min$ in the homogeneous model (Panels a-c).

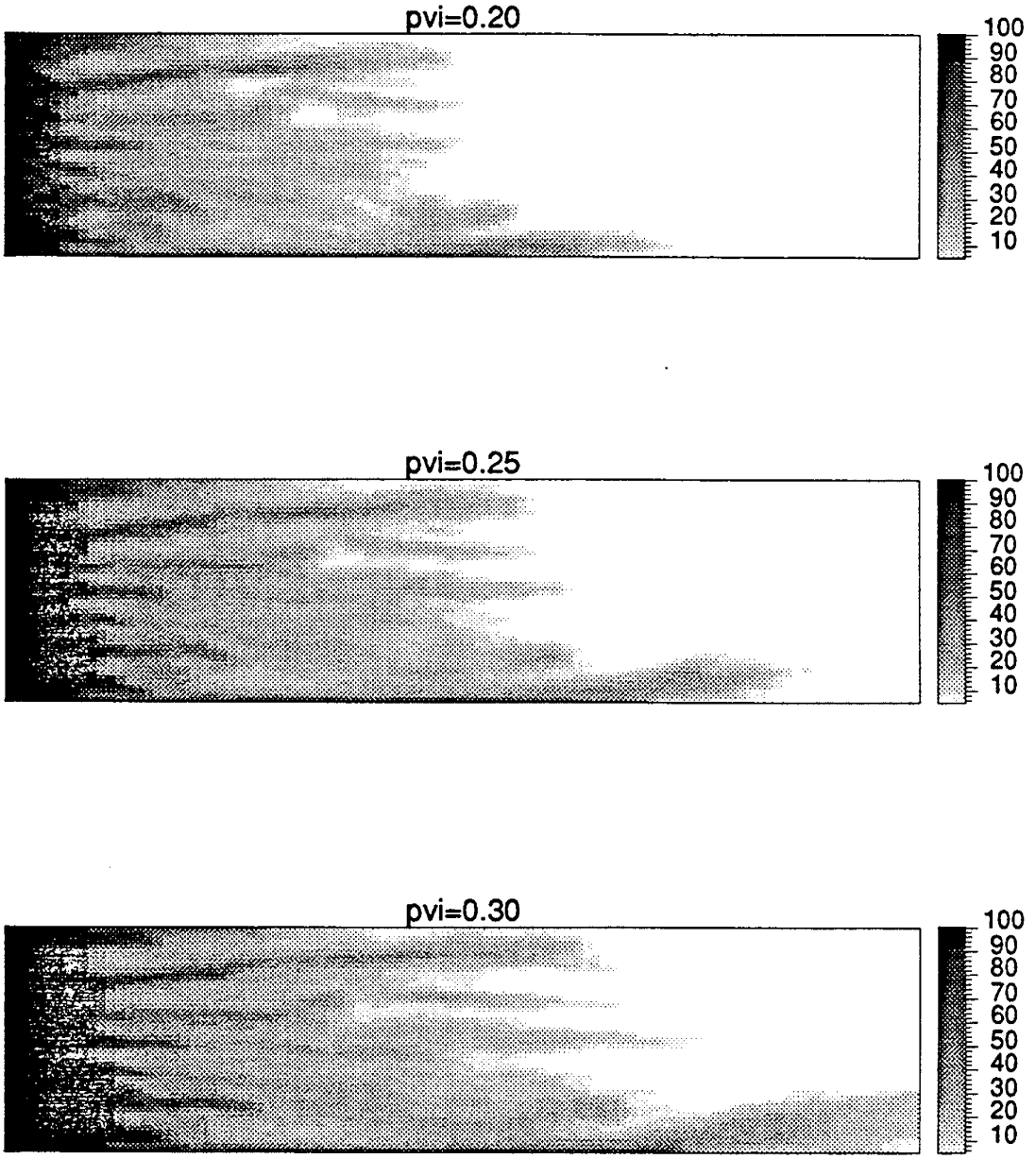

Figure 4.7: Injected fluid concentrations in an experimental displacement at M=40 and q = 6 cm^3 / min in the homogeneous model (Panels d-f).

smaller fingers (Fig. c in Fig. 4.6). Most of the fingers that were formed in this way, however, did not grow, but instead were shielded from growth by larger fingers. At 0.20 PVI (Fig. d in Fig. 4.7), coalescence of fingers left behind isolated unswept zones. By 0.30 PVI, four fingers persisted, with the longest growing in the higher permeability zone along the lower edge of the model.

Results of a simulation of the displacement are shown in Fig. 4.8. In that simulation, the dispersion and longitudinal dispersion coefficients were set from the correlations of Pozzi and Blackwell [110] as $D_t = 0.15 x 10^3\ cm^2/s$ and $D_l = 3.6 x 10^3\ cm^2/s$. The finger growth mechanisms identified in the experiment were also seen in the simulations. Of the many fingers that formed initially, only six remained at 0.115 PVI (Fig. c in Fig. 4.8). The fingers in the simulation clearly show spreading at the tips. By 0.25 PVI (Fig. e in Fig. 4.9), there were two main fingers, one in the middle and one along the lower edge, and at 0.30 PVI, most of the other fingers were coalescing into the wakes of the main fingers. In a perfectly homogeneous model, one would not expect simulated fingers to match the locations of experimental fingers, because finger locations are determined by random perturbations. Here, there was a slightly higher permeability detected along the lower edge. That higher permeability was responsible for the strong finger growth along the lower edge in experiment and simulation. At 0.20 PVI, the similarity of the appearance of the front in the experiment (Fig. f in Fig. 4.7) and simulation (Fig. f in Fig. 4.9) is striking. Both had a dominant finger along the lower edge, with three or four slower fingers.

Penetration rates—the rates at which the tips of fingers advanced—did not show such good agreement. Fig. 4.10 shows a comparison between the experiment and simulation of the base case at 0.30 PVI. In the experimental fingers, a low concentration had penetrated farther than in the simulation. In the experiment, however, much of the finger showed low concentrations of injected fluid. Comparison of the cross-sectional averaged compositions (Fig. 4.11) indicates that the largest discrepancy is indeed in the low (<15%) concentrations, while the rest of the concentrations match much better. Comparison of the 20% contours (Fig. 4.12), for example, gives satisfactory agreement. Fig. 4.13 is a comparison of effluent composition in experiment and simulation. The experiment had breakthrough at 0.28 PVI, and effluent composition rose steadily thereafter. The simulation did not break through until 0.38 PVI. However, its effluent curve rose rapidly until it reached the experimental curve at 0.50 PVI, at an effluent composition of approximately 25%. Thereafter, the curves agreed well. Thus, agreement between the experiments and simulations was poor only at low concentrations. While the difference could imply a shortcoming in the method with which the simulator handles low concentrations, it is more likely that the difference arose from limitations of the experiment. It is probable that in the porous model, a higher permeability existed along the faces where glass beads met flat glass plate. Such a high permeability zone could cause an apparent low concentration to move quickly, while the rest of the solvent in the bulk of the pack moved more slowly at predictable rates determined by the porous media.

Two-Layer Model

Fig. 4.14 shows results of the unstable displacement at M = 40 and q = 6 cm^3/min in the two-layer model. As early as 0.05 PVI (Fig. a in Fig. 4.14), two fingers had already formed from the many fingers initially present. By 0.1 PVI (Fig. b of Fig. 4.14), the finger near the interface dominated flow in the fast layer. Spreading and splitting was evident,

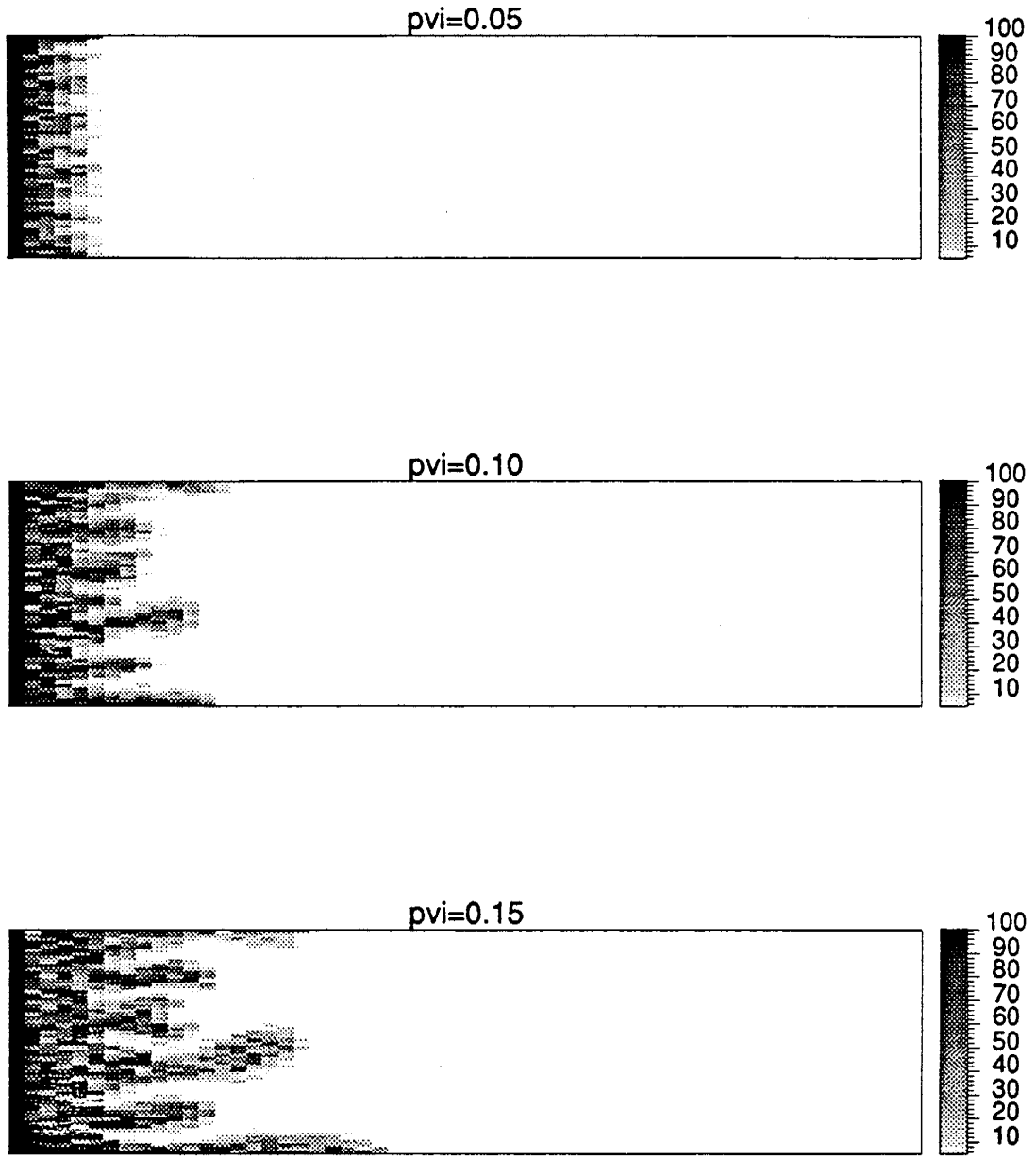

Figure 4.8: Simulated concentration distributions for a displacement at M=40 in the homogeneous model (Panels a-c).

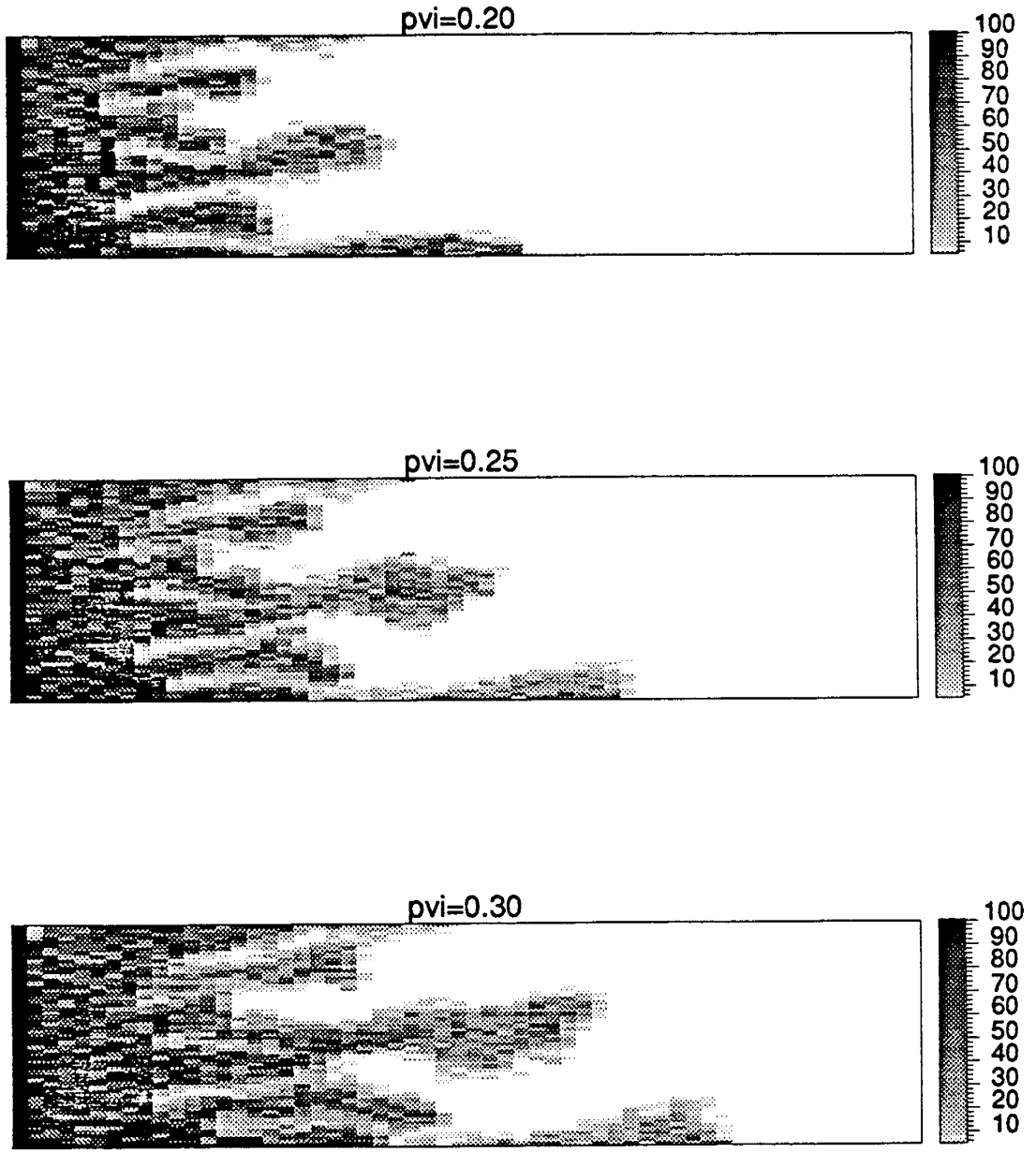

Figure 4.9: Simulated concentration distributions for a displacement at M=40 in the homogeneous model (Panels d-f).

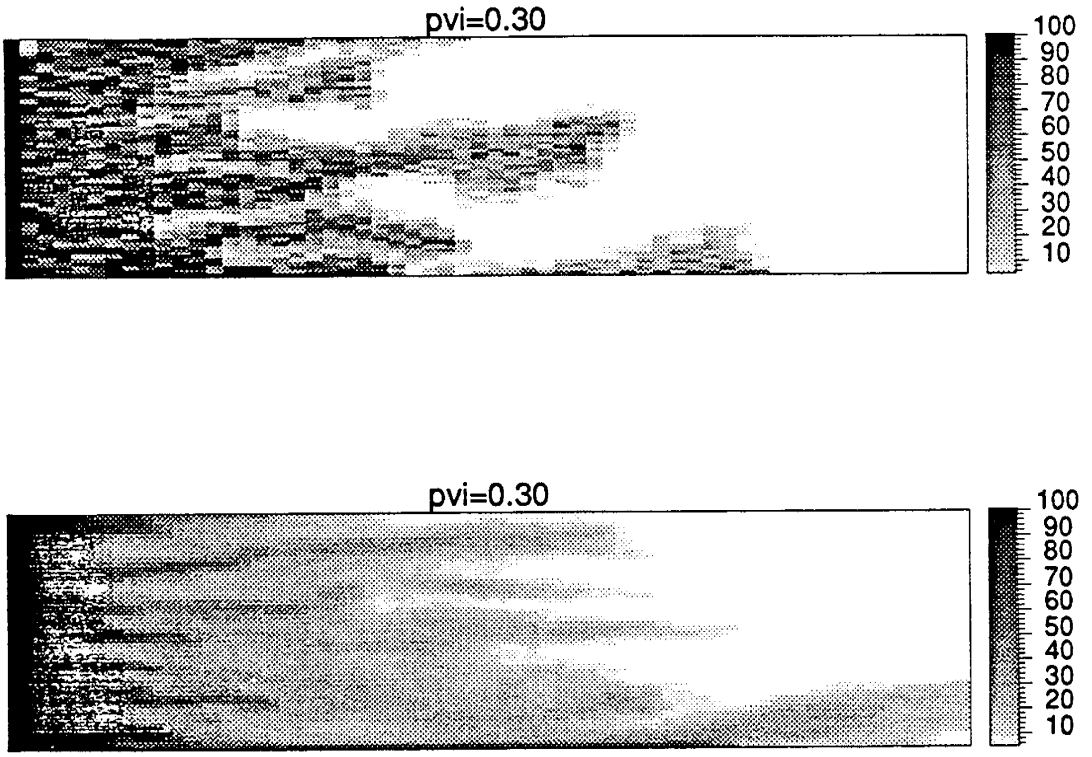

Figure 4.10: Comparison of the appearance of fingers in the simulation (a) and experiment (b) for a displacement at M=40 and q $= 6\,\mathrm{cm}^3/\mathrm{min}$ in the homogeneous model.

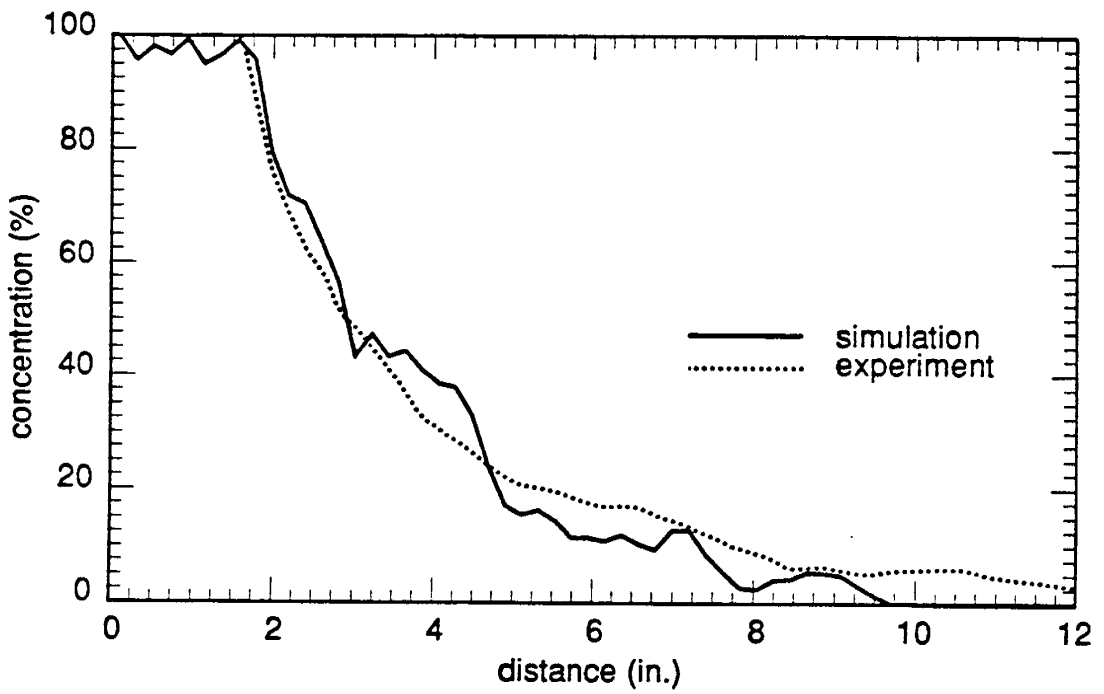

Figure 4.11: Comparison of cross-sectional averaged compositions in experiment and simulation of a displacement at M=40 and q $= 6\,\mathrm{cm}^3/\mathrm{min}$ in the homogeneous model.

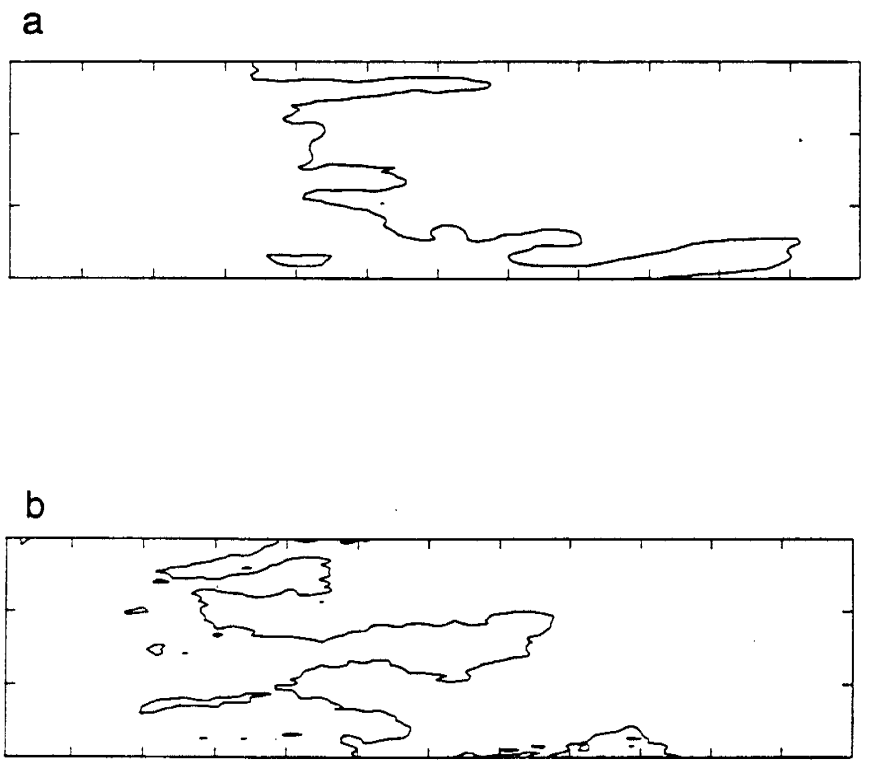

Figure 4.12: Comparison of the 0-2 concentration contour in experiment (a) and simulation (b) at M=40 and q = 6 cm^3 / min in the homogeneous model.

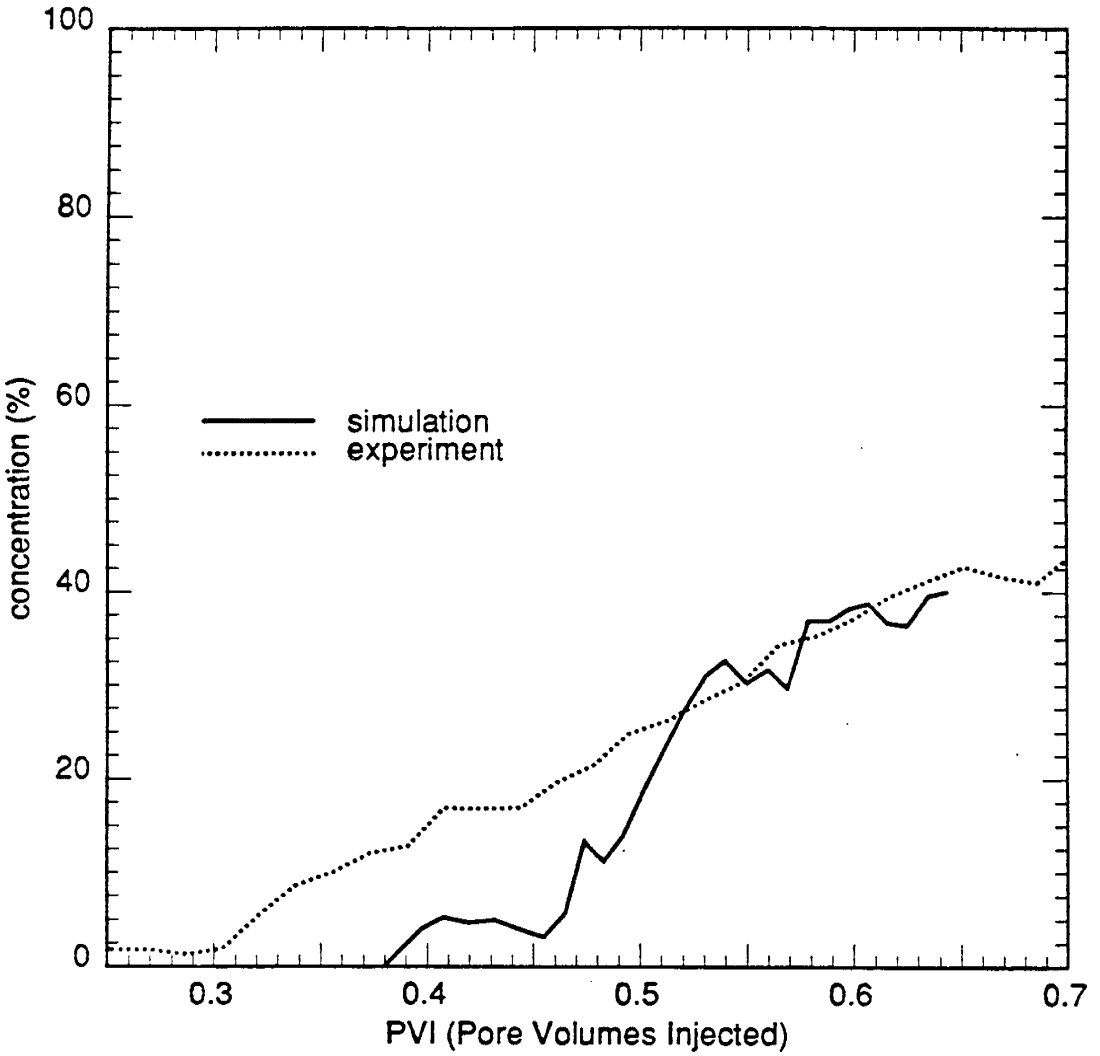

Figure 4.13: Comparison of the effluent composition curves in experiment and simulation at M=40 and q = $6\,cm^3/min$ in the homogeneous model.

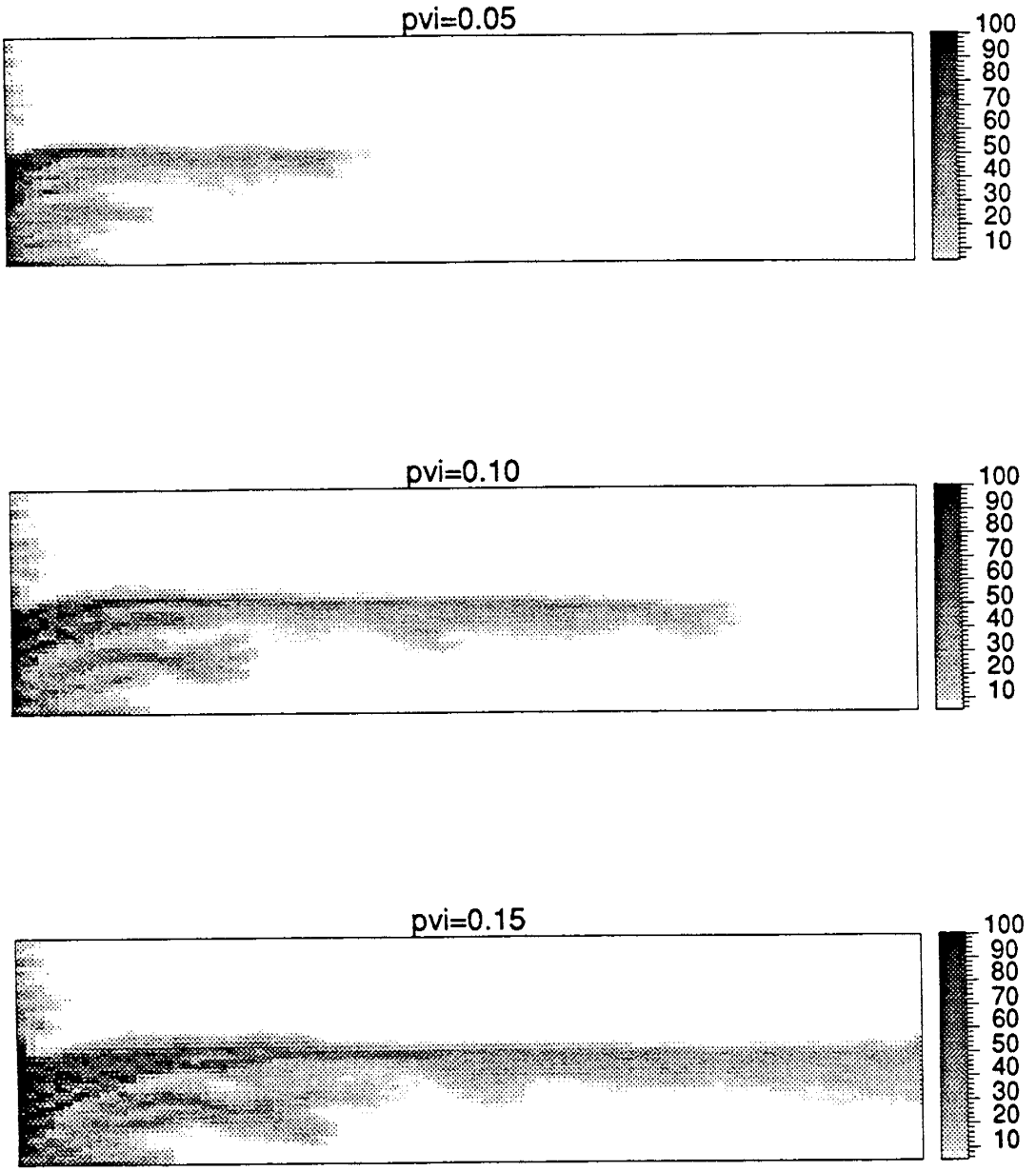

Figure 4.14: Injected fluid concentration in an experimental displacement at M=40 and $q = 6\,cm^3/min$ in the two-layer model (Panels a-c).

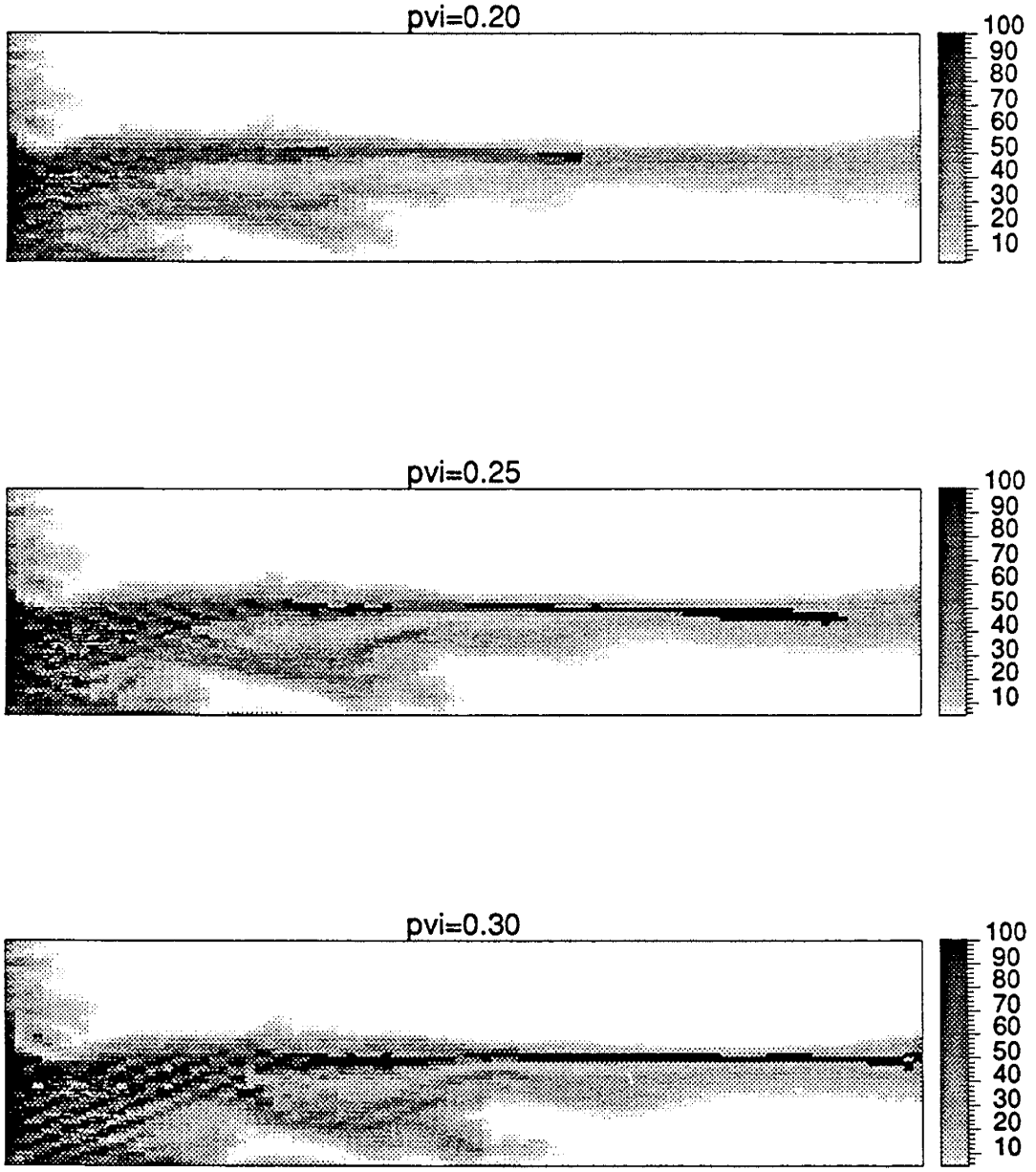

Figure 4.15: Injected fluid concentration in an experimental displacement at M=40 and q = 6 cm^3 / min in the two-layer model (Panels d-f).

especially in the slower finger. The slow layer was nearly stagnant, due to the high mobility fluid filling the high permeability layer. Later, at 0.15 PVI (Fig. c of Fig. 4.14), the smaller finger began to coalesce into the wake of the long finger. Much later, at 0.3 PVI, injected fluid contacted most of the fast layer, and growth in the slow layer was virtually stopped. The simulation of that displacement is shown in Fig. 4.15, 4.16. As in the experiment, flow occurred mainly in the fast layer with a single main finger established at 0.05 PVI (Fig. a in Fig. 4.15), with two small fingers also growing. By 0.15 PVI (Fig. c in Fig. 4.15), the main finger grew along the layer interface, with a single smaller finger growing below. The smaller finger coalesced into the main finger at 0.20 PVI (Fig. d in Fig. 4.16). Also as in the experiments, hardly any flow occurred in the slow layer. The correspondence of finger positions in the experiment and simulation is striking, with the main finger near the layer interface and the secondary finger coalescing below, and almost no penetration into the slow layer.

High Permeability Streak Model

Displacements were performed in a model with uniform permeability except for a thin higher permeability streak from inlet to outlet (streak model). The same bead sizes were used as in the two-layer model. Thus, the streak had approximately four times higher permeability than the rest of the model. While the permeability contrast and direction of layering are the same as in the previous model, the high permeability streak is thin, with width approximately 0.1 of the total width. Fig. 4.17, 4.18 shows results of a displacement at M = 40. Very quickly, at 0.025 PVI, flow began in the streak (Fig. a in Fig. 4.17) as two fingers grew along the layer interfaces, presumably due to crossflow. Not much later in the experiment (0.05 PVI, Fig. b in Fig. 4.17), more of the streak was flooded with the higher mobility fluid, and a single "finger" had spread and coalesced to occupy the entire streak. At 0.10 PVI (Fig. d in Fig. 4.18), injected fluid broke through. Note also that crossflow had carried small amounts of injected fluid into the surrounding slow zone. Much later, at 0.50 PVI (Fig. f in Fig. 4.18) displacement in the slow zones continued to be pulled slowly toward the high-permeability streak by crossflow.

Simulation results are shown in Fig. 4.19, 4.20 for this model. As in previous cases, the permeability field estimated from the matched mobility displacement was used for the simulations. The simulation shown in Fig. 4.19, 4.20 is nearly identical to the experiment. The main finger progressed quickly down the high permeability streak, while little flow occurred in the slow layer. Penetration rates in the simulation (Figs. b and c in Fig. 4.19 were closer to those of the experiments, but the finger was still not as diffuse as the experimental finger. The simulator showed the same small amount of invasion into the slow layers.

Random Checkerboard Model

The previous heterogeneous models had layers extending completely from inlet to outlet, so that permeabilities in the flow direction were highly correlated at a scale of the total model length. To examine the effects of permeability heterogeneities that have shorter correlation lengths, a model consisting of blocks of different-sized beads (checkered model) was built.

First, a permeability field was created. The smallest feasible block sizes were 1-inch squares, leading to 36 blocks, 12 in the flow direction, but 3 in the transverse direction. A

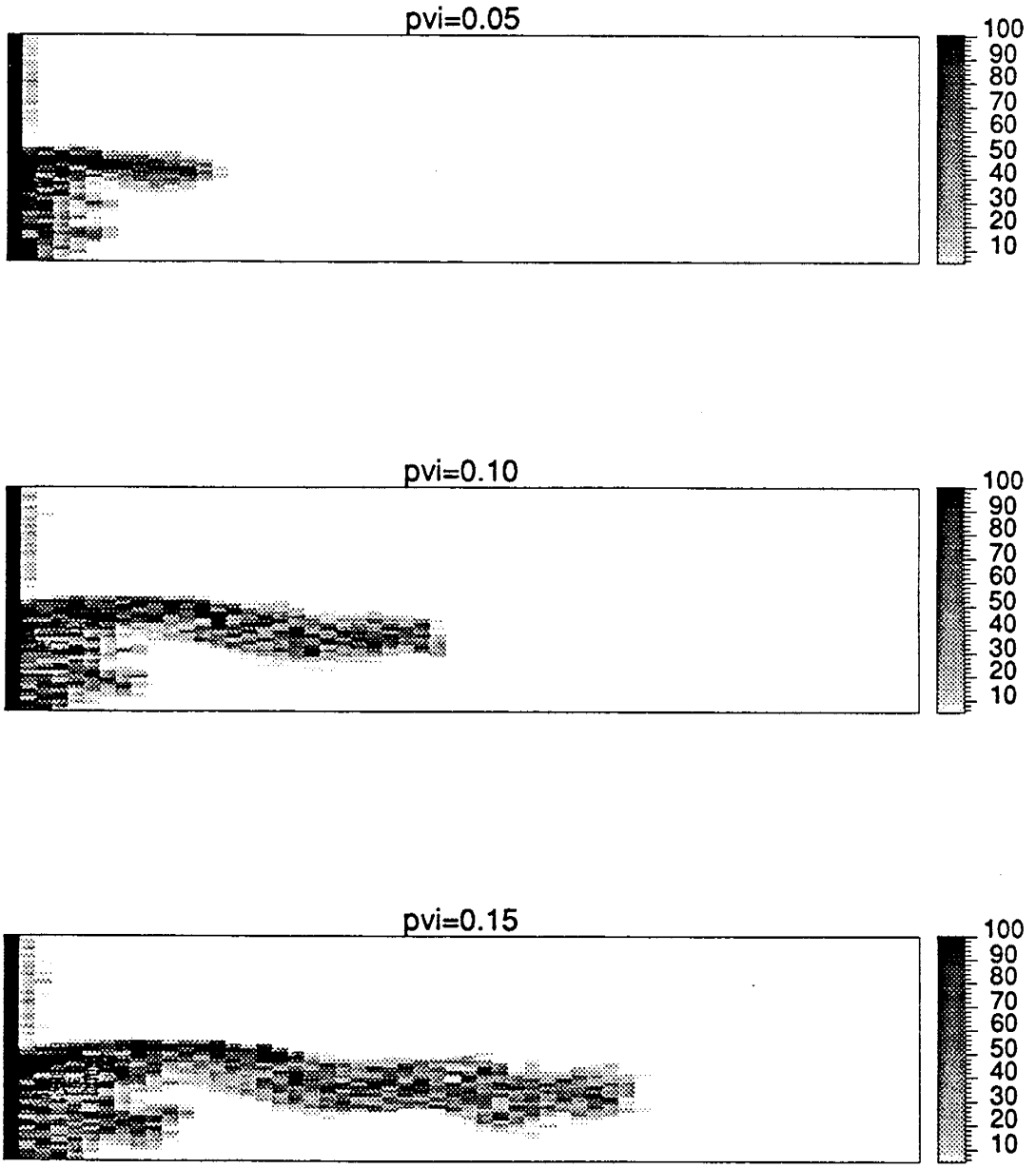

Figure 4.16: Simulated concentration distributions for displacement at M=40 in the two-layer model (Panels a-c).

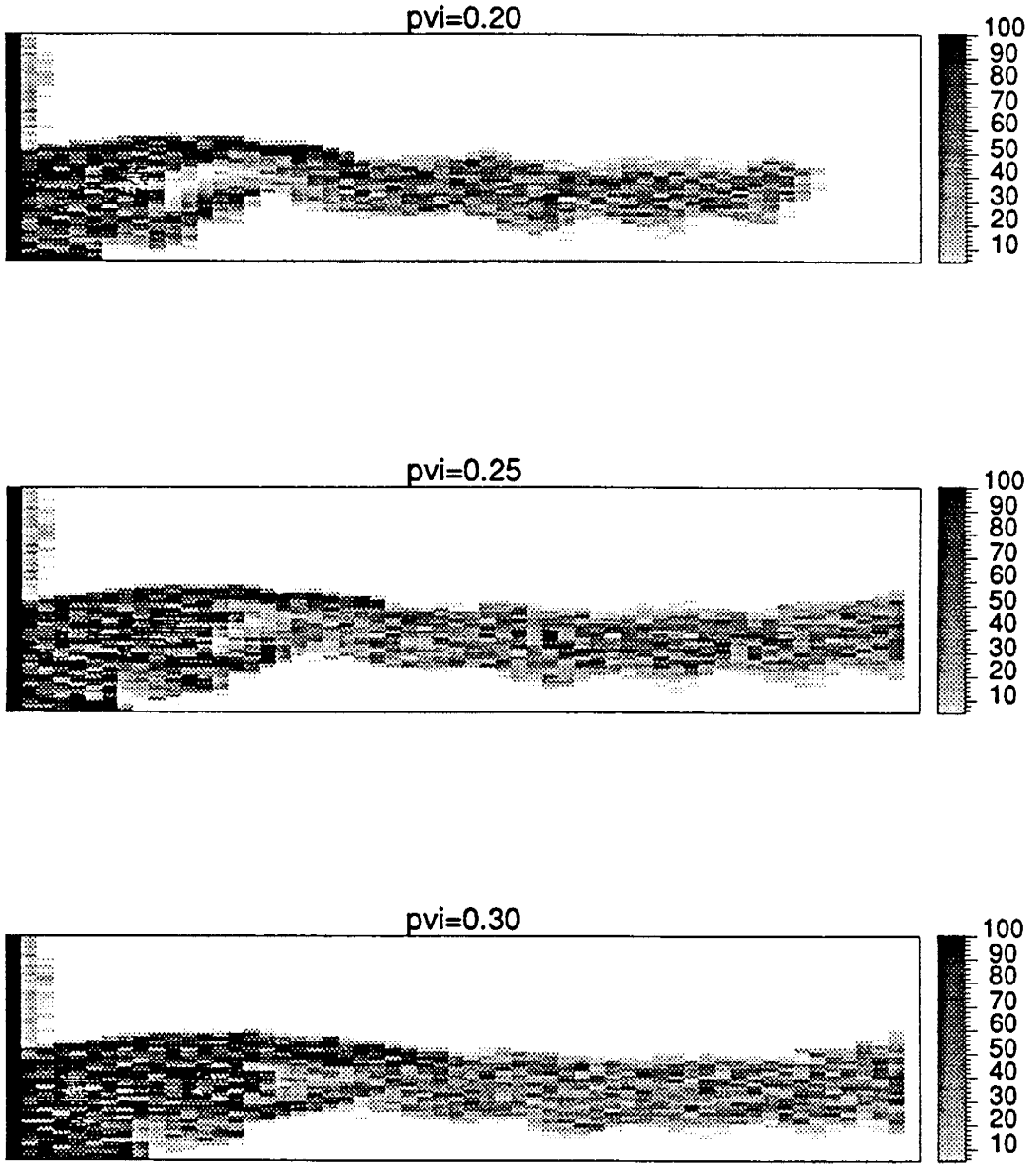

Figure 4.17: Simulated concentration distributions for displacement at M=40 in the two-layer model (Panels d-f).

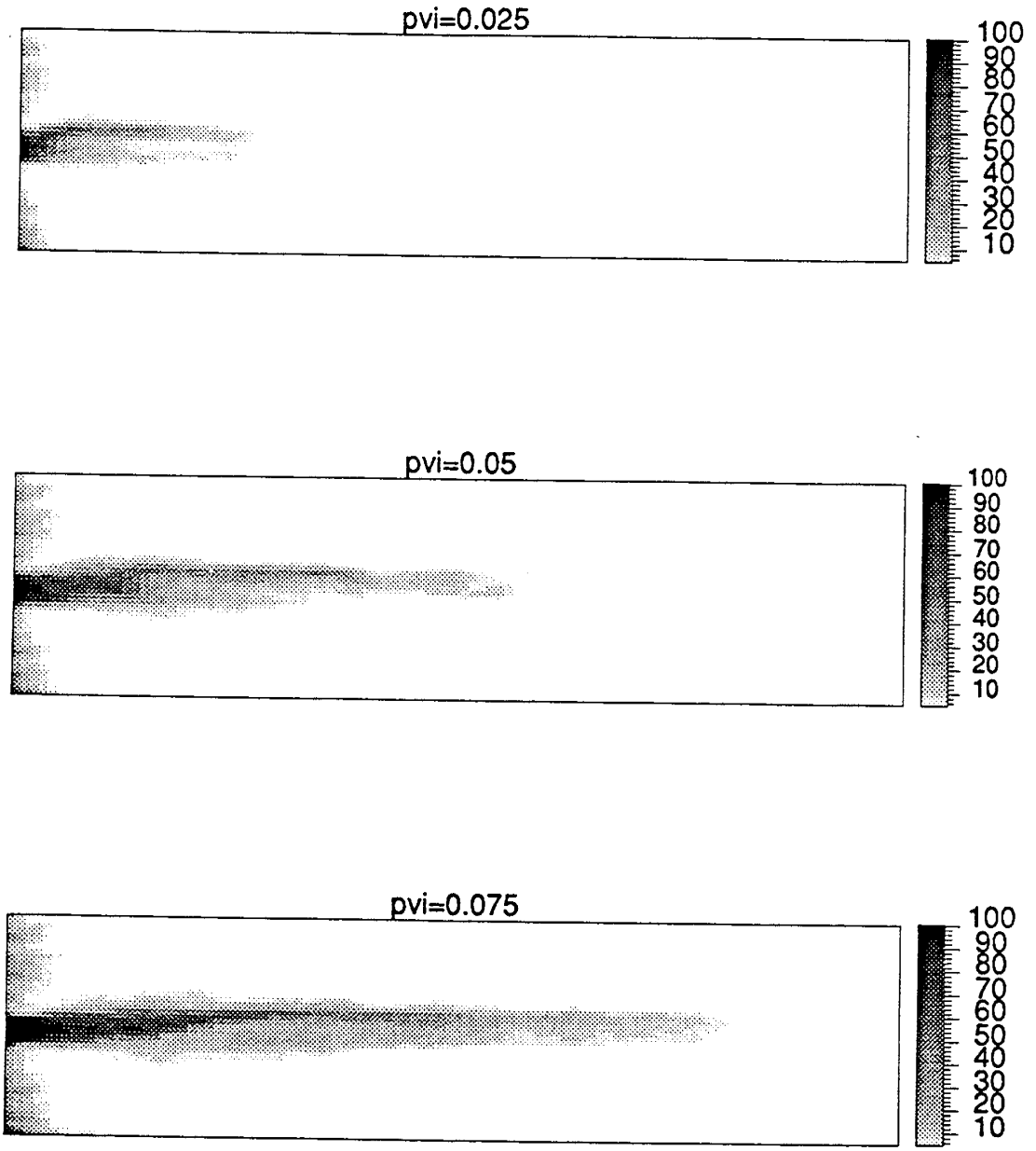

Figure 4.18: Injected fluid concentration in an experimental displacement at M=40 and $q = 6\,cm^3/min$ in the streak model (Panels a-c).

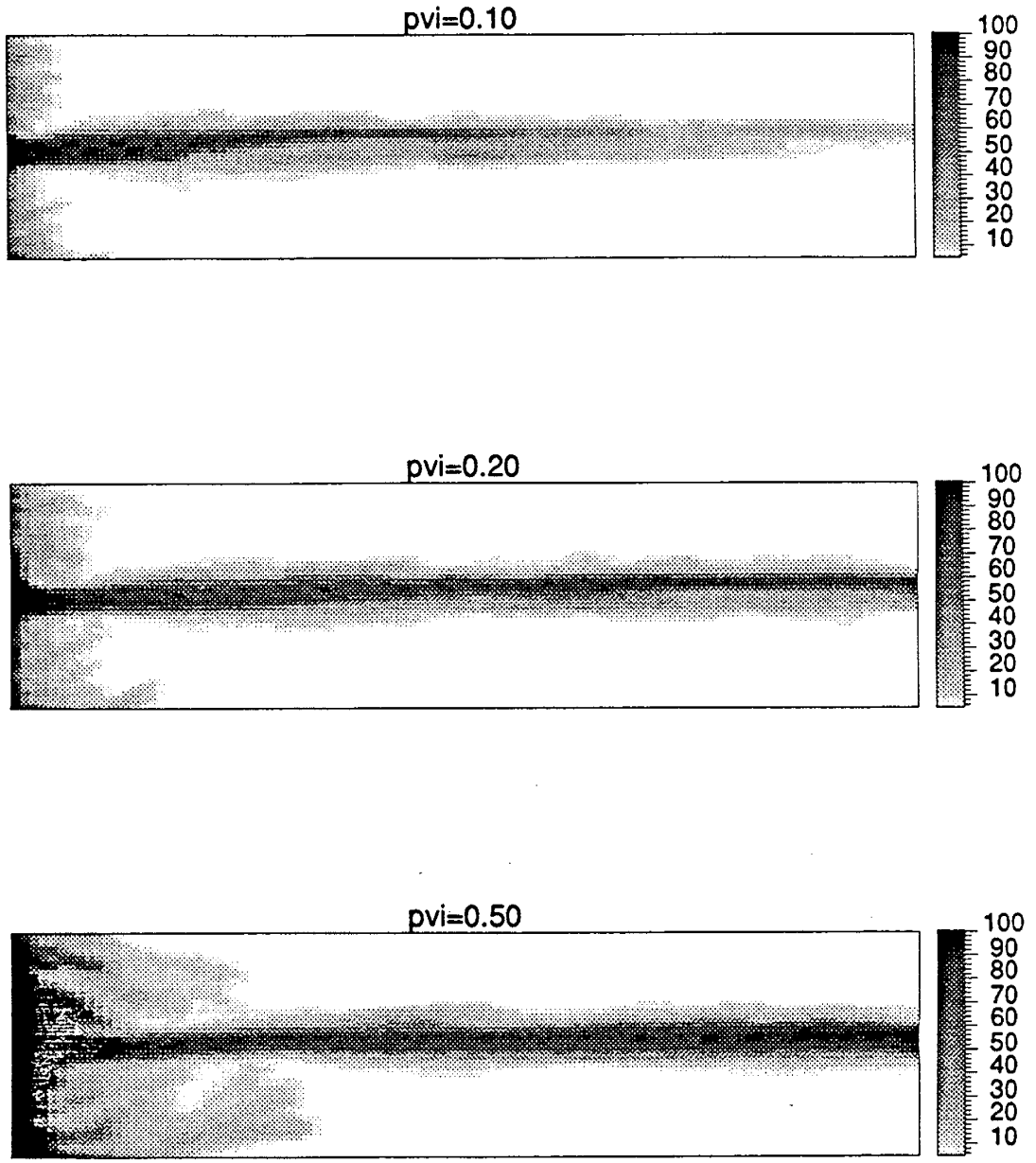

Figure 4.19: Injected fluid concentration in an experimental displacement at M=40 and q = 6 cm^3 / min in the streak model (Panels d-f).

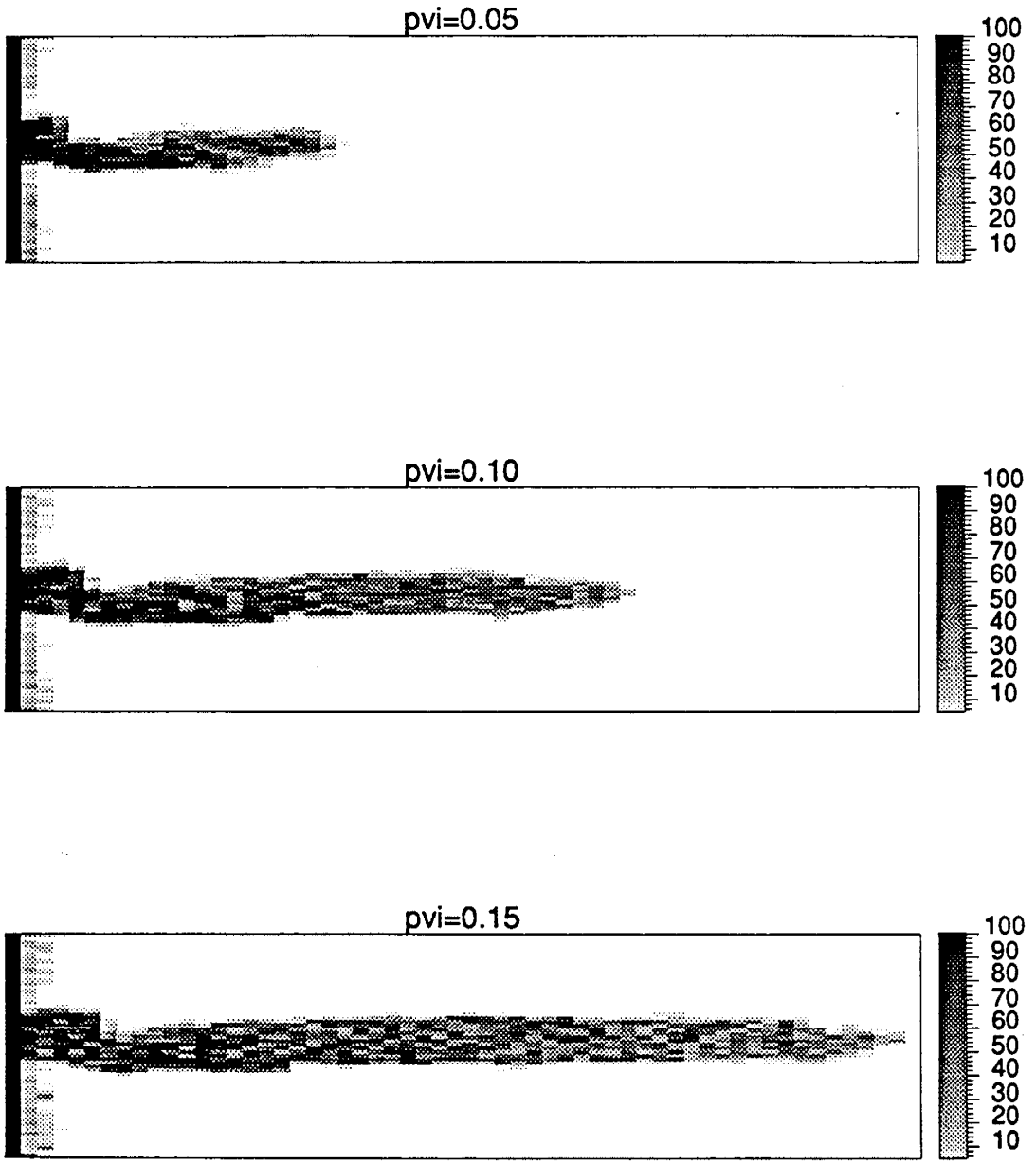

Figure 4.20: Simulated concentration distributions for displacement at M=40 in the streak model (Panels a-c).

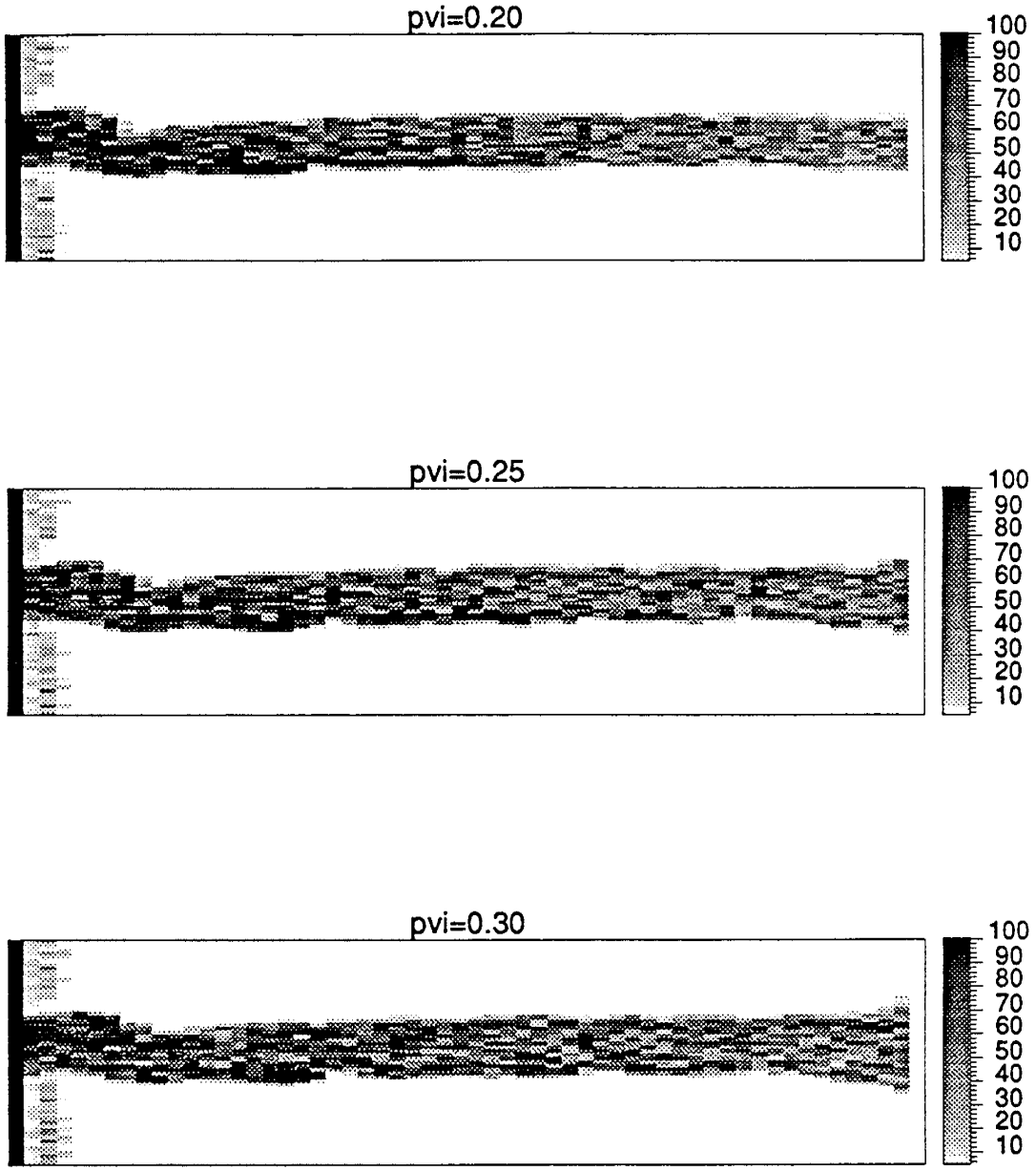

Figure 4.21: Simulated concentration distributions for displacement at M=40 in the streak model (Panels d-f).

permeability field was created by generating a 12-by-3 pattern using the software of Mishra [81]. The program generates a log-normally distributed permeability field, then imposes spatial correlation using the moving circle averaging technique. For use in this system of only two bead sizes, blocks with permeability values higher than the mean were assigned high permeability, and those under the mean were assigned low permeability. The resulting ideal permeability field is shown in Fig. 4.5, where the light blocks represent high permeability and the dark blocks represent low permeability.

A matched mobility displacement was run in the model. The gray-scale visualization of the displacement is shown in Fig. 4.22, 4.23. At 0.05 PVI (Fig. a in Fig. 4.22), fast and slow stable fronts had begun in the first blocks. As flow continued, the front curved to follow the high permeability path, first upward at 0.10 PVI (Fig. b in Fig. 4.22) and back downward at 0.15 PVI (Fig. c in Fig. 4.22). Recall that the model was horizontal during the flow experiments, so "upward" and "downward" refer to the composition maps drawn, not the models themselves. At 0.20 PVI (Fig. d in Fig. 4.23), the finger encountered the end of closely connected high permeabilities and began to move across the low permeability gap to meet the closest high permeability zone ahead of it. Note that a stable front continued to grow in the slow entry zone. This frontal profile is an example of a permeability induced instability. The fluids were of matched mobility, using the same fluid except for dye, so there was no tendency for viscous fingering. However, the heterogeneities caused a front which appeared fingered. After crossing the low permeability zone, the fastest finger followed the high permeability path (0.40 PVI, Fig. e in Fig. 4.23; 0.60 PVI, Fig. f in Fig. 4.23). Also at 0.60 PVI, other slow flow that started in the slow entry zone extended into a secondary finger. In contrast to the unstable displacements, the secondary finger did not coalesce because there was no mobility difference to cause viscous crossflow.

Results of the displacement with $M = 40$ and $q = 6\,cm^3/min$ are reported in Fig. 4.24, 4.25. Initially, the flow was similar to the matched mobility case. It took only until 0.03 PVI (Fig. c in Fig. 4.24), however, for the fast flow to move through the two high permeability entry blocks. Because of the small flow width, no distinct fingers formed. At 0.04 PVI, (Fig. d in Fig. 4.25), the fast finger made the upward turn as did the finger in the stable case. Instead of simply turning back down to the closest high permeability block, as did the finger in the stable case, the tip split, with one finger following the lower path and one following the upper (Figs. e and f in Fig. 4.25). As flow continued, some viscous fingers developed through tip splitting (Fig. g in Fig. 4.26), but the dominant fingers clearly followed the same high permeability paths as did the flow in the stable case. Thus, in this case as well, the location and pattern of fingering was strongly influenced by the permeability distribution, though viscous instabilities also added an overlay of fingers on the flow pattern seen for $M = 1$.

Fig. 4.27, 4.28 shows results of the numerical simulation of the flow in the random checkerboard model. In the simulation, the displacement front moved quickly in the fast inlet blocks (Fig. a in Fig. 4.27). At 0.10 PVI (Fig. b in Fig. 4.27), the finger followed the same path as the dominant finger in the experiments, but without the tip split seen there. As flow progressed, at 0.15 PVI (Fig. c in Fig. 4.27) the main finger continued to follow the high permeability path, and some splitting was seen. By 0.25 PVI (Fig. e in Fig. 4.28), despite the fact that the early tip split did not occur, the fingers look very similar to those in the experiment (Fig. h in Fig. 4.26). Again, the experiment had diffuse fingers, while the simulator gave fingers with higher solvent concentrations. Thus, in this case as well, the

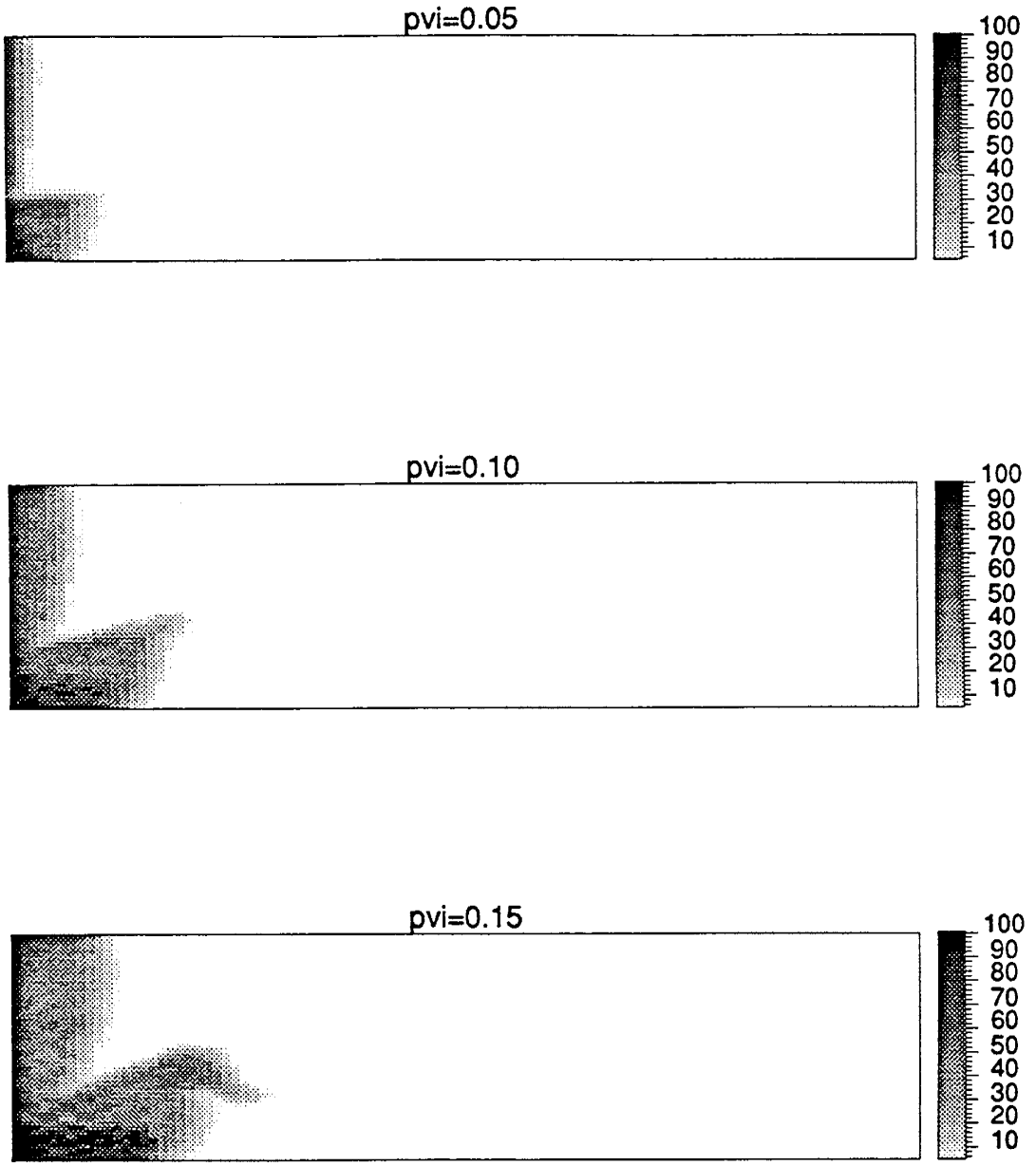

Figure 4.22: Injected fluid concentration in an experimental displacement at M=1 and q = 6 cm^3 / min in the checkered model (Panels a-c).

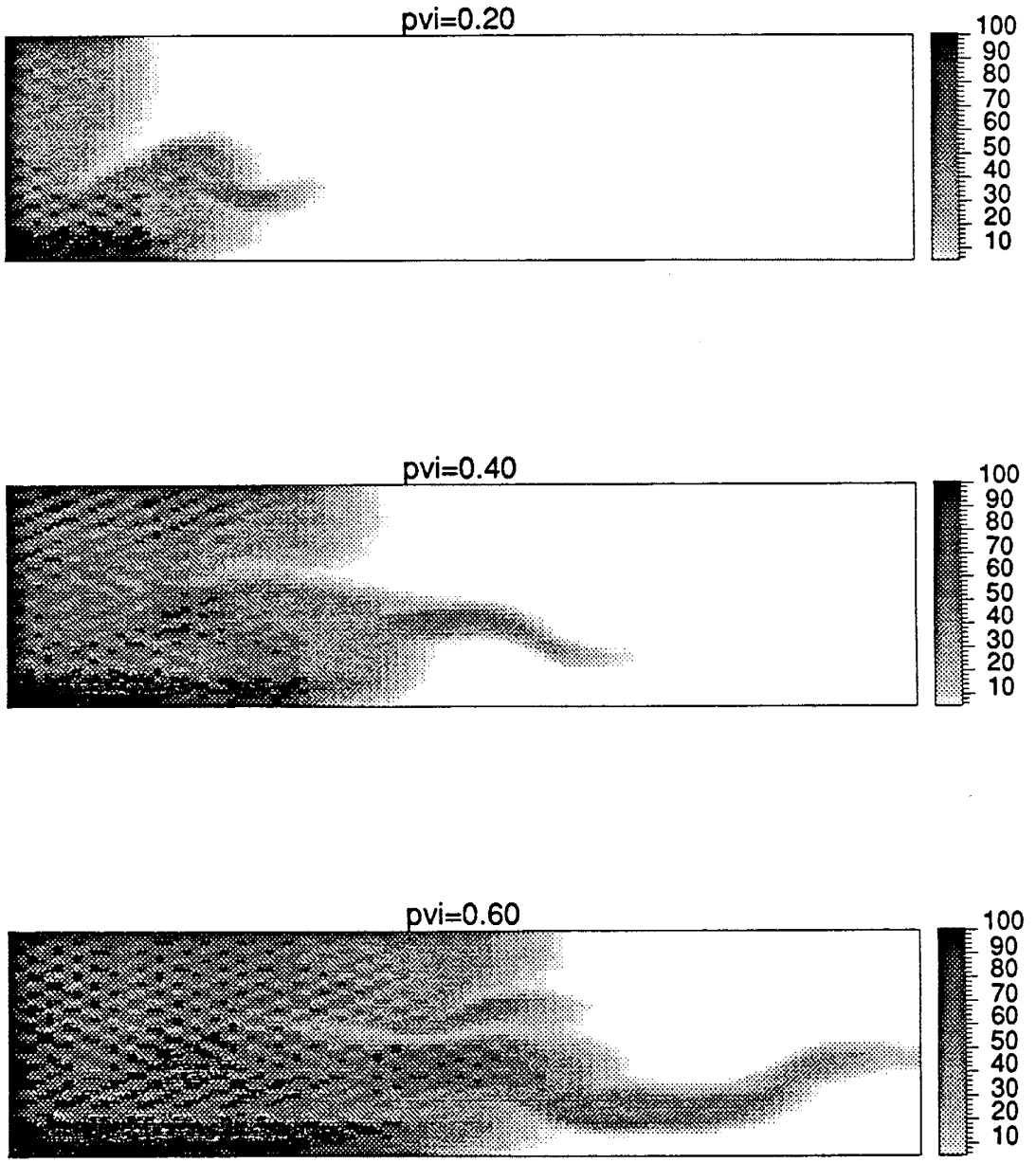

Figure 4.23: Injected fluid concentration in an experimental displacement at M=1 and q = 6 cm^3 / min in the checkered model (Panels d-f).

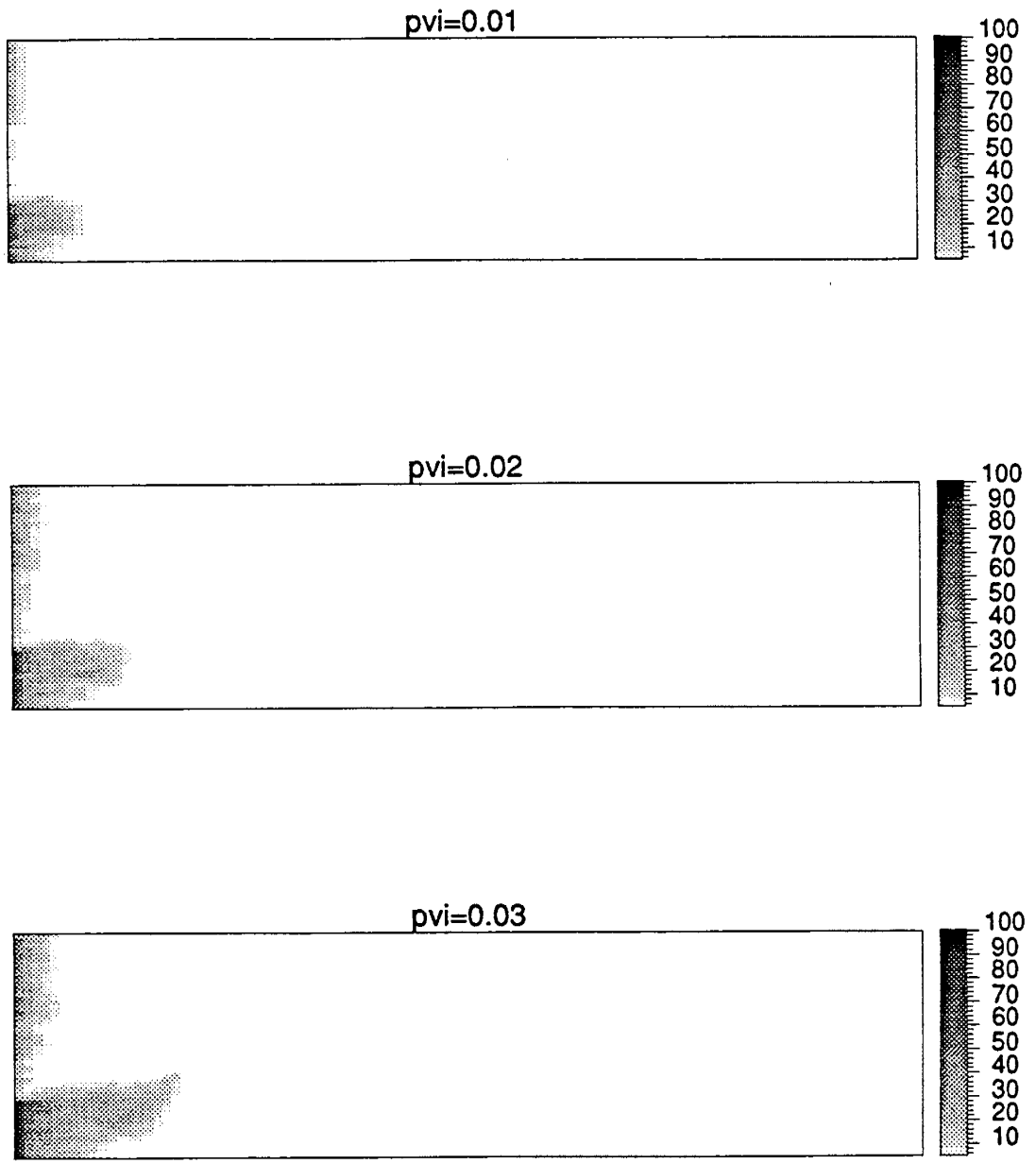

Figure 4.24: Injected fluid concentration in an experimental displacement at M=40 and $q = 6\,cm^3/min$ in the checkered model (Panels a-c).

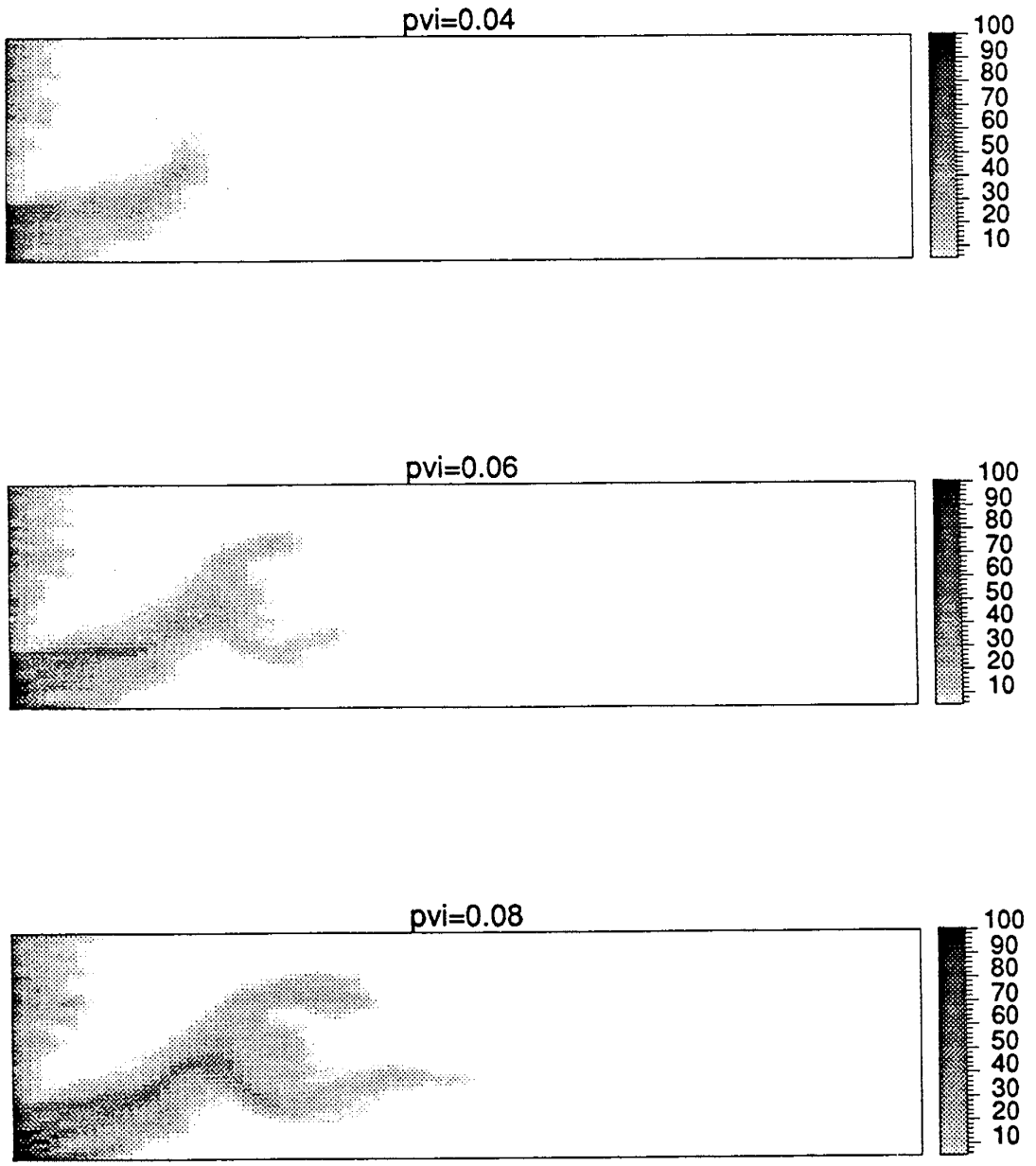

Figure 4.25: Injected fluid concentration in an experimental displacement at M=40 and $q = 6\,cm^3/min$ in the checkered model (Panels d-f).

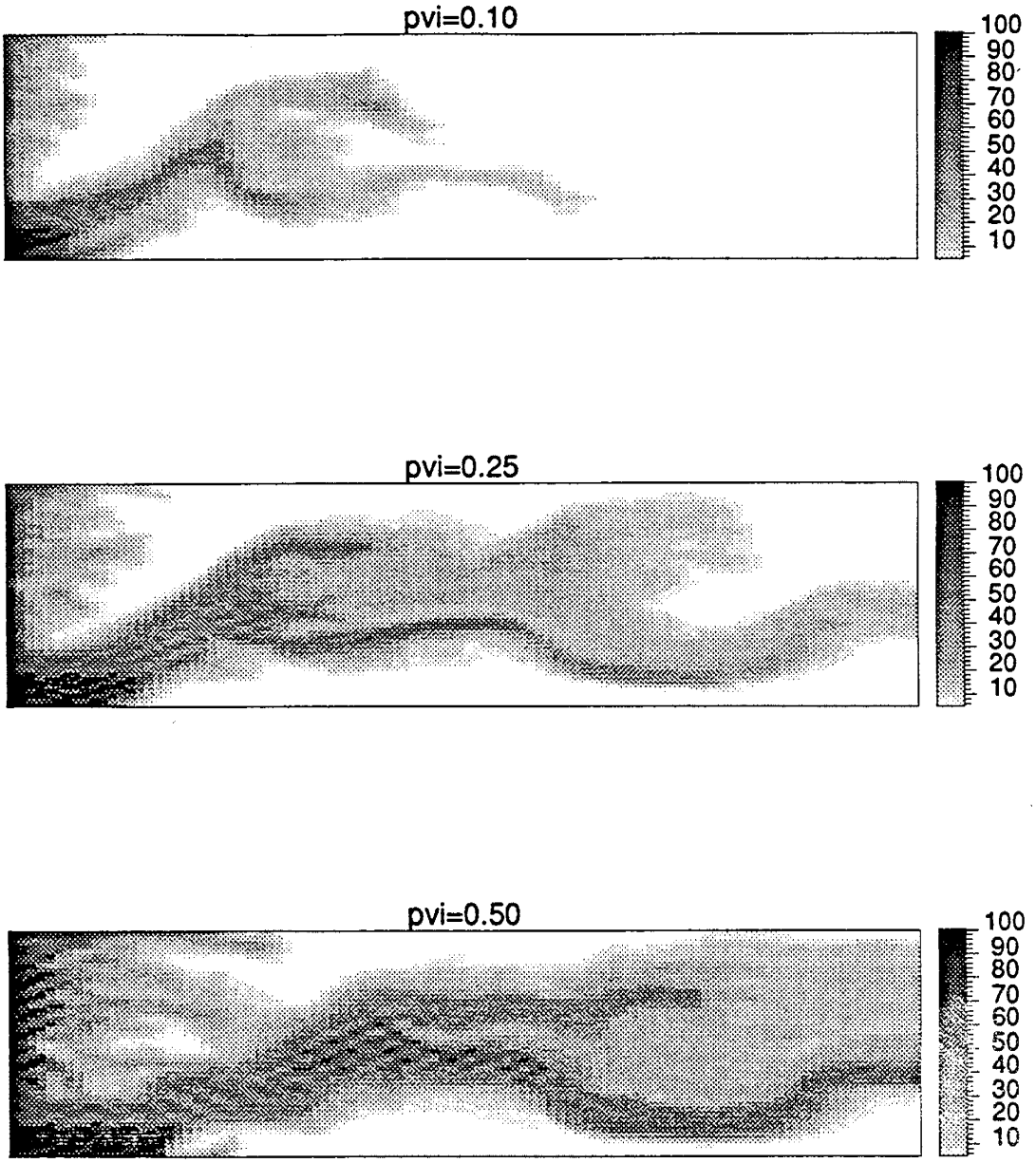

Figure 4.26: Injected fluid concentration in an experimental displacement at M=40 and q = 6 cm^3 / min in the checkered model (Panels g-i).

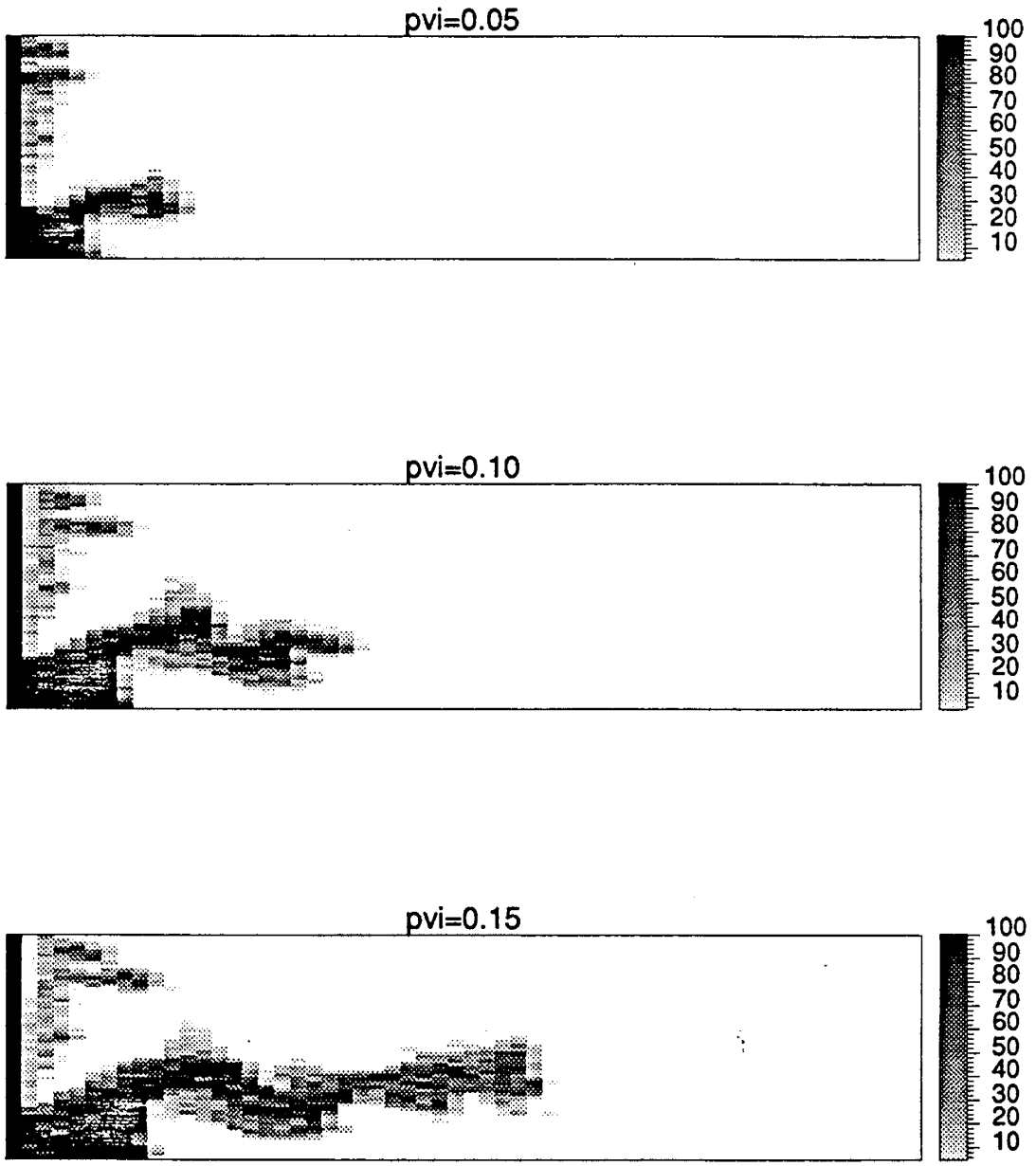

Figure 4.27: Simulated concentration distributions for displacement at M=40 in the checkered model (Panels a-c).

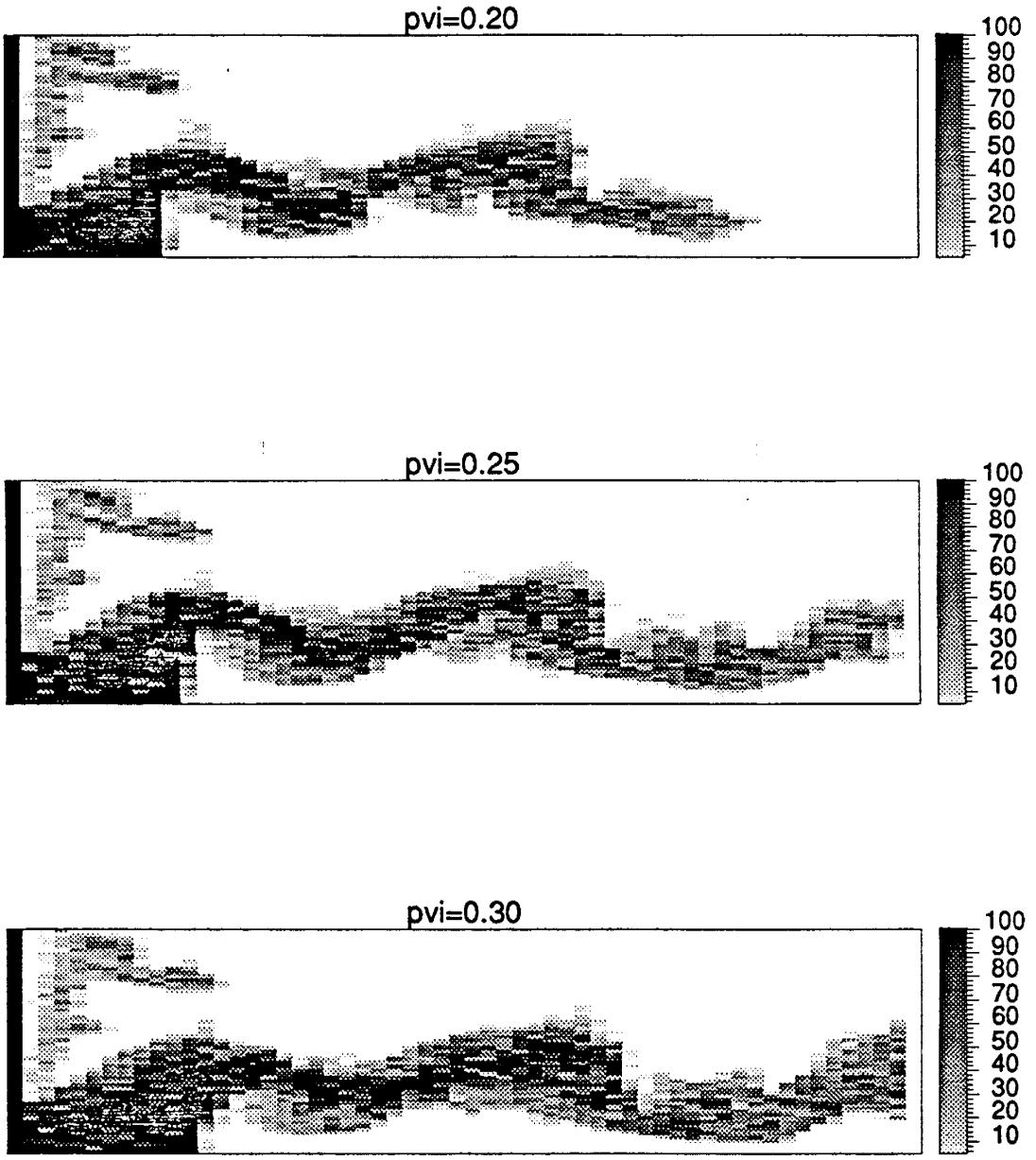

Figure 4.28: Simulated concentration distributions for displacement at M=40 in the checkered model (Panels d-f).

simulations showed reasonable agreement with experimental observations.

4.1.4 Discussion

The three heterogeneous models were designed to examine the effects of three types of heterogeneity. Since all were created with only two sizes of beads, the permeability contrasts were the same in all models. Differences were in overall variance of the permeability field and geometry of heterogeneities. The two-layer and checkered models had roughly equal areas of high and low permeability, while the streak model had only a small amount of high permeability and therefore a smaller variance of permeabilities. Both the two-layer and streak models had permeability correlation lengths equal to the flow length. The checkered model had roughly a 3.8-cm correlation length, 1/8 of the flow length.

In the layer and streak models, the flow was virtually all in the high permeability layer. In the two-layer model, the layer was wide enough that viscous fingers could form. In the streak model, there was no room in the narrow high permeability layer for splitting to occur. Flow in both did not deviate greatly from the overall flow direction. In the checkered model, finger paths curved so fingers could follow high permeability paths. The permeability field in each case affected the fingering patterns. Specifically, the appearance of the displacements was dictated not only by the permeability contrast but by the way in which the high permeabilities were connected. Both the two-layer and checkered models were characterized by flow determined by the permeability field, with viscous fingering superimposed. Thus, these models should be categorized as in the transition between viscous-dominated and heterogeneity-dominated regimes. The flow in the streak model did not display viscous fingering within the high permeability streak, because the width of the streak was not large enough for viscous fingering to develop. In that case, the flow was dominated by the permeability distribution.

While the model displacements described here were not completely scaled to represent reservoir scale flows, some of the observations made above may have important ramifications for field-scale displacements. The experiments and simulations showed that a fairly mild, four-to-one permeability contrast was enough to have a significant impact on the form and location of fingers. Both the experiments and simulations indicate that, in addition to permeability contrast, the geometry and connectivity of high- and low-permeability zones will strongly influence unstable flow. Thus, an important question is: To what extent does permeability variation dominate unstable flow patterns in field-scale displacements? The answer to that question has important implications for simulation of large-scale flows. If a reservoir is like the high permeability streak model with heterogeneity acting so strongly that it determines fingering, with only a faint overlay of viscous fingers, then a simulator would have to calculate only plug flow within a specific layer. If, however, the reservoir somewhere between that observed for the homogeneous and checkered models where heterogeneities affect finger locations and paths, but the flow is also influence by viscous fingers, accurate simulations of process performance might also require a more detailed representation of finger growth. Thus, it will be important to determine, probably by simulations, which length scales of heterogeneity and what levels of permeability contrast are most important to flow at reservoir scales. The results presented indicate that the simulation technique used here adequately models the transition from viscous-dominated to permeability-dominated unstable flow, and, therefore, it is a logical choice for such an investigation.

4.1.5 Conclusions

The experimental and numerical simulation results given here for stable and unstable displacements lead to the following conclusions:

1. In homogeneous porous media, viscous fingers grow by spreading and splitting at their tips. Fingers that outpace others nearby shield them from further growth and some fingers are eliminated by coalescence into the wake of faster moving fingers. Hence, in rectilinear flow, at least, the number of fingers declines as the flow progresses. Numerical simulations show similar mechanisms and numbers of fingers.

2. In heterogeneous porous media, fingering patterns develop along the same streamlines followed during flow at unit mobility in the same porous medium.

3. Even a relatively modest permeability contrast of 4:1 is sufficient to dominate flow if the high permeability is arranged in long thin layers.

4. Particle-tracking simulations of unstable flows reproduce with reasonable accuracy the transition from instability-dominated to permeability-dominated flow.

4.2 Dispersion, Permeability Heterogeneity and Viscous Fingering: Acoustic Experimental Observations and Particle-tracking Simulations

Hamdi Tchelepi, Nicole Rakotomalala[1], Robert Woumeni[1], Dominique Salin[1], and F.M. Orr, Jr.

The subject of miscible displacement in porous media has been examined in an extensive literature with applications that range from contaminant transport in aquifers to enhanced oil recovery to the performance of packed bed adsorbers and reactors. Despite the attention given to miscible displacement, many important questions remain to be resolved concerning the representation of flow behavior in heterogeneous porous media that arise in natural systems. In this section we examine how dispersion and permeability heterogeneity are related in both stable and unstable flows. To do so, we consider experimental displacements with a wide range of viscosity ratios performed in sandstone and limestone core samples with quite different spatial distributions of permeability. In addition, we use particle-tracking simulations of the displacement experiments to interpret and explain the observed behavior under stable and unstable flow conditions.

Dispersion coefficients for sedimentary rock samples are usually measured in laboratory displacement experiments in which a tracer is injected into a core sample and the concentration of the tracer is measured at the core outlet. The spreading of the transition zone in tracer concentration is usually taken to be due to a combination of molecular diffusion and variations in flow velocity at the microscopic (pore) scale. When the transition zone along the mean flow direction is symmetric about the mean displacement position, $x = \overline{u}t$,

[1]Laboratoire d'Acoustique et Optique la Matière Condensée, Université Pierre et Marie Curie

the growth of the transition zone can be modeled by a one-dimensional convection-dispersion (CD) equation

$$\frac{\partial c}{\partial t} + \overline{u}\frac{\partial c}{\partial x} - D_L \frac{\partial^2 c}{\partial x^2} = 0 . \tag{4.1}$$

Eq. 4.1 describes a concentration distribution that follows a normal distribution with a variance proportional to time. Eq. 4.1 is consistent with the assumption that the dispersive flux is described by Fick's law and that dispersion can be modeled as a diffusional process [8]. In addition, the dispersion coefficient is frequently assumed to be proportional to the average flow velocity, $D_L = \alpha_L \overline{u} + D_m$. Thus, the dispersivity, α_L, can be taken as a property of the porous medium [8]. The dispersivity is the correlation length of the local velocity. Thus, for a homogeneous (uniform permeability) medium, the dispersivity reflects the length scale of the pore structure. Eq. 1 and its multi-dimensional extensions have also been used to describe macroscopic dispersion in heterogeneous porous media. Use of Eq. 4.1 is appropriate when the correlation length of the permeability and in turn that of the local velocity variation is small compared to the flow length [8, 42]. Moreover, for the dispersivity to be constant, the correlation length must be constant (stationarity).

Laboratory cores used in displacement experiments may or may not satisfy the assumptions inherent in Eq. 4.1 that the flow is one dimensional, and that correlation lengths of permeability variations are small compared to the flow length. Experimental measurements of dispersion coefficients rarely examine whether the flow is really one-dimensional. Instead, effluent composition data, which are, in effect, transversely averaged concentration measurements at a single location are fit to Eq. 4.1.

In the first part of this section, we investigate the applicability of Eq. 4.1 for stable laboratory-scale displacements in two porous media. First, we report acoustic measurements of transversely averaged mixture composition histories at several locations along sandstone and limestone core samples. In addition, displacement results for a variety of superstable displacements, those in which the displaced fluid is less viscous than the displacing fluid, are reported. Furthermore, we use results from particle-tracking simulations of the displacement experiments to argue that the dependence of α_L on the viscosity ratio, M, (or lack thereof) indicates whether significant correlation of permeability exists at the scale of the displacement.

For displacements with M > 1, the displacement is hydrodynamically unstable and viscous fingering contributes to the growth the transition zone. Unstable displacements are presented in the second part of the section. We also report acoustic measurements of transversely averaged compositions, and we compare local concentration history data with predictions obtained from random-walk particle-tracking simulations. The results of both experiment and simulation show how permeability heterogeneity, dispersion, and viscous fingering interact as the viscosity ratio, M, varies in miscible displacements.

4.2.1 Experimental Apparatus and Procedures

The acoustic technique of Bacri et. al. [3] was used to measure the space and time dependence of concentration during stable and unstable miscible displacements. Fig. 4.29 is a schematic of a cross-section across the apparatus. The concentration at a particular cross-section was determined from velocity variations of a longitudinal sound wave. Ten

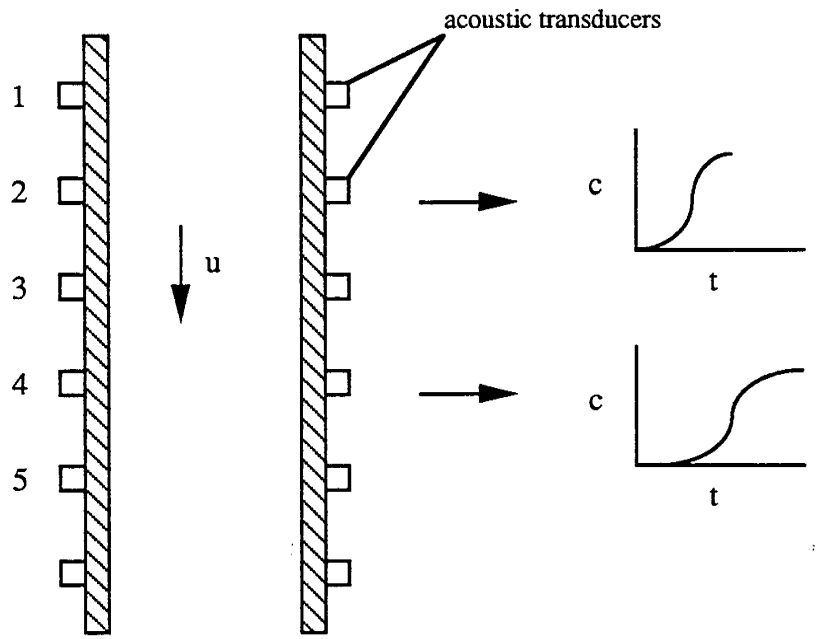

Figure 4.29: Schematic of a cross-section of the experimental apparatus and typical data.

transmitter-receiver transducer pairs generated and recorded the signal as a function of time. The ten locations were sampled in less than one minute. Calibration curves relating variations in the sound velocity to volumetric concentration were used to convert acoustic velocity measurements to local concentration measurements. The concentrations reported are estimated to be accurate to within 1% with a spatial resolution of 3 mm in the width of the sampled section. The resulting transversely averaged concentration history curves at the ten locations along the core sample provide detailed information on the concentration distribution in the transition zone.

Displacement experiments under stable ($M \leq 1$) and unstable ($M > 1$) conditions were performed for a wide range of mobility ratios and displacement rates. Water and water-glycerol mixtures constituted the fluid system. In stable displacements, a water-glycerol mixture displaced water, and in the unstable displacements, the reverse was true. The displacing fluid was driven vertically downward when water displaced a water-glycerol mixture ($M > 1$), and vertically upward when a water-glycerol mixture displaced water ($M < 1$). In other words, density differences were always stabilizing.

All the experimental curves presented in this paper are for displacements at rates that are well within the region where the contribution of molecular diffusion to the dispersion coefficients is negligible. At such conditions, viscous fingering behavior is nearly independent of flow velocity [12]. Consequently, the effect of rate on fingering behavior is not considered here.

Acoustic measurements on limestone and millstone core samples are reported here. The limestone sample dimensions were 4.5 x 4.5 x 25.4 cm^3. The transducer pairs were placed at ten equally spaced locations, $x_i = 2.55 + 2.1(i-1)$ cm, along the core length. The dimensions of the millstone were 4.1 x 4.05 x 25.4 cm^3, and the transducers were placed at $x_i = 1.5 + 2.5(i-1)$ cm.

An additional limestone core sample (4.5 x 4.5 x 25.4 cm^3) from the same block

as the sample on which the displacement experiments were performed was obtained, and minipermeameter measurements on three faces were made. The diameter of the permeameter probe tip was 1 cm. Similar measurements were also made on a slab of millstone (1.0 x 8.0 x 25.0 cm^3). The permeability maps for both samples are shown in Fig. 4.30. While these measurements do not provide a complete description of the permeability distribution in the truly three dimensional cores used in the displacement experiments, they do illustrate the major features of the two rock types under investigation.

4.2.2 Particle-Tracking Simulations

The numerical solution to the unstable displacement problem employed here is based on particle-tracking.

The model used is based on the following assumptions:

1. The porous medium is incompressible.
2. Fluids are incompressible and first-contact miscible, but have differing densities and viscosities.
3. Flow takes place in two or three dimensions, and the local flow velocity is given by Darcy's law.
4. Local velocity variations at scales smaller than a grid block can be represented adequately through the use of longitudinal and transverse dispersivities.
5. There is no volume change on mixing, and viscosities of mixtures can be represented by a quarter power blending rule.

For conservative solute transport, a material balance on the injection component gives

$$\frac{\partial(\phi c)}{\partial t} + \nabla\cdot(c\mathbf{v}) - \nabla\cdot(\phi\mathbf{D}\cdot\nabla c) = 0\,. \tag{4.2}$$

If the porosity is independent of time and space, then Eq. 4.2 becomes

$$\frac{\partial c}{\partial t} + \nabla\cdot(c\mathbf{u}) - \nabla\cdot(\mathbf{D}\cdot\nabla c) = 0\,, \tag{4.3}$$

where the dispersion tensor, $\mathbf{D}$, is given by

$$\mathbf{D} = (\alpha_T|\mathbf{u}| + D_m)\mathbf{I} + (\alpha_L - \alpha_T)\frac{\mathbf{uu}}{|\mathbf{u}|}\,. \tag{4.4}$$

For incompressible flow, the continuity equation is

$$\nabla\cdot\mathbf{v} = -q\,, \tag{4.5}$$

where $\mathbf{v}$ is given by Darcy's law

$$\mathbf{v} = -\lambda(\nabla p - \rho g\nabla z)\,, \tag{4.6}$$

and the mobility, λ, is defined as

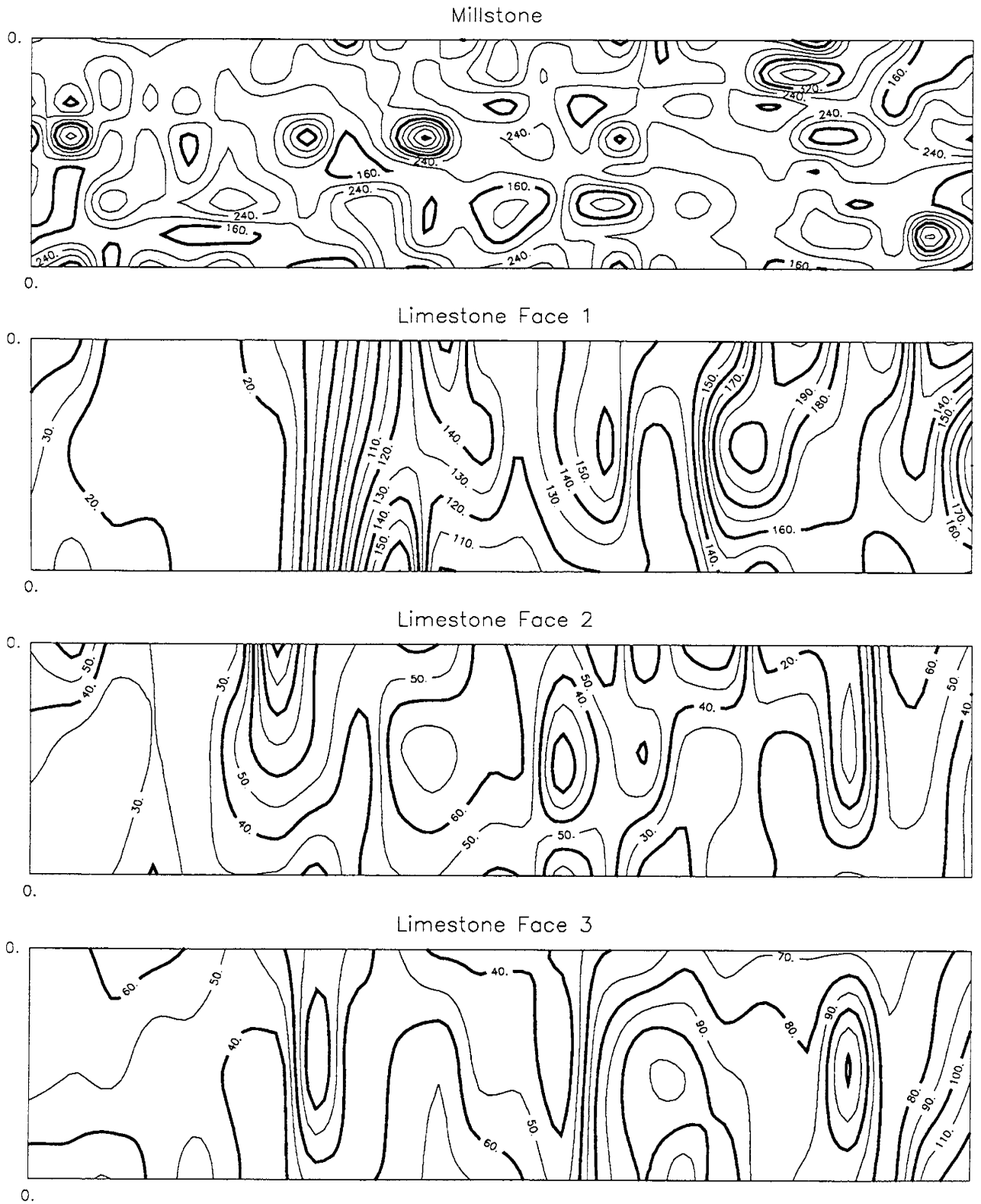

Figure 4.30: Permeability maps of the millstone slab and three faces of a limestone core

$$\lambda = \lambda(c(\mathbf{x}, t)) = \frac{k(\mathbf{x})}{\mu(c(\mathbf{x}, t))}. \tag{4.7}$$

Substitution of Eq. 4.6 into Eq. 4.5 gives the pressure equation,

$$\nabla \cdot \lambda \nabla p = q - \nabla \cdot \lambda \rho g \nabla z. \tag{4.8}$$

Analytical solutions to the convection-dispersion equation (Eq. 4.3) for a variety of boundary and initial conditions are available for simple geometries with uniform properties [64, 73]. In domains with spatially dependent properties, however, the convection-dispersion equation must be coupled with the pressure equation in order to obtain the velocity distribution in the domain. Inspection of Eqs. 4.7 and 4.8 indicates clearly where the spatial distribution of permeability comes into play. Furthermore, if variations in the viscosity, μ, and density, ρ, exist, then the pressure distribution changes as the spatial distribution of these properties changes with time.

Approaches to obtain accurate numerical solutions (minimize numerical dispersion) to the coupled system of equations formed by Eqs. 4.8 and 4.3 for $M > 1$ include among others: 1) Mixed finite difference/particle-tracking [2], 2) Finite difference schemes with flux corrected transport [19]. 3) Mixed finite elements with a modified method of characteristics [34, 82], and 4) Spectral methods based on a vorticity formulation [133, 158].

A random-walk particle-tracking numerical method is used here. Bear [8] demonstrated that there is an analogy between the normal probability distribution and the concentration distribution obtained from the solution of Eq. 4.3 for tracer flow in a homogeneous domain. As a result, a random-walk particle-tracking method that treats dispersion as a random process can be used to solve convection-dispersion problems [111]. The analogy can be more rigorously represented by casting the convection-dispersion equation into the form of a stochastic Fokker-Planck equation [140, 141, 61, 137]. The probability density, P, governed by a deterministic force $\mathbf{A}$ and a Gaussian noise scaled by a deterministic tensor $\mathbf{B}$ is expressed by the Fokker-Planck equation

$$\frac{\partial P}{\partial t} + \nabla \cdot (\mathbf{A}P) - \nabla\nabla : (\frac{1}{2}\mathbf{B} \cdot \mathbf{B}^T P) = 0. \tag{4.9}$$

The solution to Eq. 4.9 is

$$\mathbf{x}^n = \mathbf{x}^{n-1} + \mathbf{A}(\mathbf{x}^{n-1}, t_{n-1})\Delta t + \mathbf{B}(\mathbf{x}^{n-1}, t_{n-1}) \cdot \mathbf{Z}\sqrt{\Delta t}. \tag{4.10}$$

According to Eq. 4.10, the new particle position is obtained by adding two components to the previous position: a deterministic component governed by $\mathbf{A}$, and a probabilistic Gaussian component scaled by a deterministic tensor $\mathbf{B}$.

Expansion of Eq. 4.3 indicates that if the terms involving second-order spatial derivatives of the dispersion tensor, $\mathbf{D}$, are neglected, then the convection-dispersion equation (Eq. 4.3) can be cast into a Fokker-Planck equation (Eq. 4.9) if $\mathbf{A}$ and $\mathbf{B}$ are chosen to be

$$\mathbf{A} = \mathbf{v} + \nabla \cdot \mathbf{D}, \quad \frac{1}{2}\mathbf{B} \cdot \mathbf{B}^T = \mathbf{D}. \tag{4.11}$$

The mathematical model was implemented numerically using an explicit finite difference scheme to solve the pressure equation (Eq. 4.8) on a point-distributed grid. A constant

total injection rate was imposed at the inlet boundary. In effect, the potential at a given time across the inlet face was held constant. The outlet boundary was held at a constant potential. Particle positions were obtained using Eq. 4.10 with **A** and **B** given by Eq. 4.11.

The required input data include the following physical conditions: flow domain dimensions, dispersivities, flow rate, and the mobility ratio. The following additional information may be included, if needed: permeability and/or porosity distributions, effective diffusion coefficient and densities. Requirements specific to the numerical implementation include grid size and the number of particles taken to represent a unit concentration of the injected component.

The algorithm that implements the model is:

1. For the mobility distribution in the flow domain, solve Eq. 4.8 for the specified boundary conditions and calculate the internodal velocity field.

2. Calculate the time step size.

3. Introduce new particles corresponding to the amount injected.

4. Compute particle velocities, and move all particles according to Eq. 4.10.

5. Until the desired displacement time is reached: If the mobility ratio is unity and the densities of the resident and injected fluid are the same, then go to step (3). Otherwise, go to step (1).

It is important to establish whether the particle-tracking technique resolves adequately the growth of fingers in the onset period and in the subsequent nonlinear growth period. Some guidance for the onset period can be found in the linear stability analyses performed by a number of authors [105, 151, 118, 48, 108, 40, 132, 22]. Explicit attempts to account for the fact that the base state solution is time dependent due to dispersion were made by Wooding [151], Chouke (as reported by Gardner and Ypma [40]), and Tan and Homsy [132]. Tan and Homsy [132] found that a cutoff wavenumber at inception is present due to, and determined by, transverse dispersion. They also showed that a shift to smaller wavenumbers (larger wavelengths) with slower growth occurs with time.

The diffusive scales are small. For example, laboratory scale longitudinal dispersivities are frequently smaller than a centimeter (typically $\alpha_L < 0.1$ cm), and for displacement velocities in the mechanical (convective mixing) dispersion regime $\alpha_T \approx \alpha_L/20$. Hence, high resolutions will be required if the numerical solutions are to represent accurately the onset period. In numerical simulations the cutoff wavelength is set by the grid size. Thus, it is important to choose grid Peclet numbers, $\Delta x/\alpha_L$ and $\Delta y/\alpha_T$, that allow as small an unstable mode as can be tolerated. The effects of grid resolution were examined in a series of grid refinement simulations. These simulations indicate that when $\Delta x/\alpha_L < 20$, and $\Delta y/\alpha_T < 100$, finger resolution is adequate. Finer grids produced no significant changes in fingering characteristics.

In the case of stable ($M \leq 1$) displacements, the requirement is less stringent. However, grid block sizes that are also many times smaller than the correlation scales of the permeability are needed in order to resolve the pressure field accurately. The grid Peclet

numbers in all the simulations presented here are: $\Delta x/\alpha_L = 4$ and $\Delta y/\alpha_T = 40$. These numbers correspond to a dispersion anisotropy, α_L/α_T, of 25.

The random walk particle-tracking method was used by Araktingi and Orr [2] to model unstable displacements. They demonstrated excellent agreement with the recovery curves reported by Blackwell et. al. [11] for a wide range of mobility ratios. They also showed that there is a transition from unstable flow dominated by viscous forces to flow dominated by the permeability distribution (sometimes called channeling [145, 122]) as the variance and correlation length of the permeability field increase. Brock showed that particle-tracking simulations also agree well with spatial distributions of fingers observed in flow visualization experiments in homogeneous and layered unconsolidated media (see Section 4.1 and references [12] and [13]). Thus, the simulation approach used here has been shown to reproduce with reasonable accuracy the interaction of viscous instability with variable permeability.

The simulation code used here was written specifically for a massively parallel, Single Instruction Multiple Data (SIMD) machine (MasPar). The mesh used for all simulations presented here was 128 by 64. And the number of particles representing unit concentration of the injected component in a gridblock was 64.

4.2.3 Stable Displacements

Fig. 4.31 shows the apparent longitudinal dispersivities for a variety of mobility ratios obtained from concentration data of the form shown in Fig. 4.29 by taking the slope at the 50% concentration value. The reported value of α_L at each mobility ratio is the average of the values at ten locations. A small reduction in α_L with mobility ratio for the millstone core was observed for $M \leq 0.1$. Thus, α_L was nearly independent of M in the millstone. In the limestone, the dispersivity, α_L, decreased by a factor of 2.5 as M varied from 0.8 to 0.04. We argue that the dependence of α_L on M in the limestone core is the direct result of the heterogeneity of the sample.

The x-directional semivariograms for the permeability distributions in Fig. 4.30 are shown in Fig. 4.32. The millstone semivariogram reflects a permeability distribution with random character and a correlation length shorter than the nearest neighbor permeability. The semivariograms of Faces 1 and 3 of the limestone core, however, display increased variance with lag. A constant slope is shown for Face 1, while Face 3 exhibits a slope that decreases with lag. On the other hand, Face 2 of the limestone approaches stationary behavior with a correlation length of about two centimeters. The variety in the variograms observed for the limestone faces make it difficult to characterize the permeability stochastically because the permeability field is not stationary, and it probably includes correlation length scales on the order of the core sample. Moreover, it is clear that significant differences in the permeability structure occur in the third dimension, as is reflected by the differences between the faces. However, it is obvious from Figs. 4.30 and 4.32 that the limestone is much more heterogeneous than the millstone.

Concentration histories from particle-tracking simulations for permeability distributions in Fig. 4.30 were used to estimate longitudinal dispersivities using a regression fit to Eq. 4.1. Fig. 4.33 shows concentration grayscale maps and the corresponding transversely averaged concentration profiles for mobility ratios of 1 and 0.08 in Face 1 at 0.4 pore volumes injected (PVI). Fig. 4.34 is a similar plot, but for Face 3. Limestone Face 1 showed dispersive

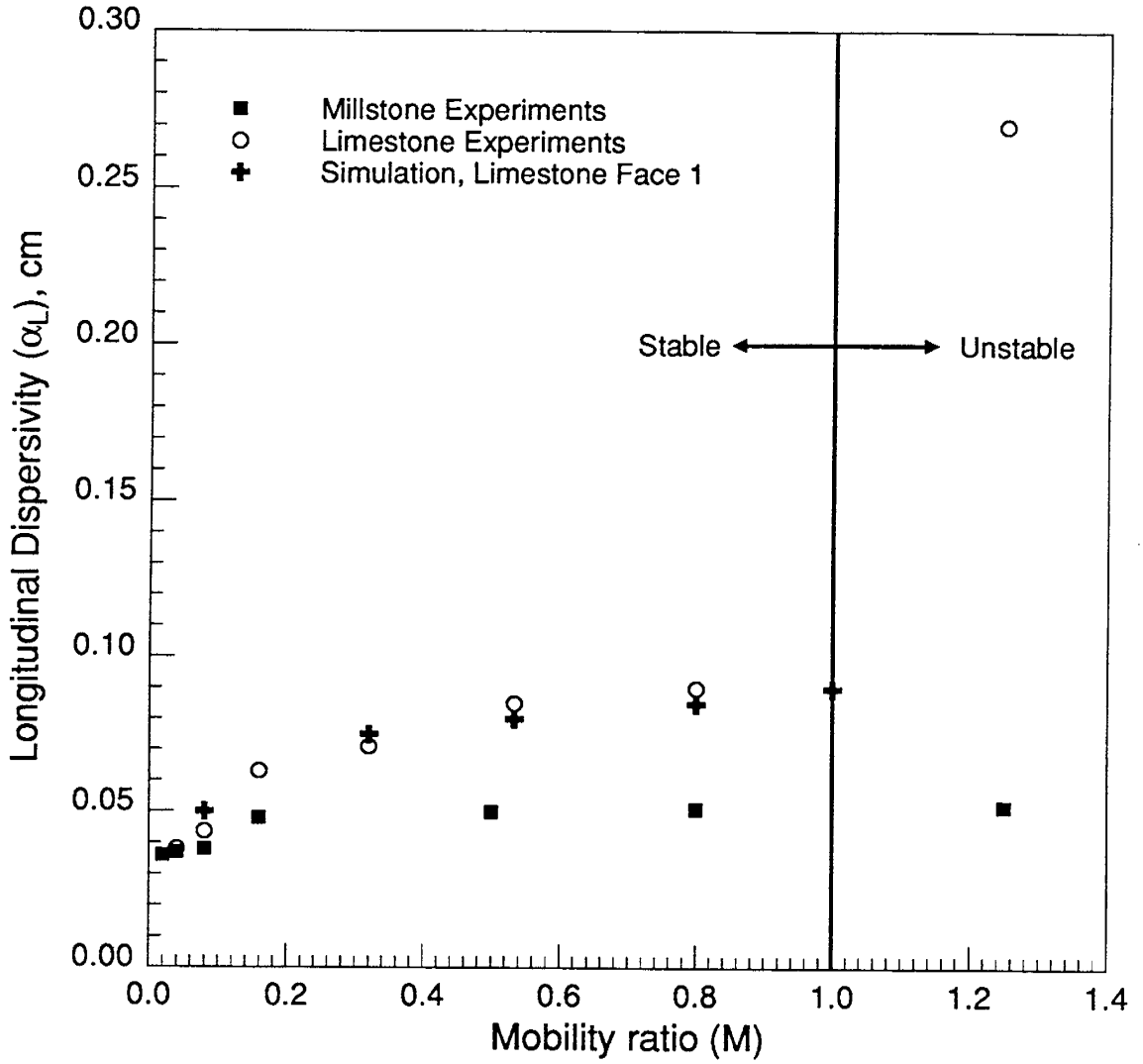

Figure 4.31: Dispersivity (α_L) vs. mobility ratio (M) from flow experiments in the millstone and limestone cores, and from simulations using limestone Face 1.

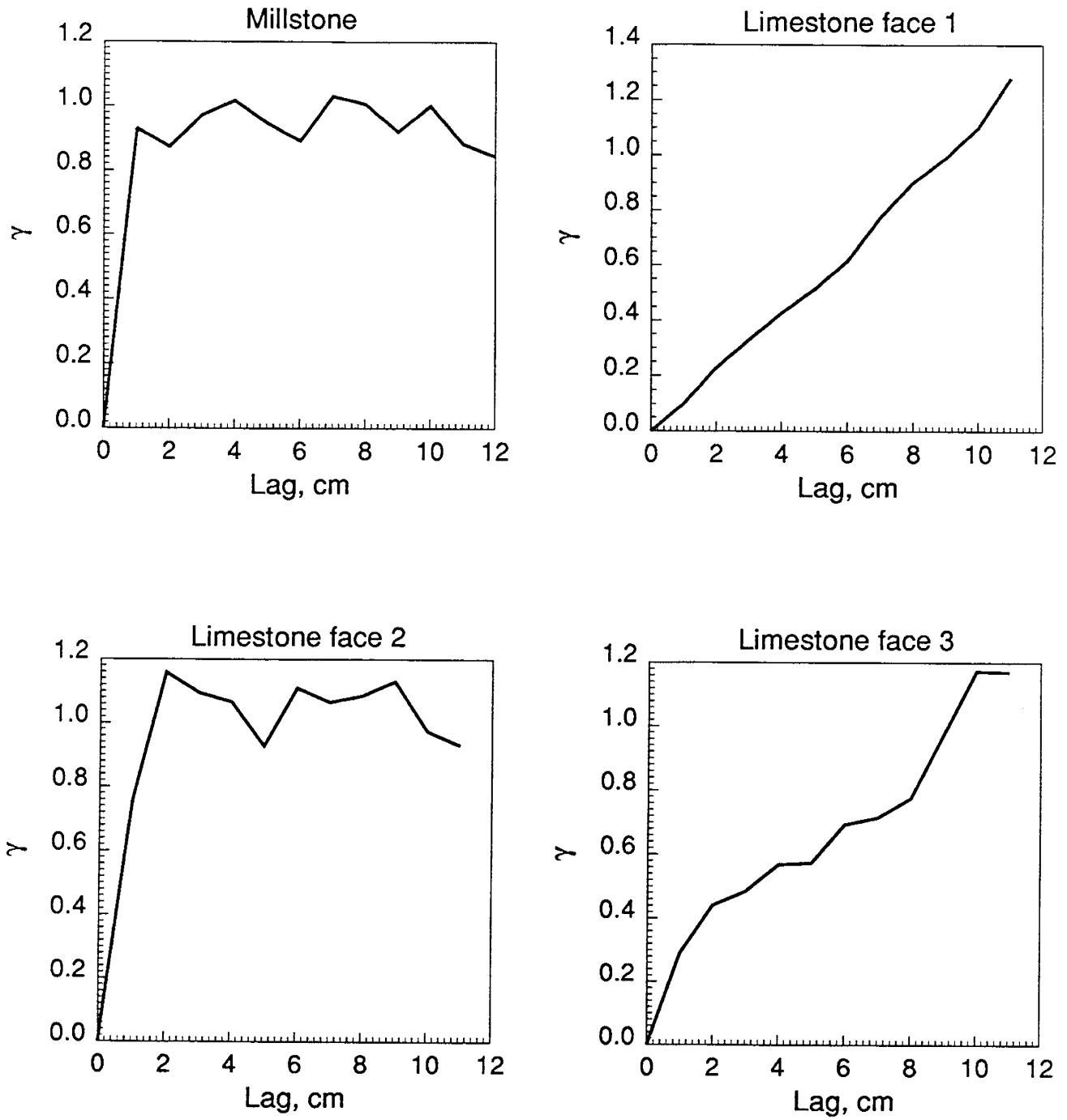

Figure 4.32: Semivariograms for the permeability distributions of the millstone slab and limestone core.

behavior for all simulated displacements with $M \leq 1$. The average apparent dispersivities for Face 1 are also plotted in Fig. 4.31. Fig. 4.31 indicates that flow simulations in Face 1 reproduce well the observed dependence of α_L on M. Thus, it is clearly possible to have flow that appears to be dispersive even though the porous medium does not satisfy the definitions of dispersive flow derived from analysis of stochastically generated correlated permeability fields. The permeability distribution of Face 1 (see Fig. 4.30) in fact shows highly correlated laminations transverse to the flow direction with a trend in the mean value along the flow direction resulting in uniform displacement fronts. The concentration histories of unit mobility displacement in Face 3 did not exhibit dispersive growth of the transition zone. Instead, preferential flow along high permeability paths caused the transversely averaged concentration profile to differ substantially from solutions to the convection-dispersion equation and regressions to determine α_L failed to converge. At M = 0.08, simulations for Face 3 did show apparently dispersive spreading region, as is demonstrated in Fig. 4.34. Thus, if M is small enough, apparently dispersive behavior can be observed for a porous medium that shows clear evidence of nonuniform flow at M = 1.

The apparent dependence of α_L on M arises from the effects of viscous crossflow. Fig. 4.35 shows the pressure distribution obtained for a stable displacement (M = 0.1) for the initial composition distribution shown in the schematic above it. Such a distribution can be imagined to arise, for example, due to a high permeability region upstream. We use a crossflow argument similar to that of Zapata and Lake [155] to explain the behavior observed here for super-stable displacements. In Fig. 4.35 the black region is the high viscosity fluid. At the tip of the high viscosity zone, the pressure in the surrounding low viscosity fluid is higher than the pressure in the high viscosity region. As a result, crossflow of the low viscosity fluid toward the tip slows the penetration of the high viscosity fluid. On the other hand, at the rear of the high-viscosity layer, high viscosity fluid is forced out into the adjacent low viscosity regions. The combined effects of slowing the penetration at the tip and depriving the high viscosity zone of support at the rear act, therefore, to shrink the transition zone when M < 1.

As M is reduced further below unity, the forces working to reduce the length of the transition zone increase in magnitude, and suppression of the influence of heterogeneity is enhanced. Thus, when permeability variations with short correlation lengths (especially short transverse correlation lengths) are present in a core, the shrinkage of the transition zone as M is reduced below unity is reflected as apparent values of α_L that decrease with M. In fact, Face 3 behavior in Fig. 4.34 shows that the reduction in M from unity to 0.08 was sufficient to eliminate significant distortions of the mean displacement front. As a result, the displacement displays apparently dispersive behavior.

Similar simulations of Face 2, which has an x-directional variogram reflecting stationary behavior, did not show apparently dispersive growth of the transition zone at any location even for mobility ratios as small as 0.04. Extensive simulations using permeability fields generated by unconditional Gaussian sequential simulations show that stationary permeability with significant correlation lengths (especially transverse) rarely show dispersive growth. In such fields, simulation results show that the permeability field dominates the early spreading of the transition zone, which grows linearly with displacement length as the permeability field dominates the pressure distribution. As a result, the pressure field fails to organize itself to eliminate this influence as the displacement proceeds.

If the reduction in mobility ratio were to eliminate completely the distortions in the

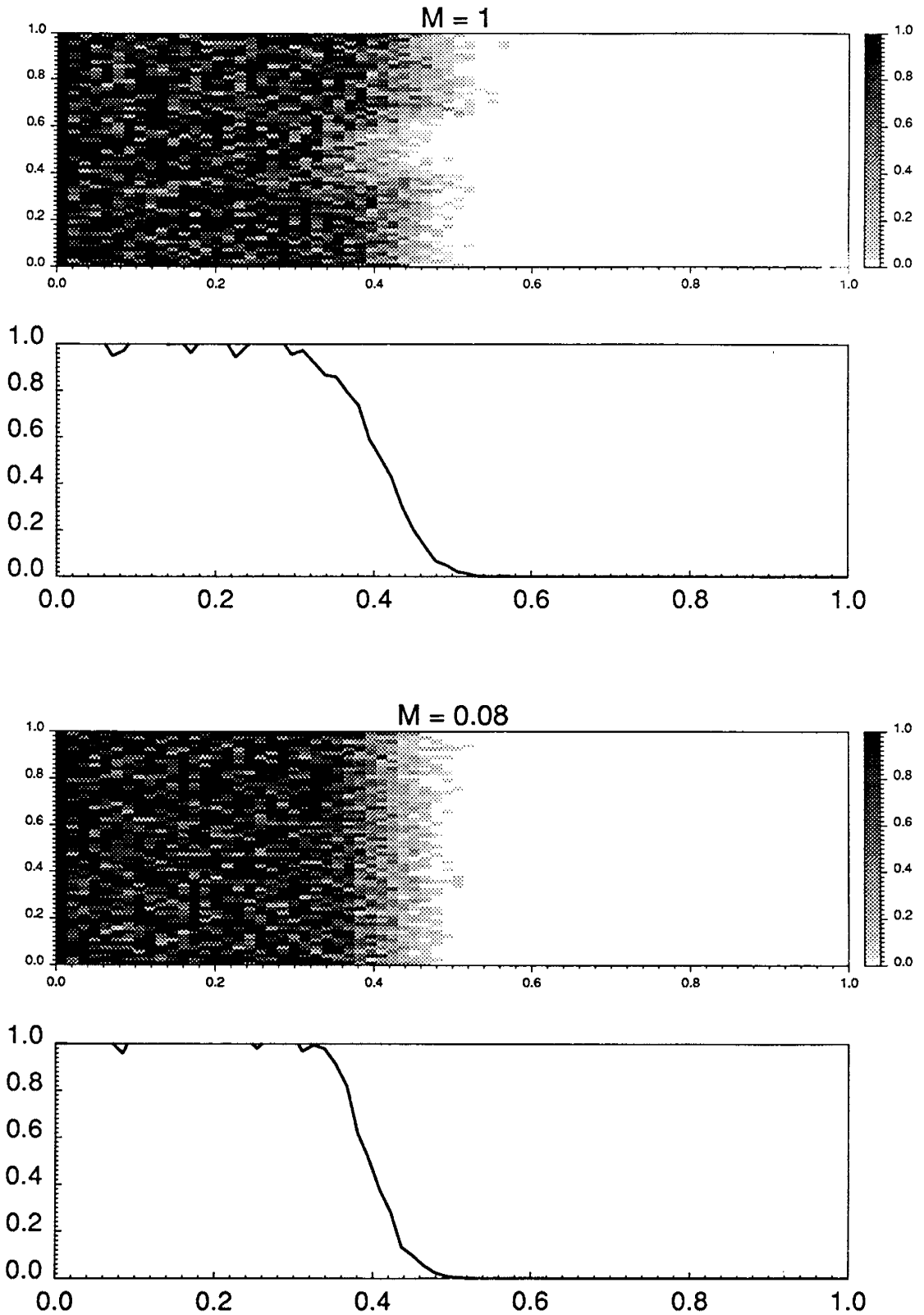

Figure 4.33: Concentration grayscale maps and transversely averaged concentration profiles for M = 1 and 0.08 at 0.4 PVI from simulations of limestone Face 1.

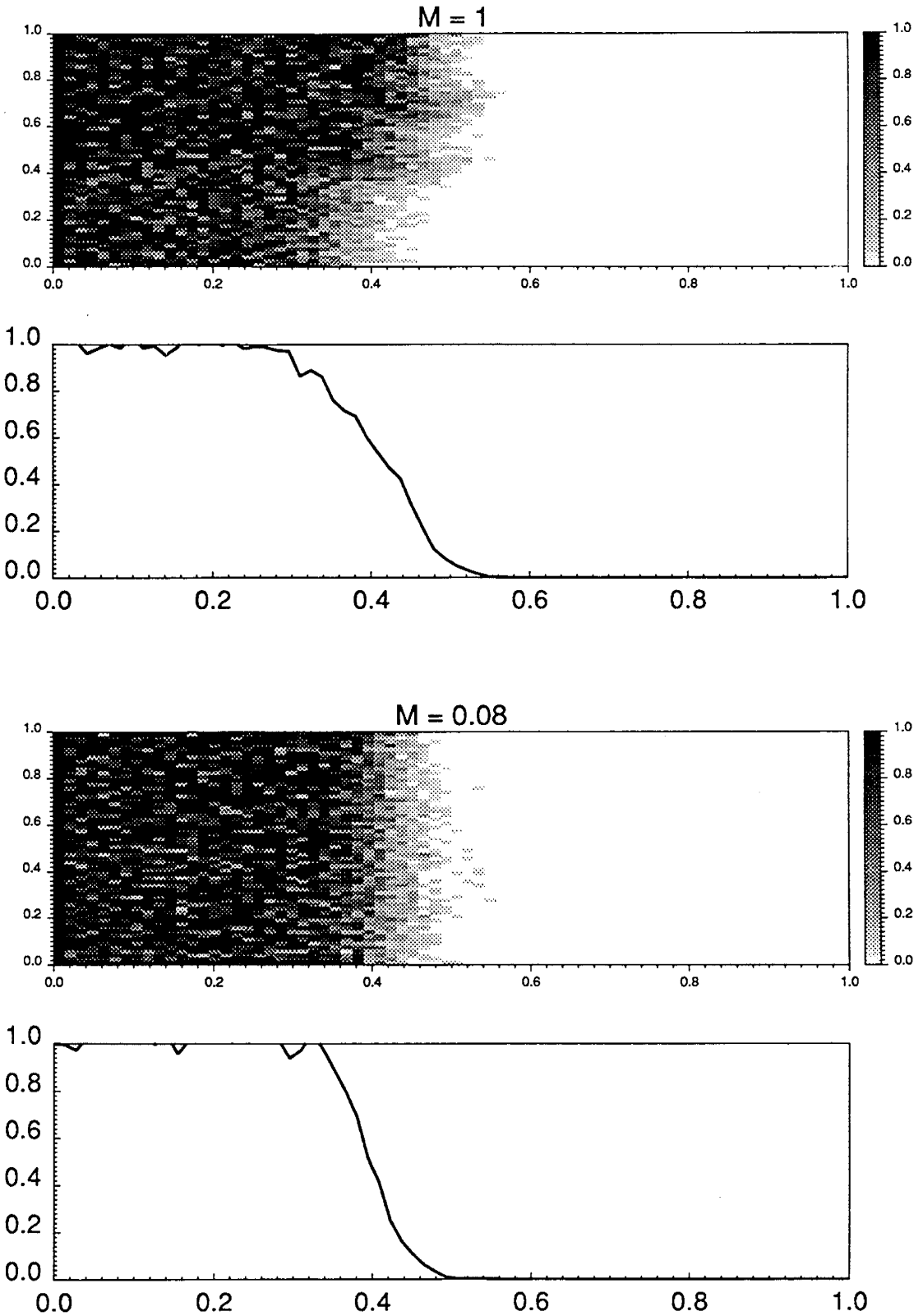

Figure 4.34: Concentration grayscale maps and transversely averaged concentration profiles for M = 1 and 0.08 at 0.4 PVI from simulations of limestone Face 3.

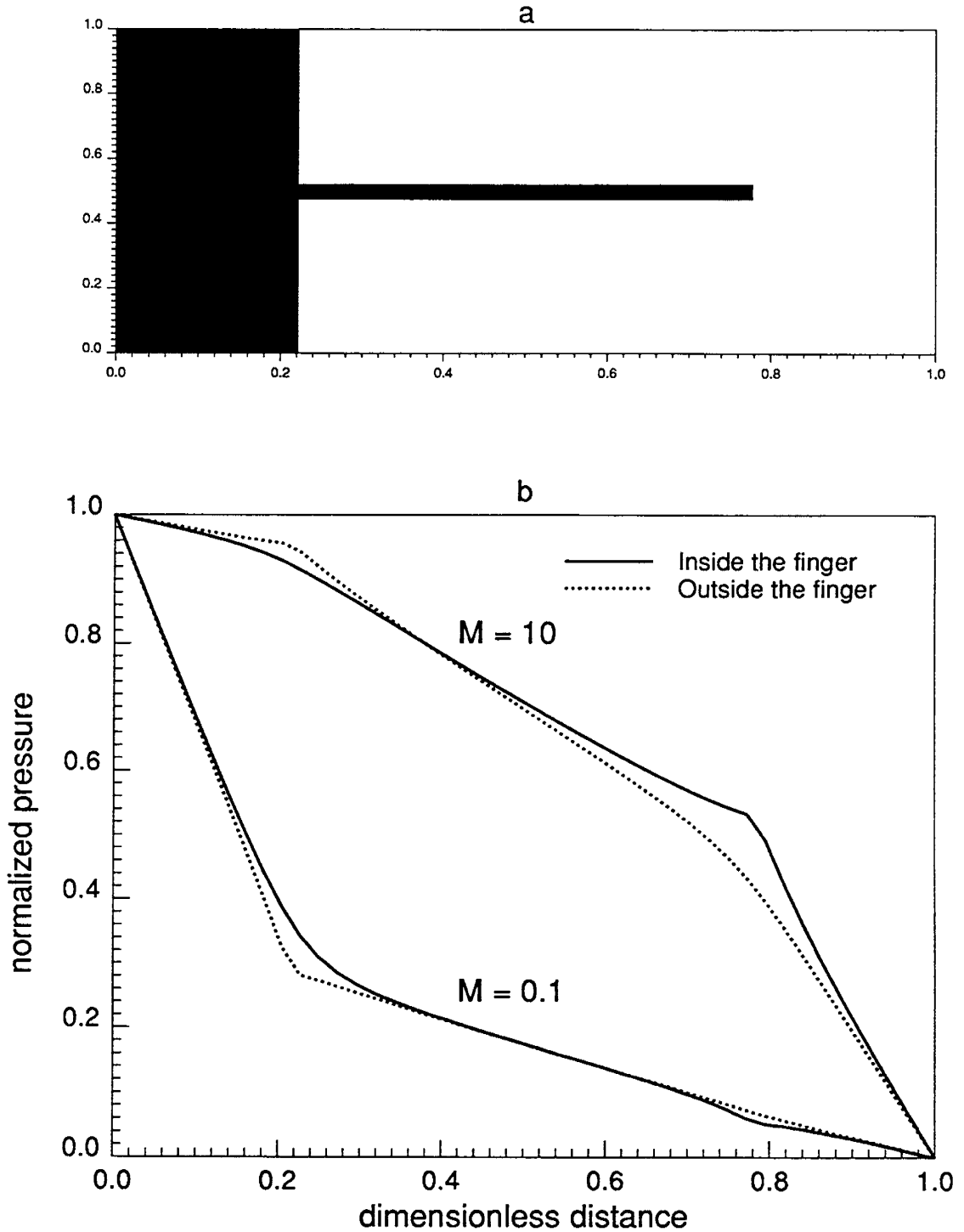

Figure 4.35: (a) Concentration distribution (black = 1, white = 0), and (b) Pressure distribution for unstable (M = 10) and stable (M = 0.1) displacements.

plane moving with the average flood velocity, $\overline{u}$, then the dispersivity value would reflect the microscopic length scale of porous medium. If so, further reductions in the mobility ratio would not change the dispersivity further. Fig. 4.31 provides limited evidence that there is some limiting value of dispersivity at sufficiently low values of M. First, the values of α_L for the millstone do not appear to vary for M < 0.08. Second, the value of α_L for the much more heterogeneous limestone is essentially equal to α_L for the relatively homogeneous millstone for M < 0.08. The results in Fig. 4.31 suggest that at the microscopic (pore) scale, variations in local velocity are comparable in the limestone and millstone samples.

4.2.4 Unstable Displacements

When M > 1, the less viscous fluid displaces the more viscous one, and the displacement is unstable. Viscous fingering then interacts with whatever heterogeneity is present to cause much faster growth of the transition zone than would be observed for displacements where $M \leq 1$. Figs. 4.36 and 4.37 show results of random-walk particle tracking simulations for a homogeneous medium that illustrate the effect of viscous fingering on transversely averaged concentrations for M = 3.1 and M = 13.5. At both values of M, the length of the transition zone grows rapidly with displacement length, with a higher growth rate for the larger mobility ratio.

For a fixed location, x_i, the time difference between the arrival times of the leading ($c > 0$) and trailing edges ($c \approx 1$) of the fingered region will be referred to as the length of the fingered zone, Δt_i.

Fig. 4.38 reports the concentration histories at the ten transducer locations for the millstone and limestone cores at mobility ratios of 3.1 and 3.4 respectively. The dips and kinks in Fig. 4.38 are more pronounced for the limestone histories than in their counterparts in the millstone. Fig. 4.39 shows the experimental fingered zone lengths for the curves in Fig. 4.38. Also shown are the fingered zone lengths for a displacement experiment at M = 2.2 in the limestone. The fingered zone lengths for the limestone core are consistently larger than their counterparts in the millstone core at comparable locations and mobility ratios. In fact, inspection of Fig. 4.39 indicates that the displacement experiment at M = 2.2 in the limestone exhibited larger fingered zone lengths for the further locations than the M = 3.1 experiment in the millstone.

Figs. 4.38 and 4.39 indicate clearly that the fingering is more severe in the limestone core. To examine the reasons for the differences between the cores, the particle-tracking simulator described in section 4.2.2 was used. We begin with an examination of fingering behavior in the relatively uniform millstone, and then turn to the more heterogeneous limestone.

Millstone

Based on the measurements of permeability distributions given in Fig. 4.30, simulations of the millstone core were performed with a homogeneous permeability field. The longitudinal dispersivity value used in the simulations was 0.05 cm. The simulations at mobility ratios of 3.1 and 13.5 are shown in Figs. 4.40, 4.41 and 4.42. These figures show that the concentration histories predicted by the simulation display trends similar to the corresponding experimental curves. The simulation is predictably more erratic in its dips and kinks, but overall the simulations reproduce the observations quite well.

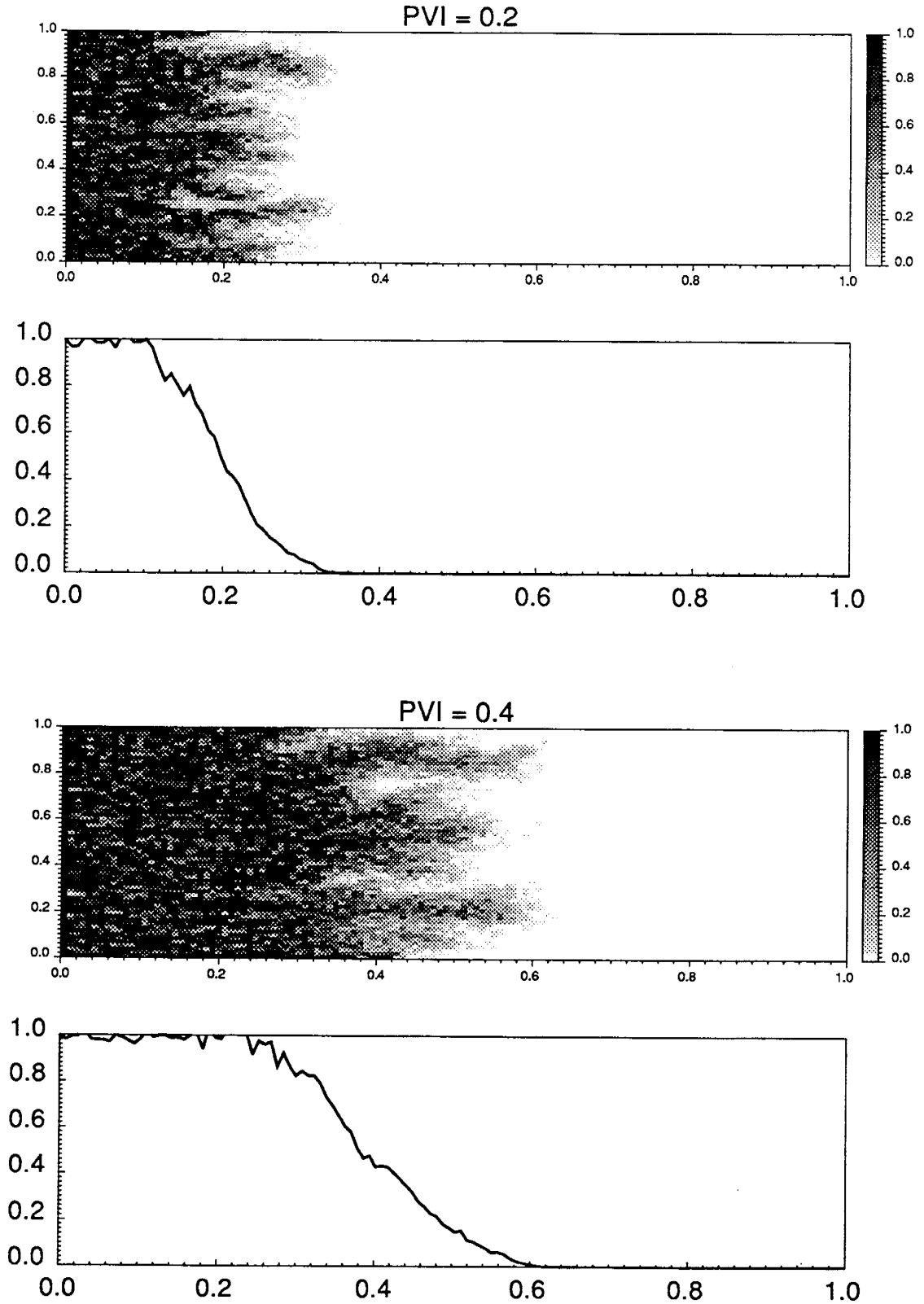

Figure 4.36: Concentration grayscale maps and transversely averaged concentration profiles at 0.2 and 0.4 PVI in a homogeneous medium for M = 3.1.

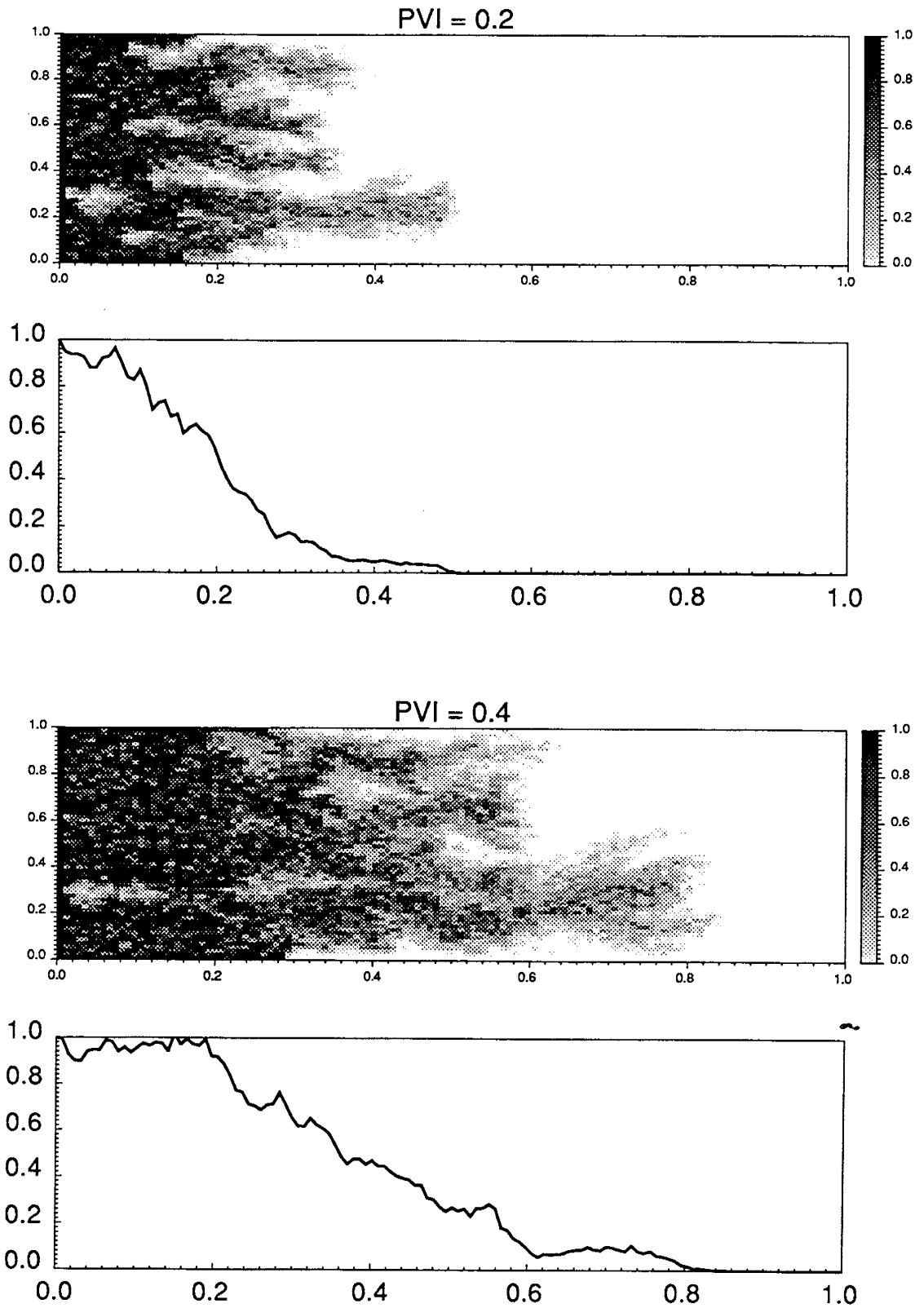

Figure 4.37: Concentration grayscale maps and transversely averaged concentration profiles at 0.2 and 0.4 PVI in a homogeneous medium for M = 13.5.

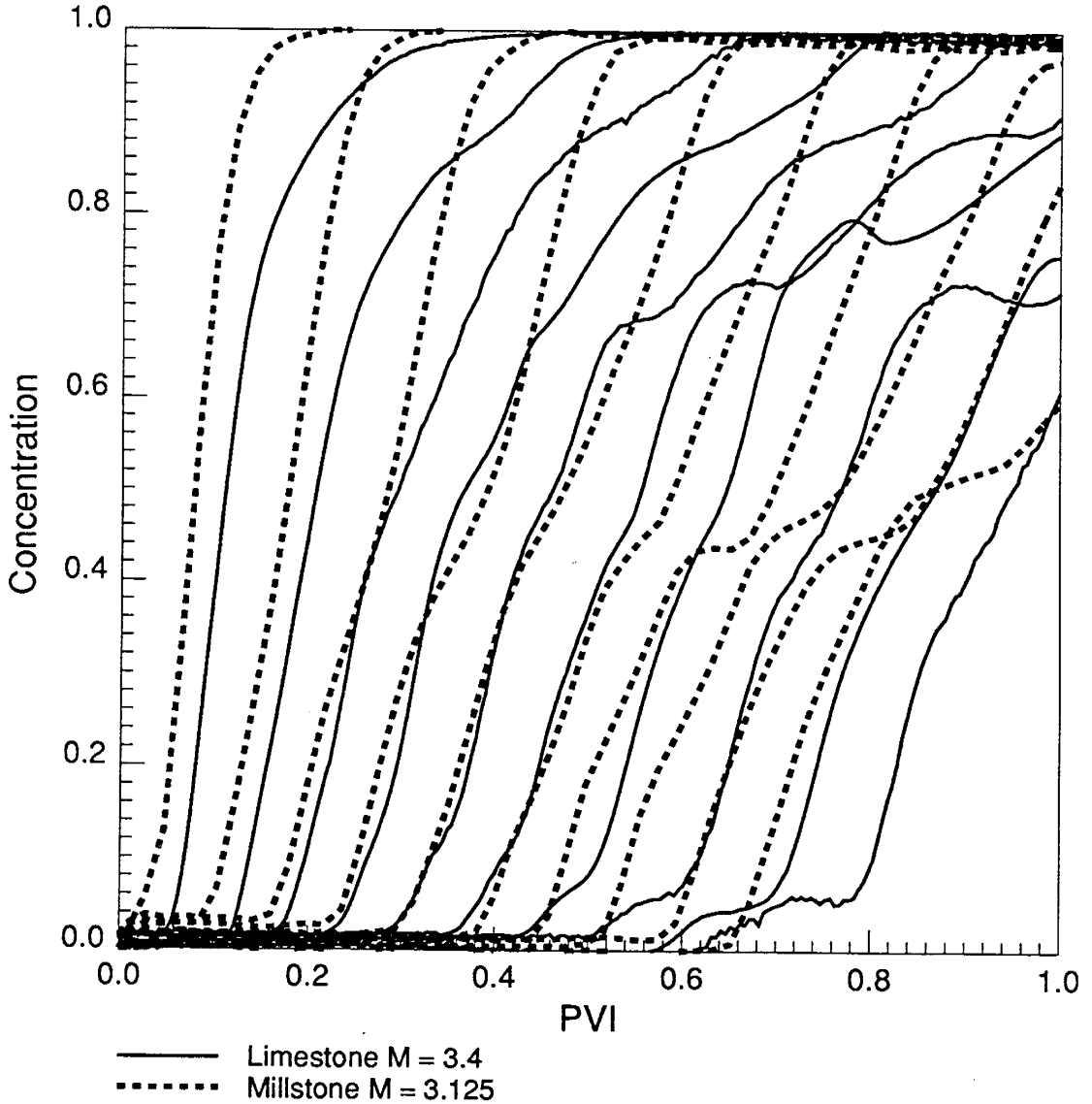

Figure 4.38: Experimental concentration histories at the ten locations for the millstone (M = 3.1) and limestone (M = 3.4) cores.

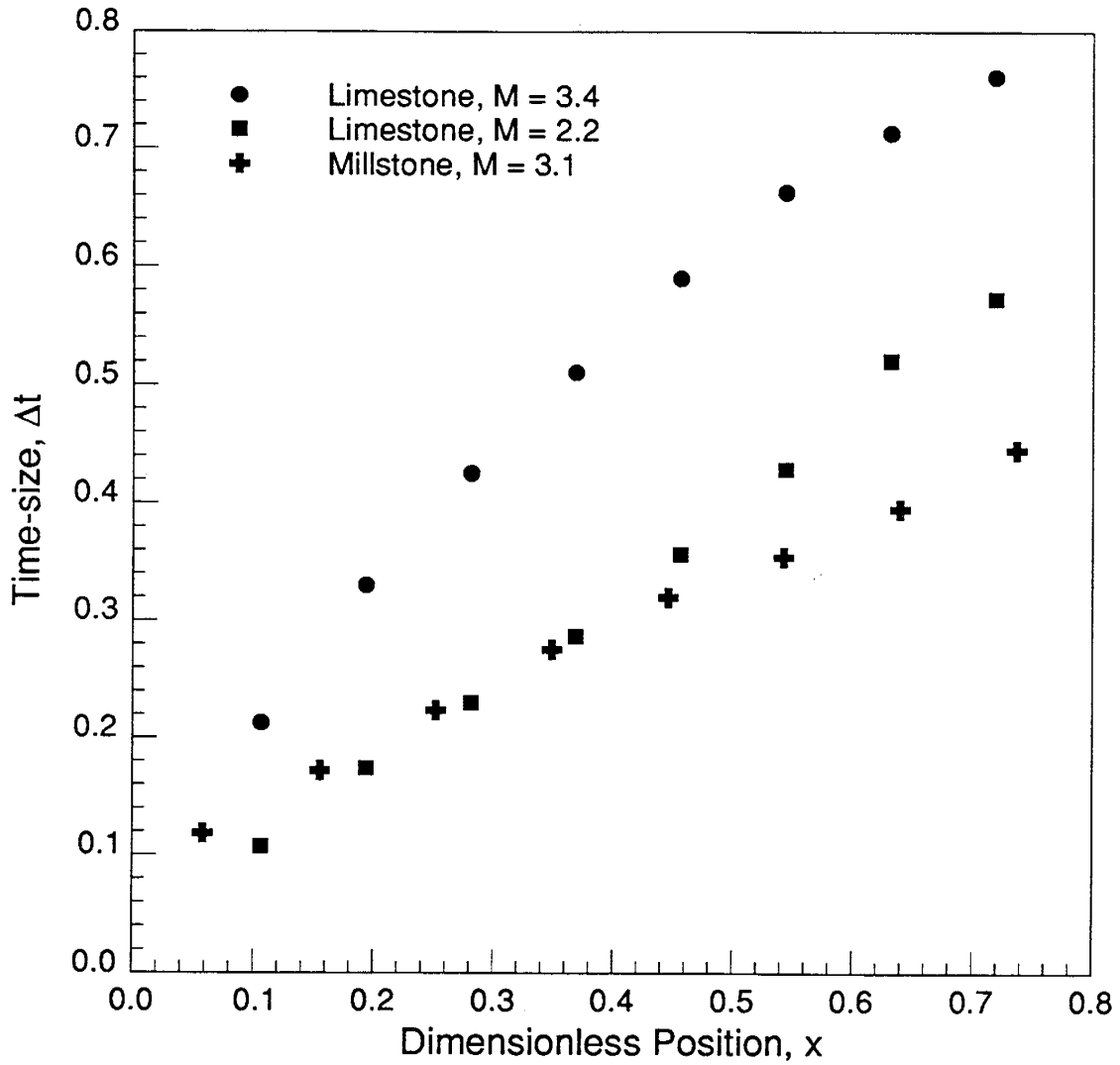

Figure 4.39: Fingered zone time-sizes from experimental concentration histories for limestone (M = 2.2 & 3.4), and millstone (M = 3.1).

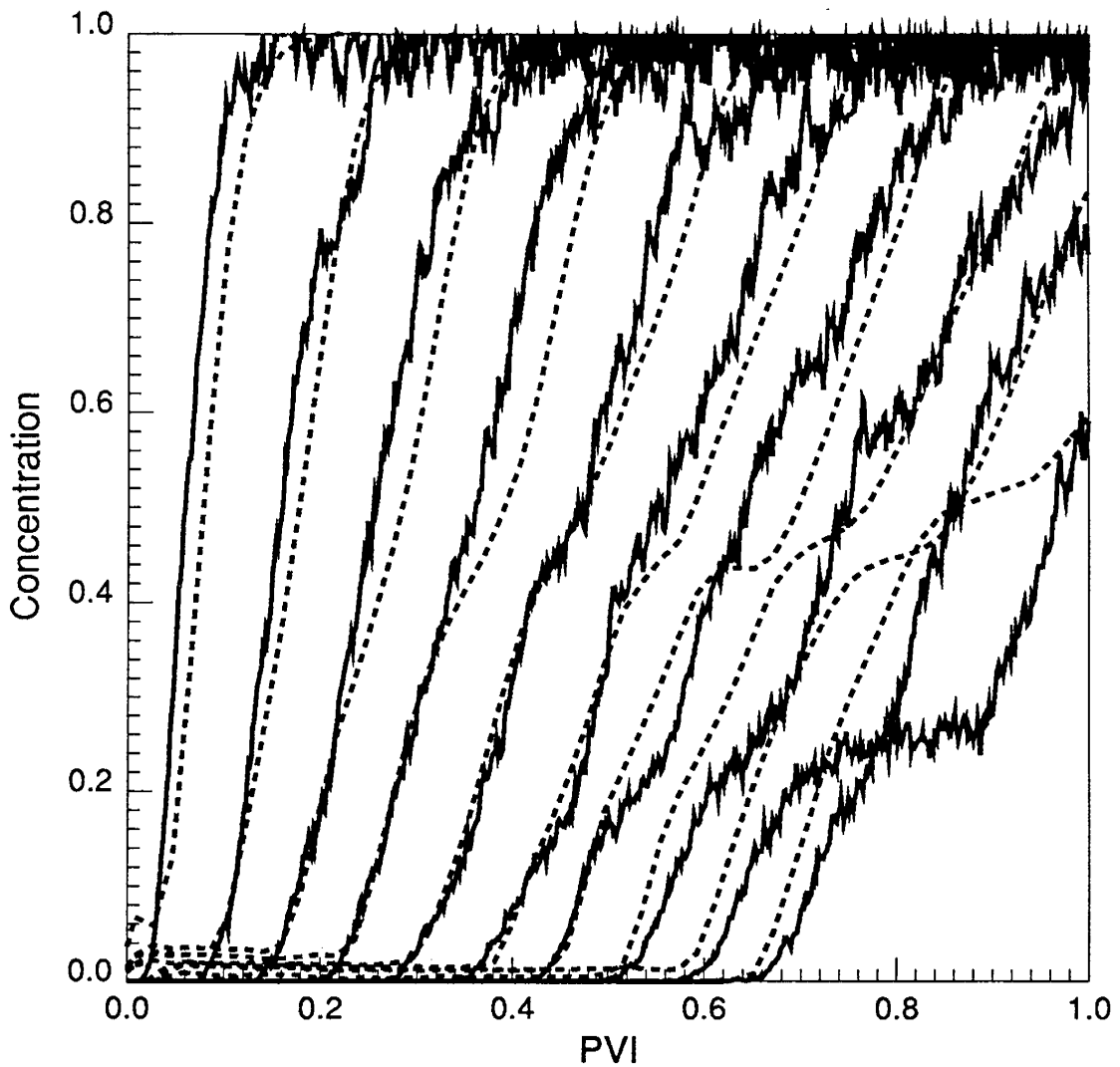

Figure 4.40: Millstone core. Experimental (dashed) and simulation (solid) concentration histories for M = 3.1.

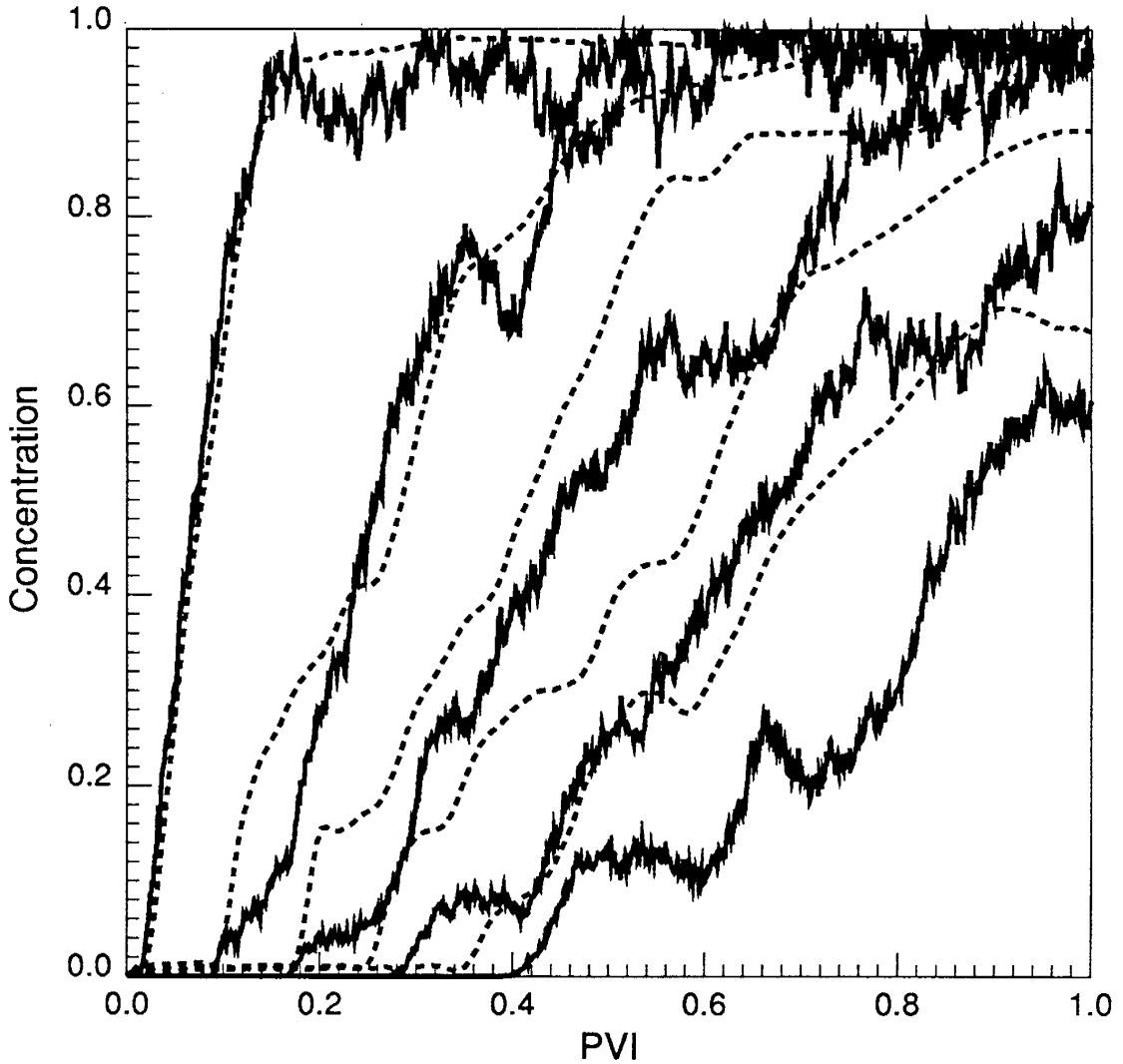

Figure 4.41: Millstone core. Experimental (dashed) and simulation (solid) concentration histories. for M = 13.5. Locations 1, 3, 5, 7, 9.

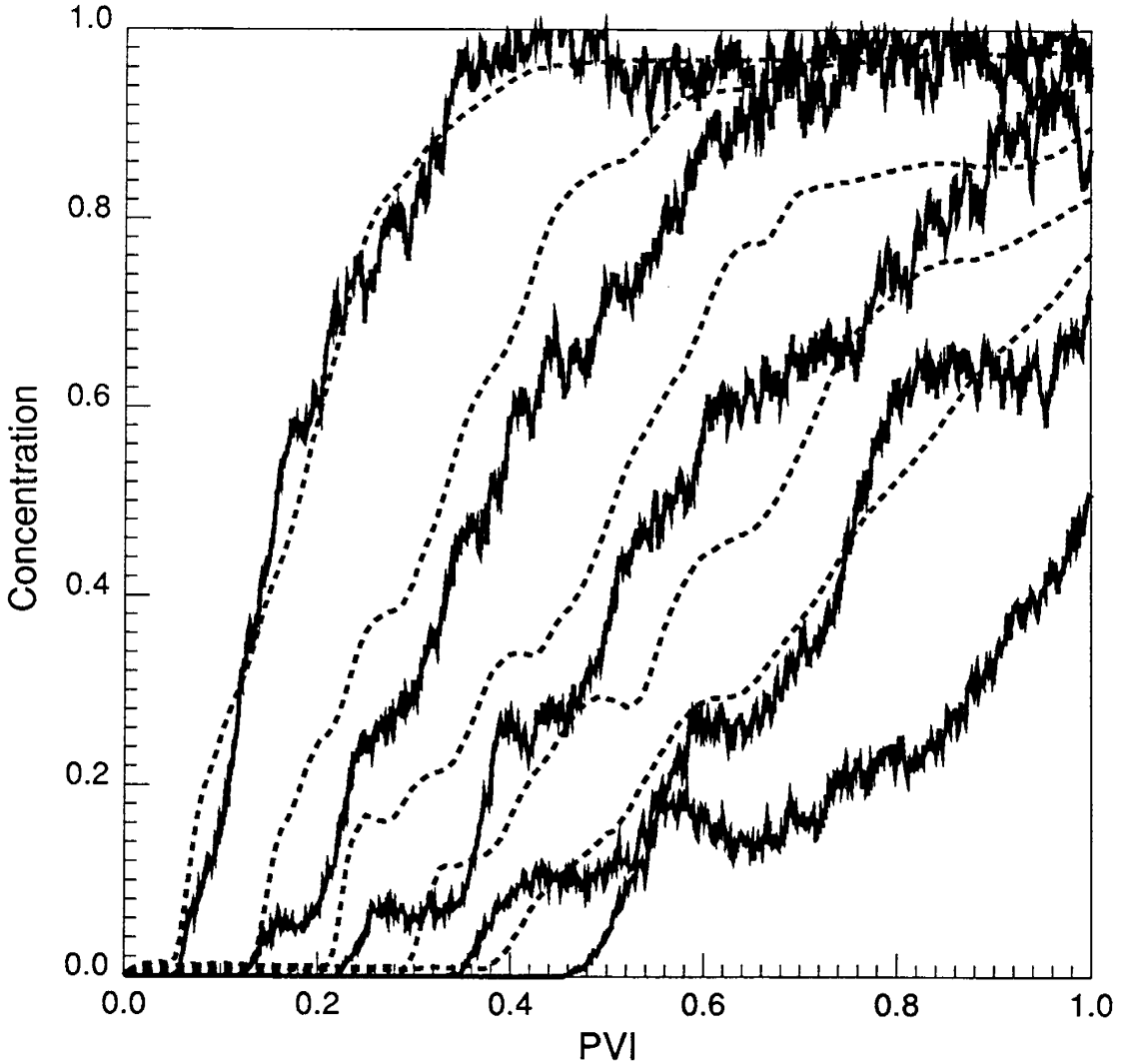

Figure 4.42: Millstone core. Experimental (dashed) and simulation (solid) concentration histories. for M = 13.5. Locations 2, 4, 6, 8, 10.

The key features of the experimental observations and the corresponding simulations as reflected by Figs. 4.40, 4.41 and 4.42, are:

1. The history curves for locations further along the core show more variability than the curves closer to the inlet, an indication of well-defined, large-scale fingers of varying length. The reason for that behavior is illustrated in Figs. 4.36 and 4.37, which show that fingering at the later time is more pronounced.

2. Fast concentration buildup of a history curve indicates well defined fingers of comparable size for the locations further from the inlet (late times). The snapshot at 0.4 PVI and the corresponding profile in Fig. 4.36 provide an example of such a case, since if the history at, say, $x = 0.6$ were recorded, the period just following $t = 0.4$ would appear as a fast buildup in the average concentration. Fast concentration buildup at locations close to the inlet indicates the arrival of a relatively uniform front.

3. Nearly constant concentrations point to regions where a few fingers (possibly one) of comparable size move ahead of the pack. For example, if two well defined fingers, where one is longer than the other, are propagating through the porous medium, the region of separation between their leading edges will be recorded at a particular location as a nearly constant concentration.

4. Concentration dips are more pronounced for long flow lengths and large mobility ratios. These dips occur mainly in regions behind the leading dominant fingers as smaller fingers twist and attempt to merge with the dominant flow paths. Concentration dips can also be recorded close to the leading edge as the dominant finger experiences a tip split. Tip-splits may be due to viscous instability (especially under isotropic dispersion conditions) [133] and/or low permeability streaks whose scales are smaller than the width of the dominant finger.

The displacement experiments in the millstone core incorporate the effects of fingering in three dimensions, but the simulations performed were two-dimensional. The quantitative agreement shown in Figs. 4.40 - 4.42 suggests that the two-dimensional simulation captures the essential features of the fingering behavior.

To examine the effect of the third dimension, a fine grid, three-dimensional simulation was performed with 128 X 64 X 64 grid blocks. Fig. 4.43 presents cross-sectionally averaged concentration histories at the ten locations from the three dimensional simulation of a displacement at M = 3.1 in a homogeneous medium (25.4 X 4.1 X 4.05 cm^3). The quantitative agreement between the two- and three-dimensional simulations is good. Thus, three-dimensional simulations also suggest that a two-dimensional calculation represents the essential features of fingering in a porous medium with modest, randomly distributed heterogeneities.

Christie [18] and Zimmerman and Homsy [159] provide results that also indicate no major differences in the average one dimensional concentration behavior between two and three dimensional fingering in homogeneous media.

In heterogeneous domains with significant correlation scales, however, the permeability variation and connectivity in the third dimension may influence the spatial distribution of mobility and, in turn, the fluid distribution in the flow domain, enough to alter the average and detailed character of the displacement. Three-dimensional modeling would then be

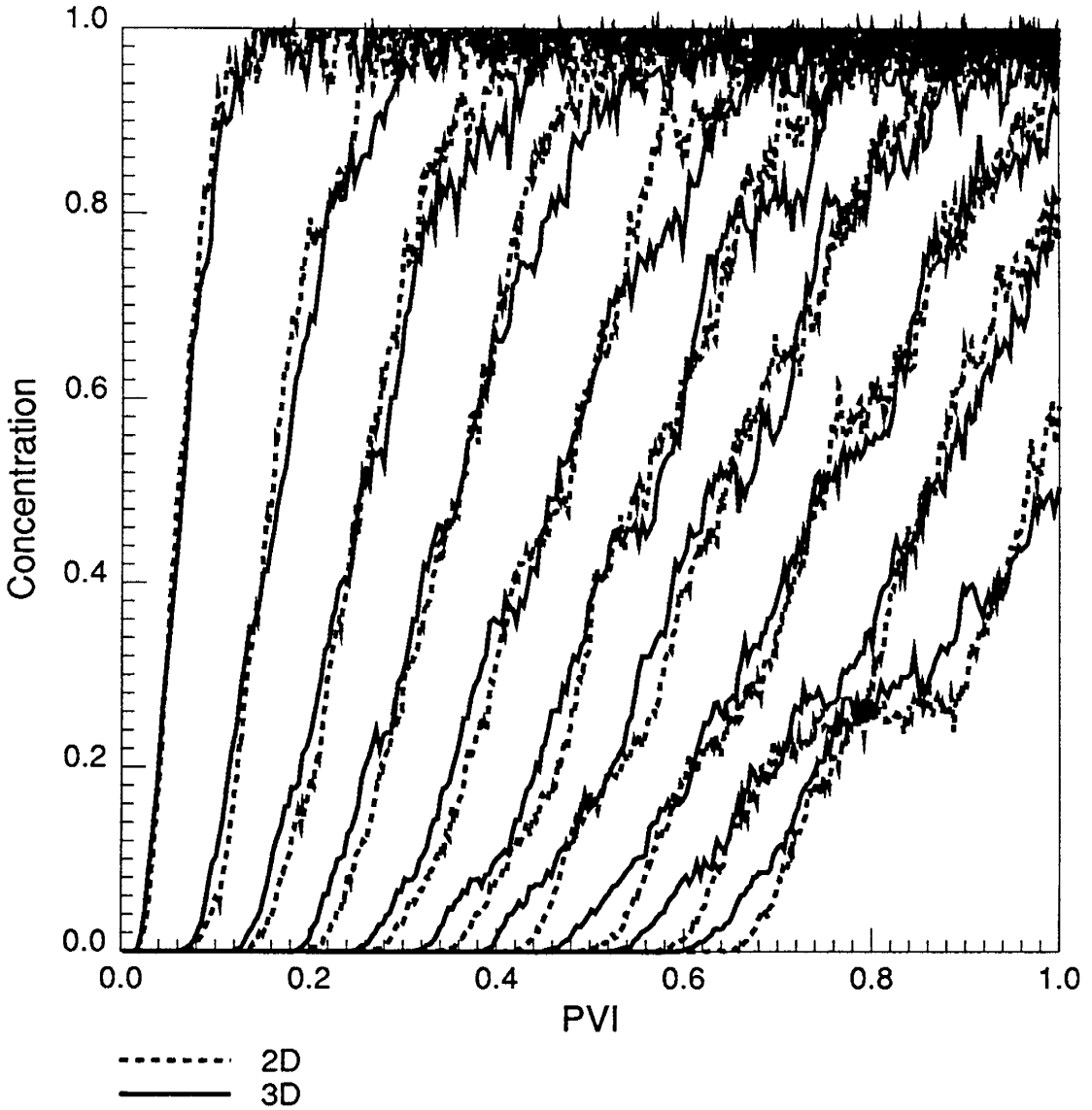

Figure 4.43: Concentration histories at 10 locations from 2D (dashed) and 3D (solid) simulations in a homogeneous medium at M =3.1.

necessary for simulations to reproduce experimental observations accurately. In such flow simulations, the relative orientation in space of the permeability correlation structure with respect to the mean direction of flow in the domain will play a significant role in unstable displacements. Three-dimensional modeling would also be required for homogeneous domains if density differences between the displacing and resident fluid exist and the mean direction of flow is not vertical.

Limestone

Fig. 4.44 reports concentration histories for the limestone core at five locations for three mobility ratios, 2.2, 3.4 and 12.5. At a particular location along the core, Fig. 4.44 clearly shows more variability and wider fingered zones as the mobility ratio increases. The curves at and beyond location 6 for M = 12.5 in Fig. 4.44 flatten at low concentration levels, an indication of severe bypassing.

The permeability distribution of Face 1 was used to simulate the displacement at a mobility ratio of 3.4. Fig. 4.45 compares the history curves from this simulation with the experimental curves at the five even locations for a mobility ratio of 3.4. Fig. 4.45 indicates that a two-dimensional simulation using the permeability distribution of Face 1 reproduces with reasonable accuracy the evolution and growth of the fingered zone the three-dimensional porous medium. Recall that for a particular mobility ratio, the variability of the history curves and the transition zone length were larger in the limestone than in the millstone (Figs. 4.38 and 4.39). The simulation reproduces the more rapid growth, as Fig. 4.45 demonstrates.

Fig. 4.46 shows two snapshots and profiles for the M = 3.4 simulation using the permeability distribution of Face 1. Large fingers completely dominate the flow, leading to more bypassed resident fluid. Contrast Fig. 4.46 with Figs. 4.36, a simulation in a homogeneous porous medium.

The agreement between the experimental observation and simulation in Fig. 4.45 indicates that permeability distribution of Face 1 represents reasonably well the average influence of the heterogeneity of the core on spreading of the transition zone. Given the complexity of the heterogeneity illustrated in Fig. 4.30, and the three dimensional nature of the core sample, the agreement shown in Fig. 4.45 is surprising. Numerical simulations for Face 1 at a variety of mobility ratios different from 3.4 also agree reasonably well with the experimental observations.

A final observation can be seen in Fig. 4.44, which indicates that the arrival times of the leading edge in Fig. 4.44 do not show a strong dependence on mobility ratio. This behavior is not matched in the simulations at the high end of mobility ratios. The details of the heterogeneity are probably responsible for this behavior.

Discussion

A frequently used measure of viscous fingering behavior is the growth rate of the length of the transition zone. Figs. 4.40-4.42 show that the agreement in the arrival times of the leading edge between the simulation and experiment is excellent. Because the transducers are evenly spaced, the difference in arrival times between two adjacent locations reflects changes in the velocity.

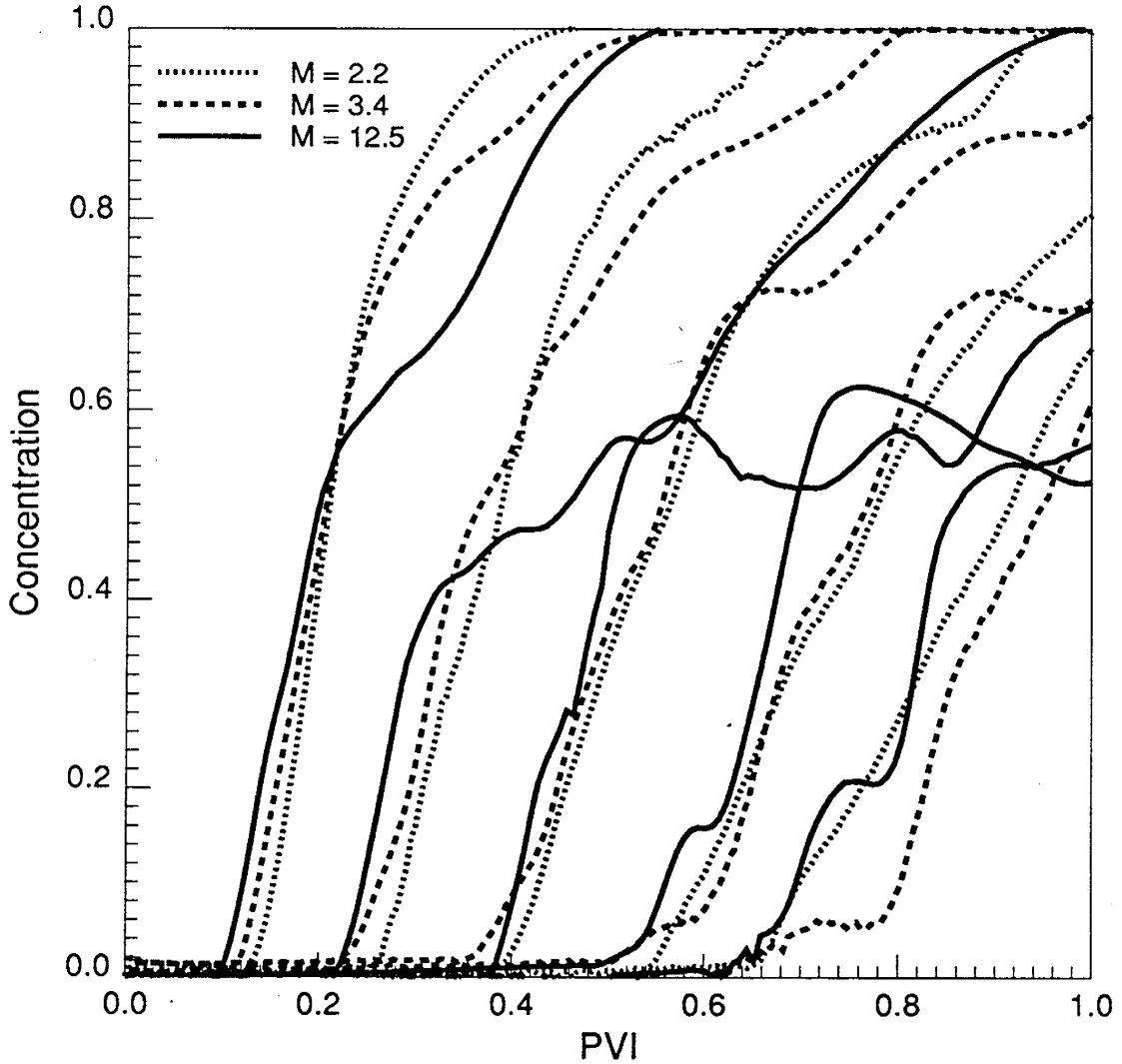

Figure 4.44: Experimental concentration histories at locations 2, 4, 6, 8, 10 in the limestone core at M = 2.2, 3.4 and 12.5.

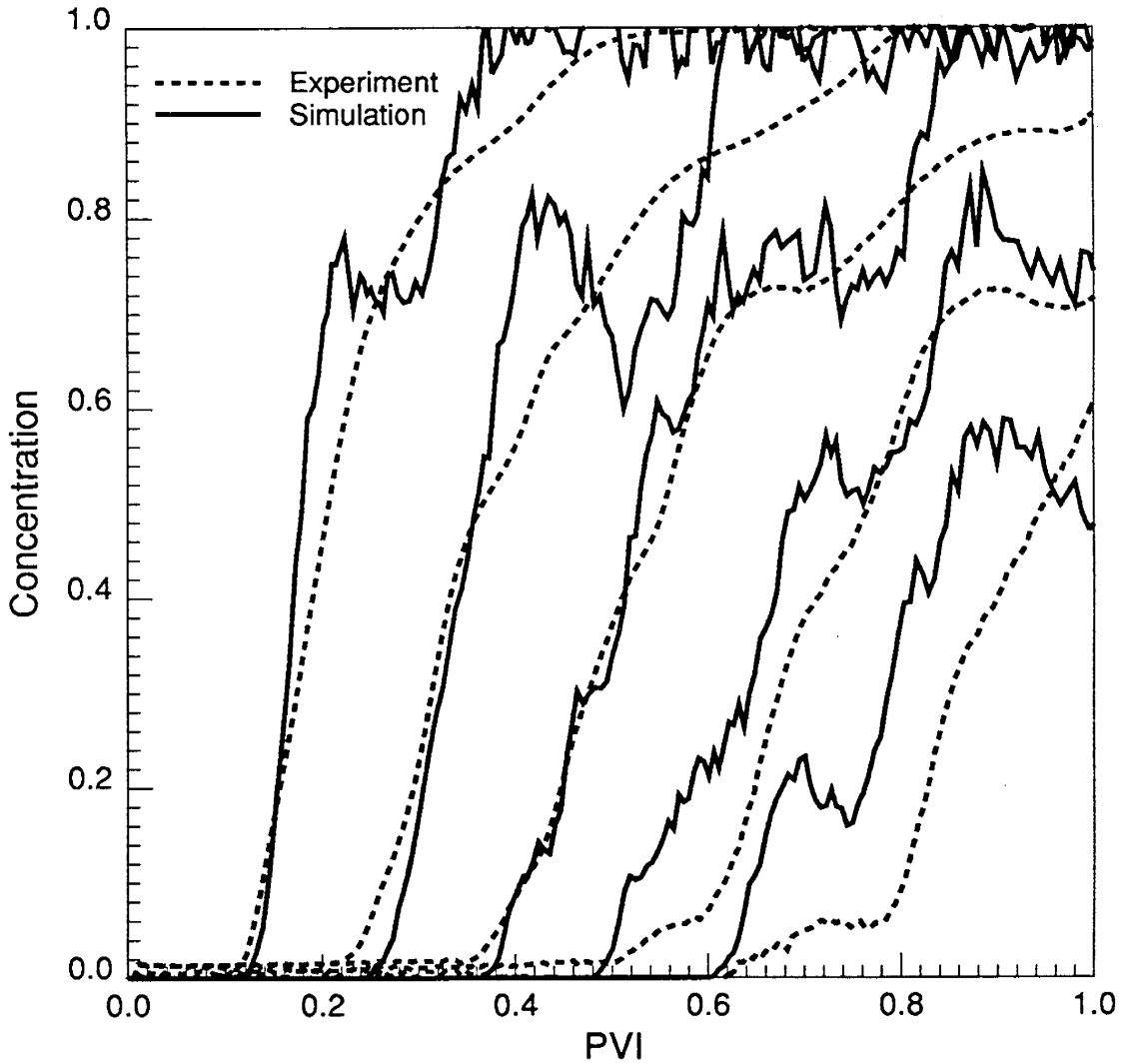

Figure 4.45: Limestone experimental concentration histories and Face 1 simulation at locations 2, 4, 6, 8, 10 for M = 3.4.

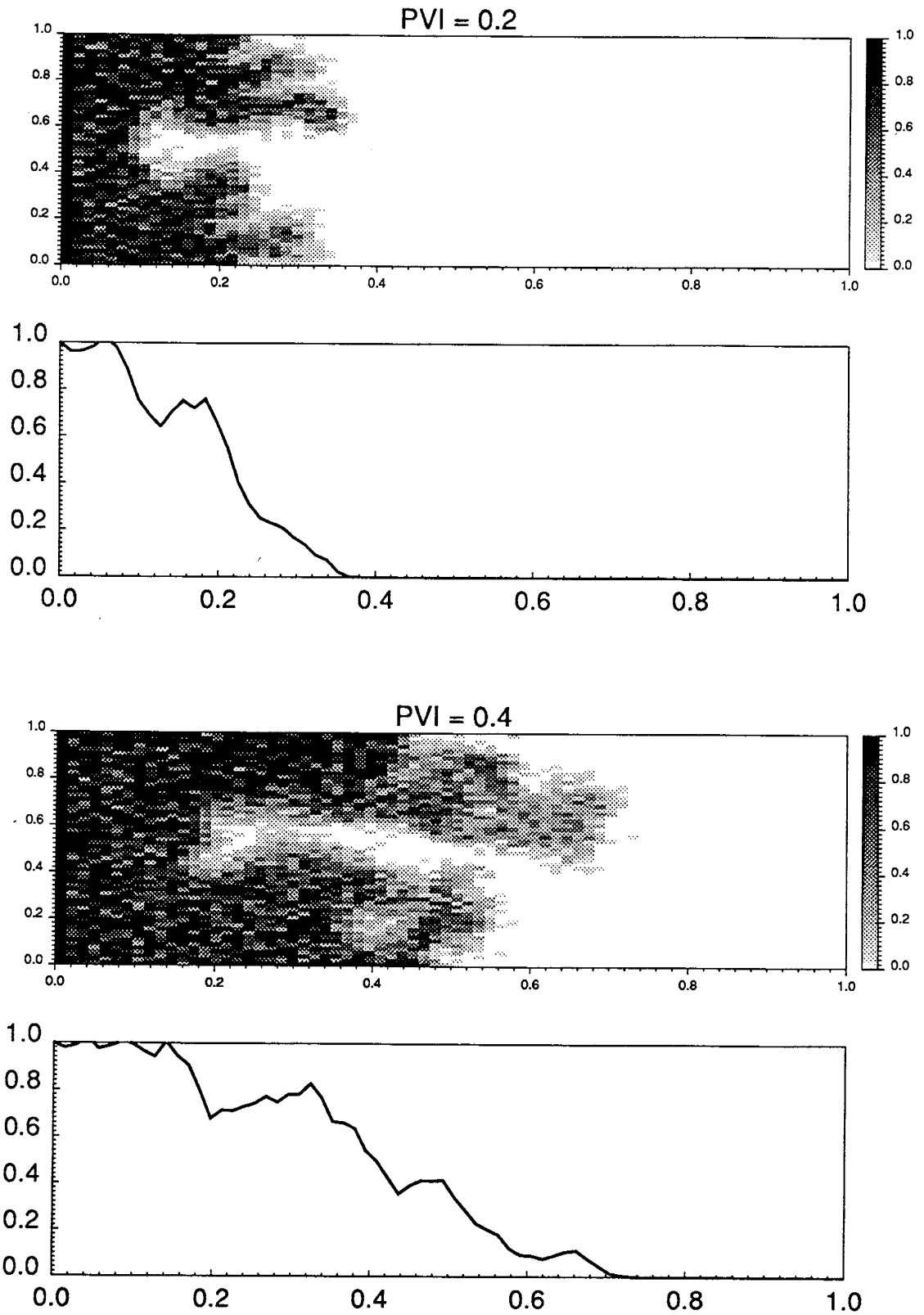

Figure 4.46: Concentration grayscale maps and transversely averaged concentration profiles at 0.2 and 0.4 PVI using Face 1 permeability distribution for M = 3.4.

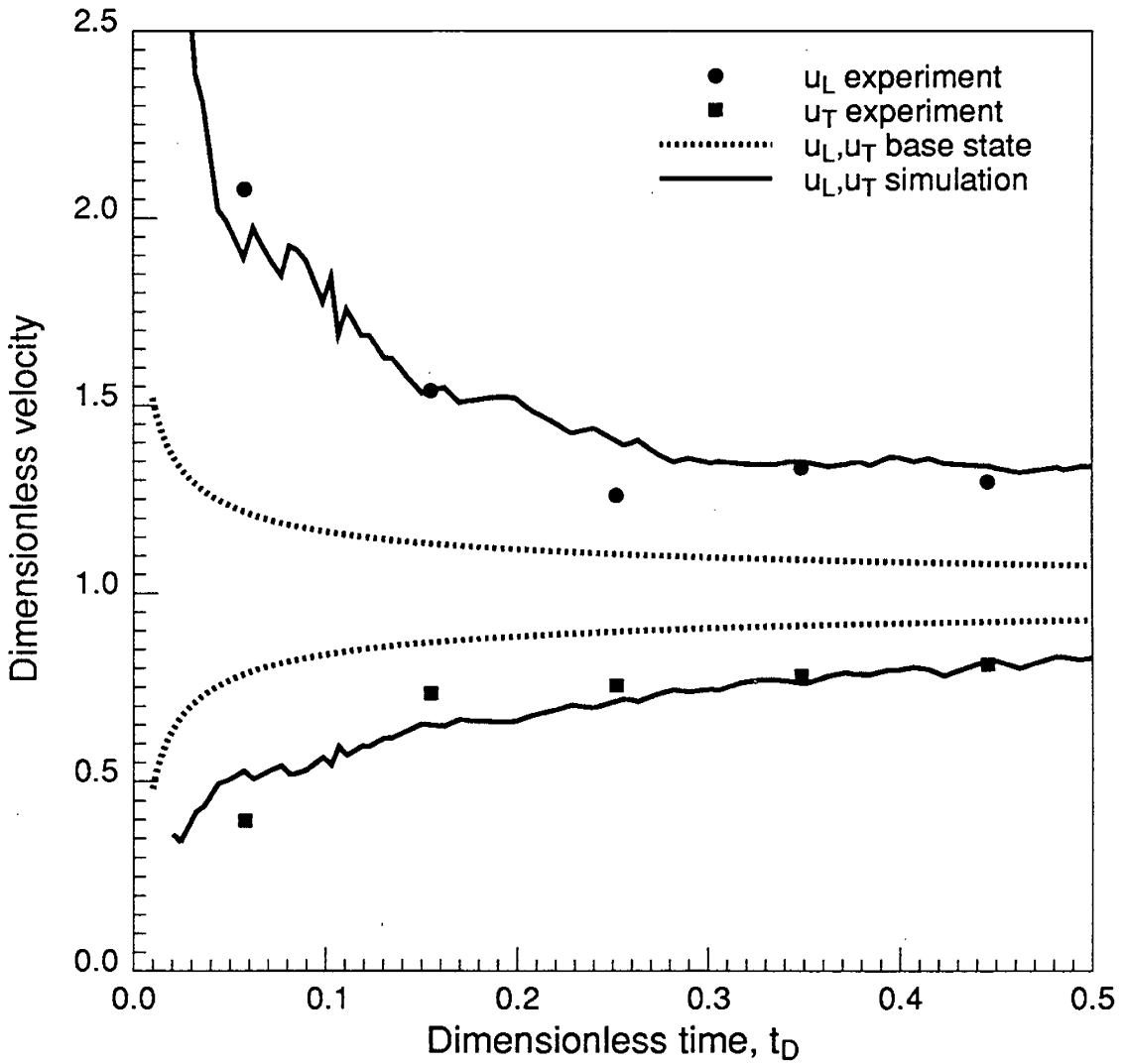

Figure 4.47: Leading (c = 5%) and trailing (c = 95%) edge velocities extracted from the millstone experimental curves and numerical simulations at M = 3.1. The corresponding base-state solution velocities are also shown.

For example, Fig. 4.47 shows the leading-edge and trailing-edge velocities, u_L and u_T, estimated from the millstone experimental curves and the numerical simulation for M = 3.1. For that case, u_L and u_T beyond the third location are nearly constant at 1.35 and 0.75 respectively. The experimental observations and simulation results of Figs. 4.40 and 4.47 indicate two regimes of flow: (1) An early time regime of fast but decreasing velocities of the leading concentrations, and slow but increasing velocities of the trailing concentrations, and (2) a subsequent regime, which persists thereafter, where tranversely averaged concentrations travel at nearly constant velocities. A third regime must exist for very long flow lengths in a sample of fixed width. In that regime, variations in local concentration in the transverse direction are negligible because diffusion, dispersion and viscous crossflow have reduced the concentration gradients to the point that wavelengths smaller than the core dimensions are no longer unstable. This third regime was not observed in the experiments or simulations. For the M = 3.1 displacement experiment in the millstone (Fig. 4.47), the flow length required for the crossover from the first to the second regime is about 5 cm or 20% of the total length. The first flow regime is also present in the simulations at M = 13.5; however, it was too small to be delineated conclusively. For the M = 13.5 case, u_L and u_T stabilized at 2.1 and 0.5 respectively.

As Fig. 4.47 also shows, the early rapid growth period is apparent in the particle-tracking simulations. However, linear stability theory and previously reported numerical simulations of fingering do not predict such rapid early growth. Thus, it is of interest to consider what physical mechanisms produce the rapid growth, why linear stability theory does not predict it, and why the simulations do.

The linear stability theory of Tan and Homsy [132] is based on a quasi-steady-state approximation (QSSA) with which the stability of a base state is tested. The base state is a solution to Eq. 4.3. Tan and Homsy obtained an expression for the exponential growth rate of an initial disturbance which indicated that perturbations with wavelength larger than a cutoff grow fastest when the concentration gradient is steepest. Thus, the fastest growth occurs at time zero. At later times, dispersion spreads the transition zone, the most unstable wavelength increases, and the growth rate decreases. Thus, the linear theory is consistent with a decreasing growth rate, but the magnitude of the growth rate predicted by Tan and Homsy [132] is much too small to explain the initial growth rate shown in Fig. 4.47. In fact, to be consistent with the linear theory, the perturbation velocities would require amplitudes larger than the length of the transition zone, which clearly violates the assumptions of the theory. Yortsos and Zeybek [154] also used the QSSA and included in their analysis the dependence of the local dispersion coefficient on the local flow velocity. While their analysis leads to slightly larger growth rates, the difference is still insufficient to explain the observations in Fig. 4.47. Thus, we conclude that the flow conditions in the initial rapid growth period were not consistent with the assumptions of linear stability theory, and therefore that nonlinear fingering phenomena were responsible for the observed behavior.

Another approach was taken by Tan and Homsy [133] and Zimmerman and Homsy [158], who used a spectral representation to obtain high accuracy numerical simulations of unstable displacements well past the initiation period. They also discerned two regimes of flow: (1) an initial period in which the transition zone grew as the square root of the distance travelled followed by (2) an extended period where the transition zone stretched linearly.

Zimmerman and Homsy [158] noted that the length of the initial "diffusive" period

depended on the amplitude of the initial concentration disturbances. When that amplitude was sufficiently large, no "diffusive" regime was observed. Furthermore, the length of time (or distance) required for macroscopic fingers to develop also depended on the level of transverse dispersion. Fig. 4.48 shows the positions of the 20% concentration contour for a displacement at M = 5 at two times (0.05 and 0.1 PVI) for three dispersivities. It is clear that macroscopically visible fingerlets appear early for the smaller dispersion levels. Evidently, the combination of low dispersivity with the perturbations introduced at each time step in the particle-tracking simulations, which are scaled by the dispersivity to represent the magnitude of the local velocity fluctuations, was sufficient to make any initially "diffusive" growth regime very short. Apparently, those perturbations are also more or less consistent with the amplitudes of perturbations that initiated fingers in the experiments. We argue that the reduction in the growth rate of the transition zone leading to the second regime was the result of the interplay of dispersive mixing with nonlinear crossflow phenomena. At the beginning of a displacement, a steep concentration gradient along with significant velocity fluctuations initiates fingering via the instabilities described by Tan and Homsy [132] and Yortsos and Zeybek [154]. As fingers develop, mixing that results from viscous crossflow illustrated in Fig. 4.35 and dispersion moderates the viscosity contrasts at finger boundaries. Because the rate of advance of a fluid front (leading or trailing edge) depends on the viscosity contrast, the velocities of leading edges decrease, while those of the trailing edge increase. At later times, fingers become larger and fewer, the mixing around the boundaries of fingers changes much less rapidly, and the leading and trailing edges travel at nearly constant speeds, leading to the second regime.

Clear experimental evidence for this linear growth was presented by Benham and Slobod [10] and Perkins et. al. [104]. Handy, as reported by Dougherty [29], Scott and Read [119] and Perrine [106] made the specific observation that transversely averaged injected fluid concentrations appear to move at nearly constant speeds. As a result, empirical models based on a one-dimensional hyperbolic conservation equation appeared [63, 29, 136, 35].

For a fixed mobility ratio, the flow length required to reach the stable growth of the mixing zone is independent of the system length due to the lack of influence of the outlet boundary on the local behavior of the instability [134]. As a result, the flow length required for the crossover from the first to the second regime becomes a smaller fraction of the length of the domain. If the second regime, once established, persists throughout the displacement in a long domain, the first regime could be neglected and empirical models will succeed in describing the average flow behavior.

The first regime was observed for M = 1.75 in the limestone core, but was not detected in the experimental curves or simulations for M $\geq$ 2.2 in the limestone. The growth rates of the transition zone were nearly constant, and the displacements for M $\geq$ 2.2 showed approximately linear growth throughout their histories. However, deviations in the growth rates, especially late in the displacement, were observed. Such variations reflect the influence of locally preferred permeability paths that established fingers move quickly to invade.

We postulate that the reason the first regime appeared at M = 1.75 and was absent at higher mobility ratios is the interaction of heterogeneity and mobility ratio at early time. The diffusive scales of wavelengths growing initially cannot compete with the perturbations due to the permeability distribution near the inlet. Thus, fingers get established more quickly and the first regime would be observed only if the mobility ratio (level of instability) were not too large.

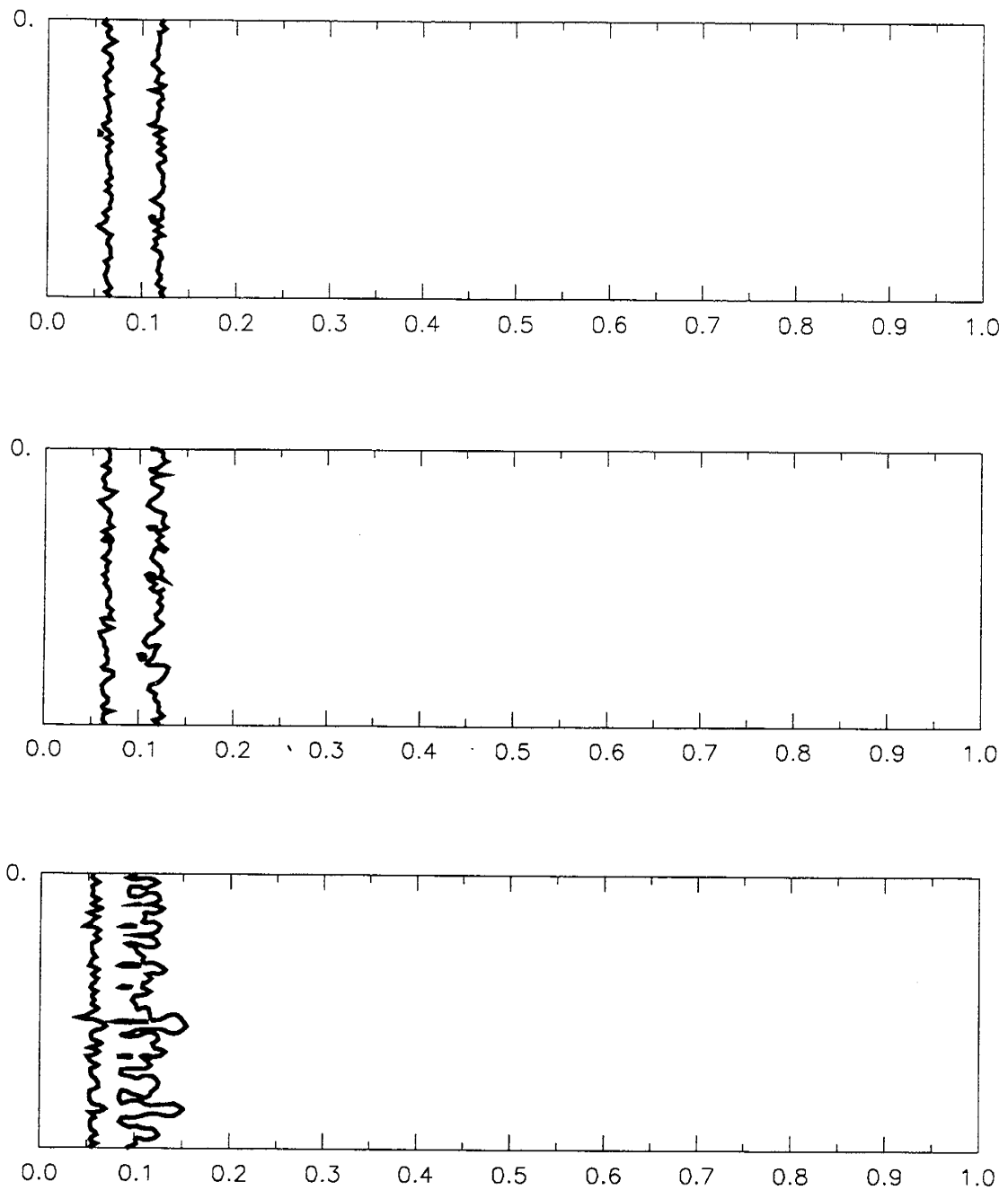

Figure 4.48: 20% concentration contour at PVI = 0.05 and 0.10 for a dispersion anisotropy 20. M = 5. α_L (cm) = 0.10 (top), 0.075 (middle), 0.05 (bottom)

4.2.5 Conclusions

The experimental observations and numerical simulations of stable and unstable displacement experiments in millstone and limestone cores indicate that:

1. Convective crossflow reduces the size of the transition zone during super stable (M < 1) displacements in heterogeneous porous media with significant correlation length scales. As a result, apparent dispersivity values decrease as the mobility ratio decreases below unity. The limiting value of α_L is the microscopic value reflecting the pore length scale.

2. Fine grid two-dimensional random-walk particle-tracking simulations of unstable displacements in the millstone core, which exhibited random heterogeneity, represent with reasonable accuracy the scale, size and growth of the viscous fingers. Two-dimensional simulations show reasonable agreement with experimental observations of three dimensional unstable flow in homogeneous and randomly heterogeneous media and with three-dimensional simulations.

3. Two regimes of flow are observed for unstable displacements in homogeneous and randomly heterogeneous porous media. The first is an early time regime of fast frontal velocities. The second, which persisted once established, is the regime where concentration velocities reach nearly constant values. The flow length required to reach the crossover from the first to the second regime was about 20% of the domain length.

4. The observed experimental differences between the millstone and limestone cores were due to the heterogeneity of the limestone.

5. In three-dimensional heterogeneous media with significant correlation lengths, a detailed description of the permeability field is required for accurate prediction of fingering behavior. If such a description is available, the particle-tracking technique can be used to make quantitative predictions of displacement behavior.

4.3 Summary

In this chapter results of particle-tracking simulations to investigate the behavior of viscous fingering in linear flow are reported. The experiments of Section 4.1 demonstrate conclusively that there is, in fact, a transition from fingering dominated by viscous forces in nearly homogeneous porous media to flow dominated by the spatial distribution of permeability when there is sufficient spatial correlation of high and low permeability. Thus, the experiments confirm the theoretical predictions of Araktingi and Orr [2] and Waggoner and Lake [145]. In addition, excellent agreement was observed between predictions of fingering behavior made with a particle-tracking simulator and the spatial patterns of fingering in heterogeneous porous media. That agreement did not require any adjustment of parameters or history matching. Hence, we conclude that the particle-tracking simulator represents the physics of fingering in heterogeneous porous media with good accuracy. Hence, such a simulator can be used with confidence to examine the scaling behavior of viscous fingering in such porous media.

The experiments of Section 4.1 also demonstrate that a modest permeability variation, only four to one, is sufficient to organize fingering patterns even when the correlation length

is also modest. Permeabilities in reservoir rocks frequently vary by much more than a factor of four, of course. Hence, it is likely that field-scale flows will be dominated by the permeability distribution. That conclusion has important implications for the design of reservoir simulators. It suggests that it will be more important to represent permeability variations than to attempt to resolve the details of the viscous instability.

The interplay of dispersion, heterogeneity and viscous forces was examined for real porous media in Section 4.2. The particle-tracking simulation approach was used there to interpret an extensive set of displacement experiments. The simulations demonstrate that the interplay of heterogeneity and crossflow can lead to an apparent dependence of dispersivity on mobility ratio. In addition, the simulations confirm directly the effects of greater heterogeneity in a limestone core sample than in a sandstone sample. That heterogeneity leads to significantly faster growth of the transition zone in unstable miscible displacements. The combination of experimental observations and interpretations demonstrates again the power of the particle-tracking simulation approach.

5. Crossflow: Effects of Gravity, Capillary and Viscous Forces in Heterogeneous Porous Media

In this chapter, we examine the interplay of forces that drive flow between zones with differing permeability. Consider, for example, a nearly miscible flood in a system with two layers. Because the displacement is not quite miscible, two-phase flow occurs. The displacement proceeds more rapidly in the high permeability layer. Thus, the permeability difference creates differences in composition and saturation between the two layers. Those differences lead to crossflow. Differences in mobility induce viscous crossflow. Differences in phase density cause gravity segregation of the phases. Differences in saturation cause capillary-pressure differences that also drive crossflow, and composition variations will induce interfacial tension (IFT) gradients that contribute to that crossflow. Diffusion and dispersion will also contribute to transverse mixing. Because all the crossflow mechanisms will mix fluids of different compositions, the development of miscibility, described in detail for one-dimensional flow in Chapter 3, will also be affected. Thus, understanding of the scaling of crossflow is of considerable importance to the description of miscible flood performance.

In Section 5.1 we examine the combined effects of gravity and capillary crossflow. Results of experiments with equilibrated phases are reported, as are results for crossflow in systems with IFT gradients. We show that as IFT is reduced to modestly low levels (10^{-1} mN/m), there is a transition to gravity-dominated flow that produces very high displacement efficiency. In Section 5.2 we report results of flow visualization experiments that illustrate the scaling of the interaction of heterogeneity, dispersion, and gravity-driven crossflow. In addition, simple, limiting-case analyses of the flows described in Sections 5.1 and 5.2 are also given. The combination of experimental and theoretical results presented, therefore, provides a foundation for understanding of the complex interactions of phase equilibrium, viscous instability, and crossflow in heterogeneous reservoirs.

5.1 Capillary Imbibition and Gravity Drainage in Low IFT Systems

David S. Schechter

CO_2 is an excellent solvent for some components of a crude oil if the pressure is near the minimum miscibility pressure (MMP), as the experimental results of Chapter 2 show. Slim tube displacement results indicate that crude oil is efficiently displaced by CO_2 at pressures near the MMP. In a reservoir displacement setting, however, some nonuniform flow is inevitable. Viscous instabilities will cause bypassing of some oil, and spatial variabilty in permeability will affect significantly the arrival time of the injected gas at the production wells. The high mobility of CO_2 in comparison with oil in the reservoir will cause the injected gas to flow rapidly through any high permeabilty channels in heterogeneous reservoirs, possibly leaving a significant portion of the oil saturated zone uncontacted. The extreme of

this situation is a fractured reservoir in which very high permeability fractures coexist with low permeability matrix blocks. Thus, "miscible" gas injection into a fractured reservoir has been largely ignored as a process option due to the fear that the injected gas would flow primarily through the high permeability fracture network and breakthrough rapidly to the production wells. Subsequent production would then require a large amount of recycled gas to recover the cost.

In this section we examine how gas injection processes might be used effectively in fractured reservoirs. The key idea is to promote effective gravity drainage from the rock matrix. We argue that if sufficient vertical communication exists, ideally in the form of vertically oriented fractures, the low IFT's created as the injected CO_2 extracts hydrocarbons from the crude oil can allow efficient gravity drainage to occur from matrix blocks, if the matrix blocks are of height large enough for the hydrostatic pressure to overcome the drainage capillary pressure threshold.

In the following sections, we review imbibition and drainage literature, present experimental results, and discuss the important points of rate and final recovery for the various flow regimes.

5.1.1 Literature Review

Imbibition

Imbibition has been long recognized as an important recovery mechanism during waterflooding of a fractured reservoir in which the matrix is water wet. The high capillary pressure associated with oil and water in porous media results in spontaneous imbibition of water into the oil saturated matrix. Conventional wisdom has led researchers to believe that lowering the IFT would be unprofitable since by doing so both the gravity and capillary forces which provide the mechanism for fluid exchange would decrease, thereby reducing the recovery rates and ultimately, the amount recovered.

Mattax and Kyte [78] , for example, reported results of experiments performed with oil and water having a large value of IFT. They showed that the time dependence of recovery depends on the matrix geometry and physical properties of the fluids. It was argued that for a given rock type (k,ϕ), block size (L^2) and fluid properties (μ_w, μ_o, σ), the time scale for imbibition is given by

$$t_d = t\sqrt{\frac{k}{\phi}}\left[\frac{\sigma}{\mu_w L^2}\right] \tag{5.1}$$

According to the scaling implied by Eq. 5.1, displacements in which values of t_d are equal should show equivalent recovery. A key assumption for this scaling relation is that the flow is governed by capillary forces and that gravity forces are negligible. According to Eq. 5.1, if the IFT (σ) is reduced, the time required to recover a given fraction of the oil increases. Hence, recovery rate decreases with IFT when capillary imbibition dominates the flow. This perception has been the reason that so few investigations have considered the effects of lowering the IFT between the imbibing and displaced phase. Also, imbibition experiments have typically been performed on small core samples in which the effects of gravity were purposefully kept negligible. In a reservoir, of course, it is likely that a combination of

capillary, gravity and viscous forces will interact to determine the flow characteristics of a given situation.

An experimental investigation of the effect of changes in IFT was reported by Cuiec et al.[24] for imbibition in low permeability chalk samples. They found that lowering the IFT (by addition of alcohol) between the imbibing brine phase and the oil phase in the chalk sample reduced the rate of oil recovery, in accordance with the scaling theory of Eq. 5.1. However, their experiments were performed on small samples with permeabilities between 1 and 3 md.

Du Prey [32] conducted the most extensive investigation into scaling the capillary and gravity forces during imbibition. The centrifuge was used to increase the gravitational force artificially. This method has been used widely for both drainage and imbibition experiments to reduce the long times required to reach equilibrium in larger core samples.

The controlling dimensionless group used to correlate du Prey's data was the capillary to gravity ratio[1] defined as

$$\pi_3 = \frac{P_{ct}}{\Delta\rho g h} \tag{5.2}$$

where P_{ct} is the displacement capillary pressure, and $\Delta\rho$gh is the gravitational potential. If the value of π_3 were small (gravity effects significant compared to capillary forces), the recovery curves should superimpose or scale if the reference time (dimensionless time required to recover a given fraction of the oil) is scaled in relation to gravity as

$$t_g = \frac{h\phi\Delta S\mu_o}{\Delta\rho g k_{omax}} \tag{5.3}$$

where h is the height of the block, ϕ is the porosity, ΔS is the difference between the initial and final oil saturation, μ_o is the oil phase viscosity and k_{omax} is the maximum relative permeability of the oil phase. If imbibition is capillary dominated, the reference time may be defined as

$$t_c = \frac{h^2\phi\Delta S\mu_o}{\Delta\rho g k_{omax}} \tag{5.4}$$

Du Prey noted that large blocks will have a low value of π_3 but dismissed this method of reducing π_3 due to the experimental difficulty involved. π_3 may also be decreased by lowering the capillary pressure between the fluids or artificially increasing the acceleration due to gravity with the centrifuge. Du Prey chose the latter method because centrifugation "cannot lead to changes in wettability." In summary, du Prey's interpretation of the experiments on small samples, used to predict behavior of imbibition in large fractured blocks demonstrated that

1. For small block sizes, capillarity is the dominant force and recovery time is proportional to the square of the block size,

2. For large blocks, gravity becomes the dominant force and recovery becomes proportional the the size of the block,

[1] In the text that follows, we will denote the capillary to gravity ratio as the inverse Bond Number, N_B^{-1}

3. For small samples of identical size subjected to centrifugation, theoretical predictions match recovery behavior, but

4. It was noticed that at high centrifugation speeds, experiment and theory no longer were in accordance.

In the capillary-dominated region the recovery times were in good agreement with Eq. 5.4. and scaled according to h^2. However, at low values of capillary to gravity ratio, scaling was not in good agreement with Eq. 5.3. Du Prey warned that scaling up to large blocks from centrifuge experiments may not be valid due to the high rates of centrifugation required to obtain low values of π_3.

Drainage

Almost all drainage experiments in the literature have been conducted in the forced manner. That is, the nonwetting phase was injected at some pressure above the capillary threshold pressure in order to force the nonwetting phase into the porous medium. If the capillary threshold is lowered sufficiently the gravitational pressure difference of the fluid in the fracture can exceed the entry pressure and "free-fall" drainage will occur until capillary-gravity equilibrium is established.

Jacquin et. al [52] investigated free fall drainage with gas/oil systems not in equilibrium, and Nectoux [87] performed drainage experiments with crude oil. Pavone et al. [101] conducted low IFT gravity drainage experiments in long core samples. Initially, the oil phase drained rapidly when the saturation of the gas phase was still low. As the gas saturation increased, there was a sharp break in the drainage recovery curve in which 20% of the oil recovered continued to drain, but at a much slower rate. The rapid initial recovery was attributed to bulk flow as the larger pores emptied. The breakpoint and slow drainage occuring over a lengthy period was interpreted as film flow. During the course of their experiments, the IFT was kept constant between the gas and oil phases at 0.53 mN/m. The amount of connate water was varied to investigate the effect of water saturation on drainage efficiency. The slope of the recovery curve decreased as the amount of connate water increased, an indication that increasing amounts of connate water slowed film drainage. Gravity drainage in this case may be highly efficient in the ultimate recovery of the oil phase. Residual oil saturations as low as 3% have been measured in the presence of connate water during gravity drainage experiments [30].

Capillary and Gravity Desaturation

Capillary desaturation has been measured in many laboratories. Chatzis and Morrow [16] provide the most comprehensive desaturation data for both continuous and trapped oil. Usually such experiments are conducted on horizontally oriented core samples, and the effects of gravity are neglected. The capillary desaturation curve (CDC) graphically demonstrates the capillary number, ($N_c = \frac{v\mu}{\sigma}$), required to reduce the residual saturation from high IFT values of 30-40% to values near zero at ultra-low IFT's. For most core samples, desaturation begins at capillary numbers in the neighborhood of 10^{-4} and is complete for values near 10^{-2} [69].

The addition of gravitational forces can reduce the residual saturation further. For example, Foulser et al.[37] showed that changing the orientation of a core from horizontal

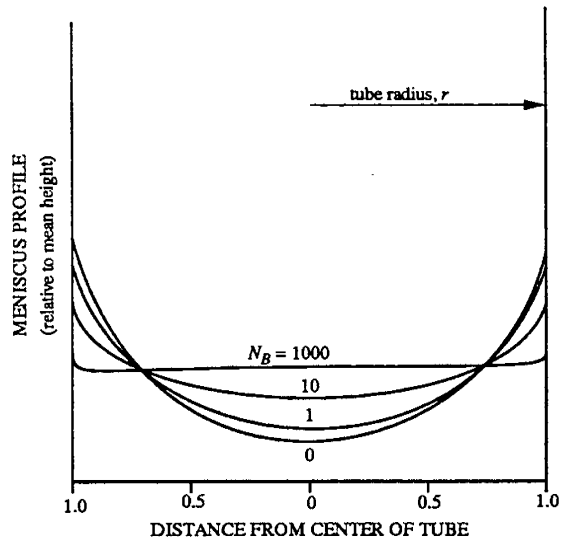

Figure 5.1: Interfacial profiles for different Bond numbers (after Concus[21]).

to vertical greatly increased recovery in gas drive experiments. Morrow and Songkran [84] investigated the relative effects of capillary number and Bond number ($N_B = \frac{\Delta\rho g R^2}{\sigma}$) on desaturation where R is the particle radius of glass beads used to pack columns. In their experiments, air was displaced from the top of the column by injecting the wetting oil phase from the bottom. By changing the bead size, the Bond number could be varied as the capillary number was kept constant. Morrow and Songkran found that the residual saturation remained constant for inverse Bond numbers greater than 200. Decreases in the Bond number at a constant capillary number less than 3×10^{-6} caused the residual saturation to decrease to zero when the inverse Bond Number was about 3.

The reduction in residual saturation was attributed to the increased importance of gravity at large pore throat radii, which they argued caused a change in fundamental trapping mechanisms. If the Bond number is large enough, for instance, in a column packed with marble-size spheres, and gas is being displaced by injecting liquid from the bottom, the interface will appear flat and no trapping of the gas will occur. Concus [21] calculated interfacial profiles as a function of Bond Number. Fig. 5.1 demonstrates the effect of increasing the Bond number on the curvature of a meniscus in a tube of radius, r. The diagram shows that the curvature of the interface depends on the Bond number. At large values of N_B (gravity dominated), the interface is flat, while for small or negligible gravity effects, the meniscus assumes the familiar shape observed in a capillary tube. In Fig. 5.2, a conceptualization of the suppression of entrapment presented by Morrow and Songkran is shown. In a gravity stable displacement of a gas by a liquid, stranding will occur if, for instance, the pore throats are small, and the capillary pressure is large. As the Bond number is increased, the gravitational pressure acting at the bottom of a strand of liquid of height Δh will prevent snap-off and subsequent isolation.

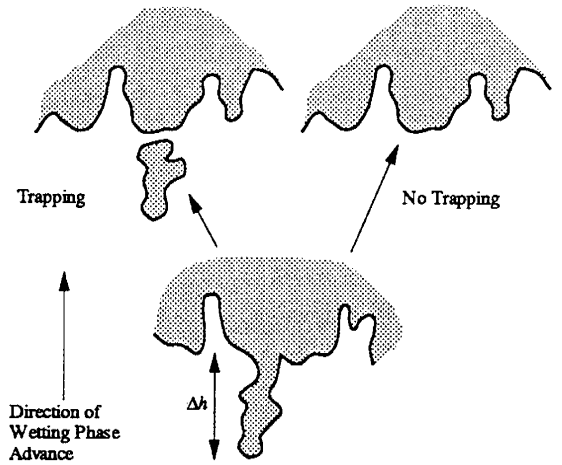

Figure 5.2: Entrapment on the left if capillary effects dominate. Suppression of entrapment on the right for large values of Bond number. After Morrow and Songkran [84].

5.1.2 Experimental Procedure

Cylindrical cores (described in Table 5.1) about 60 cm in length and 6.35 cm in diameter were mounted vertically in a plexiglass holder. In a typical imbibition experiment, the core was saturated with oil, and then it was rapidly immersed in water. The less dense oil phase was then produced by a combination of gravity segregation and capillary imbibition. For drainage experiments, the core was saturated with the aqueous or wetting phase and rapidly immersed in the nonwetting phase. (More detailed descriptions of the experimental procedures and results are given in references [117] and [92]).

Table 5.1: Core Properties

Sample	Permeability (md)	Length (cm)	Porosity (ϕ)	Pore Volume (cm^3)
Indiana Limestone	15	61	0.158	305
Berea Sandstone	100	57	0.187	335
Berea Sandstone	500	57	0.213	385
Brown Sandstone	700	61	0.184	353

To investigate how oil recovery changes with IFT, experiments were performed with the mixtures of isooctane (IC_8), brine (2 wt.% $CaCl_2$) and isopropanol (IPA). The imbibition experiments were performed with equilibrated fluids on three tie lines shown in Fig. 5.3. Properties of the phases are summarized in Table 5.2. As Table 5.2 and Fig. 5.3 show, as IPA is added, the IFT is reduced. On tie line 1 in Fig. 5.3, for example, the brine and IC_8 with no IPA have an IFT of 38 mN/m and a density difference of 0.33 g/cm^3, while tie line 3 exhibits an IFT two orders of magnitude lower with a density difference that is three times lower.

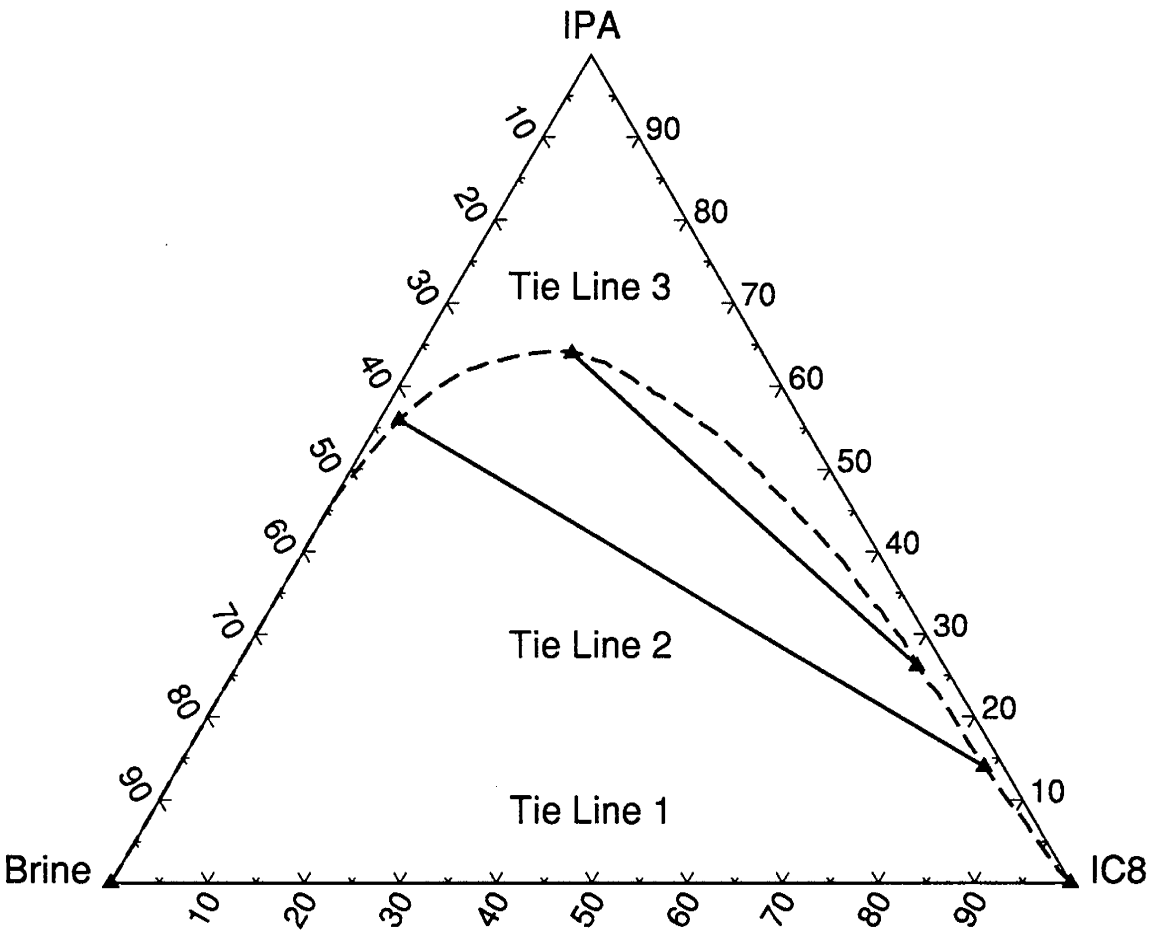

Figure 5.3: Phase diagram for IC_8, IPA and brine system.

Table 5.2: Phase Properties for Three Equilibrium Tie-Lines

Tie Line	$\Delta\rho$ (g/cm^3)	IFT (mN/m)	Viscosity Ratio (μ_w/μ_o)
1	0.33	38.1	2.0
2	0.21	1.07	6.25
3	0.11	0.10	3.71

5.1.3 Results and Discussion

Imbibition

The imbibition experiments for the three values of IFT are shown for the 15 md core in Fig. 5.4. Fig. 5.4 demonstrates that as IFT was reduced, the rate of imbibition slowed in the 15 md limestone core. At high IFT, the brine rapidly imbibed into the core with completion of imbibition occurring after four hours. During that experiment at high IFT, oil droplets were observed to exit from the lateral faces of the core. At the intermediate IFT, drops were observed to exit the core from both the lateral and the top face of the core. The final recovery was slightly higher than that of the high IFT case although imbibition occurred more slowly over several days. At low IFT there was a substantial increase in total oil produced, but completion required approximately 40 days. For the limestone core, rate behavior is therefore in qualitative agreement with Eq. 1.

Results of experiments in a Berea sandstone core with a permeability of 100 md are shown in Fig. 5.5. The trend in rate behavior shown in Fig. 5.5 differs sharply from that implied by Eq. 1. In this case, the high IFT brine imbibed more slowly than either the intermediate or the low IFT brines. Initially, the recovery rate was greatest at the intermediate IFT. For the first two days, the low IFT experiment showed a lower rate than the intermediate IFT case, but a much larger fraction of the oil originally in place (%OOIP) was eventually recovered at low IFT. In the high IFT experiment, nearly 60% of the oil was recovered, but the recovery rose to 95% for imbibition of the low IFT brine.

An important change in the flow behavior was observed for the intermediate and low IFT experiments in the cores investigated. Oil was no longer produced from all faces as was the case at high IFT. Instead, the oil produced in these experiments was a result of cocurrent flow in which oil droplets exited the core only from the top face. Despite the fact that both the capillary and density driving forces decreased as the IFT was reduced, the total recovery and the rate both increased. For additional experimental results that show similar behavior, see Schechter et al. [117, 92].

Gravity Desaturation

Fig. 5.5 shows that reducing the IFT between the imbibing brine phase and the oil phase increases the ultimate recovery. Such behavior is akin to capillary desaturation. A similar plot to demonstrate gravity desaturation may be obtained by plotting the remaining oil saturation at the end of an imbibition experiment against N_B^{-1} as shown in Fig. 5.6 for the various values of IFT. The value of capillary to gravity ratio was calculated as

$$N_B^{-1} = \frac{\sigma\sqrt{\frac{\phi}{k}}}{\Delta\rho g h} \tag{5.5}$$

As the IFT decreases, the N_B^{-1} decreases. With increasing permeability the value of N_B^{-1} also decreases as would be expected considering that pore throat sizes ultimately determine the permeability. The larger the pore throat, the more important gravity effects become as was shown in Section 5.1.1. The values of N_B^{-1} for each of the experiments in the four core samples may be found in Table 5.3.

The data indicate trends similar to those observed by Morrow and Songkran. As observed in Fig. 5.6, the residual saturation normalized to the saturation obtained at the

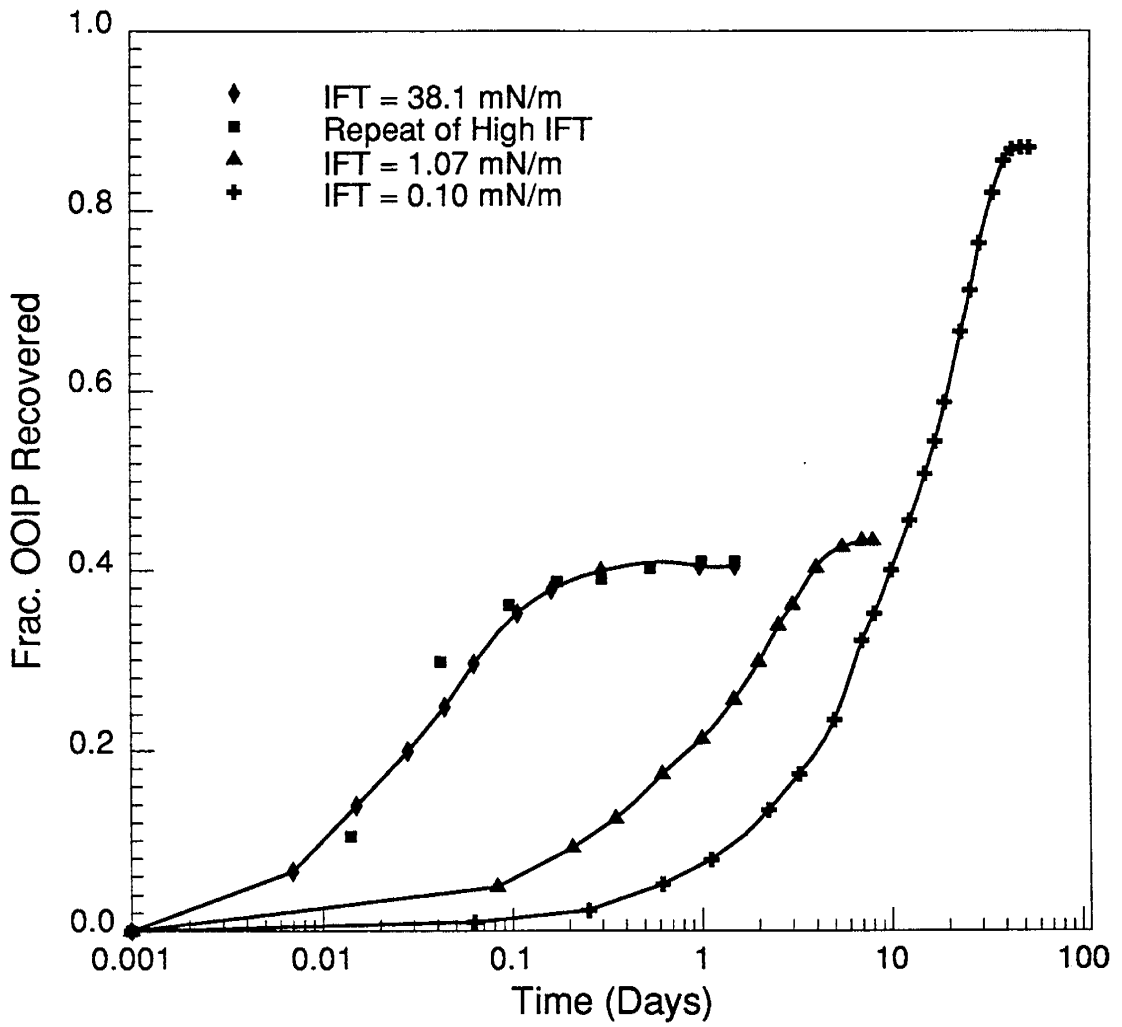

Figure 5.4: Recovery curve for 15 md limestone at three different IFT's.

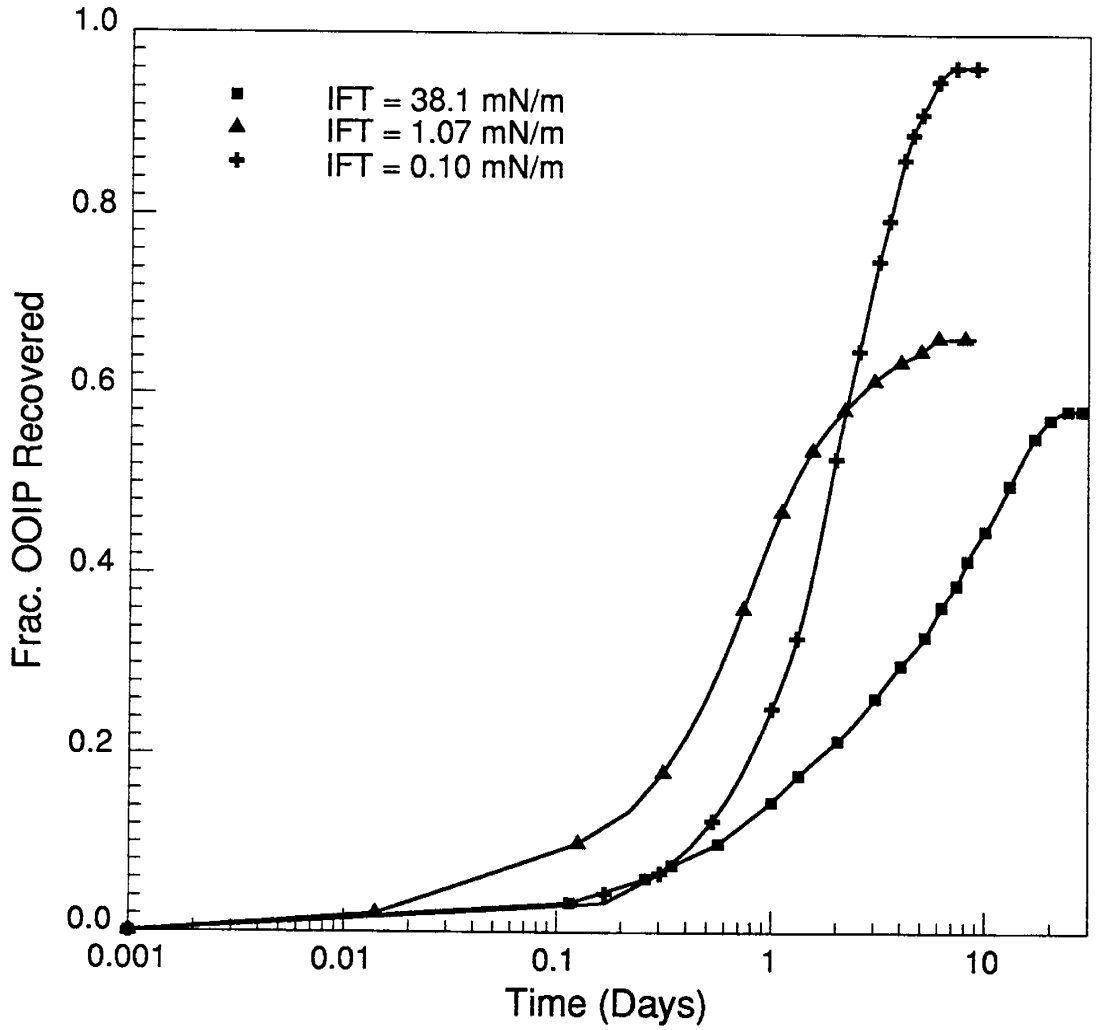

Figure 5.5: Recovery curve for 100 md Berea at three different IFT's.

Table 5.3: Inverse Bond Number for Imbibition Experiments

K (md)	Tie-line 1	Tie-line 2	Tie-line 3
15	25.66	1.13	0.202
100	10.81	0.477	0.085
500	5.13	0.227	0.04
700	4.05	0.179	0.032

end of high IFT imbibition reaches a threshold value of N_B^{-1} and any further decreases in the capillary to gravity ratio result in significant decreases in the residual saturation.

Calculation of the capillary number was straightforward in the work of Morrow and Songkran. The injection rate was monitored, and the velocity times the viscosity of the injected phase was considered the viscous contribution to the capillary number. Since there was no injection in the imbibition experiments described here, various methods of calculating the viscous contribution during imbibition were used. The capillary number may be defined according to either of the following equations,

$$N_c = \frac{\Delta P \mu}{h\sigma} = \frac{\Delta \rho g}{\sigma} \tag{5.6}$$

or

$$N_c = \frac{Q\mu}{A\sigma} \tag{5.7}$$

where ΔP is the pressure drop, μ is the viscosity of the invading phase, Q is the flow rate, A is the cross-sectional area, and h is the length of the core sample. In the first case, we obtain ΔP as the gravitational potential, $\Delta\rho$gh. Upon substitution of the gravitational term into the equation, the capillary number may be calculated. An example calculation of this number for the 500 md core at low IFT conditions gives 5.3×10^{-6}. To verify this number, we also used the second definition of capillary number. The flow rate was determined to be the maximum flow rate of oil expulsion during imbibition. In a typical slug process, the area would be the cross-sectional area of the core. During imbibition, all faces of the cylindrical core are open for imbibition. One would assume that only a fraction of this total surface area would actually accommodate the wetting phase as it imbibed in the pores yet a calculation of N_c using the entire surface area available gives 3.0×10^{-6}, a value comparable to the calculation using the gravitational potential. Results of this calculation for the 500 md core are shown in Fig. 5.7. The cross-sectional area of the core was used for calculation of the imbibition capillary numbers.

To investigate further the interplay of gravity, capillary, and viscous forces, injection tests were performed with the core placed inside an overburden sleeve and oriented vertically. The core was initially saturated with oil phase, which was displaced from below with the pre-equilibrated aqueous phase. The value of capillary number was varied by adjusting the

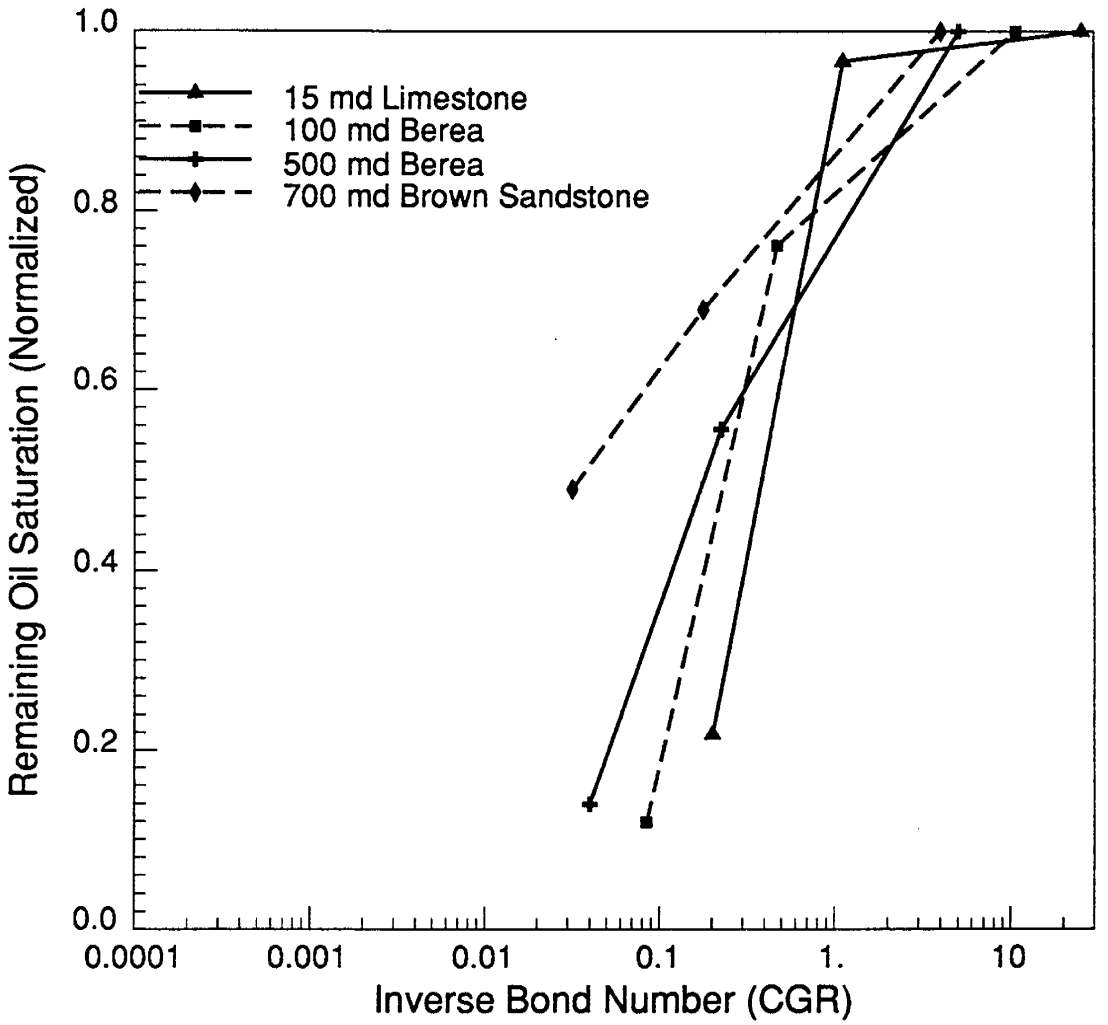

Figure 5.6: Residual saturation vs. capillary to gravity ratio for imbibition experiments.

Table 5.4: Capillary Number for Injection Experiments in 500 md Berea

Injection Rate (cm^3/sec)	Capillary Number (N_c)	Remaining Oil Saturation
0.083	6.9E-7	35.8
0.0013	1.1E-5	27.3
0.0062	4.4E-5	24.4
0.0107	8.78E-5	14.3
0.0139	1.14E-4	7.0
0.022	1.76E-4	0

flow rate for low IFT phases. The residual saturation at high IFT was measured so that the normalized saturation could be calculated. Results of six injections are plotted in Fig. 5.7 and tabulated in Table 5.4. A comparison to the data of Chatzis and Morrow [16] in their desaturation experiments in 500 md, horizontally oriented Berea cores is also presented in Fig. 5.7.

Fig. 5.7 shows that the capillary number for complete desaturation of the core during imbibition appears to be much lower than capillary numbers required to desaturate similar cores by viscous forces, according to the measurements of Chatzis and Morrow [16]. In the experiments described by Chatzis and Morrow, desaturation of continuous oil was measured. The cores were horizontally oriented, and a connate water saturation was established prior to desaturation. In the experiments reported here, the cores were initially saturated with 100% nonwetting phase and the injection was performed with the core oriented vertically. These two factors shift the desaturation curve to the left of Chatzis and Morrow, as is shown in Fig. 5.7. Linear combination of the Bond and Capillary Numbers, as suggested by Morrow and Songkran for glass bead packs, does not account for the difference. The differences between the data of Morrow and Chatzis and those presented here suggest that connate water and film behavior play an important role in snap-off events. We speculate that the dependence of snap-off on IFT results from an interaction between competing mechanisms: the increased importance of buoyancy at low IFT's or large pore throats and the wetting collars which grow in pore throats and eventually coalesce and strand droplets of nonwetting phase. The influence of changes in film thickness with changes in IFT and the corresponding effects on the time scales associated with snap-off in a gravitational field remain to be explored. Additional experiments are in progress to describe the mechanism of snap-off in the presence of gravity with varying IFT.

5.1.4 Drainage

The experimental results in Fig. 5.5 indicate that relatively rapid and high recovery is possible even when the IFT is only moderately low. As the IFT is reduced gravity forces become more important compared to the capillary forces [117, 92]. It is important to recognize that when capillary pressure is diminished, both the wetting and nonwetting phases segregate by gravity, which can lead to efficient production rates and high final recoveries. Fig. 5.8 shows, for example, that when the equilibrated fluids of Tie Line 3 were used,

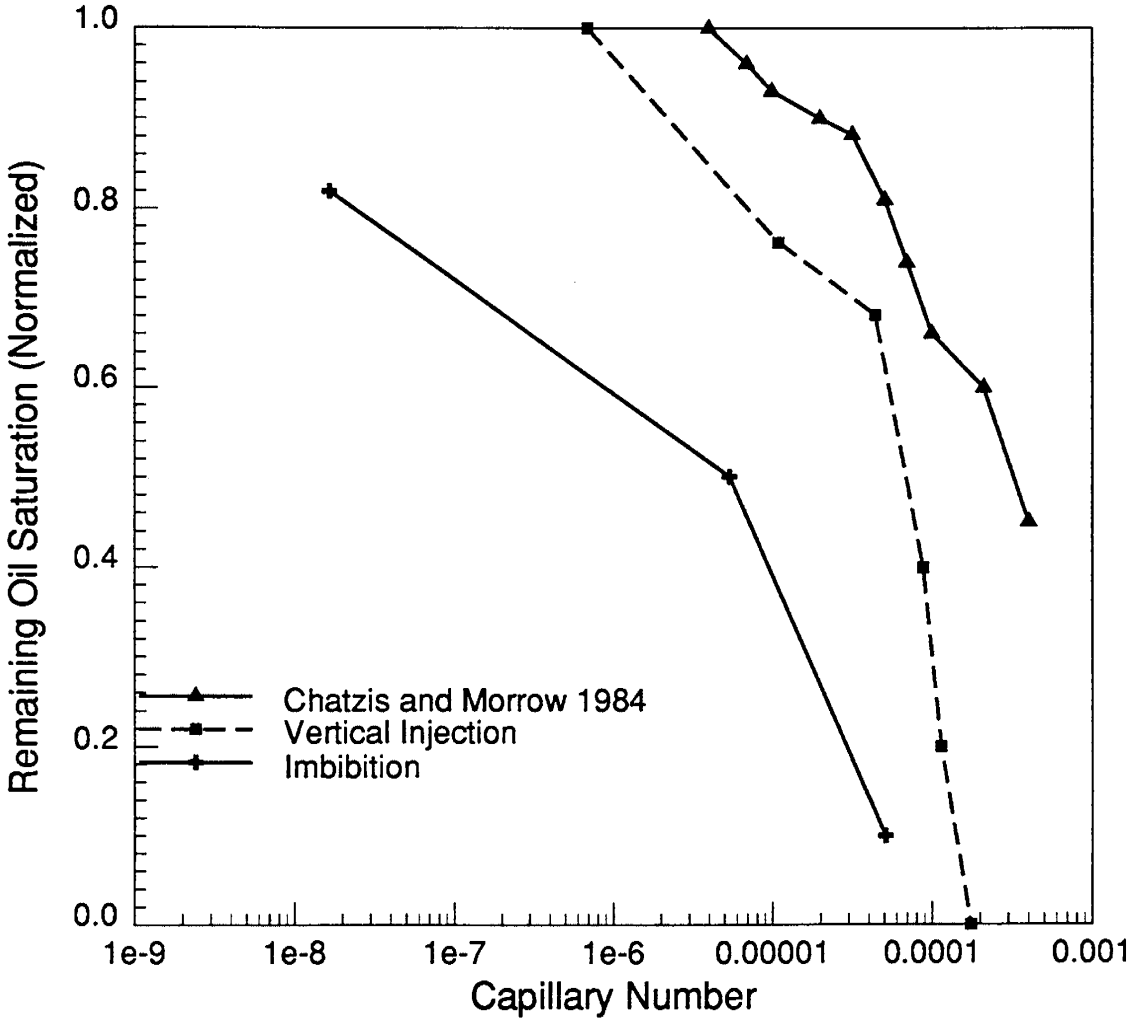

Figure 5.7: Capillary desaturation curve of continuous oil for imbibition and injection compared with data obtained from Chatzis and Morrow.

the wetting brine phase initially present in the core could be removed by gravity drainage, just as oil phase could by gravity imbibition.

Also shown is drainage at the same IFT performed with both the lateral face open and wrapped in teflon. In contrast to imbibition, where the rate of recovery is proportional to the surface area available for imbibition, covering the lateral face increased the rate of drainage and final recovery. This result suggests that nonwetting phase was penetrating the lateral face and interfering with the downward gravity stabilized front. Such interference is responsible, in turn, for the lower recoveries observed during open face drainage.

An additional drainage experiment was performed in which the 500 md Berea core was saturated with wetting phase on Tie Line 2. Results of that experiment are also shown in Fig. 5.8. Thus, the IFT between the two phases was an order of magnitude greater (1.0 mN/m) than that of the low IFT drainage experiment. At higher IFT the recovery rate was unchanged during the initial stages of drainage. The recovery curves at different IFT's are superimposed until the breakpoint, at which bulk flow was presumably completed and slower drainage from wetting films continued. However, the slope of the recovery curve in the film flow regime changed with IFT. The lower IFT drainage took place more rapidly after the breakpoint. Apparently, increasing the IFT did not affect the rate of gravity drainage or the recovery until the breakpoint. Thus, ultra-low IFT's are not necessary in order to overcome the capillary threshold in the cores investigated.

Similar data are plotted in Fig. 5.9. The result for imbibition at 0.1 mN/m is compared with drainage experiments at IFT's of 0.1 and 1.0 mN/m in the 700 md brown sandstone core. As demonstrated previously, the larger pores empty at approximately the same rate for the two drainage experiments. In this case, the breakpoint denoting the onset of film drainage is not as clearly defined as in the 500 md Berea core. The high degree of surface heterogeneity present on the 700 md brown sandstone core is consistent with this observation.

Fig. 5.10 shows the imbibition data previously presented for the 100 md Berea core. Included in this plot are drainage data for the same fluids at an IFT of 0.1 mN/m. Once again as in the case of the higher permeability Berea core, drainage occurs less rapidly than imbibition. However, the time scale for low IFT drainage was not very different from the high IFT recovery curve for imbibition, though the final recovery is much greater in the drainage experiment.

5.1.5 Discussion

A summary of the mechanisms, along with the resulting recovery curves for both the imbibition and drainage processes, is shown in Fig. 5.11. As the permeability and fracture length increase, and the IFT decreases, the transition from capillary driven, countercurrent imbibition to gravity driven cocurrent segregation is demonstrated. For the cores examined here, the transition region has been identified as the N_B^{-1} varies from the capillary dominated region of around 5 to the gravity dominated region around 0.1. In Fig. 5.6 the residual saturation was unaffected until values of N_B^{-1} were near 5. Reductions in residual saturation continued as N_B^{-1} was reduced further until values were less than 0.1 at which point most of the oil was recovered from the Berea samples. Recovery curves that show typical shapes and final recoveries are also shown in Fig. 5.11.

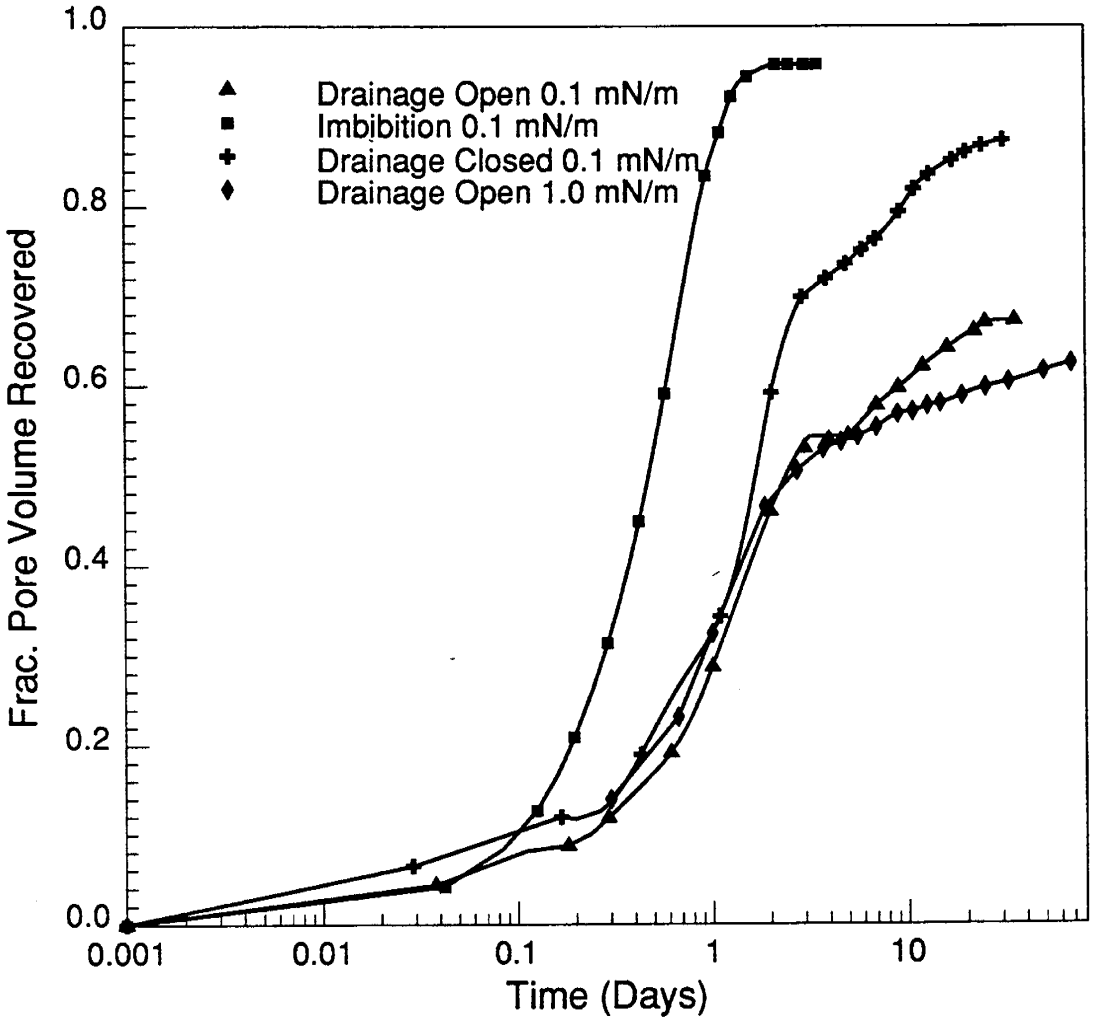

Figure 5.8: Drainage of brine, IFT = 0.1 and 1.0 mN/m, from 500 md Berea.

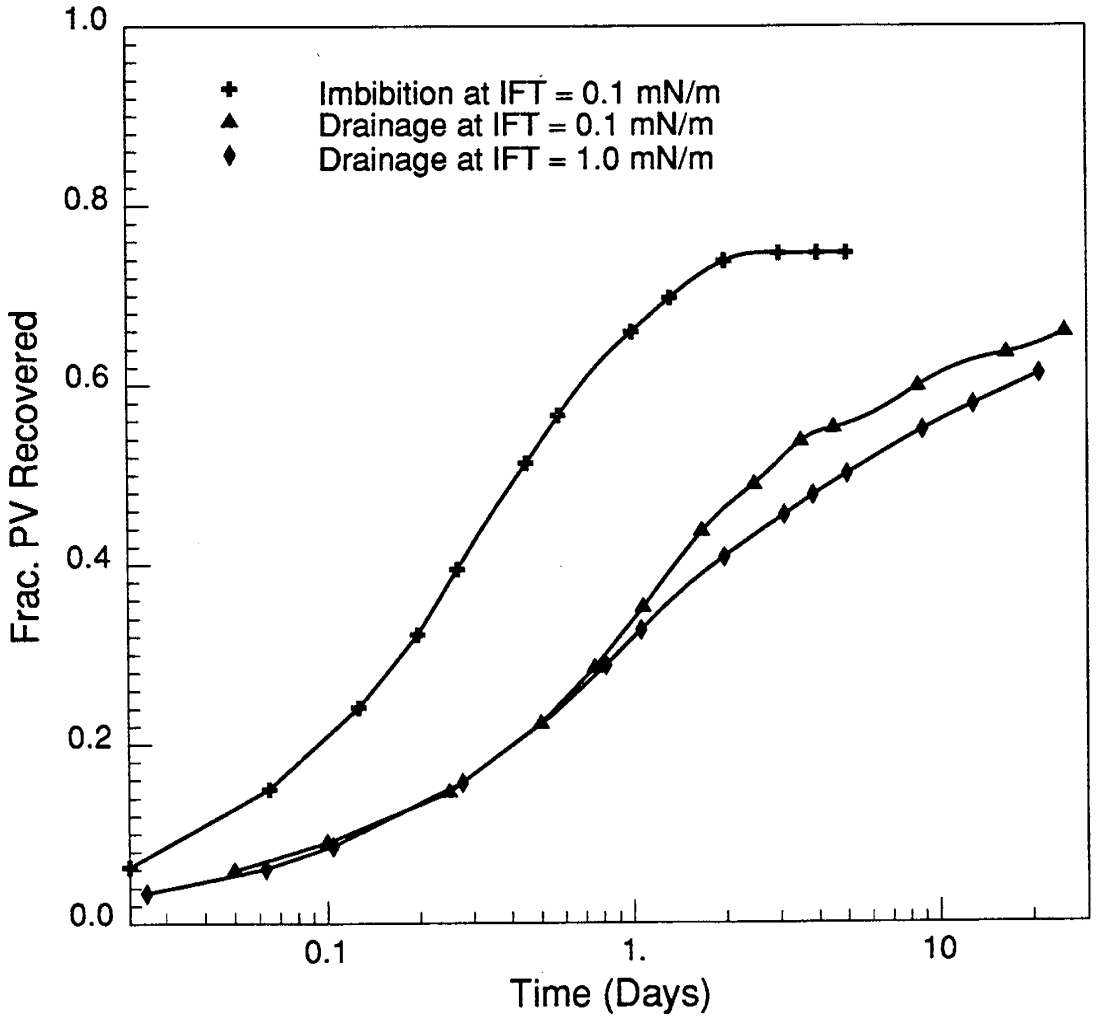

Figure 5.9: Drainage recovery curves for 700 md Brown sandstone at two different IFT's compared to imbibition at 0.1 mN/m.

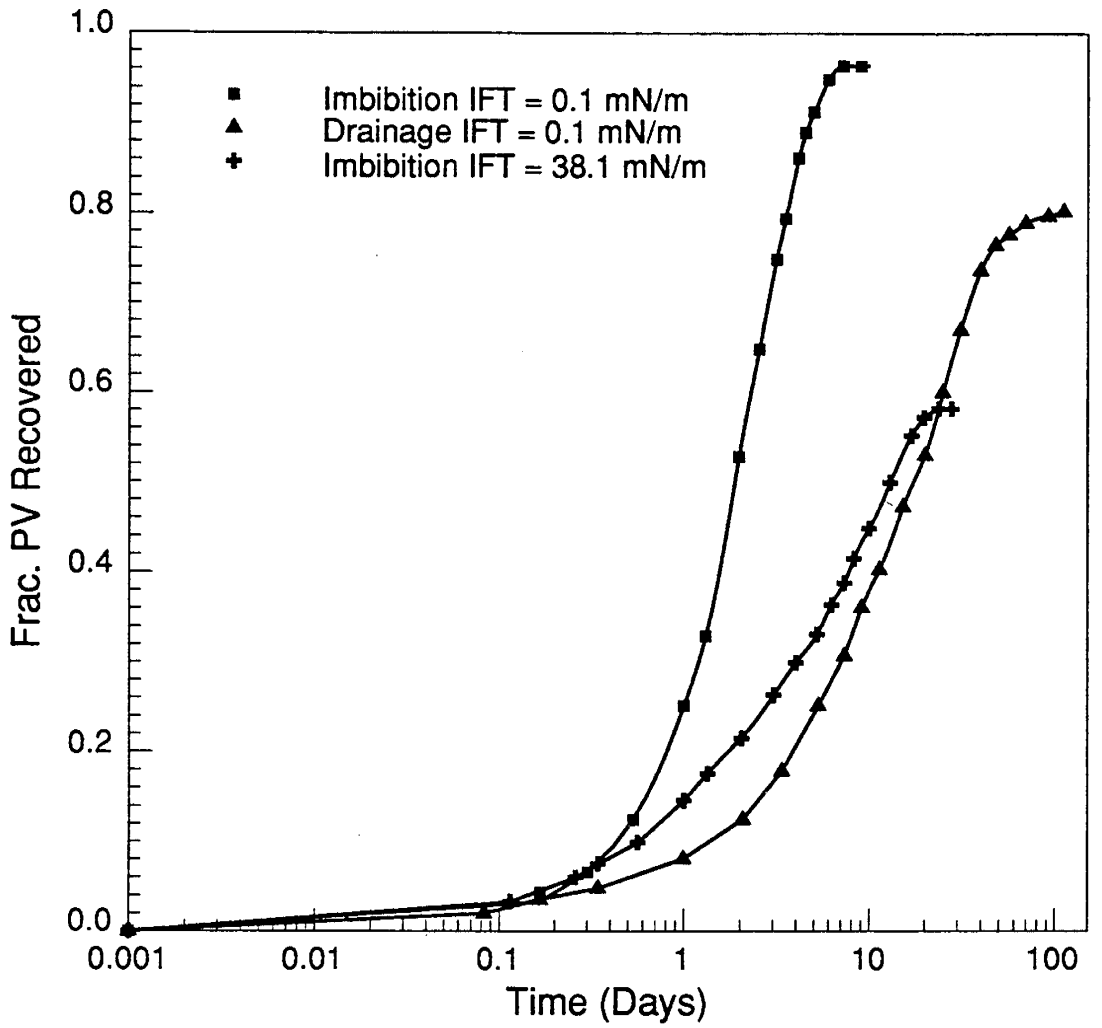

Figure 5.10: Imbibition recovery curves for 100 md Berea at high and low IFT's compared to drainage at an IFT = 0.1 mN/m.

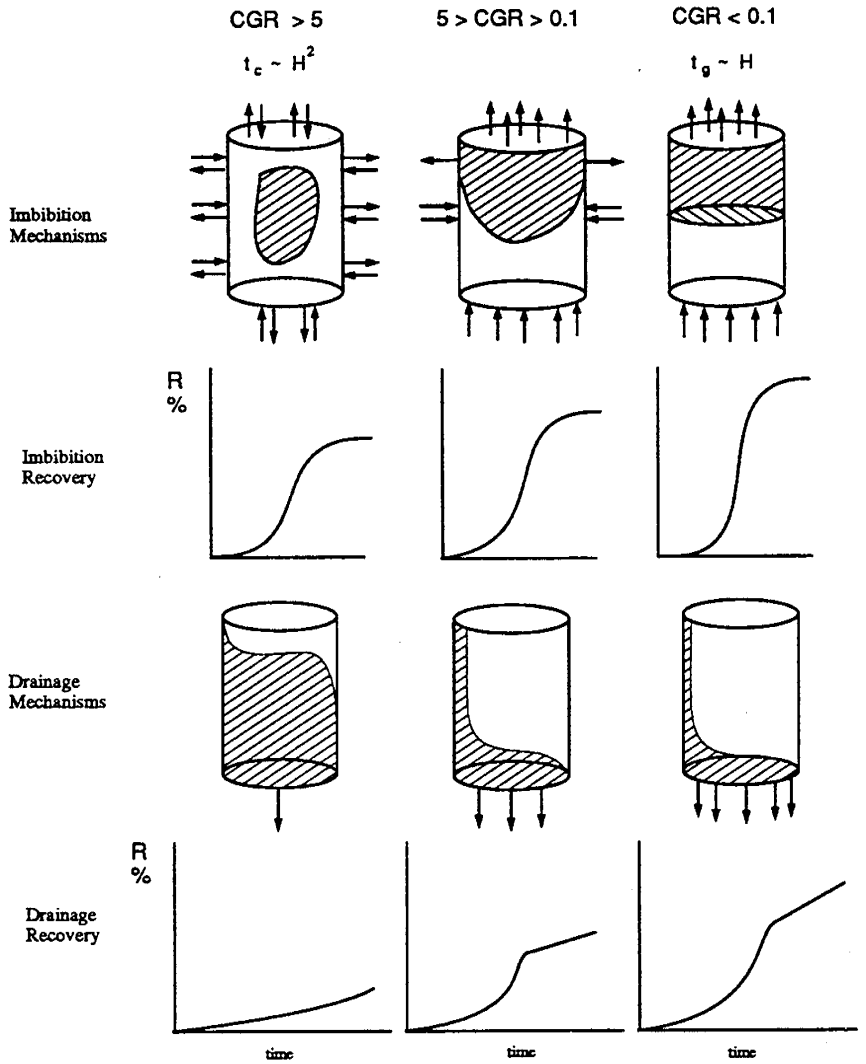

Figure 5.11: Summary of flow behavior for imbibition and drainage experiments.

Even though the experiments outlined were performed with analog fluids, they indicate that similar behavior will be quite important in MCM displacement processes in heterogeneous reservoirs. The explanation of this phenomenon comes from the fundamental principles of near-critical phase transitions. An analysis of the scaling behavior of the density difference and IFT of coexisting phases near their critical point of miscibility indicates that as a critical point is approached, IFT decreases more rapidly than density difference [120]. For instance, Fig. 5.12 shows a plot of IFT against density difference between phases for oil-water-alcohol systems [24, 85, 116]. It demonstrates the relationship between density difference and IFT in the near-critical region and also shows the slope of the straight line of 3.8, which is consistent with critical scaling theory [120].

According to that theory, the same behavior will be observed for gas-oil systems near a critical point. Haniff and Pearce verified critical scaling [45] on a gas-condensate mixture near miscibility. The phase equilibrium mechanism of a successful MCM process will generate mixtures that are near a critical point, (see Chapter 3) and hence, there will be regions of the flow where gravity forces will be more important than capillary forces. In these regions, then, gravity-driven crossflow can be used to invade zones not swept by longitudinal flow if adequate vertical communication exists. This argument suggests that a miscible gas injection process could be used effectively in a fractured reservoir. We argue that near miscible conditions in a highly fractured network will cause efficient gravity drainage, which can result in transfer of the nonwetting phase into the matrix block.

In fact, a successful field application of CO_2 injection in a fractured reservoir was recently reported by Beliveau and Payne [9]. The observations reported are consistent with the mechanisms described here. They described a pilot test currently underway in the Midale field in which CO_2 was injected at a pressure above the MMP in a fractured carbonate reservoir. Before injection of CO_2 was initiated, water with tracers was injected in the pilot area. The tracers broke through rapidly to the producing wells, in some cases, in less than one day. Hence there was clearly complete communication between the injecting and producing wells and the fracture network. When CO_2 was injected, however, it broke through much later, a clear indication that CO_2 was invading low permeability matrix blocks. Actual oil production in the pilot test indicated that CO_2 utilization was only about 3 MCF/STB. At reservoir conditions 1.7 MCF were required to produce a barrel of oil, so the observed CO_2 utilization is remarkable. It is much lower than is typical in other miscible flood applications. Cross-well tomography indicated that gravity drainage was occurring throughout the pilot area. The estimated value of N_B^{-1} for the Midale project is approximately 0.1. According to the arguments presented, the calculation of the N_B^{-1} indicates the Midale pilot is well into the region where gravity effects dominate. Hence it is clear that the reasons for success at Midale should be explored in detail, so that similar successes can be achieved in other fractured reservoirs.

The objective of a recovery method for fractured reservoirs should be to use the fracture network as a delivery system to carry injected fluid to the matrix regions to be swept and to move oil recovered from the matrix to production wells by gravity drainage. If a MCM gas is injected into a vertically fractured network, the gas will rise through the highly permeable fracture paths. If sufficient fracture heights exist, and the combination of the hydrostatic pressure and reduced IFT's can overcome capillary entry pressures, then gravity drainage can become an extremely effective recovery mechanism, as the experiments

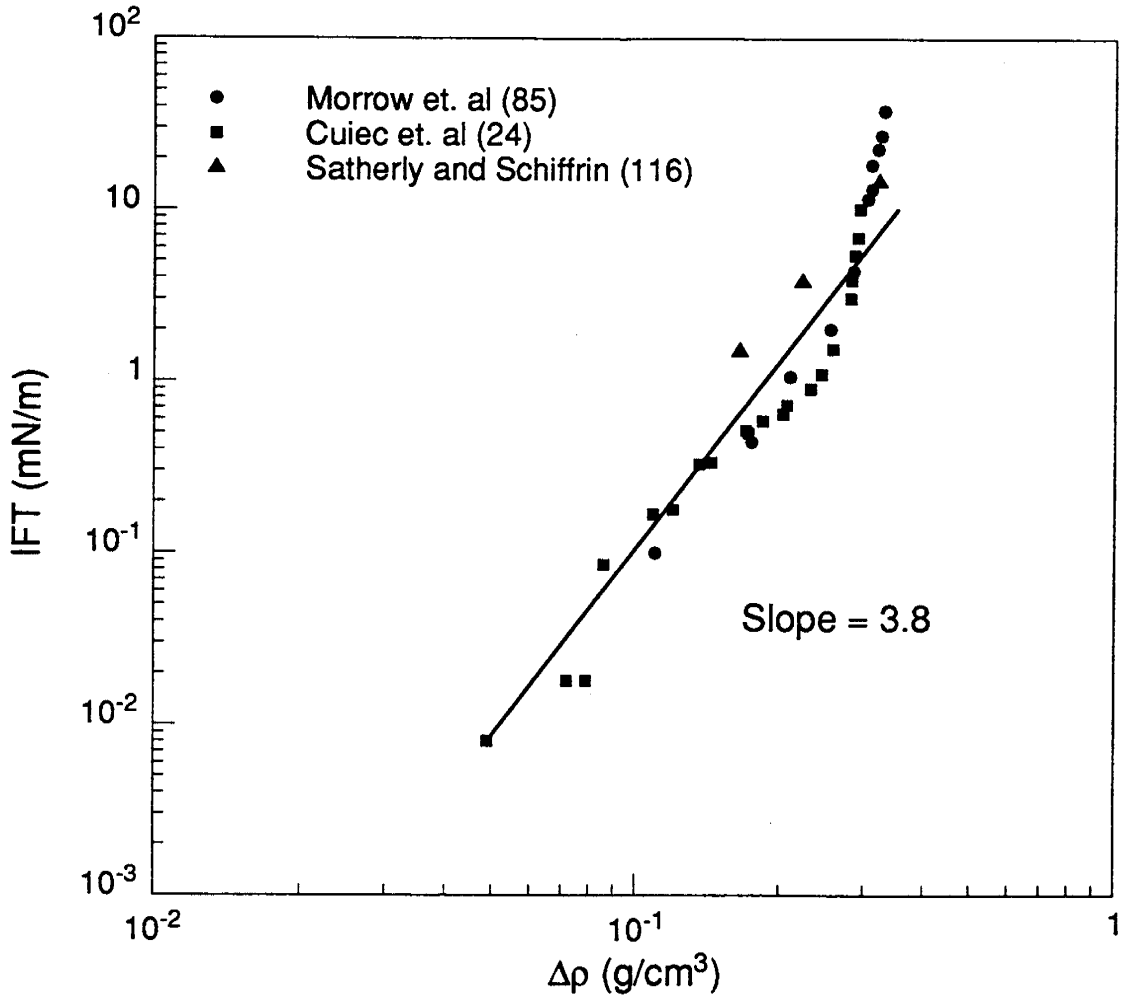

Figure 5.12: IFT vs. density difference for phases approaching miscibility.

described here show. The experience at Midale is consistent with the idea that low IFT gravity drainage can contribute substantially to recovery in relatively low permeability reservoirs.

Real miscible floods will be more complex still because crossflow and its interactions with phase behavior will induce IFT gradients. Additional experiments reported by Schechter et al. [117] indicate that IFT gradients can help or hinder crossflow significantly, depending on whether the direction of the gradient aids or impedes the flow. Thus one objective of design of processes that make use of crossflow should be to take advantage of IFT gradients. Consider a fractured reservoir, for example. If relatively low IFT's can be created inside a matrix block, as would happen as CO_2 at a pressure above the MMP invaded the block, then higher IFT's at the edge of the block would cause faster flow of oil phase toward the fracture [117]. To design such a process, the details of the interaction of crossflow with phase equilibrium must be worked out.

5.1.6 Conclusions

1. Reduction of the IFT for imbibing fluids may increase or decrease the rate of imbibition substantially depending on the relative contribution of capillary and gravity forces.

2. Only a moderate reduction in IFT is required to induce a crossover from capillary-driven to gravity stabilized imbibition in high permeability sandstones.

3. The crossover from capillary-driven to gravity stabilized imbibition is characterized by an optimal IFT in which both forces contribute, and the rate of imbibition into the matrix is greatest.

4. Imbibition at high IFT and low permeability occurs due to countercurrent flow whereas at low IFT and high permeability, oil is recovered by cocurrent flow.

5. In gravity stabilized cocurrent flow at low IFT, total recoveries may be very high due to supression of entrapment mechanisms. The N_B^{-1} required for reduction of the remaining oil saturation is approximately 5 in the imbibition experiments described.

6. Gravity drainage at low IFT in cores of moderate height and permeability is an efficient recovery process. As in the case of imbibition, it does not require ultra-low values of IFT to initiate the drainage process in the cores being studied.

5.2 Visualization of Gravity Segregation, Capillary and Viscous Crossflow in Near-Miscible Displacement in a Two-Layered Model

Dengen Zhou

Many factors influence the displacement performance of a near-miscible gas flood. According to the accepted description of development of miscibility, phase behavior acts to generate high local displacement efficiency in the zone swept by the injected fluid. The fraction of a reservoir swept at given time in a flood is determined partly by injection and

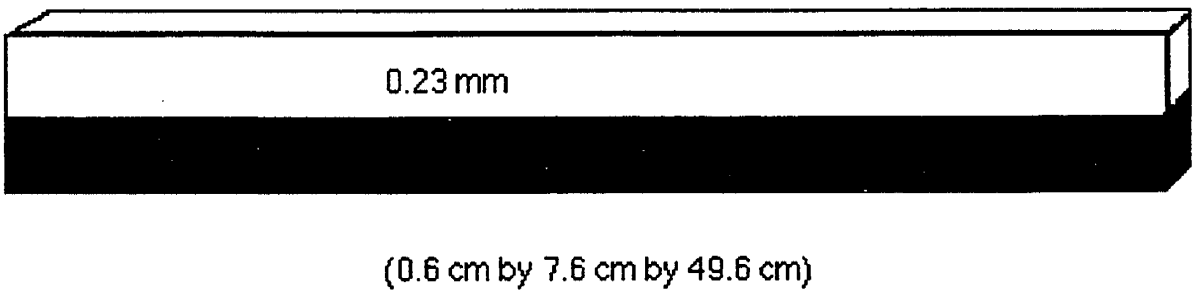

Figure 5.13: Schematic Diagram of the Glass-bead Pack.

production well patterns, permeability variations in the rocks, gravity segregation, capillary crossflow and viscous fingering arising from unfavorable ratio of displaced oil mobility to injected fluid mobility. Understanding the relative importance of such factors is a key part of scaling the performance of a near-miscible flood. This section describes an experimental study to investigate the relative importance of gravity segregation, capillary and viscous crossflow in a layered system.

5.2.1 Experimental Apparatus and Procedures

In order to study gravity, capillary, and viscous crossflow in layered porous media, visualization experiments were performed in a two-layered pack of glass beads. The model shown in Fig. 5.13 was packed in such a way that the flow is unformly distributed at both the inlet and outlet. The two layers were filled with beads of two diameters (0.23 and 0.46 mm), which resulted in a permeability ratio of 4 to 1. The permeability estimation and packing procedure are discussed in Section 4.1 and in more detail by Brock [12]. The details of the experimental apparatus and procedures are also reported by Brock [12].

Both first contact miscible (FCM) and near-miscible displacements were performed in this study. The IPA-IC_8-Brine system described in Section 5.1 was also used in the near-miscible displacements. Experiments were carried out at an injection rate of 2.0 ml/min to study the compositional effects on recovery efficiency. Fig. 5.14 shows the compositions of the oil used in this work. IC_8 was injected in all near-miscible displacements. Gas chromatography was employed to measure compositions of produced fluid for the near-miscible displacements.

Three sets of FCM fluids were employed to investigate the effects of viscosity ratio, injection rates and density difference. The sets of fluids used here are IPA and IC_8, a light mineral oil (LMO) and n-decane (C_{10}), and LMO and IC_8, with mobility ratios of 4.7, 13.4 and 27.0 respectively. The injection rates varied from 0.5 to 4.0 ml/min to obtain different gravity to viscous force ratios. The mixing properties of the fluids were measured at the

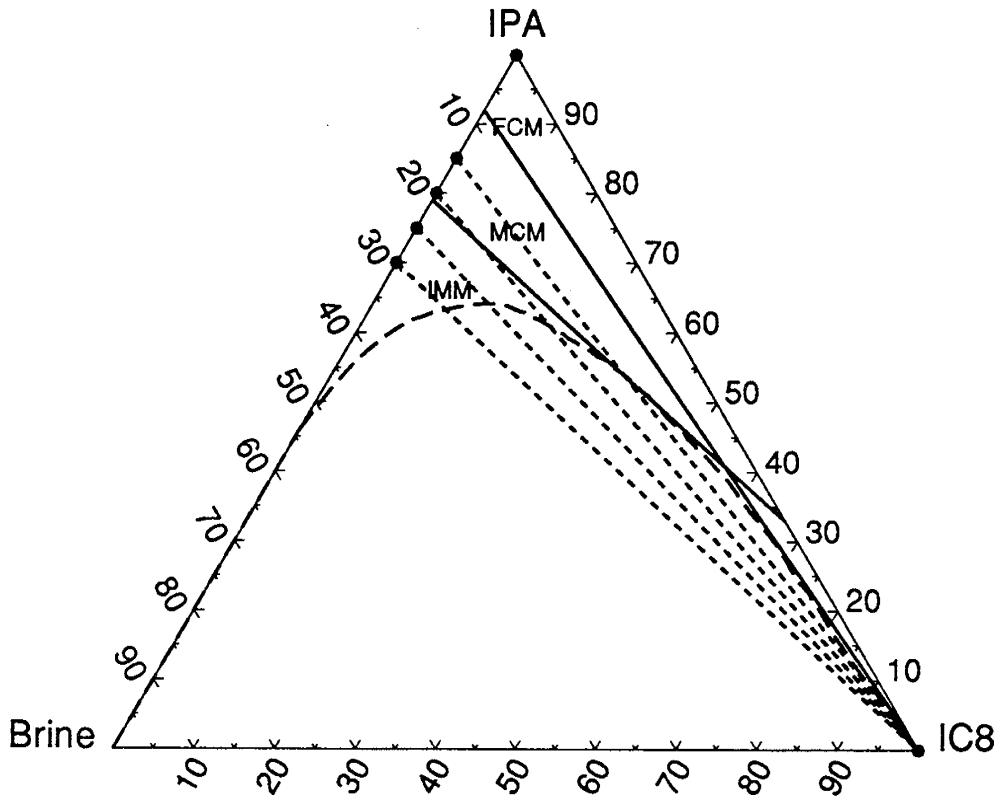

Figure 5.14: IPA-Brine-IC_8 phase diagram.

experimental temperature 22°C. Fig. 5.15 shows the results of density measurements for the mixtures. The mixing densities are well correlated by ideal mixing rules. This ideal mixing allows us to measure production curves using an electronic balance for FCM displacements. Fig. 5.16 shows viscosity variations for the mixtures, which are well correlated by a quarter-power interpolation.

In order to visualize fluid distributions within the bead pack, the injected fluid was dyed with Oil-Red, which was chosen to ensure that there would be no chromatographic separation between the injected fluid and the dye. The displacements were then recorded on video tape. Special care was taken to fill the header with the injected fluid prior to each displacement. Completely filling the header with the injected fluid allowed the displaced fluid to be uniformly distributed within the header.

5.2.2 Experimental Results

Layer ordering in a stratified system determines the interplay of gravity and viscous crossflow, depending upon the densities of the injected and displaced fluids. For example, if the injected fluid is less viscous and less dense, gravity will force the injected fluid to form overriding tongues. If the less-permeable layer is on top of the more-permeable one, viscous forces drive the injected fluid into the more-permeable layer, while gravity forces the injected fluid into the upper layer. In such systems, gravity forces aid injected fluid crossflow from the high permeability layer to the less-permeable layer. Thus, crossflow improves sweep

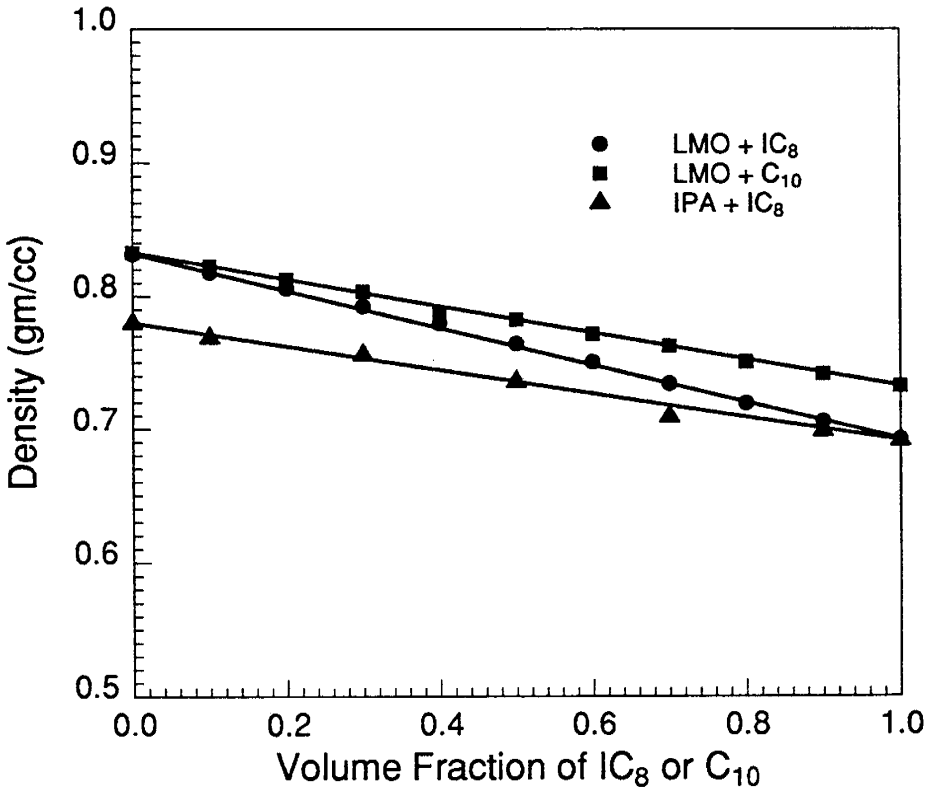

Figure 5.15: Dependence of mixture density on composition.

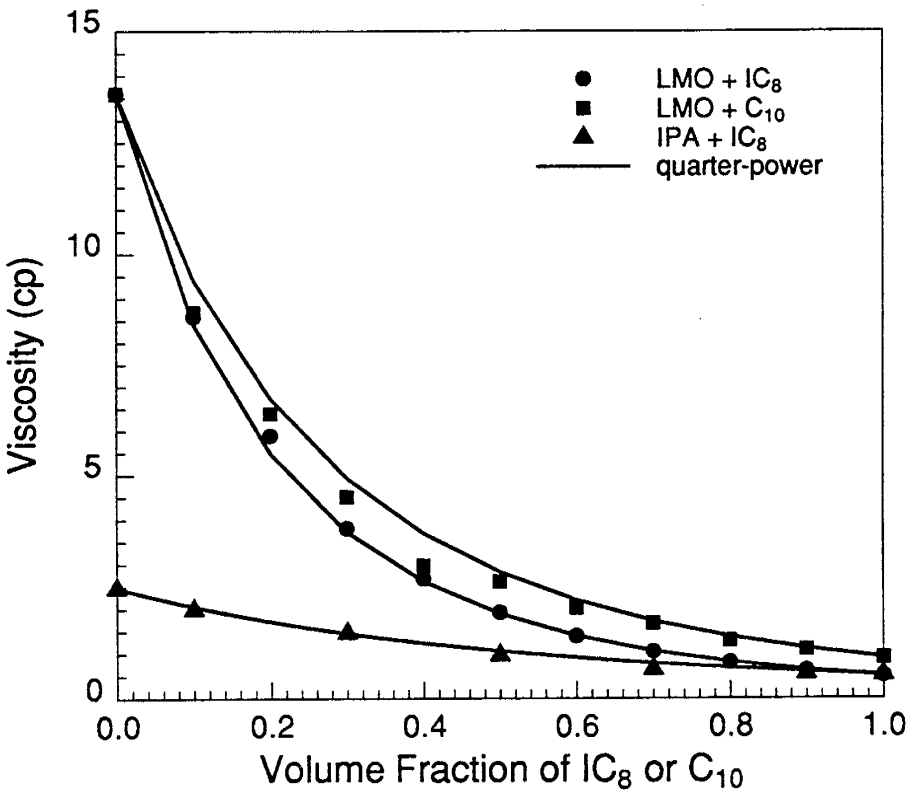

Figure 5.16: Dependence of viscosity on composition.

efficiency in the less-permeable layer. However, if the more-permeable layer is on top of the less-permeable layer, both gravity and viscous forces drive the injected fluid into the high permeability layer, which reduces sweep efficiency in the less-permeable layer. In this study, the model was placed in such a way that the gravity forces enhance crossflow. That is, the less-permeable layer was on top of the more-permeable layer.

In the subsections, experimental results are reported for first-contact-miscible displacements (FCM) or near-miscible displacements, depending on the amount of brine in the fluid in place.

FCM Displacements

Low Mobility Ratio Displacements

Low mobility ratio (M=4.7) displacements were performed using IPA and IC8 as the displaced and displacing fluids. Figs. 5.17 to 5.20 report the fluid distributions during low mobility ratio displacements. Fig. 5.17 shows the fluid distribution during the low-rate displacement at 0.5 ml/min. The injected fluid preferentially flowed into the upper layer and formed a gravity tongue in that layer. The injected fluid in the high permeability layer moved more slowly than that in the less-permeable layer, as gravity forces caused vertical crossflow at a rate that was significant compared to the injection rate. After 0.3 pore volumes injected (PVI), the front of the displacement developed into gravity-segregation, although there was a small jump at the front of the interface between the layers. Thus, gravity segregation dominated the flow process in this displacement.

Increasing the injection rate to 1.0 ml/min changed the fluid distribution substantially, as Fig. 5.18 shows. The injected fluid flowed into both layers at the beginning of the injection. Significant amounts of crossflow of the injected fluid occurred from the bottom layer to the top layer after 0.2 PVI. The displacing fluid formed a number of small fingers during the crossflow. These fingers were tilted at an angle of about 50° from the horizontal direction. After 0.4 PVI, the injected fluid crossflowing from the bottom layer met with the gravity tongue in the top layer. Comparison of Figs. 5.17 and 5.18 indicates that vertical sweep efficiency improved significantly with increase in rate.

A further increase of the injection rate to 2.0 ml/min (Fig. 5.19) resulted in the formation of a single finger in the more-permeable layer. The injected fluid forming the finger crossflowed upward into the less-permeable layer. As in the previous displacement, the injected fluid crossflowing formed a number of small fingers, but the tilt angle was smaller. Downward crossflow of IPA from the upper layer to the bottom layer was observed under the gravity tongue in the upper layer. There was one area in the low-permeability layer into which the injected fluid did not flow. The gravity tongue in the upper layer was much smaller than that observed at the lower injection rates. Similar observations were obtained from a high rate displacement (4.0 ml/min), as Fig. 5.20 shows, but the impact of gravity-driven flow was still smaller. The upward crossflow fingers also displayed a still smaller angle (36°). Comparisons of Figs. 5.17 to 5.20 indicate that downward crossflow of IPA was more pronounced and upward crossflow became less significant as the injection rate increased.

Fig. 5.21 shows the production curves at the four injection rates. The production curve at low injection rate (0.5 ml/min.) crosses over with those at higher injection rates (1.0 and 2.0 ml/min.). The crossover results from gravity segregation during the low-rate

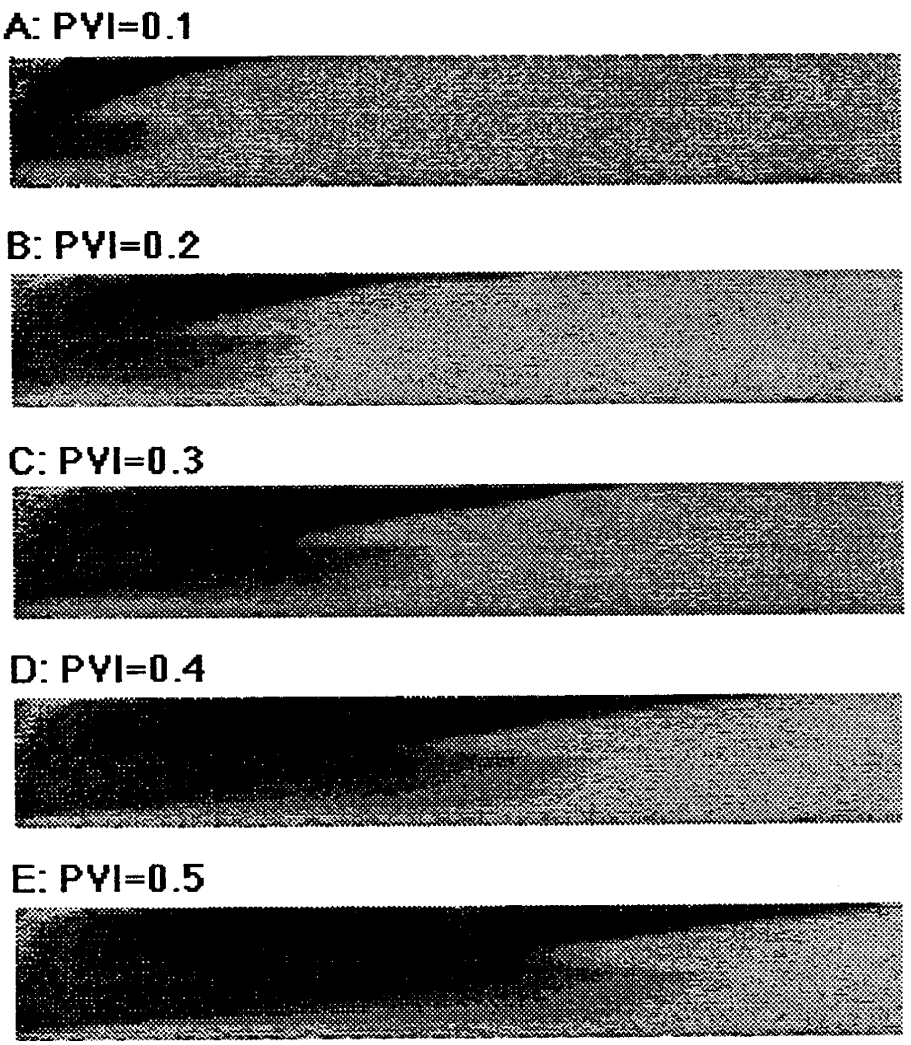

Figure 5.17: Fluid distributions during displacement of IPA by IC_8 at 0.5 ml/min.

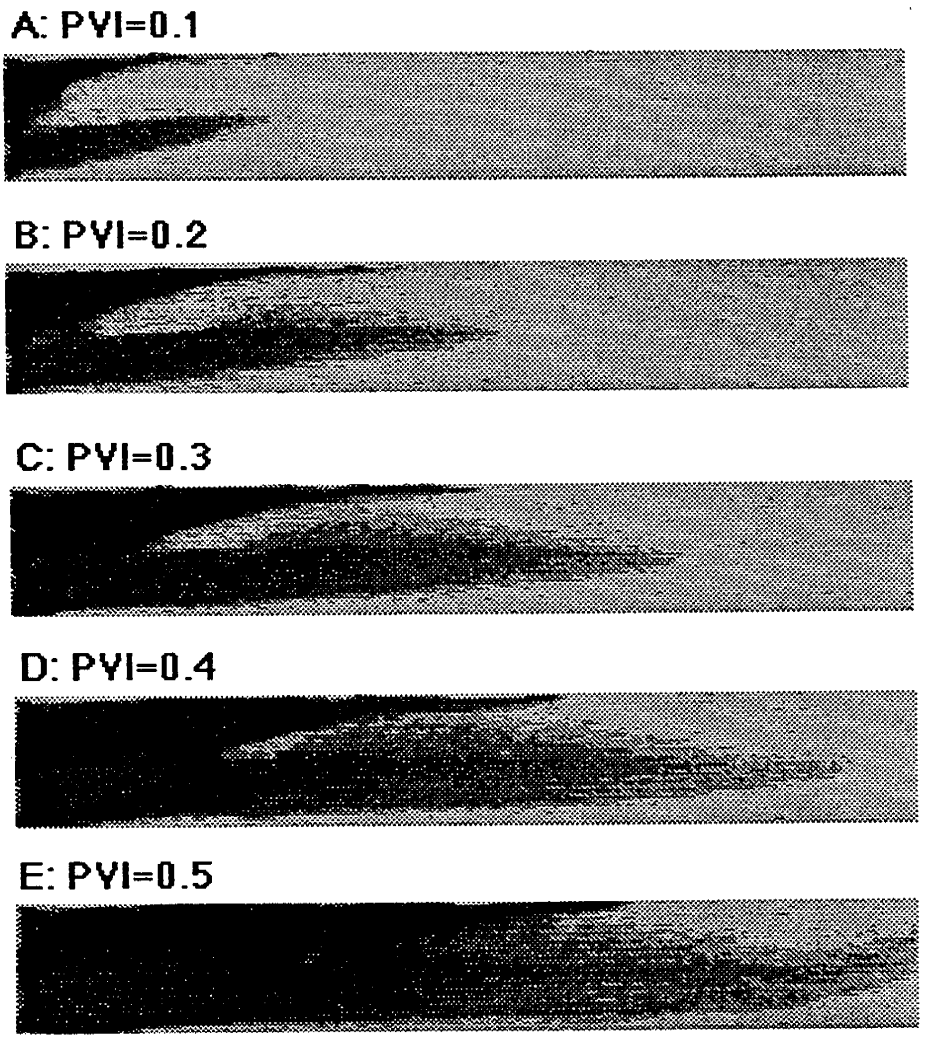

Figure 5.18: Fluid distributions during displacement of IPA by IC_8 at 1.0 ml/min.

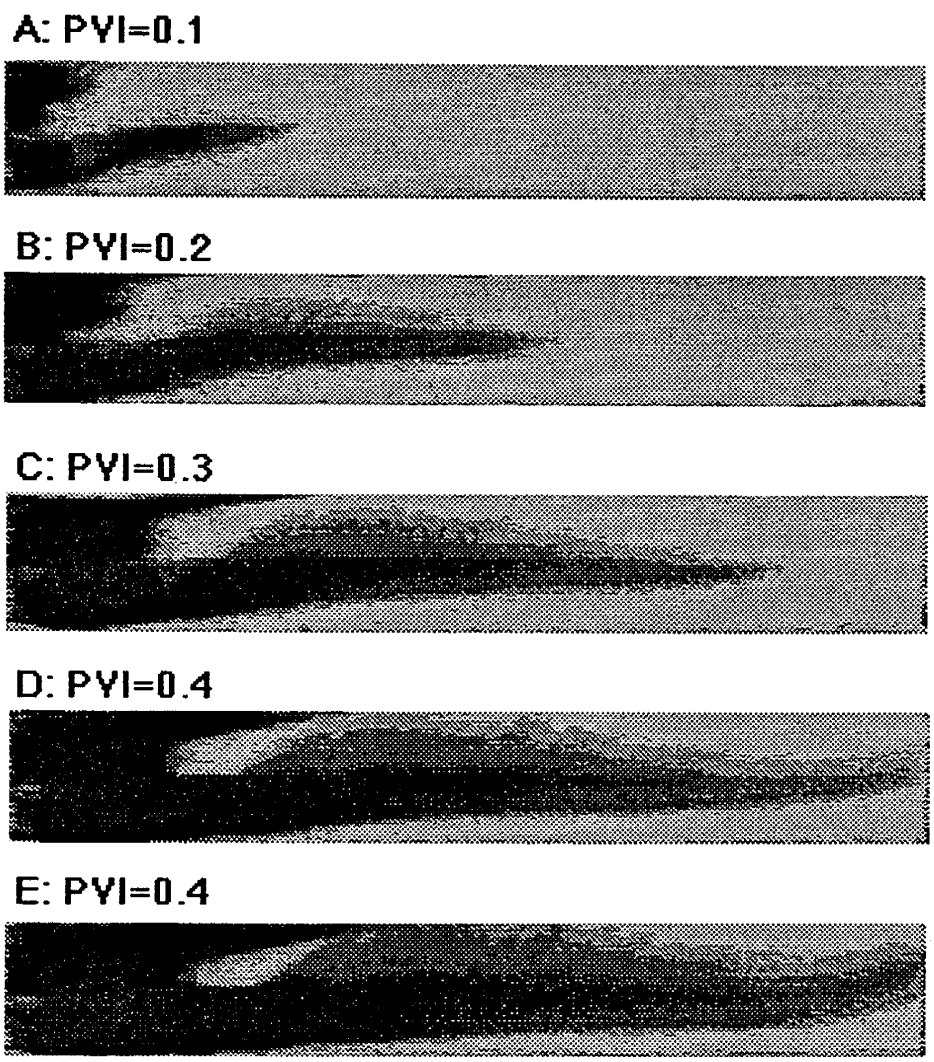

Figure 5.19: Fluid distributions during displacement of IPA by IC_8 at 2.0 ml/min.

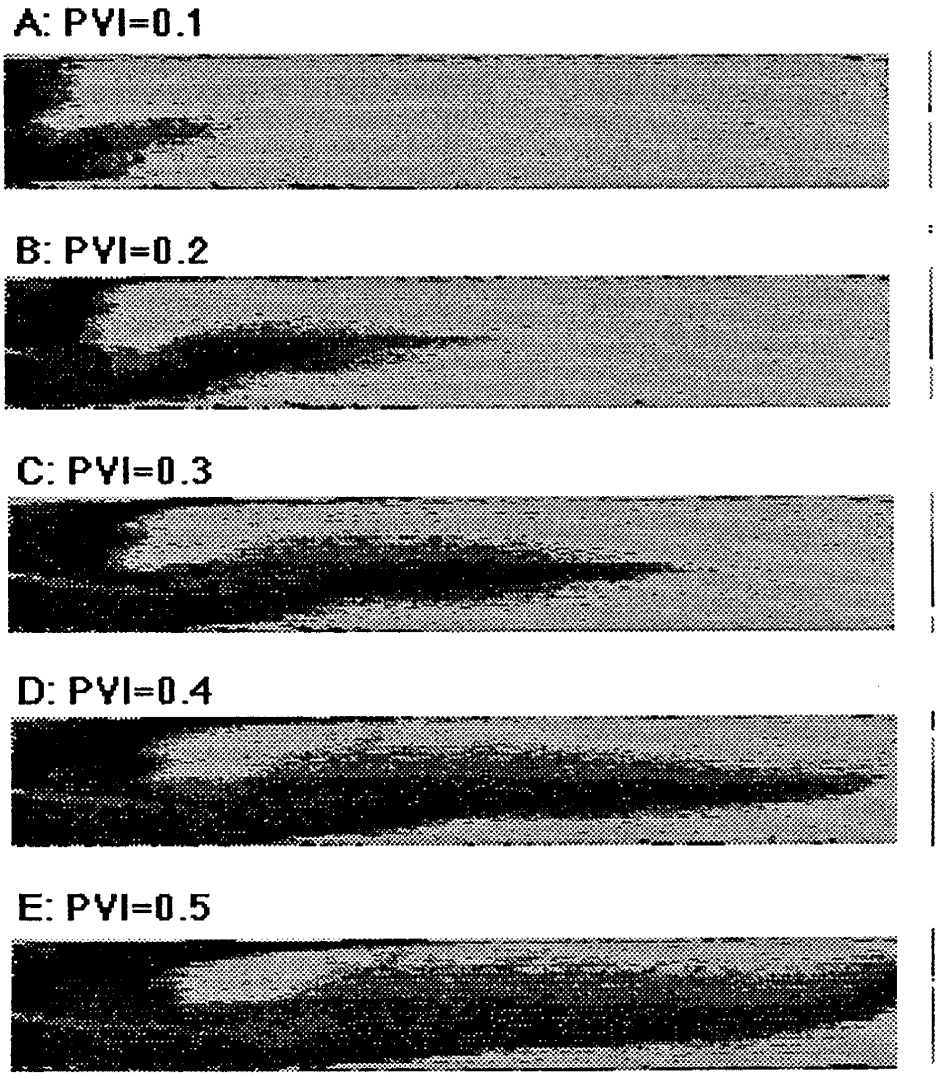

Figure 5.20: Fluid distributions during displacement of IPA by IC_8 at 4.0 ml/min.

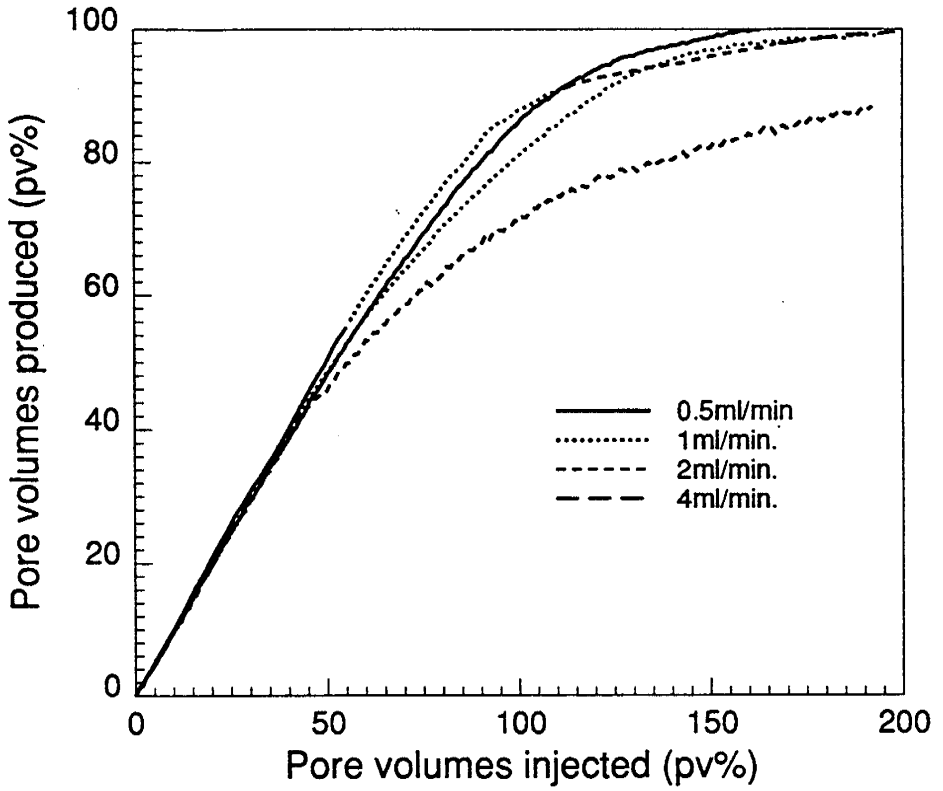

Figure 5.21: Production curves for the displacements of IPA by IC_8.

displacement. According to Fig 5.21 the optimum displacement rate for the layer structure and fluid pair was around 1.0 ml/min.

High Mobility Ratio Displacements

Displacements were carried out at high mobility ratio with a light mineral oil (LMO) as the displaced fluid and n-decane (C_{10}) and IC_8 as the displacing fluids with mobility ratios of 13.4 and 27.0 respectively. Three injection rates were employed for high mobility ratio displacements, 1.0, 2.0, and 4.0 ml/min. Figs. 5.22 to 5.24 are the fluid distributions observed during displacement of LMO by C_{10} at several rates. A large finger formed in the more-permeable layer, while a small gravity tongue formed in the less-permeable layer. Downward crossflow of LMO was observed at the front in the upper layer. Upward crossflow was apparent after 0.2 PVI. Instability in the upward crossflow was more significant at the higher mobility ratio. For example the fingers in Fig. 5.22 are larger and more separated than those observed in the low mobility displacements. Figs. 5.23 and 5.24 show that with further increase in injection rates the finger in the more-permeable layer became more dispersed, and the tip of the finger was more blunt than at lower rates. Those observations suggest that gravity had smaller effect on the development of fingering. There was much less upward crossflow, and the gravity tongue in the upper layer was smaller. At the high injection rate (4.0 ml/min.), that trend continued. Little viscous fingering was observed at the displacement front in the upper layer during the high rate displacements. Viscous fingering in the high-permeability layer started to dominate the displacements. Fig. 5.25 reports the production curves of LMO by C_{10} at the three injection rates.

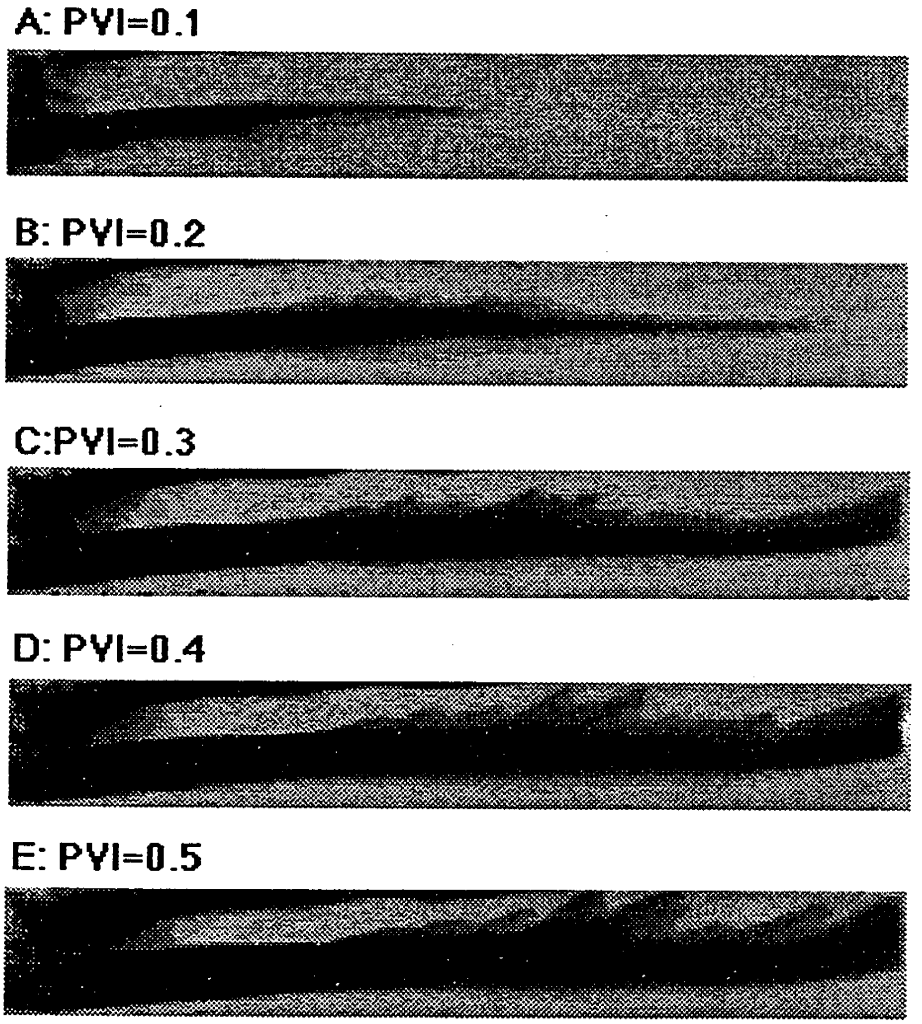

Figure 5.22: Fluid distributions during displacement of LMO by C_{10} at 1.0 ml/min.

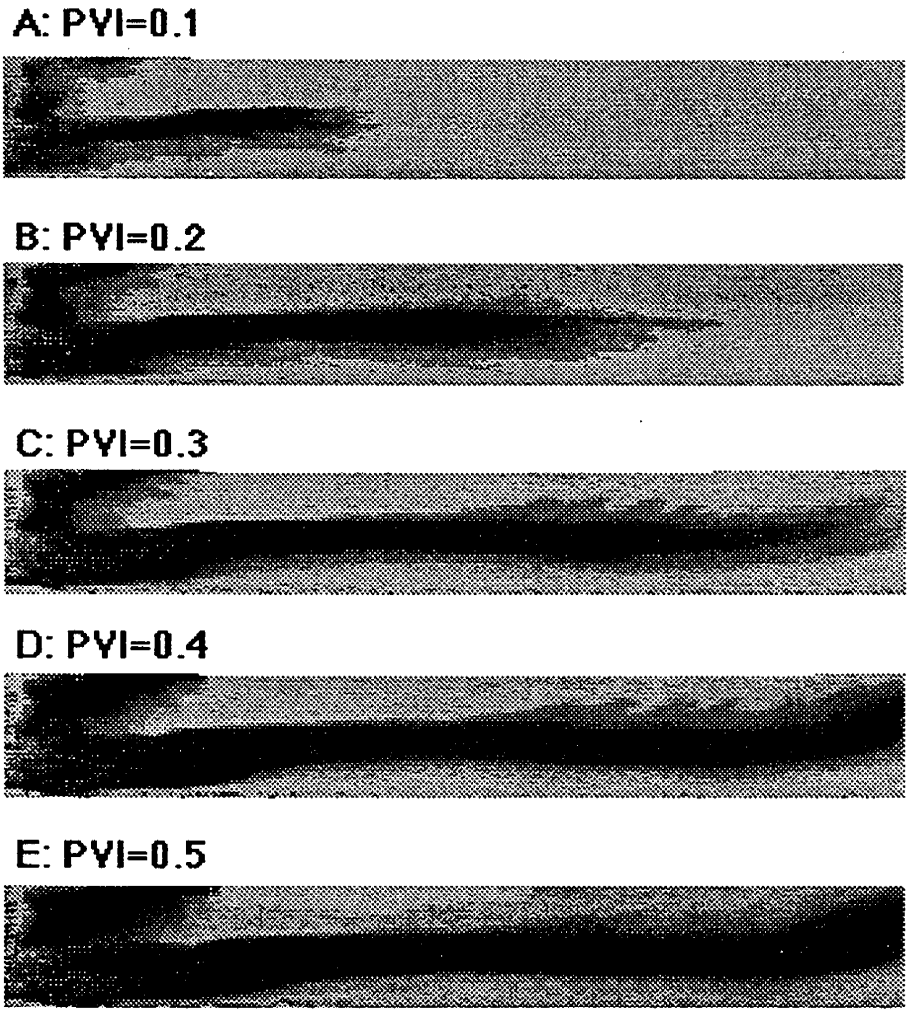

Figure 5.23: Fluid distributions during displacement of LMO by C_{10} at 2.0 ml/min.

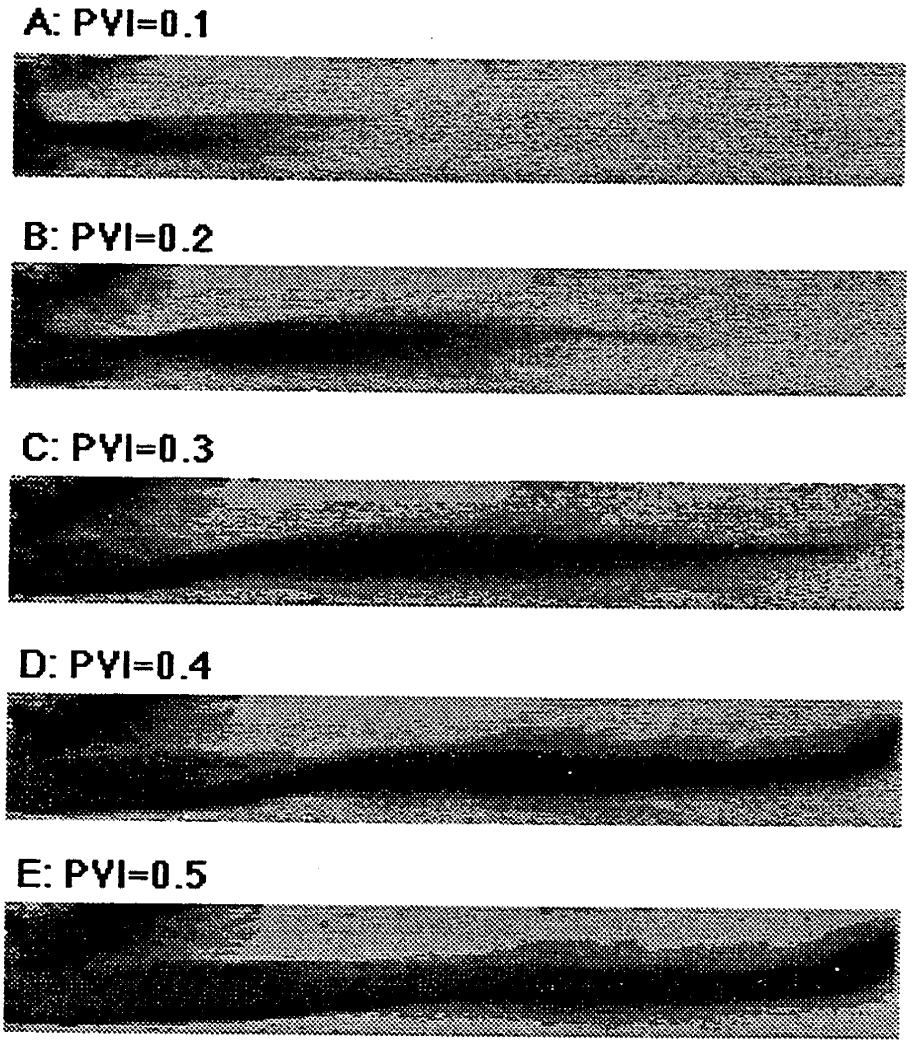

Figure 5.24: Fluid distributions during displacement of LMO by C_{10} at 4.0 ml/min.

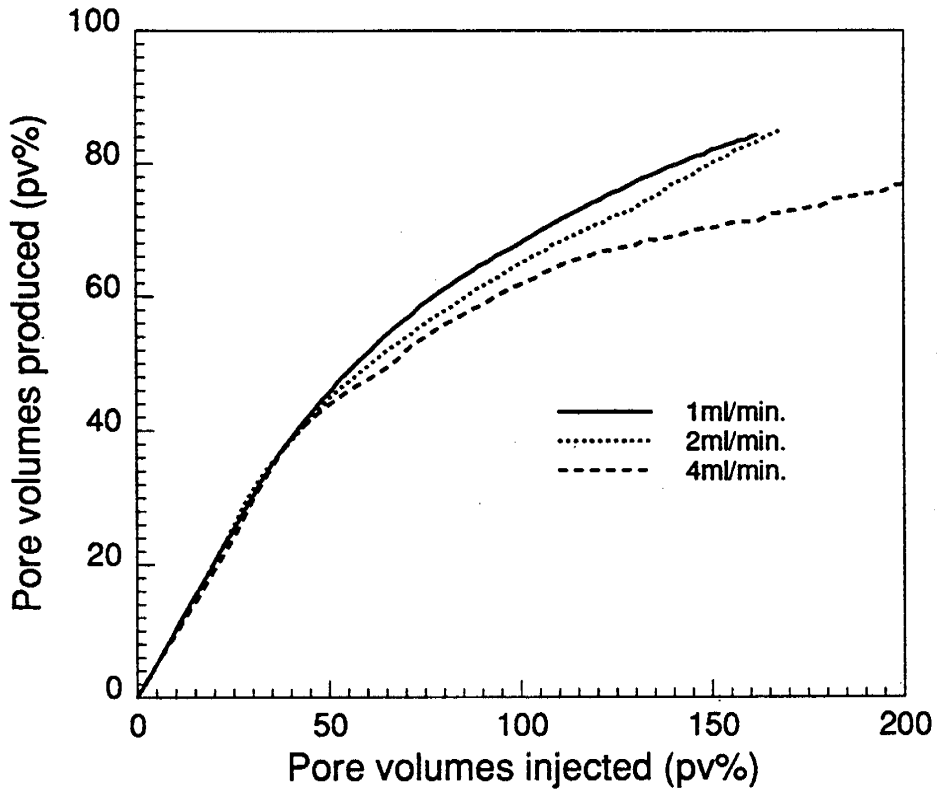

Figure 5.25: Production curves for the displacements of LMO by C_{10}.

Figs. 5.26 to 5.28 show the fluid distribution in the displacements of LMO by IC_8. The mobility ratio in this case was 27.0. The displacement behavior was similar to that shown in Figs. 5.22 to 5.24 except that additional vertical crossflow was apparent, due to the larger density difference of LMO and IC_8 (0.133 g/ml) over that of LMO and decane (0.09g/ml). Comparison of the two high mobility ratio systems indicates that more vertical fingering occurred at high mobility ratio than at lower mobility ratio, as might be expected from unstable displacements driven solely by viscous forces. Fig. 5.29 reports the production curves for the displacements of LMO by IC_8 at three different rates.

Near-Miscible Displacements

To demonstrate the effects of phase equilibrium on crossflow in near-miscible displacements, the IPA-Brine-IC_8 system was employed. The corresponding phase diagram is given in Fig. 5.14. The estimated critical tie-line extension is also shown in Fig. 5.14. That tie-line intersects the IPA-Brine axis at about 21% brine. All near-miscible displacements were conducted at an injection rate of 2.0 ml/min. Five fluid compositions (0, 15, 20, 25, 30% of brine) were investigated. Those compositions cover the range from first-contact-miscible (FCM) to immiscible flow. Figs. 5.30 to 5.33 show the fluid distributions during displacements of the different initial compositions. Fig. 5.30 gives the fluid distributions after 0.1 PV injection. The length of the viscous finger in the more-permeable layer decreases with increases in the initial brine concentration. Downward crossflow occurred for the initial brine concentration less than 25%. However, after 0.2 PV injection (Fig. 5.31), the length of the finger in the more-permeable layer decreased with increases in the initial brine concentration up to 20% then increased with additional increases in brine concentration. An interesting

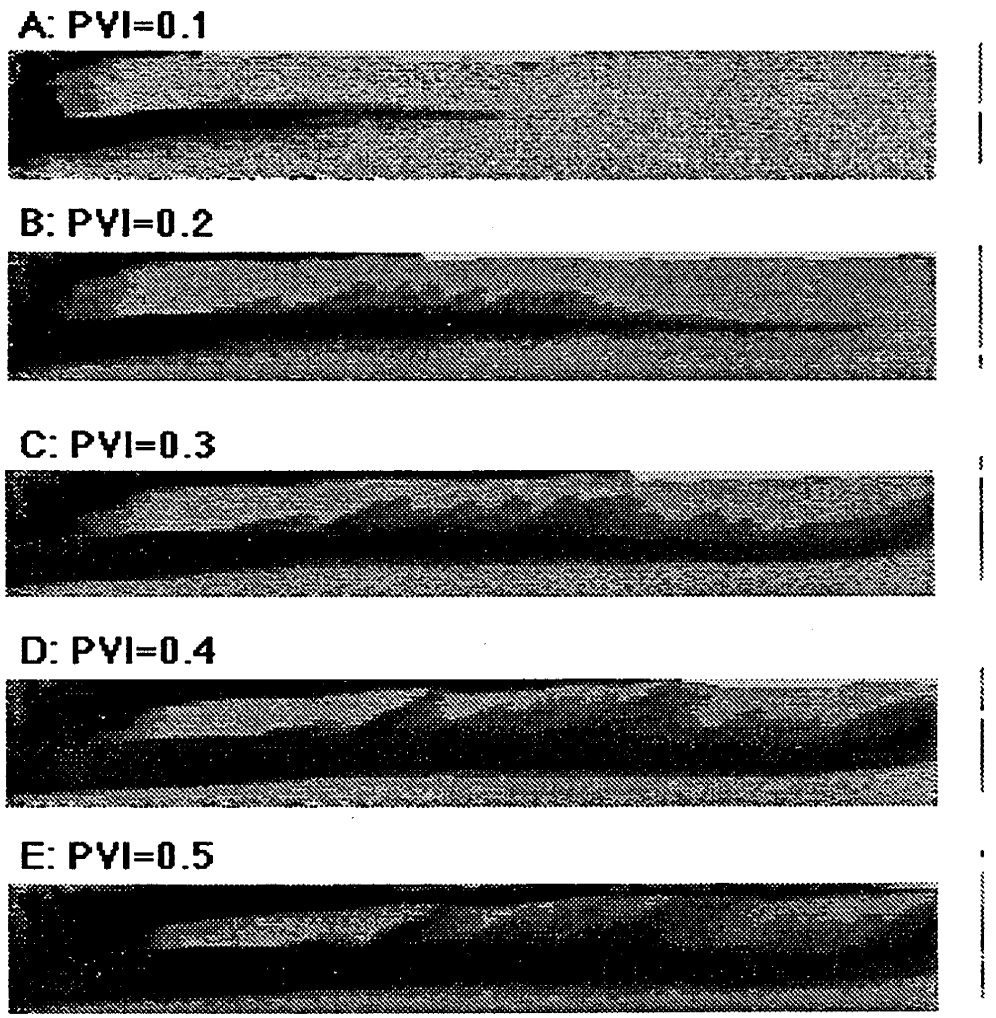

Figure 5.26: Fluid distributions during displacement of LMO by IC_8 at 1.0 ml/min.

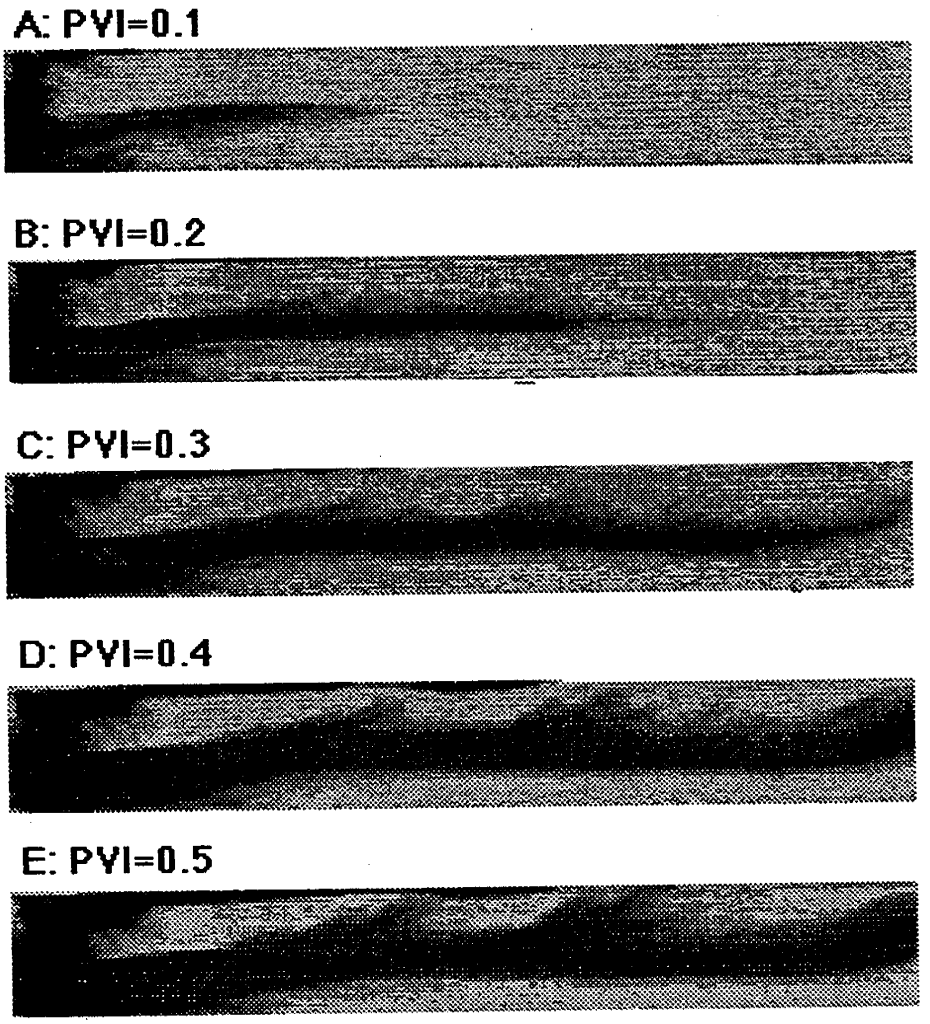

Figure 5.27: Fluid distributions during displacement of LMO by IC_8 at 2.0 ml/min.

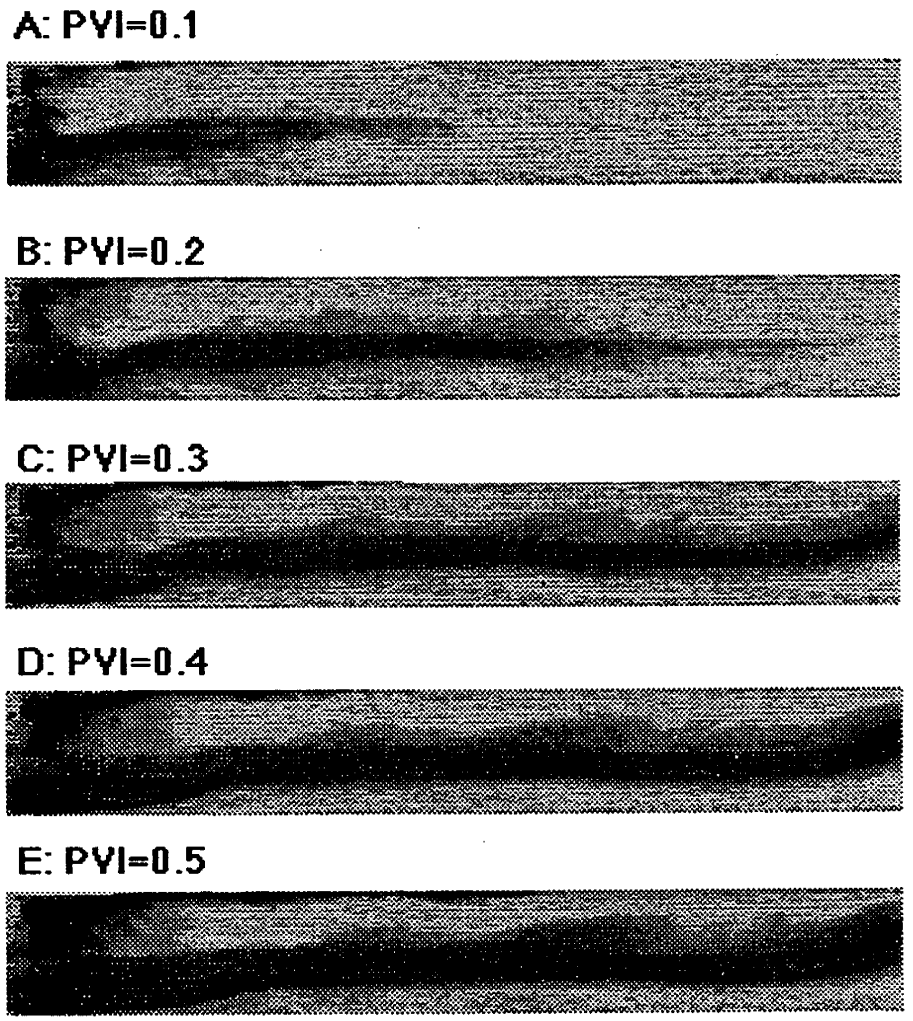

Figure 5.28: Fluid distributions during displacement of LMO by IC_8 at 4.0 ml/min.

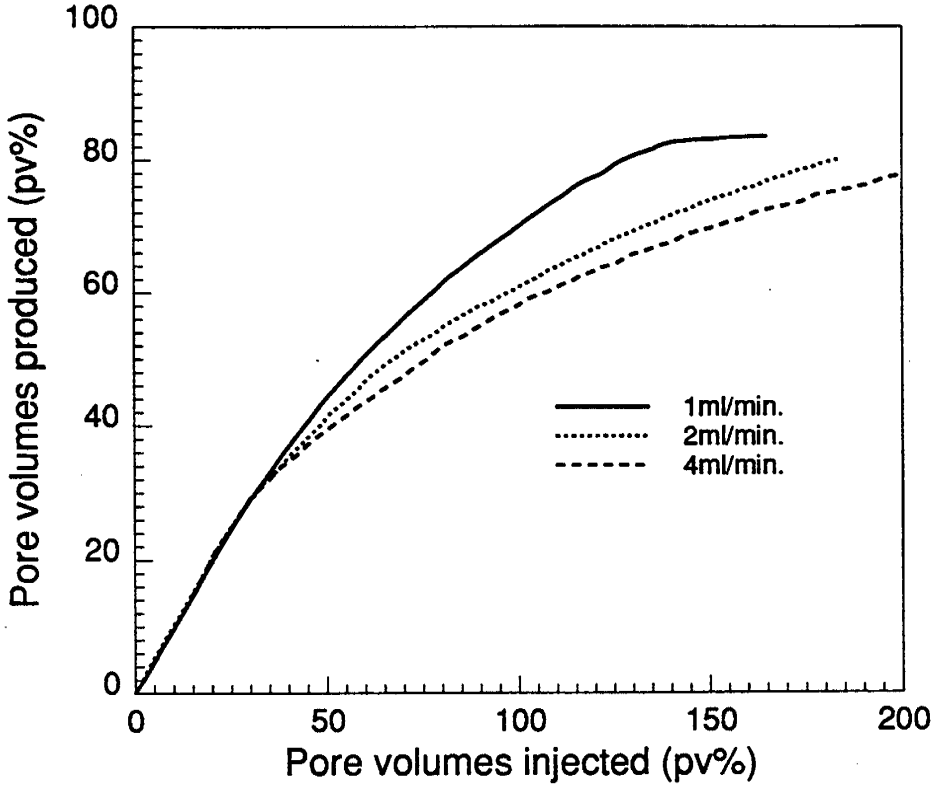

Figure 5.29: Production curves for the displacements of LMO by IC_8.

phenomenon was observed during the displacement of 20% brine and IPA where a slug of initial fluid (IPA and brine) formed in the lower, more-permeable layer due to downward crossflow. At early times (less than 0.2 PV), upward crossflow was observed only in the pure IPA displacements. After 0.3 PV injection, upward crossflow occurred in both 0.0 and 15% brine cases. As the fluid distributions indicate, a series of slugs of fluid in place formed in the displacement of 20% brine cases with continued injection. Little upward crossflow was observed in displacements when the brine concentration was greater than 20%.

Fig. 5.34 shows the production curves for the near-miscible displacements. The production curves for the FCM displacements are almost identical, although the viscosity ratio increases with the increase in brine concentration. However, the density of the fluid in place increases with increase in brine concentration, which may reduce the negative effects of high viscosity ratio. The production curves in Fig. 5.34 show significant differences for brine concentrations greater than 20%, however. Production at a given injection was consistently reduced with increases in brine concentration for brine concentrations greater than 20%.

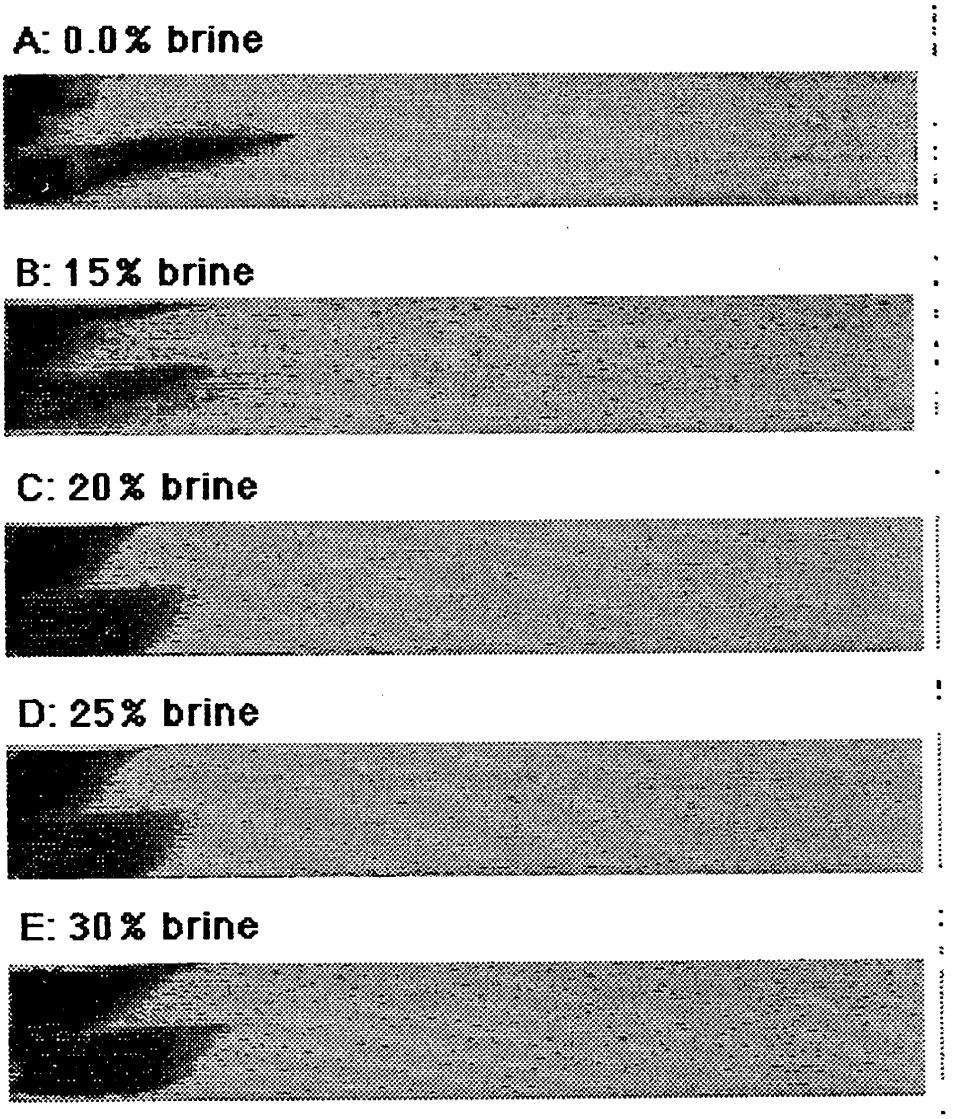

Figure 5.30: Fluid distributions of near-miscible displacements after 0.1 PVI.

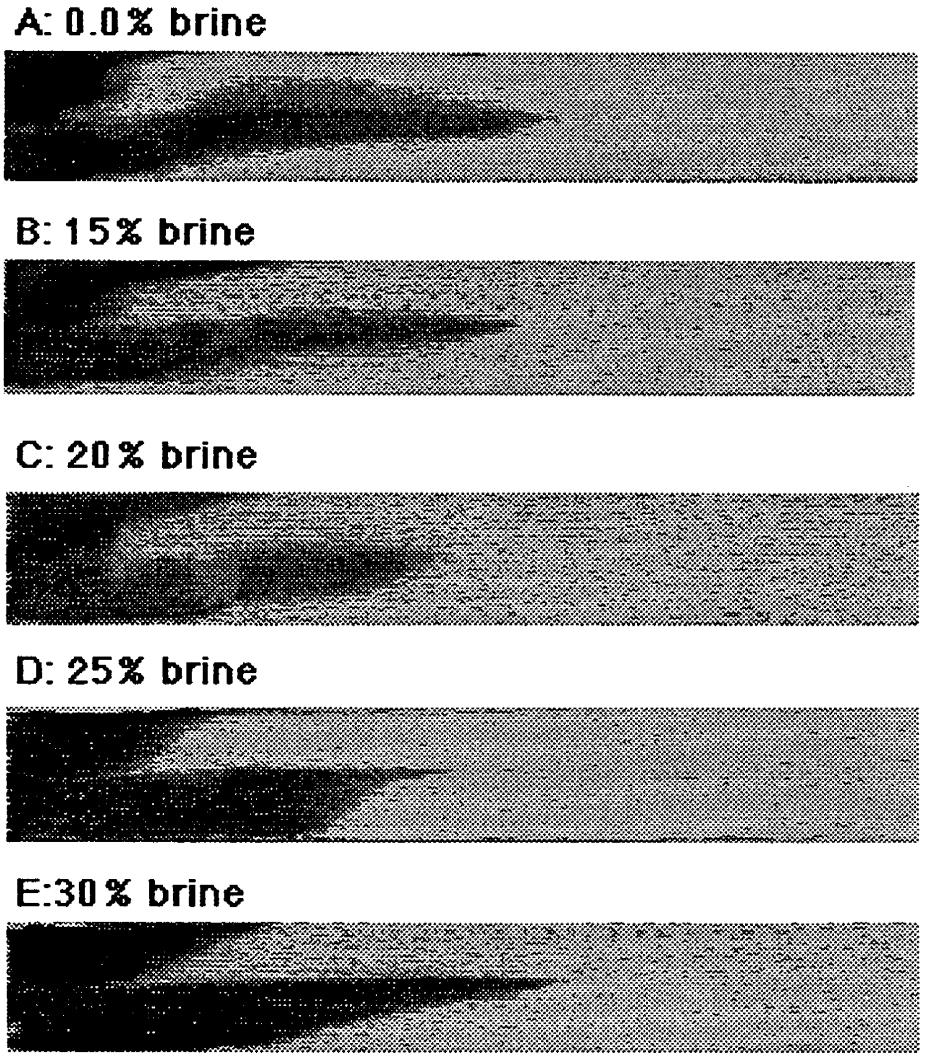

Figure 5.31: Fluid distributions of near-miscible displacements after 0.2 PVI.

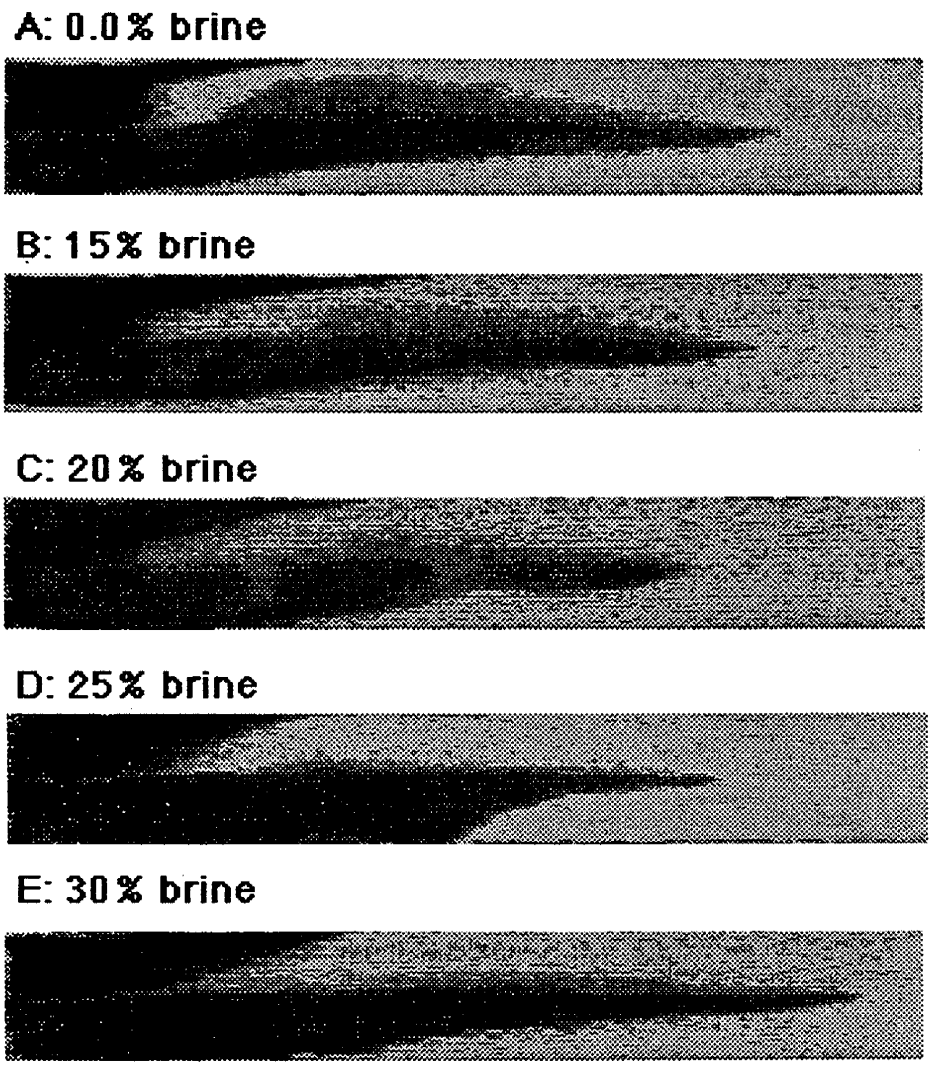

Figure 5.32: Fluid distributions of near-miscible displacements after 0.3 PVI.

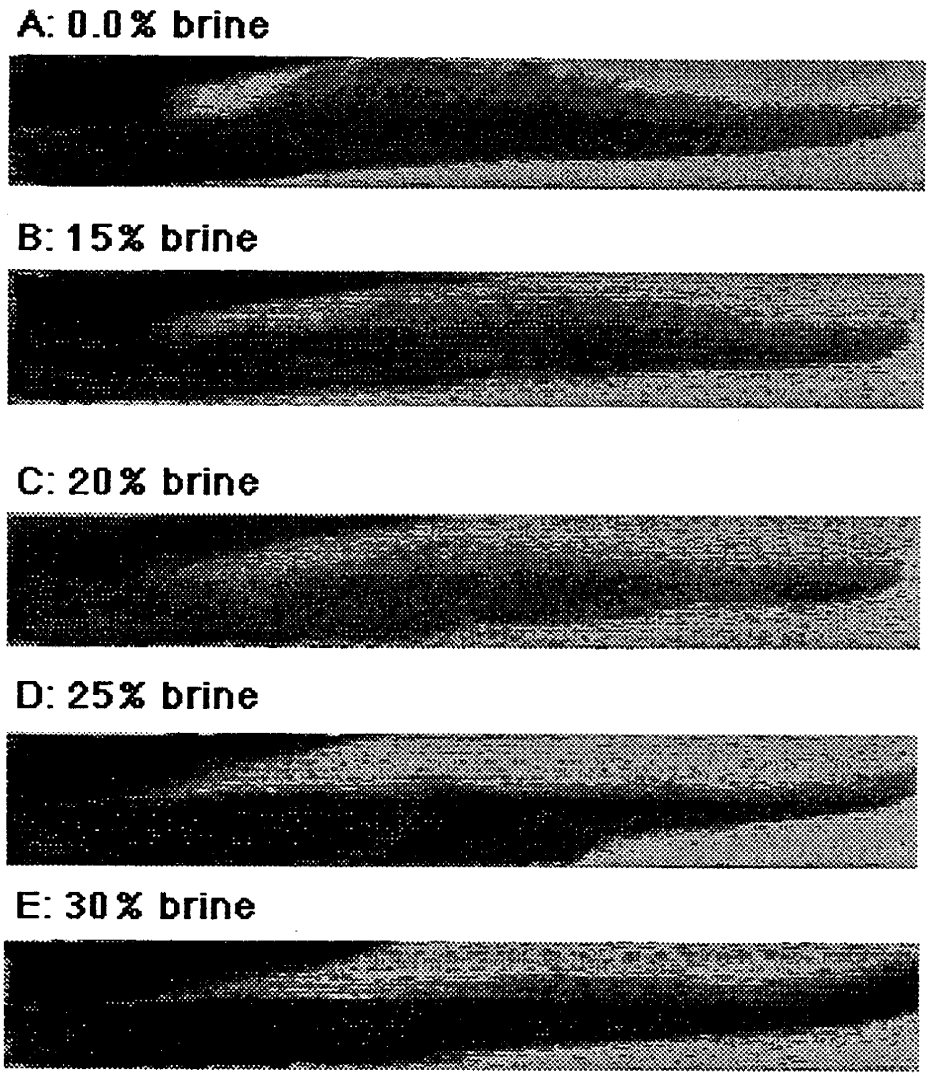

Figure 5.33: Fluid distributions of near-miscible displacements after 0.4 PVI.

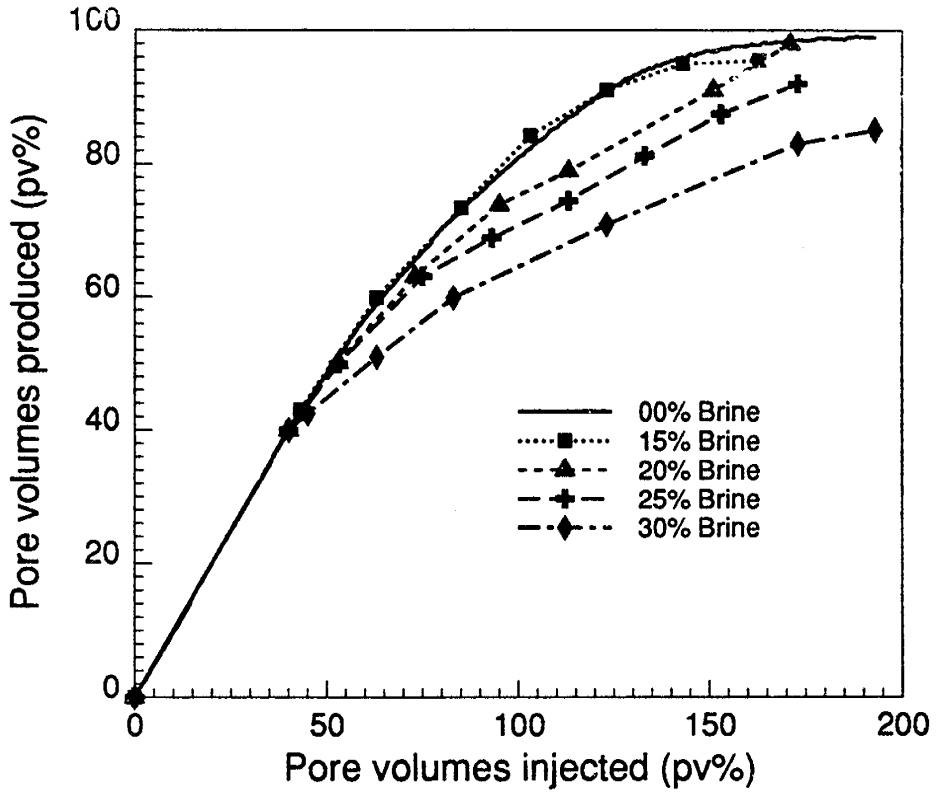

Figure 5.34: Production curves for near-miscible displacements.

5.2.3 Discussion

FCM Displacements

Scaling of miscible displacements in an homogeneous cross-section was investigated by Fayers and Muggeridge [36]. A dimensionless number, $N_G = 2\frac{H}{L}\frac{(M-1)q\mu_o}{Mk\Delta\rho g}$ (the viscous to gravity ratio), was defined for homogeneous media. Fine grid simulations suggested that transition of flow in a vertical cross-section from gravity-dominated to viscous-dominated flow occurs in the range of $1.0 < N_G < 10$ [36]. For heterogeneous media, the dimensionless number N_G can be redefined as

$$N_G = 2\frac{(M-1)}{M}\frac{Lq\mu_o}{k_{ah}\Delta\rho g H}\frac{1}{R_l^2} \tag{5.8}$$

where $R_l = \frac{L}{H}\left(\frac{k_{av}}{k_{ah}}\right)^{1/2}$ is a shape factor of the medium, k_{ah} and k_{av} are the average permeabilities in the horizontal and vertical directions, M is the mobility ratio, and μ_o is the oil viscosity. The corresponding values of N_G for the miscible displacements in this work are in the range of 0.128 to 5.71. The fluid distributions shown in Fig. 5.17 indicate that when the value of N_G is as low as 0.128, the flow behavior is dominated by gravity segregation. For displacements with values of N_G from 0.256 to 0.8 (< 1.0), the injected fluids advanced faster in the bottom layer, which suggests that the flow in those cases was dominated by viscous forces. Apparently, therefore, the transition from gravity-dominated to viscous-dominated flow occurs at lower N_G in stratified media than in homogeneous media. Fig. 5.35 shows the production of oil in place at 1.5 PVI. The recovery, at first increases, and then decreases with

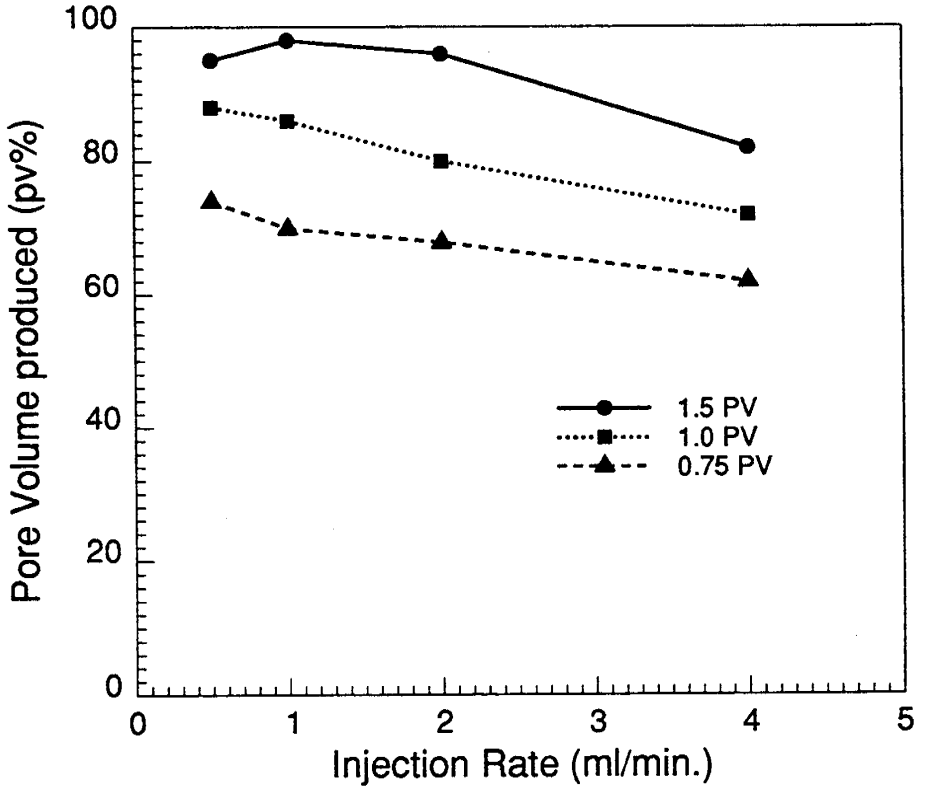

Figure 5.35: Recoveries of IPA after 0.75, 1.0 and 1.5 PVI.

increasing values of N_G. Clearly there is an optimum injection rate for oil recovery when lower density fluid is injected into a two-layer system with the high-permeability layer below the low-permeability layer. In contrast, recovery from a homogeneous medium increases with increasing rate of injection. By definition, the value of N_G is proportional to the injection rate, therefore, the recovery from a homogeneous medium increase with increasing of N_G. As has long been known, gravity-driven crossflow can interact significantly with heterogeneity to increase or decrease recovery depending on whether crossflow acts to increase or decrease sweep efficiency.

The difference in flow behavior in stratified and homogeneous media results from the interaction of gravity segregation and viscous instability with the permeability contrast. In displacements in homogeneous media at low values of N_G, gravity segregation causes formation of a single tongue, and the higher the mobility ratio, the more rapidly it penetrates. As N_g is increased, however, a transition occurs to flow that is dominated by the viscous instability. Both experiments and theory [127, 2] indicate that recovery at breakthrough is better if viscous fingering dominates, although the improvement decreases as mobility ratio increases. Thus, the viscous crossflow [12] that is so important in the development of fingering improves breakthrough recovery in a homogeneous medium.

When layers are present, gravity segregation can increase or decrease recovery depending on the vertical arrangement of permeability. When gravity augments crossflow into a low-permeability layer, as in the experiments described here, then the competition between viscous forces and gravity segregation creates the optimum. Again, it is crossflow that makes possible the improved recovery.

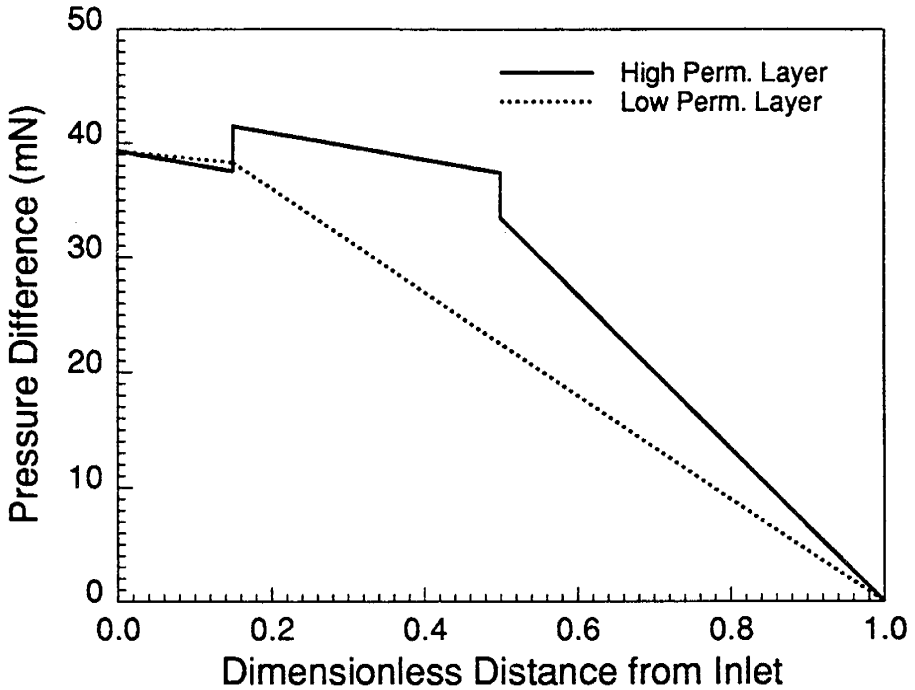

Figure 5.36: Pressure distribution during flow in a two-layered system with gravity effects.

To show the relative importance of gravity compared with viscous forces, we assume that at the beginning of the displacement process, the model was placed horizontally and after a certain period of injection, the model was turned on edge. The pressure profile in these two layers before and after the rearrangement is shown in Fig. 5.36. It is clear that when the model is vertically oriented, there is an additional force that aids the crossflow ahead of the front in the low-permeability layer. The ratio of the gravity head to the pressure difference across the section is

$$\frac{P_1 - P_2}{\Delta\rho g h} = \frac{2\mu_o l_1 Q}{k_2 A \Delta\rho g h}\left(\frac{f}{K_r} - 1\right)\frac{1}{1+f} \tag{5.9}$$

where A is the cross-sectional area of the medium, K_r is the ratio of k_1 and k_2, h is the thickness of the low-permeability layer and f is defined as

$$f = \frac{l_1 + M(L - l_1)}{l_2 + M(L - l_2)} \tag{5.10}$$

where M is the mobility ratio, and the l's are the distance of the injected fluid advanced in each layer. According to Eq. 5.10, in the displacement of IPA by IC_8 at a injection rate of 1.0 ml/min, the gravity head can be as much as 70 percent of the transverse pressure difference. Only 3 percent of the transverse pressure difference, however, is attributed to the gravity head for the high-rate (4.0 ml/min) displacement of LMO by decane. Clearly, more upward crossflow occurs at low injection rates. The same argument can be used to explain the observations for downward crossflow.

Near-miscible Displacement

In near-miscible displacements, the interplay of gravity, capillary and viscous forces determines the flow behavior. Capillary force affects crossflow depending, of course, on the wetting behavior of the system. For the system considered here, the injected fluid is the nonwetting phase, and hence capillary pressure differences suppress upward crossflow, while the gravity head enhances upward crossflow. The relative contribution to crossflow may be represented by the ratio of gravity to capillary forces, namely the Bond number $N_B = \frac{\Delta\rho g h}{\sigma}\left(\frac{k}{\phi}\right)^{1/2}$. According to critical scaling arguments, the IFT, σ, between two phases near a critical point is correlated to the density difference, $\Delta\rho$ as $\sigma = c(\Delta\rho)^{3.8}$, where c is a constant. Substitution of this expression into the definition of the Bond number gives

$$N_B = \frac{gh}{c\Delta\rho^{2.8}}\left(\frac{k}{\phi}\right)^{1/2}. \tag{5.11}$$

It is interesting to note that the Bond number is inversely proportional to the value of $\Delta\rho^{2.8}$. Thus, in the neighborhood of a critical point, where the density difference becomes very small, the value of N_B can be large. That is, gravity effects can be significant in near-miscible displacements, while for compositions farther from the critical point, the displacements will be affected more by capillary than gravity forces.

Theoretical calculations of the effects of phase behavior and crossflow [97, 98] indicate that crossflow will induce two-phase flow in displacements that would be MCM in strictly one-dimensional, dispersion-free flow, as mixing of fluids in the two layers pulls the displacement path back into the two-phase region. The displacements for 20 and 25 % brine in the initial mixtures were clearly affected by that crossflow and mixing. When two phase were created in those displacements, the interfacial tensions were evidently high enough that the capillary entry pressure for the low permeability layer did not permit much crossflow, and hence crossflow was reduced considerably below that observed for 0 and 15% brine mixtures. The displacement of the 15% brine mixture is particularly instructive. It too was MCM according to one-dimensional theory, and presumably, crossflow still caused some two-phase flow, but the phases created were close enough to the critical point that the resulting low IFT's allowed crossflow to continue. Fig. 5.33, for example, shows that substantial crossflow occured for 15% brine, less was observed for 20% brine, and almost no crossflow occured for 25 and 30% brine. Similar effects can be expected in gas injection processes, which rely on composition paths that pass near critical points, as the theory of Chapter 3 demonstrates.

5.2.4 Conclusions

The experiments performed to investigate gravity segregation, viscous and gravity crossflow in a two-layered bead pack, lead to the following conclusions:

1) For FCM displacements, the transitions of flow from gravity dominated to viscous dominated occur in the range of $0.2 < N_G < 5$ for the two-layered medium investigated in this work.

2) For FCM displacements in the transition region, gravity-driven crossflow produces optimum sweep efficiency when the rate of vertical crossflow is comparable to horizontal invasion velocity.

3) For MCM displacements, crossflow is very sensitive to the composition of the fluid in place, due to the dramatic variations of IFT and density difference of the two phases in the near-miscible region.

4) Phase behavior can alter crossflow, and therefore sweep efficiency, significantly. MCM displacements yield optimum recovery when viscous- and gravity-driven crossflow interact with phase behavior to produce near-critical mixtures with low IFT's.

5.3 Summary

The experimental results and simple, limiting case analyses of transport mechanisms and rates reported in this chapter illustrate how capillary and gravity-driven crossflow can move fluid between regions of differing permeability. The coreflood experiments of Section 5.1 show that there is a significant interaction of gravity-driven flow with capillary imbibition. When interfacial tension (IFT) is high, capillary crossflow dominates, residual saturations are typical of flow at low capillary number, and oil recovery rate is controlled by countercurrent flow of oil and water. When IFT is low, on the other hand, gravity maintains segregated flow, snap-off of residual oil droplets is suppressed, and recovery can be much higher than when IFT is high. Those results are important for scaling of miscible floods, because any successful multicontact miscible (MCM) flood will generate composition paths that pass near a critical point (see Chapter 3). Hence, low IFT's will exist within the transition zone during MCM displacements. Furthermore, that transition from capillary to gravity-dominated flow begins at only moderately low IFT's, even for permeabilities as low as 15 md. Thus, transverse transport of fluids between layers of high and low permeability is likely to be controlled by gravity forces in part of the transition zone and by some combination of capillary and gravity forces elsewhere. Composition, and hence IFT, gradients will also exist. As a result, substantial quantities of crossflow are possible in reservoirs with sufficient vertical permeability.

The first-contact miscible displacements of Section 5.2 also show how complex the flow and mixing patterns can be when low density solvent is injected into a layered system with low permeability above high permeability. In such displacements, viscous and gravity forces controlled the scaling of crossflow. At low injection rates, gravity-driven crossflow leads to significant override even in the low permeability layer. At high rates, viscous forces dominate, and most of the injected fluid enters the high permeability layer. At intermediate rates, viscous crossflow and gravity segregation both contribute to transverse flow, and hence there is an optimum rate at which the adverse effects of heterogeneity are minimized. The experimental results presented here suggest that the presence of heterogeneity in the form of layers alters significantly the range of N_G over which the transition from gravity-dominated to viscous-dominated flow takes place from that of a homogeneous porous media. When the injection rate can be set at a level near that of the optimum value of N_G, the high permeability layer can be used to deliver fluid to the low permeability layer by crossflow, which is more rapid than the corresponding longitudinal flow in the low permeability layer. In such displacements, however, there will be considerable transverse mixing of oil and solvent, as the experiments of Section 5.2 show. In MCM displacements, substantial interaction of chromatographic compositional effects (Chapter 3) with crossflow can be expected. For such systems, therefore, a detailed compositional representation of the flow will be required if the

details of the scaling behavior of heterogeneity and crossflow are to be understood. The experimental results reported here can be used to test such theories as they are developed.

6. Summary

This report outlines research results in four areas that involve physical mechanisms that play pivotal roles in the performance of gas injection processes:

1. Characterization of crude oils and prediction of multicomponent phase equilibrium,
2. Development of miscibility in multicomponent systems,
3. Viscous fingering in homogeneous and heterogeneous porous media, and
4. Crossflow driven by capillary, gravity, and viscous forces.

All four areas contribute in important ways to determine the performance of a miscible flood in a given reservoir. Furthermore, the individual physical mechanisms act (and interact) on different length and time scales, a fact that greatly complicates the analysis of scaling behavior. For example, phase equilibrium operates on relatively short-length scales. Molecular diffusion insures that phases are equilibrated at the pore scale. At the microscopic scale then, the calculation of phase equilibrium with an equation of state is completely appropriate. The experimental approaches described in Chapter 2 show how compositional information about a crude oil can be acquired efficiently by chromatography and mass spectrometry methods and how that information can be used to build a characterization of the oil for equation-of-state calculations of phase equilibria.

The next step beyond the strictly local pore scale is the extension to flow lengths in one space dimension. That step is taken in Chapter 3, where the interplay of phase equilibrium and two-phase flow is examined. The analysis of the flow behavior of four-component systems by the method of characteristics reveals a very important aspect of the development of miscibility that cannot be discerned from the traditional analysis of three-component systems. Development of multicontact miscibility requires that some key tie-line approach a critical point. In ternary systems, that can only happen if the initial oil or the injected fluid composition lies on the extension of a critical tie line. The theory of Chapter 3 shows that as components are added, additional tie lines come into play, and hence miscibility can also develop if any one of them approaches a critical tie line. That theory explains, for example, the behavior of condensing/vaporizing gas drives. It also indicates why calculation techniques that use criteria based on the requirement that the initial oil or injected fluid lie on a critical tie line sometimes fail [76, 53].

The extension of scales to the second and third space dimensions adds considerable complexity to the flow behavior as the results presented in Chapters 4 and 5 show. Now, nonuniform flow arises from heterogeneities in porosity and permeability and from the hydrodynamic instability that causes viscous fingering. The experimental results of Chapter 4 suggest strongly that permeability variations will have greater impact on field-scale flows than will pure viscous instability. It is clear that nonuniform flow inevitably reduces displacement efficiency, as the particle-tracking calculations described in Chapter 4 and elsewhere [92, 1, 12, 2, 13] show, but that is not the only important mechanism. If there is any nonuniform flow (and the mobilities of all the fluids are not the same), then crossflow will also

occur. Crossflow can be driven by capillary forces, gravity, viscous forces and, more slowly, by diffusion and dispersion. Whatever the combination of driving forces, crossflow will induce mixing of fluid in regions where flow is rapid with fluid in adjacent zones. That mixing will deliver injected gas to areas that would be reached only much more slowly by longitudinal flow. Furthermore, the transverse mixing causes two-phase flow even in displacements that would be multicontact miscible (MCM) in one-dimensional flow [40, 97, 98, 99, 100]. It is unlikely, therefore, that MCM floods in real reservoirs are strictly single phase. Instead, the combination of dispersion and crossflow with phase behavior means that two phases will be present. While the presence of two-phase flow appears at first to be a negative response to crossflow, calculations reported previously for two-layer flow indicate the opposite. Recovery can actually be more rapid when crossflow is present than it is when layers are isolated [98, 99, 100], even though the crossflow moves the process composition path back into the two-phase region. In such cases the existence of two-phase flow actually alters local mobility distributions enough to improve displacement performance. Crossflow can also move solvent into low permability layers and oil out of those layers. Thus, crossflow is likely to be beneficial in many miscible floods.

If two phases are really present in field-scale miscible floods, then analysis of scaling behavior and crossflow must include capillary phenomena. The results of Chapter 5 have important implications for the design of miscible floods, therefore. They show that if interfacial tensions (IFT's) are only moderately low, gravity forces can move significant quantities of both the wetting and nonwetting phases. Furthermore, a combination of modestly low IFT and gravity leads to faster initial crossflow than that observed for either capillary or gravity-driven crossflow alone. It is clear from the analysis of crossover tie lines in Chapter 3 that low IFT's in the required range will be created by the chromatographic interaction of phase equilibria with two-phase flow, which insures that some tie line will be near a critical point. Furthermore, the experimental observations for crossflow induced by IFT gradients suggest that local concentration gradients will contribute to crossflow in ways that have not been explored previously.

The combination of thermodynamic, mathematical, and experimental results reported here, therefore, indicates that many design opportunities exist to harness the beneficial effects of crossflow in the design of miscible displacement processes. For example, a combination of phase behavior, low IFT's and gravity drainage could be used effectively in fractured reservoirs. In addition, the use of horizontal wells opens many avenues for more advantageous use of gravity forces along the lines suggested in Chapter 5. Furthermore, the recognition that the full interplay of compositional behavior, nonuniform flow and crossflow determine process scaling behavior is an essential step toward effective use of improved descriptions of reservoir heterogeneities that are now being produced. While much remains to be understood as the implications of the results presented here are explored further, it is clear that substantially improved descriptions of the way miscible floods operate in real reservoirs are now possible.

References

[1] Araktingi, U.G.: *Viscous Fingering in Heterogeneous Porous Media*, PhD dissertation, Stanford University, Stanford, CA (1988).

[2] Araktingi, U.G. and Orr, F.M., Jr.: "Viscous Fingering in Heterogeneous Porous Media," paper SPE 18095 presented at the 1988 SPE Annual Technical Conference and Exhibition, Houston, TX, October 2–5.

[3] Bacri, J.C., Rakotomalala, N., Salin, D., Bourlion, M., Lenormand, R. and Soucemarianadin, A.: "Ultrasonic Diagnostics in Porous Media and Suspensions," *J. Physique III, Paris* (1991) **1**, 674.

[4] Baker, L.E., Pierce, A.C. and Luks, K.D.: "Gibbs Energy Analysis of Phase Equilibria," *Soc. Pet. Eng. J.* (October 1982) **22**, 731–742.

[5] Barrick, M., Anderson, J., and Robinson, Jr., R.: "Solubilities of Carbon Dioxide in Naphthalene, Phenanthrene, and Pyrene at Pressures to 10.6 MPa and Temperatures from 373 to 433 K," *J. Chem. Eng. Data* (1987) **32**, No. 3, 372–374.

[6] Bartle, K.D., Clifford, A.A. and Jafar, S.A.: "Measurement of Solubility in Supercritical Fluids Using Chromatographic Retention: the Solubility of Fluorene, Phenanthrene, and Pyrene in Carbon Dioxide," *J. Chem. Eng. Data* (1990) **35**, 355–360.

[7] Bartmann, D. and Schneider, G.M.: "Experimental Results and Physico-Chemical Aspects of Supercritical Fluid Chromatography with Carbon Dioxide as the Mobile Phase," *J. Chromatography* (1973) **83**, 135–145.

[8] Bear, J.: *Dynamics of Fluids in Porous Media*, American Elsevier, New York (1972).

[9] Beliveau, D. and Payne, D.A.: "Analysis of a Tertiary CO_2 Flood Pilot in a Naturally Fractured Reservoir," paper SPE 22947 presented at the 1991 SPE Annual Technical Conference and Exhibition, Dallas, TX.

[10] Benham, A.L. and Olson, R.W.: "A Model Study of Viscous Fingering," *Soc. Pet. Eng. J.* (June 1963) 138–144.

[11] Blackwell, R.J., Rayne, J.R. and Terry, W.M.: "Factors Influencing the Efficiency of Miscible Displacement," *Trans., AIME* (1959) **216**, 1–8.

[12] Brock, D.C.: *An Experimental Investigation of Viscous Fingering in Heterogeneous Porous Media*, PhD dissertation, Stanford University, Stanford, CA (1990).

[13] Brock, D.C. and Orr, F.M., Jr.: "Flow Visualizations of Viscous Fingering in Heterogeneous Porous Media," paper SPE 22614 presented at the 1991 SPE Technical Conference and Exhibition, Dallas, TX, October 6–9.

[14] C. M. Jensen and Orr, Jr., F. M.: "Phase Behavior of Mixtures of CO_2 and Wasson Recombined Reservoir Fluid (312 scf/bbl) at 90, 105 & 120°F," No. 82-41, New Mexico Petroleum Recovery Research Center (1982).

[15] Ceré, A. and Zanotti, F.: "Sharpening Behavior and Dispersion in a Chemical Flooding," presented at the 1985 Third European Conference on Improved Oil Recovery, Rome, Italy, April.

[16] Chatzis, I. and Morrow, N.R.: "Correlation of Capillary Number Relationships for Sandstone," *Soc. Pet. Eng. J.* (October 1984) **5**, 555–562.

[17] Chorn, L. G.: "Simulated Distillation of Petroleum Crude Oil by Gas Chromatography. Characterizing the Heptanes-Plus Fraction," *Journal of Chromatographic Science* (1984) **22**, 17–21.

[18] Christie, M.A.: "3D Simulation of Viscous Fingering and WAG Schemes," paper SPE 21238 presented at the 1991 Eleventh Symposium on Reservoir Simulation, Anaheim, CA, February.

[19] Christie, M.A. and Bond, D.J.: "Detailed Simulation of Unstable Processes in Miscible Flooding," *Soc. Pet. Eng. Res. Eng.* (November 1987) **2**, No. 4, 514–522.

[20] Coats, K. H. and Smart, G. T.: "Application of a Regression-Based EOS PVT Program to Laboratory Data," *SPE Reservoir Engineering* (May 1986) 277–299.

[21] Concus, P.: "Static Menisci in a Vertical Right Circular Cylinder," *J. Fluid Mech.* (1968) **34**, 481–495.

[22] Coskuner, G. and Bentsen, R.G.: "An Extended Theory to Predict the Onset of Viscous Instabilities for Miscible Displacements in Porous Media," *Transport in Porous Media* (October 1990) **5**, No. 5, 473–490.

[23] CRC Press, Inc., West Palm Beach, Florida, *CRC Handbook of Chemistry and Physics*, 61st edition (1981).

[24] Cuiec, L.E., Bourbiaux, B. and Kalaydjian, F.: "Imbibition in Low-Permeability Porous Media: Understanding and Improvement of Oil Recovery," paper SPE 20259 presented at the 1990 7th Annual Symposium on Enhanced Oil Recovery, Tulsa, OK, April.

[25] Dandge, D., Heller, J., and Wilson, K.: "Structure Solubility Correlations: Organic Compounds and Dense Carbon Dioxide Binary Systems," *Ind. Eng. Chem. Prod. Res. Dev.* (1985) No. 24, 162–166.

[26] Deo, M.D., Nutakki, R. and Orr, F.M., Jr.: "Schmidt-Wenzel and Peng-Robinson Equations of State for Carbon Dioxide-Hydrocarbon Systems: Binary Interaction Parameters and Volume Translation Factors," paper SPE 18796 presented at the 1989 California Regional Meeting, Bakersfield, CA, April 5–7.

[27] Dindoruk, B.: *Analytical Theory of Multiphase, Multicomponent Displacement in Porous Media*, PhD dissertation, Stanford University, Stanford, CA (1992).

[28] Dindoruk, B., Johns, R.T. and Orr, F.M., Jr.: "Analytical Solution for Four Component Gas Displacements with Volume Change on Mixing," (June 1992) Third European Conference on the Mathematics of Oil Recovery, Delft, Holland.

[29] Dougherty, E.L.: "Mathematical Model of an Unstable Miscible Displacement," *Soc. Pet. Eng. J.* (June 1963) 155–163.

[30] Dumoré, J.M. and Schols, R.S.: "Drainage Capillary Pressure Functions and the Influence of Connate Water," *Soc. Pet. Eng. J.* (1974) 437–444.

[31] Dumoré, J.M. Hagoort, J. and Risseeuw, A.S.: "An Analytical Model for One-Dimensional, Three-Component Condensing and Vaporizing Gas Drives," *Soc. Pet. Eng. J.* (April 1984) **24**, 169–179.

[32] DuPrey, L.: "Gravity and Capillary Effects during Imbibition," *SPEJ* (1980) 927–935.

[33] Edmister, W.: "Applied Hydrocarbon Thermodynamics: Part 4: Compressibility and Equations of State," *Pet. Refiner* (April 1958) **37**, 173–179.

[34] Ewing, R.E, Russell, T.F., and Wheeler, M.F.: "Simulation of Miscible Displacement Using Mixed Methods and a Modified Method of Characteristics," paper SPE 12241 presented at the 1983 Reservoir Simulation Symposium, San Francisco, CA, November.

[35] Fayers, F.J.: "An Approximate Model with Physically Interpretable Parameters for Representing Miscible Viscous Fingering," *Soc. Pet. Eng. Res. Eng.* (May 1988) **3**, 551–558.

[36] Fayers, F.J., Muggeridge, A.H.: "Extensions to Dietz Theory and Behavior of Gravity Tongues in Slightly Tilted Reservoirs," *SPE Reservoir Engineering* (November 1990) 487–494.

[37] Foulser, R.W.S., Naylor, P. and Seale, C.: "Relative Permeabilities for the Gravity Stable Tertiary Displacement of Oil by Nitrogen," (October 4–6 1989) 10th International IEA Symposium on Enhanced Oil Recovery, Stanford, CA.

[38] Francis, A.: "Ternary Systems of Liquid Carbon Dioxide," *J. Phys. Chem.* (1954) **58**, 1099–1114.

[39] Frimodig, J., Reese, N., and Williams, C.: "Carbon Dioxide Flooding Evaluation of High Pour Point Paraffinic Red Wash Reservoir Oil," paper SPE 10272 presented at the 1981 56th Annual SPE Fall Technical Conference and Exhibition, San Antonio, TX.

[40] Gardner, J.W. and Ypma, J.G.J.: "An Investigation of Phase-Behavior/Macroscopic-Bypassing Interaction in CO2 Flooding," *Soc. Pet. Eng. J.* (October 1984) 508–520.

[41] Gasem, K.A.M. and Robinson, R.L. Jr.,: "Solubilities of Carbon Dioxide in Heavy Normal Paraffins (C_{20}–C_{44}) at Pressures to 9.6 MPa and Temperatures from 323 to 423 K," *J. Chem. Eng. Data* (1985) **30**, 53–56.

[42] Gelhar, L.W. and Axness, C.L.: "Three-Dimensional Stochastic Analysis of Macrodispersion in Aquifers," *Water Resources Research* (1983) **19**, No. 1, 161–180.

[43] Hagedorn, K.: *Component Partitioning in CO_2/Crude Oil Mixtures*, PhD dissertation, Stanford University (1992).

[44] Hagoort, J. and Dumoré, J.M.: "Determination of Minimum Miscibility Pressures with an Equation of State Program," Proc. of the European Meeting on Improved Oil Recovery, Rome (April 16-18 1985) 61–66.

[45] Haniff, M.S. and Pearce, A.J.: "Measuring Interfacial Tensions in a Gas-Condensate System with a Laser-Light-Scattering Technique," *SPE Reservoir Engineering* (Nov 1990) 589–594.

[46] Helfferich, F.G.: "Theory of Multicomponent, Multiphase Displacement in Porous Media," *Soc. Pet. Eng. J.* (February 1981) **271**, 51–62.

[47] Helfferich, F.G.: "Generalized Welge Construction for Two-Phase Flow in Porous Media in System With Limited Miscibility," paper SPE 9730 presented at the 1982 SPE Annual Technical Conference and Exhibition, New Orleans, LA, September.

[48] Heller, J.P.: "Onset of Instability Patterns Between Miscible Fluids in Porous Medium," *J. Appl. Phys.* (1966) **37**, 1566–1579.

[49] Heller, J.P., Kovarik, F.S., and Taber, J.J.: "Improvement of CO_2 Flood Performance," No. DOE/MC/21136-17, U.S. Department of Energy, Bartlesville, OK (January 1989).

[50] Holm, L. and Josendal, V.: "Effect of Oil Composition on Miscible-Type Displacement by Carbon Dioxide," *Soc. Pet. Eng. J.* (February 1982) 87–98.

[51] Hutchinson, C.A. Jr. and Braun, P.H.: "Phase Relations of Miscible Displacement in Oil Recovery," *A.I.Ch.E. J.* (March 1961) 64–72.

[52] Jaquin, C., Legait, B., Martin, J.M., Nectoux, A., Anterion, F., and Rioche, M.: "Gravity Drainage in a Fissured Reservoir with Fluids Not in Equilibrium," (Oct 1987) 4th European Symposium on Enhanced Oil Recovery, Hamburg.

[53] Jensen, F. and Michelsen M.L.: "Calculation of First Contact and Multiple Contact Minimum Miscibility Pressures," *IN SITU* (January 1990) **14**, No. 1, 1–17.

[54] Jhaveri, B.S. and Youngren, G.K.: "Three-Parameter Modification of the Peng-Robinson Equation of State to Improve Volumetric Predictions," *Soc. Pet. Eng. Res. Eng.* (August 1988) 1033–1040.

[55] Johansen, T. and Winther, R.: "Mathematical and Numerical Analysis of a Hyperbolic System Modeling Solvent Flooding," (September 1990) Second European Conference on the Mathematics of Oil Recovery, France.

[56] Johns, R.T.: *Analytical Theory of Multicomponent Gas Drives With Two-Phase Mass Transfer*, PhD dissertation, Stanford University, Stanford, CA (1992).

[57] Johns, R.T., B. Dindoruk, and Orr, F.M. Jr.: "Analytical Theory of Combined Condensing/Vaporizing Gas Drives," paper SPE 24112 presented at the 1992 SPE/DOE Eighth Symposium on Enhanced Oil Recovery, Tulsa, OK, April.

[58] Johns, R.T., Fayers, F.J. and Orr, F.M., Jr.: "Effect of Gas Enrichment and Dispersion on Nearly Miscible Displacements in Condensing/Vaporizing Drives," paper SPE 24938 presented at the 1992 SPE Technical Conference and Exhibition, Washington, D.C.

[59] Katz, D. and Firoozabadi, A.: "Predicting Phase Behavior of Condensate/Crude-Oil Systems Using Methane Interaction Coefficients," *J. Pet. Tech.* (November 1978) 1649–55.

[60] Kesler, M.G and Lee, B.I.: "Improve prediction of enthalpy of fractions," *Hydrocarbon Processing* (March 1976) **55**, 153–158.

[61] Kinzelbach, Wolfgang: "The Random Walk Method in Pollutant Transport Simulation," *Groundwater Flow and Quality Modelling*, Custodio, E. et al. (ed.), D. Reidel Publishing Company (1987) 227–246.

[62] Kosal, E. and Holder, G.: "Solubility of Anthracene and Phenanthrene Mixtures in Supercritical Carbon Dioxide," *J. Chem. Eng. Data* (1987) **32**, No. 2, 148–150.

[63] Koval, E.J.: "A Method for Predicting the Performance of Unstable Miscible Displacements in Heterogeneous Media," *Soc. Pet. Eng. J.* (June 1963) 145–154.

[64] Kreft, A. and Zuber, A.: "On the Physical Meaning of the Dispersion Equation and its Solutions for Different Initial and Boundary Conditions," *Chem. Eng. Sci.* (1978) **33**, 1471–1480.

[65] Kudchadker, A., Kudchadker, S., and Wilhoit, R.: "Anthracene and Phenanthrene," Monograph No. 708, American Petroleum Institute (1979).

[66] Kudchadker, A., Kudchadker, S., and Wilhoit, R.: "Four-ring Condensed Aromatic Compounds," Monograph No. 709, American Petroleum Institute (1979).

[67] Kuo, S.S.: "Prediction of Miscibility for the Enriched-Gas Drive Process," paper SPE 14152 presented at the 1985 SPE Annual Technical Conference and Exhibition, Las Vegas, NV, September.

[68] L. L. Larson and M. K. Silva and M. A. Taylor and F. M. Orr Jr.: "Temperature Dependence of $L_1/L_2/V$ Behavior in CO_2/Hydrocarbon Systems," *SPE Reservoir Engineering* (February 1989) 105–114.

[69] Lake, W.L.: *Enhanced Oil Recovery*, first edition, Prentice Hall, Engelwood Cliffs, NJ 07632 (1989).

[70] Larson, R.G.: "The Influence of Phase Behavior on Surfactant Flooding," *Soc. Eng. Pet. Eng. J.* (December 1979) 411–422.

[71] Larson, R.G., and Hirasaki, G.J.: "Analysis of the Physical Mechanisms in Surfactant Flooding," *Soc. Eng. Pet. Eng. J.* (February 1978) 42–58.

[72] Lee, S-T, Lo, H. and Dharmawardhana, B.T.: "Analysis of Mass Transfer Mechanisms Occurring in Rich Gas Displacement Process," paper SPE 18062 presented at the 1988 SPE Annual Technical Conference and Exhibition, Houston, TX, October 2-5.

[73] Leij, F.J. and Dane, J.H.: "Analytical Solutions of the One-Dimensional Advection Equation and Two- or Three-Dimensional Dispersion Equation," *Water Resources Research* (1990) **26**, No. 7, 1475–1482.

[74] Lien, C.-L.: "Crude Oil Analysis by HP5880 Gas Chromatograph," No. 83–82, New Mexico Petroleum Recovery Research Center (1983).

[75] Lohrenz, J., Bray, B.C. and Clark, C.R.: "The Viscosity of Pure Substances in Dense Gaseous and Liquid Phases," *J. Pet. Tech.* (1964) 1171–1176.

[76] Luks, K.D., Turek, E.A. and Baker, L.E.: "Calculation of Minimum Miscibility Pressure," *Soc. Pet. Eng. Res. Eng.* (November 1987) 501–506.

[77] Magruder, J. B., Stiles, L. H., and Yelverton, T. D.: "Review of the Means San Andres Unit CO_2 Tertiary Project," *Journal of Petroleum Technology* (May 1990) 638–644.

[78] Mattax, C.C. and Kyte, J.R.: "Imbibition Oil Recovery from Fractured Water Drive Reservoirs," *Soc. Pet. Eng. J.* (1972) 177–184.

[79] McHugh, M. and Paulaitis, M.: "Solid Solubilities of Naphthalene and Biphenyl in Supercritical Carbon Dioxide," *J. Chem. Eng. Data* (1980) **25**, 326–329.

[80] Metcalfe, R.S. and Yarborough, L.: "The Effect of Phase Equilibria on the CO2 Displacement Mechanism," *Soc. Pet. Eng. J.* (August 1979) 242–252.

[81] Mishra, S.: *On the Use of Pressure and Tracer Test Data for Reservoir Description*, PhD dissertation, Stanford University, Stanford, CA (1987).

[82] Moisses, D.E., Miller, C.A., and Wheeler, M.F.: "Simulation of Miscible Viscous Fingering Using a Modified Method of Characteristics: Effects of Gravity and Heterogeneity," paper SPE 18440 presented at the 1989 Tenth Symposium on Reservoir Simulation, Houston, TX, February.

[83] Monroe, W.W., Silva, M.K., Larsen, L.L. and Orr, F.M. Jr.: "Composition Paths in Four-Component Systems: Effect of Dissolved Methane on 1D CO_2 Flood Performance," *Soc. Pet. Eng. Res. Eng.* (August 1990) 423–432.

[84] Morrow, N.R. and Songkran, B.: "Effect of Viscous and Buoyancy Forces on Nonwetting Phase Trapping in Porous Media," *Surface Phenomena in Enhanced Oil Recovery*, D. Shah (ed.), Plenum Press, New York City, NY (1982) 387–411.

[85] Morrow, N.R., Chatzis, I. and Taber, J.J.: "Entrapment and Mobilization of Residual Oil in Bead Packs," *Soc. Pet. Eng. Res. Eng.* (1988) **3**, 927–935.

[86] Moysan, J. M., Paradowski, H., and Vidal, J.: "Prediction of Phase Behaviour of Gas-Containing Systems with Cubic Equations of State," *Chemical Engineering Science* (1986) **41**, 2069–2074.

[87] Nectoux, A.: "Equilibrium Gas-Oil Drainage: Velocity, Gravitational and Compositional Effects," (October 27–29 1987).

[88] Newley, T.M.J. and Merrill R.C. Jr.: "Pseudocomponent Selection for Compositional Simulation," *Soc. Pet. Eng. Res. Eng.* (November 1991) **6**, No. 4, 490–496.

[89] Novosad, Z. and Costain, T.: "New Interpretation of Recovery Mechanisms in Enriched Gas Drives," *Canadian Pet. Tech. J.* (March-April 1988) **27**, No. 2, 54–60.

[90] Orr, F.M., Jr.: "Reservoir Characterization for the CO_2 Enhanced Oil Recovery Process—Final Report," No. DE-AC21-85MC22042, U.S. Department of Energy, Bartlesville, OK (1989).

[91] Orr, F.M., Jr.: "Scale-Up of Miscible Flood Processes," Annual Report No. U.S. DOE Grant No. DE-FG21-89MC26253, U.S. Department of Energy, Bartlesville, OK (January 1991).

[92] Orr, F.M., Jr.: "Scale-Up of Miscible Flood Processes," Annual Report No. U.S. DOE Grant No. DE-FG21-89MC26253, U.S. Department of Energy, Bartlesville, OK (December 1991).

[93] Orr, F.M., Jr. and Taber, J.J.: "Displacement of Oil by Carbon Dioxide," No. DOE/ET/12082-9, U.S. Department of Energy, Bartlesville, OK (May 1981).

[94] Orr, F.M., Jr., Johns, R.T. and Dindoruk, B.: "Miscibility in Four-Component Vaporizing Gas Drives," paper SPE 22637 presented at the 1991 SPE Annual Technical Conference and Exhibition, Dallas, TX, October 6–9.

[95] Orr Jr., F. M. and Jensen, C. M.: "Interpretation of Pressure-Composition Phase Diagrams for CO_2/Crude-Oil Systems," *Society of Petroleum Engineers Journal* (October 1984) 485–497, Erratum: (February 1985) 132.

[96] Orr, Jr., F. and Silva, M.: "Effect of Oil Composition on Minimum Miscibility Pressure - Part 2: Correlation," *Soc. Pet. Eng. Res. Eng. J.* (November 1987) 479–491.

[97] Pande, K.K.: *Interaction of Phase Behaviour with Nonuniform Flow*, PhD dissertation, Stanford University, Stanford, CA (December 1988).

[98] Pande, K.K. and Orr, F.M., Jr.: "Interaction of Phase Behavior, Reservoir Heterogeneity and and Crossflow in CO_2 Floods," paper SPE 19668 presented at the 1989 SPE Annual Technical Conference and Exhibition, San Antonio, TX, October 8–11.

[99] Pande, K.K. and Orr, F.M., Jr.: "Analytical Computation of Breakthrough Recovery for CO_2 Floods in Layered Reservoirs," paper SPE 20177 presented at the 1990 SPE Annual Technical Conference and Exhibition, Tulsa, TX, April 22–25.

[100] Pande, K.K. and Orr, F.M., Jr.: "Effects of Permeability Heterogeneity on Miscibility Development in Condensing Gas-Drive Processes," paper SPE 22635 presented at the 1991 SPE Annual Technical Conference and Exhibition, Dallas, TX, October 6–9.

[101] Pavone, D., Bruzzi, P. and Verre, R.: "Gravity Drainage at Low IFT," (October 1989) 5th European Symposium on Enhanced Oil Recovery, Budapest.

[102] Peneloux, A., Rauzy, E. and Freze, R.: "A Consistent Correction for Redlich-Kwong-Soave Volumes," *Fluid Phase Equilibria* (1982) **8**, 7–23.

[103] Peng, D.Y. and Robinson, D.B.: "A New Two-Constant Equation of State," *Ind. Eng. Chem. Fund.* (1976) **15**, 59–64.

[104] Perkins, T.K., Johnson, O.C., and Hoffman, R.N.: "Mechanics of Viscous Fingering in Miscible Systems," *Soc. Pet. Eng. J.* (December 1965) 301–317.

[105] Perrine, R.L.: "The Development of Stability Theory for Miscible Liquid-Liquid Displacement," *Soc. Pet. Eng. J.* (March 1961) 17–25.

[106] Perrine, R.L.: "A Unified Theory for Stable and Unstable Miscible Displacement," *Soc. Pet. Eng. J.* (March 1963) 28–40.

[107] Perry, R. and Chilton, C.: *Chemical Engineers Handbook*, McGraw-Hill, New York, 5th edition (1973).

[108] Peters, E.J., Broman, W.H. Jr., and Broman, J.A.: "A Stability Theory for Miscible Displacement," paper SPE 13167 presented at the 1984 SPE Annual Technical Conference and Exhibition, Houston, TX, September 16–19.

[109] Philp, R. and Gilbert, T.: "Application of Computerized Gas Chromatography-Mass Spectrometry to Oil Exploration in Australia," *Aust. Pet. Explor. Assoc. J.* (1980) No. 20, 221–228.

[110] Pozzi, A.L. and Blackwell, R.J.: "Design of Laboratory Models for Study of Miscible Displacement," *Soc. Pet. Eng. J.* (March 1963) **3**, 28–40.

[111] Pricket, T., Naymik, T.G. and Lonquist, C.G.: "A 'Random-Walk' Solute Transport Model for Selected Groundwater Quality Evaluations," Bulletin 65, Illinois State Water Survey, Champaign, Illinois (1981).

[112] Rathmell, J.J., Stalkup. F.I. and Hassinger, R.C.: "A Laboratory Investigation of Miscible Displacement by Carbon Dioxide," paper SPE 3483 presented at the 1971 SPE Annual Meeting, New Orleans, LA, October.

[113] Reid, R., Prausnitz, J., and Poling, B.: *The Properties of Gases and Liquids*, 4th edition, McGraw-Hill, New York (1987).

[114] Reid, R.C., Prausnitz, J.M. and Sherwood, T.K.: *The Properties of Gases and Liquids*, third edition, McGraw-Hill, New York, NY (1977).

[115] Rowlinson, J. S.: *Liquids and Liquid Mixtures*, 2nd edition, Plenum Press, New York (1969).

[116] Satherly, J. and Schiffrin, D.: "The Measurement of Low IFT Values for Enhanced Oil Recovery," (August 1986) Progress Report to U.K. DOE, Winfrith.

[117] Schechter, D.S., Zhou, D. and Orr, F.M., Jr.: "Capillary Imbibition and Gravity Segregation in Low IFT Systems," paper SPE 22594 presented at the 1991 SPE Annual Technical Conference and Exhibition, Dallas, TX, October 6–9.

[118] Schowalter, W.R.: "Stability Criteria for Miscible Displacement of Fluids From a Porous Medium," *AIChE. J.* (1965) **11**, 99–105.

[119] Scott, E.Z., Jr. and Read, D.L.: "A Study of Variables in Linear Miscible Displacements," paper SPE 1377-G presented at the 1959 Regional Fall Meeting of the Los Angeles Basin, San Joaquin Valley, and Coastal Sections of SPE of AIME, Pasadena, CA, October 22–23.

[120] Shang-keng, M.: *Modern Theory of Critical Phenomena*, Benjamin Cummings, Reading, Mass. (1976).

[121] Silva, M. K., Hutter, C. E., and Lien, C. L.: "Phase Compositions and Densities of Mixtures of CO_2 with Maljamar Separator Oil at 160°F and 1600 psia," No. 85-11, New Mexico Petroleum Recovery Research Center (1985).

[122] Sorbie, K.S., Feghi, F., Pickup, G.E., Ringrose, P.S., and Jensen J.L.: "Flow Regimes in Miscible Displacement in Heterogeneous Correlated Random Fields," paper SPE 24140 presented at the 1992 SPE/DOE Eighth Symposium on Enhanced Oil Recovery, Tulsa, OK, April.

[123] Stadler, M. P.: *Prediction of Carbon Dioxide/Hydrocarbon Phase Behavior Using Supercritical Fluid Chromatography*, PhD dissertation, Stanford University (1992).

[124] Stadler, M. P., Deo, M. D., and Orr, Jr., F. M.: "Crude Oil Characterization Using Gas Chromatography and Supercritical Fluid Chromatography," paper SPE 25191 presented at the 1993 SPE International Symposium on Oilfield Chemistry, New Orleans, March 2–5.

[125] Stadler, M. P., Stessman, A. N., and Orr Jr., F. M.: "Prediction of CO_2/Crude Oil Phase Behavior Using Supercritical Fluid Chromatography," paper SPE 24111 presented at the 1992 SPE/DOE Enhanced Oil Recovery Symposium, Tulsa, April 22–24.

[126] Stalkup, F.I.: "Using Phase Surfaces to Describe Condensing Gas Drive Experiments," *Soc. Pet. Eng. J.* (May 1965) 184–188.

[127] Stalkup, F.I.: "Miscible Displacement," Monograph 8, Soc. Pet. Eng. of AIME, New York (1983).

[128] Stalkup, F.I.: "Displacement Behavior of the Condensing/Vaporizing Gas Drive Process," paper SPE 16715 presented at the 1987 SPE Annual Technical Conference and Exhibition, Dallas, TX, September.

[129] Stalkup, F.I.: "Effect of Gas Enrichment and Numerical Dispersion on Compositional Simulator Predictions of Oil Recovery in Reservoir Condensing and Condensing/Vaporizing Gas Drives," paper SPE 18060 presented at the 1988 SPE Annual Technical Conference and Exhibition, Houston, TX, October.

[130] Stessman, A.N.: "Phase Behavior of Means Crude Oil and Carbon Dioxide," Master's thesis, Stanford University, Stanford, CA (1991).

[131] *Annual Book of ASTM Standards*, R. A. Storer (ed.), American Society for Testing and Materials, Philadelphia (1991) **05.02**, Ch. ASTM D 2887: Standard Test Method for Boiling Range Distribution of Petroleum Fractions by Gas Chromatography, 474–481.

[132] Tan, C.T. and Homsy, G.M.: "Stability of Miscible Displacements in Porous Media: Rectilinear Flow," *Phys. Fluids* (November 1986) **29**, No. 11, 3549–3561.

[133] Tan, C.T. and Homsy, G.M.: "Simulation of Nonlinear Viscous Fingering in Miscible Displacements," *Phys. Fluids* (June 1988) **31**, No. 6, 1330–1338.

[134] Tchelepi, H.: "Scaling of the Growth of Viscous Fingers in Linear Flow," Annual Report No. U.S. DOE Grant No. DE-FG21-89MC26253, U.S. Department of Energy, Bartlesville, OK (December 1991) Chap. 4.2 in "Scale-Up of Miscible Flood Processes".

[135] Tiffin, D.L., Sebastian, H.M., and Bergman, D.F.: "Displacement Mechanism and Water Shielding Phenomena for a Rich-Gas/Crude-Oil System," *Soc. Pet. Eng. Res. Eng.* (May 1991) 193–199.

[136] Todd, M.R. and Longstaff, W.J.: "The Development, Testing and Application of a Numerical Simulator for Predicting Miscible Flood Performance," *Trans., AIME, 253* (1972) 874–882.

[137] Tompson, A.F.B. and Dougherty, D.E.: "On the Use of of Particle Tracking Methods for Solute Transport in Porous Media," *Computational Methods in Water Resources, vol 2., Numerical Methods for Transport and Hydrologic Processes*, Celia, M., Ferrand, L., Brebbia, C. Gray, W., and Pinder, G. (ed.), Elsevier (1988).

[138] Tsai, F.-N. and Yau, J.-S.: "Solubility of Carbon Dioxide in n-Tetracosane and in n-Dotriacontane," *J. Chem. Eng. Data* (1990) **35**, 43–45.

[139] Twu, C.H.: "An Internally Consistent Correlation for Predicting the Critical Properties and Molecular Weights of Petroleum and Coal-Tar Liquids," *Fluid Phase Equilibria* (1984) **16**, 137–150.

[140] Uffink, G.: "A Random Walk Model for the Simulation of Macrodispersion in a Stratified Aquifer," IUGG 18th General Assembly, Hamburg, Proceedings of the IAHS Symposia, Vol HS2. (1983).

[141] Uffink, G.: "Modeling of Solute transport with the Random Walk Model," *Groundwater Flow and Quality Modeling*, Custodio, E. et al. (ed.), D. Reidel Publishing Company, Dordrecht, The Netherlands (1987).

[142] Van Deemeter, J.J. and Zuiderweg, F.J. and Kinkenberg, A.: "Longitudinal Diffusion and Resistance to Mass Transfer as Causes of Nonideality in Chromatography," *Chem. Eng. Sci.* (1956) **5**, 271–289.

[143] Van Ness, H.C. and Abbott, M.M.: *Classical Thermodynamics of Nonelectrolyte Solutions With Applications to Phase Equilibrium*, McGraw-Hill, San Francisco (1982).

[144] Wachmann, C: "The Mathematical Theory for the Displacement of Oil and Water by Alcohol," *Society of Petroleum Engineers Journal* (September 1964) **231**, 250–266.

[145] Waggoner, J.R., Castillo, J.L., and Lake, L.W.: "Simulation of EOR Processes in Stochastically Generated Permeable Media," *Soc. Pet. Eng. Formation Eval.* (June 1992) 173–180.

[146] Walsh, B.W. and Orr, F.M. Jr.: "Prediction of Miscible Flood Performance: The Effect Of Dispersion on Composition Paths in Ternary Systems.," *IN SITU* (1990) **14**, No. 1, 19–47.

[147] Welge, H.J., Johnson, E.F., Hicks, A.L., and Brinkman, F.H.: "An Analysis for Predicting the Performance of Cone-Shaped Reservoirs Receiving Gas or Water Injection," *J. Pet. Tech.* (August 1962) 894–898.

[148] Whitson, C.: "Effect of Physical Properties Estimation on Equation-of-State Predictions," paper SPE 11200 presented at the 1982 57th Annual SPE Fall Technical Conference and Exhibition, New Orleans.

[149] Whitson, C. and Michelsen, M.: "The Negative Flash: Part II, Fluid Properties and Phase Equilibria for Chemical Process Design," *Fluid Phase Equilibria* (1989) **53**, 51–71.

[150] Wilson, G., Johnston, R., Hwang, S., and Tsonopoulos, C.: "Volatility of Coal Liquids at High Temperatures and Pressures," *Ind. Eng. Chem. Proc. Des. Dev.* (1981) No. 20, 94–104.

[151] Wooding, R.A.: "The Stability of an Interface Between Miscible Fluids in a Porous Medium," *Z. Agnew. Math. Phys.* (1962) **13**, 255–266.

[152] Worman, J. and Green, L.: "Simulated Distillation of High Boiling Petroleum Fractions," *Anal. Chem.* (1965) **37**, 1620–1621.

[153] Yonker, C.R., Gale, R.W. and Smith, R.D.: "Effects of Pressure on Retention in Supercritical Fluid Chromatography," *J. Phys. Chem.* (1987) **91**, 3333–3336.

[154] Yortsos, Y.C. and Zeybek M.: "Dispersion Driven Instability in Miscible Displacement in Porous Media," *Phys. Fluids* (1988) **31**, 3511–3518.

[155] Zapata, V.J. and Lake, L.W.: "A Theoretical Analysis of Viscous Crossflow," paper SPE 10111 presented at the 1981 SPE Annual Technical Conference and Exhibition, San Antonio, TX, October 5–7.

[156] Zauderer, E.: *Partial Differential Equations of Applied Mathematics*, second edition, Wiley-Interscience, New York, NY (1989).

[157] Zick, A.A.: "A Combined Condensing/Vaporizing Mechanism in the Displacement of Oil by Enriched Gas," paper SPE 15493 presented at the 1986 SPE Annual Technical Conference and Exhibition, New Orleans, LA, October.

[158] Zimmerman, W.B. and Homsy, G.M.: "Nonlinear Viscous Fingering in Miscible Displacements with Anisotropic Dispersion," *Phys. Fluids A* (1991) **3**, No. 8, 1859–1872.

[159] Zimmerman, W.B. and Homsy, G.M.: submitted to Phys. Fluids A (1992).